

# MATERIALI IN TEHNOLOGIJE

M A T E R I A L S   A N D   T E C H N O L O G Y

5

MATER.  
TEHNOLOG.  
LETNIK  
VOLUME  
51  
ŠTEV.  
NO.  
5  
STR.  
P.  
707-879  
LJUBLJANA  
SLOVENIJA  
SEP.-OCT.  
2017

70  
50  
25

70 LET INŠTITUTA ZA KOVINSKE  
MATERIALE IN TEHNOLOGIJE  
50 LET REVIJE  
MATERIALI IN TEHNOLOGIJE  
25 LET KONFERENCE O MATERIALIH  
IN TEHNOLOGIJAH ICM&T

ISSN: 1580-2949

UDK: 669+666+678+53

# MATERIALI IN TEHNOLOGIJE

5

MATER.  
TEHNOLOGIJE

LETNIK  
VOLUME  
51

ŠTEV.  
NO.  
5

STR.  
P.  
707-879

LJUBLJANA  
SLOVENIJA

SEP.-OCT.  
2017

**MATERIALI IN TEHNOLOGIJE / MATERIALS AND TECHNOLOGY** so znanstvena serijska publikacija, ki objavlja izvirne in tudi pregledne znanstvene članke ter tehnične novice, ki obravnavajo teoretična in praktična vprašanja naravoslovnih ved in tehnologije na področjih kovinskih in anorganskih materialov, polimerov, vakuumске tehnike in v zadnjem času tudi nano-materialov.

*The journal MATERIALI IN TEHNOLOGIJE / MATERIALS AND TECHNOLOGY is a scientific journal, devoted to original scientific papers, reviewed scientific papers and technical news concerned with the areas of fundamental and applied science and technology. Topics of particular interest include metallic materials, inorganic materials, polymers, vacuum technique and lately nanomaterials.*

© MATERIALI IN TEHNOLOGIJE

**Izdajatelj (Published for):**

Inštitut za kovinske materiale in tehnologije Ljubljana (IMT)

**Soizdajatelji (Associated Publishers):**

IMPOL Slovenska Bistrica, METAL Ravne, TALUM Kidričevo

Izdajanje **MATERIALI IN TEHNOLOGIJE** sofinancira: Javna agencija za raziskovalno dejavnost Republike Slovenije (ARRS) (Journal **MATERIALS AND TECHNOLOGY** is financially supported by Slovenian Research Agency (ARRS))

**Glavni in odgovorni urednik (Editor-in-Chief):** Paul John McGuinness

**Pomočnik glavnega urednika (Associate Editor-in-Chief):** Matjaž Godec

**Častna glavna urednika (Honorary Editors-in-Chief):** Franc Vodopivec, Matjaž Torkar

**Souredniki (Co-Editors):**

Igor Belič (IMT), Jaka Burja (IMT), Aleksandra Kocijan (IMT), Djordje Mandrino (IMT), Boštjan Markoli (NTF), Irena Paulin (IMT), Danijela A. Skobir Balantič (IMT), Darja Steiner Petrovič (IMT), Bojan Podgornik (IMT), Srečo Škapin (IJS), Rok Zaplotnik (IJS), Ema Žagar (KI)

**Tehnični urednik (Technical Editor):** Erika Nared (IMT)

**Lektorji (Linguistic Advisers):** Erika Nared (IMT) (slovenski jezik), Paul John McGuinness (IMT) (angleški jezik)

**Mednarodni pridruženi člani uredniškega odbora (International Advisory Board):**

Leonid B. Getsov, NPO CKT, St. Petersburg, Russia • Božo Smoljan, University of Rijeka, Croatia • David Nolan, Bluescope Steel Ltd. & University of Wollongong, Wollongong, Australia • Karlo T. Raič, University of Belgrade, Faculty of Technology and Metallurgy, Belgrade, Serbia • Nicola Gargiulo, Engineering University of Naples, Naples, Italy • Francesco Colangelo, Parthenope University of Naples, Naples, Italy • Peter Jurči, Faculty of Materials Science and Technology, STU, Trnava, Slovakia • Smilja Marković, Institute of Technical Sciences of the Serbian Academy of Sciences and Arts, Belgrade, Serbia • Stefan Zaefferer, Max-Planck Institute for Steel Research, Dusseldorf, Germany • Urban Wiklund, Uppsala University of Sweden, Sweden • Zdenka Zovko Brodarac, University of Zagreb, Metallurgical Faculty, Sisak, Croatia • Bojana Dolinar, Faculty of Civil Engineering, Transportation Engineering and Architecture, University of Maribor, Slovenia • Ivan Nazarenko, Kyiv National University of Construction and Architecture, Ukraine

**Uredniški odbor (Editorial Board):**

Igor Belič (IMT), Jaka Burja (IMT), Monika Jenko, Varužan Kevorkijan (IMPOL), Aleksandra Kocijan (IMT), Andraž Legat (ZAG), Vojteh Leskovšek (IMT), Matjaž Godec (IMT), Paul McGuinness (IMT), Djordje Mandrino (IMT), Boštjan Markoli (NTF), Jožef Medved (NTF), Peter Panjan (IJS), Irena Paulin (IMT), Danijela A. Skobir Balantič (IMT), Darja Steiner Petrovič (IMT), Tatjana Večko Pirtovšek (METAL Ravne), Bojan Podgornik (IMT), Božidar Šarler (IMT), Janez Šetina (IMT), Avgust Šibila (TALUM), Srečo Škapin (IJS), Borivoj Šuštaršič, Rok Zaplotnik (IJS), Ema Žagar (KI)

**Izdajateljski svet (Editorial Advisory Board):**

Matjaž Godec (Inštitut za kovinske materiale in tehnologije), Edvard Slaček (IMPOL), Marko Drobnič (TALUM), Andrej Gradišnik (METAL Ravne)

**Članki revije Materiali in tehnologije so indeksirani v/Articles published in Materials and Technology are indexed in: SCIENCE CITATION INDEX EXPANDED, MATERIALS SCIENCE CITATION INDEX® AND JOURNAL CITATION REPORTS/ SCIENCE EDITION.**

**Po bazi podatkov JCR16 ima Materiali in Tehnologije dejavnik vpliva 0,436. / In JCR16 Database Mater. Tehnol. has an impact factor of 0.436.**

**Članki objavljeni v periodični publikaciji MATERIALI IN TEHNOLOGIJE so indeksirani v mednarodnih sekundarnih virih: (Articles published in journal are indexed in international secondary periodicals and databases):**

- DOAJ (Directory of Open Access Journals)
- Google Scholar
- SCIRUS
- CA SEARCH® – Chemical Abstracts®
- METADEX®
- TEME – Technology and management
- Inside Conferences
- Engineered Materials Abstracts®
- Aluminium Industry Abstracts
- SCOPUS
- Civil Engineering Abstracts
- Ceramic Abstracts/World Ceramic Abstracts
- Corrosion Abstracts
- Mechanical & Transportation Engineering Abstracts
- CSA Aerospace & High Technology Database
- Solid State and Superconductivity Abstracts
- Materials Business File
- Referativnyj žurnal: Metallurgija
- COBIB

**Izhajanje:** 6 števk letno / **Published:** 6 issues per year

**Naročnina / Subscription:** 42 EUR – tujina / abroad: 85 EUR

**Naslov uredništva (Editorial Address):**

MATERIALI IN TEHNOLOGIJE

IMT Ljubljana

Lepi pot 11

1000 Ljubljana, Slovenija

Telefon: +386 1 470 18 60

Telefax: +386 1 470 19 39

Podračun pri UJP št. 01100-6030344339

**Na INTERNET-u je revija MATERIALI IN TEHNOLOGIJE dosegljiva na naslovu (ELECTRONIC ACCESS):**  
<http://mit.imt.si>

**Elektronska pošta (E-mail):** [mit@imt.si](mailto:mit@imt.si)

**Oblikovanje ovitka (Design):** Ignac Kofol

**Oblikovanje plakata na naslovnici (Poster on the Cover):** Ajda Schmidt

**Računalniški prelom in tisk (Prepress and Printed by):**

NONPAREL grafične storitve d.o.o., Medvode

**Naklada (Circulation):** 400 izvodov/issues

ISSN: 1580-2949  
UDK: 669+666+678+53



MATER. TEHNOLOG.	LETNIK VOLUME	51	ŠTEV. NO.	5	STR. P.	707–879	LJUBLJANA SLOVENIJA	SEP.–OKT. SEP.–OCT.	2017
---------------------	------------------	----	--------------	---	------------	---------	------------------------	------------------------	------

## VSEBINA – CONTENTS

## PREGLEDNI ČLANEK – REVIEW ARTICLE

**Additive manufacturing: the future of manufacturing**

Dodajalna (3D) tehnologija: prihodnost proizvodnje

S. A. Adekanye, R. M. Mahmood, E. T. Akinlabi, M. G. Owolabi ..... 709

**Pomembna obletnica revije Materiali in tehnologije: petdeset let izhajanja znanstvene periodične publikacije**

An important anniversary of the Materials and Technology journal: fifty years of publication

E. Nared ..... 717

## IZVIRNI ZNANSTVENI ČLANKI – ORIGINAL SCIENTIFIC ARTICLES

**Investigation of grain boundaries in Alloy 263 after special heat treatment**

Preiskava mej zrn v zlitini 263 po posebni toplotni obdelavi

I. Slatkovský, M. Dománková, M. Sahul ..... 721

**Fracture toughness of ledeburitic Vanadis 6 steel after sub-zero treatment for 17 h and double tempering**

Lomna žilavost ledeburitnega jekla Vanadis 6 po toplotni obdelavi s 17-urnim podhlajevanjem in dvojnim popuščanjem

J. Ptačinová, P. Jurčí, I. Dlouhý ..... 729

**Electronic and optical properties of the spinel oxides  $Mg_xZn_{1-x}Al_2O_4$  by first-principles calculations**Elektronske in optične lastnosti spinelnih oksidov  $Mg_xZn_{1-x}Al_2O_4$ , izpeljane iz teoretičnih osnov

C. Xiang, J. X. Zhang, Y. Lu, D. Tian, C. Peng ..... 735

**Surface characteristics of Invar alloy according to micro-pulse electrochemical machining**

Karakteristike površine Invar zlitine glede na mikropulzno elektrokemično obdelavo

S.-H. Kim, S.-G. Choi, W.-K. Choi, E.-S. Lee ..... 743

**Durability of materials based on a polymer-silicate matrix and a lightweight aggregate exposed to aggressive influences combined with high temperatures**

Vzdržljivost materialov na osnovi iz polimer-silikatnih matric in lahkega dodatka, izpostavljenih agresivnim vplivom v kombinaciji z visokimi temperaturami

T. Melichar, J. Bydžovský, Á. Dufka ..... 751

**Influence of thermomechanical treatment on the grain-growth behaviour of new Fe-Al based alloys with fine  $Al_2O_3$  precipitates**Vpliv termomehanske obdelave FeAl zlitin s finimi  $Al_2O_3$  izločki na rast zrn

B. Mašek, O. Khalaj, H. Jirková, J. Svoboda, D. Bublíková ..... 759

**Analysis of precipitates in aluminium alloys with the use of high-resolution electron microscopy and computer simulation**

Raziskave oborin v aluminijevih zlitinah z visokoresolucijsko elektronsko mikroskopijo in računalniško simulacijo

K. Matus, A. Tomiczek, K. Gołombek, M. Pawlyta ..... 769

**Microstructural evaluation of Ni-SDC cermet from a representative 2D image and/or a 3D reconstruction based on a stack of images**

Vrednotenje mikrostruktur Ni-SDC kermeta z 2D in/ali 3D metodo

G. Kapun, M. Marinšek, F. Merzel, S. Šturm, M. Gaberšček, T. Skalar ..... 775

**A facile method to prepare super-hydrophobic surfaces on silicone rubbers**

Preprosta metoda za pripravo superhidrofobnih površin pri silikonskih gumah

H. Y. Jin, Y. F. Li, S. C. Nie, P. Z., N. K. Gao, W. Li ..... 783

**Investigation of the static icing property for super-hydrophobic coatings on aluminium**

Preiskava lastnosti statične zaledenitve pri superhidrofobnih prevlekah na aluminiju

H. Y. Jin, S. C. Nie, Y. F. Li, T. F. Xu, P. Zhang, W. Li ..... 789

**Effect of ball milling on the properties of the porous Ti–26Nb alloy for biomedical applications**

Vpliv krogljčnega mletja na lastnosti porozne zlitine Ti–26Nb za biomedicinske aplikacije

G. Dercz, I. Matula ..... 795

**Effects of an addition of coir-pith particles on the mechanical properties and erosive-wear behavior of a wood-dust-particle-reinforced phenol formaldehyde composite**

Vplivi dodatka kokosovih vlaken fenol-formaldehidnemu kompozitu, ojačanjem z lesnim prahom, na njegove mehanske lastnosti in erozijsko obrabo

A. S. Jose, A. Athijayamani, K. Ramanathan, S. Sidhardhan ..... 805

**Optimum bushing length in thermal drilling of galvanized steel using artificial neural network coupled with genetic algorithm**

Optimalna dolžina podpore (šablone, vodila) pri termičnem vrtanju galvaniziranega jekla z uporabo umetne nevronske mreže in genetskega algoritma

N. Rajesh J. Hynes, R. Kumar, J. A. J. Sujana . . . . . 813

**Gelling polysaccharide as the electrolyte matrix in a dye-sensitized solar cell**

Želirni polisaharid kot elektrolitna osnova v solarnih celicah, občutljivih na barvila

J. P. Bantang, D. Camacho . . . . . 823

**Development of a heat treatment for increasing the mechanical properties and stress corrosion resistance of 7000 Al alloys**

Razvoj toplotne obdelave za izboljšanje mehanskih lastnosti in napetostno korozijsko odpornost 7000 Al zlitin

M. Shakouri, M. Esmailian, S. Shabestari . . . . . 831

**Corrosion resistance of as-plated and heat-treated electroless duplex Ni-P/Ni-B-W coatings**

Korozijska odpornost platiranih in neelektrično topolotno obdelanih dupleks Ni-P/Ni-B-W prevlek

B. Yüksel, G. Erdogan, F. E. Bastan, R. A. Yıldır . . . . . 837

**Short-term creep of P91 heat-resistant steels at low stresses and an instantaneous-stress-change testing**

Kratkotrajno lezenje toplotno odpornega jekla P91 pri nizkih napetostih in nenadni menjavi napetosti obremenjevanja

J. Zhe, S. Junjie, Z. Pengshuo . . . . . 843

**Effect of severe plastic and heavy cold deformation on the structural and mechanical properties of commercially pure titanium**

Učinek plastičnosti in deformacije pri podhlajevanju na strukturne in mehanske lastnosti čistega komercialnega titana

J. Palán, P. Šutta, T. Kubina, M. Dománková . . . . . 849

**Effect of yttrium and zirconium microalloying on the structure and properties of weld joints of a two-phase titanium alloy**

Učinek mikrolegiranja itrija in cirkonija na strukturo in lastnosti na spoje zavrov dvofazne zlitine titana

A. Illarionov, A. Popov, S. Illarionova, D. Gadeev . . . . . 855

**Microstructure evolution and statistical analysis of Al/Cu friction-stir spot welds**

Razvoj mikrostrukture in statistična analiza vrtilno-tornih točkastih zvarov Al/Cu

M. P. Mubiyi, E. T. Akinlabi, M. E. Makhatha . . . . . 861

**Synthesis of PMMA/ZnO nanoparticles composite used for resin teeth**

Sinteza PMMA/ZnO nanodelcev kompozitov za izdelavo zob iz umetnih smol

D. Popović, R. Bobovnik, S. Bolka, M. Vukadinović, V. Lazić, R. Rudolf . . . . . 871

ERRATUM . . . . . 879

ADDITIVE MANUFACTURING: THE FUTURE OF  
MANUFACTURING

## DODAJALNA (3D) TEHNOLOGIJA: PRIHODNOST PROIZVAJANJA

**Sheriff Adefemi Adekanye<sup>1</sup>, Rasheedat Modupe Mahamood<sup>1,2</sup>,  
Esther Titilayo Akinlabi<sup>2</sup>, Moses Gbadebo Owolabi<sup>3</sup>**<sup>1</sup>University of Ilorin, Department of Mechanical Engineering, Nigeria<sup>2</sup>University of Johannesburg, Department of Mechanical Engineering Science, South Africa<sup>3</sup>Howard University, Department of Mechanical Engineering, Washington, USA  
adekanyefm@gmail.com*Prejem rokopisa – received: 2016-08-26; sprejem za objavo – accepted for publication: 2017-03-16*

doi:10.17222/mit.2016.261

Additive manufacturing is an advanced manufacturing method used to fabricate prototypes, tooling as well as functional products. Additive manufacturing helps us produce complex parts as single-unit objects, which was not possible with the traditional manufacturing methods. There are different types of additive-manufacturing technologies, including selective laser melting, laser-metal-deposition process, fused deposition modeling and electron-beam melting. All these additive-manufacturing technologies produce three-dimensional (3D) objects by adding materials layer after layer. A 3D object is built directly from a 3D computer-aided-design (CAD) model of the object. Additive manufacturing is a very promising method for the aerospace industry, in particular because of its ability to reduce the buy-to-fly ratio. This technology is the technology of the future because it is going to change the way products are designed and manufactured. In this research, various additive-manufacturing technologies are described in detail and some of the research works in this field are also presented. The future research directions are also highlighted.

**Keywords:** additive manufacturing, fused deposition modelling, laser metal deposition, selective laser melting, selective laser sintering

Dodajalni proizvodni proces je napredna tehnologija, ki se uporablja za izdelavo prototipov, orodij in funkcionalnih izdelkov. Z naprednim proizvodnim procesom lahko izdelamo izdelke ali dele kompliciranih oblik, ki jih ni možno izdelati s tradicionalnimi metodami proizvodnje. Obstajajo različne vrste naprednih dodajalnih tehnologij, kot so na primer: selektivno lasersko nataljevanje, proces laserskega nanašanja (depozicije) kovin, modeliranje z nanašanjem staljenih kapljic in taljenje z elektronskim curkom. Vse te napredne dodajalne tehnologije omogočajo izdelavo tridimenzionalnih (3D) izdelkov z dodajanjem materialov plast za plastjo. Tridimenzionalni produkt je izgrajen neposredno s pomočjo 3D-računalniško podprtega modeliranja (angl. CAD). Napredna dodajalna proizvodnja je zelo obetavna proizvodna metoda, predvsem v letalski in vesoljski industriji, še posebej zaradi sposobnosti zmanjševanja stroškov izdelave (zmanjšanje razmerja med maso materiala, potrebnega za izdelavo določenega izdelka in njegovo dejansko maso).

**Ključne besede:** dodajalna proizvodnja, modeliranje z nanašanjem staljenih materialov, laserska depozicija kovin, selektivno lasersko nataljevanje, selektivno lasersko sintranje

**1 INTRODUCTION**

The additive-manufacturing process is an advanced manufacturing process that produces three-dimensional (3D) objects directly from the 3D computer-aided-design (CAD) digital information of the parts by adding materials layer by layer.<sup>1-3</sup> This is different from the traditional manufacturing that involves material removal or an energy-intensive process such as machining, casting and forging. With additive manufacturing, a complex-shaped product can be produced as a single object, which was not possible in the past.

For the traditional manufacturing process, complex parts have to be designed based on the ease of manufacturing the parts. Complex parts are usually broken down into smaller parts because of the ease of manufacturing those parts and the pieces are assembled at the later stage through various joining processes. This practice does not only involve labor-intensive processes but also results in wastage of materials, in addition to the materials re-

moved during shaping and cutting operations; the excess materials added for joining also contribute to material wastage. The net weight of a product is also very large because of the excess materials used during the assembly. The additive-manufacturing technology, on the other hand, can make a product directly from the 3D CAD model of the product by just adding materials layer by layer. Irrespective of the complexity, any part that can be drawn using any computer-aided-design software can be made and as a single-unit object. Additive-manufacturing technologies are classified into seven main groups, namely: powder-bed fusion, directed energy deposition, sheet lamination, material extrusion, binder jetting, material jetting and vat photopolymerization.<sup>1</sup> A designer does not need to worry about the manufacturability of a product; he/she is only concerned with the functionality of the part being designed.

At the inception, the additive manufacturing process was used to make prototypes because of the limitation in

the choice of the materials that could be used on an additive-manufacturing machine at that time.<sup>2–4</sup> There are a number of industries benefiting from this revolutionary manufacturing technology,<sup>5</sup> such as the aerospace, automobile and biomedical industries.<sup>6–9</sup> In this study, some of these additive-manufacturing technologies are reviewed with the aim of throwing light on these technologies and describing their systems of operation as well as their advantages, limitations and areas of applications.

The rest of the paper is organized as follows: section 2 of the paper presents the powder-bed-based process. The extrusion-based process and sheet-lamination process are presented in sections 3 and 4, respectively. Directed-energy-deposition process is presented in section 5. Material development in additive manufacturing is presented in section 6, while conclusions are presented in section 7.

## 2 POWDER-BED-BASED PROCESS

This class of additive manufacturing technology uses the energy from an electron beam or laser beam to fuse or melt powder materials for the manufacturing of parts.<sup>10,11</sup> The additive-manufacturing technologies in this class include direct metal laser sintering (DMLS), electron-beam melting (EBM), selective heat sintering (SHS), selective laser melting (SLM) and selective laser sintering (SLS). Each of these technologies is described in this section.

### 2.1 Direct metal laser sintering (DMLS)

A schematic diagram of direct laser sintering is shown in **Figure 1** below. This process manufactures parts by compacting a metal powdered material with a power source such as laser, without melting but by binding the material together to create a solid structure defined by the 3D CAD model of the part.<sup>12</sup> The working principle of this technology makes it capable of designing and producing complex geometry of both internal and external intricacies. In this process, to avoid the collision of the recoater blade when moving, the building and dispenser platforms are lowered by the layer thickness. The powder metal needed to create a layer of the material is supplied by the dispenser platform after it

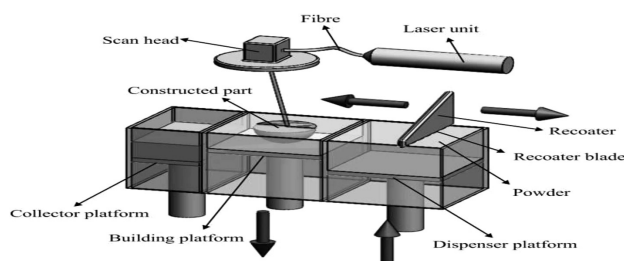


**Figure 1:** Schematic diagram of the direct metal laser sintering system<sup>14</sup>

has been ensured that the recoater stands in the right position. The spreading of the metal powder from the dispenser to the building platform is done by the recoater, moving from the right to the left position, and the excess metal powder falls into the excess-powder collector. The scan head moves the laser beam through the two-dimensional (2D) cross-section, which is switched on and off during the exposure of designated areas. The powdered metals are generated, cured and sintered by the solidified areas through the absorption of energy.<sup>13</sup> This process continues to create layer after layer until the part is completed. Using this process, parts have been successfully made from the materials such as aluminium alloys – AlSi10Mg, stainless steel, titanium alloys and cobalt chrome superalloy.<sup>13</sup> Some of the advantages of this additive-manufacturing process are highlighted below.<sup>12,13</sup>

High speed: parts are produced easily within hours since special tools are not required.

Complex geometry: this technology allows designs of both internal and external features.

High quality: it creates parts with high accuracy and detailed resolution.

It provides parts with better mechanical strength.

In spite of all these advantages, some of the limiting factors are as follows: the process is expensive and power intensive, the surface needs to be polished and the metal support structure removed, and the thermal post-processing is time consuming.<sup>14,15</sup>

### 2.2 Electron-beam melting

**Figure 2** shows a schematic presentation of an electron-beam process. Parts are developed by adding material layer by layer, following the path described by the 3D CAD data program.<sup>16</sup> Electron beam is generated within an electron-beam gun; the tungsten filament is heated to an extremely high temperature so that it releases electrons; the electrons are accelerated with an electric field and then focused with electromagnetic coils.<sup>17,18</sup> The electron beam melts each layer of the

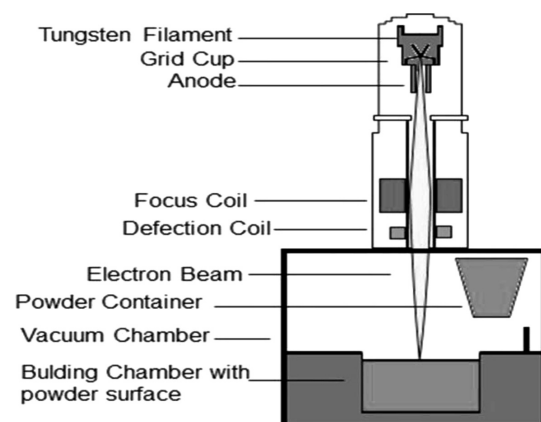


**Figure 2:** Schematic drawing of an electron-beam additive-manufacturing machine<sup>18</sup>



metal powder to the desired geometry in a vacuum; the process in the vacuum eliminates impurities and yields high-strength properties of the material under processing.<sup>16</sup> The materials used for electron-beam melting are mainly steel and titanium alloy. The following advantages are characteristic of this technology:<sup>17</sup>

- an increased efficiency of the raw-material use,
- the vacuum eliminates impurities and provides a good thermal environment for a freeform fabrication,
- it significantly reduces the amount of finishing operations,
- freedom in design – design for functionality,
- processing of high-melting-point and highly reactive materials,
- decreased lead times for design and fabrication,
- a high degree of component customization.

Some of the disadvantages of the electron-beam technology include the following:<sup>19</sup>

- It requires a vacuum, another system to the machine, which must be maintained, leading to a high cost.
- It produces X-rays while in operation, which is hazardous.

### 2.3 Selective laser sintering

Selective laser sintering is also a powder-bed-based technology that involves the spreading of powder and the subsequent compaction. A schematic diagram of the selective laser sintering is shown in **Figure 3**. The set-up is made up of a laser, an automatic powder-layering apparatus, and a computer system for process control.<sup>20</sup>

Selective laser sintering uses a substrate for the part fabrication, which is fixed onto the building platform and leveled. The sealed building chamber containing oxygen has a reduced amount of oxygen due to the protective inert gas such as argon, which is fed into the chamber. A thin layer of a loose powder is deposited on the substrate by the layering mechanism. The laser beam scans the powder-bed surface through the CAD program forming layers of the material to be produced. The powder spreading and laser-treatment process are repeated and

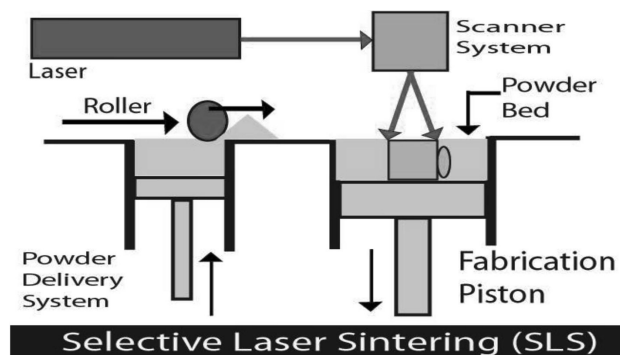


**Figure 3:** Schematic presentation of a selective-laser-sintering apparatus<sup>21</sup>

the parts are built layer by layer until completion.<sup>21–23</sup> This technology allows a variety of materials, the most common are: wax, paraffin, polymer-metal powders or various types of steel alloys, polymers, nylon and carbonates.<sup>24</sup> The advantages of using selective laser sintering include:

- parts can be created out of a wide selection of materials,
- complex geometry is made easy as long as the non-sintered powder can be removed easily,
- when printing overhanging, unsupported structures, supports are not needed because the unused powder provides the necessary support.

Disadvantages of selective laser sintering are:

- the equipment is very expensive,
- the most common problem of this technology is that the fabricated parts are porous and the surface could be rough, depending on the materials used,
- thermal distortion occurs on polymer parts and can cause shrinking and warping of the fabricated parts.

### 2.4 Selective heat sintering

**Figure 4** shows a schematic presentation of the selective-heat-sintering process, which operates by selectively fusing a thin layer of polymer powder through a thermal print-head assembly. This assembly operates bi-directionally and incorporates thermal print heads at point A as shown in the diagram. The part labelled as B is the powder-deposition mechanism, C is the layer heater, D is the chamber for the material built up in an internal build volume, E is the floor that is a vertically movable building platform; at F, fresh powder is supplied via scoops to the powder-deposition mechanism from the powder containers.<sup>25</sup> The heated building platform builds up the parts, using the layer technology, with the roller spreading across the plastic powders in layers. The thermal print head of the apparatus forms a part in its full cross-section with the already laid powder. The heat at the building platform sinters the top layer of the powder; once completed, the process is repeated until a complete 3D object is produced. The complex geometries pro-

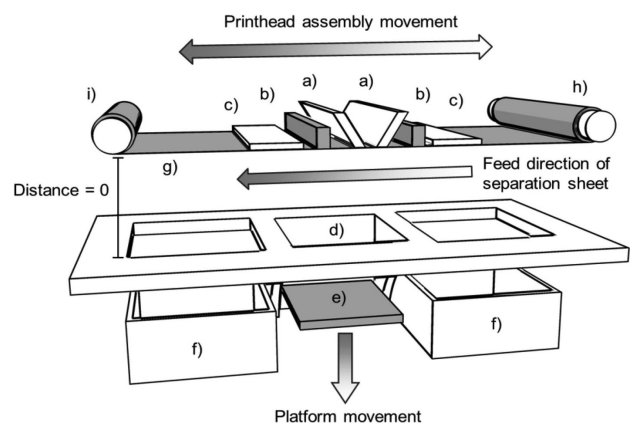


**Figure 4:** Schematic presentation of selective heat sintering<sup>25</sup>

duced are supported by the excess material surrounding the object.<sup>26</sup>

This technology uses thermoplastic powder as its working material. The benefits of this technology are as follows: it allows inexpensive manufacturing and a good concept evaluation; the thermal print heads are less expensive and the overall cost is affordable.

### 2.5 Selective laser melting

Selective laser melting is similar to the selective-laser-sintering process, with the main difference being between full melting and fusing in selective laser sintering. The process begins with designing a 3D CAD model; the model is broken down into parts to form a number of finite layers. For each layer, the laser scan path is calculated, defining both the boundary contour and the form of the fill sequence called the raster pattern. Layers are formed by spreading powder on the build platform and then the laser melts the powder with the scanning laser beam; the melted powder solidifies to form a 3D solid component.<sup>27</sup> A schematic diagram of the process is shown in **Figure 5**.<sup>28</sup>

Different materials used with this technology include steel, titanium, aluminium, cobalt-chromium and nickel alloys. The benefits of using the selective-laser-melting technology are as follows:

- it minimizes material wastage and saves costs,
- improved production-development cycle,
- it allows for complex geometry to be made,
- ideal process for a low-volume production,
- improved buy-to-fly ratio,
- functionally graded parts can be produced,
- it allows for fully customized parts that suit individuals.

The disadvantages of selective laser melting are as follows:

- it is an expensive and a very slow process,
- tolerances and surface finishes are limited because of the sticking of the unused powder on the surface of the produced part.

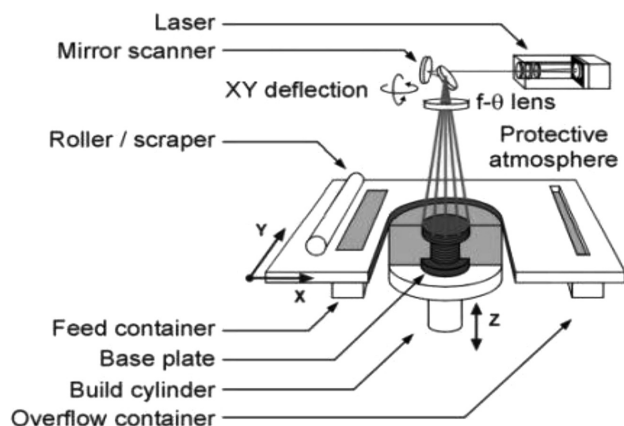


**Figure 5:** Schematic presentation of selective laser melting<sup>28</sup>

### 3 EXTRUSION-BASED SYSTEM

An extrusion-based system uses material extrusion where the material is heated to the molten state and then extruded through a nozzle to form parts layer by layer. The most common technology is fused deposition modeling (FDM). A schematic diagram of the process is shown in **Figure 6**.

Fused deposition modeling produces components by depositing extruded material in layers through a nozzle. Fused deposition modeling uses a 3D CAD program to prepare and build a model; the material is heated to the molten state and forced through the nozzle under pressure to build up a component.<sup>29</sup> The advantages of fused deposition modeling are as follows:

- the technology supports complex geometries and cavities,
- the technology produces high-grade parts,
- it is simple to use.

The limitations of fused deposition modeling are:

- limitation on the materials that can be used,
- limited size,
- the cost of the actual machine.

This technology uses different materials for component fabrication, including acrylonitrile butadiene styrene (ABS), polylactic acid (PLA), polycarbonate (PC), polyamide (PA), polystyrene (PS), lignin, rubber, nylon and others.<sup>29</sup>

### 4 SHEET-LAMINATION PROCESS

This is an additive-manufacturing technology, which mainly uses metal sheets or paper for the manufacturing process. This technology is characterized by a low cost of production, high strength of the model, possibilities to

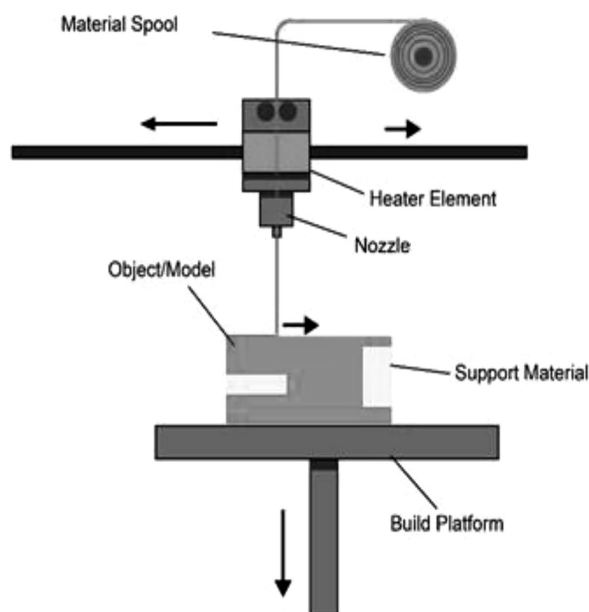


**Figure 6:** Presentation of an extrusion-based system<sup>29</sup>

control the range of speed of the process to create the outcome desired. Apart from the benefits achieved when using this technology, there are also limitations: the properties of the outcome product depends on the material used and the process of fusing the material together needs improved techniques.<sup>30</sup>

There are two variants of this process, namely: ultrasonic additive manufacturing (UAM) and laminated object manufacturing (LOM). Ultrasonic additive manufacturing (UAM) uses metal as its working material and employs the layer-by-layer techniques, whereby the layers are welded together ultrasonically. This process uses metals like aluminum, copper, stainless steel and titanium alloy. Laminated object manufacturing (LOM) incorporates the layer-by-layer lamination technique, using sheets of paper as the working material and CO<sub>2</sub> laser for cutting a sheet that has been joined together by an adhesive to form layers of CAD-model parts. The excess material that is not part of the component being built is sliced into cubes, using a cross-hutch cutting operation.<sup>31</sup>

## 5 DIRECTED ENERGY DEPOSITION

Directed energy deposition is a type of additive manufacturing that uses the energy from a laser or electron beam to create a melt pool on the surface of the substrate, where coaxial powder or wire is deposited, following the path described by a CAD profile. An example of this process is laser metal deposition, also known as laser engineered net shaping (LENS), a process with high material-utilization efficiency and cost efficiency.<sup>32–41</sup> The laser, or electron beam, leaves a solid track of the melted powder. A schematic diagram of this process is shown in **Figure 7**. The advantages of directed energy deposition include the ability to carry out a high-value repair on a part that was cost prohibitive in the past; it can also be used to manufacture parts with functionally graded materials or functionally graded

coatings.<sup>39–41</sup> The materials that can be used for this technology include metals, alloys, ceramics and composites.

Other additive-manufacturing processes are material jetting, binder jetting and the vat photopolymerization process. These types of additive manufacturing use non-metallic based materials and their applications are limited. For further reading about these and other additive-manufacturing processes, the reader can consult references.<sup>42–52</sup>

A new 3D printing technology was developed and it will help us create metallic, free-standing 3D structures. This technology was developed by the researchers at Harvard University.<sup>53</sup> The existing direct ink writing 3D printing technology is combined with laser annealing to ensure accurate and stable free-standing 3D structures. This technology is very useful in the applications where free-standing 3D microstructures are required, e.g., in sensors, electronics and also in biomedical applications.

## 6 MATERIAL DEVELOPMENT FOR ADDITIVE MANUFACTURING

There is constant demand for light materials with improved properties, especially in the automobile and aerospace industries, with the aim of reducing the global warming. The advent of additive manufacturing is the beginning of a new dawn in the manufacturing industries. A number of restrictions were placed on material development in the past because of thermodynamic limitations as well as the difficulties in processing some materials in the bulk form. With additive-manufacturing technologies, new materials are now being developed without any restriction. A number of complex metallic alloys are now being developed and used for the fabrication of important light-weight structures with impressive properties, using the additive-manufacturing process.<sup>54</sup> Complex metallic alloys are intermetallic compounds with unique thermal and transport properties that cannot be found in any metal system.<sup>55</sup>

Complex metallic alloys are needed in a number of applications because of their excellent properties, but they cannot be used with the conventional manufacturing processes because of their brittleness that makes them difficult to process. These materials have low coefficients of friction, good corrosion resistance, good wear-resistance properties and can now be processed using additive manufacturing. New composite materials with improved properties are introduced and used in additive-manufacturing processes, with the functional-part production now being commercialized.<sup>54</sup> The traditional manufacturing process presents a lot of challenges when processing these materials because of the segregation of constituent materials due to the thermodynamic properties of individual materials, but additive-manufacturing technologies can be used to process these materials without such problems.

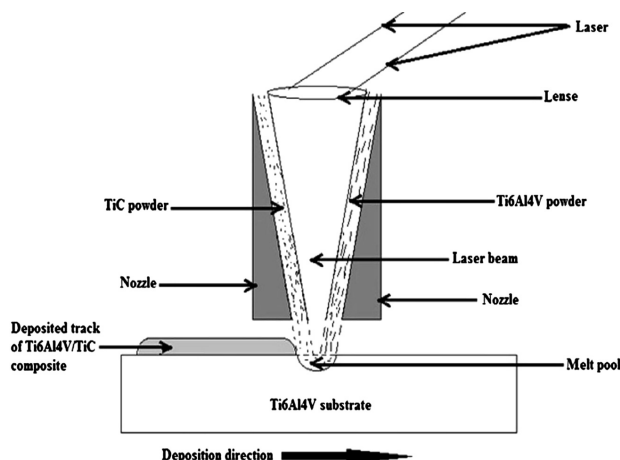


**Figure 7:** Schematic diagram of directed energy deposition<sup>41</sup>

A number of new materials with improved properties and performances are now being developed for the additive-manufacturing technologies. These new materials include the high-temperature copper alloy, developed by NASA, with excellent properties such as retention of high strength at elevated temperatures, used in rocket engines. Other materials that present challenges with the conventional manufacturing processes and are now successfully processed using the additive-manufacturing technologies include titanium aluminide, used in the fabrication of high-speed gas-turbine blades, reactor-grade pure niobium and NiTi.

## 7 CONCLUSIONS

The concept of additive manufacturing has provided solutions to most engineering problems, especially the problems faced by product designers in the past when products needed to be designed and redesigned because of the limitations imposed by the available manufacturing process. Designers can now freely design parts without having to worry about how they will be made. This research paper presents a review on various additive-manufacturing technologies. The aim of this paper is to provide a clear description of this novel manufacturing process – the additive-manufacturing process. Each of the technologies is described in this paper, including the materials suitable for use in each technology, advantages, disadvantages. Application areas and the new material development relating to the additive-manufacturing technologies are presented. In summary, additive manufacturing is a reliable technology that can be used to manufacture prototypes, tooling and functional parts, as it is less time consuming, allowing an easy fabrication of a complex geometry, an easy production of customized and personalized parts, without any need for special tools, and low material wastage that reduces the overall cost of the production. Improvements in the computing power and the reduction in mass-storage costs paved the way for processing the large amounts of data typical of modern 3D CAD models within reasonable time frames.

A new 3D printing technology has recently been developed at Harvard University. This new additive-manufacturing technology combines the existing direct ink writing 3D printing technology and the annealing process. The innovation was born out of the necessity for flexible and wearable electronic devices such as sensors and in biomedical applications. The technology uses the 3D printing technology to create complex architectures, while a printed structure is simultaneously annealed in midair. This helps to increase the accuracy of the printed material, also allowing the printed material to be created in free air without the need for any support structure. This technology has opened up possibilities of creating microscopic metallic free-standing 3D structures without an auxiliary support and in a single manufacturing run.

## 8 REFERENCES

- <sup>1</sup> J. Scott, N. Gupta, C. Wember, S. Newsom, T. Wohlers, T. Caffrey, Additive manufacturing: status and opportunities, Science and Technology Policy Institute, 2012, [https://www.ida.org/stpi/occasional-papers/papers/AM3D\\_33012\\_Final.pdf](https://www.ida.org/stpi/occasional-papers/papers/AM3D_33012_Final.pdf)
- <sup>2</sup> J. P. Kruth, M. C. Leu, T. Nakagawa, Progress in additive manufacturing and rapid prototyping, *CIRP Annals*, 47 (1998), 2, doi:10.1016/S0007-8506(07)63240-5
- <sup>3</sup> T. Wohlers, T. Caffrey, Additive manufacturing: going mainstream, manufacturing engineering, <http://advancedmanufacturing.org/additive-manufacturing-going-mainstream/>, 2013
- <sup>4</sup> F. Liou, K. Slattery, M. Kinsella, J. Newkirk, H. N. Chou, R. Landers, Applications of a hybrid manufacturing process for fabrication of metallic structures, *Rapid Prototyping Journal*, 13 (2007), 4, doi:10.1108/13552540710776188
- <sup>5</sup> R. M. Mahamood, E. T. Akinlabi, M. Shukla, S. Pityana, Revolutionary additive manufacturing: an overview, *Lasers in Engineering*, 27 (2014), 3–4, 161–178
- <sup>6</sup> N. Hopkinson, P. Dickens, Rapid prototyping for direct manufacture, *Rapid Prototyping Journal*, 7 (2001), 4, doi:10.1108/EUM0000-000005753
- <sup>7</sup> Y. L. Hou, T. T. Zhao, C. H. Li, Y. C. Ding, The manufacture of rapid tooling by stereo lithography, *Advanced Materials Research*, 102–104 (2010), 578–582
- <sup>8</sup> L. Hao, S. Dadbakhsh, Materials and process aspects of selective laser melting of metals and metal matrix composites: a review, *Chinese Journal of Lasers*, 36 (2009), 12, doi:10.3788/CJL2009-3612.3192
- <sup>9</sup> V. Petrovic, J. V. H. Gonzalez, O. J. Ferranda, J. D. Gordillo, J. R. B. Puchades, L. P. Grinan, Additive layered manufacturing: sectors of industrial application shown through case studies, *International Journal of Production Research*, 49 (2011), 4, doi:10.1080/00207-540903479786
- <sup>10</sup> S. F. S. Shirazi, S. Ghanekhani, M. Mehrabi, H. Yarmand, H. S. C. Metselaar, N. A. Kadri, N. A. A. Usman, A review on powder-based additive manufacturing for tissue engineering: selective laser sintering and inkjet 3D printing, *Science and Technology of Advance Materials*, 16 (2015), 3, doi:10.1088/1468-6996/16/3/033502
- <sup>11</sup> M. Dickson, Soft strain sensors fabricated through additive manufacturing, *MRS Bulletin*, 40 (2015), 6, doi:10.1557/mrs.2015.124
- <sup>12</sup> A. R. R. Bineli, A. P. G. Peres, L. F. Bernardes, A. L. Jardini, R. Filho, Design of microreactor by integration of reverse engineering and direct metal laser sintering process, *Proceedings of the 5th international workshop on hydrogen and fuel cells*, Campinas, 2010
- <sup>13</sup> O. Nyhila, Characterization of Process Parameter for Direct Metal Laser Sintering, Ph.D. Thesis, Nagoya Institute of Technology, 2005
- <sup>14</sup> A. Bineli, A. Peres, A. Jardini, R. Filho, Direct metal laser sintering: technology for design and construction of microreactors, *Proceedings of the 6th Brazilian Conference on Manufacturing Engineering*, 2011
- <sup>15</sup> R. Aulus, R. Maciel, Direct metal laser sintering (DMLS): technology for design and construction of microreactors, *Science and Technology of Advance Materials*, 7 (2015), 2
- <sup>16</sup> L. Morgan, L. Ulf, H. Ola, Rapid manufacturing with electron beam melting (EBM) – a manufacturing revolution, 2006, 433–438, <https://sffsymposium.engr.utexas.edu/Manuscripts/2003/2003-41-Larsson.pdf>
- <sup>17</sup> L. Ladani, L. Roy, Mechanical behavior of Ti-6Al-4V manufactured by electron beam additive fabrication, *Proceedings of the ASME International Manufacturing Science and Engineering Conference*, Madison, 2013
- <sup>18</sup> S. Biamino, A. Penna, U. Ackelid, S. Sabbadini, O. Tassa, P. Fino, M. Pavese, P. Gennaro, C. Badini, Electron beam melting of Ti-48Al-2Cr-2Nb alloy: microstructure and mechanical properties investigation, *Intermetallics*, 19 (2010), 6, doi:10.1016/j.intermet.2010.11.017



- <sup>19</sup> A. Neira, Thermal Modeling and Simulation of Electron Beam Melting for Rapid Prototyping on Ti6Al4V Alloys, Ph.D. Dissertation, North Carolina State University, Raleigh, NC, 2012
- <sup>20</sup> D. Bouk, H. Kaal, Selective Laser Sintering of Metals, Proceedings of ASME, American Society of Mechanical Engineers, New York, 2015
- <sup>21</sup> H. J. Niu, I. T. H. Chang, Selective laser sintering of gas atomized M2 high speed steel powder, *Journal of Materials Science*, 35 (2000), 1, doi:10.1023/A:1004720011671
- <sup>22</sup> M. Peterson, A. Kalz, Characterization and comparison of materials of selective laser sintering, *Journal of Materials Processing Technology*, 21 (2013) 3, 21–22
- <sup>23</sup> C. Telenko, C. C. Seepersad, Assessing energy requirements and material flows of selective laser sintering of nylon parts, Proceedings of the Solid Freeform Fabrication Symposium, Austin, USA, 2010, 289–297
- <sup>24</sup> S. Caroly, Design rules for selective laser sintering, [https://www.me.utexas.edu/~ppmdlab/files/designers\\_guide.sls.pdf](https://www.me.utexas.edu/~ppmdlab/files/designers_guide.sls.pdf)
- <sup>25</sup> M. Baumann, C. Tuck, R. Hague, Selective heat sintering versus laser sintering: comparison of deposition rate, process energy consumption and cost performance, <https://sffsymposium.engr.utexas.edu/sites/default/files/2015/2015-9-Baumann.pdf>
- <sup>26</sup> R. M. Mahamood, E. T. Akinlabi, M. Shukla, S. Pityana, Material efficiency of laser metal deposited Ti6Al4V: effect of laser power, *Engineering Letters*, 21 (2013), 1, [http://www.engineeringletters.com/issues\\_v21/issue\\_1/EL\\_21\\_1\\_03.pdf](http://www.engineeringletters.com/issues_v21/issue_1/EL_21_1_03.pdf)
- <sup>27</sup> A. Diatlov, D. Buchbinder, W. Meiners, K. Wissenbach, Towards surface topography: Quantification of Selective Laser Melting (SLM) built parts, Review of selected measurement methods and ongoing report on development of measurement specifications, 2011
- <sup>28</sup> Additive Manufacturing Processes, [www.slidehot.com/9673714743](http://www.slidehot.com/9673714743)
- <sup>29</sup> A. K. Sood, R. K. Ohdar, S. S. Mahapatra, Parametric appraisal of mechanical property of fused deposition modeling processed parts, *Materials and Design*, 31 (2010), 201–246
- <sup>30</sup> L. Gibson, D. W. Rosen, B. Stucker, Sheet lamination processes: additive manufacturing technologies, *Journal of Materials and Manufacturing*, 23 (2012) 3, 223–252
- <sup>31</sup> C. M. Cheah, Rapid sheet metal manufacturing, *International Journal of Advanced Manufacturing Technology*, 19 (2002), 510–515
- <sup>32</sup> R. M. Mahamood, E. T. Akinlabi, Effect of processing parameters on wear resistance property of laser metal deposited titanium-alloy composite, *Journal of Optoelectronics and Advanced Materials*, 17 (2015) 9–10, 1348–1360
- <sup>33</sup> R. M. Mahamood, E. T. Akinlabi, Process parameters optimization for material deposition efficiency in laser metal deposited titanium alloy, *Lasers in Manufacturing and Materials Processing*, 3 (2016), 1, doi:10.1007/s40516-015-0020-5
- <sup>34</sup> R. M. Mahamood, E. T. Akinlabi, Effect of laser power and powder flow rate on the wear resistance behaviour of laser metal deposited TiC/Ti6Al4V composites, *Materials Today: Proceedings*, 2 (2015) 4–5, 2679–2686
- <sup>35</sup> R. M. Mahamood, E. T. Akinlabi, M. Shukla, S. Pityana, Characterization of Laser Deposited Ti6Al4V/TiC Composite, *Lasers in Engineering*, 29 (2014) 3–4, 197–213
- <sup>36</sup> R. M. Mahamood, E. T. Akinlabi, S. A. Akinlabi, Laser power and scanning speed influence on the mechanical property of laser metal deposited titanium-alloy, *Lasers in Manufacturing and Materials Processing*, 2 (2014) 1, 43–55
- <sup>37</sup> R. M. Mahamood, E. T. Akinlabi, M. Shukla, S. Pityana, Scanning Velocity Influence on Microstructure, Microhardness and Wear Resistance Performance on Laser Deposited Ti6Al4V/TiC Composite, *Materials and Design*, 50 (2013), 656–666
- <sup>38</sup> R. M. Mahamood, E. T. Akinlabi, M. Shukla, S. Pityana, Characterizing the Effect of Laser Power Density on Microstructure, Microhardness and Surface Finish of Laser Deposited Titanium Alloy, *Journal of Manufacturing Science and Engineering*, 135 (2013), 6, doi:10.1115/1.4025737
- <sup>39</sup> J. Scott, N. Gupta, C. Weber, S. Newsome, T. Wohlers, T. Caffrey, Additive Manufacturing: Status and Opportunities, [https://cgsr.llnl.gov/content/assets/docs/IDA/AdditiveM3D\\_33012\\_Final.pdf](https://cgsr.llnl.gov/content/assets/docs/IDA/AdditiveM3D_33012_Final.pdf)
- <sup>40</sup> R. M. Mahamood, E. T. Akinlabi, Laser metal deposition of functionally graded Ti6Al4V/TiC, *Materials & Design*, 84 (2015), 402–410
- <sup>41</sup> R. M. Mahamood, E. T. Akinlabi, M. Shukla, S. Pityana, Functionally graded material: An overview, Proceedings of the World Congress on Engineering, London, UK, 2012, 1593–1597
- <sup>42</sup> A. D. Halvorsen, P. Vaidya, M. Robinson, D. L. Schulz, Transforming a laser micromachine into a direct-write tool for electronic materials, *Journal of Micro-Electronics and Electronic Packaging*, 5 (2008), 116–121
- <sup>43</sup> K. K. B. Hon, L. Li, I. M. Hutchings, Direct writing technology – advances and developments, *CIRP Annals*, 57 (2008) 2, 601–620
- <sup>44</sup> A. Lutfurakhmanov, G. K. Loken, D. L. Schulz, I. S. Akhatov, Capillary-based liquid microdroplet deposition, *Applied Physics Letters*, 97 (2010) 12, 1–3
- <sup>45</sup> D. B. Chrisey, A. Pique, R. Modi, H. D. Wu, R. C. Y. Auyeung, H. D. Young, Direct writing of conformal microscopic electronic device by MAPLE DW, *Applied Surface Science*, 168 (2000) 1–4, 345–352
- <sup>46</sup> M. Burns, Automated Fabrication: Improving Productivity in Manufacturing, Prentice Hall, Eaglewood Cliffs, NJ, 1993
- <sup>47</sup> Wohlers Report, Additive manufacturing and 3D printing state of the industry, <https:// WohlersAssociates.com/state-of-the-industry-reports.html>
- <sup>48</sup> J. P. Kruth, M. C. Leu, T. Nakagawa, Progress in additive manufacturing and rapid prototyping, *CIRP Annals – Manufacturing Technology*, 47 (1998) 2, 525–540
- <sup>49</sup> J. Kietzman, L. Pitt, P. Berthon, Disruptions, decisions, and destinations: Enter the age of 3-D printing and additive manufacturing, *Business Horizons*, 58 (2015) 2, 201–210
- <sup>50</sup> K. Chan, Metal Additive Manufacturing: A Review, *Journal of Materials Engineering and Performance*, 31 (2016) 6, 1917–1928
- <sup>51</sup> R. M. Mahamood, E. T. Akinlabi, Influence of scanning speed intermetallic produced in-situ in laser metal deposited TiC/Ti6Al4V composite, *Mater. Tehnol.*, 51 (2017) 3, 473–478, doi:10.17222/mit.2016.096
- <sup>52</sup> Y. Zhai, D. A. Lados, J. L. Lagoy, Additive Manufacturing: Making Imagination the Major Limitation, *JOM*, 66 (2014) 5, 808–816
- <sup>53</sup> M. A. Skylar-Scott, S. Gunasekaran, J. A. Lewis, Laser-assisted direct ink writing of planar and 3D metal architectures, *PNAS*, 113 (2016) 22, doi:10.1073/pnas.1525131113
- <sup>54</sup> S. Kenzari, D. Bonina, J. M. Dubois, V. Fournée, Complex metallic alloys as new materials for additive manufacturing, *Science and Technology of Advanced Materials*, 15 (2014) 2, 1–9
- <sup>55</sup> J.-M. Dubois, Properties and applications of quasicrystals and complex metallic alloys, *Chem. Soc. Rev.*, 41 (2012), 6760–6777



# POMEMBNA OBLETNICA REVIJE MATERIALI IN TEHNOLOGIJE: PETDESET LET IZHAJANJA ZNANSTVENE PERIODIČNE PUBLIKACIJE

## AN IMPORTANT ANNIVERSARY OF THE MATERIALS AND TECHNOLOGY JOURNAL: FIFTY YEARS OF PUBLICATION

**Erika Nared**

Inštitut za kovinske materiale in tehnologije, Lepi pot 11, 1000 Ljubljana  
erika.nared@imt.si

*Prejem rokopisa – received: 2017-08-11; sprejem za objavo – accepted for publication: 2017-09-04*

doi:10.17222/mit.2017.136

Revija Materiali in tehnologije (MIT), ki jo izdaja Inštitut za kovinske materiale in tehnologije Ljubljana, v letošnjem letu praznuje petdeseto obletnico neprekinjenega izhajanja v tiskani obliki. Tudi v elektronski obliki je revija MIT, kot jo skrajšano imenujemo, na voljo že kar precej let in sicer od leta 1996. V članku je predstavljen pregled izhajanja serijske publikacije Materiali in tehnologije (ISSN 1580-2949) v zadnjih desetih letih; od leta 2007 pa vse do danes. Opisane so nekatere spremembe v reviji v tem obdobju, njena dinamika izhajanja ter vizija njenega izhajanja v naslednjih letih.

**Ključne besede:** znanstvena periodična publikacija, zgodovinski pregled, obletnica izhajanja, uredniška politika

The Materials and Technology journal (MIT), published by the Institute of Metals and Technology Ljubljana, is celebrating 50 years of its printed version, with the online archive stretching back to 1996. This article provides an overview of the journal (ISSN 1580-2949), covering the past 10 years. Some of the new changes to the journal are described, together with its vision for the future.

**Keywords:** scientific periodical publication, historical overview, anniversary of publication, editorial policy

### 1 PREDSTAVITEV REVIJE IN NJEN RAZVOJ

Revija Materiali in tehnologije ima zelo dolgo zgodovino izhajanja, saj izhaja že od leta 1967. Železarski zbornik (ISSN 0372-8633), kakor se je imenovala pred petdesetimi leti, ko je začela izhajati, je bil strokovno glasilo Slovenskih železarn in Metalurškega inštituta Ljubljana. Četrtnik je takrat tehnično urejal Edo Žagar in sicer do leta 1980; nasledila sta ga Darko Bradašnja do leta 1987 in Jana Jamar do leta 1991. Glavni in odgovorni urednik Železarskega zbornika pa je bil vse do konca njegovega izhajanja pod tem imenom mag. Joža Arh (**Slika 1**), torej kar 24 let (1967–1991). Železarski

zbornik je objavljala prispevke s področja kovinskih in deloma nekovinskih materialov.<sup>1</sup>

Po dveh desetletjih je revija zaradi vsebinskih sprememb dobila novo ime: Kovine zlitine tehnologije (KZT) (ISSN 1318-0010). Preimenovala se je zaradi vsebinske razširitve, saj je po novem vsebovala prispevke tako s področja kovinskih materialov kot tudi s področja anorganskih materialov, polimerov in materialov za namen vakuumске tehnike. Skladno z menjavo naslova je dobila tudi novo številko ISSN.<sup>1</sup> Glavni in odgovorni urednik je bil do leta 1994 še vedno mag. Jože Arh, nasledil ga je mag. Aleš Lagoja, ki je oblikoval uredniško politiko revije v naslednjih 4 letih (**Slika 1**).



**Slika 1 (od leve proti desni):** Jože Arh – glavni urednik revije od 1967 do 1991, Aleš Lagoja – glavni urednik revije od 1991 do 1995, Franc Vodopivec – glavni urednik revije od 1995 do 2011, Matjaž Torkar – glavni urednik revije od 2012 do julija 2016 – Paul McGuinness, sedanji glavni urednik revije

Do konca izhajanja revije z imenom Kovine zlitine tehnologije (1999), je uredniško politiko vodil prof. dr. Franc Vodopivec (**Slika 1**), ki je bil na mestu urednika 16 let in tako po letih urednikovanja na drugem mestu. Tehnično uredništvo revije Kovine zlitine tehnologije je vodila Jana Jamar.

Izdajatelj revije je bil Inštitut za kovinske materiale in tehnologije Ljubljana skupaj s soizdajatelji: ACRONI Jesenice, IMPOL Slovenska Bistrica, Kemijski inštitut Ljubljana, Koncern Slovenske železarne, Metal Ravne, Talum Kidričevo, Fakulteta za strojništvo Ljubljana, Institut Jožef Stefan in Slovensko društvo za tribologijo.<sup>1</sup>

Revija z novim imenom Materiali in tehnologije (ISSN 1580-2949) je nasledila obe svoji predhodnici na prelomu tisočletja in z letom 2000 začela izhajati kot znanstvena serijska publikacija, ki objavlja izvirne in pregledne znanstvene članke ter strokovne članke, ki obravnavajo teoretična in praktična vprašanja naravoslovnih ved in tehnologije na področjih kovinskih in anorganskih materialov, polimerov, vakuumске tehnike, kompozitnih in gradbenih materialov ter nanomaterialov.<sup>2</sup>

Njen namen je bil razširiti njeno interesno področje, da ne bi delovala le na področju kovin. Odgovorni urednik revije je bil vse do leta 2011 prof. dr. Franc Vodopivec. Do istega leta je tehnično urednikovanje vodila Jana Jamar. Z letom 2012 so se v uredniškem odboru zgodile spremembe predvsem na kadrovskem področju. Uredniško delo je vse do svoje upokojitve v letu 2016 vodil dr. Matjaž Torkar (**Slika 1**), tehnična urednica v tem času je bila dr. Danijela A. Skobir Balantič.

Leta 2016 je mesto odgovornega in glavnega urednika revije prevzel dr. Paul John McGuinness (**Slika 1**), mesto pomočnika glavnega in odgovornega urednika doc. dr. Matjaž Godec, častna glavna urednika sta prof. dr. Franc Vodopivec in dr. Matjaž Torkar. Tehnično uredništvo vodi Erika Nared, ki na Inštitutu za kovinske materiale in tehnologije vodi tudi specialno knjižnico.

Souredniki revije Materiali in tehnologije so: Igor Belič, Jaka Burja, Aleksandra Kocijan, Djordje Mandrino, Irena Paulin, Danijela A. Skobir Balantič, Darja Steiner Petrovič, Bojan Podgornik iz Inštituta za kovinske materiale in tehnologije (IMT), Boštjan Markoli iz Naravoslovnotehniške fakultete (NTF), Srečo Škapin in Rok Zaplotnik iz Inštituta Jožef Stefan (IJS) ter Ema Žagar iz Kemijskega inštituta (KI).<sup>3</sup> Osvežen je tudi uredniški odbor in zasedba članov mednarodnih pridruženih članov uredniškega odbora ter izdajateljskega sveta.

Članki revije MIT so indeksirani v bazah podatkov, kot so: Science Citation Index Expanded, Materials Science Citation Index in Journal Citation Reports (Science Edition). Po slednji, bazi podatkov JCR, ima revija trenutno faktor vpliva 0.436. Članki, objavljeni v reviji, so indeksirani tudi v mednarodnih in domačih sekundarnih virih/bazah: DOAJ (Directory of Open

Access Journals), Google Scholar, SCOPUS, WoS, COBIB in dLib.si (Digitalna knjižnica Slovenije).

Revija si, tako kot že večino časa svojega izhajanja, še vedno prizadeva za višjo citiranost, saj bi bila posledično vsekakor bolj zanimiva, tako za slovenske raziskovalce kot tudi tuje, in bi pritegnila uveljavljene domače in tuje raziskovalce, da bi v njej objavljali svoje znanstvene članke.<sup>3</sup>

## 2 PREGLED IZHAJANJA REVİJE IN OPIS SPREMEMB V OBDOBJU 2007–2017

Revijo Materiali in tehnologije danes izdaja Inštitut za kovinske materiale in tehnologije Ljubljana (IMT), skupaj s soizdajatelji: IMPOL - Industrija aluminija Slovenska Bistrica, SIJ METAL Ravne in TALUM Kidričevo. Izdajanje revije sofinancira Javna agencija za raziskovalno dejavnost Republike Slovenije (ARRS), prej Javna agencija za knjigo (JAK). Inštitut za kovinske materiale in tehnologije sodeluje na javnih razpisih, ki jih razpiše ARRS ter tako pridobi sofinanciranje izdajanja revije.

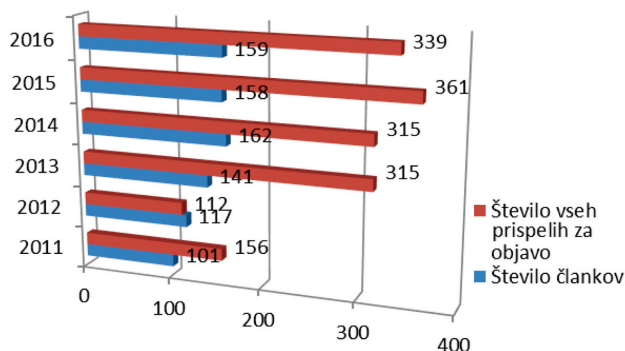
Periodika izhajanja je 6 števil letno. V vsaki številki je povprečno objavljenih od 20 do 25 člankov in prispevkov, ki so: večinoma izvirni znanstveni članki, pregledni članki in strokovni članki ter uvodne besede urednika ob posebnih priložnostih. Takšen obseg omogoča korekten in kvaliteten potek procesa objave člankov, od oddaje članka v uredništvo, do recenzije, prevodov in končno objave.

V letu 2016 so z novim vodstvom prišle tudi spremembe.<sup>4</sup> S številko 6/2016 smo po mnogih letih brezplačnega objavljanja člankov, začeli objavo člankov zaračunavati. Eden od razlogov je tudi krčenje sredstev za sofinanciranje pri ARRS. Za običajne članke je tako cena objave 300 EUR, za tiste članke, ki bodo predstavljeni na letni Mednarodni konferenci o materialih in tehnologijah, ki poteka vsako leto v Portorožu, pa je cena za objavo 150 EUR. Druga sprememba je sprejemanje in objavljanje le izvirnih znanstvenih in preglednih člankov.<sup>4</sup> Vzrok za odločitev uredništva, da uvede objavljanje le znanstvenih prispevkov, je ta, da gre pri strokovnih člankih zgolj za strokovna poročila brez znanstvenega pristopa, in kot tako ti bolj sodijo v strokovna ali druga interna glasila.

V desetletnem obdobju (2007–2017) je število oddaje člankov naraščalo in v zadnjih štirih letih naraslo do skoraj 400 letno (**Slika 2**), zato so se časovni roki za objavo podaljšali skoraj na obdobje enega leta ali več, kar je po mnenju uredništva absolutno predolgo.

Zato smo, v pomoč avtorjem, posodobili Navodila za avtorje, ki so objavljena tako v tiskani reviji (na zadnjih straneh vsake številke) kot na spletni strani revije.<sup>5</sup> Predstavili smo vzorec oz. predlogo, kako naj bo članek napisan in, da poleg oddaje članka želimo od avtorjev prejeti tudi kontrolni seznam, s katerim avtor potrdi, da je seznanjen z veljavno politiko uredništva. Oddaja





**Slika 2:** Grafikon s prikazom števila člankov prispelih za objavo po letih (rdeča barva) in število dejansko objavljenih (modra barva)

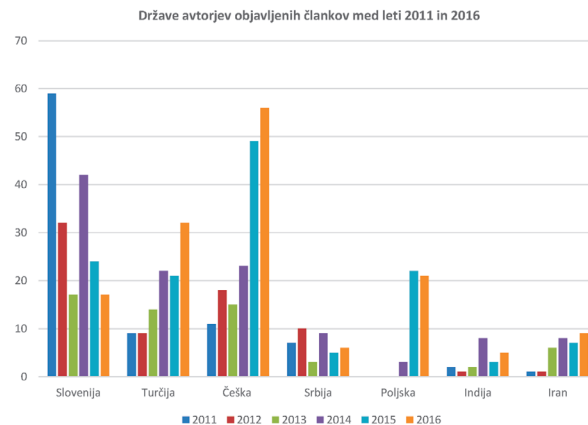
člankov še vedno poteka preko e-pošte: mit@imt.si, si pa uredništvo revije prizadeva, da bi v prihodnje v celoti uveljavili spletno oddajanje člankov. Glede na želje in zahteve mnogih avtorjev, smo v zadnjem letu uspeli skrajšati obdobje čakanja na objavo člankov in čakalne vrste iz enega leta na 2 do 3 mesece in tako stopiti naproti tako avtorjem, kot tudi bralcem oz. ciljni publiki, ki ima v krajšem času možnost slediti novim spoznanjem in novostim na področju materialov in tehnologij.

V obdobju od leta 2007 do 2016 je v reviji *Materiali in tehnologije* izšlo 1.071 člankov, kar je veliko več kot v desetletnem obdobju pred letom 2007. V zadnjih letih se je število objavljenih člankov povečevalo, saj smo v uredništvo prejeli vedno več člankov, katerih avtorji so želeli objavo. Nemara je bil najpogostejši razlog ravno brezplačna objava člankov. Največji dvig je bil leta 2008, ko je izšla posebna številka revije, v katero so bili vključeni članki iz druge mednarodne konference o toplotni obdelavi in površinski obdelavi (2nd International Conference on the Heat Treatment and Surface Engineering of Tools and Dies), ter ponoven porast med letoma 2013 in 2014, ko so še vedno velik delež člankov predstavljali prispevki udeležencev Mednarodne konference o materialih in tehnologijah v Portorožu, katerih članki so bili objavljeni še v reviji, četudi so nekateri vsebinsko predstavljali zgolj poročila o eksperimentih in ne toliko rezultatov raznih raziskav (**Slika 2**). Namen tovrstnih objav je bil med drugim dati priložnost tudi mladim, še ne uveljavljenim raziskovalcem, da na ta način predstavijo svoja dela.

Interne evidence od leta 2011 dalje kažejo, koliko člankov je vsakoletno prispelo na naslov uredništva revije v želji za objavo. Ta številka je dosegla vrh leta 2015. S spremembami v lanskem letu (2016), ko je uredniški odbor določil zaračunavanje objave, se je število prispelih člankov, pričakovano, postopoma začelo nižati.

### 2.1 Število objavljenih člankov

V prihodnje si v uredništvu revije *Materiali in tehnologije* želimo več objav domačih raziskovalcev in strokovnjakov ter tudi tistih iz ožjega evropskega prostora. V obdobju med 2011 in 2016 so avtorji člankov najpogosteje iz naslednjih držav (**Slika 3**).



**Slika 3:** Države avtorjev objavljenih člankov med leti 2011–2016

V letu 2011 je največje število člankov avtorjev iz Slovenije, ta številka se je v zadnjih letih zelo znižala, v zadnjem času namreč prevladujejo predvsem objave avtorjev iz Češke, Turčije in Poljske. Povečuje se torej število tujih avtorjev glede na domače.

### 2.2 Pregled revije po letih izhajanja v obdobju od 2007 do 2017

Temeljiti pregled revije postopno po letih izhajanja, od začetka pa do leta 2007, je moč najti v že objavljeni literaturi<sup>1</sup>, zato se bomo na tem mestu dotaknili let, ki so sledila kasneje, torej v obdobju od 2007 do danes (**Tabela 1**). Statistična analiza kaže, da število člankov na splošno zelo narašča (2007:43 in 2015:159), število znanstvenih člankov je višje kot število strokovnih, večje je tudi število člankov v angleškem jeziku.

Z uvedbo sprememb v letu 2016 je uredništvo odločilo tudi, da bo pri člankih še vedno povzetek v slovenskem in angleškem jeziku, ravno tako tudi naslov ter ključne besede, ki označujejo vsebino članka v obeh jezikih Od 4. številke letnika 51 pa podnapisi k slikam in tabelam ne bodo več v dveh jezikih, pač pa le enem – in sicer v angleškem jeziku.

**Tabela 1:** Pregled po letih izhajanja, 2007–2017

Letnik	Leto	Število zvezkov in številke	Znanstveni in strokovni članki
41	2007	6 (1–6)	43
42	2008	6 (1–6)	38
43	2009	6 (1–6)	46
44	2010	6 (1–6)	45
45	2011	6 (1–6)	76
46	2012	6 (1–6)	142
47	2013	6 (1–6)	138
48	2014	6 (1–6)	157
49	2015	6 (1–6)	159
50	2016	6 (1–6)	156
51	2017	6 (1–2)	72*
		<b>SKUPAJ:</b>	<b>1.072</b>

\*število člankov do številke 4 (2017)

### 2.3 Pregled revije po tipologiji

Število člankov, ki spadajo v skupino izvirnih znanstvenih člankov se je z leti višalo, največ jih je bilo v letu 2016, najmanj pa v letu 2007. Število strokovnih člankov, ki so z letom 2016, po odločitvi uredništva ukinjeni, je obdržalo konstantno številko, od 30 do 40 letno.

**Tabela 2:** Pregled prispevkov v letih od 2007 do 2017 po tipologiji

Leto	Tipologija			
	1.01 (izvirni znanstveni članek)	1.02 (pregledni znanstveni članek)	1.04 (strokovni članek)	1.20 (predgovor, spremna beseda)
2007	39	4	1	0
2008	30	6	8	0
2009	38	3	9	0
2010	43	8	7	0
2011	79	4	14	0
2012	81	0	30	3
2013	98	6	30	0
2014	118	2	39	0
2015	114	6	35	0
2016	125	2	30	2
2017 (do št. 3)*	46	2	10	1

\*podatki pridobljeni pred izidom 4. številke

### 3 DOSTOPNOST REVİJE

Revija *Materiali in tehnologije* je že v devetdesetih letih prejšnjega stoletja, ko se je imenovala še *Kovine zlitine tehnologije*, stopila naproti ideji, da bi bila bolj odprta in lažje dostopna širši javnosti. V skladu z željami in dejanji uredništva in navsezadnje težnjami širše javnosti ter splošnih trendov tistega časa, je v letu 1998 postala dostopna na svetovnem spletu v celotnem besedilu in jo je bilo sprva moč najti na spletni strani Centralne tehniške knjižnice (repozitorij CTK), kasneje pa na spletni strani [www.imt.si](http://www.imt.si), kjer je revija dostopna še danes.

Revija (njeni predhodniki *Železarski zbornik* in *Kovine zlitine tehnologije*) je bila v Narodni in univerzitetni knjižnici (NUK) vključena v projekt digitalizacije in je danes na voljo v digitalni obliki tako na spletnem portalu pri Digitalni knjižnici Slovenije pri NUK, kot tudi na spletni strani revije MIT. Ob petdeseti obletnici izhajanja revije smo se v uredništvu odločili, da na spletni strani revije uredimo celoten arhiv vseh števil revije, tudi števil njenih predhodnic, ki so doslej manjkale: *Železarski zbornik* (ISSN 0372-8633) in *Kovine zlitine tehnologije* (ISSN 1318-0010). Revija *Materiali in tehnologije* je mogoče prelistati kadarkoli in od koderkoli (če le imate v bližini internet), in sicer od prve številke *Železarskega*

zbornika iz leta 1967 pa do vseh člankov revije MIT do danes. Večino števil revije v tiskani obliki hranimo tudi v knjižnici IMT. Skupno je bilo tako pripravljenih, in v spletni arhiv dodanih, 123 datotek; 102 številke *Železarskega zbornika* in 21 številke revije KZT.<sup>6</sup>

### 4 ZAKLJUČEK

Začetki revije in objava člankov samo iz področja železarstva in metalurgije pred petdesetimi leti, ko je industrija jekla in železarstva predstavljala največji delež tovrstne dejavnosti v gospodarstvu takratne Jugoslavije in kasneje države Slovenije, so bili med drugim ravno tako podlaga za nadaljnje raziskovanje in uveljavljanje metalurgije kot panoge, ki je do danes počasi, a vztrajno prešla v skoraj vse pore industrije in je v današnjem času razvoja tehnologije na izredno visoki ravni. Danes tako z visoko tehnološkimi principi in najnovejšimi tehnologijami na področju tako kovinskih, kot tudi drugih materialov, dosegamo zavidljive rezultate. Napredni materiali, napredne proizvodne tehnologije, nanotehnologije in biotehnologije so ključna področja, identificirana v strategiji pametne specializacije, ki bodo omogočala evropski in slovenski industriji ohraniti mednarodno globalno konkurenčnost in izkoristiti nove trge. Z njimi sta metalurgija in kemijska industrija neločljivo povezani in sta del opredeljenih ključnih tehnologij. Pri tem razvoj novih materialov in tehnologij pomeni vstop novih, do sedaj neznanih možnosti, na tržišče, kjer imajo raziskave, razvoj in inovacije zelo pomembno vlogo.<sup>7</sup> Del raziskav in preizkusov, je predstavljen tudi skozi prispevke in članke v reviji MIT in tudi v drugih medijih,<sup>8</sup> ki s tem širi nova dognanja, spoznanja in znanja na širši krog raziskovalcev, znanstvenikov in drugo potencialno publiko. Revija *Materiali in tehnologije* je danes sicer priznana tudi izven meja Slovenije, vendar pa si v prihodnje še vedno želimo, da bi v reviji objavljalo večje število strokovnjakov in raziskovalcev iz Slovenije in evropskega prostora.

### 5 LITERATURA

- <sup>1</sup> N. Jamar, J. Jamar, Zgodovina znanstvene serijske publikacije *Materiali in tehnologije/Materials and Technology* = Historical overview of the scientific journal *Materiali in tehnologije/Materials and Technology*, *Mater. Tehnol.*, 41 (2007) 1, 13–19
- <sup>2</sup> <http://mit.imt.si/Revija/index-slo.html>, 28.7.2017
- <sup>3</sup> <http://mit.imt.si/Revija/information-slo.html>, 28.7.2017
- <sup>4</sup> P. McGuinness, Predgovor urednika=Editor's preface, *Mater. Tehnol.*, 50 (2016) 5, str. 639–640
- <sup>5</sup> <http://mit.imt.si/Revija/authors-slo.html>, 28.07.2017
- <sup>6</sup> <http://mit.imt.si/Revija/archive.html>, 29.07.2017
- <sup>7</sup> <https://www.gzs.si/Novice/ArticleId/58642/srip-matpro>, 29.7.2017
- <sup>8</sup> M. Godec, Največji hit je 3D tisk, *Glas gospodarstva*, Naj materiali, panožna številka, april (2017), 30–31

INVESTIGATION OF GRAIN BOUNDARIES IN ALLOY 263  
AFTER SPECIAL HEAT TREATMENTPREISKAVA MEJ ZRN V ZLITINI 263 PO POSEBNI TOPLOTNI  
OBDELAVI

Ivan Slatkovský, Mária Dománková, Martin Sahul

Slovak University of Technology Bratislava, Faculty of Materials Science and Technology, Institute of Materials Science,  
Bottová 25, 917 24, Trnava, Slovak Republic  
ivan.slatkovsky@stuba.sk*Prejem rokopisa – received: 2016-06-20; sprejem za objavo – accepted for publication: 2017-01-24*

doi:10.17222/mit.2016.115

Alloy 263 is well known for its very good creep resistance and also for its weldability. These kinds of properties are appreciated in the power-plant industry where Alloy 263 is used for shafts in a high-pressure circle. One of the possible ways to improve the properties of superalloys, including Alloy 263, is through the effect of the grain-boundary serration (GBS) which, as research indicates, is associated with the improvement of the creep resistance that can lead to an increased efficiency of coal power plants. Grain-boundary serration was observed in different kinds of superalloys although the formation mechanism of serration has not been clearly explained yet. Some researchers reported that the formation of serration is associated with the change in the character of the precipitates at grain boundaries. This paper deals with an investigation of the grain boundaries in Alloy 263 using two different kinds of heat treatment. To form serrated grain boundaries in Material A (MA), slow controlled cooling from the temperature of solution annealing to 800 °C was carried out. Standard heat treatment of Alloy 263 was performed on material B (MB). Experimental techniques of scanning electron microscopy (SEM) and transmission electron microscopy (TEM), including electron diffraction, were used to analyze the microstructure, determine the character of the grain boundaries and identify the secondary particles at the grain boundaries.

Keywords: Alloy 263, grain-boundary serration, precipitates

Zlitina 263 je znana po zelo dobri odpornosti proti lezenju in tudi po dobri varivosti. Te vrste lastnosti so zelo cenjene v termoelektrarnah, kjer se zlitina 263 uporablja za gredi v visokotlačnem delu turbin. Eden od možnih načinov za izboljšanje lastnosti superzlitin, vključno z zlitino 263, je tvorba (nastanek) nazobčanih kristalnih mej (angl. GBS). Preiskava je pokazala, da je ta fenomen povezan z izboljšanjem odpornosti proti lezenju, kar lahko vodi k večji učinkovitosti termoelektrarn na premog. Učinek nazobčanosti mej kristalnih zrn so opazili pri različnih vrstah superzlitin, čeprav mehanizem tvorbe še ni popolnoma pojasnjen. Nekateri raziskovalci so ugotovili, da je tvorba nazobčanosti povezana s spremembo lastnosti izločkov na mejah med zrn. Prispevek se ukvarja s preiskavo mej med kristalnimi zrn v zlitini 263 z dvema različnima vrstama toplotne obdelave. Nastanek nazobčanih mej kristalnih zrn materiala A (MA), je bil povzročen s počasnim kontroliranim ohlajanjem iz temperature raztopnega žarjenja, ki je bila 800 °C. Standardna toplotna obdelava se je izvajala za zlitino 263 - material B (MB). Za analizo mikrostrukture so uporabili vrstični elektronski mikroskop (SEM) in presežno elektronsko mikroskopijo (TEM), vključno z elektronsko difrakcijo. Na ta način so določili lastnosti mej kristalnih zrn in sekundarnih delcev na mejah zrn.

Ključne besede: zlitina 263, nazobčanost mej kristalnih zrn, izločki

## 1 INTRODUCTION

It is a well-known fact that a reduction in the CO<sub>2</sub> emissions produced by coal power plants is one of the major goals for the countries all over the world. A possible way to reduce the CO<sub>2</sub> emissions is to improve thermal efficiencies through super critical and ultra-super critical technologies in power plants, where efficiencies above 40 % could be reached. Hence, to achieve this kind of efficiency, the materials like nickel-based superalloys are considered to be used (**Figure 1**).<sup>1–3</sup>

To prolong the life time of parts when the temperature exceeds 700 °C, scientists are looking for new paths of material processing. In the case of heat treatment, one of the possible ways is a modification of grain boundaries (GBs) when the character of the boundaries changes from straight to zigzag.

The phenomenon of grain-boundary serration (GBS) was observed in the nickel-based superalloys and in austenitic stainless steels. The formation of serrations on grain boundaries (GBs) has not been fully described yet. However, it is a known fact that in the case of nickel-based superalloys, the GBS is closely related to the slow controlled cooling from the temperature of the solution annealing.

Early studies of serration in the nickel-based alloys were focused on the interaction between the grain boundary and  $\gamma'$  phase.<sup>4,5</sup> Until now, researchers have found that the serration is associated not only with the presence of the  $\gamma'$  phase, but also with other precipitates like M<sub>23</sub>C<sub>6</sub> carbide, the  $\sigma$  phase or the  $\gamma''$  phase on the GBs that were observed in different kinds of superalloys. The formation of these secondary particles could be highly related to the serrated grain boundaries and their formation.<sup>6–13</sup> Recently, contemporary authors have

**Table 1:** Nominal chemical composition of Alloy 263

Chemical-composition limits									
Weight %	Ni	Cr	Co	Mo	C	Al	Ti	Al+Ti	Mn
263	Bal	19–21	19–21	5.6–6.1	0.04–0.08	0.60 max	1.90–2.40	2.40–2.80	0.60 max
Weight %	Si	Fe	Cu	B	Pb	S	Ag	Bi	
263	0.40 max	0.07 max	0.020 max	0.005 max	0.0020	0.007 max	0.005 max	0.0001 max	

found that in some alloys, in the early stages of the formation, GBS occurred in the absence of the adjacent coarse  $\gamma'$  particle or  $M_{23}C_6$  carbide.<sup>12–14</sup> Furthermore, H. U. Hong et al.<sup>15</sup> observed in their research that the serrations on GBs were formed in the material after a long solution annealing (2000 min) without any slow controlled cooling. Also, no secondary particles were observed.

As reported by the authors of references,<sup>10–13</sup> GBS leads to a morphological change of the carbides on GBs, from granular to planar. A growth of secondary particles on the serrated grain boundaries was observed mostly at a low angle and on special GBs. The authors of references<sup>10,11</sup> reported that the formation of planar  $M_{23}C_6$  carbides is orientated in the  $\{111\}$  plane. Also, the orientation relationship between the carbides and the matrix was observed.

Therefore, the purpose of this study is to investigate the effect of special heat treatment on GBs and identify the secondary phases formed at the GBs in Alloy 263.

## 2 EXPERIMENTAL PART

In order to investigate GBS, commercially available hot-rolled nickel-based superalloy 263 was used in the study. The chemical composition of the examined alloy is given in **Table 1**.

A two-stage special heat-treatment method was designed to form a GBS in material A, based on the previous studies.<sup>6–13</sup> The solution heat treatment followed by slow cooling at a carefully controlled rate (until the aging temperature was reached) was found to be necessary to generate serrated GB structures.

Material A was solution annealed at 1150 °C for 80 min and cooled slowly to 800 °C at a cooling rate of 3 °C/min, followed by water quenching. After that,

precipitation hardening at 800 °C for 4 h was performed and followed by air cooling.

On material B, the standard two-stage heat treatment of Alloy 263 (solution annealing at 1150 °C for 80 min followed by water quenching and precipitation hardening at 800 °C for 4 h, cooled in the air) was applied.

For a SEM analysis, the samples were sliced, mechanically grinded and polished. The etching solution for the SEM observation was a solution containing 5 g  $FeCl_3$ , 15 mL  $HCl$ , 2 mL  $HNO_3$  and 60 mL ethanol used for 10–15 s in order to reveal the GB configuration and carbides. A JEOL 7600 F scanning electron microscope was used for the observation of the GBs.

Thin foils were prepared for a detailed grain-boundary observation using mechanical grinding to a thickness of about 0.1 mm, and then electrolytically etched. Etching was done on TENUPOL 5 in a solution of perchloric acid and methanol (1:9). The temperature during etching was -30 °C and the voltage was 25 V. For the detailed observation, a transmission electron microscope, JEOL 200 CX with an accelerating voltage of 200 kV, was used. To identify secondary particles at the GBs, an electron-diffraction analysis was applied.

Extraction replicas were prepared in the following route: samples were first prepared using standard metallographic techniques. After that, they were etched with the above-mentioned solution for 15 s. A thin carbon film was sputtered onto the etched surface of the samples. The carbon film (replica) was subsequently electrolytically extracted, using 8 % perchloric acid, at a bias of 10 V.

## 3 RESULTS

**Figure 2** shows the microstructure of material A after the special heat treatment. Light microscopy revealed a polyhedral grain, the presence of twins as well as the grain-size heterogeneity in material A. Two types of grain-boundary morphology were observed with light microscopy. Straight boundaries with a percentage share of approximately 38 % of the total of 254 observed grain boundaries were located in the structure of material A. Serrated boundaries, as the second type, covered approximately 39 % of the noticed boundaries. In some cases, the type of boundary could not be determined owing to the state of the boundary.

As a reference sample, material B (**Figure 3**) was processed with the conventional heat treatment. In material B, we also observed the base microstructure

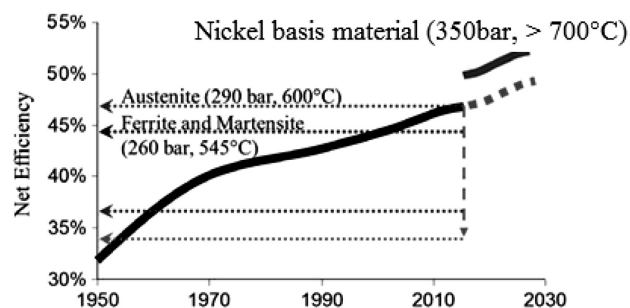


**Figure 1:** Net efficiency development in the case of hard coal-fired power plants considering different structural alloys<sup>3</sup>



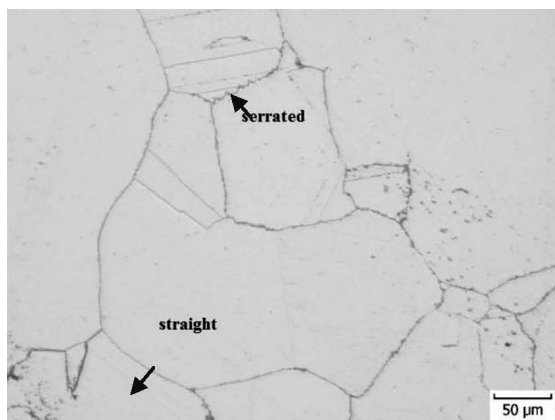


Figure 2: Material A

with polyhedral grains with the heterogeneity of the grain size and twins similar to those in material A. As expected, no serrated boundaries were observed in material B after the conventional heat treatment.

The grain-boundary details taken with SEM indicate the presence of precipitates on the serrated and straight grain boundaries in material A as well as in material B (Figures 4 and 5). Results of the EDX analysis taken from material A (Figure 6) reveal the eventual presence of carbon-rich secondary particles, which could possibly indicate the presence of carbides at the grain boundaries. The occurrence of the other elements at the grain boundaries was not significant. Comparable results were also noticed for material B. To confirm the presence of the secondary particles formed at the boundaries and to identify the chemical nature of these particles, ED and EDX using the TEM were taken for materials A and B, and the results are shown below.

The authors of reference<sup>16</sup> predicted and identified typical kinds of the secondary particles for this alloy, allowing us to expect mainly the presence of the MC,  $M_6C$  and  $M_{23}C_6$  carbides.

Figures 7 to 9 summarize the identified phases on the replicas for material A. Electron diffraction spectra as well as the EDX analysis of the extracted precipitates



Figure 3: Material B

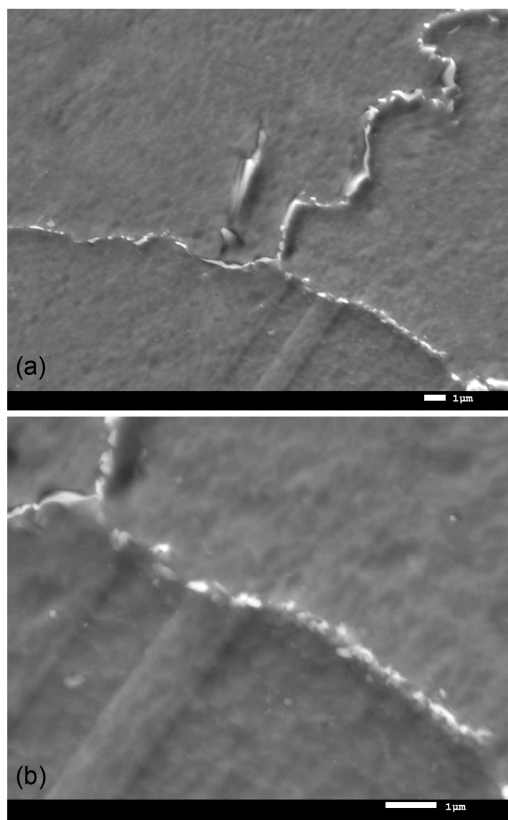


Figure 4: SEM, material A: a) serrated grain-boundary triple point and b) detail of precipitates

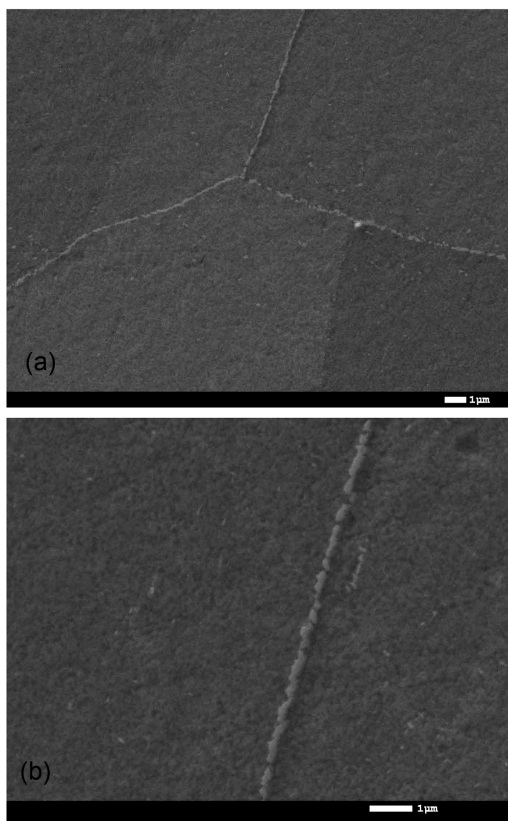


Figure 5: SEM, material B: a) straight grain-boundary triple point and b) detail of precipitates

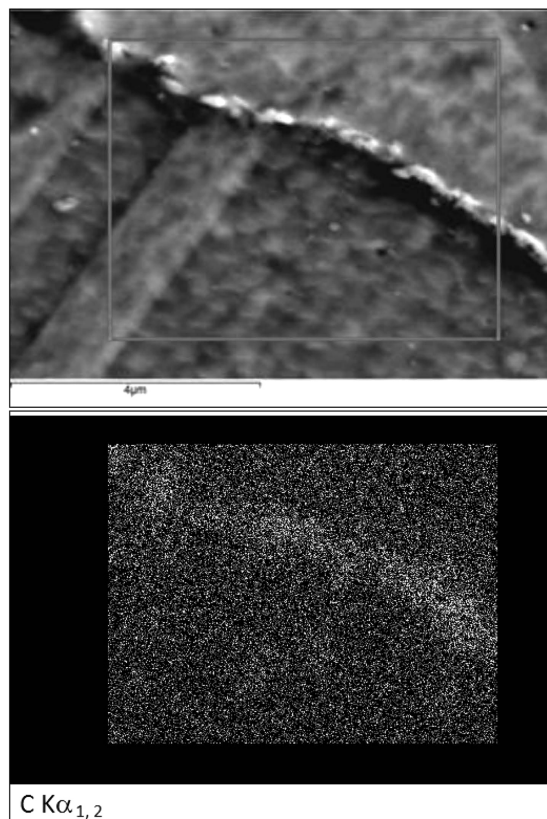


Figure 6: EDX map, carbon-rich grain boundary, material A

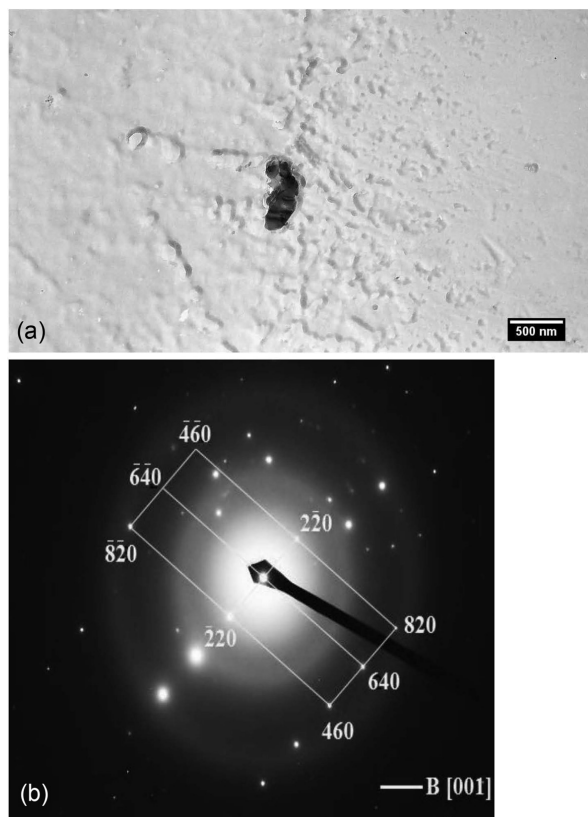


Figure 7: a) Detail of a precipitate at the grain boundary, material A and b) point-diffraction spectra of  $M_{23}C_6$  carbide

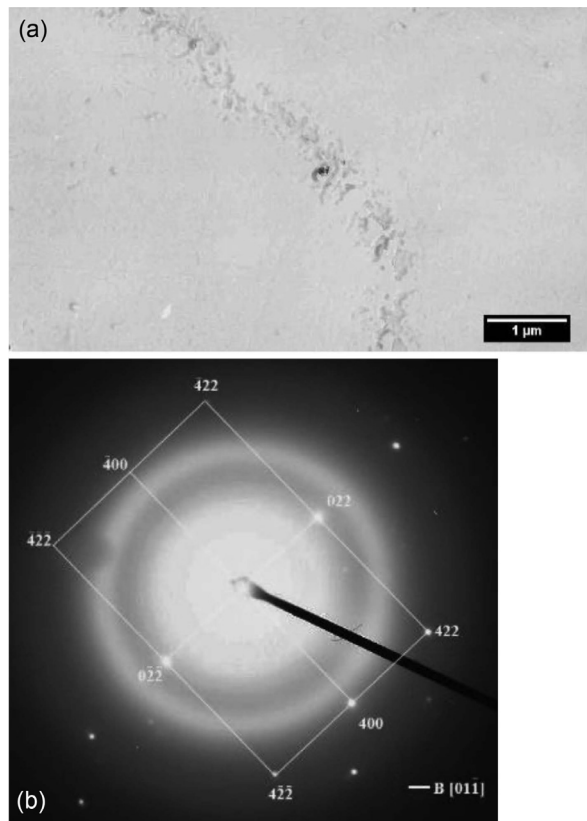


Figure 8: a) Extracted small particles of irregular shapes at the grain boundary, material B and b) point-diffraction spectra of MC carbide

extracted at the grain boundaries confirmed the presence of carbides. The carbides contained minor elements such as Mo, Cr and Ni (Table 2).

The  $M_6C$  ( $(Co,Ni)_3Mo_3C$ ) carbide was not confirmed by electron diffraction (confirmed only by the EDX anal-

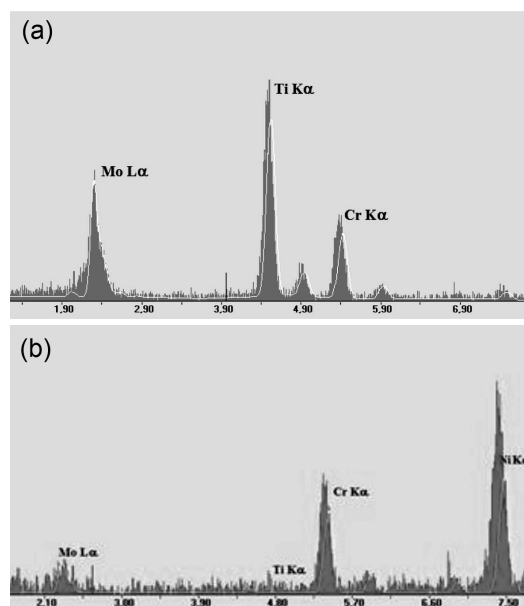


Figure 9: Typical EDX spectra of precipitates in material A: a) carbide MC and b) carbide  $M_6C$

ysis); a slight difference between the lattice parameters of the  $M_{23}C_6$  and  $M_6C$  ( $a_{M_{23}C_6} = 0.1065$  nm  $a_{M_6C} = 0.1085$  nm) carbides makes the identification difficult.

**Table 2:** Approximate chemical composition of carbides in Material A

	$M_{23}C_6$		MC		$M_6C$	
	Avr. (w/%)	$\sigma$	Avr. (w/%)	$\sigma$	Avr. (w/%)	$\sigma$
Mo	28.6	$\pm 6.1$	64.7	$\pm 6.3$	22.9	$\pm 5.0$
Ti	4.6	$\pm 3.6$	26.0	$\pm 5.0$	3.3	$\pm 1.3$
Cr	66.8	$\pm 9.6$	8.8	$\pm 4.3$	27.5	$\pm 3.6$
Ni					46.3	$\pm 6.8$

Details of the serrated boundaries and precipitates in Material A, observed with TEM on the foils, can be seen in **Figures 10a** to **10b**. As shown in the figures, the asymmetry of the serration was observed on some parts of the serrated boundaries when the irregularity of the serration exhibited a high difference in  $\lambda$  at the observed parts of the boundary (on the edges,  $\lambda = 800$ – $900$  nm; in the middle of the boundary,  $\lambda = 150$ – $200$  nm).

On the serrated grain boundary documented in **Figure 10b**, secondary particles of different sizes were noticed. The shape of the particles copied the serration of the boundary. Using electron diffraction, the particles were identified as the  $M_{23}C_6$  carbide and the matrix as the  $\gamma$ -phase (**Figure 11**). Electron diffraction also revealed the existence of the orientation relationship between the matrix and carbide:  $\{200\}_{\gamma} \parallel \{200\}_{M_{23}C_6}$ .

**Figure 12a** documents a straight grain boundary with discrete secondary particles in material A. Along the full

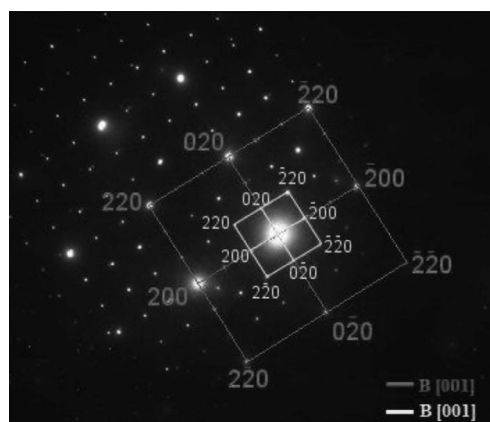


**Figure 11:** Point diffraction spectra – phase  $\gamma$  and  $M_{23}C_6$  carbide

length of the boundary, the particles of triangular or rectangular shapes were observed. As shown in **Figure 12b**, this kind of particles does not copy the shape of the boundary as in the case of the precipitates at the serrated boundaries. The size of the precipitates was approximately 300 nm. The particles were identified, with electron diffraction (**Figure 13**), as  $M_{23}C_6$  carbide and the matrix as phase  $\gamma$ . However, in the case of the straight grain boundary, no orientation relationship between the matrix and the precipitate was spotted.

The precipitates extracted at the grain boundary in material B as  $M_{23}C_6$  carbide were identified on the replicas using electron diffraction, as documented below

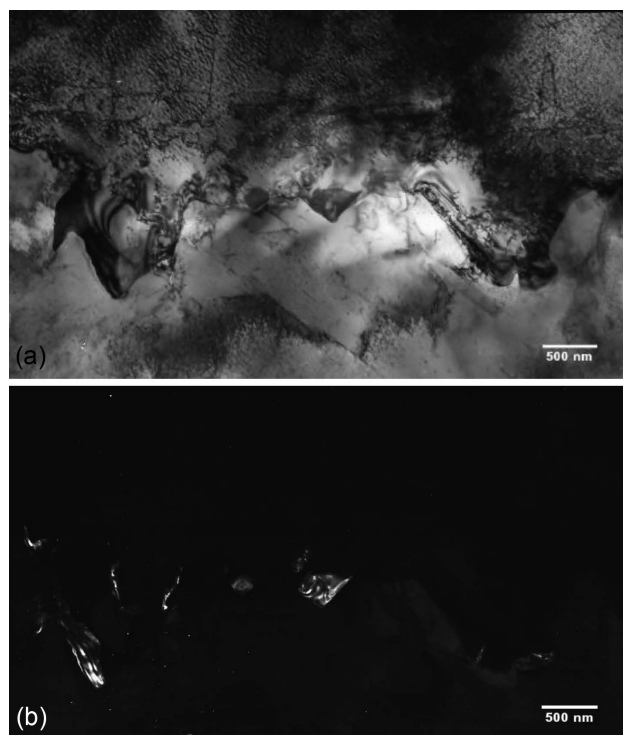


**Figure 10:** Detail of serrated grain boundary, material A, bright field; b) detail of precipitates at the grain boundary, material A, dark field; reflection  $(2\ 0\ 0)_{M_{23}C_6}$  was used for the dark-field display

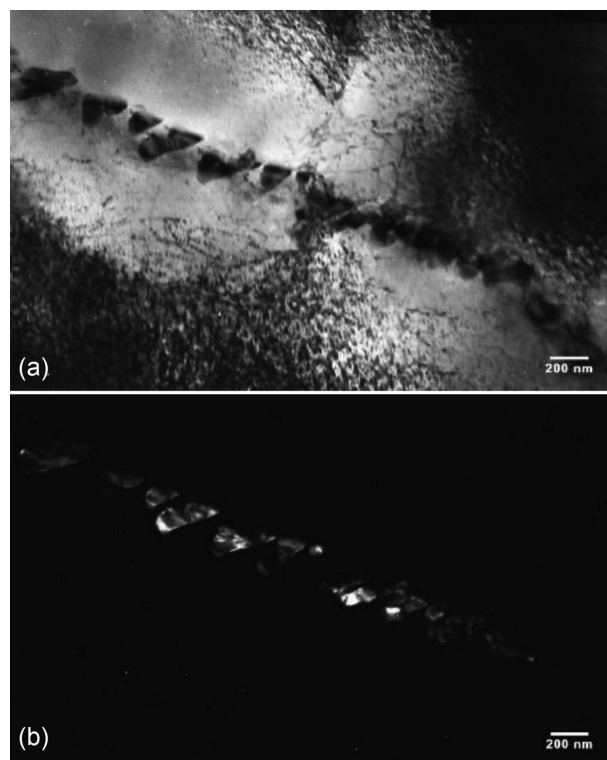


**Figure 12:** Detail of straight grain boundary, material A, bright field; b) detail of precipitates at the grain boundary, material A, dark field; reflection  $(2\ -2\ 4)_{M_{23}C_6}$  was used for the dark-field display



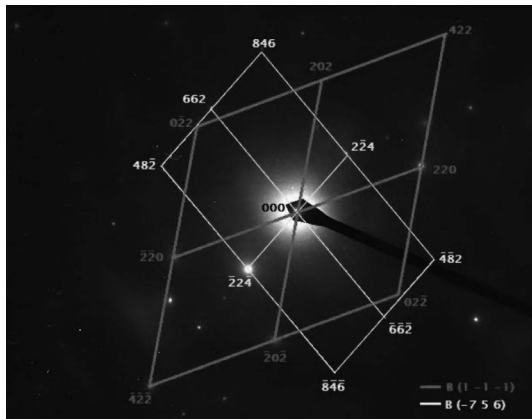


Figure 13: Point diffraction spectra – phase  $\gamma$  and  $M_{23}C_6$  carbide

in Figure 14. Other precipitates were not identified, which does not exclude their presence in Material B.

From the results of the EDX analysis (Figure 15, Table 3) of the observed precipitates in Material B, the presence of MC and  $M_6C$  carbides is also possible.

Figures 16a to 16b document details of straight boundaries and precipitates at the grain boundary in material B on the foils. It can be noticed that the secondary particles extracted at the grain boundaries have a polyhedral or rectangular shape, and none of the observed particles copies the shape of the boundary. The size of these precipitates is in range of 100–200 nm.

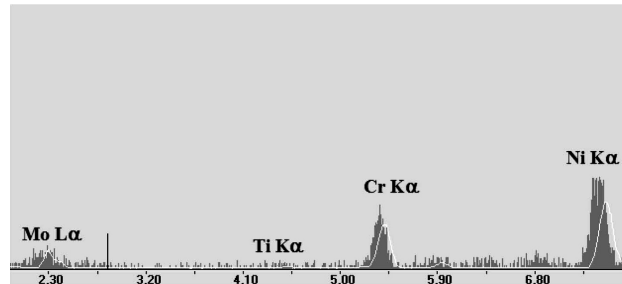
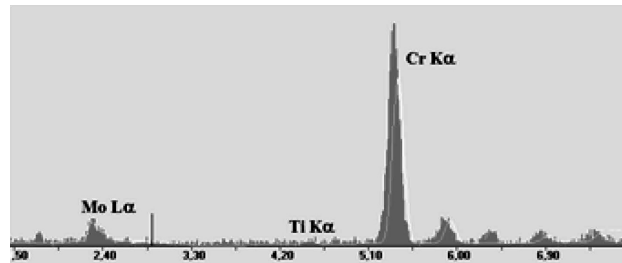


Figure 15: Typical EDX spectra of precipitates in material B: a)  $M_{23}C_6$  carbide, b)  $M_6C$  carbide

Table 3: Approximate chemical composition of carbides in material B

	$M_{23}C_6$		MC		$M_6C$	
	Avr. (w/%)	$\sigma$	Avr. (w/%)	$\sigma$	Avr. (w/%)	$\sigma$
Mo	27.3	$\pm 6.4$	62.9	$\pm 5.6$	24.6	$\pm 3.2$
Ti	4.3	$\pm 4.9$	25.0	$\pm 4.7$	4.1	$\pm 1.8$
Cr	61.7	$\pm 9.4$	10.5	$\pm 3.5$	26.0	$\pm 3.1$
Ni					42.6	$\pm 5.1$

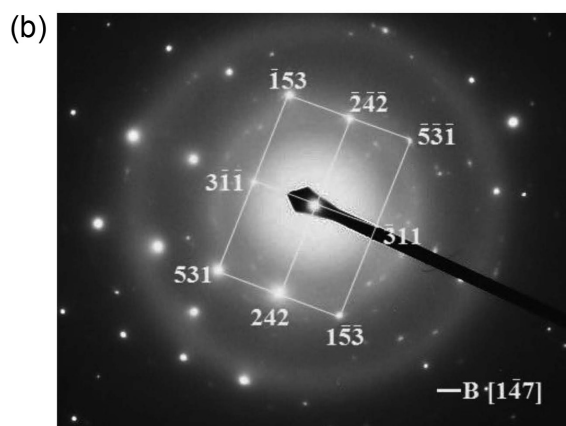
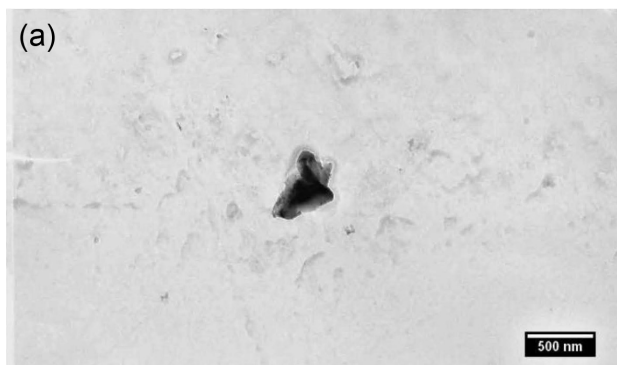


Figure 14: Extracted small particle of an irregular shape at the grain boundary, material A; b) point diffraction spectra of  $M_{23}C_6$  carbide

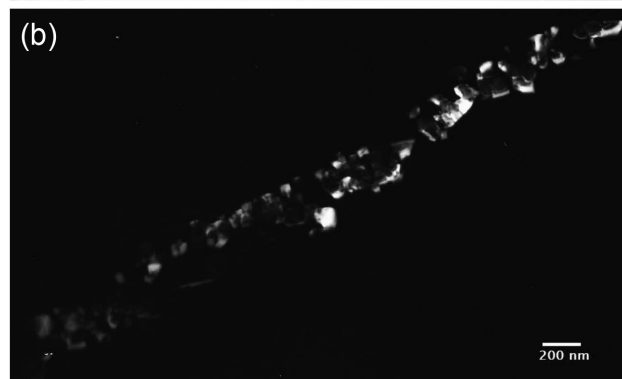
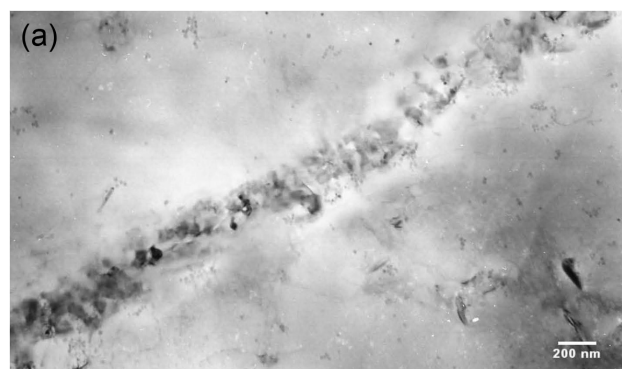


Figure 16: Detail of straight grain boundary, material B, bright field; b) detail of precipitates at the grain boundary, material B, dark field; reflection  $(5 -1 -3)_{M_{23}C_6}$  was used for the dark-field display

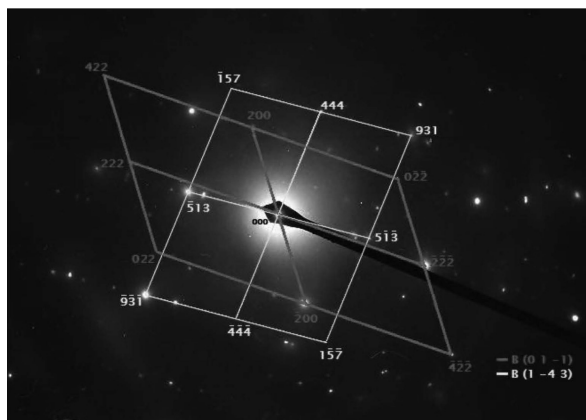


Figure 17: Point diffraction spectra – phase  $\gamma$  and  $M_{23}C_6$  carbide

From the diffraction spectra (Figure 17), secondary particles at the grain boundaries were identified as  $M_{23}C_6$  carbide. No relationship between the matrix and precipitate was observed in all the diffraction spectra in material B.

#### 4 CONCLUSION

To study the serration and precipitates at the grain boundaries and identify secondary particles in Alloy 263, both SEM and TEM were used in the research. To form serrated grain boundaries, material A was heat treated under special conditions, based on the studies from the literature. Material A was compared with material B, which underwent the conventional heat treatment based on the material list for Alloy 263. The experimental results can be summarized as follows:

- Serrated and straight grain boundaries were observed in material A. Approximately 39 % of the observed boundaries were serrated. In material B, only straight grain boundaries were observed.
- In both cases, precipitates at the grain boundaries were identified as carbide  $M_{23}C_6$  using electron diffraction. In material A, carbide MC was also observed.
- The EDX analysis revealed three types of carbides, based on their chemical compositions, in both materials: MC,  $M_6C$  and  $M_{23}C_6$ .
- Electron diffraction also revealed the orientation relationship between the matrix and the precipitate at the serrated grain boundaries:  $\{200\}_{\gamma} \{200\}_{M_{23}C_6}$ . No orientation relationship was observed at the straight grain boundaries.

#### Acknowledgments

The authors wish to thank the financial support of the Slovak Republic Scientific Grant Agency (VEGA) within Grant No. 1/0402/13.

#### 5 REFERENCES

- <sup>1</sup> P. J. Maziasz, I. G. Wright, J. P. Shingledecker, T. B. Gibbons, R. R. Romanosky, Defining the materials issues and research needs for ultra-supercritical steam turbines, Proc. 4<sup>th</sup> Inter. Conf. Advances in Materials Technology for Fossil Power Plants, Hilton Head Island, USA, 2005, 602–622
- <sup>2</sup> R. J. Campbell, Increasing the Efficiency of Existing Coal-Fired Power Plants, <https://fas.org/sgp/crs/misc/R43343.pdf>, 14.06.2017
- <sup>3</sup> G. Stein-Brzozowska, D. M. Flórez, J. Maier, G. Scheffknecht, Nickel-base superalloys for ultra-supercritical coal-fired power plants: Fireside corrosion. Laboratory studies and power plant exposures, Fuel, 108, (2013), 521–533, doi:10.1016/j.fuel.2012.11.081
- <sup>4</sup> A. K. Koul, G. H. Gessinger, On the mechanism of serrated grain boundary formation in Ni-based superalloys, Acta Metallurgica, 31, (1983) 7, 1061–1069, doi:10.1016/0001-6160(83)90202-X
- <sup>5</sup> H. L. Danflou, M. Marty, A. Walder, Formation of serrated grain boundaries and their effect on the mechanical properties in a P/M nickel base superalloy, Proc. 7<sup>th</sup> Inter. Symp. on Superalloys, Seven Springs Mountain, USA, 1992, 63–72, doi:10.7449/1992/ Superalloys\_1992\_63\_72
- <sup>6</sup> R. J. Mitchell, H. Y. Li, Z. W. Huang, On the formation of serrated grain boundaries and fan type structures in an advanced polycrystalline nickel-base superalloy, Journal of Materials Processing Technology, 209 (2009) 2, 1011–1017, doi:10.1016/j.jmatprotec.2008.03.008
- <sup>7</sup> C. L. Qiu, P. Andrews, On the formation of irregular-shaped gamma prime and serrated grain boundaries in a nickel-based superalloy during continuous cooling, Materials Characterization, 76 (2013), 28–34, doi:10.1016/j.matchar.2012.11.012
- <sup>8</sup> A. C. Yeh, K. W. Lu, C. M. Kuo, H. Y. Bor, C. N. Wei, Effect of Serrated Grain Boundaries on the Creep Property of Inconel 718 Superalloy, Materials Science and Engineering A, 530 (2011), 525–529, doi:10.1016/j.msea.2011.10.014
- <sup>9</sup> D. H. Ping, Y. F. Gu, C. Y. Cui, H. Harada, Grain boundary segregation in a Ni-Fe-based (Alloy 718) superalloy, Materials Science and Engineering A, 456 (2007) 1–2, 99–102, doi:10.1016/j.msea.2007.01.090
- <sup>10</sup> L. Jiang, R. Hu, H. Kou, J. Li, G. Bai, H. Fu, The effect of  $M_{23}C_6$  carbides on the formation of grain boundary serrations in a wrought Ni-based superalloy, Materials Science and Engineering A, 536 (2012), 37–44, doi:10.1016/j.msea.2011.11.060
- <sup>11</sup> Y. S. Lim, D. J. Kim, S. S. Hwang, H. P. Kim, S. W. Kim,  $M_{23}C_6$  precipitation behavior and grain boundary serration in Ni-based Alloy 690, Materials Characterization, 96 (2014), 28–39, doi:10.1016/j.matchar.2014.07.008
- <sup>12</sup> H. U. Hong, I. S. Kim, B. G. Choi, M. Y. Kim, C. Y. Jo, The effect of grain boundary serration on creep resistance in a wrought nickel-based superalloy, Materials Science and Engineering A, 517 (2009) 1–2, 125–131, doi:10.1016/j.msea.2009.03.071
- <sup>13</sup> H. U. Hong, I. S. Kim, B. G. Choi, Y. S. Yoo, C. Y. Jo, On the role of grain boundary serration in simulated weld heat-affected zone liquation of a wrought nickel-based superalloy, Metallurgical and Materials Transactions A, 43 (2012) 1, 173–181, doi:10.1007/s11661-011-0837-2
- <sup>14</sup> H. U. Hong, I. S. Kim, B. G. Choi, Y. S. Yoo, C. Y. Jo, On the Mechanism of Serrated Grain Boundary Formation in Ni-Based Superalloys with Low  $\gamma'$  Volume Fraction, Proc. 12th Inter. Symp. on Superalloys, Seven Springs Mountain, USA, 2012, 53–61, doi:10.1002/9781118516430.ch6
- <sup>15</sup> H. U. Hong, F. H. Latief, T. Blanc, I. S. Kim, B. G. Choi, C. Y. Jo, J. H. Lee, Influence of chromium content on microstructure and grain boundary serration formation in a ternary Ni-xCr-0.1C model alloy, Materials Chemistry and Physics, 148 (2014) 3, 1194–1201, doi:10.1016/j.matchemphys.2014.09.047
- <sup>16</sup> J. C. Zhao, V. Ravikumar, A. M. Beltran, Phase Precipitation and Phase Stability in Nimonic 263, Metallurgical and Materials Transactions A, 32 (2001) 6, 1271–1282, doi:10.1007/s11661-001-0217-4





# FRACTURE TOUGHNESS OF LEDEBURITIC VANADIS 6 STEEL AFTER SUB-ZERO TREATMENT FOR 17 H AND DOUBLE TEMPERING

## LOMNA ŽILAVOST LEDEBURITNEGA JEKLA VANADIS 6 PO TOPLOTNI OBDELAVI S 17-URNIM PODHLAJEVANJEM IN DVOJNIM POPUŠČANJEM

Jana Ptačinová<sup>1</sup>, Peter Jurčí<sup>1</sup>, Ivo Dlouhý<sup>2</sup>

<sup>1</sup>Institute of Materials Science, Faculty of Materials Science and Technology Trnava, Jána Bottu 25, 917 24 Trnava, Slovakia

<sup>2</sup>Institute of Physics of Materials, Academy of Sciences of the Czech Republic, Žitkova 22, 61662 Brno, Czech Republic  
jana.ptacinova@stuba.sk

*Prejem rokopisa – received: 2016-06-20; sprejem za objavo – accepted for publication: 2017-03-01*

doi:10.17222/mit.2016.118

The influence of sub-zero treatment on the fracture toughness of Cr-V ledeburitic steel Vanadis 6 was examined, in comparison with the same material processed without the sub-zero period. The microstructure of the material consists of the matrix and several types of carbides – eutectic carbides (ECs), secondary carbides (SCs) and small globular carbides (SGCs). Small amounts of retained austenite were also present in the microstructure, but only in the untempered or low-temperature tempered steel. Sub-zero treatment increases the amount of small globular carbides. On the other hand, tempering results in a decrease in the population density of these particles. The fracture toughness of conventionally heat-treated steel firstly increases with the tempering, but then it decreases rapidly when the steel is tempered at the temperature of secondary hardening. In the case of the sub-zero treated material, the fracture toughness is correspondingly lower when the material is tempered at low temperatures, but it becomes slightly higher in the temperature range normally used for secondary hardening. Generally, one can say that the fracture toughness follows well the values of the hardness of the material, except in the narrow temperature range in the case of the sub-zero treated steel, where a "window" for a simultaneous enhancement of hardness and toughness exists.

Keywords: ledeburitic steel, sub-zero treatment, fracture toughness, carbides, fracture surface

Avtorji so preučevali vpliv standardne toplotne obdelave v kombinaciji s podhlajevanjem na lomno žilavost Cr-V ledeburitnega jekla Vanadis 6 v primerjavi z enakim materialom brez podhlajevanja. Mikrostruktura materiala sestoji iz matrice in več vrst karbidov – evtektičnih karbidov (angl. ECs), sekundarnih karbidov (angl. SCs), in manjših globularnih karbidov (angl. SGCs). Majhne količine zaostalega avstenita so bile prisotne v mikrostrukturi, vendar le v nepopuščnem ali v nizkotemperaturno-popuščnem jeklu. Podhlajevanje povečuje količino manjših globularnih karbidov. Po drugi strani pa se s popuščanjem zmanjšuje populacijska gostota teh delcev. Lomna žilavost konvencionalno toplotno obdelanega jekla se najprej povečuje s poviševanjem temperature popuščanja vendar se prične hitro zmanjševati (zniževati), ko je prekoračena temperatura sekundarnega utrjevanja. Pri toplotni obdelavi materiala s podhlajevanjem, se lomna žilavost posledično znižuje, ko je le-to popuščeno na nižjih temperaturah, vendar se rahlo povečuje v območju temperature, ki se navadno uporablja za sekundarno utrjevanje. V splošnem je možno reči, da lomna žilavost sledi vrednostim trdote materiala, razen v primeru toplotno obdelanega jekla v kombinaciji s podhlajevanjem, kjer v zelo ozkem temperaturnem intervalu obstaja "temperaturno okno". Tam dosežemo istočasno povečanje žilavosti in trdote.

Ključne besede: ledeburitno jeklo, podhlajevanje, lomna žilavost, karbidi, lomna površina

## 1 INTRODUCTION

In modern tooling, it is necessary that the tool materials have a good wear performance and high hardness, accompanied with at least acceptable toughness. Otherwise the tools might fail very early, before any wear damage can occur.

The toughness of steels quantifies their resistance to the initiation of brittle fracture under given conditions. For real tools made of Cr- and Cr-V ledeburitic steels, the toughness determines their capability to resist either the chipping or a total failure. The toughness, being expressed by the three-point bending strength,  $\sigma_b$ , of brittle ledeburitic steels is the highest when the material is soft-annealed and it decreases as a consequence of the application of heat treatment. However, the higher the

austenitizing temperature ( $T_A$ ), the lower is the toughness and, at a constant  $T_A$ , the tempering first results in an increase in the toughness, which is followed by its decrease at the maximum secondary hardening.<sup>1</sup> Hence, the application of proper heat treatment is a compromise between the requirements for the maximum hardness and at least acceptable toughness.

There is a shortage of literature pertaining to the effect of the sub-zero treatment (SZT) on the toughness. D. N. Collins and J. Dormer reported that the toughness of the AISI D2 steel decreased with an application of the SZT up to the temperature of  $-70\text{ }^{\circ}\text{C}$ , which was followed by a moderate increase in the toughness when a lower processing temperature was used for the SZT.<sup>2,3</sup> It should be noticed here that the samples were low-temperature tempered at  $200\text{ }^{\circ}\text{C}$ .

The fracture toughness ( $K_{IC}$ ) (the resistance against the crack propagation) of the ledeburitic steels can be quantified using either pre-cracked (bend) specimens or chevron-notch technique.<sup>4–6</sup> The fracture toughness of ledeburitic steels is very low, whereas the  $K_{IC}$  values usually follow the three-point bending strength.

The effect of the SZT on the fracture toughness was reported by several groups of investigators. D. Das et al., for instance, pointed out that the SZT carried out at temperatures of (–75, –125 and –196) °C led to a decrease in the fracture toughness compared to conventionally heat-treated samples when low-temperature tempered at 210 °C for 2 h.<sup>6</sup> The variations in the fracture toughness were attributed to the reduction of the retained-austenite amount and to the increase in the population density of SGCs in the microstructure after the SZT. In our recent paper, it was demonstrated that the effect of the SZT on the toughness is marginal, but the effect of this processing on  $K_{IC}$  is rather positive when the material is tempered at the temperature normally used for secondary hardening.<sup>7</sup>

The main goal of the current investigations is to characterize the variations in the toughness and fracture toughness of powder-metallurgy (PM) ledeburitic steel Vanadis 6, as a result of different heat-treatment schedules (austenitizing, sub-zero treatment, tempering) and to relate them to the microstructural alterations, due to these treatments, like the reduction of the retained-austenite amount, increase in the carbide count and others.<sup>8–10</sup>

## 2 MATERIAL AND EXPERIMENTAL METHODS

### 2.1 Material and processing

The experimental material was tool steel Vanadis 6 with nominally 2.1 % C, 1.0 % Si, 0.4 % Mn, 6.8 % Cr, 1.5 % Mo, 5.4 % V and Fe as balance, made with PM. The conventional heat treatment (CHT) consisted of the following steps: heating up the material to the desired  $T_A$  (1050 °C) in a vacuum furnace, holding it at the temperature for 30 min and nitrogen gas quenching (5 bar). One set of samples was processed without the inclusion of the SZT between quenching and tempering, while the other samples were subjected to the SZT carried out at the temperature of –196 °C for 17 h. Double tempering (2 h + 2 h) was performed at temperatures in the range of 100–600 °C.

### 2.2 Experimental methods

Metallographic samples were prepared in the standard way and etched with a picric-acid reagent for the SEM observation. The microstructure was recorded using a JEOL JSM 7600 F device equipped with an EDS detector (Oxford Instruments), at an acceleration voltage of 15 kV. Details of the categorization of the carbides have been published recently.<sup>10,11</sup> Macro-hardness measurements were completed using the Vickers (HV10) method. Five measurements were made on the metallo-

graphic specimens processed with any combination of heat-treatment parameters, and both the mean values and the standard deviations were then calculated. For the fracture-toughness determination, pre-cracked specimens predetermined for bending, with dimensions of 10 mm × 10 mm × 55 mm were used. For the pre-cracking of the samples, four bending fixtures and a resonance frequency machine (Cracktronic 8024) were used, which allowed the fatigue-crack initiation and further propagation through the actual frequency of the cycling to be controlled.

In addition, the crack development was checked on both sides of a sample using digital long-distance microscopic methods. Both the pre-crack preparation and bend tests were carried out at room temperature according to the ISO12137 standard.<sup>12</sup> For the test, an Instron 8862 machine was used and a loading rate of 0.1 mm/min was applied. Specimen deflection was measured by means of an inductive transducer integrated directly into the loading axis. In total, five samples were tested for each investigated condition. Fracture-surface morphology was investigated with a scanning electron microscope JEOL JSM 7600F with an EDS detector (Oxford Instruments). The topography of fracture surfaces was studied with a confocal laser scanning microscope Zeiss LSM 700. Three-dimensional topographical resolution was achieved using the ZEN 2009 software.

## 3 RESULTS AND DISCUSSION

### 3.1 Microstructure

SEM micrographs, **Figure 1**, show an example of the microstructure evolution of the material after the sub-zero treatment in liquid nitrogen (for 17 h) and tempering at different temperatures. The microstructure after the sub-zero treatment consists of a matrix made of martensite, a small amount of retained austenite and carbides (**Figure 1a**). As expected, the character of the matrix microstructure changes with increasing tempering temperature (**Figures 1b to 1f**). Due to the tempering, the martensite becomes more sensitive to the etching agent (the so-called tempered martensite). This is a commonly known fact and it is related to the precipitation of carbides during tempering. Retained austenite is transformed into martensite. The portion of carbides is also changed due to the tempering. The volume fractions of both eutectic carbides and secondary carbides are invariant over the range of the heat-treatment parameters used in the experiments. The population density of the small globular carbides increased with the application of the sub-zero treatment, but rapidly decreased with the increasing temperature of the tempering (**Figure 2**).

### 3.2 Hardness characteristics

The bulk hardness of the non-SZT and SZT Vanadis 6 steel, as a function of the tempering temperature, is

shown in **Table 1**. The as-quenched hardness of the conventionally heat-treated steel that was not tempered was  $838 \pm 4.33$  HV10. The hardness of the SZT steel soaked in liquid nitrogen for 17 h and not tempered was correspondingly higher, e.g.,  $917 \pm 7.58$  HV10. These results show that the as-quenched bulk hardness of the Vanadis 6 steel was improved due to the sub-zero treatment. The hardness of all the samples then decreases with the increasing tempering temperature. Here it is interesting that the hardness of the SZT steel remains higher up to the tempering temperature of 450 °C and then it drops more intensely than that of the conventionally quenched samples. As a result, the hardness of the specimens tempered in the range of the temperatures commonly used for secondary hardening is lower for the SZT steel than for the steel achieved after conventional quenching and tempering.

### 3.3 Evaluation of the SZT effect on the fracture toughness

The fracture toughness vs. heat treatment schedules are presented in **Figure 3a** (CHT) and **Figure 3b** (SZT). In the case of the CHT, the fracture toughness of the untempered material was measured to be  $16.4 \text{ MPa m}^{1/2}$  and it firstly increased, due to the tempering, to  $19.6 \text{ MPa m}^{1/2}$  with a subsequent slight decrease; however, the decrease in the fracture toughness markedly accelerated, at the temperature normally used for secondary hardening, to a value of  $14.8 \text{ MPa m}^{1/2}$ . For the material subjected to the SZT in liquid nitrogen for 17 h, the fracture toughness before tempering was  $13.3 \text{ MPa m}^{1/2}$

(i.e., lower than that of the CHT steel). Then, the fracture toughness increased with the tempering temperature to more than  $15 \text{ MPa m}^{1/2}$  and just slightly decreased at a tempering temperature of 450 °C. It is interesting that the  $K_{IC}$  values were higher for the SZT steel than for the CHT steel at the temperature of secondary hardening (530 °C).

**Table 1:** Hardness of the Vanadis 6 ledeburitic steel

Tempering of samples	CHT		SZT	
	HV10	±	HV10	±
untempered	838	4.3	917	7.6
tempered at 170 °C	784	3.7	870	5.4
tempered at 330 °C	736	7	851	15.7
tempered at 450 °C	724	3	816	7.8
tempered at 530 °C	758	5.9	701	3

The behaviour of fracture toughness vs. heat treatment schedules can be classified as logical because one can expect higher  $K_{IC}$  at lower hardness and lower  $K_{IC}$  at elevated hardness. In other words, the application of the SZT decreases  $K_{IC}$  when the steel is low-temperature tempered. This fact should be considered by toolmakers and users of tools in all the cases when they expect an increase in the wear resistance due to a high hardness resulting from the sub-zero treatment. A very interesting fact was found for the material tempered at the temperature of secondary hardening –  $K_{IC}$  was higher for the SZT material. This is in good agreement with the recently published results where a similar tendency was found for the same SZT steel treated for 4 h and 10 h.<sup>7</sup> One can say that this kind of  $K_{IC}$  behaviour can be expected because of the lower hardness of the SZT steel when tempered in this temperature range; however, in the mentioned paper, it was also found that the increase of  $K_{IC}$  is accompanied with a better wear performance of the material, due to the presence of a higher amount of carbides. The enhanced number of carbides, compared to the material after the conventional quenching, was also identified in the current work. Hence, one can expect that a sub-zero treated material would have a better wear performance, too. These results are also interesting from

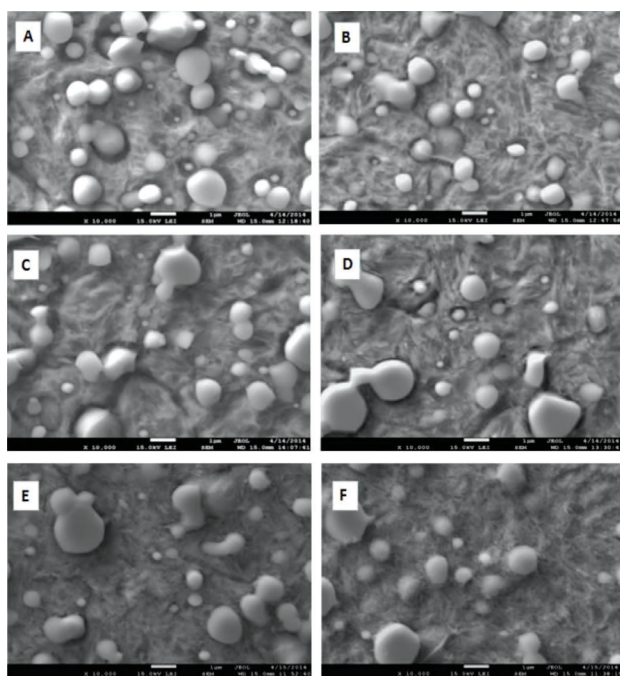


**Figure 1:** SEM micrographs showing the microstructure of Vanadis 6 ledeburitic steel: a) after quenching, subsequent SZT and b) tempering at 170 °C, c) 330 °C, d) 450 °C, e) 530 °C, f) 600 °C

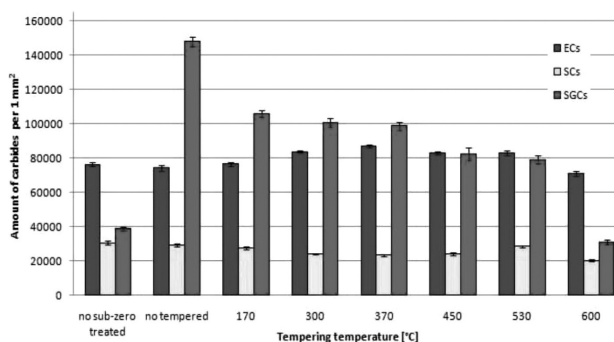


**Figure 2:** Amount of carbides in the Vanadis 6 steel after conventional quenching, SZT for 17 h and SZT and subsequent tempering at different temperatures



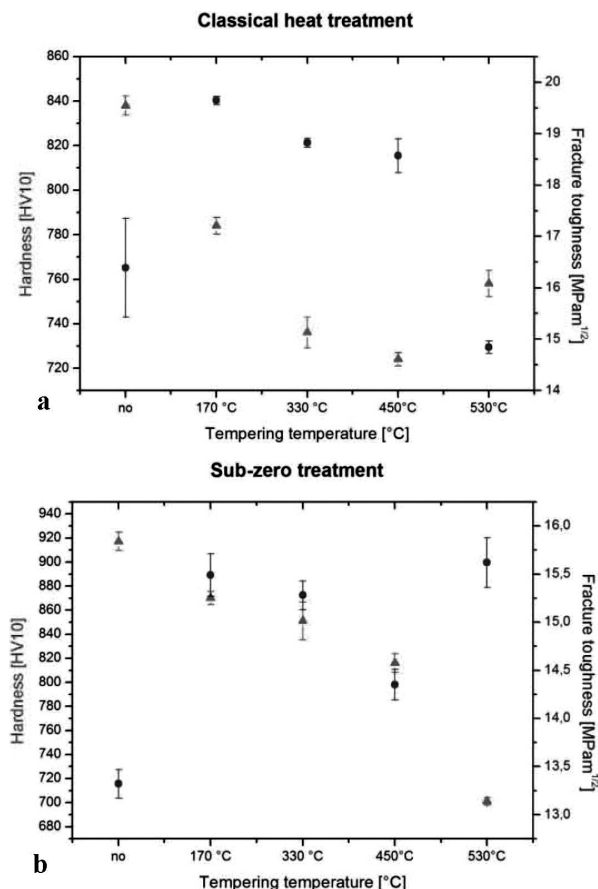


**Figure 3:** Hardness HV10 and fracture toughness  $K_{IC}$  of Vanadis 6 steel in dependence on the heat treatment applied: a) conventional quenching, b) sub-zero treatment

the point of view of industrial practice. They indicate that it is possible to increase the wear performance, along the toughness, of the material in a certain tempering-temperature range.

### 3.4 Fracture-surface morphology

The micro-mechanics of fracture propagation is demonstrated through representative SEM micrographs showing how the fractures appear in the cases of the steel that was sub-zero treated at  $-196\text{ °C}$  for 17 h and not

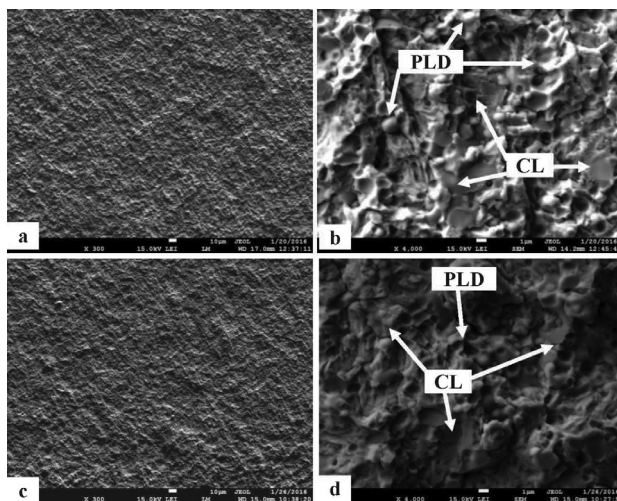


**Figure 4:** Representative SEM micrographs of the fracture surfaces of the specimens processed with: a) b) SZT at  $-196\text{ °C}$  for 17 h and tempered at  $170\text{ °C}$  and c) d) SZT at  $-196\text{ °C}$  for 17 h and not tempered

tempered (the lowest  $K_{IC}$ ) and the steel that was sub-zero treated at  $-196\text{ °C}$  for 17 h and tempered at  $170\text{ °C}$  (higher  $K_{IC}$ ). The fracture surface of the sample that was not tempered and the one that was tempered at  $170\text{ °C}$  are shown in **Figure 4**.

At first glance, there is not any difference between the mentioned fracture surfaces; they appear flat and shiny, **Figures 4a** and **4c**. However, a more detailed observation, at higher magnifications, makes it clear that the fracture surface of the sample after low-temperature tempering contains an enhanced number of sites with micro-plastic deformation (PLD), located mainly at the carbide/matrix interfaces, **Figure 4b**. On the other hand, there are very few such sites on the fracture surface of the untempered specimen, **Figure 4d**, and the fracture surface contains a number of cleavage facettes/regions (CL).

The topographies of the fracture surfaces of the CHT Vanadis 6 steel tempered at  $170\text{ °C}$  and sub-zero treated, and the untempered one, expressed with surface roughness  $R_a$  are shown in **Table 2** and **Figure 5**. The average roughness of the fracture surface of the conventionally quenched steel tempered at  $170\text{ °C}$  was  $4.2703 \pm 0.248\text{ mm}$ .

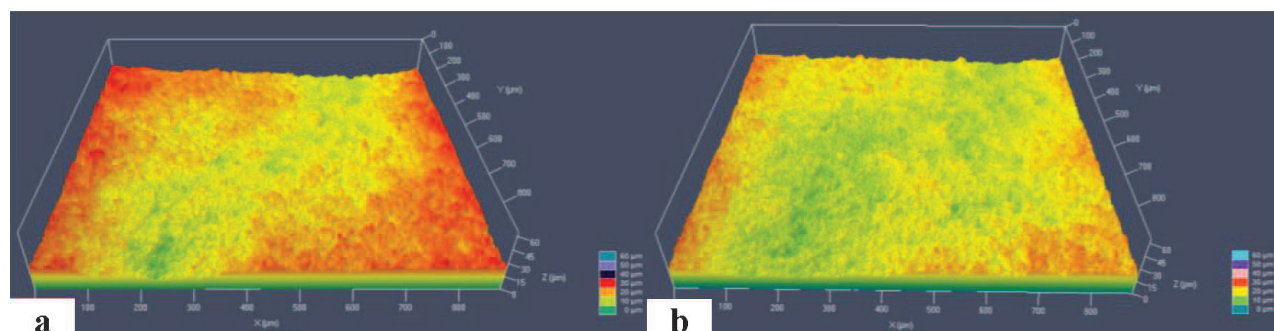


**Figure 5:** Confocal-microscope micrographs showing the fracture surfaces of  $K_{IC}$  specimens: a) CHT and tempered at  $170\text{ °C}$ , b) SZT and not tempered

The roughness of the sub-zero treated and untempered Vanadis 6 steel was lower, i.e.,  $2.918 \pm 0.323 \mu\text{m}$ . At this point, it should be noted that in this stage of experimental efforts, only the materials with the highest  $K_{IC}$  and the one with the lowest  $K_{IC}$  were checked with confocal microscopy. However, the measurements gave unambiguous differences in the roughness, where the higher roughness corresponded to the higher  $K_{IC}$ , i.e., to the conventionally quenched and low-temperature tempered sample.

**Table 2:** Roughness of the fracture surface of Vanadis 6 ledeburitic steel

No. of measurement	Tempered at 170 °C	SZT and untempered
1.	4.136	2.591
2.	4.750	3.507
3.	3.925	2.656
$R_a (\mu\text{m})$	$4.2703 \pm 0.248$	$2.918 \pm 0.323$

## 4 CONCLUSIONS

The main conclusions based on the presented results are as follows:

- Sub-zero treatment reduces the amount of retained austenite and increases the population density of small globular carbides in the microstructure.
- The amount of small globular carbides decreases with the application of tempering treatment. The higher the tempering temperature, the more significant is the reduction of the carbide count.
- The hardness of the sub-zero treated material is higher than that of the conventionally quenched one. Also, this tendency is preserved when steel is low-temperature tempered.
- On the other hand, the hardness of the conventionally quenched steel becomes higher than that of the SZT one when tempered at the temperature of secondary hardening.
- The fracture toughness is generally higher for the conventionally quenched steel Vanadis 6 except in the case when the material is tempered to the secondary hardness. One can conclude that  $K_{IC}$  follows the reciprocal value of the hardness, i.e., the harder the material the lower is the fracture toughness.
- The differences in  $K_{IC}$  are reflected in the topographies of the fracture surfaces, represented by the

surface roughness – the higher the fracture toughness, the higher is the roughness of the fracture surface.

## Acknowledgements

This paper is the result of implementing project CE for development and application of advanced diagnostic methods in processing of metallic and non-metallic materials, ITMS: 26220120048, supported by the Research & Development Operational Programme funded by the ERDF. This research was supported by the grant project VEGA 1/0735/14.

## 5 REFERENCES

- <sup>1</sup> P. Jurči, Cr-V Ledeburitic Cold-Work Tool Steels, *Mater. Tehnol.*, 45 (2011) 5, 383–394
- <sup>2</sup> D. N. Collins, Cryogenic treatment of tool steels, *Advanced Materials and Processes*, 12 (1998), 24–29
- <sup>3</sup> D. N. Collins, J. Dormer, Deep Cryogenic Treatment of a D2 Cold-Work Tool Steel, *Heat Treatment of Metals*, 24 (1997) 3, 71–74
- <sup>4</sup> H. Berns, C. Bröckmann, Fracture of Hot Formed Ledeburitic Chromium Steels, *Engineering Fracture Mechanics*, 58 (1997), 311–325, doi:10.1016/S0013-7944(97)00118-5
- <sup>5</sup> I. Dlouhý, M. Holzmann, J. Valka, Using chevron notched specimens for determining fracture toughness of bearing steels, *Kovove materiály/Metallic materials*, 32 (1994), 3–13
- <sup>6</sup> D. Das, R. Sarkar, A. K. Dutta, K. K. Ray, Influence of sub-zero treatments on fracture toughness of AISI D2 steel, *Materials Science and Engineering, A* 528 (2010), 589–603, doi:10.1016/j.msea.2010.09.057
- <sup>7</sup> J. Sobotová, P. Jurči, I. Dlouhý, The effect of subzero treatment on microstructure, fracture toughness and wear resistance of Vanadis 6 tool steel, *Materials Science and Engineering, A* 652 (2016), 192–204, doi:10.1016/j.msea.2015.11.078
- <sup>8</sup> K. Amini, A. Akhbarizadeh, S. Javadpour, Investigating the effect of holding duration on the microstructure of 1.2080 tool steel during the deep cryogenic treatment, *Vacuum*, 86 (2012), 1534–1540, doi:10.1016/j.vacuum.2012.02.013
- <sup>9</sup> D. Das, A. K. Dutta, K. K. Ray, Sub-zero treatments of AISI D2 steel: Part I, Microstructure and hardness, *Materials Science and Engineering, A* 527 (2010), 2182–2193, doi:10.1016/j.msea.2009.10.070
- <sup>10</sup> P. Jurči, M. Dománková, L. Čaplovič, J. Ptačinová, J. Sobotová, P. Salabová, O. Prikner, B. Šuštaršič, D. Jenko, Microstructure and hardness of sub-zero treated and untempered P/M Vanadis 6 ledeburitic tool steel, *Vacuum*, 111 (2015), 92–101, doi:10.1016/j.vacuum.2014.10.004
- <sup>11</sup> P. Bílek, J. Sobotová, P. Jurči, Evaluation of the Microstructural Changes in Cr-V Ledeburitic Tool Steel Depending on the Austenitization Temperature, *Mater. Tehnol.*, 45 (2011), 489–493
- <sup>12</sup> ČSN EN ISO 12137: 2010 – Metallic materials – determination of plane strain fracture toughness, European Committee for Standardization, Brussels



ELECTRONIC AND OPTICAL PROPERTIES OF THE SPINEL OXIDES  $\text{Mg}_x\text{Zn}_{1-x}\text{Al}_2\text{O}_4$  BY FIRST-PRINCIPLES CALCULATIONSELEKTRONSKE IN OPTIČNE LASTNOSTI SPINELNIH OKSIDOV  $\text{Mg}_x\text{Zn}_{1-x}\text{Al}_2\text{O}_4$ , IZPELJANE IZ TEORETIČNIH OSNOVChao Xiang<sup>1</sup>, Jianxiong Zhang<sup>1</sup>, Yun Lu<sup>2</sup>, Dong Tian<sup>3</sup>, Cheng Peng<sup>1</sup><sup>1</sup>Yangtze Normal University, School of Mechanical and Engineering, Fuling 408000, China<sup>2</sup>Chiba University, Institute of Material Science and Engineering, Chiba 2790000, Japan<sup>3</sup>Kunming University of Science and Technology, Faculty of Science, Kunming 650093, China  
1254618608@qq.com

Prejem rokopisa – received: 2016-10-07; sprejem za objavo – accepted for publication: 2017-02-10

doi:10.17222/mit.2016.296

The structural, electronic and optical properties of perfect  $\text{Mg}_x\text{Zn}_{1-x}\text{Al}_2\text{O}_4$  oxides have been studied by first-principles calculations within the generalized gradient approximation of the density functional theory. It is interesting to note that a linear increase of cell volume ( $V$ ) with increasing doping amount ( $x$ ) occurs. The band gap increases in the series from 3.851 eV to 5.079 eV, which is in agreement with theoretical and experimental values. In addition, a blue shift of the absorption shoulder is observed in the UV region with the increase of  $x$ , as predicted by the imaginary part  $\epsilon_2(\omega)$  of the dielectric function at zero frequency as well as bandgap. This can be explained by the threshold of the electronic transition from O-2p to the empty Mg-3p electron states due to the substitution of Zn with Mg. The real part  $\epsilon_1(\omega)$  of the dielectric function located at zero frequency has a square fit relationship with refractive index  $n(0)$ , which is 1.71–1.77 from  $x=0$  to  $x=1$ . The energy-loss function shows that the replacement of Zn by Mg is responsible for a decrease in the intensity of the sharp peaks. The reflectivity shows that a higher coefficient of reflectivity ( $R(0)$ ) at zero frequency corresponds to a smaller bandgap.

Keywords: electronic transitions, dielectric function, refractive index, adsorption shoulder

Preiskovali smo strukturne, elektronske in optične lastnosti idealnih  $\text{Mg}_x\text{Zn}_{1-x}\text{Al}_2\text{O}_4$  oksidov, izpeljane iz teoretičnih osnov znotraj posplošene gradientne aproksimacije funkcionalne teorije gostote. Opazili smo linearno povečanje celičnega volumna ( $V$ ) z naraščajočo koncentracijo Mg ( $x$ ). Širina prepovedanega pasu narašča od 3.851 eV do 5.079 eV v skladu s teoretičnimi in eksperimentalnimi vrednostmi. Poleg tega ob naraščanju deleža Mg opazimo modri premik dodatnega absorpcijskega vrha v UV območju, kakor napovedujeta vrednosti imaginarnega dela  $\epsilon_2(\omega)$  dielektrične funkcije pri frekvenci 0 in prepovedanega pasu. To je mogoče pojasniti s pragom elektronskega prehoda elektronov iz O-2p v prazen Mg-3p zaradi nadomestitve Zn z Mg. Kvadrat realnega dela  $\epsilon_1(\omega)$  dielektrične funkcije pri frekvenci 0 se ujema z lomnim količnikom  $n(0)$ , ki je 1.71–1.77 za  $x=0$  do  $x=1$ . Funkcija izgube energije, kaže, da zamenjava Zn z Mg povzroča zmanjšanje intenzitete ostrih vrhov. Reflektivnost kaže, da višji koeficient refleksije ( $R(0)$ ) pri frekvenci 0 odgovarja manjši širini prepovedanega pasu.

Ključne besede: prehodi elektronov, dielektrična funkcija, lomni količnik, dodatni absorpcijski vrh

## 1 INTRODUCTION

Spinel oxides with the general chemical formula  $\text{AB}_2\text{O}_4$  have a close-packed, face-centered-cubic structure (space group  $\text{Fd}\bar{3}\text{m}$ ) characterized by two symmetrically distinct polyhedra: a tetrahedron and an octahedron. They are widely used in various fields such as catalysis, gas sensor, semiconductor, biomedical, catalyst carrier, as well as electroluminescent displays owing to their catalytic, physical, structural, electronic and optical properties.<sup>1,2</sup> Among them,  $\text{MgAl}_2\text{O}_4$  and  $\text{ZnAl}_2\text{O}_4$  have high-temperature resistance,<sup>3,4</sup> and they are highly reflective for wavelengths in the ultraviolet (UV) region, which make them candidate materials for reflective optical coating in aerospace applications.<sup>5</sup> In particular,  $\text{MgAl}_2\text{O}_4$  is one of the potential candidates for the full wave band transparent window materials with high transmittance in IR- and visible-wavelength even extending to microwave ranges,<sup>6,7</sup> and it also can be used as lamps and lasers,<sup>8</sup> transparent ceramic material for high-temperature,<sup>9</sup> transparent armor and glass.<sup>10</sup>

Similarly,  $\text{ZnAl}_2\text{O}_4$  can be used as a ceramic material similar to  $\text{MgAl}_2\text{O}_4$ . It can be used as a transparent conductor, optical material and dielectric material,<sup>11,12</sup> and it is suitable for UV photoelectronic applications.<sup>13</sup> Simultaneously, much work has been done on the structural, electronic and optical properties of  $\text{MgAl}_2\text{O}_4$  and  $\text{ZnAl}_2\text{O}_4$  over the past few years.<sup>14–27</sup> The effect of point vacancies on the spectral properties of  $\text{MgAl}_2\text{O}_4$  has been studied by S. L. Jiang et al.<sup>14</sup> They revealed that the absorption peak at 5.3 eV is attributed to the neutral oxygen vacancy  $V_o^0$ , while two peaks at 3.2 eV and 4.75 eV are attributed to the 1+ charged oxygen vacancy  $V_o^{1+}$ . A related mechanism of transparency in  $\text{MgAl}_2\text{O}_4$  nanoceramics prepared by sintering under high pressure and low temperature has been studied by J. Zhang et al.<sup>15</sup>, who suggested that the decrease in the transparency with increasing temperature ( $>700^\circ\text{C}$ ) is therefore a result of the light scattering at large pores. The low-temperature, high-pressure preparation of transparent nanocrystalline  $\text{MgAl}_2\text{O}_4$  ceramics has been investigated by T. C. Lu et



al.,<sup>16</sup> indicating that the nanoceramics are highly transparent even though their relative densities are all less than 99 %, owing to the low or negligible light scattering from the nanosized grains and pores. The optical properties of  $\text{ZnAl}_2\text{O}_4$  nanomaterials obtained by the hydrothermal method have been investigated by Miron and co-workers,<sup>17</sup> demonstrating that the band gap is determined from the absorbance spectra, and it depends strongly on the temperature used for further heating the samples. A first-principles study on structural, electronic and optical properties of spinel oxides  $\text{ZnAl}_2\text{O}_4$ ,  $\text{ZnGa}_2\text{O}_4$  and  $\text{ZnIn}_2\text{O}_4$  has been carried out by F. Zerarga and co-workers,<sup>18</sup> implying that the peaks and structures in the optical spectra are assigned to interband transitions. The fabrication of transparent polycrystalline  $\text{ZnAl}_2\text{O}_4$  – a new optical bulk ceramic – has been investigated by Goldstein and co-workers<sup>19</sup>, who suggested that specimens have a high transparency ( $\text{ILT} \approx 78\%$ ;  $\lambda = 800 \text{ nm}$ ;  $t = 2 \text{ mm}$ ). Plus, the differences in structural, electronic and optical performance between aluminum spinel  $\text{MgAl}_2\text{O}_4$  and  $\text{ZnAl}_2\text{O}_4$  have been presented.<sup>28–30</sup> To the best of our knowledge, the structure, electronic and optical properties of  $\text{Mg}_x\text{Zn}_{1-x}\text{Al}_2\text{O}_4$  ( $0 < x < 1$ ), expressed quantitatively, which is that  $\text{Zn}^{2+}$  of  $\text{ZnAl}_2\text{O}_4$  is replaced by  $\text{Mg}^{2+}$ , has not been investigated. The main aim of this investigation is to study the effect of the replacement of Zn by Mg on the structural, electronic and optical properties of  $\text{ZnAl}_2\text{O}_4$ .

## 2 MODEL AND COMPUTATIONAL DETAILS

In our calculations a 56-atom unit cell was modeled for the investigation of spinel  $\text{Mg}_x\text{Zn}_{1-x}\text{Al}_2\text{O}_4$  in **Figure 1**. All the calculations were performed using the Cambridge Serial Total Energy Package (CASTEP) program,<sup>31</sup> based on density functional theory (DFT).

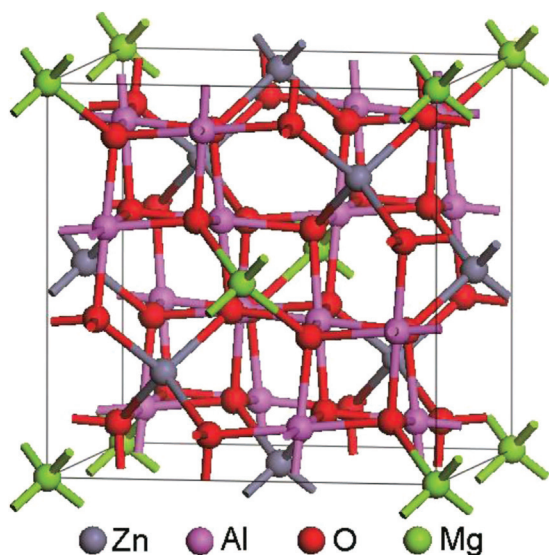


**Figure 1:**  $\text{Mg}_x\text{Zn}_{1-x}\text{Al}_2\text{O}_4$  crystal structure. The gray, pink, green and red represent Zn, Al, Mg and O atoms, respectively.

Electron-ion interaction for cations and anions was described by the ultra-soft pseudo-potential. The Mg-3s and -3p, Zn-3d and -4s, Al-3s and -3p, as well as O-2s and -2p states were treated as valence electrons. The exchange-correlation potential was calculated by the generalized gradient approximation (GGA) developed by the Perdew, Burke, and Ernzerhof functional (PBE).<sup>32</sup> The Engel-Vosko scheme (GGA+U) was applied to electronic properties calculations.<sup>33</sup> The on-site Coulomb Hubbard interaction  $U = 1 \text{ eV}$  is used to treat correctly the localized 3d electrons in the  $\text{Mg}_x\text{Zn}_{1-x}\text{Al}_2\text{O}_4$ . The unit cell was optimized using the Broyden, Fletcher, Goldfarb, Shanno (BFGS) method,<sup>34</sup> and convergence tolerance of energy charge, maximum force and stress were  $1 \times 10^{-5} \text{ eV}$ ,  $0.03 \text{ eV/nm}$ , and  $0.05 \text{ GPa}$ , respectively.<sup>18,35</sup> The plane-wave basis set cutoff energy was set to  $340 \text{ eV}$ .<sup>18,35,36</sup> The Brillouin-zone integration was implemented within Monkhorst-Pack scheme using a  $4 \times 4 \times 4$  mesh to optimize structures and calculate the electronic and optical properties.

## 3 RESULTS AND DISCUSSION

### 3.1 Structure and electronic properties

To obtain the stable structure of  $\text{Mg}_x\text{Zn}_{1-x}\text{Al}_2\text{O}_4$  spinel, the internal coordinates and lattice parameters of crystals were relaxed during geometry optimization. Structure parameters such as average bond lengths, cell volumes and lattice constants are presented, in comparison with the experimental data and values available from other calculations. As can be seen from **Tables 1** and **2**, the calculated equilibrium lattice constants  $a_0$  of both  $\text{ZnAl}_2\text{O}_4$  and  $\text{MgAl}_2\text{O}_4$  are larger than the experimental values with less than 2 % deviation. Plus, substitution of Zn with Mg causes a slight increase in the lattice constant of  $\text{ZnAl}_2\text{O}_4$ . This is in agreement with the previous report.<sup>28</sup> In addition, one can see that the substitution of Zn with Mg is responsible for the formation of the pseudo-cubic, spinel-type structure. The average bond lengths of  $d_{\text{Al-O}}$  increases with increasing doping con-

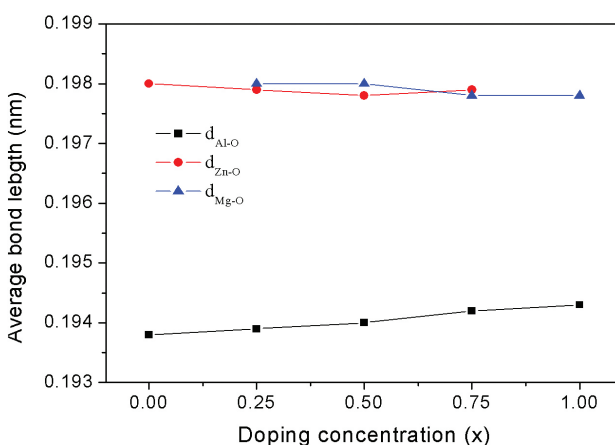


**Figure 2:** Calculated average bond length (nm) of  $\text{Mg}_x\text{Zn}_{1-x}\text{Al}_2\text{O}_4$

centration (from  $x=0$  to  $x=1$ ) in **Figure 2**. In contrast, both  $d_{\text{Zn-O}}$  and  $d_{\text{Mg-O}}$  are nearly unchanged. This suggests that the increase of lattice constants is mostly due to an increase of  $d_{\text{Al-O}}$ . The minimum  $d_{\text{Al-O}}$  in  $\text{MgAl}_2\text{O}_4$  is 0.1938 nm, which indicates that the strength of the chemical bond (Al-O) of  $\text{MgAl}_2\text{O}_4$  is stronger than that of  $\text{Mg}_x\text{Zn}_{1-x}\text{Al}_2\text{O}_4$ . The cell volume ( $V$ ) is listed in **Table 2**. The volume- $x$  curve is plotted, where  $x$  is the concentration of Mg. It is interesting to note that the unit-cell volume ( $V$ ) changes linearly with the doping amount  $x$  (**Figure 3**).

**Table 1:** Calculated structure parameters for  $\text{Mg}_x\text{Zn}_{1-x}\text{Al}_2\text{O}_4$  ( $x=0$ ,  $x=1$ ), experimental measurement and other available theoretical values

	$\text{ZnAl}_2\text{O}_4$			$\text{MgAl}_2\text{O}_4$		
	Present	Expt.	Calc.	Present	Expt.	Calc.
$a_0$ (nm)	0.8194	0.8086 <sup>38</sup>	0.80911 <sup>37</sup>	0.8208	0.806 <sup>45</sup>	0.8032 <sup>18</sup>
			0.8032 <sup>18</sup>			0.80836 <sup>43</sup>
			0.7995 <sup>28</sup>			0.8027 <sup>28</sup>
			0.8193 <sup>39</sup>			0.80844 <sup>44</sup>
			0.80215 <sup>40</sup>			0.81074 <sup>25</sup>
			0.8018 <sup>41</sup>			0.814627 <sup>m</sup>
			0.802 <sup>42</sup>			0.80934 <sup>14</sup>
						0.82 <sup>46</sup>

The calculated band gaps are presented in **Figure 4**. From the figure it is easy to see that the bottom of the conduction band and the top of the valence band for  $\text{Mg}_x\text{Zn}_{1-x}\text{Al}_2\text{O}_4$  occurs at  $\Gamma$  point with a direct band gap. Among them,  $\text{ZnAl}_2\text{O}_4$  ( $x=0$ ) has a band gap value of 3.851 eV, which is very close to the experimental value.<sup>48</sup> The  $\text{MgAl}_2\text{O}_4$  ( $x=1$ ) has a band gap value of 5.079 eV, which is underestimated with respect to the experimental value of 7.8 eV.<sup>49</sup> A similar issue has been addressed in previous theoretical calculations for  $\text{MgAl}_2\text{O}_4$  such as 5.30 eV<sup>14</sup>, 5.1 eV<sup>27</sup> and 5.36 eV.<sup>28</sup> This is mostly due to the fact that the calculated band gaps are related to DFT limitations, not considering the discontinuity in the exchange-correlation potential,<sup>50</sup> as mentioned in <sup>35</sup>. The calculations also show that the band-gap value increases due to changing the cation Zn with Mg. The band gap is 4.078 for  $x=0.25$ , 4.349 for  $x=0.50$  and 4.638 eV for  $x=0.75$ .

As discussed above, the band gap of optimized  $\text{Mg}_x\text{Zn}_{1-x}\text{Al}_2\text{O}_4$  is different (from  $x=0$  to  $x=1$ ). This is attributed to the difference in the density of states (DOS). To further elucidate the nature of the electronic band structure, we calculated the total density of states

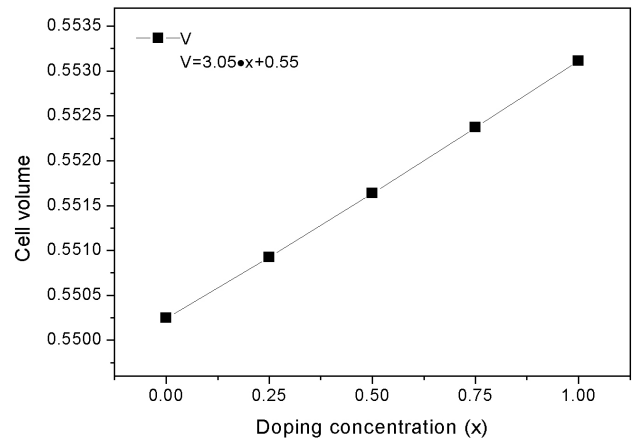


**Figure 3:** Calculated the unit cell volume  $V$  ( $\text{nm}^3$ ) as a function of composition  $x$

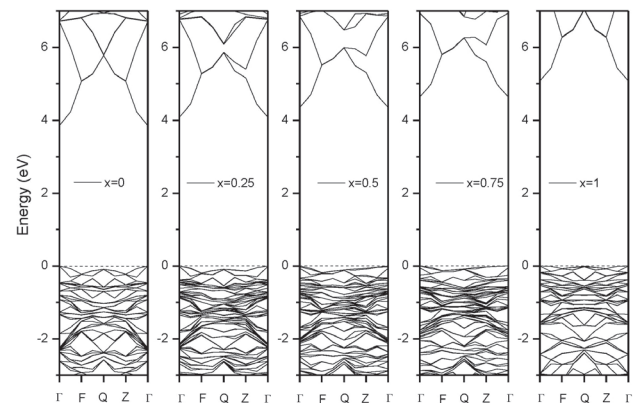


**Figure 4:** Calculated electronic band structure of  $\text{Mg}_x\text{Zn}_{1-x}\text{Al}_2\text{O}_4$  ( $x=0$ ,  $x=0.25$ ,  $x=0.5$ ,  $x=0.75$ ,  $x=1$ )

(DOS) and partial density of states (PDOS) of O, Zn, Mg and Al for the spinel oxides. As can be seen from **Figure 5**, the Fermi level is set to zero. It is mostly created by Zn-3d and O-2p states for  $x=0$ , with small contributions coming from Al-3p, and it is mostly created by Mg-3p and O-2p states for  $x=1$ , with small contributions of Al-3p. The character of the upper valence band is localized between -6.2 eV and 0 eV, which is mainly due to hybridization between the Zn-3d and O-2p states and due less to hybridization of O-2p with Zn-3p, Zn-4s, Mg-3s, Mg-3p, Al-3s and Al-3p as well. The lower valence band in the energy range -18.8 eV to -16.3 eV is

**Table 2:** Calculated structure parameters for  $\text{Mg}_x\text{Zn}_{1-x}\text{Al}_2\text{O}_4$

	0.000			0.250	0.500	0.750	1000		$\text{Al}_2\text{O}_3$
$a(\text{nm})$	0.8194			0.8198	0.8202	0.8205	0.8208		
$b(\text{nm})$	0.8194			0.8197	0.8202	0.8205	0.8208		
$c(\text{nm})$	0.8194			0.8197	0.8199	0.8203	0.8208		
$d_{\text{Zn-O}}(\text{nm})$	0.1980	0.2019 <sup>18</sup>		0.1979	0.1978	0.1979		0.2032 <sup>18</sup>	
$d_{\text{Al-O}}(\text{nm})$	0.1938	0.1963 <sup>18</sup>	0.188 <sup>b</sup>	0.1939	0.1940	0.1942	0.1943	0.19419 <sup>25</sup>	0.192 <sup>47</sup>
$d_{\text{Mg-O}}(\text{nm})$				0.1980	0.1980	0.1978	0.1978	0.19569 <sup>25</sup>	
Volume ( $\text{nm}^3$ )	550.25			0.55092	0.55164	0.55237	0.55312		

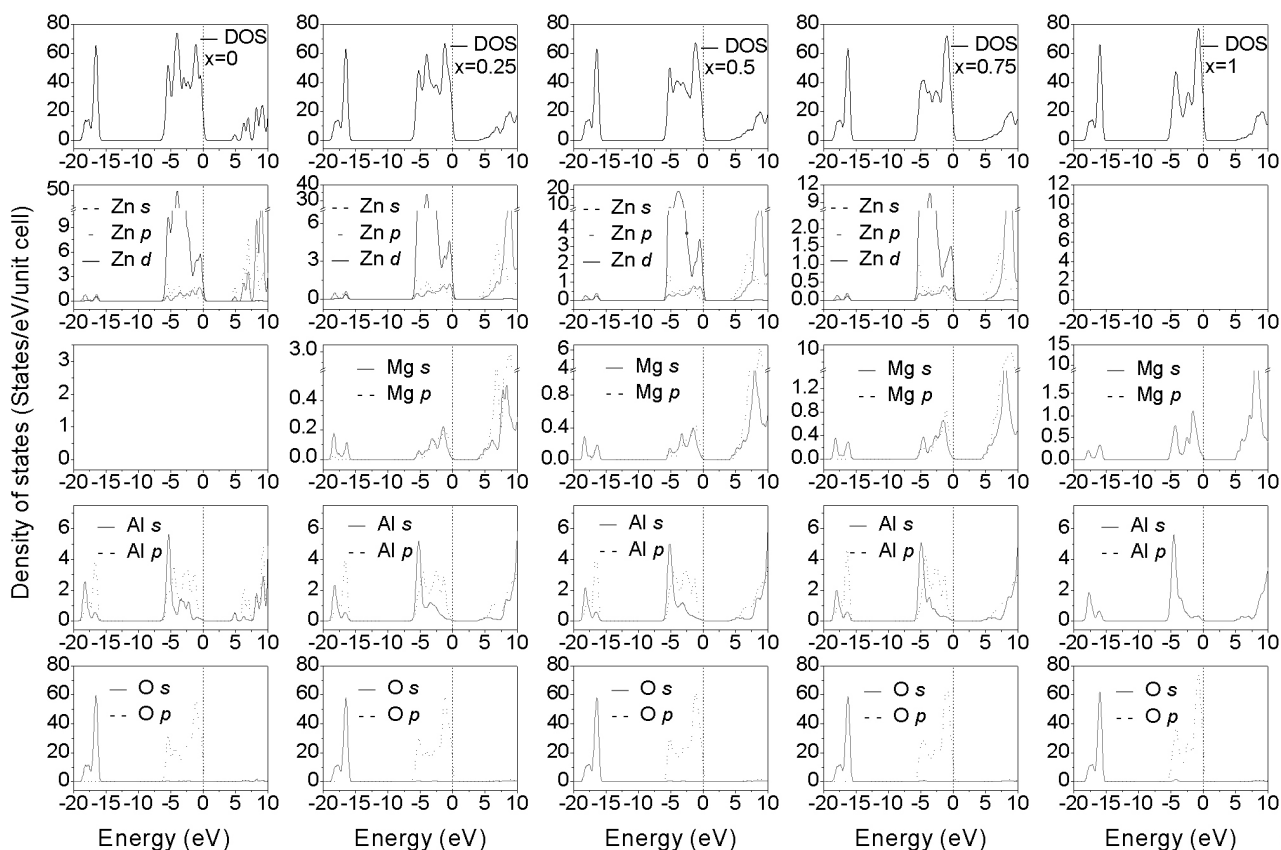


**Figure 5:** Calculated total (DOS) and partial densities (PDOS) of states for  $\text{Mg}_x\text{Zn}_{1-x}\text{Al}_2\text{O}_4$  ( $x=0, x=0.25, x=0.5, x=0.75, x=1$ )

mostly attributed to the O 2s states which split into two: a sharp peak at -17.8 eV and a lower part 2.3 eV wide with double peaks for  $x=0$ . A similar issue appears for  $x=1$ , from which we can see that the lower valence band located at approximately -15.4 eV – -18.1 eV is mostly due to the O 2s states, which split into two: a sharp peak at -16.1 eV and a lower double peak with a width of 2.1 eV. This is in agreement with other theoretical calculations.<sup>14,25</sup> Moreover, we note that Zn-4s and Al-3p states play the main role in the conduction band above the Fermi level (between 3.8 eV and 8.2 eV) for  $x=0$ , while conduction band is mainly created by Mg-3p states for  $x=1$ .

### 3.2 Optical properties

The common response from both electronic and ionic polarization are taken into account in the condition of a low-frequency electric field, although only electronic polarization is considered as the dielectric function, and phonon contributions to the optical is not taken into account, when calculating optical properties in CASTEP package. It is well known that the optical properties are determined considering only direct interband transitions. One of the main optical characteristics of a solid is its dielectric function, which can express other optical properties and describe the optical response of the medium. The dielectric function,  $\varepsilon(\omega)$ , is given in Equation (1):

$$\varepsilon(\omega) = \varepsilon_1(\omega) + \varepsilon_2(\omega) \quad (1)$$

Here  $\varepsilon_1(\omega)$  and  $\varepsilon_2(\omega)$  are the real and imaginary parts of the dielectric function, respectively. The complex  $\varepsilon_2(\omega)$  is defined as Equation (2):<sup>39</sup>

$$\varepsilon_2(\omega) = \frac{2e^2\pi}{V\varepsilon_0} \sum_{k,v,c} \langle \varphi_k^c | \mathbf{u} \cdot \mathbf{r} | \varphi_k^v \rangle^2 \delta(E_k^c - E_k^v - \hbar\omega) \quad (2)$$

where  $V$  is the unit cell volume,  $\mathbf{u}$  is the vector defining the polarization of the incident electric field,  $c$  and  $v$  are the valence band and conduction band, respectively,  $\mathbf{r}$  is the momentum operator, and both  $E_k^c$  and  $E_k^v$  are eigenstates. This expression is similar to Fermi's golden rule for time-dependent perturbations. The  $\varepsilon_2(\omega)$  can be thought of as detailing the real transitions between the unoccupied and occupied electronic states. The imaginary and real parts of the dielectric function are linked by a Kramers-Kronig transform because the dielectric function describes a causal response. Furthermore, the Kramers-Kronig transform is also used to obtain the  $\varepsilon_1(\omega)$ , which is:<sup>18</sup>

$$\varepsilon_1(\omega) = 1 + \frac{2}{\pi} P \int_0^\infty \frac{\omega' \varepsilon_2(\omega')}{(\omega')^2 - \omega^2} d\omega' \quad (3)$$

Both imaginary parts and the real of the dielectric function can also be used to calculate important optical

functions, such as the refractive index  $n(\omega)$  and the reflectivity  $R(\omega)$ .<sup>18</sup>

$$n(\omega) = \left[ \frac{\varepsilon(\omega)}{2} + \frac{\sqrt{\varepsilon_1^2(\omega) + \varepsilon_2^2(\omega)}}{2} \right]^2 \quad (4)$$

$$R(\omega) = \left[ \frac{\varepsilon(\omega)^{0.5} - 1}{\varepsilon(\omega)^{0.5} + 1} \right]^2 \quad (5)$$

The peak of the imaginary part of the dielectric function corresponds to electronic transitions from the valence to conduction bands, depending on the electronic transition energy of the conduction and valence band, i.e., the band-gap energies. The instrumental smearing of 0.3 eV is used to simulate the broadening effects. The dielectric functions for various  $x$  are displayed in **Figure 6**. It can be seen that the first critical point starts at (3.49, 3.61, 3.90, 4.22 and 4.63) eV from  $x=0$  to  $x=1$ . These are known as the edge of the optical absorption. Furthermore, the different widths of the non-zero part of  $\varepsilon_2(\omega)$  are related with different widths of the adsorption spectra, as shown in **Figure 6**, suggesting that absorption region for  $\text{Mg}_x\text{Zn}_{1-x}\text{Al}_2\text{O}_4$  ( $x=0$ ) is wider than that of  $\text{Mg}_x\text{Zn}_{1-x}\text{Al}_2\text{O}_4$  ( $x=1$ ). Other peak locates at (7.38, 10.87, 14.63 and 15.54) eV for  $x=0$ , (7.49, 7.37, 11.65, 12.83 and 14.22) eV for  $x=0.25$ , (6.83, 7.84, 10.31, 12.81 and 15.36) eV for  $x=0.5$ , (5.81, 10.16, 12.85 and 15.85) eV for  $x=0.75$  and (6.25, 7.69, 10.01, 12.91 and 16.16) eV for  $x=1$ , in comparison with other theoretical values listed in **Table 3**. These peaks of origins and features on

the basis of decomposing each spectrum to its individual pair contribution from each pair of valence and conduction bands are obtained by the analysis of  $\varepsilon_2(\omega)$ .<sup>18</sup> The calculated real part of  $\varepsilon_1(\omega)$  in infinite wavelength (i.e., the limit of zero energy) for  $x=0$  is 3.15 and for  $x=1$  is 2.93, which are in agreement with previous theoretical values such as 2.6691 for  $\text{ZnAl}_2\text{O}_4$ <sup>18</sup> and 3.112 for  $\text{MgAl}_2\text{O}_4$ .<sup>25</sup> In addition, the  $\varepsilon_1(\omega)$  in infinite wavelength is 3.09 for  $x=0.25$ , 3.03 for  $x=0.5$ , and 2.98 for  $x=0.75$ , signaling a negative trend with the increase of the doping amount  $x$ . These can also indicate that the real part  $\varepsilon_1(\omega)$  of the limit of zero energy has a square fit relationship with the refractive index  $n$  localized zero energy. The  $\varepsilon_1(\omega)$  reaches a maximum value of 4.22 at about 6.15 eV for  $x=0$ , 4.28 at 8.88 eV for  $x=0.25$ , 4.30 at 8.82 eV for  $x=0.5$ , 4.29 at 8.84 eV for  $x=0.75$  and 4.39 at 8.73 for  $x=1$ .

**Table 3:** The imaginary part ( $\varepsilon_2(\omega)$ ) of dielectric function for  $\text{Mg}_x\text{Zn}_{1-x}\text{Al}_2\text{O}_4$  ( $x=0, x=1$ ).

	$\text{ZnAl}_2\text{O}_4$			$\text{MgAl}_2\text{O}_4$		
	Present	Calc. <sup>18</sup>	Calc. <sup>40</sup>	Present	Calc. <sup>23</sup>	Calc. <sup>25</sup>
Threshold Peak position	3.49	4.31	~4.25	4.63	7.4	
	7.38	7.82	~8.01	6.25		6.27
	10.87	10.98		7.69		7.44
	14.63	14.08		10.01		9.42
	15.54			12.91		10.19

The refractive index and the extinction coefficient are shown in **Figure 7**. One can see that the static refractive

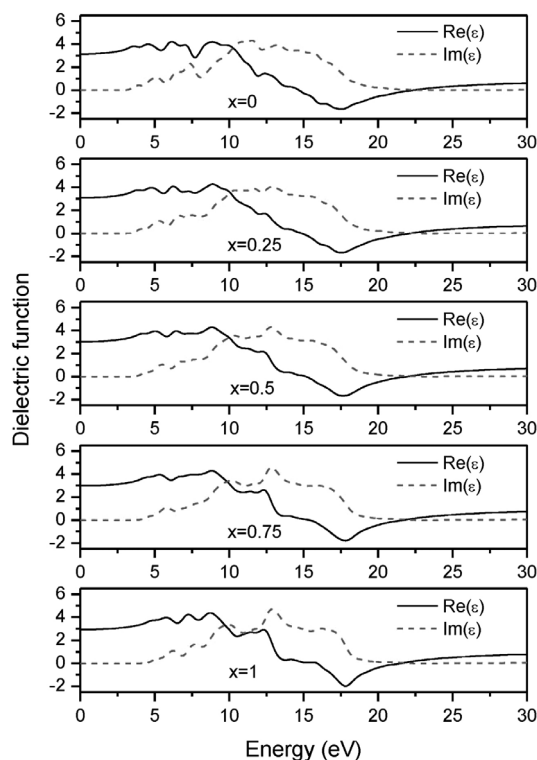


**Figure 6:** Dielectric function of Mg doped ions at different doping concentration

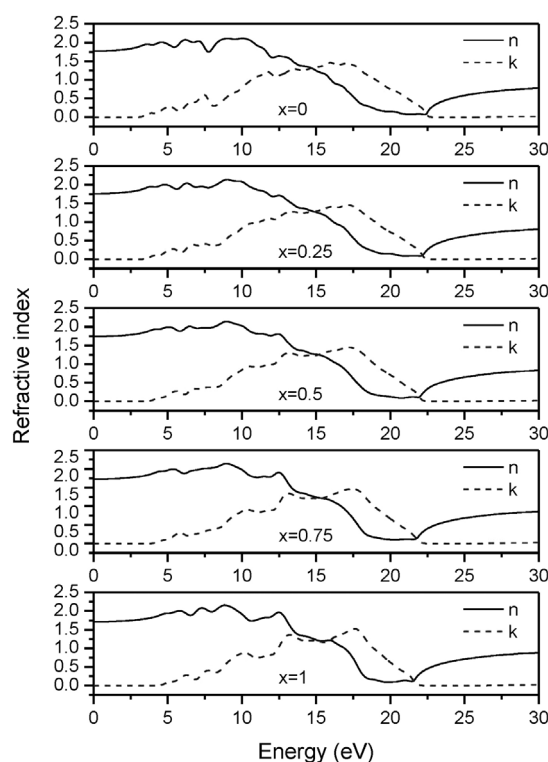


**Figure 7:** Refractive index of Mg doped ions at various doping concentration



index  $n(0)$  at the zero frequency limits is 1.77, 1.76, 1.73, 1.72 and 1.71 from  $x=0$  to  $x=1$ , which are consistent with values derived from the real part  $\varepsilon_1(\omega)$  of the dielectric function mentioned above. They reach a maximum value of 2.12 at 10.05 eV for  $x=0$ , 2.14 at 9.01 eV for  $x=0.25$ , 2.13 at 8.97 eV for  $x=0.5$ , 2.14 at 8.95 eV for  $x=0.75$  and 2.16 at 8.84 eV for  $x=1$ , compared to other theoretical values listed in **Table 4**. We note that the refractive index  $n(0)$  decreases with an increase of  $x$ . It indicates that the  $n(0)$  likely is decided by the bond length of Zn-O, Al-O, Mg-O and the volume of  $\text{Mg}_x\text{Zn}_{1-x}\text{Al}_2\text{O}_4$ .

**Table 4:** Calculated refractive index for  $\text{Mg}_x\text{Zn}_{1-x}\text{Al}_2\text{O}_4$  ( $x=0, x=1$ )

	$n(0)$	$n$	
		Maximum	Energy(eV)
$\text{ZnAl}_2\text{O}_4$			
Present	1.77	2.13	10.15
Calc.	1.63	2.16	10.71
Calc.	1.74		
$\text{MgAl}_2\text{O}_4$			
Present	1.71	2.16	8.84
Calc. <sup>53</sup>	1.61	2.40	11.35
Calc. <sup>25</sup>	1.763		
Expt. <sup>54</sup>	1.71		

The different band structure is responsible for different structure in the optical spectra because the optical spectra originates from the transitions from the top valence band to the bottom conduction band. For instance, a different band gap corresponds to different absorption edge. The relationship between the absorption edge and the band gap is described by Equation (6):

$$\left(\frac{hc}{\lambda}\right)^2 \left(\frac{1}{d}\right)^2 \ln^2\left(\frac{1}{T}\right) = A \left(\frac{hc}{\lambda} - E_g\right) \quad (6)$$

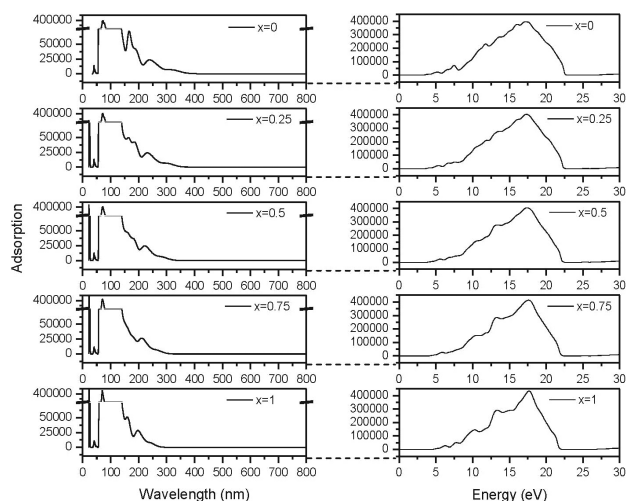


**Figure 8:** Absorption spectra of Mg doped ions at various doping concentration: a) the unit of the vertical axis for absorption spectra is wavelength (nm), b) the unit of abscissa is energy (eV)

where  $\lambda$  is the wavelength,  $T$  is the transmissivity,  $A$  is the transition coefficients of the direct band gap,  $d$  is the thickness and  $E_g$  is the value of the band gap. As shown in **Figure 8a**, it is found that  $\text{Mg}_x\text{Zn}_{1-x}\text{Al}_2\text{O}_4$  ( $x=0$ ) shows an absorption shoulder around 360 nm, which is in agreement with the experimental value. For instance, the optical absorbance spectrum of  $\text{ZnAl}_2\text{O}_4$  was detected in the 250–400 nm region at room temperature,<sup>17</sup> and its adsorption shoulder was also observed in the 290–375 nm wavelength region for the sample calcined at 700 °C.<sup>52</sup>  $\text{Mg}_x\text{Zn}_{1-x}\text{Al}_2\text{O}_4$  ( $x=1$ ) shows an absorption shoulder around 270 nm, meaning that the absorption shoulder undergoes a small blue shift. This is in agreement with the imaginary part  $\varepsilon_2(\omega)$  of the dielectric function, and also suggests that perfect  $\text{MgAl}_2\text{O}_4$  spinel is a transparent crystal, and its transparency is higher than that of  $\text{ZnAl}_2\text{O}_4$  in the visible region. Meanwhile, the absorption shoulder is 340 nm for  $x=0.25$ , 310 nm for  $x=0.50$ , 290 nm for  $x=0.75$  and 270 nm for  $x=1$ . Moreover, as shown in **Figure 8b**, where it seems that the absorption region shifts towards lower energy for  $\text{ZnAl}_2\text{O}_4$  than  $\text{MgAl}_2\text{O}_4$  due to the smaller band gap of the former than the latter, as predicted by the imaginary part of the dielectric function as well as the data derived from Equation (6). The absorption edge starts from about (3.66, 3.95, 4.18, 4.50 and 4.86) eV from  $x=0$  to  $x=1$ . This is mainly attributed to electronic transitions from the O-2p located at the top of the valence band to the empty Zn-4s electron states dominating the bottom of the conduction band for  $x=0$ . Since Zn is replaced by Mg, electronic transitions from O-2p to the empty Mg-3p electron states, yielding an increase in band gap, so that absorption edge starts at higher energy (4.86 eV), due to Mg-3p electron states dominating the bottom of the conduction band for  $x=1$ . Other peaks locates at (7.46, 11.77, 13.80, 16.05 and 17.15) eV for  $x=0$ , (6.75, 7.57, 11.91, 13.63 and 17.30) eV for  $x=0.25$ , (5.61, 13.41 and 17.35) for  $x=0.5$ , (5.85, 10.49, 13.21 and 17.58) eV for  $x=0.75$  and (6.28, 7.76, 10.21, 13.33, 15.11 and 17.66) eV for  $x=1$ , in comparison with other theoretical values listed in **Table 5**.

**Table 5:** The adsorption spectra of perfect  $\text{Mg}_x\text{Zn}_{1-x}\text{Al}_2\text{O}_4$  ( $x=0, x=1$ ).

	$\text{ZnAl}_2\text{O}_4$			$\text{MgAl}_2\text{O}_4$	
	Present	Calc. <sup>18</sup>	Calc. <sup>40</sup>	Present	Calc. <sup>14</sup>
Threshold Peak position	3.66	4.20	~4.31	4.86	~5.05
	7.46	7.83	~8.03	6.28	~6.14
	13.80	14.17		7.76	~7.03
	16.05	16.41		10.21	~10.15
	17.15	17.35		13.33	13.75

The energy-loss function has a large effect on usage of material. For example, the sharper peak of energy loss, explained narrower scope, the better the optical storage efficiency. Besides, energy loss function is an important factor for describing the energy loss of a fast electron traversing in a material, and the prominent

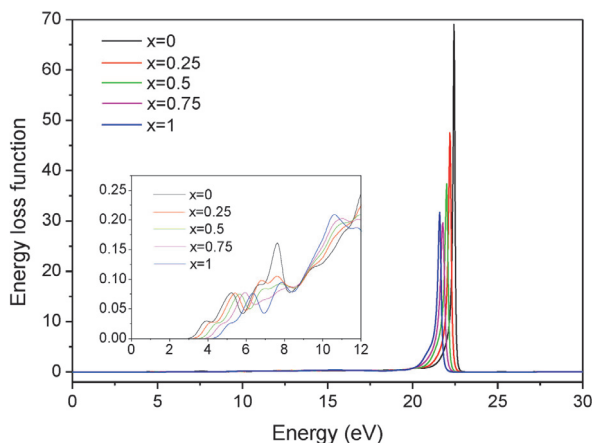


**Figure 9:** Calculated energy loss function of  $\text{Mg}_x\text{Zn}_{1-x}\text{Al}_2\text{O}_4$  obtained from the CASTEP calculations

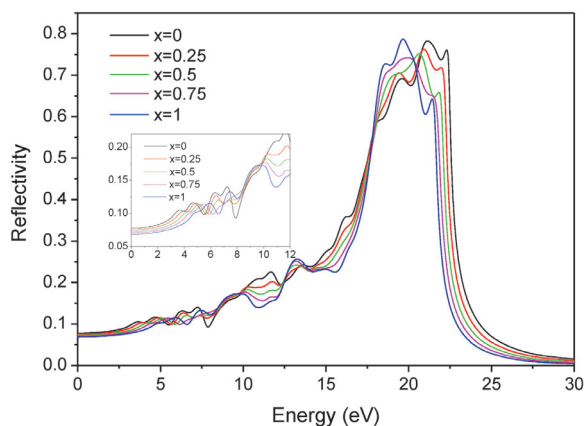


**Figure 10:** Calculated reflection of  $\text{Mg}_x\text{Zn}_{1-x}\text{Al}_2\text{O}_4$  obtained from the CASTEP calculation

peaks in the energy-loss function representing a characteristic associated with the plasma resonance (a collective oscillation of the valence electrons).<sup>51</sup> The energy-loss function is displayed in **Figure 9**. It can be seen that the primary peak emerges at 22.43 eV for  $x=0$  ( $\text{ZnAl}_2\text{O}_4$ ), which is consistent with the theoretical value of 20.99 eV.<sup>18</sup> Additionally, the energy-loss function for  $\text{ZnAl}_2\text{O}_4$  between 0 eV and 12 eV is in agreement with a previous report.<sup>40</sup> Other peaks are located at 22.19 eV for  $x=0.25$ , 22.00 eV for  $x=0.5$ , 21.78 eV for  $x=0.75$  and 21.60 eV for  $x=1$ .

There is close relationship between reflectivity and band gap, i.e., the higher coefficient of reflectivity ( $R(0)$ ) at zero frequency corresponds to a smaller band gap. Additionally, the reflection takes an important role in optical losses. As can be seen from **Figure 10** the high reflectivity localizes between 18.61 eV and 22.32 eV, which is consistent with the energy-loss function mentioned above.

## 4 CONCLUSIONS

The effect of  $\text{Mg}^{+2}$  versus  $\text{Zn}^{+2}$  by comparing the structural, electronic and optical properties of  $\text{Mg}_x\text{Zn}_{1-x}\text{Al}_2\text{O}_4$  (from  $x=0$  to  $x=1$ ) has been implemented using the DFT+U method. The calculations show that the volume of the unit cell changes linearly with increasing Mg-doping amount ( $x$ ). The Al-O bond length of  $\text{Mg}_x\text{Zn}_{1-x}\text{Al}_2\text{O}_4$  increases with  $x$ , suggesting it has a weaker bond stiffness. On the basis of the imaginary parts of the dielectric function, it is found that critical points occur at about 3.49 eV for  $\text{ZnAl}_2\text{O}_4$ , which is lower than that for Mg-doped  $\text{ZnAl}_2\text{O}_4$ , indicating that absorption shoulder undergoes a blue shift in the UV region as evidenced by the absorption spectra. The blue shift is probably due to the electronic transition from O-2p to the empty Mg-3p electron states. For real parts of dielectric function, the limit of zero energy has a square fit relationship with the refractive index ( $n(0)$ ) localized zero energy, which is verified by the reflectivity spectra. Furthermore, the absorbance spectra, reflectivity spectra and the refractive index show that these compounds are suitable for UV reflective coatings. The peak of the energy-loss function shows that  $\text{Mg}_x\text{Zn}_{1-x}\text{Al}_2\text{O}_4$  can be a candidate for optical storage materials.

## Acknowledgment

This work is supported by the project from Chongqing Municipal Education Commission (No. KJ1601218), Young Foundation of Yangtze Normal University (No. 2015XJXM29) and Talent Program of Yangtze Normal University (No. 2015KYQD03).

## 6 REFERENCES

- N. Bouropoulos, I. Tsiaoussis, P. Pouloupoulos, P. Roditis, S. Bakoutas, ZnO controllable sized quantum dots produced by polyol method: an experimental and theoretical study, *Mater. Lett.*, 62 (2008), 3533–3535, doi:10.1016/j.matlet.2008.03.044
- W. S. Tzing, W. H. Tuan, The strength of duplex  $\text{Al}_2\text{O}_3\text{-ZnAl}_2\text{O}_4$  composite, *J. Mater. Sci. Lett.*, 15.16 (1996), 1395–1396, doi:10.1007/BF00275286
- S. A.T. Redfen, R. J. Harrison, H. S. C. O'Neill, D. R. R. Wood, Thermodynamics and kinetics of cation ordering in  $\text{MgAl}_2\text{O}_4$  spinel up to 1600 °C from in situ neutron diffraction, *Amer. Mineral.*, 84.3 (1999), 299–310, doi:10.2138/am-1999-0313
- H. Cynn, S. K. Sharma, T. F. Cooney, M. Nicol, High-temperature Raman investigation of order-disorder behavior in the  $\text{MgAl}_2\text{O}_4$  spinel, *Phys. Rev. B*, 45.1 (1992), 500–502, doi:10.1103/PhysRevB.45.500
- QivaStar. Inc, Ridgecrest. CA, and Hugest Space and Communication CO., El. Segundo, CA, U. S. Pat. N0. 5820669, 1998
- K. P. Surendran, P.V. Bijumon, P. Mohanan, M.T. Sebastian,  $(1-x)\text{MgAl}_2\text{O}_4\text{-}x\text{TiO}_2$  dielectrics for microwave and millimeter wave applications, *Appl. Phys.*, A 81.4 (2005), 823–826, doi:10.1007/s00339-005-3282-5
- P. Fu, W. Z. Lu, W. Lei, Y. Xu, X. H. Wang, J. M. Wu, Transparent polycrystalline  $\text{MgAl}_2\text{O}_4$  ceramic fabricated by spark plasma sintering: Microwave dielectric and optical properties, *Ceram. Int.*, 39.3 (2013), 2481–2487, doi:10.1016/j.ceramint.2012.09.006

- <sup>8</sup> G. Gilde, P. Patel, P. Patterson, D. Blodgett, D. Hahn, Evaluation of hot pressing and hot isostatic pressing parameters on the optical properties of spinel, *J. Am. Ceram. Soc.*, **88.10** (2005), 2747–2751, doi: 10.1111/j.1551-2916.2005.00527.x
- <sup>9</sup> J. G. Li, T. Ikegami, J. H. Lee, T. Mori, Fabrication of translucent magnesium aluminum spinel ceramics, *J. Am. Ceram. Soc.*, **83.11** (2000), 2866–2868, doi:10.1111/j.1151-2916.2000.tb01648.x
- <sup>10</sup> W. Miao, Y. Wu, H. Zhou, W. Han, F. Ru, Low-temperature sintering of AlN ceramics with shock wave treated powder, *Mater. Lett.*, **30.5-6** (1997), 411–414, doi:10.1016/s0167-577x(96)00232-7
- <sup>11</sup> N. J. Van der Laag, M. D. Snel, P. C. M. M. Magusin, G. de With, Structural, elastic, thermophysical and dielectric properties of zinc aluminate ( $\text{ZnAl}_2\text{O}_4$ ), *J. Eur. Ceram. Soc.*, **24.8** (2004), 2417–2424, doi:10.1016/j.jeurceramsoc.2003.06.001
- <sup>12</sup> X. Y. Chen, C. Ma, Spherical porous  $\text{ZnAl}_2\text{O}_4$ :  $\text{Eu}^{3+}$  phosphors: PEG-assisted hydrothermal growth and photoluminescence, *Opt. Mater.*, **32.3** (2010), 415–421, doi:10.1016/j.optmat.2009.10.001
- <sup>13</sup> Y. Wang, Q. Liao, H. Lei, X. P. Zhang, X. C. Ai, J. P. Zhang, K. Wu, Interfacial reaction growth: morphology, composition, and structure controls in preparation of crystalline  $\text{Zn}_x\text{Al}_y\text{O}_z$  nanonets, *Adv. Mater.*, **18.7** (2006), 943–947, doi:10.1002/adma.200502154
- <sup>14</sup> S. L. Jiang, T. C. Lu, J. Zhang, First-principles study on the effects of point vacancies on the spectral properties of  $\text{MgAl}_2\text{O}_4$ , *J. Chen, Solid State Commun.*, **151** (2011), 29–32, doi:10.1016/j.ssc.2010.10.030
- <sup>15</sup> J. Zhang, T. C. Lu, X. H. Chang, N. Wei, W. Xu, Related mechanism of transparency in  $\text{MgAl}_2\text{O}_4$  nano-ceramics prepared by sintering under high pressure and low temperature, *J. Phys. D: Appl. Phys.*, **42** (2009) 052002 (5pp), doi:10.1088/0022-3727/42/5/052002
- <sup>16</sup> T. C. Lu, X. H. Chang, J. Q. Qi, X. J. Luo, Low-temperature high-pressure preparation of transparent nanocrystalline  $\text{MgAl}_2\text{O}_4$  ceramics, *Appl. Phys. Lett.*, **88.21** (2006), 213120, doi:10.1063/1.2207571
- <sup>17</sup> I. Miron, C. Enache, M. Vasile, I. Grozescu, Optical properties of  $\text{ZnAl}_2\text{O}_4$  nanomaterials obtained by the hydrothermal method, *Phys. Scr.*, **T149** (2012) 014064 (3pp), doi:10.1088/0031-8949/2012/T149/014064
- <sup>18</sup> F. Zerarga, A. Bouhemadou, R. Khenata, S. Bin-Omran, Structural, electronic and optical properties of spinel oxides  $\text{ZnAl}_2\text{O}_4$ ,  $\text{ZnGa}_2\text{O}_4$  and  $\text{ZnIn}_2\text{O}_4$ , *Solid State Sci.*, **13.8** (2011), 1638–1648, doi:10.1016/j.solidstatesciences.2011.06.016
- <sup>19</sup> A. Goldstein, Y. Yeshurun, M. Vulfson, H. Kravits, Fabrication of transparent polycrystalline  $\text{ZnAl}_2\text{O}_4$ —a new optical bulk ceramic, *J. Ceram. Soc.*, **95**(2012) 3, 879–882, doi:10.1111/j.1551-2916.2011.05063.x
- <sup>20</sup> S. L. Jiang, T. C. Lu, Y. Long, J. Chen, Ab initio many-body study of the electronic and optical properties of  $\text{MgAl}_2\text{O}_4$  spinel, *J. Appl. Phys.*, **111.4** (2012), 043516, doi:10.1063/1.3686727
- <sup>21</sup> L. Zhang, G. F. Ji, F. Zhao, Z. Z. Gong, First-principles study of the structural, mechanical and electronic properties of  $\text{ZnX}_2\text{O}_4$  ( $X=\text{Al}$ ,  $\text{Cr}$  and  $\text{Ga}$ ), *Chin. Phys. B.*, **20** (2011), 4, doi:10.1088/1674-1056/20/4/047102
- <sup>22</sup> C. Ragupathi, J. J. Vijaya, A. Manikandan, L. J. Kennedy, Phytosynthesis of nanoscale  $\text{ZnAl}_2\text{O}_4$  by using sesamum (*Sesamum indicum* L.) optical and catalytic properties, *J. Nanosci. Nanotechnol.*, **13** (2013) 12, 8298–8306, doi:10.1166/jnn.2013.7922
- <sup>23</sup> M. Arbi, N. Benramdane, Z. Kebbab, R. Miloua, F. Chiker, First principles calculations of structural, electronic and optical properties of zinc aluminum oxide, *Mater. Sci. Semicond. Process.*, **15** (2012) 3, 301–307, doi:10.1016/j.mssp.2012.03.010
- <sup>24</sup> H. Dixit, N. Tandon, S. Cottenier, R. Saniz, D. Lamoens, B. Partoens, V. V. Speybroeck, M. Waroquier, Electronic structure and band gap of zinc spinel oxides beyond LDA:  $\text{ZnAl}_2\text{O}_4$ ,  $\text{ZnGa}_2\text{O}_4$  and  $\text{ZnIn}_2\text{O}_4$ , *New J. Phys.*, **13.6** (2011) 063002 (11pp), doi:10.1088/1367-2630/13/6/063002
- <sup>25</sup> S. M. Hosseini, Structural, electronic and optical properties of spinel  $\text{MgAl}_2\text{O}_4$  oxide, *phys. Status Solidi B* **245.12** (2008), 2800–2807, doi:10.1002/pssb.200844142
- <sup>26</sup> A. Goldstein, Correlation between  $\text{MgAl}_2\text{O}_4$ -spinel structure, processing factors and functional properties of transparent parts (progress review), *J. Eur. Ceram. Soc.*, **32.11** (2012), 2869–2886, doi:10.1016/j.jeurceramsoc.2012.02.051
- <sup>27</sup> D. L. Zhang, X. G. Xu, W. Wang, X. Zhang, H. L. Yang, Y. Wu, C. Z. Ma, Y. Jiang, Electronic structures of new tunnel barrier spinel  $\text{MgAl}_2\text{O}_4$  first-principles calculations, *Rare Metals* **31.2** (2012), 112–116, doi:10.1007/s12598-012-0473-z
- <sup>28</sup> R. Khenata, M. Sahnoun, H. Baltache, M. Réshak, A. H. Reshak, Y. Al-Douri, B. Bouhafs, Full-potential calculations of structural, elastic and electronic properties of  $\text{MgAl}_2\text{O}_4$  and  $\text{ZnAl}_2\text{O}_4$  compounds, *Phys. Lett. A* **344.2** (2005), 271–279, doi:10.1016/j.physleta.2005.06.043
- <sup>29</sup> Y. Y. Jiang, J. W. Zhang, Z. Q. Hu, J. X. Liu, Synthesis and Visible Light Photocatalytic Activity of Spinel  $\text{MAI}_2\text{O}_4$  ( $M=\text{Mg}$ ,  $\text{Zn}$ ,  $\text{Cu}$ ), *Appl. Mech. Mater.* **455** (2014), 99–105, doi:10.4028/www.scientific.net/AMM.455.99
- <sup>30</sup> F. Y. Zhang, Z. Zeng, J. Q. You, The Electronic and Optical Properties of  $\text{Al}_2\text{O}_3$ ,  $\text{MO}$ , and  $\text{MAI}_2\text{O}_4$  ( $M=\text{Zn}$ ,  $\text{Mg}$ ), *J. Nanosci. Nanotechnol.*, doi: 10 (2010), 5475–5478
- <sup>31</sup> M. D. Segall, P. J. D. Lindan, M. J. Probert, C. J. Pickard, P. J. Hasnip, S. J. Clark, M. C. Payne, First-principles simulation: ideas, illustrations and the CASTEP code, *J. Phys-Condens. Mat.*, **14** (2002), 2717–2743, doi:10.1088/0953-8984/14/11/301
- <sup>32</sup> J. P. Perdew, K. Burke, M. Ernzerhof, Generalized gradient approximation made simple, *Phys. Rev. Lett.*, **77.18** (1996), 3865–3868, doi:10.1103/PhysRevLett.77.3865
- <sup>33</sup> E. Engel, S. H. Vosko, Exact exchange-only potentials and the virial relation as microscopic criteria for generalized gradient approximations, *Phys. Rev. B*, **47.20** (1993), 13164, doi:10.1103/PhysRevB.47.13164
- <sup>34</sup> B. G. Pfrommer, M. Côté, S. G. Louie, M. L. Cohen, Relaxation of crystals with the quasi-Newton method, *J. Comput. Phys.*, **131.1** (1997), 233–240, doi:10.1006/jcph.1996.5612
- <sup>35</sup> M. G. Briki, First-principles calculations of electronic, optical and elastic properties of  $\text{ZnAl}_2\text{O}_4$  and  $\text{ZnGa}_2\text{O}_4$ , *J. Phys. Chem. Solids*, **71.10** (2010), 1435–1442, doi:10.1016/j.jpcs.2010.07.007
- <sup>36</sup> A. Bouhemadou, R. Khenata, Pseudo-potential calculations of structural and elastic properties of spinel oxides  $\text{ZnX}_2\text{O}_4$  ( $X=\text{Al}$ ,  $\text{Ga}$ ,  $\text{In}$ ) under pressure effect, *Phys. Lett. A* **360** (2006) 2, 339, A. doi:10.1016/j.physleta.2006.08.008
- <sup>37</sup> D. Errandonea, R. S. Kumar, F. J. Manjón, V. V. Ursaki, E. V. Rusu, Post-spinel transformations and equation of state in  $\text{ZnGa}_2\text{O}_4$ : determination at high pressure by in situ x-ray diffraction, *Phys. Rev. B*, **79.2** (2009), doi:10.1103/PhysRevB.79.024103
- <sup>38</sup> R. J. Hill, J. R. Graig, G. V. Gibbs, Systematics of the spinel structure type, Physics and chemistry of minerals, *Phys. Chem. Miner.*, **4** (1979), 317–339, doi:10.1007/BF00307535
- <sup>39</sup> C. Xiang, H. L. Tan, J. S. Lu, Y. X. Yang, C. L. Ni, First-principles calculations of structural, electronic and optical properties of  $\text{ZnGa}_{1-x}\text{Al}_x\text{O}_4$  spinel-type oxides, *J. Alloys Compd.* **581** (2013), 139–145, doi:10.1016/j.jallcom.2013.05.040
- <sup>40</sup> S. Z. Karazhanov, P. Ravindran, Ab initio study of double oxides  $\text{ZnX}_2\text{O}_4$  ( $X=\text{Al}$ ,  $\text{Ga}$ ,  $\text{In}$ ) having spinel structure, *J. Am. Ceram. Soc.* **93** (2010), 3335–3341, doi:10.1111/j.1551-2916.2010.03864.x
- <sup>41</sup> A. Seko, K. Yuge, F. Oba, A. Kuwabara, I. Tanaka, Prediction of ground-state structures and order-disorder phase transitions in II-III spinel oxides: A combined cluster-expansion method and first-principles study, *Phys. Rev.* **73.18** (2006), 184117, doi:10.1103/PhysRevB.73.184117
- <sup>42</sup> S. López, A. H. Romero, First-principles study of the high-pressure phase transition in  $\text{ZnAl}_2\text{O}_4$  and  $\text{ZnGa}_2\text{O}_4$ : From cubic spinel to orthorhombic post-spinel structures, *Phys. Rev. B*, **79** (2009), 21, doi:10.1103/PhysRevB.79.214103
- <sup>43</sup> N. Kashii, H. Maekawa, Y. Hinatsu, Dynamics of the cation mixing of  $\text{MgAl}_2\text{O}_4$  and  $\text{ZnAl}_2\text{O}_4$  spinel, *J. Am. Ceram. Soc.*, **82** (1999) 7, 1844–1848, doi:10.1111/j.1151-2916.1999.tb02007.x

- <sup>44</sup> A. Navrotsky, B. A. Wechsler, K. Geisinger, F. Seifert, Thermochemistry of  $\text{MgAl}_2\text{O}_4$ - $\text{Al}_2\text{O}_3$  Defect Spinel, *J. Am. Ceram. Soc.*, 69 (1986) 5, 418–422, doi:10.1111/j.1151-2916.1986.tb04772.x
- <sup>45</sup> P. Fischer, Neutronenbeugungsuntersuchung der Strukturen von  $\text{MgAl}_2\text{O}_4$ -und  $\text{ZnAl}_2\text{O}_4$ -Spinellen, in Abhängigkeit von der Vorgesichte, *Z. Krist.-Cryst. Mater.*, 124 (1967) 1–6, 275–302, doi:10.1524/zkri.1967.124.4-5.275
- <sup>46</sup> H. Sukegawa, H. X. Xiu, T. Ohkubo, T. Furubayashi, T. Niizeki, W. H. Wang, S. Kasai, S. Mitani, K. Inomata, K. Hono, Tunnel magnetoresistance with improved bias voltage dependence in lattice-matched Fe/spinel  $\text{MgAl}_2\text{O}_4/\text{Fe}$  (001) junctions, *Appl. Phys. Lett.* 96 (2010) 21, 212–205, doi:10.1063/1.3441409
- <sup>47</sup> R. E. Newnham, Y. M. de Haan, Z. Kristallogr, Refinement of the  $\text{Al}_2\text{O}_3$ ,  $\text{Ti}_2\text{O}_3$ ,  $\text{V}_2\text{O}_3$  and  $\text{Cr}_2\text{O}_3$  structures, *Z. Krist.-Cryst. Mater.*, 117.1–6 (1962), 235–237, doi:10.1524/zkri.1962.117.2-3.235
- <sup>48</sup> S. K. Sampath, J. F. Cordaro, Optical properties of zinc aluminate, zinc gallate, and zinc aluminogallate spinels, *J. Am. Ceram. Soc.*, 81 (1998) 3, 649–654, doi:10.1111/j.1151-2916.1998.tb02385.x
- <sup>49</sup> M. L. Bortz, R. H. French, D. J. Jones, R.V. Kasowski, F. S. Ohuchi, Temperature dependence of the electronic structure of oxides:  $\text{MgO}$ ,  $\text{MgAl}_2\text{O}_4$  and  $\text{Al}_2\text{O}_3$ , *Phys. Scr.* 41 (1990), 537–541, doi:10.1088/0031-8949/41/4/036
- <sup>50</sup> J. P. Perdew, M. Levy, Physical content of the exact Kohn-Sham orbital energies: band gaps and derivative discontinuities, *Phys. Rev. Lett.* 51 (1983) 20, 1884, doi:10.1103/PhysRevLett.51.1884
- <sup>51</sup> M. Fox, *Optical Properties of Solids*. Academic Press, New York, 1972
- <sup>52</sup> S. Mathur, M. Veith, M. Haas, H. Shen, N. Lecerf, V. Huch, Single-Source Sol-Gel Synthesis of Nanocrystalline  $\text{ZnAl}_2\text{O}_4$ : Structural and Optical Properties, *J. Am. Ceram. Soc.* 84 (2001), 1921–1928, doi:10.1111/j.1151-2916.2001.tb00938.x
- <sup>53</sup> B. Amin, R. Khenata, A. Bouhemadou, Iftikhar Ahmad, M. Maqbool, Opto-electronic response of spinels  $\text{MgAl}_2\text{O}_4$  and  $\text{MgGa}_2\text{O}_4$  through modified Becke-Johnson exchange potential, *Phys. B* 407 (2012), 2588–2592, doi: 10.1016/j.physb.2012.03.075
- <sup>54</sup> GEMSELECT, <http://www.gemselect.com/gem-info/spinel/spinel-info.php>, 1.10.2016





SURFACE CHARACTERISTICS OF INVAR ALLOY ACCORDING  
TO MICRO-PULSE ELECTROCHEMICAL MACHININGKARAKTERISTIKE POVRŠINE INVAR ZLITINE GLEDE NA  
MIKROPULZNO ELEKTROKEMIČNO OBDELAVO

Seong-Hyun Kim, Seung-Geon Choi, Woong-Kirl Choi, Eun-Sang Lee

Inha University, Department of Mechanical Engineering, 253 Yonghyun-Dong, Nam-Gu, Incheon 402-751, Republic of Korea  
kimseonghyun@inha.edu, leees@inha.ac.kr*Prejem rokopisa – received: 2016-07-15; sprejem za objavo – accepted for publication: 2017-01-24*

doi:10.17222/mit.2016.187

Invar is a 36 % nickel iron alloy that has a low thermal expansion, compared to other metals and alloys, at temperatures ranging from room temperature up to approximately 230 °C. Invar alloy is ductile, easily weldable and its machinability is similar to that of austenitic stainless steel. Due to the low thermal expansion of Invar, it is used for shadow masks for display devices such as UHDTV – organic light-emitting diode. In this study, micro-pulse electrochemical machining (MPECM), which is a non-contact ultra-precision machining method, was developed to manufacture Invar sheets; optimum parameters of MPECM were defined and the basic MPECM experiments were carried out on an Invar sheet. The optimum parameters were determined with pulse-on time and duty-ratio analysis. The experimental results show that MPECM is hard to control. Therefore, using ultrashort charging times and very high pulses, it is possible to achieve a successful anodic dissolution at a very small electrode gap. Hence, a longer pulse-on time and a small electrode gap may provide the scope for further improvement of the machining accuracy by controlling the localization effect. Furthermore, the machining depth and MPECM efficiency were investigated with respect to various parameters and pulse-on time, considering different duty-ratio conditions.

Keywords: Invar alloy, electrochemical machining, surface characteristics

Invar je 36 % zlitina niklja in železa, ki ima v primerjavi z vsemi kovinami in zlitinami, nizek koeficient toplotnega raztezka v območju sobne temperature pa do okoli 230 °C. Invar zlitina je duktilna, primerna za enostavno varjenje in njena obdelovalnost je podobna avstenitnemu nerjavnemu jeklu. Zaradi nizkega koeficienta termičnega raztezka, se zlitina Invar uporablja v maskah za senčenje displejev v OLED-UHD TV (angl.: Organic Light Emitting Diode – Ultra High Definition TeleVision) napravah. V tej študiji je bila razvita metoda mikropulzne elektrokemične obdelave kovin (angl. MPECM), ki je brezkontaktna ultraprecizna tehnologija mehanske obdelave. Izvedeni so bili osnovni poskusi na zlitini Invar. Določeni so bili optimalni parametri postopka. Eksperimentalni rezultati kažejo, da je obdelovalnost z MPECM težko nadzorovati. Izjemno kratki časi, z zelo visokimi napetostnimi impulzi, omogočajo nastanek pogojev za uspešno anodno raztapljanje kovine pri zelo majhni reži elektrode. Zato se pri zelo visokem številu impulzov in manjšem razmiku elektrod, lahko zagotovi nadaljnje izboljšanje točnosti obdelave z MPECM. Nadalje je bila raziskana obdelovalna globina in obdelovalnost z MPECM pri različnih procesnih parametrih (napetost-čas-storilnost).

Ključne besede: Invar zlitina, elektrokemična obdelava, površinske karakteristike

## 1 INTRODUCTION

Invar is an alloy of 64 % iron and 36 % nickel. Its coefficient of expansion is very low, namely  $1.8 \times 10^{-6}$  cm/°C, at temperatures ranging from a cryogenic temperature of –196 °C to a Currie temperature of 260 °C. This value is 10 times lower than that of stainless steel and 100 times lower than that of iron, which makes Invar appropriate for applications in various fields of study. Invar is used in ultra-high-definition televisions, display shadow masks, organic light-emitting diodes, controllers for quality, colors, and for the definition of images in mobile devices and other instruments that require precise measurements.<sup>1–3</sup> Invar is also used in electron-gun electrodes (devices that eject an electron beam into the hole in a shadow mask), lead frames (to protect semiconductor chips from external damage) and other industrial devices.

Invar is currently manufactured with mechanical processes or electroforming; other methodologies have also

been suggested. To maintain the specific characteristics of Invar alloys, advanced machining methods are being studied, such as laser machining, supersonic-wave machining, micro-end mills/drilling, electropolishing and electrochemical machining.<sup>4–6</sup> Moreover, the effects of hydrodynamics and temperature on the electrode position of Fe–Ni (Invar) alloys has been investigated with DC, pulse, and pulse-reverse electrodeposition techniques.<sup>7,8</sup> MPECM has seen a resurgence of industrial interest within the last decade, due to its many advantages, such as no tool wear, stress-free and smooth surfaces, and the ability to machine complexly shaped products made from different materials, regardless of their hardness and high strength, high tension, or whether they are heat-resistant materials.<sup>9</sup> In this study, the possibility of pulse electrochemical machining is investigated by analyzing the machinability characteristics of processed Invar prior to pulse electrochemical machining.

## 2 EXPERIMENTAL PART

### 2.1 Theory of the MPECM system

**Figure 1** shows a schematic diagram of the combined electrochemical process and the MPECM set-up with a previously developed microprobe. A pulsed voltage from a high-voltage pulse generator (Hewlett-Packard HP8116A) is applied to the gap between the anode and cathode, and the electrolyte solution is supplied through a hole in the cathode or an external electrolyte supplier. This homogenizes the electrochemical reaction and removes the gas and heat generated. The anode is the Invar alloy with a thickness of 30  $\mu\text{m}$  and the cathode is stainless steel with a 1-mm diameter.

The fully programmable 50 MHz pulse generator has a variable pulse width (10 ns min) and the maximum output amplitude of the maximum voltage of 32 V p-p (in an open circuit). The high-speed data-acquisition system was provided by a TDS 2002C digital oscilloscope (Tektronix) with a bandwidth of 200 MHz and a sampling rate of 500 MS/s. Typical experimental conditions are shown in **Table 1**.

**Table 1:** Experimental conditions

Parameter	Value
Pulse generator spec.	HP8116A (Hewlett-Packard), 50MHz, 32 V p-p, various (10 ns) pulse widths
Workpiece (anode)	Invar (Fe 64 %, Ni 36 %) 30- $\mu\text{m}$ thickness
Electrode (cathode)	Stainless steel 304 ( $\phi$ 1 mm) Non-insulation, Insulation
Digital oscilloscope	Tektronix TDS 2002C
MPECM time	40 min (pulse-on time: 500 ns-2 $\mu\text{s}$ , Duty factor: 33–66 %)
Applied voltage (V)	16
Electrode gap ( $\mu\text{m}$ )	50
Electrolyte	Sodium nitrite + sodium tartrate + DI water
Measurement	Optical microscopic analysis, Scanning electron microscopy (SEM), Non-contact 3D profile

### 2.2 Electrode type

The concentration of the current at the edges and irregular parts of an electrode can lead to localized sedimentation on the anode surface. A specially designed electrode is recommended for electrochemical micro-machining to control the dimensions of the Invar surface. **Figure 2** compares the surfaces that were electrochemically micro-machined using two different electrodes. Electrode 1, with the traditional design, had a concentrated current at the edge, which is marked as a 2. Electrode 2 has a non-conducting part that is marked as a 3. The current distribution for electrode 2 is uniform on the surface, which is marked as a 4. Localized sedimentation was identified on the anode workpiece surface in the shape profile created by electrode 1, but none was

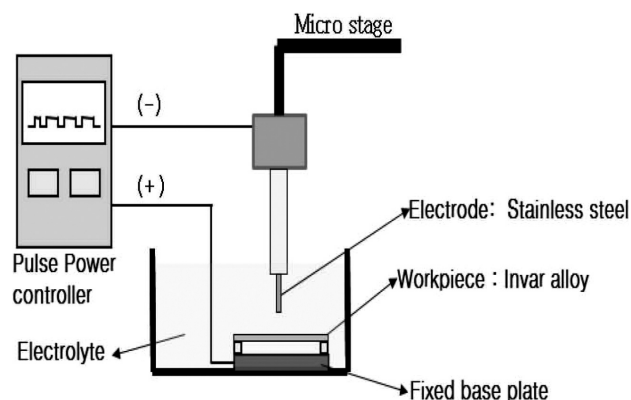


**Figure 1:** Micro-pulse electrochemical machining system

identified for electrode 2. This results from non-conducting part 3 on the side of the electrode. The cathode design should be taken into account to precisely control the shape and prevent sedimentation.

When the electrodes are far apart, the voltage flows in the regions other than the processed area, even when no machining is intended. To reduce the unwanted voltage flowing in these regions, an electrode that is coated on the top can be used as the tool. To minimize this voltage and observe the behavior of the machining current, the sides of the tool need to be completely insulated.

## 3 RESULTS AND DISCUSSION

### 3.1 Machining characteristics versus the pulse-on time using a non-insulated electrode

The machining characteristics were studied using a voltage of 16 V, a gap of 50  $\mu\text{m}$  a pulse-off time of 1  $\mu\text{s}$  and a machining time of 40 min. An insulated electrode was used, and the pulse-on time was changed from 500 ns to 2  $\mu\text{s}$ . **Figure 3** shows that the machining radius was larger as the pulse-on time increased. The processed radius was 559.04  $\mu\text{m}$  at the pulse-on time of 500 ns, 620.76  $\mu\text{m}$  at 600 ns, 675.21  $\mu\text{m}$  at 800 ns, 689.73  $\mu\text{m}$  at 1  $\mu\text{s}$ , 693.36  $\mu\text{m}$  at 1.5  $\mu\text{s}$ , and 715.14  $\mu\text{m}$  at 2  $\mu\text{s}$ . When the pulse-on time was 1  $\mu\text{s}$  or higher, the machining radius drastically increased. **Figure 4** shows the results after the machining with respect to the pulse-on time.

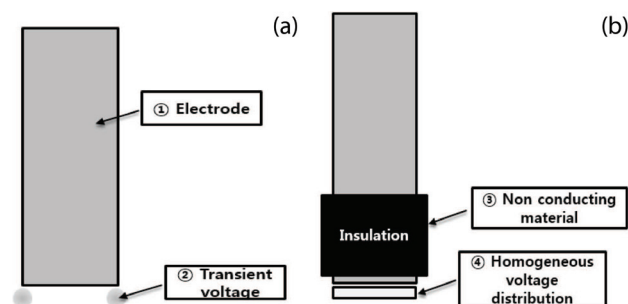


**Figure 2:** Comparison between two different electrodes

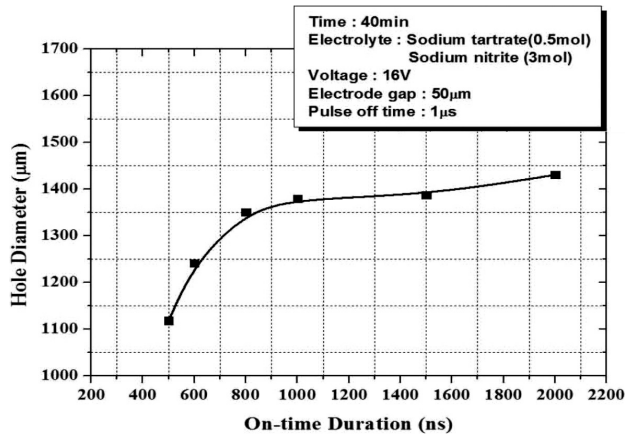


Figure 3: Increase of hole-diameter size versus pulse-on time

When the pulse-on time was 500–800 ns, the machinability declined due to a low current density, but at 1–2 μs, the machinability improved due to a high current density. The precision and the resulting image became better and better.

### 3.2 Machining characteristics versus the pulse-on time using an insulated electrode

The machining characteristics were also examined using an insulated electrode, with the other conditions

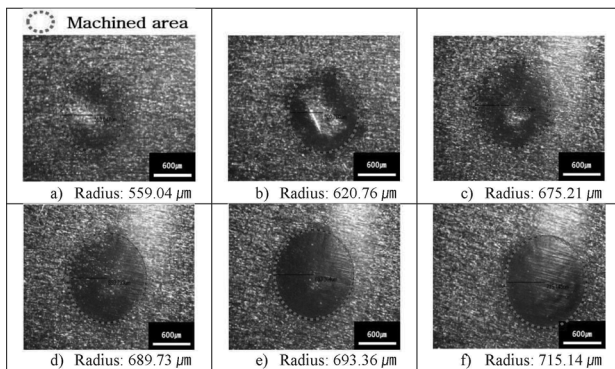


Figure 4: Crater-shape patterns with pulse-on time / duty factor and non-insulated electrode: a) 500 ns / 33 %, b) 600 ns / 37 %, c) 800 ns / 44 %, d) 1 μs / 50 %, e) 1.5 μs / 60 %, f) 2 μs / 66 %

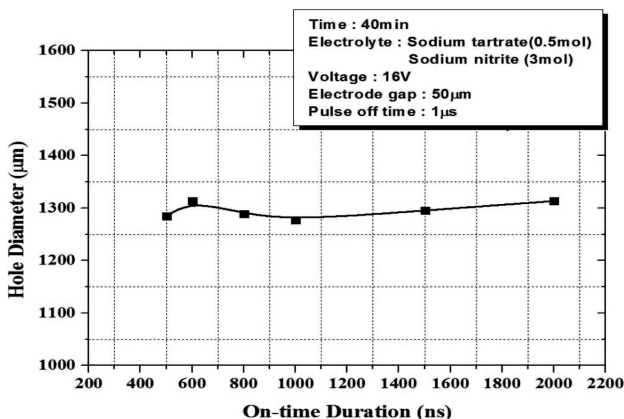


Figure 5: Increase of hole-diameter size versus pulse-on time

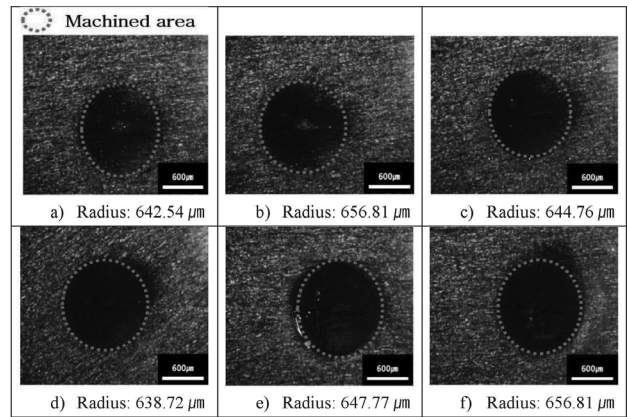


Figure 6: Crater-shape patterns with pulse-on time / duty factor and insulated electrode: a) 500 ns / 33 %, b) 600 ns / 37 %, c) 800 ns / 44 %, d) 1 μs / 50 %, e) 1.5 μs / 60 %, f) 2 μs / 66 %

kept the same as in the previous experiment. **Figure 5** shows that the machining radius was consistent with the increase in the pulse-on time. The processed radius was 642.54 μm at 500 ns, 656.81 μm at 600 ns, 644.76 μm at 800 ns, 638.72 μm at 1 μs, 647.77 μm at 1.5 μs, and 656.81 μm at 2 μs.

**Figure 6** shows the results after the machining. The machining may occur on the sides of the electrode without the insulation, but the insulated electrode prevents this and makes the machining consistent with a very fine outcome.

### 3.3 Surface analysis versus the pulse-on time using insulated and uninsulated electrodes

**Figure 7a** shows a SEM image of the Invar film surface after the machining with the uninsulated electrode. The processed area is clearly displayed. **Figure 7b** shows the non-contact 3D profile measured. The tapering remained on the side of the Invar film surface after the experiment. **Figure 7c** shows the results for the pulse-on time of 2 μs, which allowed the best machinability with both types of electrode. **Figure 8** shows the equivalent results obtained with the insulated electrode. The voltage in **Figure 8c** is slightly increased compared to **Figure 7c**.

With the uninsulated electrode, the processed radius is increased, with almost no influence on the depth. This is attributable to the parts other than the intended machining area with the repeated charging and discharging in the dual layer of electricity because the voltage pulse is exhausted on the other sides of the uninsulated electrode. However, with the insulated electrode, the voltage is concentrated only in the machining area, so the radius is consistently maintained and the machining depth increases. **Figures 7c** and **8c** show that the voltage permitted during the actual machining is lower with the uninsulated electrode than with the insulated one.



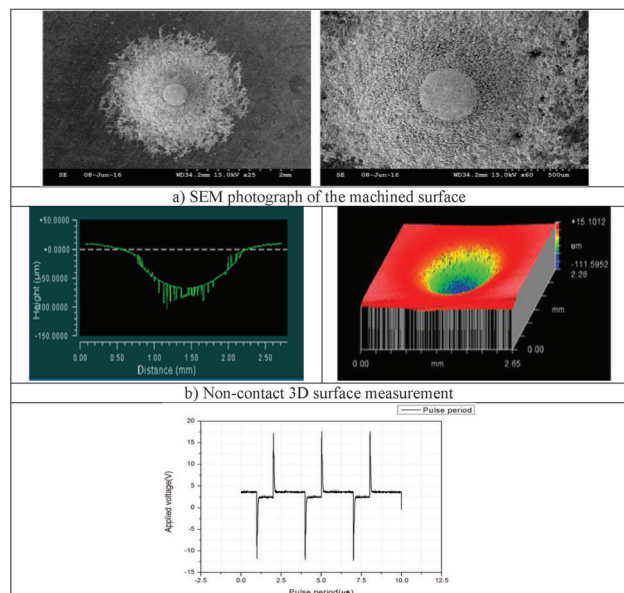


**Figure 7:** SEM images and non-contact 3D profiles of crater-shaped patterns at different pulse-on times using the uninsulated electrode

#### 4 CONCLUSIONS

This study demonstrated that MPECM has suitable process characteristics for machining Invar-alloy surfaces. The machined shape and surface qualities, such as the surface condition and the machining defect, were observed. The important factors influencing the hole-shape quality of the Invar alloy are the pulse-on time, the duty factor, the shape of the cathode and the electrolytic process parameters. During the application of MPECM to a fine sheet metal, the electrochemical machining characteristics of the surface of the alloy were revealed and analyzed with respect to different electrode shapes, pulse-on times and applied voltages.

When the uninsulated electrode was used, the machining speed differed depending on the area of the tool electrode that was submerged in the liquid. With a greater machining depth, the machining speed was reduced and there was almost no machining after reaching a certain limit. This is attributable to the current being exhausted because of the repeated charging and discharging in the dual layer of electricity by the pulse, for any part other than the intended machining part.

The insulated electrode prevents the permitted voltage from being exhausted and improves the machinability with the increasing machining depth. In addition, since the voltage flows only into the machining area, a taper does not occur since the sides of the electrode are well insulated. Accordingly, if insulated electrodes are used, it is possible to increase the precision of the form and the processing depth.

This study indicates that the electrode shape and suitable MPECM conditions affect the machinability, and that there is a close interrelation between the electric field on the Invar-alloy surface and the polishing rate. A comparison of the insulated and uninsulated electrodes

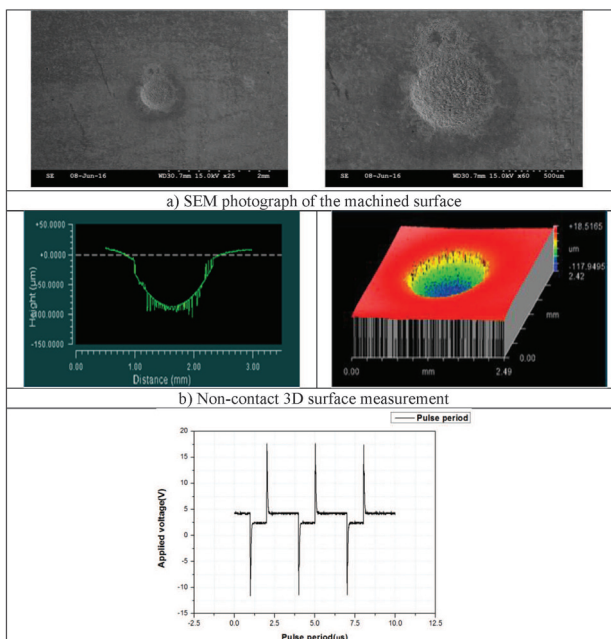


**Figure 8:** SEM images and non-contact 3D profiles of crater-shaped patterns at different pulse-on times using the insulated electrode

was made, and the effect of the pulse-on time on the electrochemical machinability was determined. MPECM can be recommended to practitioners in different fields to improve the conditions for making holes in the Invar alloy.

The electrolyte of sodium nitrite + sodium tartrate + DI water was used and holes with a  $\phi 1$  mm diameter were made into the 30- $\mu$ m-thick Invar alloy. The future work, therefore, can be made when more engineering data has been gathered. In addition, more research needs to be done on the related factors, such as the surface roughness and the shape accuracy, using controlled micro-pulses.

#### Acknowledgment

This work was supported by the Inha University Research Foundation, Korea.

#### 5 REFERENCES

- <sup>1</sup> D. Grimmertt, M. Schwartz, K. Node, A comparison of DC and pulsed Fe–Ni alloy deposits, *Journal of The Electrochemical Society*, 140 (1993) 4, 973–978, doi:10.1149/1.2056238
- <sup>2</sup> A. Stupnik, M. Leisch, Study on the surface topology of vacuum-fired stainless steel by scanning tunnelling microscopy, *Vacuum*, 81 (2007) 6, 748–751, doi:10.1016/j.vacuum.2005.11.061
- <sup>3</sup> L. S. Andrade, S. C. Xavier, R. C. Rocha-Filho, N. Bocchi, S. R. Biaggio, Electropolishing of AISI-304 stainless steel using an oxidizing solution originally used for electrochemical coloration, *Electrochimica Acta*, 50 (2005) 13, 2623–2627, doi:10.1016/j.electacta.2004.11.007
- <sup>4</sup> Y. N. Hu, H. Zhou, L. P. Liao, H. B. Deng, Surface quality analysis of the electropolishing of cemented carbide, *Journal of Materials Processing Technology*, 139 (2003) 1–3, 253–256, doi:10.1016/S0924-0136(03)00230-9

- <sup>5</sup> D. Grimmer, M. Schwartz, K. Node, A Comparison of DC and Pulsed Fe-Ni Alloy Deposits, *Journal of The Electrochemical Society*, 140 (1993) 4, 973–978, doi:10.1149/1.2056238
- <sup>6</sup> S. Fujimoto, K. Tsujino, T. Shibata, Growth and properties of Cr-rich thick and porous oxide films on Type 304 stainless steel formed by square wave potential pulse polarisation, *Electrochimica Acta*, 47 (2001) 47, 543–551, doi:10.1016/S0013-4686(01)00782-4
- <sup>7</sup> T. Koyano, M. Kunieda, Ultra-Short Pulse ECM Using Electrostatic Induction Feeding Method, *Procedia CIRP*, 6 (2013), 390–394, doi:10.1016/j.procir.2013.03.066
- <sup>8</sup> M. Boxhammer, S. Altmannshofer, Model Predictive Control in Pulsed Electrochemical Machining, *Journal of Process Control*, 24 (2014) 1, 296–303, doi:10.1016/j.jprocont.2013.11.003
- <sup>9</sup> E. Lee, T. Shin, B. Kim, S. Baek, Investigation of short pulse electrochemical machining for groove process on Ni-Ti shape memory alloy, *International Journal of Precision Engineering and Manufacturing*, 11 (2010) 1, 113–118, doi:10.1007/s12541-010-0014-3



# DURABILITY OF MATERIALS BASED ON A POLYMER-SILICATE MATRIX AND A LIGHTWEIGHT AGGREGATE EXPOSED TO AGGRESSIVE INFLUENCES COMBINED WITH HIGH TEMPERATURES

## VZDRŽLJIVOST MATERIALOV NA OSNOVI IZ POLIMER-SILIKATNIH MATRIC IN LAHKEGA DODATKA, IZPOSTAVLJENIH AGRESIVNIM VPLIVOM V KOMBINACIJI Z VISOKIMI TEMPERATURAMI

**Tomáš Melichar, Jiří Bydžovský, Ámos Dufka**

Brno University of Technology, Faculty of Civil Engineering, Veveří 331/95, 602 00 Brno, Czech Republic  
melichar.t@fce.vutbr.cz

*Prejem rokopisa – received: 2016-07-15; sprejem za objavo – accepted for publication: 2017-03-16*

doi:10.17222/mit.2016.190

The paper presents the results and findings of the research focused on an examination of progressive degradation of newly developed composite materials. These materials consisted of a polymer-silicate matrix and a mix of fillers with a considerable proportion of a porous aggregate. The matrix also contained a larger amount of alternative raw materials, in particular high-temperature fly ash and blast furnace slag. Prepared mixes were tested after different periods of exposure to an aggressive environment – for 45 d and 90 d (50 and 100 cycles). First, after 45 d and 90 d, reference materials (i.e., those not exposed to aggressive influences) were tested. In parallel, tests were carried out with materials exposed to a solution of chloride ions and subjected to cyclic freeze and thaw. The last mode of testing in this research included materials exposed to cyclic freeze and thaw, chloride-ion solution and the consequent thermal load of up to 1000 °C. The level of degradation was evaluated by means of physico-mechanical, physico-chemical and microstructural test methods. It was found that the exposure to cyclic freeze and thaw, water and chloride ions has no considerable influence on the reduction of the thermal resistance of the developed mix designs of polymer-silicate-based composites.

**Keywords:** durability, porous aggregate, polymer-silicate matrix, long-term exposure, chloride ions, water, frost, fire, micro-structure

Članek predstavlja rezultate in izsledke raziskave, osredotočene na preverjanje napredujočega slabšanja na novo razvitih kompozitnih materialov. Ti materiali so sestavljeni iz polimer-silikatnih matric in mešanice polnil z znatnim deležem poroznih agregatov. Matrica je vsebovala tudi večjo količino alternativnih surovih materialov, visokotemperaturni dimniški pepel in žlindro. Pripravljene mešanice so bile testirane po različnih časih izpostavljanja agresivnemu okolju – 45 d in 90 d (v 50 in 100 ciklih). Najprej so bili, po 45 d in 90 d, testirani referenčni materiali, tisti, ki niso bili izpostavljeni agresivnim vplivom. Vzporedno pa so bila izvedena testiranja materialov, ki so bili izpostavljeni raztopini kloridnih ionov ter nato ciklično zamrznjeni in nato staljeni. Zadnji način testiranja v tej raziskavi je bilo izpostavljanje materialov cikličnemu zamrzovanju in taljenju, kloridni raztopini ionov in ter toplotni obremenitvi do 1000 °C. Stopnja degradacije je bila ocenjena glede na fizikalno-mehanske, fizikalno-kemične in mikrostrukturne testne metode. Ugotovljeno je bilo, da izpostavljenost cikličnemu zamrzovanju in taljenju, vodi in kloridnim ionom, nima večjega vpliva na zmanjšanje termične odpornosti na razvite mešanice iz polimer-silikatnih kompozitov.

**Ključne besede:** vzdržljivost, porozne mešanice, polimer-silikatna osnova, daljše izpostavljanje, kloridni ioni, voda, led, ogenj, mikrostruktura

## 1 INTRODUCTION

Technical papers, stating results of the research focused on the problems of the resistance of silicate (cement) matrix based composites, focus mainly on an assessment of the influences of individual adverse factors and aggressive environments. Scientists do not focus on a synergic action of more than two types of adverse influences, one of which is extremely high temperature. Several factors are crucial for a gradual degradation of polymer-silicate composites exposed to chloride ions, frost and high temperature. The first of them is mechanical deterioration of the composite caused by freeze-thaw cycles together with the water containing chloride

ions. A water solution with chlorides penetrates through the surface and subsequently deeper into the structure of a composite material with a capillary-porous system. Depending on the depth of the ingress of the mentioned solution, affected areas are damaged during the temperatures changes above and below zero. The depth of penetration depends on the components used, in particular, the material base of the matrix, the used additions, their activities and the structure of the aggregate.

This problem is solved, in considerable detail, by J. G. Jang et al.<sup>1</sup> Apart from the influence of individual factors, the authors also described a combination of aggressive CO<sub>2</sub> and Cl<sup>-</sup> ions, and it was proved that when the two act in synergy, the penetration of Cl ions is



increased. This implies that the testing of a synergic action of negative influences affecting a given material is quite important because it is impossible to give an exact prediction only on the basis of an evaluation of individual aggressive substances. M. Maes et al.<sup>2</sup> confirmed that a replacement of Portland cement with blast-furnace slag in amounts of 50 % and 70 % considerably increases the resistance to the actions of  $\text{Cl}^-$  and  $\text{SO}_4^{2-}$ . It is also interesting that increasing the contents of sulfates in a solution increases the attack of chlorides. On the other hand, the concentration of chlorides has no influence on the sulfate attack on the mortar with blast-furnace slag. Slag generally has good resistance to sulfate attack, which was proved by M. Maes et al.<sup>2</sup>, inter alia, with negligible changes in the volume and expansion. This finding is quite important from the viewpoint of a positive influence of blast-furnace slag on the resistance of a cement matrix to extreme temperatures.

The presence of  $\text{Cl}^-$  ions in silicates is also important for a possible formation of Friedel's salt –  $3\text{CaO} \cdot \text{Al}_2\text{O}_3 \cdot \text{CaCl}_2 \cdot 10\text{H}_2\text{O}$ . This chemical compound can develop from free  $\text{Cl}^-$  ions, which bind to  $\text{C}_3\text{A}$  or  $\text{C}_4\text{AF}$ . However, the reaction of the mentioned components is considerably influenced by several factors. As A. Delagrave et al.<sup>3</sup> and D. Izquierdo et al.<sup>4</sup>, Q. Yuan<sup>5</sup> and L. Tang<sup>6</sup> state, concentration of chloride ions, type of cement, replacement of cement, temperature or water-cement ratio are important. According to F. P. Glasser et al.<sup>7</sup>, a penetration of chloride ions with the consequent formation of Friedel's salt can, inter alia, cause a gradual filling of the porous structure of a given composite, which eventually slows down the transportation of  $\text{Cl}^-$  ions. The filling of pores is critical particularly for the thermal resistance where a porous structure is an advantage. The thermal decomposition of Friedel's salt is also important, i.e., gases developed during the dissociation, components remaining as residua and their capability for a further reaction with water consequently lead to an increase in the volume.

Durability of mortars with blast-furnace slag as the filler is described by Santamaría-Vicario et al.<sup>8</sup> The research focused on the influence of a combination of several adverse environments – frost with water, alternating between humid and dry environment, simulation of a marine environment or crystallization of salts and gaseous  $\text{SO}_2$ . Based on the results and findings, the possibility of using slag as a replacement of the aggregate was confirmed. The development and research of mortars with blast-furnace slag resistant to fire up to a temperature of 900 °C is presented by S. Aydin<sup>9</sup>. The tests involving blast-furnace slag as a replacement of the binder included mortars containing up to 80 % of the slag. Pumice was used as the filler. Mortars with 40 % of the slag showed the best test results. The residual compressive strength of these mortars exposed to 900 °C was 44 %, after they were gradually cooled down. After rapid cooling with water, the residual compressive strength of

the mortar was around 40 %. The replacement of a fine aggregate with industrial by-products is a part of the research described by I. Yüksel et al.<sup>10</sup> The amount of the substitution was from 10–50 %, with the subsequent thermal load of up to 800 °C at the age of 90 d. A positive influence of the replacement of the commonly used dense aggregate with byproducts of the energy and foundry industry was unambiguously proved. The bottom ash showed the best results. One of the few publications, in which the authors provide the results of a research focused on the synergic action of high temperature and adverse environment (in particular  $\text{CO}_2$ ), was published by G. Yuan and Q. Li<sup>11</sup>. The authors focus on the problems of concrete with various water-cement ratios exposed to temperatures of up to 700 °C. One of the subsequent testing methods was the exposure to an environment with a higher concentration of  $\text{CO}_2$ . The aim of the research presented by G. Yuan and Q. Li<sup>11</sup> was the verification of the influence of a possible surface treatment of the tested concrete after its exposure to heat. The results show that as the exposure temperature grows, the resistance to carbonization decreases.

## 2 METHODOLOGY OF EXPERIMENTAL WORK

As the aim of the research was to design a material resistant to adverse environmental influences and possible fire at the same time, the selected matrix contained an increased amount of blast-furnace slag and high-temperature fly ash. Fly ash as a substitution binder increasing the thermal resistance was researched by A. Nadeem et al.<sup>12</sup> Microsilica was used as a supporting addition and stabilizing component; its positive effect in cement-based composites on the resistance to high temperatures was proven, for example, by T. Harun and C. Ahmet.<sup>13</sup> Two types of aggregate were used. The coarser fraction of 1–2 mm was amphibolite, which is mined as a primary raw material. The fine-grained residue from washing the aggregate, produced as a by-product of adjusting the granulometric composition of the mined amphibolite, was used. The remaining part – a fine fraction of 0–1 mm – was fly-ash agloporite; the dominant part of agloporite is an energy-industry by-product – fly ash. As agloporite is created, through a self-burning process, from alternative raw-material resources, it can be characterized as an advantageous and cheap raw material, which is relatively environmentally friendly. The suitability of agloporite as a filler for materials with an assumed thermal resistance can be presumed, for example, on the basis of the results stated by V. Černý and Š. Kepřdová.<sup>14</sup> Mix designs of tested composite materials are listed in **Table 1**. Agloporite was saturated with water before its application in the mix. This fact was taken into account when correcting the water-cement ratio, which was adjusted to achieve good

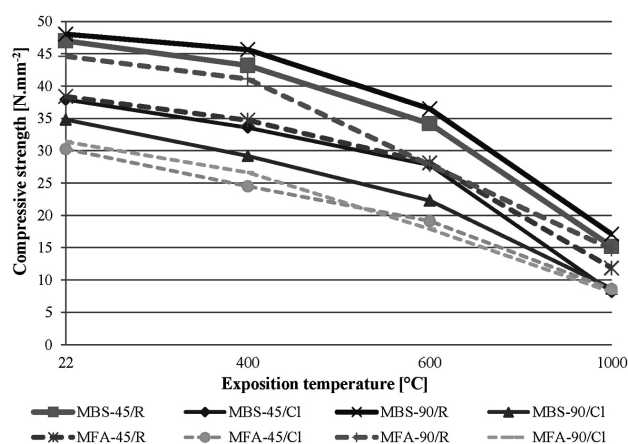


**Figure 1:** Compressive strengths of mixtures MBS and MFA after 45 d and 90 d (R – temperature exposure; CI – combination of chloride ions, frost and exposure to extreme temperatures)

**Table 1:** Composition of mixtures MBS and MFA

Component	Unit	Mixture	
		MBS	MFA
Cement	kg m <sup>-3</sup>	443	443
Blast furnace slag	kg m <sup>-3</sup>	251	–
Fly ash	kg m <sup>-3</sup>	–	238
Vinyl acetate copolymer	% (W <sub>C+FBS, FA</sub> )	3	3
Microsilica	% (W <sub>C+FBS, FA</sub> )	7	7
Amphibolite (by-product) <0,063 mm	kg m <sup>-3</sup>	33	33
Porous aggregate 0–1 mm	kg m <sup>-3</sup>	641	641
Amphibolite 1–2 mm	kg m <sup>-3</sup>	792	792
Polypropylene fibres	kg m <sup>-3</sup>	1.1	1.1
Water	kg m <sup>-3</sup>	193	201

workability of the fresh mix (a slump of around 160 mm).

Out of each mix design, four sets of test specimens of (40 × 40 × 160) mm were made. The first and the second sets were treated in standardized conditions; then, after 28 d of maturing, the specimens were exposed to an adverse environment. In the adverse environment, the

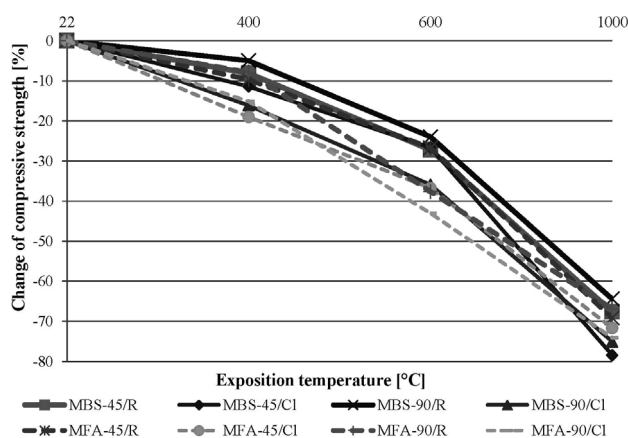


**Figure 2:** Percentage change of compressive strength due to chloride-ion solution and frost attack – weight change of mixtures MBS and MFA after 45 d and 90 d

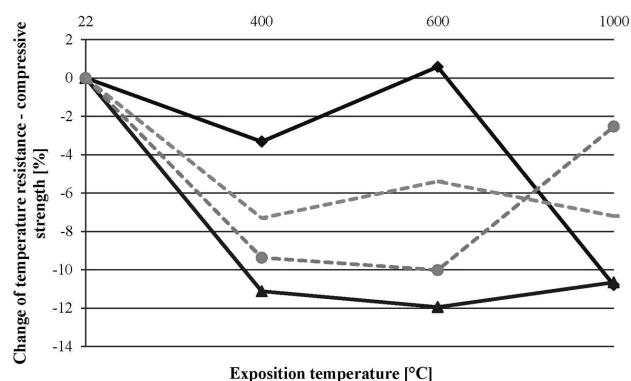


**Figure 3:** Change of temperature resistance (compressive strength) due to chloride-ion solution and frost attack – weight change of mixtures MBS and MFA after 45 d and 90 d

temperature was cyclically changing (above and below zero), combined with a saturation of the solution with chloride ions (in accordance with ČSN EN<sup>17</sup>). After 50 cycles (and after 45 d elapsed from the standardized maturation), half of the specimens were subjected to tests of strength characteristics. The other half of the test specimens were exposed to temperatures of (22, 400, 600 and 1000) °C. The rate of the temperature increase was around 10 °C min<sup>-1</sup> with an isothermal dwell time of 90 min and slow cooling down. A similar procedure was also applied for the third and fourth set, where the test conditions were different regarding the number of cycles: 100 cycles were made in an adverse environment so that the specimens could be tested after 90 d. It is important to emphasize that the testing was carried out after 45 d or 90 d; however, the cycles were counted after the standardized age of 28 d. The reason for this was the exposure of the test specimens to the adverse environment after the maturing process. The end of the cyclical exposure at the ages of 45 d or 90 d simulated the early age of a real structure.

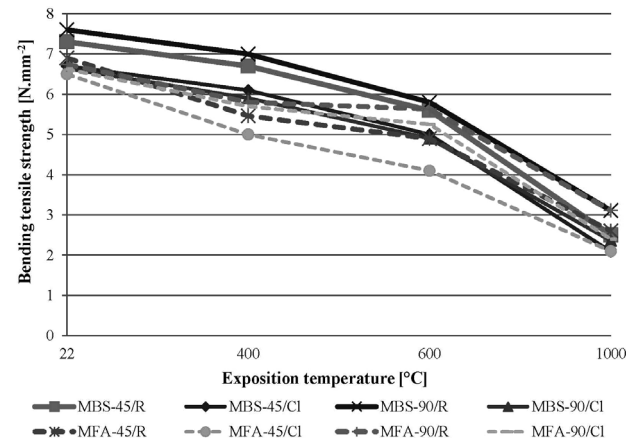


**Figure 4:** Bending tensile strengths of mixtures MBS and MFA after 45 d and 90 d (R – temperature exposure; CI – combination of chloride ions, frost and exposure to extreme temperatures)

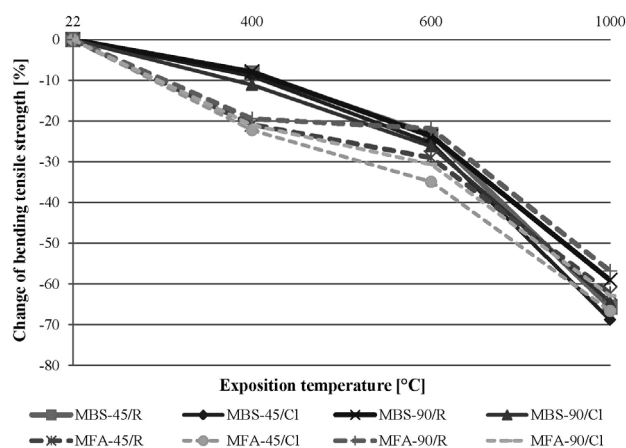


**Figure 5:** Percentage change of bending tensile strength due to chloride-ion solution and frost attack – weight change of mixtures MBS and MFA after 45 d and 90 d

### 3 RESULTS

The diagrams below show the dependency of individual observed parameters on the exposure to aggressive environments and high temperatures, including their combination (**Figures 1 to 6**). The first compressive strength and tensile bending strength were examined. The first diagram of a given set – observed parameters (**Figures 1 to 4**) – shows the development of the above-mentioned parameters in a given environment and at a given temperature (labeling: R – with no aggressive exposure, Cl – exposed to a solution of chlorides and frost). The second diagram of a given set shows the percentage changes of a particular parameter (**Figures 2 and 5**). The last diagram of a given parameter (**Figures 3 and 6**) shows the development of the temperature resistance (which is characterized by the percentage decrease of a given parameter). The curves presented as a solid line (dash line) denote mix designs MBS (MFA), i.e., the binder modified with blast-furnace slag (high-temperature fly ash).

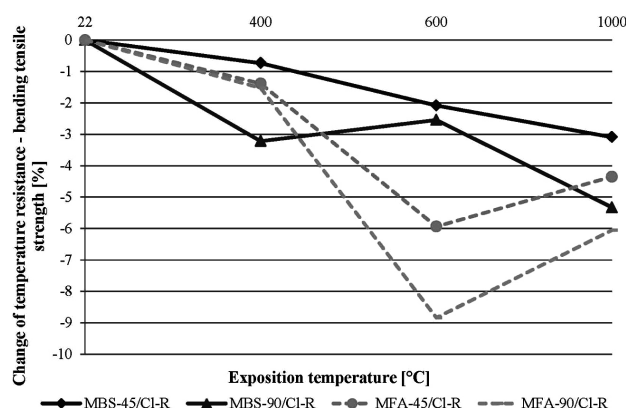


**Figure 6:** Change of temperature resistance (bending tensile strength) due to chloride-ion solution and frost attack – weight change of mixtures MBS and MFA after 45 d and 90 d

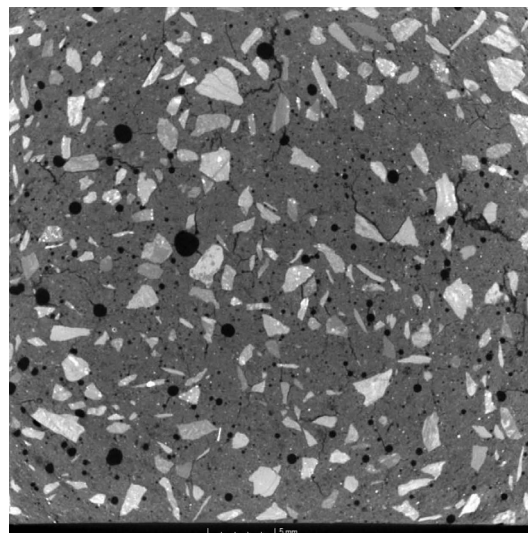


**Figure 7:** CT picture – slice of MBS-45/R (45 d, R – reference sample without chloride solution and frost environment), exposure to 1000 °C

Due to the chloride-ion solution and frost, failures are possible even inside the composite. The formation of cracks is the most likely failure. One of the key methods of the assessment of the structure of a material exposed to high temperatures is X-ray tomography (and CT). The CT examination focused on the presence of cracks, in particular, their number, width and orientation. It was important to determine where the cracks were found: the matrix, the aggregate or the transition zone. The location of cracks is also important: close to the surface or in the inner structure. **Figures 7 to 10** show the test specimens exposed to adverse conditions. To identify and evaluate phase changes, an X-ray diffraction analysis was used (hereinafter referred to as XRD). The observed parameters were phase changes and the formation of new chemical compounds as products of the reaction of

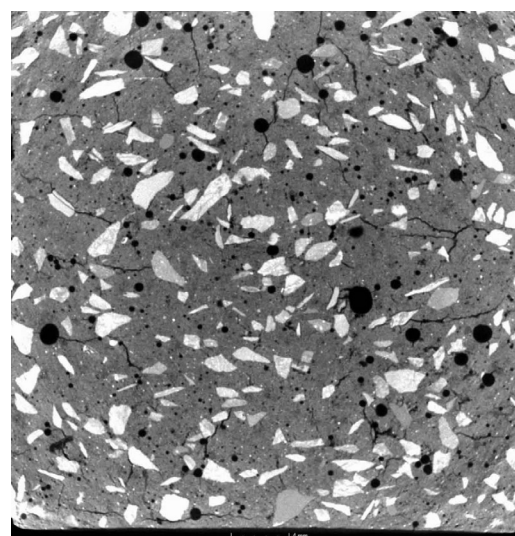


**Figure 8:** CT picture – slice of MBS-45/Cl (45 d, Cl – exposure to chloride solution and frost environment, 50 cycles), exposure to 1000 °C



chlorides with the matrix of a composite (**Table 2**). To make the picture complete, electron microscopy was used (hereinafter referred to as SEM). SEM focused on the formation of micro-cracks and the products related to the crystallization of chloride ions or their residua (**Figures 11 and 12**).

**Table 2:** XRD – mineralogical composition of mixtures MBS and MFA – selected samples

Mixture-age/ environment, temperature	Identified components
MBS-90/R, 22	portlandite, calcite, $\beta$ -quartz, ettringite, mullite, chlorite, actinolite, anorthite, hematite, akermanite, merwinite, gehlenite, CSH, amorphous phase
MBS-90/R, 1000	$\beta$ -quartz, mullite, chlorite, actinolite, anorthite, hematite, akermanite, merwinite, wolastonite, amorphous phase
MBS-90/Cl, 22	portlandite, calcite, $\beta$ -quartz, ettringite, mullite, chlorite, hematite, akermanite, actinolite, wolastonite, gehlenite, biotite CSH, amorphous phase
MBS-90/Cl, 1000	$\beta$ -quartz, mullite, actinolite, anorthite, hematite, gehlenite, amorphous phase wolastonite
MFA-90/R, 22	portlandite, calcite, $\beta$ -quartz, ettringite, mullite, chlorite, actinolite, anorthite, hematite, biotite CSH, amorphous phase
MFA-90/R, 1000	$\beta$ -quartz, mullite, chlorite, actinolite, amorphous phase, anorthite, hematite, wolastonite
MFA-90/Cl, 22	portlandite, ettringite, mullite, calcite, $\beta$ -quartz, anorthite, biotite, hematite CSH, amorphous phase
MFA-90/Cl, 1000	$\beta$ -quartz, mullite, amorphous phase, anorthite, hematite, wolastonite

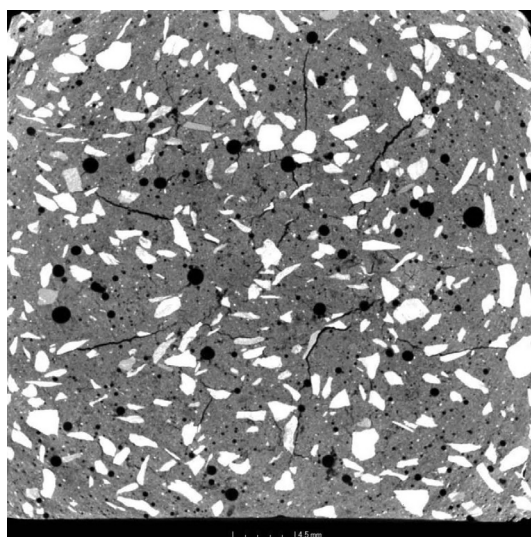


**Figure 9:** CT picture – slice of MBS-90/Cl (90 d, Cl – exposure to chloride solution and frost environment, 100 cycles), exposure to 1000 °C

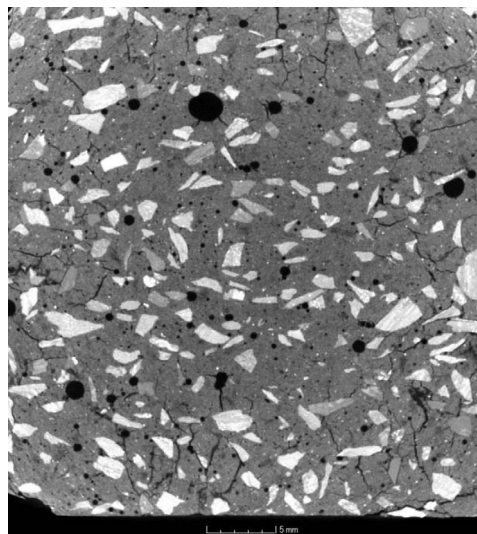


**Figure 10:** CT picture – slice of MFA-90/Cl (90 d, Cl – exposure to chloride solution and frost environment, 100 cycles), exposure to 1000 °C

#### 4 DISCUSSION

The diagrams (**Figures 1 to 6**) show the development of individual parameters and differences between the tested mix designs at a given age and exposed to a given environment.

Reference materials MBS-90 and MFA-90 showed compressive strengths of 48 N mm<sup>-2</sup> and 45 N mm<sup>-2</sup>. As the diagram shows (**Figure 1**), the compressive strength decreases more considerably after an exposure to an aggressive environment. This fact is supported by the test results of the materials stored in laboratory conditions (in

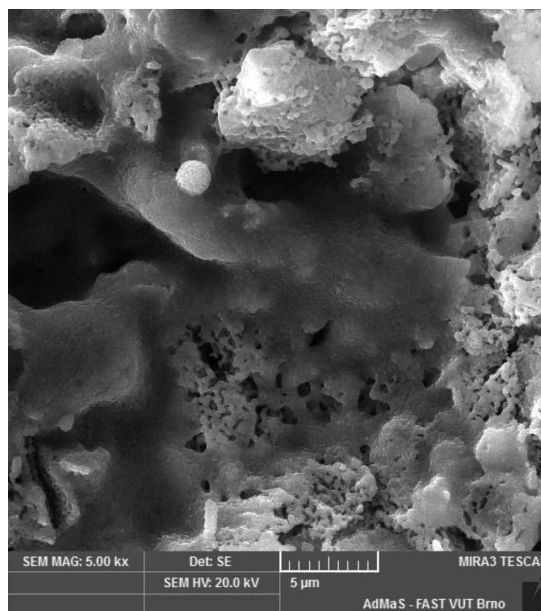


**Figure 11:** Microstructure of MBS-45/Cl (45 d, Cl – exposure to chloride solution and frost environment, 50 cycles), exposure to 1000 °C, 5000× magnification



diagram "22"). A combination of frost and chloride ions caused a decrease in the strength of 27.5 % (MBS-90Cl) and 29.6 % (MFA-90Cl). These values can be assessed as adequate for the given type of material (i.e., the material with a porous aggregate) after a given number of cycles. The thermal resistance (a relative decrease in the compressive strength) of the materials in individual environments after being exposed to 1000 °C was approximately 64–69 % (72–78 %) for the reference samples (the samples exposed to the aggressive environment). It is interesting that slag (i.e., MBS) showed better results than the other reference material; however, after the exposure to the aggressive environment and high temperature, fly ash was better (i.e., MFA). For illustration, MBS-90/Cl (MFA-90/Cl) showed a decrease in the compressive strength of 75.1 % (74.1 %; **Figure 2**). A slight increase in the thermal resistance developed over time in spite of the higher number of cycles in the aggressive environment. The only exception was MFA-90/Cl. An evaluation of the relative change in the thermal resistance caused by the aggressive environment shows an irregular development of the curves (**Figure 3**). This is particularly clear for temperatures of 600 °C and above. It is evident that the exposure to an aggressive environment and 1000 °C caused a decrease in the observed parameter of MBS (MFA) of approximately 11 % (2.5–7.2 %).

Further, the bending tensile strength was evaluated. The differences are less obvious compared to the development of the compressive strength (**Figures 1 and 4**). The increase in the bending strength in time was also less considerable than the increase in the compressive strength. The bending strengths of the test specimens not exposed to aggressive environments and a thermal load were from 7.3 N mm<sup>-2</sup> to 7.6 N mm<sup>-2</sup> (6.9 N mm<sup>-2</sup> to

7.2 N mm<sup>-2</sup>) for mix designs MBS (MFA). After the exposure of the samples to the aggressive environment with chloride ions, the decrease was 12.6 % for MBS-90 and 13.9 % for MFA-90.

The decrease in the tensile bending strength caused by the exposure to aggressive environments is then much lower than that of the compressive strength. The negative impact on the thermal resistance was also smaller. The decrease in the tensile bending strength was 65.8 % (62.3 %) for MBS-90/R (MFA-90/R) after the exposure to 1000 °C (**Figure 5**). These facts imply that the substitution of the primary binder with fly ash had a more positive effect from the viewpoint of a combined exposure involving an aggressive environment and a thermal load. On the other hand, comparing the changes in the thermal resistance in time and after the exposure to adverse environments shows (**Figure 6**) that blast-furnace slag had better results (MBS). The reduction in the thermal resistance after the exposure to 1000 °C was 5.3 % for MBS-90/Cl-R and 6.1 % for MFA/Cl-R. The reduction in the thermal resistance of MFA after the exposure to 600 °C is also interesting for both tested ages. It can be assumed that used high-temperature fly ash contains components that react with chloride solutions, possibly only during the thermal load. It could also be a synergy reaction of both mentioned influences.

The synergy effect of an aggressive environment and extreme temperatures causes a considerable degradation of the structures of the materials based on a silicate matrix and a porous aggregate. The given case is confirmed with the results of physico-mechanical tests of materials MBS and MFA. The CT examination proved the above character of the crack changes after the exposure to the aggressive environment (chlorides and frost) and the subsequent extreme thermal load. On the reference materials, only a small amount of randomly oriented cracks was identified (**Figure 7**). The cracks were rather small, i.e., with a smaller width. These cracks mostly did not reach the transition zone between the matrix and dense aggregate. On the contrary, the number of cracks of the materials exposed to the aggressive environment was larger (**Figures 8 to 10**). An increase in the width and number of the cracks is evident as the number of aggressive cycles and age of the samples grow. However, the increase was not considerable. The orientation of the cracks was easily observable; the cracks pointed towards the center of a test specimen (**Figures 8 and 9**). The width and number of the cracks and more cracks in the transit zone between the dense aggregate and the matrix were evident compared to the reference materials.

The last representative sample was FMA-60/Cl (**Figure 10**). It is interesting that its cracks are more close to the surface, with an orientation similar to that of MBS. Chloride ions combined with frost and the subsequent thermal shock damaged more considerably the surface areas of MFA, whereas MBS was damaged more evenly throughout the whole structure.

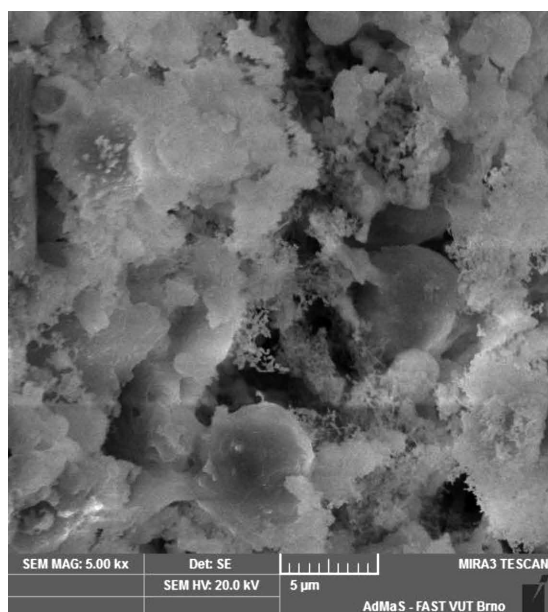


**Figure 12:** Microstructure of MBS-90/Cl (90 days, Cl – exposure to chloride solution and frost environment, 100 cycles), exposure to 1000 °C, 5000× magnification

The XRD analysis was used for the identification of crystal phases and their changes. XRD did not identify Friedel's salt in any of the tested specimens. The crucial factor of the formation of this chemical compound is the temperature, which is, *inter alia*, mentioned by Delagrave et al.<sup>3</sup>, Izquierdo et al.<sup>4</sup>, Yuan<sup>5</sup> and Tang<sup>6</sup>. It is then evident that the damage of the structure caused by the combination of frost and the solution with chloride ions is purely mechanical. The salt in the solution – NaCl – is transported into the porous structure of the composite by equalizing the concentration gradient. Sudden changes of the temperatures above and below zero then cause the crystallization of the salt and the change of the phase of water, which necessarily causes a decrease in the mechanical properties of the given material. This corresponds with the findings determined with CT. As regards the changes in the structures of the analyzed materials, a decomposition of chemical compounds (in particular mineralogical phases) typical for silicates and the used aggregate, due to the increasing temperature, was observed. The development shows peaks with a decreasing intensity and a gradual ceasing of portlandite, calcite and CSH phases. At temperatures over 600 °C, new phases were observed (like  $\beta$ -C<sub>2</sub>S).

SEM together with an element analysis showed the presence of Cl<sup>-</sup> ions in some areas. Microcracks and the degree of decomposition of the hydration products of the matrix or the changes in the structure of the used aggregate were marked, as shown in **Figures 11 and 12**. Almost no failures were observable in the transit zone between the porous aggregate (agloporite) and the matrix. As regards the age of the tested materials/number of cycles, no considerable differences in the microstructure were observed. A 5000× magnification clearly shows a degraded polymer-silicate matrix. SEM images clearly show spherical particles of fly ash also in MBS. This was caused by an imperfect manufacturing process of agloporite, during which not all granules (for the production of the aggregate) were perfectly compacted and fired. However, as this fly ash had gone through the thermic process twice, it is almost an inert filler from the viewpoint of high temperature. Only few microscopic cracks were observed in the matrix.

## 5 CONCLUSIONS

The influence of a combination of an aggressive environment (chloride solution and freeze-thaw cycles) and a thermal load (of up to 1000 °C) was tested and analyzed in detail on newly designed materials as it is not a thoroughly examined area. Fly-ash agloporite is a promising aggregate and its influence on polymer-silicate materials is still not quite clear. The advantage of agloporite is its thermal resistance and very good interaction with a polymer-silicate matrix. However, an exposure to cyclic changing of temperatures above and below zero, intensified by a salt solution, makes the use of the porous aggregate difficult. Blast-furnace slag (MBS) and fly ash (MFA) were used for a modification

of the matrix composition. Physico-chemical and microstructural analyses proved that the action of the above-mentioned environment disturbs the structures of MBS and MFA in a mechanical way, causing an expansion due to the change of the phase of water or crystallization of salt rather than the formation of new chemical compounds. The extreme temperature then only intensifies these phenomena by degrading the structures, in particular that of the matrix. It was proved that CT is crucial for the explanation of the changes/failures of the inner structure. This analytical method is quite suitable for examining the three-dimensional structure of a given material. It is particularly applicable for revealing various cracks, their orientation, localization or number. The tested materials have a large potential for future research. An examination of the behavior of the materials over a longer time (e.g., 180 d and 360 d) would also be very interesting.

## Acknowledgements

This paper has been worked out with the financial support of The Czech Science Foundation (GAČR), project GA15-07657S, "Study of kinetics of processes occurring in the composite system at extreme temperatures and exposed to an aggressive environment", as well as under project No. LO1408 "AdMaS UP – Advanced Materials, Structures and Technologies", supported by the Ministry of Education, Youth and Sports under the National Sustainability Programme I.

## 6 REFERENCES

- <sup>1</sup> J. G. Jang, H. J. Kim, H. K. Kim, H. K. Lee, Resistance of coal bottom ash mortar against the coupled deterioration of carbonation and chloride penetration, *Materials & Design*, 93 (2016), 160–167, doi:10.1016/j.matdes.2015.12.074
- <sup>2</sup> M. Maes, N. De Belie, Resistance of concrete and mortar against combined attack of chloride and sodium sulphate, *Cement and Concrete Composites*, 53 (2014), 59–72, doi:10.1016/j.cemconcomp.2014.06.013
- <sup>3</sup> A. Delagrave, J. Marchand, J. P. Ollivier, S. Julien, K. Hazrati, Chloride binding capacity of various hydrated cement paste systems, *Advanced Cement Based Materials*, 6 (1997), 28–35, doi:10.1016/S1065-7355(97)90003-1
- <sup>4</sup> D. Izquierdo, C. Alonso, C. Andrade, M. Castellote, Potentiostatic determination of chloride threshold values for rebar depassivation – experimental and statistical study, *Electrochim. Acta*, 49 (2004) 17–18, 2731–2739, doi:10.1016/j.electacta.2004.01.034
- <sup>5</sup> Q. Yuan, Fundamental studies on test methods for the transport of chloride ions in cementitious materials, Doctoral Thesis, Ghent, Ghent University, 2009
- <sup>6</sup> L. Tang, Chloride transport in concrete-measurement and prediction, Doctoral Thesis, Göteborg, Chalmers University of Technology, 1996
- <sup>7</sup> F. P. Glasser, J. Marchand, E. Samson, Durability of concrete – degradation phenomena involving detrimental chemical reactions, *Cem. Concr. Res.*, 38 (2007) 2, 226–246, doi:10.1016/j.cemconres.2007.09.015
- <sup>8</sup> I. Santamaría-Vicario, A. Rodríguez, C. Junco, S. Gutiérrez-González, V. Calderón, Durability behavior of steelmaking slag masonry mortars, *Materials & Design*, 97 (2016), 307–315, doi:10.1016/j.matdes.2016.02.080

T. MELICHAR et al.: DURABILITY OF MATERIALS BASED ON A POLYMER-SILICATE MATRIX ...

- <sup>9</sup> S. Aydin, Development of a high-temperature-resistant mortar by using slag and pumice, *Fire Safety Journal*, 43 (2008), 610–617, doi:10.1016/j.firesaf.2008.02.001
- <sup>10</sup> İ. Yüksel, R. Siddique, Ö. Özkan, Influence of high temperature on the properties of concretes made with industrial by-products as fine aggregate replacement, *Construction and Building Materials*, 25 (2011), 967–972, doi:10.1016/j.conbuildmat.2010.06.085
- <sup>11</sup> G. Yuan, Q. Li, The use of surface coating in enhancing the mechanical properties and durability of concrete exposed to elevated temperature, *Construction and Building Materials*, 95 (2015), 375–383, doi:10.1016/j.conbuildmat.2015.07.120
- <sup>12</sup> A. Nadeem, S. A. Memon, T. Yiu Lo, Mechanical performance, durability, qualitative and quantitative analysis of microstructure of fly ash and Metakaolin mortar at elevated temperatures, *Construction and Building Materials*, 38 (2013), 338–347, doi:10.1016/j.conbuildmat.2012.08.042
- <sup>13</sup> T. Harun, C. Ahmet, An experimental investigation of bond and compressive strength of concrete with mineral admixtures at high temperature, *Arab. J. Sci. Eng.*, 33 (2008) 2B, 443–449
- <sup>14</sup> V. Černý, Š. Keprdová, Usability of fly ashes from Czech Republic for sintered artificial aggregate, *Advanced Materials Research*, (2014), 805–808
- <sup>15</sup> ČSN EN 1504-3, Products and systems for the protection and repair of concrete structures – Definitions, requirements, quality control and evaluation of conformity – Part 3: Structural and non-structural repair, ČNI, 2006
- <sup>16</sup> ČSN EN 1363-1, Fire resistance tests – Part 1: General requirements, ČNI, 2013
- <sup>17</sup> ČSN 73 1326, including Z1, Resistance of cement concrete surface to water and defrosting chemicals, ČNI, 2003
- <sup>18</sup> ČSN EN 12190, Products and systems for the protection and repair of concrete structures – Test methods – Determination of compressive strength of repair mortar, ČNI, 1999
- <sup>19</sup> ČSN EN 196-1, Methods of testing cement – Part 1: Determination of strength, ČNI, 2005

INFLUENCE OF THERMOMECHANICAL TREATMENT ON THE  
GRAIN-GROWTH BEHAVIOUR OF NEW Fe-Al BASED ALLOYS  
WITH FINE  $\text{Al}_2\text{O}_3$  PRECIPITATESVPLIV TERMOMEHANSKE OBDELAVE FeAl ZLITIN S FINIMI  
 $\text{Al}_2\text{O}_3$  IZLOČKI NA RAST ZRNBohuslav Mašek<sup>1</sup>, Omid Khalaj<sup>1</sup>, Hana Jirková<sup>1</sup>, Jiří Svoboda<sup>2</sup>,  
Dagmar Bublíková<sup>1</sup><sup>1</sup>University of West Bohemia, Regional Technology Institute, Univerzitní 22, 306 14 Pilsen, Czech Republic<sup>2</sup>Institute of Physics of Materials, Academy of Sciences of the Czech Republic, Žitkova 22, 616 62 Brno, Czech Republic  
svobj@ipm.cz*Prejem rokopisa – received: 2016-07-20; sprejem za objavo – accepted for publication: 2017-04-20*

doi:10.17222/mit.2016.232

To obtain the superior-high-temperature creep strength, a transformation of a fine-grained structure to large grains due to abnormal grain growth or recrystallization is an important process in oxide-dispersion-strengthened (ODS) alloys. The processing of steel is enabled with powder metallurgy, which utilizes powders consisting of a Fe-Al metal matrix with a large O content, prepared with mechanical alloying, and their hot consolidation due to rolling. The thermomechanical characteristics of new ODS alloys with a Fe-Al matrix are investigated in terms of the changes in the grain-size distribution. The recrystallization and grain growth were quantified after heating up to 1200 °C, which is the typical consolidation temperature for standard nanostructured ferritic steels. The results show that new ODS alloys are significantly affected by the thermomechanical treatment leading to microstructural changes. Recrystallization is mostly affected by decreasing the deformation and increasing the holding time, which leads to a growth of the grain size.

Keywords: grain growth, ODS alloys, steel, Fe-Al,  $\text{Al}_2\text{O}_3$ 

Da bi pridobili najvišjo temperaturo moči lezenja, je transformacija drobnozrnate strukture v večja zrna ali celo v abnormno velika oziroma rekristalizacija pomemben proces pri zlitinah, ojačanih z oksidno disperzijo (angl. ODS). Obdelava jekla je omogočena z metalurgijo v prahu, ki pomaga prahom, ki vsebujejo metalno matrico Fe-Al z veliko vsebnostjo kisika, pripravljeno z mehanskim legiranjem in njihovo vročo konsolidacijo pri valjanju. Termomehanske karakteristike novih ODS-zlitin s Fe-Al matrico so bile preiskovane, ker je prišlo do sprememb v velikosti porazdelitve zrn. Rekristalizacija in rast zrn sta bili ovrednoteni po segretju do 1200 °C, ki je tipična temperatura konsolidacije za nanostrukturirana feritna jekla. Rezultati kažejo, da na ODS-zlitine zelo vpliva termomehanska obdelava, ki pripelje do sprememb v mikrostrukturi. Na rekristalizacijo največkrat vpliva deformacija in povečanje časa zadržanosti, ki povzroči rast velikost zrn.

Ključne besede: rast zrn, ODS-zlitine, jeklo, Fe-Al,  $\text{Al}_2\text{O}_3$ 

## 1 INTRODUCTION

Historically, ODS alloys have been employed to improve high-temperature mechanical properties. In 1910, the first utilization of an oxide dispersion was reported by W. D. Coolidge. Using the classical powder metallurgy, a tungsten-based alloy reinforced with thorium oxides was developed to impede high-temperature grain growth and therefore increase the life span of a tungsten-filament lamp.<sup>1</sup> After this first development, several other applications with various metallic matrices such as aluminium or nickel were implemented over the decades. A notable improvement in the field was made by J. S. Benjamin at the International Nickel Company (INCO) laboratory: he proposed a new process based on high-energy-milling powder metallurgy – later called mechanical alloying.<sup>2</sup> This process was introduced to obtain a fine and homogeneous oxide dispersion within a nickel matrix. Its aim was to produce high-temperature-resistant materials for gas-turbine applications.<sup>3</sup>

Currently, mechanical alloying is still considered to be the most effective process for obtaining fine and homogeneously distributed particles. The volume fraction of dispersed spherical oxides (usually  $\text{Y}_2\text{O}_3$ ) is typically below 1 % and the oxides typically have a mean size of 5–30 nm. The mechanically alloyed powder is then consolidated at high temperatures and pressures to produce the bulk material in the form of a bar or tube stock. Subsequently, different thermomechanical treatments are applied to optimize its microstructure and mechanical properties.

Oxides are much more resistant to coarsening in the coarse-grained ferrite than the  $\gamma'$ -precipitates in superalloys, and the limiting temperature for a long-term operation is between 1000 °C and 1100 °C when the mean size of oxides is 20–30 nm. This clearly indicates that oxides are extremely stable and the microstructural stability of ODS alloys is much higher than that of nickel-based superalloys. However, a loss of mechanical properties due to the coarsening of oxides was also



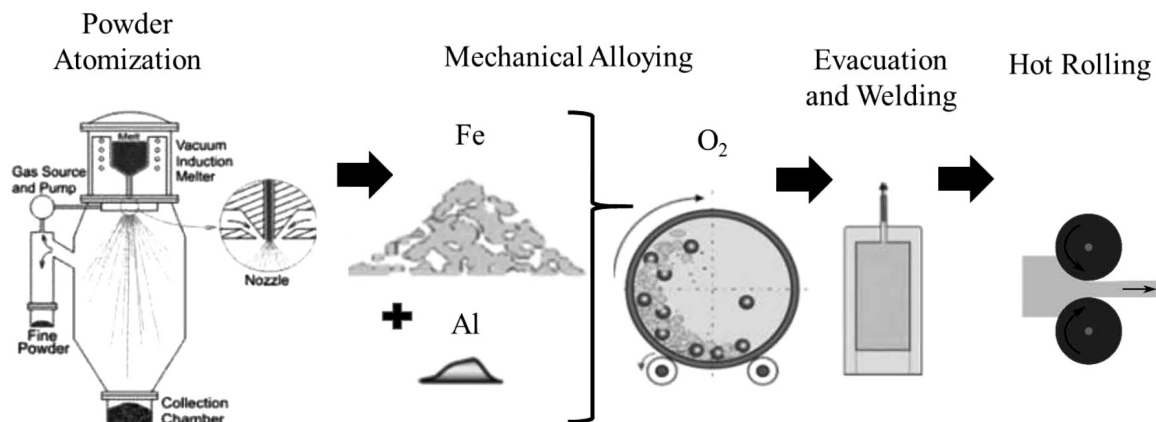


Figure 1: Material-preparation process

observed in fine-grained ODS steels at temperatures of about 800 °C for the systems with an extremely fine oxide dispersion (about 5 nm).<sup>4</sup> Thus, the size of oxides as well as the grain size are also important for the stability of the microstructure – coarser oxides are much more stable than fine ones, which is in line with the cubic law for coarsening kinetics.

In the consolidation step, the processing temperatures are critical in order to retain the nanocrystalline structure generated during the mechanical alloying and to impede the particle coarsening and grain growth.<sup>5–9</sup> The Ni- and F-based ODS alloys rely on the formation of slowly growing and strongly adherent chromium and aluminium scales for their high temperature oxidation/corrosion resistance. In the present study, the ODS alloys consist of a ferritic Fe-Al matrix strengthened with about 4 % volume fraction of  $\text{Al}_2\text{O}_3$  particles.<sup>10–15</sup> In order to obtain a more detailed insight into these new groups of materials, this paper will concentrate on both the general microstructure and mechanical properties of ODS steels, the phenomenon of recrystallization and the related microstructural evolutions.

## 2 EXPERIMENTAL PART

### 2.1 Material preparation

The classical processing route used to produce Fe-Al based alloys with fine  $\text{Al}_2\text{O}_3$  precipitates is highly dependent on powder metallurgy (Figure 1). The first step of the elaboration is the mechanical alloying of powders consisting of Fe-11 w/% Al matrix (90 w/% Fe and 10 w/% Al) and 1 w/% of  $\text{O}_2$  in gas, which is absorbed, in a low-energy ball mill developed by the authors, enabling evacuation and filling with oxygen. It has two steel containers (each holding 24 L) and each container is filled with 80 steel balls with a diameter of 40 mm. The revolution speed varies between 20–75  $\text{min}^{-1}$ . However, the speed for our research was kept constant (75  $\text{min}^{-1}$ ) for all the material preparations.

This step allows the powder to be forced into a solid solution. The milled powder is then deposited into a steel

container with a diameter of 70 mm, evacuated (degassed) and sealed by welding. The steel container is then heated up to a temperature of 750 °C and rolled in a hot rolling mill to a thickness of 20 mm in the first rolling step, then heated up to a temperature of 900 °C and rolled to a thickness of 8 mm in the second step. A 6-mm-thick sheet of the ODS alloy covered on both sides with a 1-mm-thick scale from the rolling container was produced in this way. Afterwards, the specimens were cut with a water jet (Figure 5).

Eight types of material were used in this research as described in Table 1. They are all based on a Fe-10w/% Al ferritic matrix with different particle sizes and 4 % volume fraction of  $\text{Al}_2\text{O}_3$ .

$\text{Al}_2\text{O}_3$  powder was added to prepare the composite; fine oxides in the ODS alloys were obtained with the internal oxidation during mechanical alloying and precipitated during hot consolidation. It should be noted that in the case of Material 1, the  $\text{Al}_2\text{O}_3$  particles were added, but in all the other materials, oxides were produced due to internal oxidation as shown in Figure 1. Different sizes of the oxides in ODS steels are due to different heat treatments after hot rolling. SEM observations indicated several inhomogeneities due to the material sticking to the walls of the milling container during mechanical alloying.

Table 1: Material parameters

Material No.	Material type	Milling time (hours)	Ferritic matrix	Vol.% of $\text{Al}_2\text{O}_3$	Typical particle size (nm)
1	ODS Alloy	100	Fe10wt%Al	10	300
2	ODS Alloy	100	Fe10wt%Al	6	50-200
3	ODS Alloy	150	Fe10wt%Al	6	50-150
4	ODS Alloy	200	Fe10wt%Al	6	30-150
5	ODS Alloy	245	Fe10wt%Al	7	20-50
6*	ODS Alloy	245	Fe10wt%Al	7	20-50
7*	ODS Alloy	245	Fe10wt%Al	7	20-50
8*	ODS Alloy	245	Fe10wt%Al	7	20-50

\* Different rolling conditions

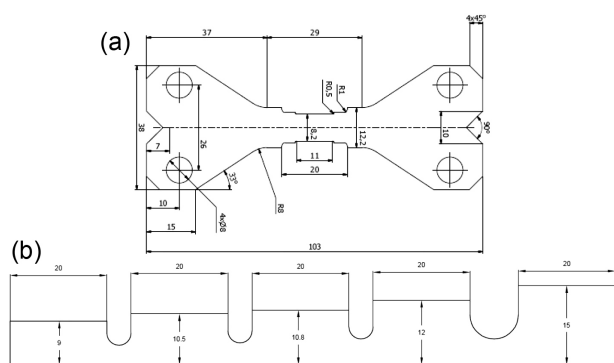


**Figure 2:** Specimen dimensions in mm: a) type 1, b) type 2

These inhomogeneities can also influence the mechanical properties of the material, but the mechanical alloying process is steadily optimized with respect to the homogeneity of the materials.

## 2.2 Specimen preparation

Two specimen types (**Figure 2**) were selected from several examples, which exhibited the most homogeneous temperature fields for specimen type 1 and simplicity of tests for specimen type 2. Specimen type 1 was chosen from six types of specimen shapes with different active parts in the middle. All the samples were carefully monitored using a thermal camera to see how the temperature field is distributed within the active part when heated up to 1200 °C. So, regarding the results, specimen type 1 (5a) has the best homogeneity regarding the temperature distribution. On the other hand, specimen type 2 is designed to have four different deformations (5, 8, 20 and 50) % at the same time. The shortest part (9 mm) is designed to have no deformation during the pressing and the rest have appropriate values of deformation. This specimen is held in a hydraulic



**Figure 3:** Positions of specimens between holding plates



**Figure 4:** Positions of specimens on a rolled semi-product: a) type 1, b) type 2

forging press with two positioning side plates (10 mm thick) (**Figure 3**) in order not to apply more deformation than required. The prepared containers were annealed at 1000 °C over 16 h. After normal cooling at room temperature, all the specimens were cut by a water-jet machine in the longitudinal direction (**Figure 4**) and then all the specimens were removed from the steel containers. After grinding, the thickness of the specimens was approximately 6 mm.

### 2.3 Testing equipment

In order to speed up the tests, a hydraulic forging press (**Figure 5**) was used to apply four different deformations at the same time on the type-2 specimens. Also, in order to investigate the thermomechanical treatment of the specimens, a servo-hydraulic MTS thermomechanical simulator (**Figure 6**) was used, which allows various temperature-deformation paths to be run in order to find the conditions leading to, e.g., the most effective grain coarsening due to recrystallization. The thermo-

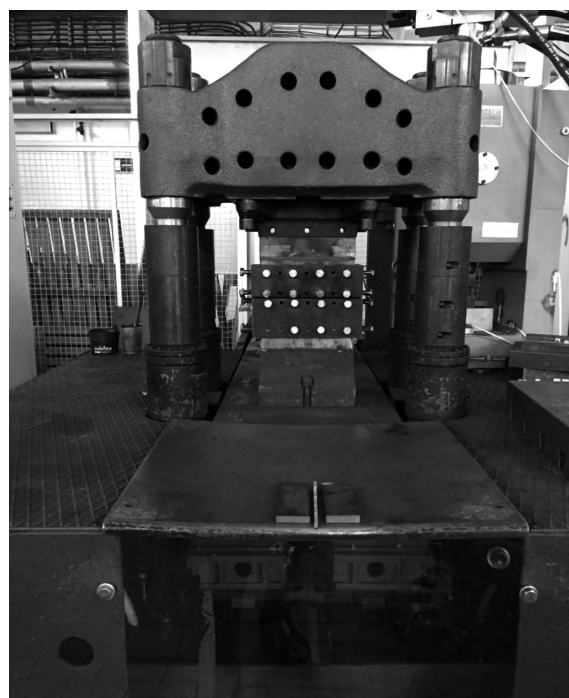


**Figure 5:** Hydraulic forging press

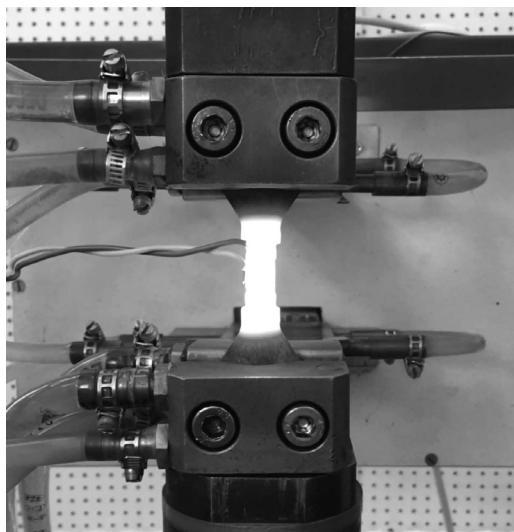


Figure 6: Treatment with a thermomechanical simulator

mechanical simulator also allows a combination of tensile and compressive deformation, thus accumulating a high plastic deformation (and a high dislocation density) in a specimen.

## 2.4 Testing programme

The testing programme involved two different groups. The tests are summarized in **Table 2**.

Tests in group A were carried out to investigate the thermomechanical behaviour of different materials (1–8) at different temperatures, looking at a single tensile and compression loading with a constant strain rate of  $1 \text{ s}^{-1}$  (**Figure 7**). In order to give a clearer comparison of the results, only the results at room temperature (RT), (800, 1000 and 1200) °C are presented.

Tests in group B were performed to investigate the effects of the holding time at 1000 °C and the deformation percentage on materials 7 and 8 with the type-2 specimen shape (**Figure 2b**). The specimen was designed in order to apply four different deformations (5, 8, 20 and 50 %) at the same time (**Figure 8**), and subsequently one specimen from each material was quenched in water for immediate cooling and the rest were kept in the furnace at three different holding times (10, 20, 40) h, after which they were cooled slowly to room temperature.

Treatment No. 1 was designed to apply three different single deformations on each sample at different temperatures. The specimen is first heated up to the

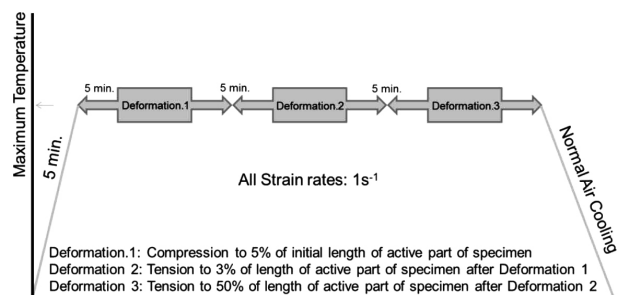


Figure 7: Treatment No. 1

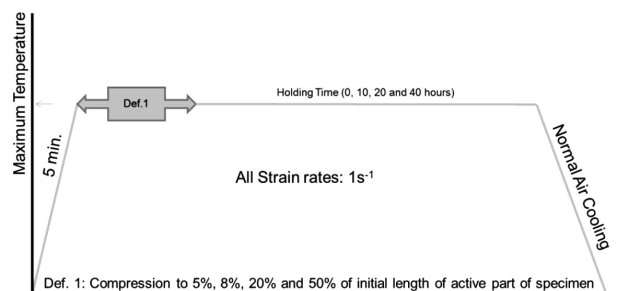


Figure 8: Treatment No. 2

desired temperature in 5 min and is then held for another five minutes. Immediately after these 10 min, the first deformation (5 % compression) is applied to the specimen and then the temperature is held for another five minutes. The second deformation (3 % tension) is applied immediately after 5 min and again the temperature is held for five minutes and after that the last deformation (50 % tension) is applied and the specimen is left to cool down to room temperature.

Treatment No. 2 was designed to apply four different deformations (5, 8, 20 and 50) % at the same time on a specimen. First, the specimen is heated to the desired temperature in 5 minutes and immediately after that, the deformation is applied. The temperature is kept for different holding times (0, 10, 20, 40) h and then the specimen is left to cool down to room temperature.

## 3 RESULTS AND DISCUSSION

### 3.1 Test group A

**Figure 9** shows the stress-strain curves for all the materials at different temperatures, with 5 % compression, corresponding to Treatment No. 1. Material 2 exhibits better strength at 30 °C (almost 500 MPa) and 800 °C (almost 300 MPa); at 1200 °C, material 1 still

Table 2: Parameters of the testing programme

Test group	Material No.	Treatment No.	Holding time (h)	Maximum temperature (°C)	Number of tests	Purpose of tests
A	1, 2, 3, 4, 5, 6, 7, 8	1	–	1200, 1100, 1000, 900, 800, RT	48	Investigation of thermomechanical behaviour
B	7,8	2	0, 10, 20, 40	1000	40	Investigation of grain-size growth



shows better strength (almost 60 MPa), but not very different from material 2 (almost 50 MPa). It seems that the difference in the compression strength between these two materials is almost 37 % at RT; however, this difference increased to 137 % at 800 °C. On the other hand, all the materials have almost the same elastic modulus and none of them fails at the 5 % compression. However, material 4 shows a strange behaviour at 800 °C. The microstructure analysis shows that this occurred because of an inhomogeneous formation of the particles in the specimen.

The hot-working behaviour of alloys is generally reflected by flow curves, which are a direct consequence of microstructural changes: the nucleation and growth of new grains, dynamic recrystallization (DRX), the generation of dislocations, work hardening (WH), the rearrangement of dislocations and their dynamic recovery (DRV). In deformed materials, DRX seems to be the prominent softening mechanism at high temperatures. DRX occurs during the straining of metals at high temperatures, characterized by a nucleation of low-dislocation-density grains and their posterior growth, producing a homogeneous grain structure when dynamic equilibrium is reached. Material 4 showed a strange curve shape at 800 °C. The test was repeated several times and similar behaviour was observed each time. It was concluded that this happens because of the inhomogeneity of the microstructure of this material.

**Figure 10** shows the stress-strain curves at different temperatures corresponding to the 3 % tension of Treatment No. 1. As can be seen in **Figure 10**, material 2 shows a higher strength at 30 °C (almost 650 MPa) and 800 °C (almost 270 MPa), but at 1200 °C, material 1 again shows a better strength (almost 65 MPa). This value was 35 % lower when the temperature was increased. In **Figure 10**, the strain at the maximum tension is almost 2 % at RT (**Figure 10a**), then it increases to almost 3 % at 800 °C (**Figure 10b**); however, it decreases to almost 1 % at 1200 °C (**Figure 10c**). All the

materials have almost the same elastic modulus and none of them failed at the 3 % deformation. The yield stress and the shape of the flow curves are sensitive to temperature. Comparing all these curves, it is found that decreasing the deformation temperature increases the yield-stress level. In other words, it prevents softening due to dynamic recrystallization (DRX) and dynamic recovery (DRV) and allows the deformed metals to exhibit work hardening (WH). For every curve, after a rapid increase in the stress to the peak value, the flow stress decreases monotonically towards a steady-state regime with a varying softening rate, which typically indicates the onset of DRX, **Figure 10c**.

**Figure 11** shows the stress-strain curves at different temperatures for the 50 % tension of Treatment No. 1. All eight materials failed at RT, but only four materials failed below the 50 % tension at higher temperatures. Material 2 failed at the 34 % strain, materials 4 and 5 failed at around 45 % strain and material 8 failed at around 50 % at 800 °C. At 1200 °C, only material 1 failed at 41 % and material 2 failed at the 45 % strain. From these curves, it can also be seen that the stress evolution with strain exhibits three distinct stages.

Work hardening (WH) predominates in the first stage and causes dislocations to polygonise into stable subgrains. The flow stress exhibits a rapid increase with the increasing strain up to the critical value. Then DRX occurs due to a large difference in the dislocation density within subgrains or grains. When the critical driving force of DRX is attained, new grains are nucleated along the grain boundaries, deformation bands and dislocations, resulting in the formation of equiaxed DRX grains.

In the second stage, the flow stress exhibits a smaller and smaller increase until the peak value, or an inflection of the work-hardening rate is reached. This shows that thermal softening becomes more and more important due to DRX and dynamic recovery (DRV) and it exceeds WH.

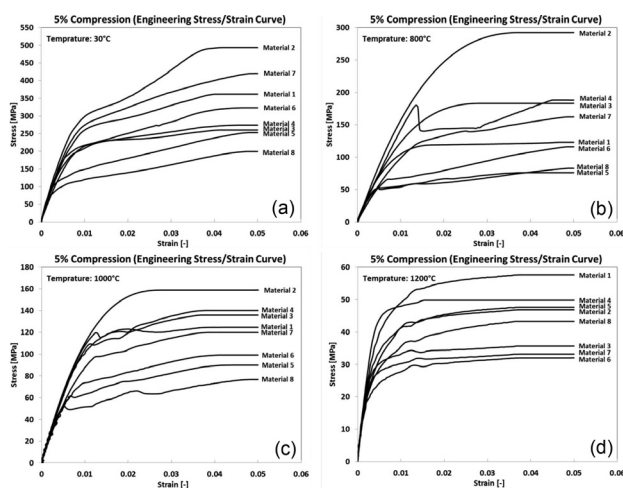


**Figure 9:** Stress-strain curves (5 % compression) for: a) RT, b) 800 °C, c) 1000 °C, d) 1200 °C

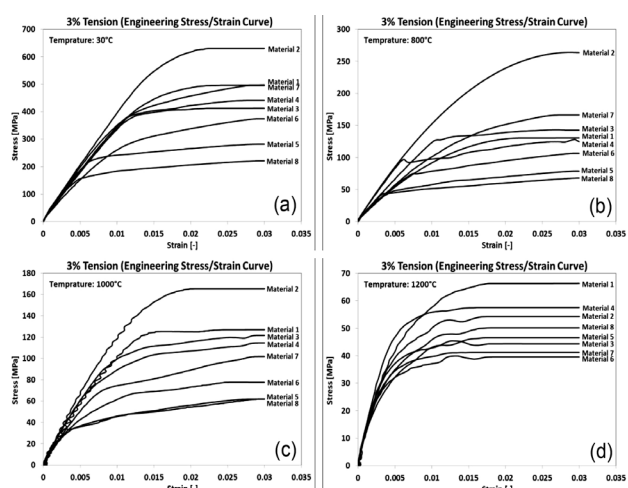


**Figure 10:** Stress-strain curves (3 % tension) for: a) RT, b) 800 °C, c) 1000 °C, d) 1200 °C



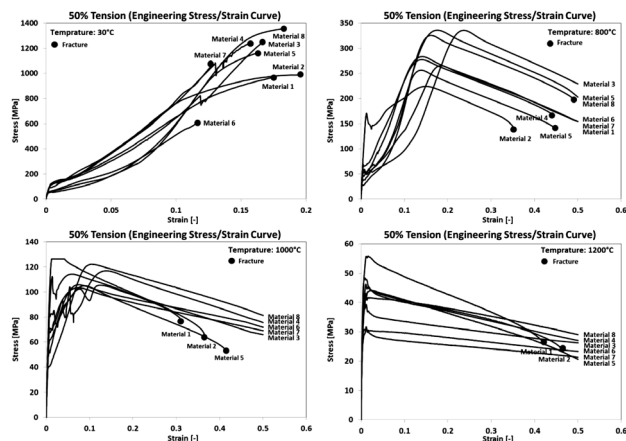


**Figure 11:** Stress-strain curves (50 % tension) for: a) RT, b) 800 °C, c) 1000 °C, d) 1200 °C

In the third stage, three types of curves can be recognized:

- A gradual decrease to a steady state with DRX softening (**Figure 11c**).
- A continuous increase with significant work-hardening (**Figure 11a**).
- A continuous decrease with significant DRX softening (**Figure 11b**).

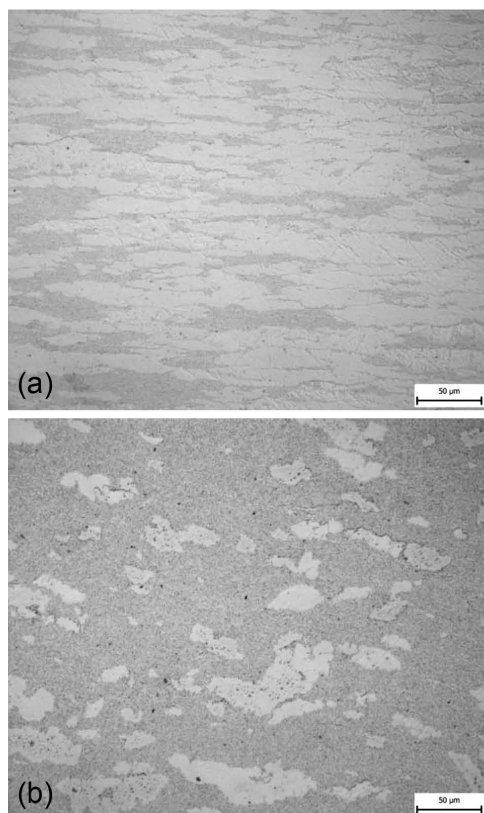


**Figure 12:** Microstructure for material 7 without annealing a) without deformation, b) with 50 % deformation

### 3.2 Test group B

**Figures 12 to 19** show the microstructures of materials 7 and 8 without deformation and with the 50 % deformation at different annealing times of (0, 10, 20 and 40) h at 1000 °C. It can be seen that by increasing the annealing time, the number of low-angle grain boundaries ( $<15^\circ$ ) decreased. This indicates that recrystallization does not occur at the zones with shorter annealing times (**Figure 12a**). A few banding zones with a high density of low-angle grain boundaries are observed in **Figures 14a** and **16a** showing that recrystallization occurs in most zones. **Figure 18a** shows that the banding zones with a high density of low-angle grain boundaries cannot be observed, indicating that almost completely recrystallized ferrite grains can be obtained after annealing at 1000 °C for 40 h.

Similar results were achieved for the rest of the specimens; however, there is a major difference between the microstructures. Material 7 is partially recrystallized, but material 8 retained fine grains. Both materials were prepared using the same procedure, but with different rolling pressures during the hot-rolling process. During the rolling process, a specimen passes through different stages. In the first stage of rolling, the material is under a considerable mechanical stress, resulting from an internally balanced elastic strain. This elastic strain is

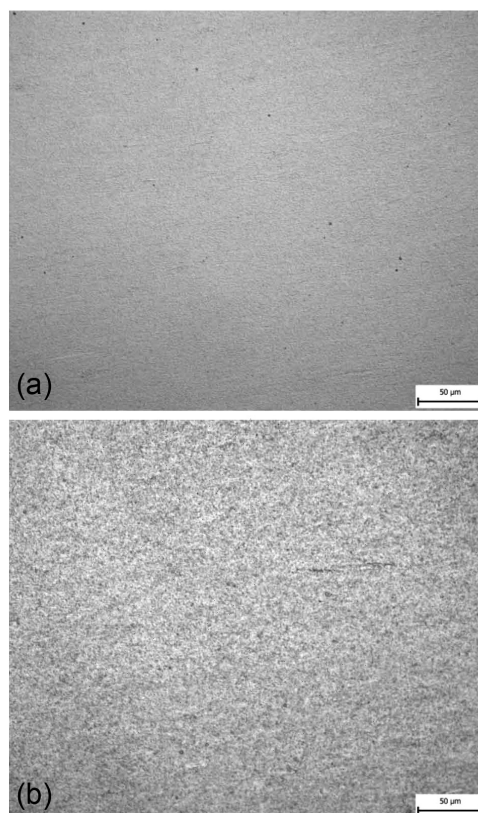


**Figure 13:** Microstructure of material 8 without annealing: a) without deformation, b) with 50 % deformation

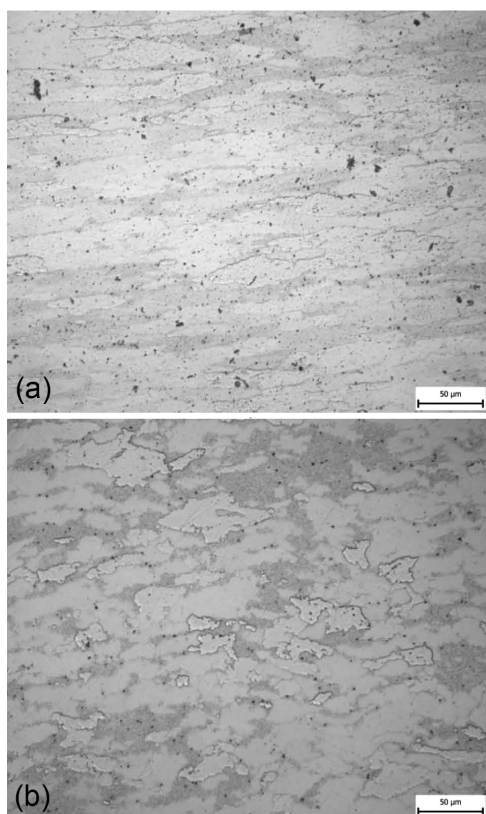


**Figure 14:** Microstructure for material 7 after 10 h annealing: a) without deformation, b) with 50 % deformation

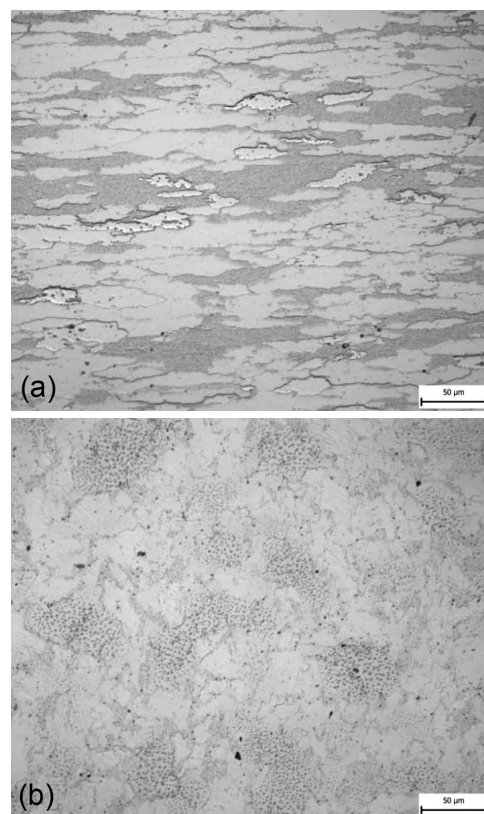


**Figure 16:** Microstructure for material 7 with 20 h annealing: a) without deformation, b) with 50 % deformation

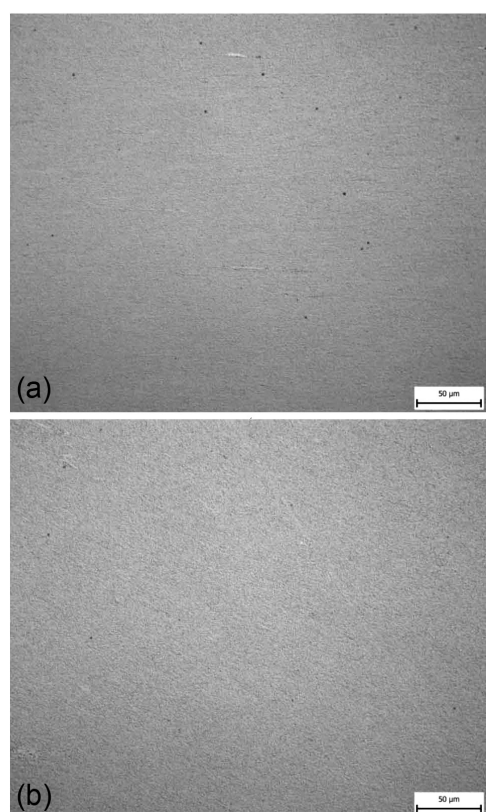


**Figure 15:** Microstructure for material 8 after 10 h annealing: a) without deformation, b) with 50 % deformation

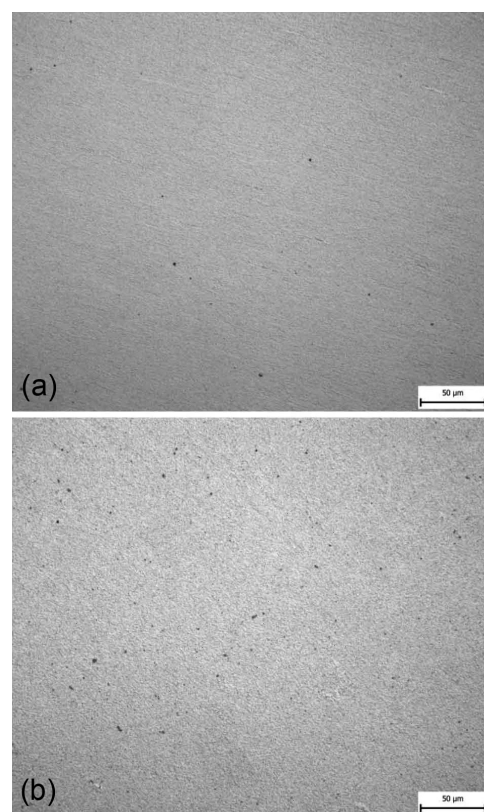


**Figure 17:** Microstructure for material 8 with 20 h annealing: a) without deformation, b) with 50 % deformation



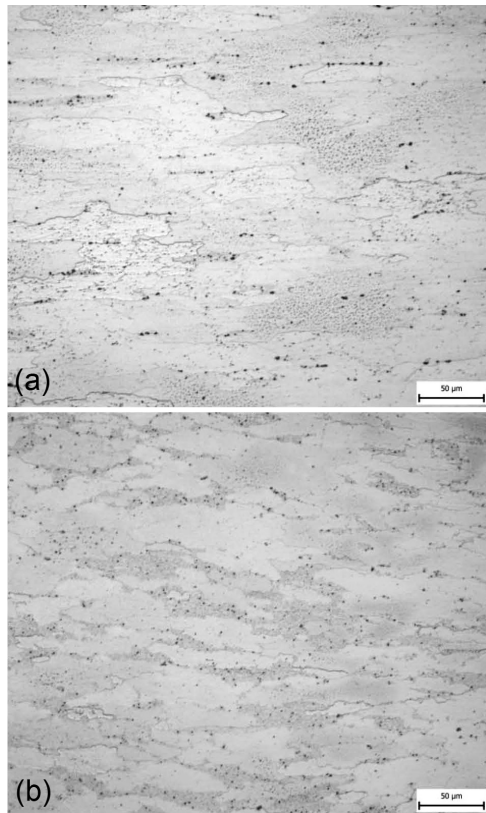


**Figure 18:** Microstructure for material 7 with 40 h annealing: a) without deformation, b) with 50 % deformation

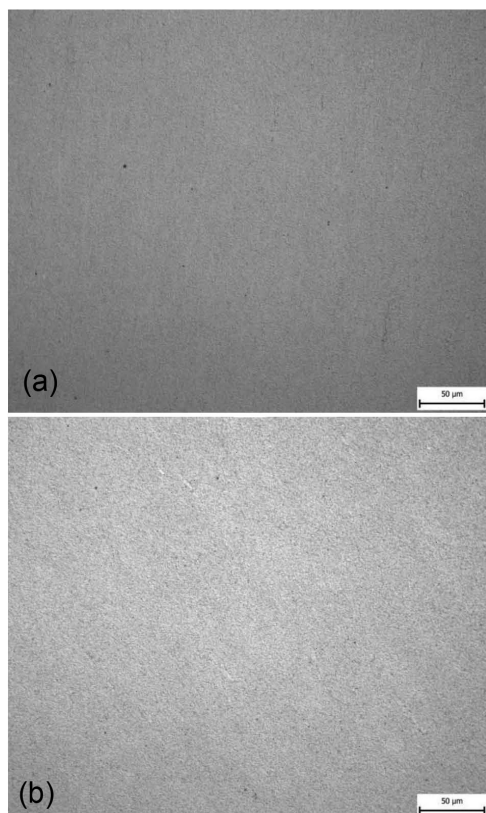


**Figure 19:** Microstructure for material 8 with 40 h annealing: a) without deformation, b) with 50 % deformation

added to the jamming of the dislocation, which occurred during cold forming.

In **Figures 12, 14, 16 and 18**, there is a visible alternation in the distorted shape of the cold-work crystals at the stress-relief stage (**Figures 12a, 14a, 16a and 18a**). In this stage, new crystals begin to grow in the deformed crystals. In the next stage (**Figures 12b, 14b, 16b and 18b**), the small crystals that formed in the previous stage gradually grow into bigger crystals by absorbing each other in the cannibal fashion, thus making the structure relatively coarse grained.

**Figures 12 to 19** show that with the increasing strain, a cellblock structure gradually develops and the sizes of the cellblocks and the cells decrease. In other words, in material 7 (**Figures 12, 14, 16 and 18**), there is a great transformation. It can be seen that with the increasing strain, there are changes in the spacing of the dense dislocation walls and micro-bands (DDW-MBs) and in the cell size. It is seen that after a 50 % deformation, the spacing of the DDW-MBs decreased to almost 50 µm, close to the cell size. In addition, the rate of the decrease in spacing with the increasing strains is much larger for geometrically necessary boundaries (GNBs) than for incidental dislocation boundaries (IDBs). However, in material 8 (**Figures 13, 15, 17 and 19**), there was no serious transformation and the structure still shows ferrite and pearlite. The grain size is relatively similar for both deformations. The grain boundaries can no longer be seen clearly, as the ferrite precipitated with the pearlite, creating a grey shade instead of a clear black-and-white contrast.

**Figure 20** gives an overview of the grain sizes of materials 7 and 8 with different deformations and annealing times. It can be seen that as material 7 is almost recrystallized, it has a bigger grain size than material 8. From **Figure 20** it is clear that by increasing

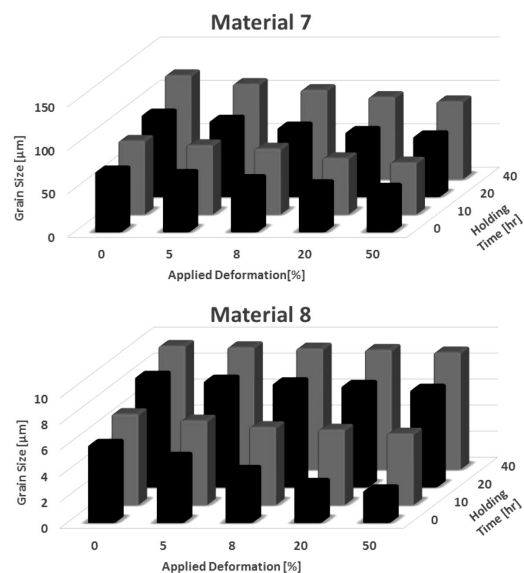


**Figure 20:** Grain size for: a) material 7, b) material 8

the annealing time, the grain size increases significantly for material 7 (**Figure 20a**), however the rate of increase in grain size is lower for material 8 (**Figure 20b**). The grain size reached almost 120  $\mu\text{m}$  after 40 hours annealing without any deformation in material 7, while the grains in material 8 reached almost 10  $\mu\text{m}$  under the same conditions. On the other hand, by increasing the applied deformation, the grain size of both materials decreased smoothly. Material 7 reached 50  $\mu\text{m}$  by applying 50 % deformation without annealing while material 8 reached almost 3  $\mu\text{m}$  under the same conditions. One can thus conclude that the stability of grain microstructure can be significantly influenced by the processing. The analysis of the reasons for this will be the topic of future work by the team.

#### 4 CONCLUSIONS

If you mean that why we didn't present the microstructure of material 1-6, because all the materials except 7 has fine microstructure similar to material 8, that is why we decide to present only the microstructure results from material 7 and 8 and compare them in this view point.

This paper outlines the influence of thermomechanical treatment on the grain growth of new Fe-Al based alloys with fine  $\text{Al}_2\text{O}_3$  precipitates. Eight materials differing in the amount and size of the oxides embedded in the ferritic matrix were tested under different conditions. The advantages of all the materials are their low-cost, simplicity of preparation and significant mechanical properties together with micro structures, due to the Fe-Al based ferritic matrix of the ODS alloy. The results from material 1-6 described in the relevant section (3.1. test group A) and the results from material 7-8 in case of microstructure described in section (3.2 test group B). As all the materials except 7 has fine microstructure similar to material 8, only the microstructure results from material 7 and 8 compared in this view point. It can be concluded that in general the oxide dispersion significantly strengthens the material. However, the typical form of the flow curve with DRX softening, including a single peak followed by a steady state flow as a plateau, is more recognizable at high temperatures than at low temperatures. This is because at high temperatures the DRX softening compensates for the work hardening (WH), and both the peak stress and the onset of steady state flow are therefore shifted to lower strain levels. The characteristics of softening flow behaviour coupled with DRX were investigated for eight materials and can be summarized as follows:

Decreasing deformation temperature causes the flow stress level to increase. In other words, it prevents the occurrence of softening due to DRX and dynamic recovery (DRV) and causes the deformed metals to exhibit work hardening (WH).

For every curve, after a rapid increase in the stress to a peak value, the flow stress decreases monotonically towards a steady state regime (a steady state flow as a

plateau due to DRX softening is more recognizable at higher temperatures). A varying softening rate typically indicates the onset of DRX, and the stress evolution with strain exhibits three distinct stages.

At higher temperatures, a higher DRX softening compensates the WH, and both the peak stress and the onset of steady state flow are therefore shifted to lower strain levels.

The elastic part of the total strain amplitude is always higher than the plastic part in all specimens tested, even for the highest total strain amplitudes of 15 %. This is further confirmation of the strong strengthening effect of oxide particles.

Material 7 is more crystallised than material 8. Thus, it has a larger grain size compared to the fine grains of material 8.

#### Acknowledgements

This paper includes results from projects 14-24252S Preparation and Optimization of Creep Resistant Submicron-Structured Composite with Fe-Al Matrix and  $\text{Al}_2\text{O}_3$  Particles subsidised by the Czech Science Foundation.

#### 5 REFERENCES

- <sup>1</sup> M. Mohan, R. Subramanian, Z. Alam, P. C. Angelo, Evaluation of the Mechanical Properties OF A Hot Isostatically Pressed Yttria-Dispersed Nickel-Based Superalloy, *Mater. Tehnol.*, 48 (2014) 6, 899–904
- <sup>2</sup> W. Quadackers, Oxidation of ODS alloys, *Journal de Physique IV*, 03 (1993) C9, 177–186, doi:10.1051/jp4:1993916
- <sup>3</sup> F. Pedraza, Low Energy-High Flux Nitridation of Metal Alloys: Mechanisms, Microstructures and High Temperatures Oxidation Behaviour, *Mater. Tehnol.*, 42 (2008) 4, 157–169
- <sup>4</sup> O. Khalaj, B. Mašek, H. Jirkova, A. Ronesova, J. Svoboda, Investigation on New Creep and Oxidation Resistant Materials, *Mater. Tehnol.*, 49 (2015) 4, 173–179, doi:10.17222/mit.2014.210
- <sup>5</sup> F. D. Fischer, J. Svoboda, P. Fratzl, A thermodynamic approach to grain growth and coarsening, *Journal of Philosophical Magazine*, 83 (2003) 9, 1075–1093, doi:10.1080/0141861031000068966
- <sup>6</sup> M. J. Alinger, G. R. Odette, D. T. Hoelzer, On the role of alloy composition and processing parameters in nanocluster formation and dispersion strengthening in nanostuctured ferritic alloys, *Acta Material*, 57 (2009) 2, 392–406, doi:10.1016/j.actamat.2008.09.025
- <sup>7</sup> P. Unifantowicz, Z. Oksiuta, P. Olier, Y. de Carlan, N. Baluc, Microstructure and mechanical properties of an ODS RAF steel fabricated by hot extrusion or hot isostatic pressing, *Fusion Engineering and Design*, 86 (2011), 2413–2416, doi:10.1016/j.fusengdes.2011.01.022
- <sup>8</sup> M. A. Auger, V. de Castro, T. Leguey, A. Muñoz, R. Pareja, Microstructure and mechanical behavior of ODS and non-ODS Fe-14Cr model alloys produced by spark plasma sintering, *Journal of Nuclear Materials*, 436 (2013) 5, 68–75, doi:10.1016/j.jnucmat.2013.01.331
- <sup>9</sup> M. Kos, J. Ferčec, M. Brunčko, R. Rudolf, I. Anžel, Pressing of Partially Oxide-Dispersion-Strengthened Copper using the ECAP Process, *Mater. Tehnol.*, 48 (2014) 3, 379–384, UDK 621.777.2:669.35\*71
- <sup>10</sup> B. Mašek, O. Khalaj, Z. Nový, T. Kubina, H. Jirkova, J. Svoboda, C. Štádlr, Behaviour of New ODS Alloys under Single and Multiple Deformation, *Mater. Tehnol.*, 50 (2016) 6, 891–898, doi:10.17222/mit.2015.156



B. MAŠEK et al.: INFLUENCE OF THERMOMECHANICAL TREATMENT ON THE GRAIN-GROWTH BEHAVIOUR ...

- <sup>11</sup> Marmy, P., Kruml, T., Low cycle fatigue of Eurofer 97, *Journal of Nuclear Materials*, 377 (2008) 1, 52–58, doi:10.1016/j.jnucmat.2008.02.054
- <sup>12</sup> M. Mišović, N. Tadić, M. Jaćimović, M. Janjić, Deformations and Velocities during the Cold Rolling of Aluminium Alloys, *Mater. Tehnol.*, 50 (2016) 1, 59–67, doi:10.17222/mit.2014.250
- <sup>13</sup> A. Grajcar, Microstructure Evolution of Advanced High-Strength Trip-Aided Bainitic Steel, *Mater. Tehnol.*, 49 (2015) 5, 715–720, doi:10.17222/mit.2014.154
- <sup>14</sup> B. Šuštaršič, I. Paulin, M. Godec, S. Glodež, M. Šori, J. Flasker, A. Korošec, S. Kores, G. Abramovič, DSC/TG of Al-based Alloyed Powders for P/M Applications, *Mater. Tehnol.*, 48 (2014) 4, 439–450
- <sup>15</sup> F. Tehovnik, J. Burja, B. Podgornik, M. Godec, F. Vode, Microstructural evolution of Inconel 625 during hot rolling, *Mater. Tehnol.*, 49 (2015) 5, 899–904, doi:10.17222/mit.2015.274

ANALYSIS OF PRECIPITATES IN ALUMINIUM ALLOYS WITH  
THE USE OF HIGH-RESOLUTION ELECTRON MICROSCOPY  
AND COMPUTER SIMULATIONRAZISKAVE OBORIN V ALUMINIJEVIH ZLITINAH Z  
VISOKORESOLUCIJSKO ELEKTRONSKO MIKROSKOPIJO IN  
RAČUNALNIŠKO SIMULACIJO

Krzysztof Matus, Anna Tomiczek, Klaudiusz Golombek, Mirosława Pawłyta

Silesian University of Technology, Institute of Engineering Materials and Biomaterials, 18A Konarskiego Str.,  
44100 Gliwice, Poland  
krzysztof.matus@polsl.pl*Prejem rokopisa – received: 2016-07-27; sprejem za objavo – accepted for publication: 2017-01-27*

doi:10.17222/mit.2016.226

This paper presents the results of the tests using high-resolution transmission electron microscopy (HRTEM) with both transmission and scanning modes, as well as energy-dispersive-spectroscopy (EDS) investigation of the AlSi9Cu alloy after laser surface remelting. The possibility of using a computer simulation to identify precipitates in the analysed alloy was also explored. The obtained results and computer simulations were compared. Moreover, this article presents the advantages of the computer aid in solving the diffraction patterns and precipitates in supercell simulations.

Keywords: precipitation, crystallography, TEM, computer simulations

V prispevku so predstavljeni rezultati preiskave AlSi9Cu zlitine z laserskim pretaljevanjem površin z uporabo transmissijske elektronske mikroskopije z visoko ločljivostjo (angl. HRTEM) na dva načina: s transmissijskim skeniranjem, kot tudi z energijsko disperzijsko spektroskopijo (angl. EDS). Z uporabo računalniške simulacije je bila preiskana možnost identifikacije delcev v analizirani zlitini. Dobljeni rezultati in računalniške simulacije so bili primerjani. Poleg tega članek predstavlja prednosti računalniške simulacije pri študiji vzorcev difrakcije in oborin v posameznih stanjih celic.

Ključne besede: oborine, kristalografija, TEM, računalniške simulacije

## 1 INTRODUCTION

Aluminium alloys are the most widely used alloys in modern technology, mainly due to high specific strength and low density. Other factors behind the widespread distribution of aluminium alloys are their excellent electrical conductivity and high corrosion resistance.<sup>1,2</sup> The use of laser surface treatment to improve the utility properties of aluminium alloys allows the remelting of the surface layer of the material or its enrichment with alloy elements. The remelting of the material surface and rapid crystallisation allow an improvement of the mechanical properties of alloys, mainly in the field of abrasion resistance and tribological properties of the surface. Through the generation of plenty of fine precipitates, the strength is increased as well. The influence of alloying element precipitates on aluminium alloys is a complex issue and it is still one of the most promising topics in materials science.<sup>3-7</sup>

Laser surface treatment ensures that the processed material obtains new properties due to the rapid dispersion of the heat from the melted zone. This phenomenon enables the crystallisation of very fine precipitates to occur. Laser remelting can be used for small and large elements. The most common alloyed layers have a thickness from 0.3 mm to about 3 mm. A layer formed by

remelting usually has a high homogeneity as well as a fine crystalline structure. The use of the laser technology makes it possible to obtain surface layers with high contents of alloying elements and a unique combination of elements that conventional alloys rarely contain.<sup>8-11</sup>

Generally, the laser surface treatment is accomplished with two methods, which differ from one another based on how the alloying addition is introduced to the surface layer (which is schematically presented in **Figure 1**). When the surface of a material is subjected to a laser beam and then melted, the process is called remelting (**Figure 1a**). When an alloying material is applied to a surface and then melted with a laser beam (most of the materials are added in the forms of tapes, pastes or powders), the process is called alloying (**Figure 1b**).<sup>12,13</sup>

This article aims to identify the precipitates in an aluminium alloy after the laser treatment using transmission electron microscopy and computer simulations.

## 2 EXPERIMENTAL PART

For the experimental procedure, cast AlSi9Cu aluminium alloy was used. Its average chemical composition is shown in **Table 1**. This alloy was subjected to

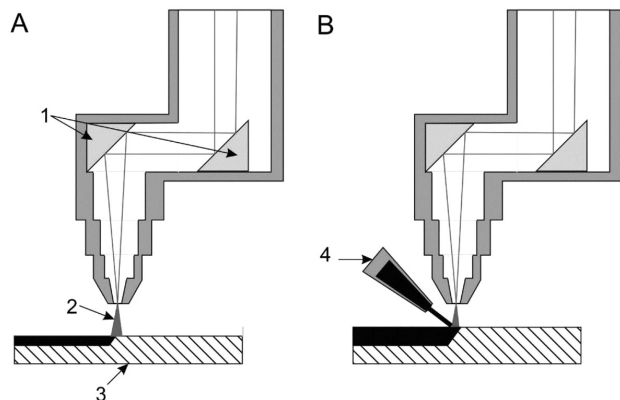


**Figure 1:** Diagram of laser treatment: a) remelting, b) alloying<sup>12,13</sup>

remelting using high-power diode laser (HPDL) ROFIN SINAR DL 020 with a radiation wavelength of  $940 \pm 5$  nm and a laser power of 2 kW with a spot size of  $1.8 \text{ mm} \times 6.8 \text{ mm}$  and argon as the shielding gas.

**Table 1:** Chemical composition of AlSi9Cu alloy, in mass fractions (w/%)

Si	Cu	Fe	Mn	Mg	Ti	Al
9.0	1.0	0.7	0.4	0.3	0.3	balance

Samples for transmission-electron-microscopy (TEM) observations were prepared as thin foils, where the Gatan PIPS 691 precision ion polishing system was used to prepare them. Studies were carried out using a scanning transmission electron microscope S/TEM Titan 80-300 type (FEI, USA), operated at 300 kV and equipped with a EDAX Li-drifted Si EDS detector (Philips Electronic Instruments Corp. PV97-61850 ME). Electron-microscopy observations were performed with a probe Cs-corrected S/TEM Titan 80-300 FEI microscope, equipped with an EDAX EDS detector (energy resolution of 132 eV). HRTEM images (300 kV, Cs = 1.2 nm, 0.2 nm point resolution) were recorded using only a condenser lens aperture, and thus without an objective lens aperture. HAADF-STEM images were obtained

with a HAADF STEM detector (Model Fischione 3000). A convergence angle of  $0.974^\circ$  was used with the HAADF detector's inner collection angle of  $5.443^\circ$ . The probe size used was about 0.1 nm. The diffraction patterns were collected by exploiting both the selected area electron diffraction (SAED) and Fourier transformations from HRTEM and HAADF images. Chemical-composition examinations were carried out using energy-dispersive spectroscopy (EDS) for the identification of the precipitates which occurred in the samples. To perform a simulation of unit cells, the CrystalMaker software was used.<sup>14</sup> The simulation of supercells and the results of electron diffraction were realised with the software "Química de Sólidos y Catalisis, Estructura y Química de Nanomateriales" developed at the University of Cadiz.<sup>15,16</sup>

### 3 RESULTS AND DISCUSSION

Despite a low content of titanium in the analysed material (0.3 %, **Table 1**), microscopic observations revealed the presence and dense occurrence of titanium nanoprecipitates in the shape of sticks, sized approximately  $250 \text{ nm} \times 50 \text{ nm}$  (**Figures 2 and 3**). The reason for this is the fact that it is a high-melting-point element. At the time of the laser alloying, the volume of the material was treated with a laser beam and then rapidly melted and cooled down. When lowering the temperature, the precipitates of titanium were the first to crystallize. After melting all the elements, including titanium, there was an even distribution. The amount of titanium is limited, so the size of the crystallites formed did not exceed 250 nm. The boundary between the matrix and the titanium precipitates is a favorable nucleation area for the other precipitates to grow on titanium rods. The EDS map presents the titanium distribution and determines the localization of titanium precipitates in the aluminium matrix (**Figure 3**).

**Figure 4** shows an enlarged view of one of the precipitates containing Ti. The size of the precipitate is

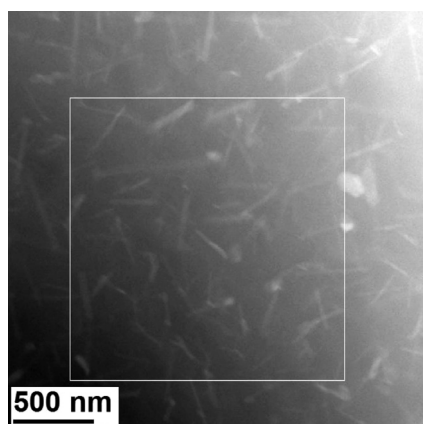


**Figure 2:** STEM-HAADF image of titanium precipitates in an aluminium-alloy matrix

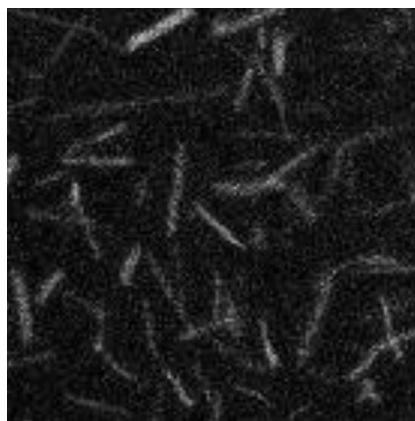


**Figure 3:** STEM-HAADF/EDS map which presents a magnification of the area from **Figure 2** and shows the distribution of titanium in the aluminium matrix

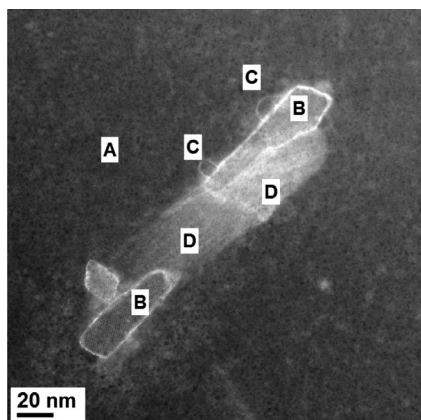


**Figure 4:** STEM-HAADF image of a complex precipitate in the aluminium matrix

approximately  $150 \text{ nm} \times 30 \text{ nm}$ . The contrast in the STEM-HAADF image indicates a difference in the chemical composition between the precipitate and the matrix. The matrix area and three areas characterised by differing contrasts (different chemical compositions) and structures (different phases) are marked by A and B–D, respectively. The results of the chemical analysis of the selected areas are presented in **Figure 5**, in graphs A–D, and **Table 2**.

**Table 2:** Chemical compositions of the areas marked with letters A–D in **Figure 5** (in amount fractions, at%)

	Al (K)	Cu (K)	Mg (K)	Si (K)	Ti (K)
point A	93.95	6.04	–	–	–
point B	18.92	15.04	39.83	26.19	–
point C	67.65	5.03	3.70	23.60	–
point D	75.64	6.35	–	5.75	12.24

In the centre of **Figure 4**, the precipitate marked with symbol D, which contains mainly Ti, Al and Si, is

shown. The observed precipitate had an irregular, elongated shape and a size of approximately  $100 \text{ nm} \times 20 \text{ nm}$ . The grain boundary between the precipitate with titanium and the matrix served as the nucleation point for the other precipitates. Copper results were affected by a holder and by the pole pieces, which were made of copper. There were at least two other types of precipitates, which were marked with symbols B and C. The phase marked as B consisted of Al, Mg, Si and Cu (**Figure 5b**). The intensities of the Mg, Si and Cu peaks (K lines) were higher than that of the matrix. At the phase boundary between the aluminium matrix and the precipitate marked as B, two smaller precipitates, marked as C, can be noticed. The chemical composition of precipitate C was similar to that of precipitate B (Al, Si, Mg and Cu), as shown in **Figure 5c**, but the relative intensities of the peaks were different. Detected Mg content in precipitate C was practically at the background level. A fast Fourier transform (FFT) of the precipitate marked with the letter B is presented in **Figure 6a**. Compared to the EDS spectrum, the measurement of the spacings and angles in the FFT, with its high-resolution image, and a computer simulation of the diffraction pattern allow the identification of the precipitate marked with letter B as the Q phase (with a chemical composition close to  $\text{Al}_3\text{Cu}_2\text{Mg}_9\text{Si}_7$ ). A comparison of the simulated electron diffraction and the experimental one allows determining the orientation of the Q-phase precipitate as  $[001]$  (**Figure 6b**).

The unit cell of the Q phase was simulated along the  $[001]$  direction (**Figure 7**). This data was necessary to create a supercell in the Q phase (**Figure 8a**) with its characteristic arrangement of atoms and marked regular shape between the copper atoms. This was then adapted to an enlarged HAADF image of the investigated precipitate (**Figure 8b**). The HAADF detector enabled the

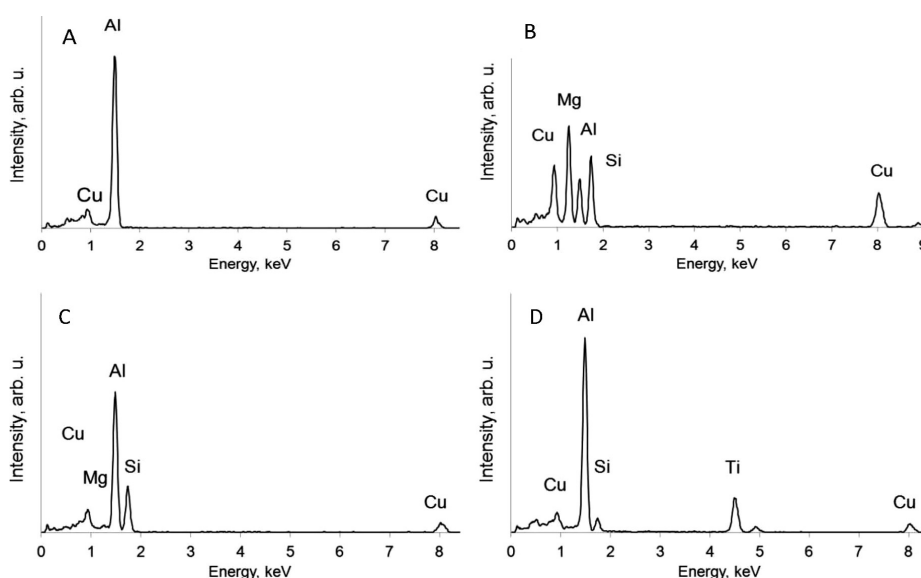


**Figure 5:** Results of the chemical analysis of the areas marked with letters A–D in **Figure 5**



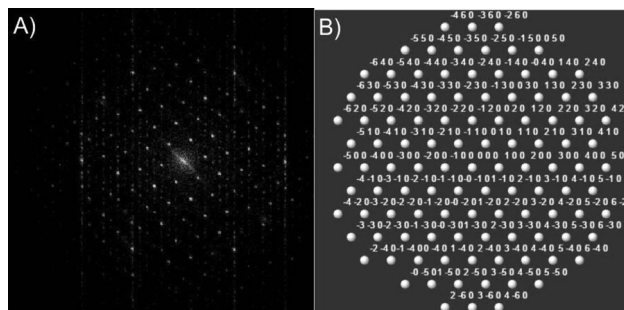


**Figure 6:** a) Fast Fourier transform (FFT) of a high-resolution image and b) simulation of the diffraction pattern of the Q-phase precipitate in the [001] direction

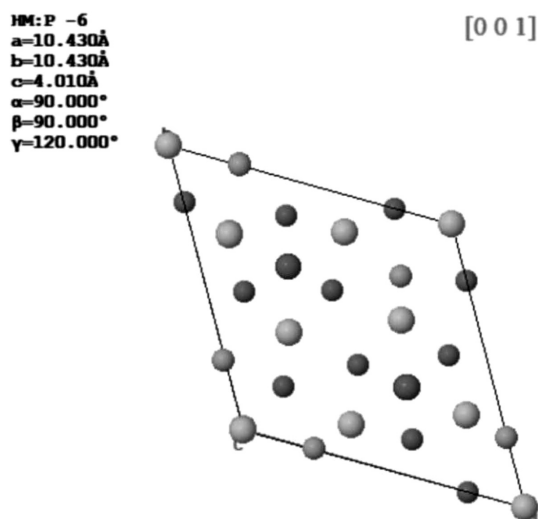


**Figure 7:** Unit cell of precipitate Q in the [001] direction

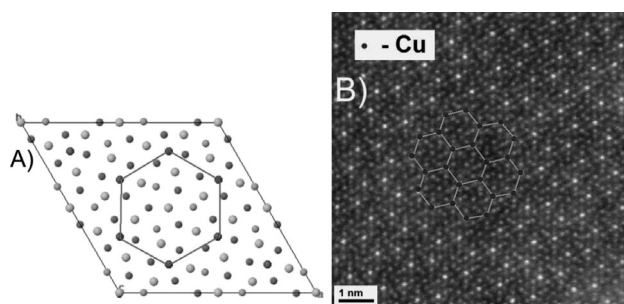


**Figure 8:** a) Q-phase supercell with the selected pattern of copper atoms and b) this pattern registered on the HAADF image

distinction and contrast between the columns of atoms containing elements of differentiated value  $Z$ . Images were obtained by recording the intensity of the scattered electrons as a function of the incident beam position on the sample surface. Cu has the highest value of  $Z$ , therefore the copper atoms were characterized as having the best contrast, or the brightest points.

Using the same method, the area marked as C in **Figure 4** was identified as the U1 phase ( $\text{MgAl}_2\text{Si}_2$ ), and area D was determined as the  $\text{TiAl}_3$  phase.<sup>17,18</sup>

The precipitates created during the laser remelting of aluminium alloys have very complex chemical compo-

sitions and crystallographic structures (**Figures 5 and 7** and **Table 2**). The interface between the matrix and the large amount of precipitation is a unique place to increase further the creation of the precipitates, which are successfully identified as the participations of the complex U1 and Q phases. Particularly the precipitates of the Q phase, which is a major equilibrium phase of the Al-Mg-Si-Cu system, are noteworthy. The Q phase belongs to the P-6 space group with lattice parameters:  $a = b = 0.1039$  nm,  $c = 0.409$  nm, and  $\alpha = \beta = 90^\circ$ ,  $\gamma = 120^\circ$ .<sup>17</sup>

## 4 CONCLUSIONS

Laser surface treatment, due to its requirement for a large amount of energy, leads to a dissolution of the surface layers of alloys due to a rapid dissipation of heat into the interior of the material. This causes the remelted material to solidify very quickly, resulting in the formation of fine precipitates of high-melting elements, which are unique places for the nucleation of other precipitates. This type of treatment can increase the hardness due to the refinement of the microstructure. The completed research determined that the phase that forms first during the cooling was  $\text{TiAl}_3$ , on which other precipitates with complex chemical compositions such as the precipitates of the Q and U1 phases grew. With the help of the computer simulations allowing the identification of the phases of the process, the process was shortened in comparison to the research using the databases on a computer. Moreover, the use of simulation software to obtain diffraction patterns simplified the processes of identifying the phases and their orientations. The simulation of unit cells and supercells allowed the matching of the simulated phases with their high-resolution images.

## Acknowledgment

This publication was financed by the Ministry of Science and Higher Education of Poland as the statutory financial grant of the Faculty of Mechanical Engineering, SUT.

## 5 REFERENCES

- <sup>1</sup> C. Cayron, P. A. Buffat, Transmission electron microscopy study of the  $\beta'$  phase (Al-Mg-Si alloys) and QC phase (Al-Cu-Mg-Si alloys): ordering mechanism and crystallographic structure, *Acta Mater.*, 48 (2000), 2639–2653, doi:10.1016/S1359-6454(00)00057-4
- <sup>2</sup> D. J. Chakrabarti, D. E. Laughlin, Phase relations and precipitation in Al-Mg-Si alloys with Cu additions, *Prog. Mater. Sci.*, 49 (2004), 389–410, doi:10.1016/S0079-6425(03)00031-8
- <sup>3</sup> A. L. Garcia-Garcia, I. Dominguez-Lopez, L. Lopez-Jimenez, J. D. O. Barceinas-Sanchez, Comparative quantification and statistical analysis of  $\eta'$  and  $\eta$  precipitates in aluminum alloy AA7075-T651 by TEM and AFM, *Mater. Charact.*, 87 (2014), 116–124, doi:10.1016/j.matchar.2013.11.007

- <sup>4</sup> N. K. Mukhopadhyay, H. J. Chang, J. Y. Lee, D. H. Kim, Electron microscopy of an icosahedral phase in a rapidly solidified Al<sub>18</sub>Mg<sub>3</sub>Mn<sub>2</sub> complex metallic alloy, *Scr. Mater.*, 59 (2008), 1119–1122, doi:10.1016/j.scriptamat.2008.07.024
- <sup>5</sup> A. Biswas, D. J. Siegel, D. N. Seidman, Compositional evolution of Q-phase precipitates in an aluminum alloy, *Acta Mater.*, 75 (2014), 322–336, doi:10.1016/j.actamat.2014.05.001
- <sup>6</sup> F. Delmas, M. J. Casanove, P. Lours, A. Couret, A. Coujou, Quantitative TEM study of the precipitation microstructure in aluminium alloy Al(MgSiCu) 6056 T6, *Mater. Sci. Eng. A*, 373 (2004), doi:10.1016/j.msea.2003.12.068
- <sup>7</sup> W. Yang, S. Ji, M. Wang, Z. Li, Precipitation behaviour of Al–Zn–Mg–Cu alloy and diffraction analysis from  $\eta'$  precipitates in four variants, *J. Alloys Compounds*, 610 (2014), 623–629, doi:10.1016/j.jallcom.2014.05.061
- <sup>8</sup> Z. Hu, L. Wan, S. Wu, H. Wu, X. Liu, Microstructure and mechanical properties of high strength die-casting Al–Mg–Si–Mn alloy, *Mater. Des.*, 46 (2013), 451–456, doi:10.1016/j.matdes.2012.10.020
- <sup>9</sup> J. Aguilar, M. Fehlbier, A. Ludwig, A. Bührig-Polaczek, P. R. Sahm, Non-equilibrium globular microstructure suitable for semisolid casting of light metal alloys by rapid slug cooling technology (RSCT), *Mater. Sci. Eng. A*, 375–377 (2004), 651–655, doi:10.1016/j.msea.2003.10.091
- <sup>10</sup> W. M. Lee, M. A. Zikry, High strain-rate modeling of the interfacial effects of dispersed particles in high strength aluminum alloys, *Int. J. Solids Struct.*, 49 (2012), 3291–3300, doi:10.1016/j.ijsolstr.2012.07.003
- <sup>11</sup> J. F. Nie, B. C. Muddle, On the form of the age-hardening response in high strength aluminium alloys, *Mater. Sci. Eng. A*, 319–321 (2001), 448–451, doi:10.1016/S0921-5093(01)01054-1
- <sup>12</sup> J. C. Betts, Laser surface modification of aluminium and magnesium alloys, *Surf. Eng. Light Alloys*, Woodhead Publishing, 2010, 444–474, doi:10.1533/9781845699451.2.444
- <sup>13</sup> H. C. Man, C. T. Kwok, T. M. Yue, Cavitation erosion and corrosion behaviour of laser surface alloyed MMC of SiC and Si<sub>3</sub>N<sub>4</sub> on Al alloy AA6061, *Surf. Coat. Technol.*, 132 (2000), 11–20, doi:10.1016/S0257-8972(00)00729-5
- <sup>14</sup> <http://www.crystallmaker.com>
- <sup>15</sup> C. López-Cartes, J. A. Pérez-Omil, J. M. Pintado, J. J. Calvino, Z. C. Kang, L. Eyring, Rare-earth oxides with fluorite-related structures: Their systematic investigation using HREM images, image simulations and electron diffraction pattern simulations, *Ultramicroscopy* 80 (1999), 19–39, doi:10.1016/S0304-3991(99)00067-4
- <sup>16</sup> S. Bernal, F. J. Botana, J. J. Calvino, C. Lopez-Cartes, J. A. Perez-Omil, J. M. Rodriguez-Izquierdo, The interpretation of HREM images of supported metal catalysts using image simulation: profile view images, *Ultramicroscopy*, 72 (1998), 135–164, doi:10.1016/S0304-3991(98)00009-6
- <sup>17</sup> R.-K. Pan, L. Ma, First-principles study on the elastic properties of B' and Q phase in Al–Mg–Si (–Cu) alloys, *Phys. Scr.*, 87 (2013), doi:10.1088/0031-8949/87/01/015601
- <sup>18</sup> S. J. Andersen, C. D. Marioara, R. Vissers, A. Frøseth, H. W. Zandbergen, The structural relation between precipitates in Al–Mg–Si alloys, the Al-matrix and diamond silicon, with emphasis on the trigonal phase U1-MgAl<sub>2</sub>Si<sub>2</sub>, *Mat. Sci. Eng. A – Struct.*, 444, (2007), 157–169, doi:10.1016/j.msea.2006.08.084



# MICROSTRUCTURAL EVALUATION OF Ni-SDC CERMET FROM A REPRESENTATIVE 2D IMAGE AND/OR A 3D RECONSTRUCTION BASED ON A STACK OF IMAGES

## VREDNOTENJE MIKROSTRUKTUR Ni-SDC KERMETA Z 2D IN/ALI 3D METODO

**Gregor Kapun<sup>1,3</sup>, Marjan Marinšek<sup>2</sup>, Franci Merzel<sup>1</sup>, Sašo Šturm<sup>3,4</sup>,  
Miran Gaberšček<sup>1</sup>, Tina Skalar<sup>2</sup>**

<sup>1</sup>National Institute of Chemistry, Laboratory for Materials Chemistry, Hajdrihova 19, Ljubljana, Slovenia

<sup>2</sup>University of Ljubljana, Faculty for Chemistry and Chemical Technology, Večna pot 113, Ljubljana, Slovenia

<sup>3</sup>Jožef Stefan International Postgraduate School, Jamova cesta 39, 1000 Ljubljana, Slovenia

<sup>4</sup>Jožef Stefan Institute, Jamova cesta 39, 1000 Ljubljana, Slovenia

Tina.Skalar@fkkt.uni-lj.si

*Prejem rokopisa – received: 2016-08-16; sprejem za objavo – accepted for publication: 2017-01-24*

doi:10.17222/mit.2016.256

This work provides an in-depth discussion on the subject of deriving microstructural parameters from a realistic 2D image or a 3D volume reconstruction based on a stack of images. As a convenient model material, a nickel/samarium-doped-ceria (Ni-SDC) cermet synthesized by the citrate-nitrate combustion reaction is tested. Field-emission scanning electron microscopy (FE-SEM) for 2D microstructure evaluation or focused-ion-beam/scanning-electron-microscopy (FIB-SEM) for 3D imaging is used for the cermet characterization. Microstructural parameters, such as the volume ratio of phases, grain morphology, contiguity of phases and triple-point boundary density, are quantitatively evaluated. These microstructural parameters reveal that a 2D microstructural evaluation provides a relatively accurate and quick analytical approach. However, it is shown that a detailed microstructural quantification of the parameters that are closely related to transport phenomena and electrochemical reactions in a porous cermet is only possible through the three-dimensional (3D) quantitative material characterization. Based on the microstructural evaluation, optimization of the Ni-SDC material used is briefly discussed.

**Keywords:** solid-oxide fuel cell, Ni-SDC anode, microstructure, FIB tomography

Ni-SDC kermeta (nikelj/cerijev oksid dopiran s samarijevim oksidom) je eden izmed najpogostejše uporabljenih anodnih materialov v gorivnih celicah s trdnim elektrolitom (angl. SOFC). Med pripravo materiala sodi tudi kvantitativno vrednotenje mikrostrukturnih parametrov kot so velikost in porazdelitev velikosti zrn, deleži faz, kontinuitete, gostota trojnih točk (angl. TPB), gostota materiala, itd. V tem prispevku želimo primerjati dva različna načina analiziranja teh parametrov. Prva t.i. 2D metoda temelji na obdelavi slik, posnetih z vrstičnim elektronskim mikroskopom s poljsko emisijo (SEM). Medtem, ko 3D metoda upošteva 3D rekonstrukcijo vzorca iz slik s pomočjo sistema s fokusiranim ionskim sklopom (FIB-SEM). Omenjeni mikrostrukturni parametri razkrivajo, da je 2D pristop razmeroma hiter in natančen. Vendar se je izkazalo, da je za natančnejšo kvantitativno analizo mikrostrukture, ki je tesno povezana s prenosom snovi in elektrokemijskimi reakcijami v anodnem materialu, potreben 3D pristop. Metodi sta bili ocenjeni glede na njuno težavnost izvedbe in časovno zahtevnost.

**Ključne besede:** SOFC, Ni-SDC anoda, mikrostruktura, FIB-tomografija

## 1 INTRODUCTION

High energy-conversion efficiency, fuel flexibility and environmental friendliness can be seen as great advantages of solid-oxide fuel cells (SOFCs), which may become one of the leading energy-conversion technologies converting chemical energy into electricity using a wide spectrum of fuels.<sup>1</sup> An SOFC system consists of two porous electrodes, which are separated by a solid ceramic electrolyte. Most commonly, the anode material is based on two-phase cermets. Due to reduced operating temperatures (600–800 °C) in modern SOFC devices, yttrium-stabilized zirconia (YSZ) based cermets, i.e., Ni-YSZ, have been typically replaced with samarium-doped ceria (SDC) cermets, i.e., Ni-SDC<sup>2</sup>; namely, at comparable temperatures samarium-doped ceria exhibits ionic conductivities approximately one order of magnitude greater than YSZ.<sup>3</sup>

Several synthesis approaches for cermet preparation are described in the literature. Certain approaches such as mechanical mixing<sup>4–6</sup> of metal oxides are associated with high costs due to fine particle milling and may lead to a non-uniform particle size distribution or insufficient continuity of ceramic, metal and pore phases in the final cermet.<sup>7</sup> Some of these issues may be avoided by using alternative methods such as co-precipitation,<sup>4,8</sup> sol-gel,<sup>9</sup> Pechini synthesis,<sup>10–12</sup> spray pyrolysis<sup>13</sup> or citrate/nitrate combustion synthesis.<sup>4</sup> All of them rely on producing small particles, which may eventually result in a homogeneous phase distribution within the cermet after thermal treatment.

The most important requirements for efficient electro-oxidation at the anode are: i) high catalytic activity for fuel electro-oxidation, ii) chemical-, morphological- and dimensional-stability, iii) electronic- and ionic-con-



ductivity, iv) chemical-, thermal- and mechanical compatibility to other cell components and v) open porosity.<sup>14,15</sup> Many of those requirements are determined by the anode microstructure. Specifically, the performance of composite cermet anodes critically depends on features like particle size distribution, contiguity and triple phase boundary length.<sup>4,16</sup> In attempts to find correlations between the anode microstructure and selected measured properties, authors usually rely on 2D cross-sectional images obtained from optical or electron microscopy.<sup>17,18</sup> From these images, 3D microstructural parameters are estimated by using porous models based on geometrical theories, such as general effective media (GEM),<sup>19</sup> the contiguity concept,<sup>20</sup> the random register network model,<sup>21</sup> the random packing spheres model<sup>22</sup> and the stochastic reconstruction.<sup>23</sup> However, these models are all based on various assumptions, which can only indirectly describe the real 3D microstructure. Recently, 3D reconstructions of SOFC electrodes have been performed by X-ray computed tomography as well as by focused-ion-beam-coupled scanning electron microscopy (FIB-SEM).<sup>24–26</sup> The recently highly improved spatial resolution of the latter method is based on the serial sectioning by FIB and SEM imaging of a sample followed by reconstruction of the SEM micrographs into a single data set, which gives 3D information of the probed volume. Direct observation of a real electrode 3D structure is a key towards the establishment of a reliable relationship between a porous anode microstructure and the cell's power-generation performance.

The aim of this work is to compare a Ni-SDC microstructure obtained by the conventional 2D method using SEM with the state-of-the-art FIB-SEM-based 3D approach. The advantages and challenges of both methods are discussed in significant detail, with a special emphasis on the accuracy and applicability of the obtained results as well as on the time required for preparation and conducting the analysis. Both approaches track well the characteristic microstructure parameters that of a porous cermet structure, such as volume fraction of phases, the average grain sizes and grain size distribution in various directions, grain shape factor, porosity (open and closed), contiguity of phases (*C*) and triple-point boundary density (TPB).

## 2 EXPERIMENTAL PART

### 2.1 Material preparation

Anode materials were synthesized via the citrate-nitrate combustion synthesis by mixing aqueous solutions of metal nitrates and citric acid. Cation precursors – hydrated metal nitrates  $\text{Ce}(\text{NO}_3)_3 \cdot 6\text{H}_2\text{O}$  (99 %, Sigma-Aldrich),  $\text{Sm}(\text{NO}_3)_3 \cdot 6\text{H}_2\text{O}$  (99.9 %, Alfa Aesar) and  $\text{Ni}(\text{NO}_3)_2 \cdot 6\text{H}_2\text{O}$  (99 %, Acros Organics) and citric acid (100%, Carlo Erba) were separately dissolved in distilled water. The mixture was prepared by taking care that the molar ratio between cerium and samarium cations was

80:20, and considering that the Ni volume content in the final composite was 50 %. In order to ensure subsequent self-sustaining combustion the molar ratio between citric acid and nitrates was set to 0.2. The prepared mixture was then held over a water bath at 60 °C under vacuum (8 mbar) for at least 6 h until it transformed into a light green brittle gel. The dried gel was grinded and compressed into pellets ( $f = 12 \text{ mm}$ ,  $h = 30 \text{ mm}$ ,  $p = 100 \text{ MPa}$ ), which were then immediately ignited at the top with a hot metal tip to start a self-sustaining combustion reaction that spread as a reaction zone throughout the pellet. The synthesized NiO-SDC powder was then crushed in an agate mortar, wet-milled (isopropanol) in a planetary mill (Fritsch pulverisette 7 premium line) for 15 min with 10 mm grinding balls and 500  $\text{min}^{-1}$  (1<sup>st</sup> milling) and additional 15 min with 1 mm grinding balls and 500  $\text{min}^{-1}$  (2<sup>nd</sup> milling). After drying the milled powder was calcined at 800 °C for 1 h and subsequently uni-axially pressed into pellets ( $f = 6 \text{ mm}$ ,  $h = 2.6 \text{ mm}$ ,  $p = 100 \text{ MPa}$ ). The formed pellets were sintered at 1400 °C for 1 h. To determine the final composite microstructure, all the sintered tablets were polished, thermally etched and reduced in an Ar-H<sub>2</sub> (5 % of volume fractions) atmosphere at 900 °C for 2 h.

### 2.2 Material characterization

The rapid increase in temperature during combustion inside the reaction zone was measured as a temperature profile using an optical pyrometer (Impac, IPE 140, based on sample brightness). The measuring range of the pyrometer is from 50 °C to 1200 °C, and it has a very quick response time (1.5 ms). The accuracy of the optically measured temperature was  $\pm 2.5$  °C below 400 °C and  $\pm 0.4$  % of a measured value (in °C) above 400 °C. The particle size observations of the as-synthesized NiO-SDC dispersion were performed on a JEOL JEM-2100 transmission electron microscope (TEM) operated at 200 kV and equipped with EDX. The TEM samples were prepared by dispersing the prepared powder in ethanol using ultrasonication followed by deposition of the obtained suspension on holey carbon-coated copper grids. Particle size distributions of unmilled and milled powders after the synthesis were obtained using a Microtrac Bluewave particle sizer and measured as aqueous suspensions. The shrinkage curve of the NiO-SDC during sintering up to 1450 °C with a constant heating rate of 10 K  $\text{min}^{-1}$  was obtained with a heating microscope (Leitz Wetzlar). FE-SEM (Zeiss, Ultra Plus) was used for a conventional 2D cross-section imaging of sintered and reduced pellets. FIB-SEM (Zeiss, Crossbeam 540) was used for the image data stack acquisition of sintered anode material to obtain 3D reconstruction of the probed volume.

### 2.3 2D microstructure analysis

The quantitative 2D microstructure analysis involved the determination of the fraction of phases ( $j_{\text{Ni}}$ ,  $j_{\text{SDC}}$ ),

intercept grain lengths in  $x$  and  $y$  directions (*Feret  $x$*  and *Feret  $y$* ), diameter of the area-analogue circle ( $\bar{d}$  which equals *D-CIRCLE*), sphericity (*F-CIRCLE*) and microstructural porosity ( $\epsilon$ ) were performed on 4–5 digital images using Axiovision 4.8 image-analysis software. The definitions and equations of these parameters are listed in **Figure 1**. Geometrical porosity ( $\epsilon_{\text{geometrical}}$ ) was calculated from the Archimedes densities of the pellets using measured dimensions (diameter, height and mass) relative to the theoretical densities. In order to determine the contiguity values ( $C$ ), which represent a frequency of contacts between grains of one or various phases, in a three-phase mixture the Gurland principle<sup>27,28</sup> modified by J. H. Lee et al.<sup>29</sup> was used. SEM micrographs of the given sample were lined (**Figure 1**) vertically and horizontally. Along with these lines contacts between different phases were counted. The final number of contacts ( $N$ ) was normalized to 1 mm length of sample. Finally, contiguities were calculated using Equations (1), (2) and (3):

$$C_{\text{Ni-Ni}} = \frac{2N_{\text{Ni-Ni}}}{2N_{\text{Ni-Ni}} + N_{\text{Ni-pore}} + N_{\text{Ni-SDC}}} \quad (1)$$

$$C_{\text{SDC-SDC}} = \frac{2N_{\text{SDC-SDC}}}{2N_{\text{SDC-SDC}} + N_{\text{SDC-pore}} + N_{\text{Ni-SDC}}} \quad (2)$$

$$C_{\text{Ni-SDC}} = \frac{2N_{\text{Ni-SDC}}}{2N_{\text{Ni-Ni}} + N_{\text{Ni-pore}} + N_{\text{Ni-SDC}} + 2N_{\text{SDC-SDC}} + N_{\text{SDC-pore}}} \quad (3)$$

#### 2.4 3D microstructure analysis

In addition to the conventional 2D microstructure analysis, a FIB-SEM serial sectioning method was used for a quantitative 3D examination of the anode microstructures. The method allows direct observation of critical microstructure parameters like phase distributions, grain connectivity and triple phase boundary density. The prepared Ni-SDC cermet was infiltrated with epoxy resin (EpoFix, Struers) under vacuum in order to easily distinguish the pores and avoid mistakes due to the depth of field during SEM imaging. Subsequently, a lamella with a thickness of 150  $\mu\text{m}$  was cut

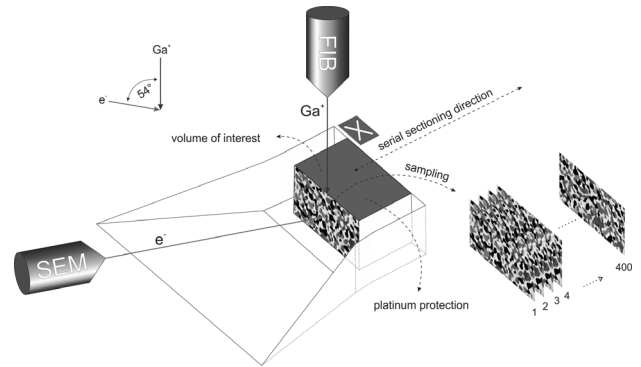


**Figure 2:** Schematic view of FIB-SEM settings and the measuring procedure

out, polished down to 50  $\mu\text{m}$  and glued directly to an aluminium stub to prevent sample drift during FIB operation. The configuration of the FIB-SEM setup is presented in **Figure 2**. Initially, a layer of platinum was "in situ" deposited on top of the region of interest to protect the surface and prevent the curtaining effect of the cross-section during milling. The volume of interest was separated using an optimised U-pattern pre-milling procedure to prevent material re-deposition and shadowing of the signals used for imaging and microanalysis. The sample was then serially sectioned using an automated slicing procedure with drift correction algorithms to obtain a series of 2D images with narrow and reproducible spacing between the individual image planes.<sup>30</sup> Experimental milling and imaging parameters were optimized in order to obtain a high-quality 3D reconstruction (10 nm  $\times$  10 nm  $\times$  20 nm voxel resolution) with phase-contrast information. Individual phases were identified from EDXS elemental maps and further segmented according to their grey level. Raw images were pre-processed with "in-house" programming using ImageJ followed by phase segmentation based on thresholding, edge detection and a region growth algorithm.<sup>31,32</sup> After phase separation, the 3D microstructure with final dimensions of 10  $\mu\text{m}$   $\times$  10  $\mu\text{m}$   $\times$  10  $\mu\text{m}$  was reconstructed using the Amira 5.4.5. software package.<sup>33,34</sup> The 3D structure was additionally separated into particles based upon a three-dimensional watershed algorithm applied to a distance measurement.<sup>35,36</sup> Volume fractions, feature size and size distributions for each individual phase were calculated directly from the 3D reconstruction. The specific surface area was calculated inside the Amira 5.4.5. software using a triangular approximation based on the marching cubes algorithm. A summary of the results is listed in **Table 1**.

In the final step of the 3D quantification, the segmented data cube with a 3D data matrix/grid of dimensions  $N_p \times N_p \times N_p$ , with  $N_p = 400$  at a resolution of 20 nm/pixel was exported for the TPB length calculation using an "in house" programming algorithm based on the centroid method.<sup>32,37,38</sup> Each grid element (pixel) gets associated with one of the three different phases: the

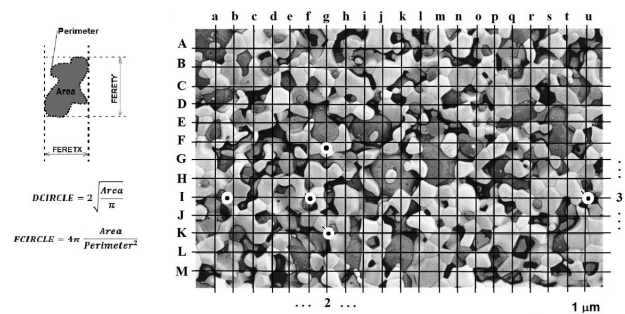


**Figure 1:** In the left-hand part the definitions of *FERTX*, *FERET*, *DCIRCLE* and *FCIRCLE* are presented. Lined SEM micrograph in the right-hand part (horizontal lines A, B, C, D, ... and vertical lines a, b, c, d, ...) with marked Ni-SDC phase contact (mark  $\odot$ ) and listed number of Ni-SDC contacts for lines "I" (left) and "g" (right)

SDC phase, the Ni phase and the pore/void "phase", respectively. We identify the three-phase boundary (TPB) elements/pixels satisfying the following condition: an element belonging to the pore is a TPB element if it has pixels on both other two phases among its first neighbours on the grid and at least one of its first neighbours also belongs to the TPB. In order to avoid multiplication of the TPB points it is important to assume that the boundary element should refer to one phase only (pore in our case). If a given TPB element is not connected to any other TPB element, it does not form a TPB line. The TPB length can be obtained, to a reasonable approximation, as a product of the number of TPB points and the grid spacing,  $N_{TPB} \times d_0$ , that corresponds to the edge summation. The corresponding TPB density is then simply  $\rho = N_{TPB} N_P^3 d_0^{-2}$ . Here we define one cubic layer of neighbouring elements around the tagged pixel represented either by a single element (Figure 3), leading to  $\rho = 7.23 \mu\text{m}^{-3}$ .

**Table 1:** Microstructural and morphological parameters of Ni-SDC determined by 2D or 3D approach

			bulk	2D	3D	
$\varphi_{\text{Ni}} / \%$			36.1	37.7	34.7	
$\varphi_{\text{SDC}} / \%$			36.1	42.8	37.4	
$feret / \mu\text{m}$	$x$	Ni		0.55	0.49	
		SDC		0.42	0.40	
	$y$	Ni		0.44	0.44	
		SDC		0.38	0.34	
	$z$	Ni		/	0.51	
		SDC		/	0.40	
$\bar{d} / \mu\text{m}$		Ni		0.52	0.48	
		SDC		0.38	0.37	
$F_{\text{CIRCLE}} /$		Ni		0.90	0.85*	
		SDC		0.78	0.71*	
$\varepsilon / \%$	geometrical			27.8	/	/
	microstructural				21.5	27.9
	open			/	27.2	
	closed			/	0.7	
$C /$	Ni-Ni			0.05	/	
	Ni-SDC			0.18	/	
	SDC-SDC			0.47	/	
TPB density / $\mu\text{m} \mu\text{m}^{-3}$				/	3.5	
$\text{SSA} / \mu\text{m} \mu\text{m}^{-3}$	Ni			/	15.4	
	SDC			/	18.7	
	pore			/	15.7	
$\text{SIA} / \mu\text{m} \mu\text{m}^{-3}$	Ni-pore			/	6.2	
	Ni-SDC			/	9.2	
	SDC-pore			/	9.5	

\* In xy projection

### 3 RESULTS AND DISCUSSION

The combustion synthesis of NiO-SDC preparation is chosen due to its major advantages over the classic calcination method. Namely, the citrate-nitrate combustion is a one-step, relatively simple method with rapid material synthesis inside the combustion zone. Typically, in

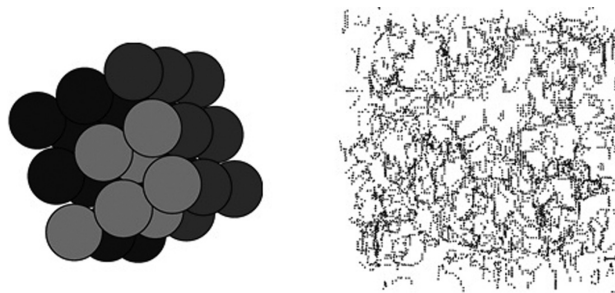


**Figure 3:** Left: an example of the TPB element defined as one central pixel surrounded by one layer of neighbouring pixels (pixels are represented by balls, dark grey balls denote the SDC phase, black the Ni phase and light grey the pores). Right: an image showing a distribution of the TPB points in the sample ( $\rho = 7.23 \mu\text{m}^{-3}$ )

the head of the combustion zone, changes from ambient temperature to combustion temperature happen in a fraction of a second, while after the combustion the product ash is also quickly cooled. In the case of NiO-SDC preparation, the measured peak combustion temperature is 1169.2 °C, the propagation wave velocity is 0.6 mm s<sup>-1</sup> and the temperature gradient in the head of the reaction zone is calculated to be 1053 °C s<sup>-1</sup>. Such rapid temperature variations limit significantly the time span during which diffusion of species in the system plays an important role. This leads to a typical nano-scaled mixture of NiO and SDC phases (Figure 4), which serves as the starting material for the final Ni-SDC cermet preparation.

The as-synthesized NiO-SDC product is partially agglomerated. The size of the average agglomerate size is about 1350 nm. The formed agglomerates of NiO-SDC are weak and can be easily reduced in size during milling (Figure 5). The first and second milling cycles produce particles with average sizes of 5.23 μm and 2.80 μm, respectively, which are still small agglomerates of nano-sized NiO and SDC one-phase regions.

The sintering behaviour of NiO-SDC during a dynamic temperature rise is presented in Figure 6. Densification of the tablet starts slightly above 800 °C, proceeds over two separate steps, and is practically

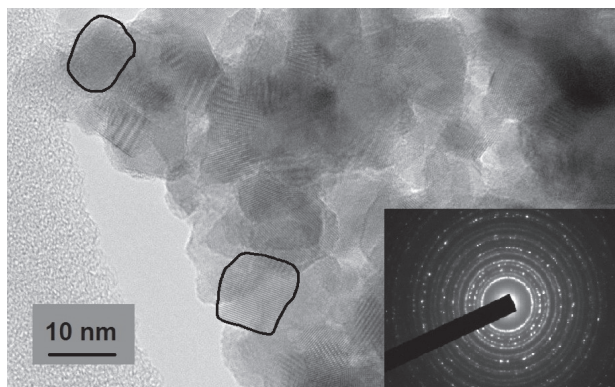


**Figure 4:** High-resolution TEM image of as synthesized product (some individual grains are encircled) and corresponding selected area electron diffraction pattern for the image (insert)



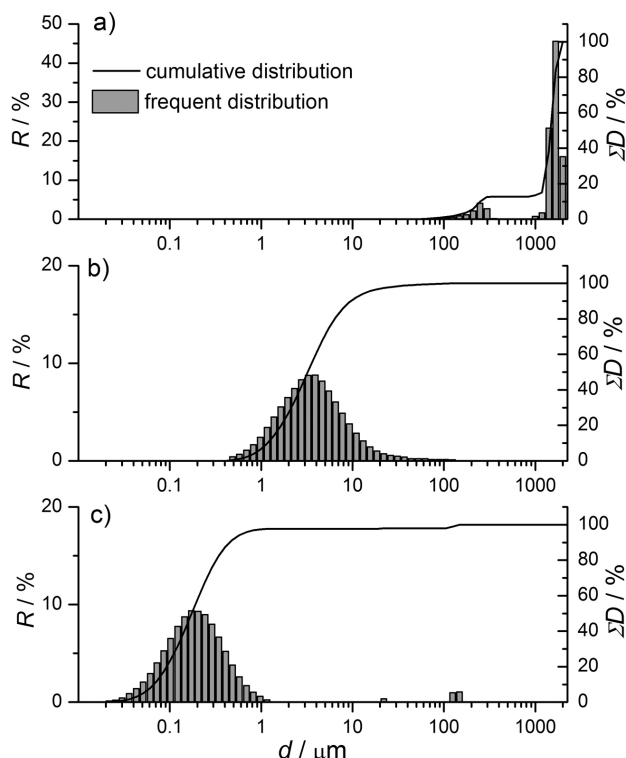


**Figure 5:** Particle size distribution of ungrounded powder (a), powder after 1<sup>st</sup> milling cycle (b) and after 2<sup>nd</sup> milling cycle (c)

completed at 1400 °C. The final shrinkage reached at 1450 °C is 24 %. Some features found in the sintering curve may be clearly associated with the state of the reacting matter during the synthesis. For example, the relatively early start of the densification is a consequence of the highly sinterable nano-sized mixture. However, due to the presence of some agglomerates, the densification first proceeds mainly as an inter-agglomerate sintering with the maximal sintering rate at 950 °C. Intra-agglomerate sintering starts at rather higher temperatures (above 1100 °C), reaching the maximum sintering rate at 1300 °C.

Among the crucial criteria for high-quality SOFC anodes are the maximization of the TPB density, as well as of the electronic and ionic conductivities. This means that sintering must provide very good contacts between the particles. Good particle-to-particle contact should appear both inside one phase as well as between both phases. Furthermore, the continuity of the Ni and SDC phases throughout the cermet additionally contributes to improved conductivities (ionic and electronic). At the same time, the TPB density can be increased by preventing excessive grain coarsening during sintering. From this point of view, the best compromise for the sintering temperature for final cermet preparation was found to be 1400 °C. Any sintering temperature below 1400 °C may result in the formation of continuous phases inside the agglomerates only, whereas the intra-agglomerate con-

nection remains poor. Sintering temperatures above 1400 °C, however, result in exaggerated grain growth.

Microstructures of sintered NiO-SDC and subsequently reduced Ni-SDC cermet are shown in **Figure 7**. Such a final Ni-SDC cermet was submitted to an in-depth microstructure analysis. The dark-grey particles seen in **Figures 7a** and **7b** are NiO or Ni in the sintered or reduced samples, respectively. The light grey is the SDC phase, whereas the pores are black. It is evident that NiO or Ni grains are homogeneously distributed between the SDC phase. Furthermore, pores are also uniformly distributed, especially in the reduced sample.

The parameters important for an exact cermet 2D analysis were extracted from the SEM micrographs by a detailed quantitative microstructure analysis (**Table 1**). Each parameter was determined on 5–10 different regions on the surface of the analysed tablets. As a whole, any quantitative calculation was based on several hundreds of grains. After sintering at 1400 °C, the remaining porosity in the NiO-SDC was around 97 %, which means that the sample was densely sintered. After the reduction, the microstructural porosity was increased to 21.5 %. The value for the porosity, however, depends to some extent on the determination method. The microstructural porosity, obtained from conventional 2D image analysis, tends to be lower than the geometrical porosity. This may be explained by the fact that microstructural porosity is determined on a limited number of images (which may be considered also as limited number of slices throughout the sample), while the geometrical porosity is a bulk property. To minimize this discrepancy one has to increase the number of images for 2D microstructure analysis. Similarly, approximate numbers are also determined for the phase fraction values ( $\varphi_{\text{Ni}}$  and  $\varphi_{\text{SDC}}$ ) and all the morphological values (*Feret*-values, *F-CIRCLE* and  $\bar{d}$ ). An interesting phenomenon may be deduced from the contiguity values' calculation. Namely, the relatively low  $C_{\text{Ni-Ni}}$  value may indicate a poor contact between the Ni grains. Such poor contact is highly undesired, since it also results in a lower electrical conductivity. However, the relatively high Ni content in

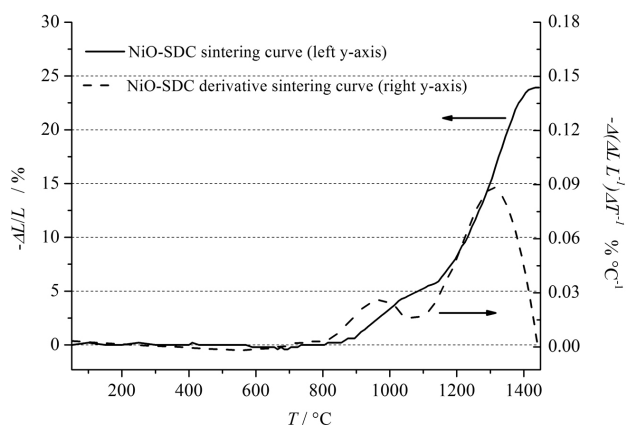


**Figure 6:** Sintering curve of NiO-SDC material calcined at 800 °C (full line) and derivative sintering curve (dashed line)



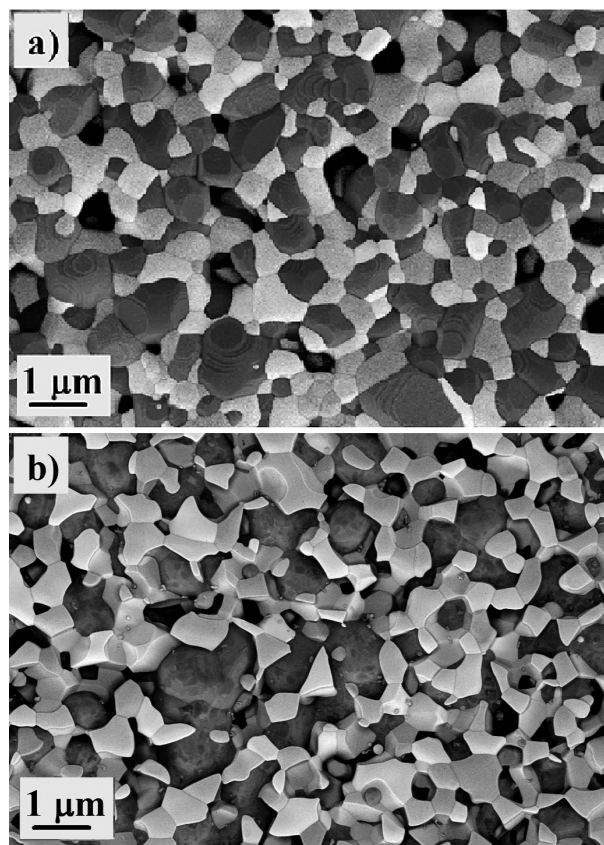


**Figure 7:** Microstructures of a) sintered (1400 °C) and b) reduced (900 °C)

the sample ( $\varphi_{\text{Ni}} = 37.7\%$ ) and its homogeneous distribution throughout the cermet should guarantee a good Ni-to-Ni particle contact. The latter suggests that a contiguity determination should consider a real 3D microstructure, since contacts between particles may continue also in the direction perpendicular to the investigated 2D plane. Generally, it is clear that after the reduction the average particle sizes remain well beneath the micrometre range; however, more precise microstructural quantization requires a more sophisticated approach.

More precise quantitative microstructural evaluation is possible by using the real 3D microstructure reconstruction based on FIB-SEM serial sectioning technique. It has to be stressed that for 3D microstructure reconstruction the back-scattered electron detector (BSC-ED) is more appropriate than the commonly used in-lens secondary electron detector (IL-SED), since BSC-ED successfully copes with the shadowing effect, which sometimes appears on the images when using IL-SED. Considering the obtained phase-extraction images (**Figure 8**), it is evident that the distribution of all three phases, namely, Ni, SDC and pores (pores may be considered as an additional phase in the cermet), is homogeneous. No larger areas of one-phase domination can be found in the cermet. Moreover, average particle sizes and pore diameters in any direction are in the

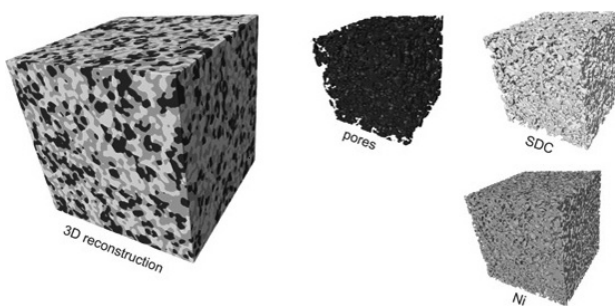


**Figure 8:** 3D microstructure reconstruction of Ni-SDC cermet and extracted phases Ni, SDC and pores

nanometre range. Similar to the 2D analytical approach, the 3D microstructural description also allows the determination of morphological parameters (**Table 1**); however, the 3D analysis additionally enables a description of microstructure also in the  $z$  axis. It appears that the  $\bar{d}$  and *Feret*-values ( $x$ ,  $y$  and  $z$ ) are somewhat lower when determined by the 3D approach. There are two main reasons for such a slight discrepancy in the results. Firstly, the computational algorithms employed for grey image segmentations and thus the separation of phases are different; and secondly, 2D statistical calculation is based on several hundreds of analysed grains, while the 3D statistics involves several tens of thousands of recognized particles. This fact makes the 3D microstructural analysis more reliable. Similar is true also for the  $\varphi_{\text{Ni}}$  and  $\varphi_{\text{SDC}}$  determination.

One of the big advantages of 3D microstructural analyses over the 2D approach is the fact that 3D microstructure reconstruction also enables an in-depth porosity description. Due to the large voxel matrix ( $2.6 \times 10^8$  voxels) in 3D reconstruction, the determined value for the microstructural porosity comes very close to the determined value of the geometrical porosity. The discrepancy of the  $\varepsilon_{\text{geometrical}}$  and  $\varepsilon_{\text{microstructural}}$  is much bigger for the 2D approach. Moreover, a detailed examination of the separated pore phase enables the overall porosity  $\varepsilon_{\text{microstructural}}$  to be separated into open- and closed-porosity. According to the results only 0.7% of the porosity belongs to closed pores, making the prepared microstructure interesting for SOFC applications.

The contiguity values may no longer be calculated from the 3D microstructure reconstruction. Instead, using an appropriate computational algorithm the much more interesting TPB density value ( $TPB_L$ ) can be obtained. In the analysed Ni-SDC cermet the  $TPB_L$  is determined as  $7.23 \mu\text{m} \mu\text{m}^{-3}$ , making this material fully comparable to other Ni-based cermets described in the literature. Further interesting information that may also be obtained from 3D microstructural reconstruction is the specific surface areas SSA of the phases (i.e., surface areas of individual phases normalized to the sample volume). For the investigated cermet the SSA values for Ni- SDC and pores are determined  $15.4 \mu\text{m}^2 \mu\text{m}^{-3}$ ,  $18.7 \mu\text{m}^2 \mu\text{m}^{-3}$ ,  $15.7 \mu\text{m}^2 \mu\text{m}^{-3}$ , respectively. The obtained

values are rather high compared to some data available in the literature and are a consequence of the relatively small grains of each individual phase. Furthermore, each phase in the cermet is in contact with the two other phases, meaning that by simple combination of the obtained SSA values specific interface areas SIA (normalized to the sample volume) between the three neighbouring phases can be calculated. For instance, the SSA of the Ni phase is divided into Ni-pore SIA  $6.2 \mu\text{m}^2 \mu\text{m}^{-3}$  and Ni-SDC SIA  $9.2 \mu\text{m}^2 \mu\text{m}^{-3}$ . Thus, about 40 % of the total Ni surface is exposed to the porous phase and can be used for surface catalytic reaction with fuel. Namely, oxidation of the fuel involves numerous reaction steps, which are not necessarily located at the TPB (i.e., adsorption and dissociation of hydrogen or hydrocarbon reforming inside an anode layer of a SOFC).

#### 4 CONCLUSIONS

This work focused on a 2D and 3D microstructural analysis of a Ni-SDC anode cermet material using SEM analysis and FIB tomography, respectively. The Ni-SDC sample was prepared by citrate-nitrate combustion synthesis, followed by milling, sintering and NiO to Ni reduction. The 2D microstructure investigation employed grey image-analysis and made it possible to obtain quantitative values of the fraction of phases, microstructural porosity, grain sizes of all phases, sphericity and contiguity. On the other hand, the 3D analysis additionally provided information on specific surface areas and specific interface areas of all the phases, as well as the triple phase boundary density. When comparing the 2D and the 3D microstructure analysis, the latter turned out to be more challenging to perform, difficult to interpret and extra time consuming in the initial step when quantification algorithms are established. Due to the fact that 3D microstructural analysis takes into the calculation a huge number of individual particles, the obtained information is also more reliable than in the case of 2D analysis. However, the biggest advantage of 3D microstructure analysis is the possibility of a complete microstructural reconstruction and determination of interface connected properties that directly determine the cermet activity in an operating SOFC.

#### 5 REFERENCES

- S. Singhal, K. Kendall, *High-Temperature Solid Oxide Fuel Cells: Fundamentals Design and Applications*, Elsevier Advanced Technology, Oxford, UK 2003
- D. Tian, Y. Chen, W. Yu, L. Yu, B. Lin, A robust NiO-Sm<sub>0.2</sub>Ce<sub>0.8</sub>O<sub>1.9</sub> anode for direct-methane solid oxide fuel cell, *Mater. Res. Bull.*, 71 (2005), 1–6, doi:10.1016/j.materresbull.2015.06.042
- W. Jung, H. Park, Y. Kang, D. Yoon, Lowering the sintering temperature of Gd-doped ceria by mechanochemical activation, *Short communication, Ceram. Int.*, 36 (2010), 371–374, doi:10.1016/j.ceramint.2009.07.020
- Y. Yin, S. Li, C. Xia, G. Meng, Electrochemical performance of gel-cast NiO-SDC composite anodes in low-temperature SOFCs, *Electrochim. Acta*, 51 (2006), 2594–2598, doi:10.1016/j.electacta.2005.07.046
- J. E. Hong, T. Inagaki, S. Ida, T. Ishihara, Improved power generation performance of solid oxide fuel cells using doped LaGaO<sub>3</sub> electrolyte films prepared by screen printing method II. Optimization of Ni-Ce<sub>0.8</sub>Sm<sub>0.2</sub>O<sub>1.9</sub> cermet anode support, *Int. J. Hydrogen Energ.*, 36 (2011) 14632–14642, doi:10.1016/j.ijhydene.2011.08.046
- S. Y. Park, C. W. Na, J. H. Ahn, R. H. Song, J. H. Lee, Preparation of highly porous NiO-gadolinium-doped ceria nano-composite powders by one-pot glycine nitrate process for anode-supported tubular solid oxide fuel cells, *J. Asian Ceram. Soc.*, 2 (2014), 339–346, doi:10.1016/j.jascer.2014.07.005
- Z. Shao, W. Zhou, Z. Zhu, Advanced synthesis of materials for intermediate-temperature solid oxide fuel cells, *Prog. Mater. Sci.*, 57 (2012), 804–874, doi:10.1016/j.pmatsci.2011.08.002
- X. Fang, G. Zhu, C. Xia, X. Liu, G. Meng, Synthesis and properties of Ni-SDC cermets for IT-SOFC anode by co-precipitation, *Solid State Ionics*, 168 (2004), 31–36, doi:10.1016/j.ssi.2004.02.010
- Y. Yin, W. Zhu, C. Xia, G. Meng, Gel-cast NiO-SDC composites as anodes for solid oxide fuel cells, *J. Power Sources*, 132 (2004), 36–41, doi:10.1016/j.jpowsour.2004.01.017
- T. Skalar, K. Zupan, M. Marinšek, B. Novosel, J. Maček, Microstructure evaluation of Ni-SDC synthesized with an innovative method and Ni-SDC/SDC bi-layer construction, *J. Europ. Ceram. Soc.*, 34 (2014), 347–354, doi:10.1016/j.jeurceramsoc.2013.08.020
- T. Skalar, A. Golobič, M. Marinšek, J. Maček, Determination of the metal concentrations in an anode material for solid-oxide fuel cells, *Materiali in tehnologije*, 47 (2013), 423–429
- D.A. Medvedev, J.G. Lyagaeva, E.V. Gorbova, A.K. Demin, P. Tsjakaras, Advanced materials for SOFC application: Strategies for the development of highly conductive and stable solid oxide proton electrolytes, *Progress in Materials Science*, 75 (2016), 38–79, doi:10.1016/j.pmatsci.2015.08.001
- M. Kawano, H. Yoshida, K. Hashino, H. Ijichi, S. Sudan, K. Kawahara, T. Inagaki, Synthesis of matrix-type NiO-SDC composite particles by spray pyrolysis with acid addition for development of SOFC cermet anode, 173 (2007), 45–52, doi:10.1016/j.jpowsour.2007.08.021
- P. I. Covin, C. T. G. Petit, R. Lan, J. T. S. Irvine, S. Tao, Recent progress in the development of anode materials for solid oxide fuel cells, *Adv. Energy Mater.*, 1 (2011), 314–332, doi:10.1002/aenm.201100108
- L. Holzer, B. Münch, B. Iwanschitz, M. Cantoni, T. Hocker, T. Graule, Quantitative relationships between composition, particle size, triple phase boundary length and surface area in nickel-cermet anodes for Solid Oxide Fuel Cells, *J. Power Sources*, 196 (2011), 7076–7089, doi:10.1016/j.jpowsour.2010.08.006
- Q. Liu, X. Dong, C. Yang, S. Ma, F. Chen, Self-rising synthesis of Ni-SDC cermets as anodes for solid oxide fuel cells, *J. Power Sources*, 195 (2010), 1543–1550, doi:10.1016/j.jpowsour.2009.09.071
- W. Z. Zhu, S. C. Deevi, A review on the status of anode materials for solid oxide fuel cells, *Mater. Sci. Eng. A*, 362 (2003), 228–239, doi:10.1016/S0921-5093(03)00620-8
- T. Skalar, M. Marinšek, M. Lubej, M. Lukežič, T. Skalar, J. Maček, Modelling of operating parameters in an SOFC testing system, *Mater. Tehnol.*, 48 (2014), 861–867
- M. Mori, T. Yamamoto, H. Itoh, H. Inaba, T. Tagawa, Thermal Expansion of Nickel-Zirconia Anodes in Solid Oxide Fuel Cells during Fabrication and Operation, *J. Electrochem. Soc.*, 145 (1988), 1374–1381
- D. S. Simwonis, F. Tietz, D. Stover, Nickel coarsening in annealed Ni/8YSZ anode substrates for solid oxide fuel cells, *Solid State Ionics*, 132 (2000), 241–251

G. KAPUN et al.: MICROSTRUCTURAL EVALUATION OF Ni-SDC CERMET FROM A REPRESENTATIVE 2D IMAGE ...

- <sup>21</sup> Z. Wu, M. Liu, Modelling of ambipolar transport properties of composite mixed ionic-electronic conductors, *Solid State Ionics*, 93 (1996), 65–84, doi:10.1016/S0167-2738(96)00521-8
- <sup>22</sup> M. Marinšek, S. Pejovnik, M. Maček, Modelling of Electrical Properties of Ni-YSZ Composites, *J. Eur. Ceram. Soc.*, 27 (2007), 959–964, doi:10.1016/j.jeurceramsoc.2006.04.165
- <sup>23</sup> J. A. Quiblier, A new three-dimensional modeling technique for studying porous media, *J. Colloid Interface Sci.*, 98 (1984), 84–102, doi:10.1016/0021-9797(84)90481-8
- <sup>24</sup> H. S. Hong, U. S. Chae, S. T. Choo, The effect of ball milling parameters and Ni concentration on a YSZ-coated Ni composite for a high temperature electrolysis cathode, *J. Alloys Compd.*, 449 (2008), 331–334, doi:10.1016/j.jallcom.2006.01.131
- <sup>25</sup> J. R. Wilson, S. A. Barnett, Solid Oxide Fuel Cell Ni-YSZ Anodes: Effect of Composition on Microstructure and Performance, *Electrochem. Solid-State Lett.*, 11 (2008), B181–B185, doi:10.1149/1.2960528
- <sup>26</sup> J. R. Wilson, M. Gameiro, K. Mischaikow, W. Kalies, P. W. Voorhees, S. A. Barnett, Three-Dimensional Analysis of Solid Oxide Fuel Cell Ni-YSZ Anode Interconnectivity, *Microsc. Microanal.*, 15 (2009), 71–77, doi:10.1017/S1431927609090096
- <sup>27</sup> J. Gurland, The measurements of grain contiguity in two phase alloys, *Trans. Metall. Soc.*, 212 (1958), 452–455
- <sup>28</sup> J. Gurland, An estimate of contact and contiguity of dispersions in opaque sample, *Trans. Metall. Soc.*, 236 (1966), 642–64
- <sup>29</sup> J. H. Lee, H. Moon, H. W. Lee, J. Kim, J. D. Kim, K. H. Yoon, Quantitative analysis of microstructure and its related electrical property of SOFC anode, Ni-YSZ cermet, *Solid State Ionics*, 148 (2002), 15–26, doi:10.1016/j.jpowsour.2011.08.083
- <sup>30</sup> M. Schaffer, J. Wagner, B. Schaffer, M. Schmied, H. Mulders, Automated three-dimensional X-ray analysis using a dual-beam FIB, *Ultramic.*, 107 (2007), 587–597, doi:10.1016/j.ultramic.2006.11.007
- <sup>31</sup> J. M. Perez, J. Pascau, *Image Processing with ImageJ*, Packt Publishing Ltd, 2013
- <sup>32</sup> J. Joos, M. Ender, I. Rotscholl, N. H. Menzler, E. Ivers-Tiffée, Quantification of double-layer Ni/YSZ fuel cell anodes from focused ion beam tomography data, *J. Power Sources*, 246 (2014), 819–830, doi:10.1016/j.jpowsour.2013.08.021
- <sup>33</sup> F. Hess, P. Fürnstahl, L. M. Gallo, A. Schweizer, 3D Analysis of the Proximal Interphalangeal Joint Kinematics during Flexion, *Computational and Mathematical Methods in Medicine*, (2013), 7 pages, doi:10.1155/2013/138063
- <sup>34</sup> A. V. Nagasekhar, C. H. Cáceres, C. Kong, 3D characterization of intermetallics in a high pressure die cast Mg alloy using focused ion beam tomography, *Mater. Charact.*, 61(2010), 1035–1042, doi:10.1016/j.matchar.2010.06.007
- <sup>35</sup> F. Tariq, R. Haswell, P. D. Lee, D. W. McComb, Characterization of hierarchical pore structures in ceramics using multiscale tomography, *Acta Mater.*, 59 (2011), 2109–2120, doi:10.1016/j.actamat.2010.12.012
- <sup>36</sup> J. E. Cates, R. T. Whitaker, G. M. Jones, Case study: An evaluation of user-assisted hierarchical watershed segmentation, *Medical Image Analysis*, 9 (2005), 566–578, doi:10.1016/j.media.2005.04.007
- <sup>37</sup> H. Iwai, N. Shikazono, T. Matsui, H. Teshima, M. Kishimoto, R. Kishida, H. Yoshida, Quantification of SOFC anode microstructure based on dual beam FIB-SEM technique, *J. Power Sources*, 195 (2010), 955–961, doi:10.1016/j.jpowsour.2009.09.005
- <sup>38</sup> N. Shikazono, D. Kanno, K. Matsuzaki, H. Teshima, S. Sumino, N. Kasagi, Numerical Assessment of SOFC Anode Polarization Based on Three-Dimensional Model Microstructure Reconstructed from FIB-SEM Images, *J. Electrochem. Soc.*, 157 (2010), B665–B672, doi:10.1149/1.3330568



## A FACILE METHOD TO PREPARE SUPER-HYDROPHOBIC SURFACES ON SILICONE RUBBERS

## PREPROSTA METODA ZA PRIPRAVO SUPERHIDROFOBNIH POVRŠIN PRI SILIKONSKIH GUMAH

Hai Yun Jin<sup>1</sup>, Yu Feng Li<sup>1</sup>, Shi Chao Nie<sup>1</sup>, Peng Zhang<sup>1</sup>, Nai Kui Gao<sup>1</sup>, Wen Li<sup>2</sup><sup>1</sup>Xi'an Jiaotong University, State Key Laboratory of Electrical Insulation and Power Equipment, Xi'an, 710049, China<sup>2</sup>Hubei Polytechnic University, Hubei Key Laboratory of Mine Environmental Pollution Control & Remediation and School of Chemical and Materials Engineering, Huangshi, 435003, PR China  
lxfzzl@126.com*Prejem rokopisa – received: 2016-09-02; sprejem za objavo – accepted for publication: 2016-10-24*

doi:10.17222/mit.2016.267

Fabricating large-scale super-hydrophobic surfaces for commercial applications is challenging due to certain limitations. In this paper, a simple and inexpensive method is developed to fabricate super-hydrophobic surfaces on silicone rubbers. Rough microstructures were prepared on the mould's inner surfaces and then sample super-hydrophobic surfaces on silicone rubbers with different surface roughness were achieved using the standard moulding process. Furthermore, the effects of roughness on the wettability were investigated. The results showed that by controlling the roughness, the fabricated surfaces exhibited a static contact angle of 150.9° and a sliding angle of 8°. Finally, the property of hydrophobicity recovery for the silicone-rubber samples was also studied. The surfaces of the samples could recover well after a sand-blasting experiment. The proposed method is low-cost, environmentally friendly and suggests promising industrial applications.

Keywords: thin films, coatings, chemical techniques, surface properties

Izdelava obsežnih superhidrofobnih površin za komercialne namene je zaradi določenih omejitev zahtevna. V članku je razvit preprost in poceni način za izdelavo superhidrofobne površine na silikonskih gumah. Grobe mikrostrukture so bile pripravljene na notranjih površinah kalupa in nato je bila dosežena vzorčna superhidrofobna površina na silikonski gumi z različno hrapavo površino z uporabo standardnega postopka modeliranja. Nadalje so bili raziskani učinki hrapavosti na omočljivost. Rezultati so pokazali, da so s krmiljenjem hrapavosti izdelane površine razstavljene pod statičnim kontaktnim kotom 150.9° in drsnim kotom 8°. Nazadnje je bila preučevana tudi lastnost okrevanja hidrofobnosti vzorcev silikonskih gum. Površine vzorcev se lahko dobro obnovijo tudi po poskusu s peskanjem. Predlagana metoda je poceni, okolju prijazna in kaže obetavne možnosti apliciranja v procese v industriji.

Ključne besede: tanke plasti, prevleke, kemijske tehnike, površinske lastnosti

## 1 INTRODUCTION

Superhydrophobic surfaces, with a water contact angle (CA) greater than 150° and a sliding angle (SA) less than 10°, have aroused increasing research interest for their promising applications.<sup>1–6</sup> By observing the microstructure of a lotus leaf surface, it was found that the combination of micro papilla and a thin wax film leads to the self-cleaning properties.<sup>4</sup> L. Jiang et al.<sup>1</sup> discovered that on top of the micro papilla also exist branch-like nanostructures and pointed out that the micro- and nanoscale hierarchical structures were the fundamental mechanism for lotus leaf's unique wetting properties. There were two main measures to fabricate superhydrophobic surfaces:

- 1) preparation of a rough surface followed by a low free-energy material coating step,
- 2) creation of a rough surface from low-surface-energy materials.<sup>1</sup>

Up to now, many approaches to fabricate rough surfaces had been developed, including the template method<sup>7</sup>, phase separation<sup>8</sup>, self-assembly<sup>9</sup>, vapour-phase deposition<sup>10</sup>, chemical etching<sup>11</sup>, laser etching<sup>12</sup>, hydro-

thermal method<sup>13</sup>, and electrospinning<sup>14</sup>. In the power system, the surfaces of insulators always work under high voltage and the sand-dust climate condition. However, some superhydrophobic coats (especially rubber-based coatings) synthesized by techniques on large-area and environmentally friendly cannot meet the operating requirements of composite insulators.<sup>15–17</sup> Therefore, it is a good way to solve this problem by synthesizing a superhydrophobic surface on the basis of not changing the insulator material. Silicon rubber was a hydrophobic material; therefore, a superhydrophobic surface could be created by only forming a special nm-μm geometry structure. The template method was a simple and convenient technique that could be used as a method to prepare superhydrophobic surfaces, and the quality of this method was easy to control; therefore, template method was suited for industrial production.

In this study, to fabricate a superhydrophobic surface on the composite insulators, a silicone-rubber superhydrophobic surface was developed with a facile template method. The creation of a rough structure on the inner surface of the mould and a special geotroy morphology was prepared on the silicone-rubber surface



through a conventional moulding process. The surface microstructures were investigated by a roughness tester and scanning electron microscope (SEM). It was found that the superhydrophobic silicone-rubber surface could be attained by creating the appropriate roughness surfaces, which lead to the lotus-leaf-like surface morphology. After samples suffered the artificial sandstorm testing, the property of hydrophobicity recovery for superhydrophobic and a common silicone-rubber surface have also been studied in this paper.

## 2 EXPERIMENTAL PART

Templates with different rough structures were prepared first. Silicon carbide particles of (63, 21, 15, and 10.5)  $\mu\text{m}$  in diameter were obtained by using test sieves of 80, 240, 600, 800 and 1200 mesh, respectively. A uniform layer of resin binder-epoxy resin was sprayed on the inner surface of a cubic mould with dimensions of 3 cm  $\times$  3 cm  $\times$  3 cm after treating with a silane coupling agent N- $\beta$ -aminoethyl- $\gamma$ -aminopropyl trimethoxysilane. The prepared silicon carbide particles were evenly sprayed on the inner surface of the mould and dried at room temperature. Then rough silicon rubber samples were prepared through a conventional moulding process. Liquid silicone rubber was poured into the mould, the mould was taken off after consolidation, and thus silicone-rubber surfaces with different surface morphologies were obtained. To avoid the superhydrophobic surface being destroyed during the mould unloading, the moulds were treated with a release agent (methyl-silicone oil). For a comparison, the smooth silicone rubber was prepared with a smooth mould.

To analyses the morphology and microstructures of the sample surfaces, SEM and a roughness tester were used. The morphological characterization was observed with a SEM (VE-9800, Keyence). The surface roughness  $R_a$  was measured with a handheld roughness tester (TR200, Times Run Bao). The roughness tester was placed at 20 different locations of the sample surface under investigation and the average value was taken as the surface roughness.

The water contact angles were investigated using a measurement system (JC2000C4, POWEREACH). Before the test the samples were washed with deionized water and ethanol, respectively, and then naturally dried. Five different locations of the sample surface were measured, and the average value was used.

The property of hydrophobicity recovery for both the superhydrophobic and the common silicone-rubber surface were tested in the artificial experimental platform, and the sand-dust sample was also prepared, as described in <sup>18</sup>. Samples of superhydrophobic silicone rubber and the common silicone rubber were placed horizontally in the experimental platform. The surfaces of the samples and the wind direction were parallel. The wind speed was 15m/s. The samples were in the artificial sandstorm

for 1 h. To accelerate the process of hydrophobicity recovery, the heat treatment for the sample was carried out in an oven at 75  $^{\circ}\text{C}$ .

## 3 RESULTS AND DISCUSSION

**Figure 1a** to **1f** show SEM micrographs of surface morphologies for the different silicone-rubber surfaces. A very flat microstructure can be seen from the surface prepared with the smooth template (**Figure 1a**). After preparing with templates, the surfaces have spongy-like rough structures and this confirmed that the morphology of the mould surface was successfully replicated. It can be seen that rough structure units (number and decrease in scale) increase with decreasing silicon carbide particle size. The silicone-rubber surface prepared with a template of particle size 63  $\mu\text{m}$  has an average diameter of 200  $\mu\text{m}$  irregular protuberances and pits (**Figure 1b**), the surface distributes on average a diameter of 100  $\mu\text{m}$  irregular papilla (**Figure 1c**), and the surface prepared with template of particle size of 15  $\mu\text{m}$  in diameter has a diameter of about 40  $\mu\text{m}$  irregular pits and protuberances (**Figure 1d**). **Figure 1e** to **1f** are higher-resolution micrographs of **Figure 1d**. **Figure 1f** and show that the randomly distributed papilla morphology (observed in **Figure 1e**) consists of sub-micron structures, which implies two-length-scale hierarchical structure on the surface. Therefore, the Cassie-Baxter superhydrophobic state was well formed.

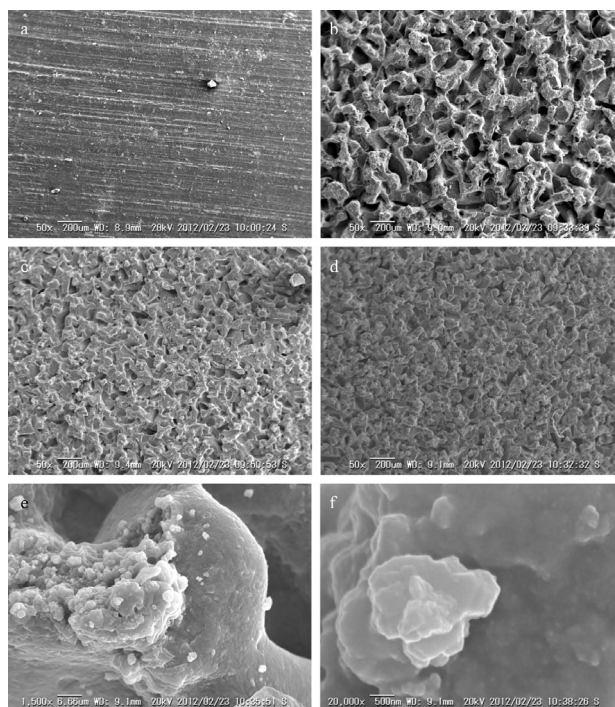


**Figure 1:** SEM micrographs of surface prepared with templates of different diameter silicon carbide particles: a) smooth, b) 63  $\mu\text{m}$ , c) 21  $\mu\text{m}$ , d) 15  $\mu\text{m}$ , e) the high magnification of d), and f) the high magnification of (e)

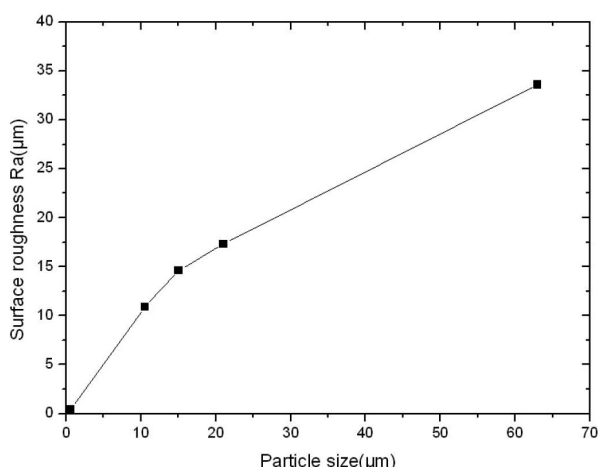


Figure 2: Relationship between particle size and surface roughness  $R_a$

Figure 2 shows the roughness of the surface morphology. The surface roughness of the smooth silicone rubber surface was  $0.42\ \mu\text{m}$ . When the templates are made by different silicon carbide particles of (10.5, 15, 21, and  $63\ \mu\text{m}$ ) in diameter, the surface roughness of the samples made by different templates are ( $10.88$ ,  $14.63$ ,  $17.32$  and  $33.61\ \mu\text{m}$ ), respectively. The results show that, after roughening with a rough template, the surface roughness of the silicone rubber increases with the increasing particle size of the sprayed silicon carbide.

Figure 3 shows the relationship between the surface wettability and the surface roughness. It is clear that the contact angle of the smooth silicone rubber surface is  $110.2^\circ$  and the sliding angle is about  $90^\circ$ . While roughening with rough templates, the surface wettability is greatly improved (the contact angle is larger than  $140^\circ$  and the sliding angle is from  $8^\circ$  to  $50^\circ$ ). The higher contact angle of the rough silicone-rubber surface can be attributed to the formation of the Wenzel wetting state (Figure 4a). According to Wenzel model ( $\cos \theta^* = r \cos \theta$ , where  $\theta^*$  is Wenzel apparent contact angle,  $\theta$  is the intrinsic contact angle of the ideal smooth material,

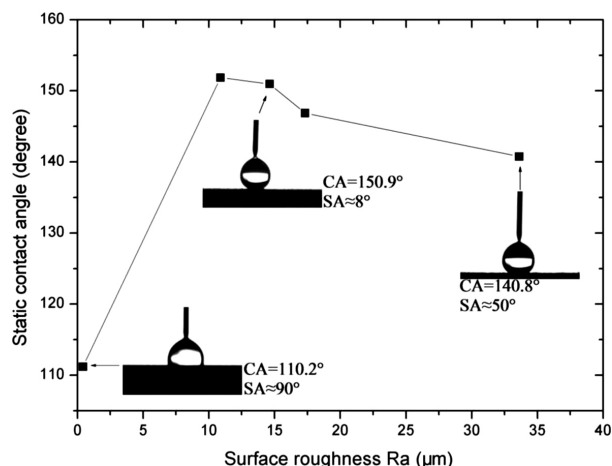


Figure 3: Relationship between static contact angle and surface roughness

which also called as Young's contact angle, and  $r$  is the ratio of the actual area to the projected area), rough structures can amplify the natural wettability tendency of the surface. Since silicone rubber is hydrophobic, the surface hydrophobic property will be improved by roughening the surface; its new contact angle becomes greater than the intrinsic contact angle. The contact angle reaches to  $150.9^\circ$  with a very small sliding angle of  $8^\circ$  for samples with a surface roughness of  $14.63\ \mu\text{m}$ . This can be explained by the formation of the Cassie-Baxter wetting state (Figure 4b), for it has a lotus-leaf-like surface morphology (Figure 1d to 1f). It is because of that there is such a micro-submicron hierarchical structure on samples, which is like the structure of the lotus leaf.<sup>1,4</sup> If a water droplet is placed upon the surface, air can be entrapped in both the hollows and interstices, resulting in the formation of a high area fraction of air-liquid interfaces. According to the Cassie-Baxter equation ( $\cos \theta_a = f_1 \cos \theta - f_2$ , where  $\theta_a$  is the apparent contact angle on a rough surface,  $f_1$  is the area fraction of the solid-liquid interface, and  $f_2$  is area fraction of the air-liquid interface), the contact angle can larger than  $150^\circ$  when the rough surface attains a large area fraction of air-liquid interface. With regards to the sliding angle, a surface exhibiting the Wenzel wetting state usually shows a larger sliding angle due to the pinning effects (Figure 4a). In contrast, a surface following the regime of the Cassie-Baxter wetting state (Figure 4b) allows a water droplet to roll off easily with a sliding angle of less than  $10^\circ$ .

Figure 3 shows that surface roughness plays an important role in the surface wettability. Since all the silicone rubber samples are prepared with a similar template structure (but different roughness), the samples present a similar surface morphology (Figure 1b to 1d). For samples with surface roughness  $R_a$  of  $10.88\ \mu\text{m}$  and  $14.63\ \mu\text{m}$ , the contact angle exceeds  $150^\circ$ , with a negligible sliding angle of about  $8^\circ$ . The contact angles reaches to a maximum value of  $151.8^\circ$ , when the surface roughness is  $10.88\ \mu\text{m}$ . When the surface roughness is larger than  $10.88\ \mu\text{m}$ , the contact angles decrease with increasing surface roughness. For the samples with a surface roughness ( $R_a$ ) of  $17.32\ \mu\text{m}$  and  $33.61\ \mu\text{m}$ , the contact angles are  $146.9^\circ$  and  $140.8^\circ$  respectively, while both of them show a sliding angle of about  $50^\circ$ . It is known that the micro-scale and nano-scale hierarchical structures affect the contact angle greatly. The micro-scale and nano-scale hierarchical structures can be

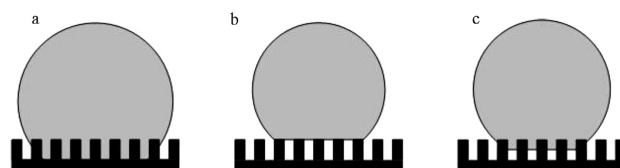
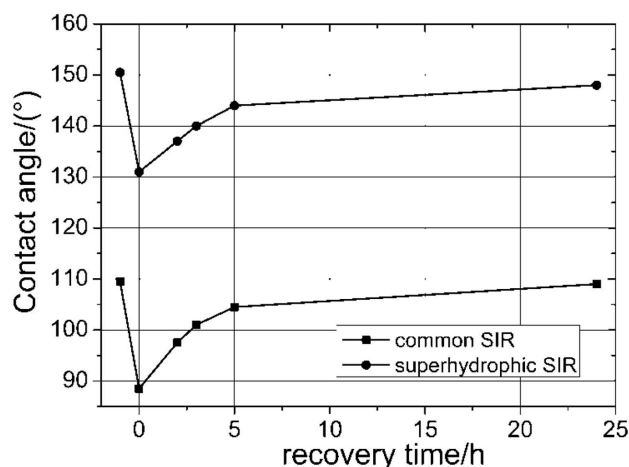


Figure 4: Various wetting state model sketch of a droplet on a rough surface: a) Wenzel state, b) Cassie-Baxter state and c) combined Cassie-Baxter/Wenzel state



**Figure 5:** The recovery curve for the hydrophobicity of the silicone-rubber samples

quantified by the surface roughness; therefore, the effect of surface structures on the contact angle can be studied by the surface roughness.<sup>19</sup> Compared with the contact angle, the sliding angle is more affected by the surface roughness. This can be attributed to the formation of the combined Cassie-Baxter and Wenzel wetting state model (Figure 4c).<sup>20,21</sup> As seen, the area fraction of air-liquid interfaces from the combined Cassie-Baxter and Wenzel wetting state model changes little (compared with Cassie-Baxter wetting state model); therefore, the contact angle will be larger than 140°. However, the sliding angle is greatly increased due to a certain extent by the pinning effects (Figure 4c). With respect to promising applications, such as anti-icing of superhydrophobic surfaces, both the contact angle and the small sliding angle are very important; therefore, the sliding angle also plays a important role.<sup>22</sup> Superhydrophobic surfaces with negligible sliding angle can be obtained by controlling the surface structure and the roughness.

Figure 5 shows the changes of the contact angle after the sandstorm experiment and the hydrophobicity recovery experiment. Because of the effects of the sand-dust, both of the contact angles decrease by approximately 20°. At the beginning of the recovering process, the hydrophobicity of samples recover quickly. Then the speed of the recovery slows down. After 24 h in a high-temperature treatment, the hydrophobicities of both superhydrophobic and common silicone rubber have basically recovered to the level of the primary sample.

The sand-dust on the silicone rubber is hydrophilic, which results in hydrophobicity degradation of the samples. Inside the silicone rubber, the large molecules polysiloxane are cracked into smaller molecules polysiloxane. And the high temperature can accelerate the cracking process. The small molecules polysiloxane with a low surface tension can migrate to the surface of the silicone rubber and cover the sand-dust particles.<sup>23,24</sup> Therefore, the hydrophobicity can be recovered after the high-temperature treatment. Considering that the contact

angle of the superhydrophobic silicone rubber has recovered to almost 150°, it shows that the micro-submicron hierarchical structure of superhydrophobic surfaces can almost not be destroyed.

## 4 CONCLUSIONS

Superhydrophobic surfaces were successfully fabricated on silicone rubbers through a facile template method. The contact angle for the surfaces can reach a maximum of 151.8° (sliding angle about 8°) with a surface roughness of 10.88 μm. When the surface roughness is larger than 10.88 μm the contact angle decreased with increasing roughness, and when the surface roughness is less than 10.88 μm, the contact angle increased with increasing roughness. The micro/sub-micron hierarchical structures of the surface were responsible for the high water contact angle and the low sliding angle. The wetting ability of the various surface roughness was different, and it could be explained by the different wetting state model. The sandstorm testing and the hydrophobicity experiment showed that the contact angle of both superhydrophobic and the common silicone rubber sample could recover.

## Acknowledgments

This research was financially supported by the National Natural Science Foundation of China (No. 51272208), the Natural Science Foundation of Hubei Province (2010CDA026), the Key Program of Hubei Provincial Department of Education (Z20104401), the Outstanding Scientific and Technological Innovation Team Project of Universities in Hubei Province (T201423), and the Talent Program of Hubei Polytechnic University (11yz04R).

## 5 REFERENCES

- L. Feng, S. Li, Y. Li, H. Li, L. Zhang, J. Zhai, Y. Song, B. Liu, L. Jiang, D. Zhu, Super-hydrophobic surfaces: From natural to artificial, *Advanced Materials*, 14 (2002) 24, 1857–1860, doi:10.1002/adma.200290020
- K. K. Varanasi, M. Hsu, N. Bhate, W. Yang, T. Deng, Spatial Control in the Heterogeneous Nucleation of Water, *Applied Physics Letters*, 95 (2009) 9, 094101, doi:10.1063/1.3200951
- L. Cao, A. K. Jones, V. K. Sikka, J. Z. Wu, D. Gao, Anti-Icing Superhydrophobic Coatings, *Langmuir*, 25 (2009) 21, 12444–12448, doi:10.1021/la902882b
- W. Barthlott, C. Neinhuis, Purity of the sacred lotus, or escape from contamination in biological surfaces, *Planta*, 202 (1997) 1, 1–8, doi:10.1007/s004250050096
- F. Arianpour, M. Farzaneh, S. A. Kulinich, Hydrophobic and ice-retarding properties of doped silicone rubber coatings, *Applied Surface Science*, 265 (2013), 546–552, doi:10.1016/j.apsusc.2012.11.042
- J. Li, Y. Zhao, J. Hu, L. Shu, X. Shi, Anti-icing Performance of a Superhydrophobic PDMS/Modified Nano-silica Hybrid Coating for Insulators, *Journal of Adhesion Science and Technology*, 26 (2012) 4–5, 665–679, doi:10.1163/016942411X574826



- <sup>7</sup> M. Jin, M. Liao, J. Zhai, L. Jiang, Super-hydrophobic polystyrene films prepared via pattern transformation, *Acta Chimica Sinica*, 66 (2008) 1, 145–148, doi:10.3321/j.issn:0567-7351.2008.01.025
- <sup>8</sup> Q. Xie, G. Fan, N. Zhao, X. Guo, J. Xu, J. Dong, L. Zhang, Y. Zhang, C. Han, Facile creation of a bionic super-hydrophobic block copolymer surface, *Advanced Materials*, 16 (2004) 20, 1830–1833, doi:10.1002/adma.200400074
- <sup>9</sup> J. Genzer, K. Efimenko, Creating long-lived super-hydrophobic polymer surfaces through mechanically assembled monolayers, *Science*, 290 (2000) 5499, 2130–2133, doi:10.1126/science.290.5499.2130
- <sup>10</sup> A. Hozumi, O. Takai, Preparation of ultra water-repellent films by microwave plasma-enhanced CVD, *Thin Solid Films*, 303 (1997) 1–2, 222–225, doi:10.1016/S0040-6090(97)00076-X
- <sup>11</sup> D. Xie, W. Li, A novel simple approach to preparation of super-hydrophobic surface of aluminum alloys, *Applied Surface Science*, 258 (2011) 3, 1004–1007, doi: 10.1016/j.apsusc.2011.07.104
- <sup>12</sup> T. Sun, G. Wang, L. Feng, B. Liu, Y. Ma, L. Jiang, D. Zhu, Reversible switching between super-hydrophilicity and super-hydrophobicity, *Angewandte Chemie International Edition*, 43 (2004) 3, 357–360, doi:10.1002/anie.200352565
- <sup>13</sup> X. Feng, L. Feng, M. Jin, J. Zhai, L. Jiang, D. Zhu, Reversible super-hydrophobicity to super-hydrophilicity transition of aligned ZnO nanorod films, *Journal of the American Chemical Society*, 126 (2004) 1, 62–63, doi:10.1021/ja038636o
- <sup>14</sup> L. Jiang, Y. Zhao, J. Zhai, A lotus-leaf-like superhydrophobic surface: a porous microsphere/nanofiber composite film prepared by electrohydrodynamics, *Angewandte Chemie International Edition*, 43 (2004) 33, 4338–4341, doi:10.1002/anie.200460333
- <sup>15</sup> M. K. Tiwari, I. S. Bayer, G. M. Jursich, T. M. Schutzius, C. M. Megaridis, Highly Liquid-Repellent, Large-Area, Nanostructured Poly(vinylidene fluoride)/Poly(ethyl 2-cyanoacrylate) Composite Coatings: Particle Filler Effects, *ACS applied materials & interfaces*, 2 (2010) 4, 1114–1119, doi:10.1021/am900894n
- <sup>16</sup> T. M. Schutzius, I. S. Bayer, J. Qin, D. Waldrup, C. M. Megaridis, Water-Based, Nonfluorinated Dispersions for Environmentally Benign, Large-Area, Superhydrophobic Coatings, *ACS applied materials & interfaces*, 5 (2013) 24, 13419–13425, doi:10.1021/am4043307
- <sup>17</sup> E. Bormashenko, V. Goldshtein, R. Barayev, T. Stein, G. Whyman, R. Pogreb, Z. Barkay, D. Aurbach, Robust method of manufacturing rubber waste-based water repellent surfaces, *Polymers for Advanced Technologies*, 20 (2009) 7, 650–653, doi:10.1002/pat.1323
- <sup>18</sup> B. He, G. Zhang, B. Chen, N. Gao, Y. Li, Z. Peng, H. Jin, The influence of the sand-dust environment on air-gap breakdown discharge characteristics of the plate-to-plate electrode, *Science China Physics, Mechanics and Astronomy*, 53 (2010) 3, 458–464, doi:10.1007/s11433-010-0078-1
- <sup>19</sup> X. Shi, T. A. Nguyen, Z. Suo, J. Wu, J. Gong, R. Avci, Electrochemical and mechanical properties of superhydrophobic aluminum substrates modified with nano-silica and fluorosilane, *Surface and Coatings Technology*, 206 (2012) 17, 3700–3713, doi:10.1016/j.surfcoat.2012.02.058
- <sup>20</sup> X. Feng, L. Jiang, Design and creation of superwetting/antiwetting surfaces, *Advanced Material*, 18 (2006) 23, 3063–3078, doi:10.1002/adma.200501961
- <sup>21</sup> C. W. Yang, F. He, P. F. Hao, The apparent contact angle of water droplet on the micro-structured hydrophobic surface, *Science China Chemistry*, 53 (2010) 4, 912–916, doi:10.1007/s11426-010-0115-y
- <sup>22</sup> S. A. Kulinich, M. Farzaneh, How Wetting Hysteresis Influences Ice Adhesion Strength on Superhydrophobic Surfaces, *Langmuir*, 25 (2009) 16, 8854–8856, doi:10.1021/la901439c
- <sup>23</sup> J. W. Chang, R. S. Gorur, Surface recovery of silicone rubber used for HV outdoor insulation, *IEEE Transactions on Dielectrics and Electrical Insulation*, 1 (1994) 6, 1039–1046, doi:10.1109/94.368659
- <sup>24</sup> T. Tokoro, R. Hackam, Loss and recovery of hydrophobicity and surface energy of HTV silicone rubber, *IEEE Transactions on Dielectrics and Electrical Insulation*, 8 (2001) 6, 1088–1097, doi:10.1109/94.971469





# INVESTIGATION OF THE STATIC ICING PROPERTY FOR SUPER-HYDROPHOBIC COATINGS ON ALUMINIUM

## PREISKAVA LASTNOSTI STATIČNE ZALEDENITVE PRI SUPERHIDROFOBNIH PREVLEKAH NA ALUMINIJU

Hai Yun Jin<sup>1</sup>, Shi Chao Nie<sup>1</sup>, Yu Feng Li<sup>1</sup>, Tian Feng Xu<sup>1</sup>, Peng Zhang<sup>1</sup>, Wen Li<sup>2</sup>

<sup>1</sup>Xi'an Jiaotong University Xi'an, State Key Laboratory of Electrical Insulation and Power Equipment, 710049, China

<sup>2</sup>Hubei Polytechnic University, Hubei Key Laboratory of Mine Environmental Pollution Control & Remediation and School of Chemical and Materials Engineering, Huangshi, 435003, China  
lxfzzl@126.com

*Prejem rokopisa – received: 2016-09-02; sprejem za objavo – accepted for publication: 2016-10-24*

doi:10.17222/mit.2016.266

An anti-icing aluminium with a super-hydrophobic surface was fabricated. A static icing system was developed to investigate the process of static icing for samples with different contact angles (CAs), and the contact state was also researched. The results showed that the water droplets' solidification time on a super-hydrophobic surface was much longer than for other surfaces at the same temperature. A water droplet on the super-hydrophobic surface had a much smaller contact area than on another surfaces. In addition, the air gap between the droplet and the super-hydrophobic surface retarded and prevented any exchange of heat. The temperature affected the transition from the Cassie state to the Wenzel state for super-hydrophobic aluminium.

Keywords: aluminium coating, static icing, solidification time, super hydrophobicity

Narejeno je bilo preprečevanje zaledenitve aluminija s superhidrofobno plastjo. Sistem statične zaledenitve je bil razvit za preiskavo procesa statične zaledenitve za vzorce z različnimi kontaktnimi koti (angl. CA), preiskano pa je bilo tudi stanje kontakta. Rezultati so pokazali, da je čas strjevanja vodnih kapljic na superhidrofobni površini precej daljši kot na drugih površinah pri enaki temperaturi. Vodna kapljica je imela na superhidrofobni površini precej manjšo kontaktno površino kot na drugih površinah. Poleg tega je zračna reža med kapljicami in superhidrofobno površino zaustavljala in preprečevala vsako izmenjavo toplote. Temperatura je vplivala na prehod iz stanja Cassie v stanje Wenzel za superhidrofobni aluminij.

Ključne besede: aluminijeva prevleka, statična zaledenitev, čas strjevanja, superhidrofobnost

## 1 INTRODUCTION

Icing is a natural phenomenon that occurs on the surfaces of objects in the bad conditions of low temperatures and freezing rain. An ice disaster is a serious natural disaster for a power system,<sup>1,2</sup> especially for abnormal weather with the El Nino and La Nina phenomena, the ice disaster became more frequently. In the past, for a long time, de-icing methods were active, and external energy was required to deal with the icing on the surfaces.<sup>3,4</sup> In recent years, anti-icing coatings that could improve the icing performance effectively received more attention, such as electric heating coatings, photo-thermal coatings and hydrophobic coatings. Two features are required for promising anti-icing materials. One is that overcooled water droplets can roll off from the surface easily before crystallization. And the other, is that the ice adhesion will be weaker when the ice is accumulated on the surface.<sup>5</sup> Super-hydrophobic coatings are promising materials due to the retardation and prevention of icing and have become a focus of study.<sup>6–16</sup>

The researches on super-hydrophobic materials for anti-icing are abundant; however, there are few reports about the process in detail of water condensing and then freezing to form ice on a cold super-hydrophobic surface.<sup>14,15</sup> M. He et al.<sup>14</sup> fabricated super-hydrophobic

surfaces with isotactic polypropylene; the results showed that the micro- and nanometre structures led to a delay of the solidification of liquid water at the three phase line region. M. He et al.<sup>14</sup> fabricated super-hydrophobic surfaces with ZnO nanorod arrays; the process of icing at different temperatures below the freezing point was studied.<sup>15</sup> However, the effect on the mechanism is unclear and needs more systemic and deep research. Furthermore, there are few reports about super-hydrophobic aluminium used in a power transmission line. Aluminium has good thermal conductivity, so different phenomenon may occur in the process of icing. S. L. Zheng et al.<sup>17,18</sup> fabricated super-hydrophobic aluminium coatings using the Electrochemical Corrosion Method. The adhesion strength of ice on coatings was researched, but the process of solidification of the droplets was not mentioned.

In this paper, super-hydrophobic coatings were fabricated using the Chemical Etching Method and a static icing system was developed to study the ice crystallization process of super-cooled water droplets on different coatings and different temperatures below the freezing point. The results are helpful to provide theoretical basis effectively for the design and fabrication of super-hydrophobic transmission aluminium conductors in the future.

## 2 EXPERIMENTAL PART

In order to fabricate samples with different hydrophobicities, a pre-treatment was necessary for the electrically pure aluminium. First, 1000 mesh sandpaper was used to polish the surface of the aluminium for the purpose of removing dense oxide layer, then using water and absolute ethyl alcohol to clean filth and grease on the surface by ultrasonic cleaning for 10 min. After pre-treatment, the aluminium can be used as a hydrophilic aluminium surface samples (A1). Using stearic acid to modify the aluminium surface, stearic acid is a kind of long-chain fatty acid and has a lower free energy. As shown in **Figure 1**, a dehydration reaction would happen between hydroxyl groups on the surface of the aluminium and the carboxyl group in stearic acid. Then a tight and thin coating with low free energy would be generated on the surface of the aluminium and hydrophobic aluminium surface samples (A2) could be obtained. As for super-hydrophobic aluminium surface samples, put the aluminium after pre-treatment to the 20 % of mass fractions of hydrochloric acid to etch for 1 min, after drying put it in the 1 % of mass fractions of stearic acid to modify the surface energy for 15 min, finally put the sample into the 90 °C oven to fabricate super-hydrophobic aluminium surface samples (A3).<sup>19</sup>

**Figure 2** shows that static icing system was made up of a Peltier chip, the cooling fan, temperature sensors and a temperature controller. The Peltier chip (TEC-1206) was supplied with power by a 12V DC power supply, the temperature difference between cold end and hot end was 75 °C and the temperature on the cold end could be –20 °C. The microprocessor in the semiconductor refrigeration temperature controller (TTC-B) was used to control the DC power in order to realize the temperature control. The test of static icing characteristics was completed at room temperature. In order to compare the process of icing, three kinds of typical aluminium wire samples (A1, A2 and A3) were observed. Detailed test steps was as follows:

1) Setting the surrounding environment in a dark-room, the entire Peltier cooling system was placed in a simple studio, the illumination was backlit bright LED projection mode, and the Peltier chip temperature was kept constant by adjusting the parameters of the PID

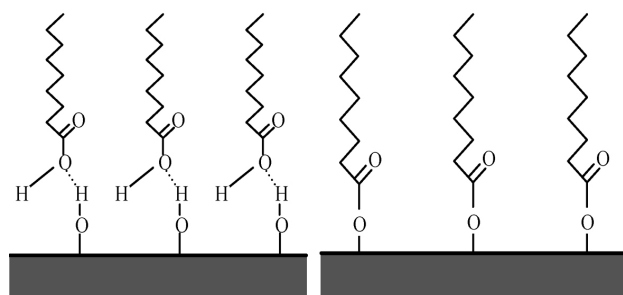


**Figure 1:** Modification mechanism of stearic acid on the aluminium surface

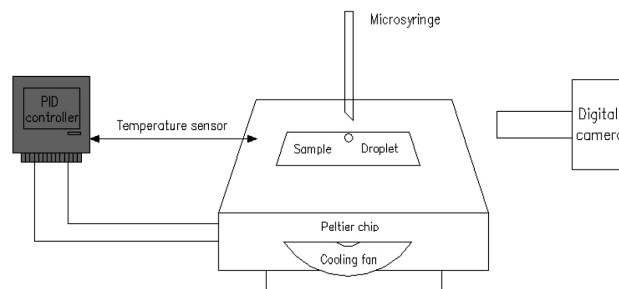


**Figure 2:** Schematic diagram of static icing test system

control system ( $-5\text{ °C} \pm 0.5\text{ °C}$ ,  $-3\text{ °C} \pm 0.5\text{ °C}$  and  $-1\text{ °C} \pm 0.5\text{ °C}$ ), and recorded both the ambient temperature and the humidity value;

2) Turning on the power of the Peltier cooling system. When the temperature of the surface was constant, we placed the samples on the Peltier surface, 15  $\mu\text{L}$  water droplets were injected onto the samples' surface rapidly by using a micro-syringe, and we recorded the solidification process of droplets using a digital camera.

## 3 RESULTS AND DISCUSSION

**Figure 3** shows the CA of droplets on 3 typical aluminium samples at room temperature. The CA on A1, A2 and A3 were 82°, 109° and 152°, respectively. Heat transfer happened between the droplets and the cold surface. Droplets placed on the surface of sample were liquid at first, and because of the results of differences of hydrophobicity, different contact states on three different surfaces were observed. As shown in **Figure 3**, the droplet on the surface of A1 was like a pan upside down, it had largest contact area; the droplet on the surface of A2 was like a semicircle, it had larger contact area and droplet on the surface of A3 was like a ball, it had the smallest contact area.

**Figure 4** shows SEM images and 3D laser scanning of A3, it can be seen that A3 had many micron structure pits and protrusions, and the size of these pits and protrusions was about 3  $\mu\text{m}$ . From **Figure 4b** and **4d**, a rough structure similar with building blocks could be observed, so the pits and protrusions connected with each other. Besides, the micron pits and protrusions had submicron even nano-sized rough structure on their surfaces. This surface structure was easy to form super hydrophobicity with a water droplet.<sup>20</sup>

**Figure 5** showed droplets' solidification process on samples (surface temperature is  $-3\text{ °C}$ ). Droplets on the surface of samples were liquid at first, as the time pro-

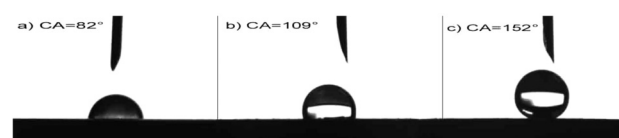


**Figure 3:** Contact angle of droplets on 3 typical aluminium samples at room temperature: a) A1, b) A2 and c) A3

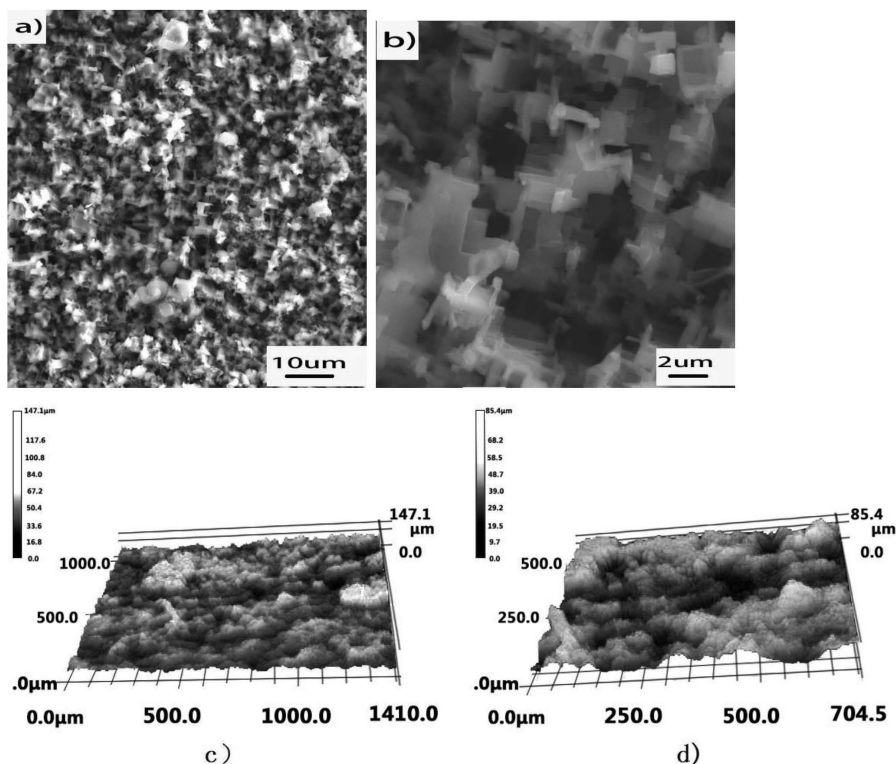


**Figure 4:** Microstructure of A3: a) The SEM image magnified 1000 times, b) the SEM image magnified 5000 times, c) the 3D laser scanning magnified 10 times and d) the 3D laser scanning magnified 20 times

longed, gas/liquid/solid three phase contact line between droplet and surface of sample expanded, and the contact area between the droplet and the surface increased, which meant the CA decreasing as the time prolonged. A phase transition occurred in the droplets because of the heat transfer between the cold surfaces and the droplets, which meant the transition from liquid to solid for the droplets. Also shown was the process of solidification after the phase transition, a clear liquid/solid line could be observed and this line grew up from bottom to the top. Under the liquid/solid line, the droplets were already frozen ice. Above the line, the droplets were still liquid. The liquid/solid line grew up at different speeds on three typical aluminium surfaces; the line grew up quickly on the A1 and A2 but relatively slowly on the A3. The line went up to the top of the droplet, and finally, a peak on the top of droplet was generated, which meant the end of solidification process.

**Figure 5** showed the phase transition time on different surfaces. The phase transition starting times for A1, A2 and A3 were 20 s, 34 s and 348 s, respectively. The phase-transition time on A3 was much longer than the other two surfaces. The solidification time for total droplet for A1, A2 and A3 were 38 s, 49 s and 404 s, respectively, the solidification time increased with increasing CA. The solidification time of the droplet for A3 was 10.6 times that of for A1 and 8.2 times that of for A2. Therefore, the solidification process of water

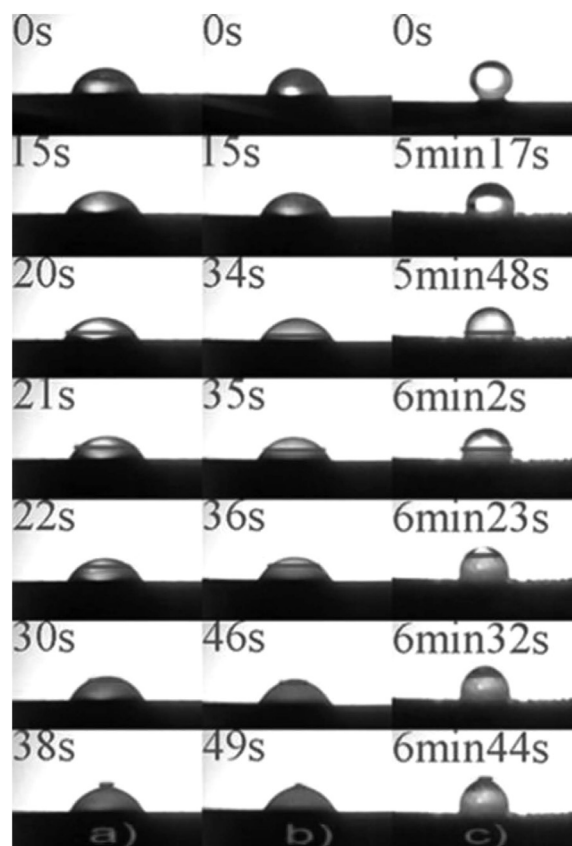


**Figure 5:** Droplets' solidification process on the surfaces of 3 typical aluminium wire samples, the red lines are the boundary of liquid and solid: a) A1, b) A2 and c) A3



droplet could be greatly delayed by the super-hydrophobic surface (A3).

The results show that the CA directly affects the freezing process of the droplets. For A1 and A2, the contact states between droplets and surfaces were the Wenzel state. The contact angle on A2 was larger than on A1, so the contact area between the droplet and A2 was smaller. For A3, the contact state of ball-like droplet made the smallest contact area. It was known that the heat-transfer rate was related to the contact area<sup>21</sup>, solidification time on A3 was the longest. At the same time, the vertical height of the droplet on A3 was greater, which meant more distance and time should be required for the solidification process from the bottom to the top of the droplet, therefore, the solidification time on A3 was the longest. On the other hand, for A3, the contact state was the Cassie state. There were a lot of air films in the contact interface and the air films played a role of energy barrier, which greatly delayed the heat exchange process between the droplets and surfaces, so the solidification time of droplets for A3 surface was also much longer than the other two surfaces.

After solidification, the top of the droplet would form a peak, and there were two main reasons for this: one was that the volume of droplets increased from liquid to solid; the other was that the droplet contained some of air, the dissolved air would form bubbles and released out of droplet during the process of phase transition and solidification. However, the peak of the droplet on the super-hydrophobic surface was more acute, which indicated that there was other air in the droplet besides the dissolved air, the explanation for this phenomenon could be the involvement of an air film between the droplet and the surface of the super-hydrophobic aluminium sample. Results might indirectly prove that the contact state of the droplet and the super-hydrophobic aluminium surface was in the Cassie contact state.

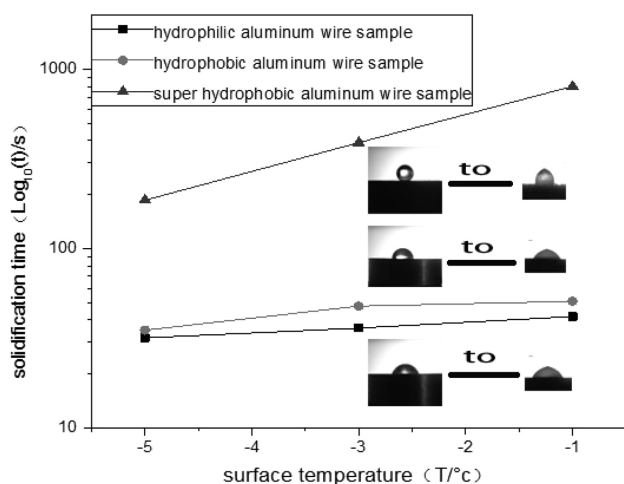


**Figure 6:** Relationship between solidification time and surface temperature: the picture shows the initial liquid state and the final solid state of the water droplets on A3 when the surface temperature is  $-3^{\circ}\text{C}$

**Figure 6** shows the relationship between the solidification time and surface temperature (the data of solidification time was average data of five experiments). When the surface temperature was  $-1^{\circ}\text{C}$ , the solidification times for A1, A2 and A3 were 41.7 s, 50.7 s and 803.7 s, respectively. When the surface temperature of the samples was  $-3^{\circ}\text{C}$ , the solidification time for A1, A2 and A3 were 36 s, 47.7 s and 390 s respectively. When the surface temperature was  $-5^{\circ}\text{C}$ , the data were 31.7 s, 35 s and 186 s, respectively. From **Figure 6** it can be seen that with the reduction of surface temperature, the solidification time of the droplets on three typical samples should decrease. This was because of the increase of the energy exchange speed and the decrease of nucleation barrier of surfaces with decreasing surface temperature. At different surface temperatures the solidification time of the droplets on A3 was much longer than A1 and A2, which showed the excellent static anti-icing performance of A3. When the surface temperatures were  $-1^{\circ}\text{C}$ ,  $-3^{\circ}\text{C}$  and  $-5^{\circ}\text{C}$ , the droplets' solidification times on A3 were 803.7 s, 390.0 s and 186.0 s, respectively. With a decreasing surface temperature, the solidification time of the droplets on A3 fell more rapidly than the other two typical surfaces. Due to the instability of the air film between the droplets and surface,<sup>22</sup> the contact state change from the Cassie state to the Wenzel state could become easier for A3, with temperature decreasing (**Figure 5c**) for 0 s and 5 min 17 s.

## 4 CONCLUSIONS

In summary, the super-hydrophobic coatings on aluminium ( $\text{CA}=152^{\circ}$ ) were fabricated by Chemical Etching and Modification Method. For the super-hydrophobic surface, the solidification and phase-change time of the droplets were much longer than the hydrophilic aluminium surface and the hydrophobic aluminium surface. This was because for the super-hydrophobic aluminium surfaces the freezing process could be retarded and prevented by both smaller contact area and air film between droplet and surface (Cassie contact state), which influenced the thermal exchange between the droplet and the surface.

Due to that the air film latched by the droplet on the super-hydrophobic surface was not stable, with the temperature decreasing, the droplet transited from the Cassie contact state to the Wenzel contact state more easily.

## Acknowledgements

This research was financially supported by the National Natural Science Foundation of China (No. 51272208), the Natural Science Foundation of Hubei Province (2010CDA026), the Key Program of Hubei Provincial Department of Education (Z20104401), the Outstanding Scientific and Technological Innovation

Team Project of Universities in Hubei Province (T201423), and the Talent Program of Hubei Polytechnic University (11yz04R).

## 5 REFERENCES

- <sup>1</sup> Y. Hu, Analysis and Countermeasures Discussion for Large Area Icing Accident on Power Grid, *High Voltage Engineering*, 34 (2008) 2, 215–219, doi:10.13336/j.1003-6520.hve.2008.02.020
- <sup>2</sup> Y. Yang, J. Li, J. Hu, Y. Zhao, X. Jiang, C. Sun, Experimental Study on Icing Properties of Superhydrophobic Coatings on Insulators, *High Voltage Engineering*, 36 (2010) 3, 621–626, doi:10.13336/j.1003-6520.hve.2010.03.013
- <sup>3</sup> J. Laforte, M. Allaire, J. Laflamme, State-of-the-art on power line de-icing, *Atmospheric Research*, 46 (1998) 1, 143–158, doi:10.1016/S0169-8095(97)00057-4
- <sup>4</sup> O. Parent, A. Ilinca, Anti-icing and de-icing techniques for wind turbines: Critical review, *Cold Regions Science and Technology*, 65 (2011) 1, 88–96, doi:10.1016/j.coldregions.2010.01.005
- <sup>5</sup> Y. Wang, J. Xue, Q. Wang, Q. Chen, J. Ding, Verification of Ice-phobic/Anti-icing Properties of a Superhydrophobic Surface, *ACS applied materials & interfaces*, 5 (2013) 8, 3370–3381, doi:10.1021/am400429q
- <sup>6</sup> G. Fang, A. Amirfazli, Understanding the anti-icing behavior of superhydrophobic surfaces, *Surface Innovations*, 2 (2014) 2, 94–102, doi:10.1680/si.13.00046
- <sup>7</sup> S. Farhadi, M. Farzaneh, S. Kulinich, Anti-icing performance of superhydrophobic surfaces, *Applied Surface Science*, 257 (2011) 14, 6264–6269, doi:10.1016/j.apsusc.2011.02.057
- <sup>8</sup> T. Kako, A. Nakajima, H. Irie, Z. Kato, K. Uematsu, T. Watanabe, K. Hashimoto, Adhesion and sliding of wet snow on a super-hydrophobic surface with hydrophilic channels, *Journal of Materials Science*, 39 (2004) 2, 547–555, doi:10.1023/B:JMSC.0000011510.92644.3f
- <sup>9</sup> Y. Tang, Q. Zhang, X. Zhan, F. Chen, Superhydrophobic and anti-icing properties under overcooled temperature of fluorinated hybrid surface prepared via sol–gel process, *Soft Matter*, 11 (2015) 22, 4540–4550, doi:10.1039/c5sm00674k
- <sup>10</sup> P. Tourkine, M. Le Merrer, D. Quéré, Delayed freezing on water repellent materials, *Langmuir*, 25 (2009) 13, 7214–7216, doi:10.1021/la900929u
- <sup>11</sup> T. Bharathidasan, S.V. Kumar, M. Bobji, R. Chakradhar, B. J. Basu, Effect of wettability and surface roughness on ice-adhesion strength of hydrophilic, hydrophobic and superhydrophobic surfaces, *Applied Surface Science*, 314 (2014), 241–250, doi:10.1016/j.apsusc.2014.06.101
- <sup>12</sup> S. Kulinich, M. Farzaneh, How wetting hysteresis influences ice adhesion strength on superhydrophobic surfaces, *Langmuir*, 25 (2009) 16, 8854–8856, doi:10.1021/la901439c
- <sup>13</sup> S. Kulinich, M. Farzaneh, Ice adhesion on super-hydrophobic surfaces, *Applied Surface Science*, 255 (2009) 18, 8153–8157, doi:10.1016/j.apsusc.2009.05.033
- <sup>14</sup> M. He, J. X. Wang, H. L. Li, X. L. Jin, J. J. Wang, B. Q. Liu, Y. L. Song, Super-hydrophobic film retards frost formation, *Soft Matter*, 6 (2010) 11, 2396–2399, doi:10.1039/c0sm00024h
- <sup>15</sup> M. He, J. Wang, H. Li, Y. Song, Super-hydrophobic surfaces to condensed micro-droplets at temperatures below the freezing point retard ice/frost formation, *Soft Matter*, 7 (2011) 8, 3993–4000, doi:10.1039/c0sm01504k
- <sup>16</sup> J. Durret, N. Fiolet, C. Gourgon, Hydrophobicity and anti-icing performances of nanoimprinted and roughened fluoropolymers films under overcooled temperature, *Microelectronic Engineering*, 155 (2016), 1–6, doi:10.1016/j.mee.2016.01.011
- <sup>17</sup> S. Zheng, C. Li, Q. Fu, M. Li, W. Hu, Q. Wang, M. Du, X. Liu, Z. Chen, Fabrication of self-cleaning superhydrophobic surface on aluminum alloys with excellent corrosion resistance, *Surface & Coatings Technology*, 276 (2015), 341–348, doi:10.1016/j.surfcoat.2015.07.002
- <sup>18</sup> S. Zheng, C. Li, Q. Fu, W. Hu, T. Xiang, Q. Wang, M. Du, X. Liu, Z. Chen, Development of stable superhydrophobic coatings on aluminum surface for corrosion-resistant, self-cleaning, and anti-icing applications, *Materials and Design*, 93 (2016), 261–270, doi:10.1016/j.matdes.2015.12.155
- <sup>19</sup> Z. Huang, Y. Li, P. Jin, M. Hu, B. He, N. Gao, H. Zhang, H. Jin, Fabrication of Aluminum Superhydrophobic Surface with Facile Chemical Etching Method, *Materials Science Forum*, 804 (2015), 103–106, doi:10.4028/www.scientific.net/MSF.804.103
- <sup>20</sup> L. Jiang, Nanostructured Materials with Super-hydrophobic Surface-from Nature to Biomimesis, *Chemical Industry and Engineering Progress*, 22 (2003) 12, 1258–1264, doi:10.3321/j.issn:1000-6613.2003.12.002
- <sup>21</sup> O. R. Enriquez, A.G. Marin, K. G. Winkels, J. H. Snoeijer, Freezing singularities in water drops, *Physics of Fluids*, 24 (2012) 9, 091102, doi:10.1063/1.4747185
- <sup>22</sup> H. Y. Jin, Y. F. Li, P. Zhang, S. C. Nie, N. K. Gao, The investigation of the wetting behavior on the red rose petal, *Applied physics Letter*, 108 (2016) 15, 151605, doi:10.1063/1.4947057



EFFECT OF BALL MILLING ON THE PROPERTIES OF THE  
POROUS Ti–26Nb ALLOY FOR BIOMEDICAL APPLICATIONSVPLIV KROGLIČNEGA MLETJA NA LASTNOSTI POROZNE  
ZLITINE Ti–26Nb ZA BIOMEDICINSKE APLIKACIJE

Grzegorz Dercz, Izabela Matuła

University of Silesia, Institute of Materials Science, 75 Pułku Piechoty Street 1 A, 41-500 Chorzów, Poland  
grzegorz.dercz@us.edu.pl*Prejem rokopisa – received: 2016-09-09; sprejem za objavo – accepted for publication: 2017-02-21*

doi:10.17222/mit.2016.269

The current study investigated the effect of the ball-milling time on the structural characteristics and pore morphology of a biomedical porous Ti–26Nb (at%) alloy. An open-cell porous material was synthesized by mechanical alloying and sintering. Commercially available elemental metal powders of Ti and Nb were used as the starting materials. Elemental metal powders with a nominal composition of Ti–26Nb (at%) were milled in a planetary ball mill. During the testing, the powders were milled for two milling times: 50 h and 70 h. During the shorter milling time, the speed of 200 min<sup>-1</sup> was applied, and during the longer milling time, the speed of 400 min<sup>-1</sup> was applied. The powders were cold pressed under a pressure of 750 MPa and then sintered at 1000 °C for 24 h. The effects of the powder milling time on the microstructure and mechanical properties of the porous structure were investigated with optic microscopy (OM), scanning electron microscopy (SEM), X-ray diffraction (XRD), microhardness, nanoindentation and nanomachining tests. The hardness and elastic modulus were calculated from the load-displacement data obtained with nanoindentation using a three-sided, pyramidal, diamond (Berkovich) indenter tip. The X-ray diffraction results confirmed the presence of the  $\alpha$  and  $\beta$  phases. An analysis of diffraction patterns revealed a decrease in the lattice parameters for the 70 h milling. In summary, it should be pointed out that the material has a hierarchical structure, obtained during the successive stages of milling. The observed grains are composed of many smaller grains, the size of which decreased with an increase in the milling time.

Keywords: mechanical alloying, porosity, nanoindentation, Ti–26Nb alloy

V študiji so preiskovali vpliv različno dolgega časa kroglíčnega mletja na strukturne značilnosti in morfologijo por biomedicinske porozne Ti–26Nb zlitine (at%). Porozni material z odprtimi celicami je bil sintetiziran z mehanskim legiranjem in sintranjem. Osnovni metalurški prahovi z nominalno vsebnostjo Ti–26Nb (at%) so bili mleti v planetarnem krogelnem mlinu. Med testiranjem so bili prahovi mleti pri dveh različnih časih: 50 h in 70 h. Med krajšim časom mletja je bila uporabljena hitrost mletja 200 min<sup>-1</sup> in med daljšim časom mletja je bila uporabljena hitrost 400 min<sup>-1</sup>. Prahovi so bili hladno stiskani pod tlakom 750 MPa in nato sintrani pri 1000 °C za 24 h. Preiskovali so vpliv različnega časa mletja prahu na mikrostrukturo in na mehanske lastnosti porozne strukture z optičnim mikroskopom, s SEM- in XRD-analizo ter določevanjem mikrotrdote in mehanske nanoobdelave. Trdoto in modul elastičnosti so izračunali iz meritev odvisnosti med obremenitvijo in globino vtisa tristranske diamantne konice (po Berkovichu). Rezultati rentgenske difrakcije so potrdili prisotnost  $\alpha$  in  $\beta$  faz. Skratka, poudariti je treba, da ima material hierarhično strukturo, ki je posledica faze mletja. Pregledana zrna so sestavljena iz mnogo manjših podzrn, katerih velikost se je zmanjševala s podaljševanjem časa mletja.

Ključne besede: mehansko legiranje, poroznost, nanoviskovanje, zlitina Ti–26Nb

## 1 INTRODUCTION

Titanium-based alloys seem to be the preferred materials for orthopaedic applications. They are characterized by high biocompatibility, great corrosion resistance, light weight and good mechanical properties and have a relatively low modulus in comparison to the other materials used as implants.<sup>1</sup> However, titanium-based alloys used for implants have important disadvantages. Firstly, popular alloying additives (Al, V) are dangerous for the health and life of a patient.<sup>2</sup> Secondly, the metals used for implants have too high an elastic modulus in comparison to the mechanical properties of the bone. This difference between the mechanical properties induces stress between the implant and the bone.<sup>3</sup> In recent years, due to intensive investigation, we have seen the production and development of various Ti-based alloys,

among which there are Ti–Mo-based, Ti–Nb-based, Ti–Zr-based and Ti–Ta-based alloys.<sup>2</sup>

This work focuses on niobium as the additive to titanium because it has been recognized as an extremely promising element. Nb is highly biocompatible, has a low ionic in-vitro cytotoxicity, and most importantly – there is no evidence of mutagenicity or carcinogenicity.<sup>4</sup> The Ti–Nb-based alloys are attracting more researchers to study them due to their low modulus, good biocompatibility and shape-memory effect. Medical applications of SME (shape-memory effect) alloys will be especially increased in the near future, so the development and basic or extensive research of the Ti-based alloys are necessary.<sup>1,2,4,5</sup> A series of studies confirmed the presence of the shape-memory effect and superelasticity in the alloys with the composition of Ti–26Nb (at%) and also in approximate compositions of the elements.<sup>4–7</sup> Most of



these alloys are obtained with a conventional method such as arc melting. One of the alternatives to the widely used arc melting is powder metallurgy (PM). In the scientific literature, there are evidences of successful preparations of titanium-based materials with this production method.<sup>8–10</sup> This production method has a number of significant advantages. It allows creating alloys of materials with large differences between their melting temperatures or densities. The most important advantages of PM for the production of biomaterials are its low cost and the possibility to produce highly porous materials.<sup>4,11</sup>

The aim of the present paper is to determine the possibility to produce a Ti–26Nb (at%) alloy using the powder-metallurgy method. Simultaneously, this research is to develop a technology of producing Ti-based alloys and estimate the influence of changing parameters during the mechanical alloying. Such research is the starting point for further development of nickel-free alloys with the shape-memory effect based on titanium and niobium. In this article, the influence of the milling time on the microstructure and mechanical properties of the produced alloy is investigated.

## 2 EXPERIMENTAL PART

Commercial elemental powders of Ti (Atlantic Equipment Engineers (AEE), 99.7 %, <20 µm) and Nb (Atlantic Equipment Engineers (AEE), 99.8 %, < 5 µm) were used as the initial materials for the synthesis of the alloy. Elemental metal powders with the nominal composition of Ti-26Nb (at%) were milled for two different milling times, 50 h and 70 h, in a planetary ball mill Fritch PULVERISETTE 7 premium line. To prevent the powder from oxidation as much as possible, the process was carried out in an argon-protective atmosphere. During the shorter milling time, the speed of 200 min<sup>-1</sup> was applied, and for the longer milling time (with additional 20 h), the speed of 400 min<sup>-1</sup> was applied. The powders were cold isostatically pressed under a 750 MPa pressure without any substances that improve the porosity (e.g., space holders). Then the material was sintered at 1000 °C for 24 h and cooled in the furnace to room temperature.

The crystalline structure and phase content of the sintered materials were tested with X-ray diffraction. The refinement of the X-ray diffraction pattern was carried out using Rietveld's whole X-ray profile fitting technique with the DBWS 9807a program.<sup>12</sup> The profile function used to adjust the calculated diffractograms to the observed ones was the pseudo-Voigt one.<sup>13,14</sup> The weight fraction of each component was determined based on the optimized scale factors with the use of the relation proposed by Hill and Howard.<sup>15,16</sup> Based on the Williamson–Hall method, the crystallite sizes (*D*) and lattice strain  $\langle \Delta a/a \rangle$  for the phases appearing in the material at various milling times were determined. The

apparatus factors were eliminated using LaB<sub>6</sub> (SRM 660a).

The morphology of the initial powders and the microstructure of the sintered material were tested using an optic microscope and scanning microscope JEOL JSM 6480 with an accelerating voltage of 20 kV. Additionally, a chemical analysis was performed using an EDS detector manufactured by IXRF using the standard calibration method.

An analysis of the microstructure was performed on microscopic images with the use of ImageJ, which is the software used for image processing and analysis. The size and shape of the grains were determined using the planimetric method. The study also included determining the inhomogeneity of the size of the grains. A quantitative analysis of the morphology of the material was performed using the stereological parameters presented below:

- the size of the area of a section of grain *a* (µm<sup>2</sup>),
- dimensionless lengthening factor (Equation (1):

$$f_{g1} = \frac{h}{w} \quad (1)$$

where: *h* – height and *w* – width of the smallest rectangle described on the object,

- dimensionless shape factor – the circularity:

$$f_{g2} = \frac{4\pi F}{L^2} \quad (2)$$

where: *F* – area of the analyzed object; *L* – perimeter of the analyzed object,

- grain-size change-ability factor:

$$v = \frac{\sigma_x}{a} \quad (3)$$

where:  $\sigma_x$  – grain-size standard deviation; *a* – grain mean value,

the number of analyzed elements per area unit of the image:  $N_A$  [1/mm<sup>2</sup>].

The thermal behavior of the martensitic transformation was studied using a differential scanning calorimeter (DSC) Mettler Toledo DSC-1. Transformation temperatures were determined from the thermograms measured at a heating rate of 10 deg/min and a thermal range of –120 °C to 600 °C.

The surface morphology, hardness and elastic modulus were tested using a Hysitron Triboindenter Ti950 with AFM QScope 250. The measurements were calculated from the load-displacement data obtained with the nanoindentation, using a three-sided, pyramidal, diamond (Berkovich) indenter tip. An area of 40 µm × 40 µm was analyzed at a scanning frequency of 0.25 Hz. The microhardness measurement was carried out parallel to the nanoindentation tests. The Vickers microhardness measurement was taken at a load of 500 N and a loading time of 10 s on a 401MVD microhardness tester.

### 3 RESULTS AND DISCUSSION

SEM micrographs of the initial metal powders are presented in **Figure 1**. The titanium-powder morphology is irregular, having sharp corners and rough surfaces. The dispersion of the Ti particles is wide and ranges from a few  $\mu\text{m}$  to even 50  $\mu\text{m}$ . The niobium powder has a much wider dispersion of the particles in comparison to the Ti powder.

Some of the particles have the size below 10  $\mu\text{m}$ , and the shape of these particles is irregular. Simultaneously, there are also very large particles, the sizes of which are greater even than 50  $\mu\text{m}$  and these particles have an irregular, polyhedral shape. As a result of the work-hardening effect and high density of defects such as dislocations and vacancies created during long ball-milling times, the fracture and welding of powders reach an equilibrium state. This state leads to the formation of rather equiaxed and small particles.<sup>16,17</sup> However, due to the higher bonding strength of the finer particles, their ability to undergo further plastic deformation is decreased and a higher force is required to fracture the small particles during the ball-milling process.<sup>18</sup> It is worth mentioning that the reduction in the particle size at a given milling time can also be influenced by the milling technique.

The morphologies of the Ti-26Nb (*a/a*%) powders at different milling stages are shown in **Figure 2**. The powder after the shortest milling time shows globular particles. In the picture with the higher magnification (**Figure 2b**), some cracks were observed, which is the beginning of the cyclic process of material milling during high-energy ball milling. In contrast, in the samples after 70 h of milling, the particles became larger and the shape of the particles became less globular. Moreover, the particles of this sample are cold welded and the powder particles, in particular, are composed of the welded layers of the material. This behavior of the material during the high-energy milling is consistent

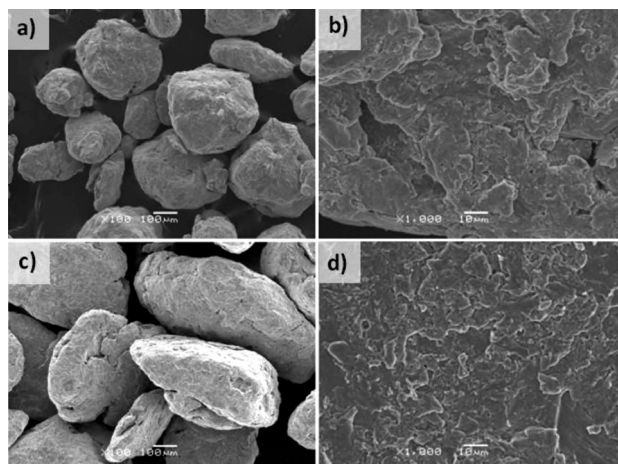


**Figure 2:** SEM micrographs of particles after different milling times: a), b) 50 h of milling and c), d) 70 h

with the conduct and following steps of mechanical alloying.<sup>19</sup> As shown by the other studies, the mechanical-alloying method leads to a decreased particle size, the  $\beta$ -Ti phase being stabilized by Nb, and an increased surface area between Ti and Nb. This promotes good homogeneity of the solid solution.<sup>20</sup>

**Figure 3** shows a summary of diffraction patterns of the material after the mechanical synthesis, depending on the milling time of the initial powders. The X-ray qualitative analysis showed that only  $\beta$  and  $\alpha$  phases are present in the material after milling for 50 h and 70 h. Change of the profile lines of individual diffraction patterns are clearly visible.

The broadening of the particle-size distribution at longer ball-milling times is a typical behavior of high-energy ball-milling process.<sup>17,19,21,22</sup> For the  $\beta$  and  $\alpha$  phases, it was observed that a decrease in the crystallite size took place simultaneously with an increase in the milling time (**Table 1**). In addition, in the case of the  $\beta$  phase there was a tendency towards a decrease in the lattice strain  $\langle\Delta a/a\rangle$  (**Table 1**). The estimated size of the crystallites for the powder after milling for 70 h is 9(1) nm and 16(2) nm for the  $\beta$  and  $\alpha$  phases, respectively. The observed  $\langle\Delta a/a\rangle$  lattice strain values indicate growth in the  $\beta$  phase ( $3.43\text{E-}03\%$ ) and in the  $\alpha$  phase

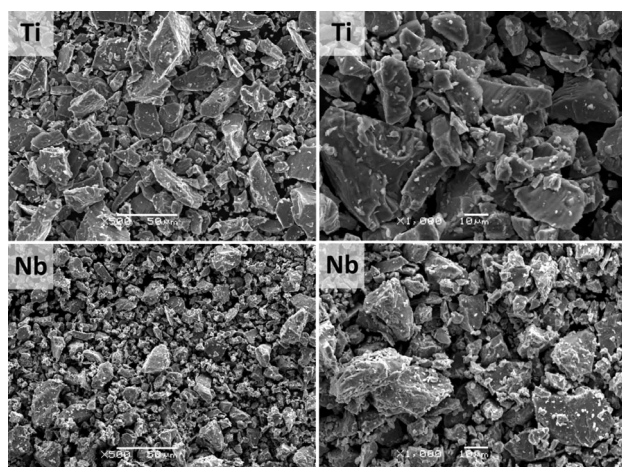


**Figure 1:** SEM micrographs of the initial Ti and Nb powders at different magnifications

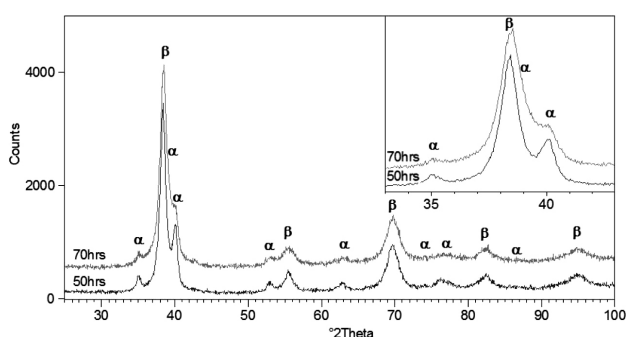


**Figure 3:** X-ray diffraction patterns of the powder after 50 h and 70 h of the milling process

(2.31E-03 %). The analysis of the diffraction patterns obtained using the Rietveld method showed that that high-energy milling has an influence on the lattice parameters.

**Table 1:** Changes of the average crystallite sizes (D) and lattice distortions ( $\langle\Delta a/a\rangle$ ) of the  $\alpha$  and  $\beta$  phases of the milled powders

Phase	Parameters		Milling time (h)	
			50	70
$\alpha$	D	(nm)	22(2)	16(1)
	$\langle\Delta a/a\rangle$	(%)	2.76E-03	3.43E-03
$\beta$	D	(nm)	15(2)	9(1)
	$\langle\Delta a/a\rangle$	(%)	2.04E-03	2.31E-03

**Table 2** presents lattice parameters determined for individual phases and the corresponding ICDD data sheets. In the case of the  $\beta$  phase, a slight deviation of the  $a_0$  lattice parameters from the catalogue data was observed. A similar type of cell contraction was discovered for the  $a_0$  parameter of the  $\alpha$  phase and for the  $c_0$  parameter, but these changes are smaller, resulting from the shift systems for the phases of the hexagonal system. It should be stressed that for the sample after 70 h of milling, the deviation of both lattice parameters can be noted. It is probably the effect of the alternate cold welding and deposition of the particles during the mechanical synthesis.

**Table 2:** Lattice parameters and contents of  $\alpha$  and  $\beta$  phases of the milled powders

Phase	Lattice parameters (nm)	
		ICDD*
$\alpha$	$a_0$	0.2970
	$c_0$	0.4720
$\beta$	$a_0$	0.3307

\* International Centre for Diffraction Data® – a scientific organization dedicated to collecting, editing, publishing and distributing powder-diffraction data for the identification of materials

The quantitative phase analysis of the material after each stage show a successive progressive synthesis of the as-prepared powders in relation to the  $\beta$  phase (77.5(11) % mass fraction and 82.6(12) % mass fraction, for 50 h and 70 h milling times, respectively).

The X-ray qualitative analysis showed that only  $\beta$  and  $\alpha$  phases are present in the samples annealed at 1000 °C for 24 h from the powder previously milled for 50 h and 70 h, as shown in **Figure 4**. The XRD shows that there were no obvious diffraction peaks of elemental Nb remaining in the sintered Ti–26Nb ( $a/\%$ ). The diffraction peaks attributable to the  $\alpha$  and  $\beta$  phases from the pattern confirm a duplex microstructure. M. Tahara et al.<sup>23</sup> confirmed only the  $\beta$  phase for Ti–26Nb ( $a/\%$ ) produced by arc melting. The predominant phase in all the samples was the body-centered-cubic (bcc)  $\beta$  phase. This indicates that Nb was diffused into Ti, thereby leading to the formation of  $\alpha + \beta$  phases after the sintering.

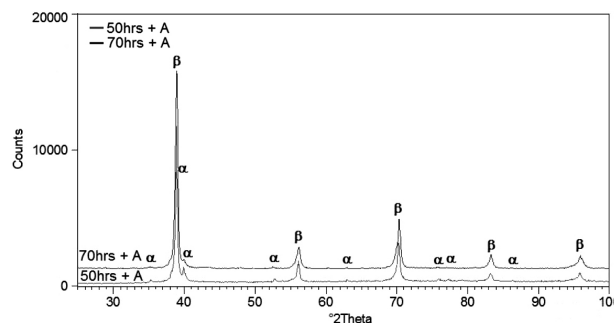


**Figure 4:** X-ray diffraction patterns for the samples annealed (+A) at 1000 °C for 24 h from the powder previously milled for 50 h and 70 h

This is significant because two-phase Ti alloys, with the major  $\beta$  phase and the minor  $\alpha$  phase, possess good comprehensive properties including high yield strength, excellent corrosion resistance and good fracture toughness.

The presence of unalloyed Ti particles in materials may arise from different facts. According to S. N. Patankar and F. H. Froes<sup>24</sup>, it could be correlated with the brittleness of the Nb particles, as compared to the Ti particles, since these brittle particles adhere to the surfaces of ductile particles. Another reason could be the limited solubility of Nb in  $\alpha$ -Ti. It is known that isomorphous  $\beta$ -stabilizer elements, such as Nb, exhibit slower diffusivities in Ti than the eutectoid elements of Fe, Co and Ni.<sup>25</sup>

The structural analysis of the diffraction patterns obtained using the Rietveld method showed that the lattice parameters for all the tested samples become reduced. In comparison to the ICDD data, it was found that high-energy milling and annealing have the smallest, but significant effect on the reduction of the size of a unit cell of the  $\alpha$  and  $\beta$  phases. The quantitative phase analysis (**Table 3**) of the material after annealing showed a significant synthesis of the as-prepared powders in relation to the  $\beta$  phase 96.6(12) w/% and 98.8(12) w/% for samples previously milled for 50 h and 70 h, respectively).

**Table 3:** Lattice parameters and contents of  $\alpha$  and  $\beta$  phases after annealing (A) the samples at 1000 °C for 24 h from the powder previously milled for 50 h and 70 h

Phase	Lattice parameters (nm)				Phase	Contents (w/%)	
		ICDD*	50 h + A	70 h + A		50 h + A	70 h + A
$\alpha$	$a_0$	0.2970	0.2898 (2)	0.2891 (2)	$\alpha$	3.4 (6)	1.2 (4)
	$c_0$	0.4720	0.4715 (4)	0.4710 (4)			
$\beta$	$a_0$	0.3307	0.3287 (2)	0.3286 (2)	$\beta$	96.6 (12)	98.8 (12)

\* International Centre for Diffraction Data® – a scientific organization dedicated to collecting, editing, publishing and distributing powder-diffraction data for the identification of materials

Optical and SEM micrographs of the studied samples are presented in **Figures 5** and **6**. They clearly show the



changes in the morphology of the material after sintering with respect to various milling times. The common feature of the samples is a hierarchical structure. After the milling, large-sized particles caused the formation of a porous material. The pores were large and interconnected (**Figures 5a** and **5c**) in spite of the applied pressure of 750 MPa during the isostatic pressing.

In the case of the sample milled for 50 h (**Figure 5b**), an anomalous grain growth was observed. SEM micrographs (**Figure 6**) revealed further differences between the obtained microstructures. The powders ball-milled for a long time cannot move and deform effectively during the compaction. This may be primarily due to the effects of the decrease in the particle size, solid-solution strengthening and work hardening of the particles during the ball-milling process.<sup>26,27</sup> Amongst these factors, the work-hardening effect appears to be the main determinant in governing the plastic behavior of the powder particles during the compaction. In the ball-milling process, work hardening is caused by the interaction of

dislocations with each other through the continuous mechanical impact of the balls on the powder particles.<sup>16</sup>

A quantitative analysis of the microstructure was conducted including the determination of the cross-sectional area of the grains and the subgrains, as well as the average circularity of the subgrains of the microsections based on microscopic images, the results of which are presented in **Tables 4** to **6**. Significant changes between the samples in the average  $a$  of the grain cross-sectional area can also be observed. For the samples milled for 50 h and 70 h, the average section area of grains was  $9.09 \mu\text{m}^2$  and  $3.55 \mu\text{m}^2$ , respectively (**Table 4**). A change in the time and rotations per minute during milling causes a difference in the parameter.

**Table 4:** Results for the cross-sectional area of the grains for the samples milled for different times

Parameter	Sample	Minimum value	Maximum value	Average value	Std. dev.
$a \text{ (}\mu\text{m}^2\text{)}$	50 h	0.51	267.57	9.09	12.68
	70 h	0.51	32.35	3.55	3.45

**Table 5:** Results for the circularity of the grains for the samples milled for different times

Parameter	Sample	Minimum value	Maximum value	Average value	Std. dev.
$f_{g2}$	50 h	0.10	1.00	0.60	0.15
	70 h	0.11	0.96	0.59	0.15

**Table 6:** Results for the dimensionless lengthening factor of the grains for the samples milled for different times

Parameter	Sample	Minimum value	Maximum value	Average value	Std. dev.
$f_{g1}$	50 h	0.32	3.31	1.06	0.37
	70 h	0.28	3.30	1.06	0.37

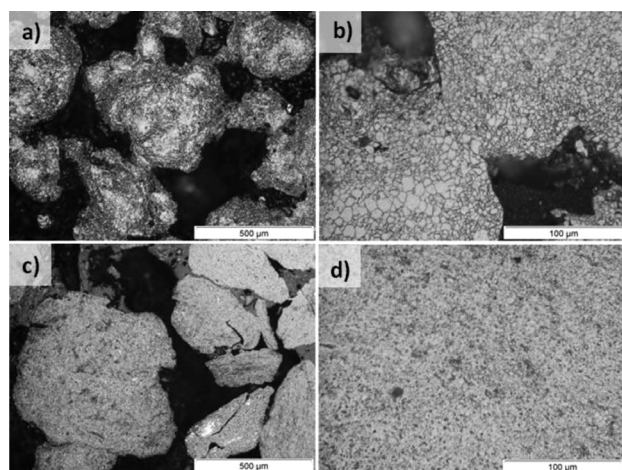


**Figure 5:** a), b) Optical micrographs of Ti-26Nb (a/l%) at different magnifications, produced in different milling times – 50 h and c), d) 70 h and annealing

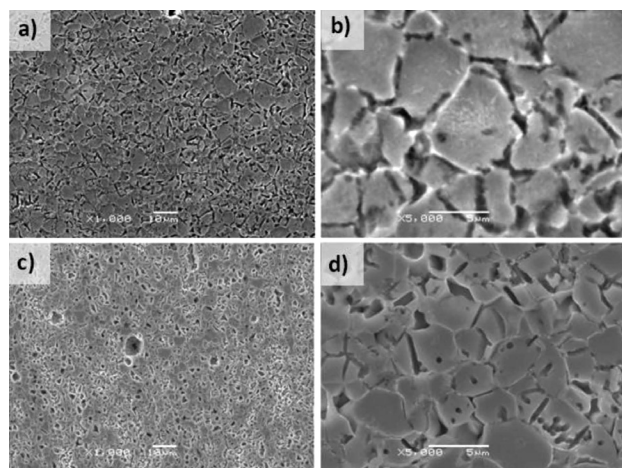


**Figure 6:** a), b) SEM micrographs of Ti-26Nb (a/l%) after different milling times – 50 h and c), d) 70 h and annealing

Histograms of the size of the area of the section of the grains in the samples milled for 50 h and 70 h are presented in **Figures 7** and **8**, respectively. For the sample milled for 70 h, a larger fraction of the grains with the section area in the range of  $0.5\text{--}35 \mu\text{m}^2$  can be observed. Milling for 70 h caused a significant fragmentation of the grains with the section area below  $30 \mu\text{m}^2$ .

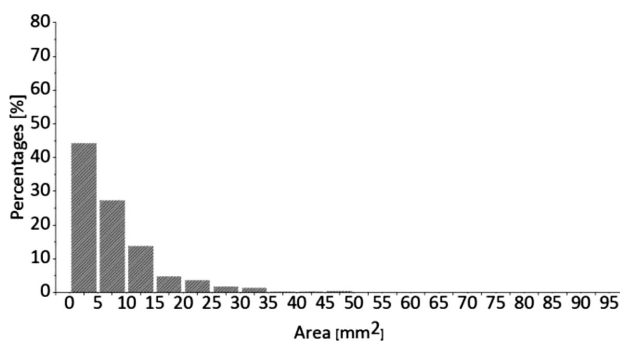


**Figure 7:** Histogram of the grain average area for the sample milled for 50 h and annealed



G. DERCZ, I. MATULA: EFFECT OF BALL MILLING ON THE PROPERTIES OF THE POROUS Ti–26Nb ...

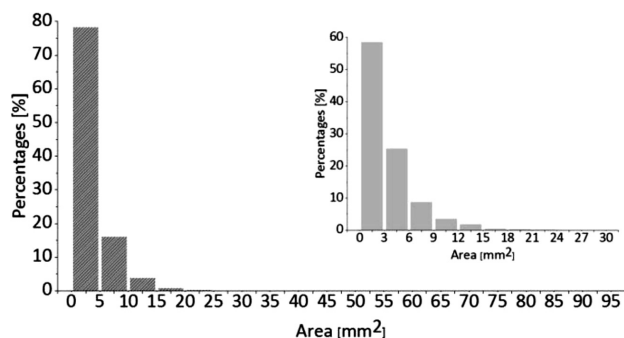


**Figure 8:** Histograms of the grain average area for the sample milled for 70 h and annealed. The upper histogram presents the distribution of the average area of the grains smaller than  $36 \mu\text{m}^2$  for this sample

The circularity of grains was 0.60 for 50 h of milling and 0.59 for 70 h of milling, which corresponds to the dimensionless lengthening factor for both samples (Tables 5 to 6). The coefficient of the grain variability was also determined. For all the samples milled for 50 h, it was 1.4, and for the sample milled for 70 h, it was 0.9. It means that for the sample milled for a shorter time, the size of the cross-sectional area is much more diversified in comparison to the sample milled for 70 h. The longer milling time (70 h) caused a greater fragmentation of the material. The difference in the average section area of the grains was significant, especially when compared to

the size of the powder after milling. No significant differences in the size of the particles depending on the milling time were noticed. The number of the elements that were tested per area unit of the image was also determined; for the samples annealed and previously milled for 50 h and 70 h, the number of elements per area was estimated to be  $82379 \text{ [1/mm}^2\text{]}$  and  $199951 \text{ [1/mm}^2\text{]}$  respectively.

Distribution maps of the elements for the sintered samples revealed single regions rich in titanium in the case of the material milled for 50 h (Figure 9). Also, a slightly higher concentration of Ti was observed inside the grains. In contrast, milling for 70 h allowed us to obtain a material with an even distribution of the elements on its surface (Figure 10). In the case of this alloy, the increase in the milling time allows a more homogeneous structure.

Figures 11 and 12 show the effect of an analysis with the Hysitron Tribotender Ti950 with AFM QScope 250, which allowed us to compare the surface topographies of the produced samples. For the material milled for 50 h and sintered, a higher diversification of the sample surface was observed. On the sample, initially synthesized for 70 h of milling, we can observe smaller and more regular grains in comparison to the sample exposed to the shorter milling time, which was confirmed with a stereological analysis.

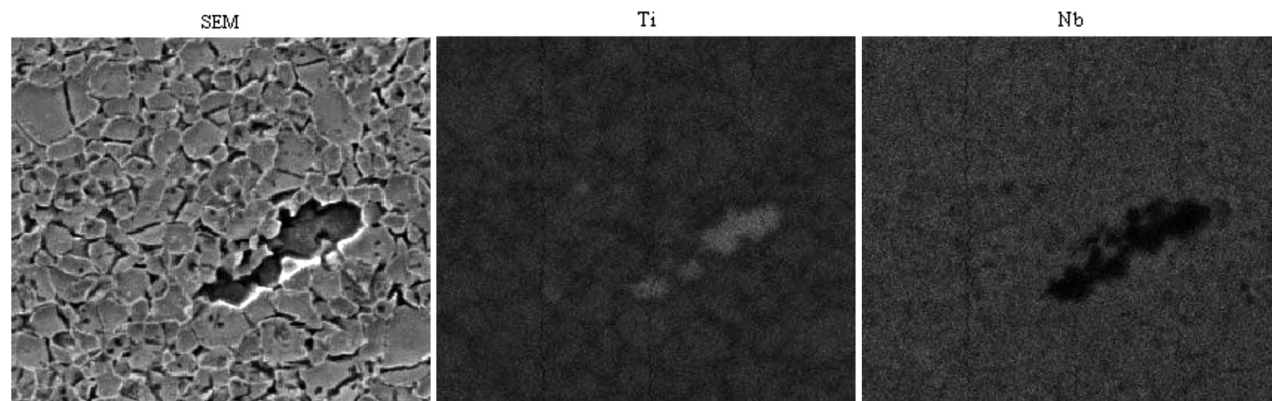


**Figure 9:** Distribution maps of the elements for the sample milled for 50 h and annealed

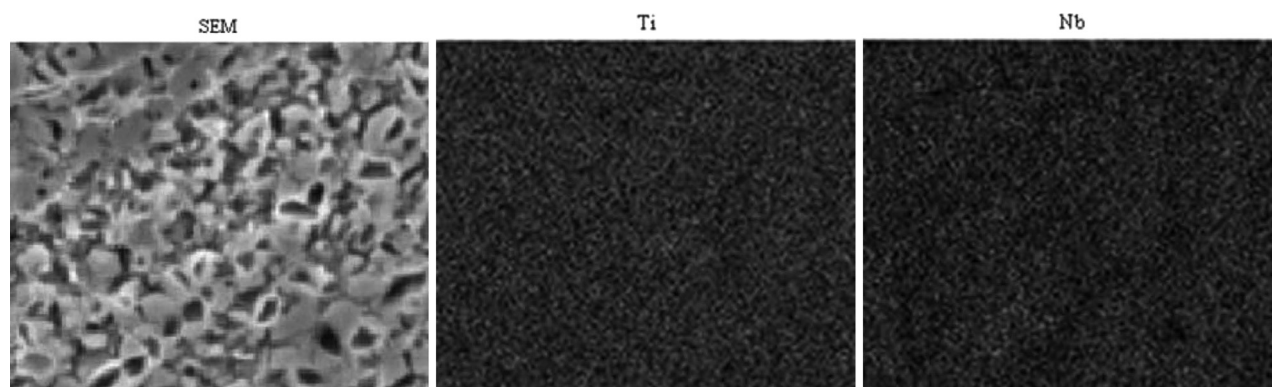


**Figure 10:** Distribution maps of the elements for the sample milled for 70 h and annealed

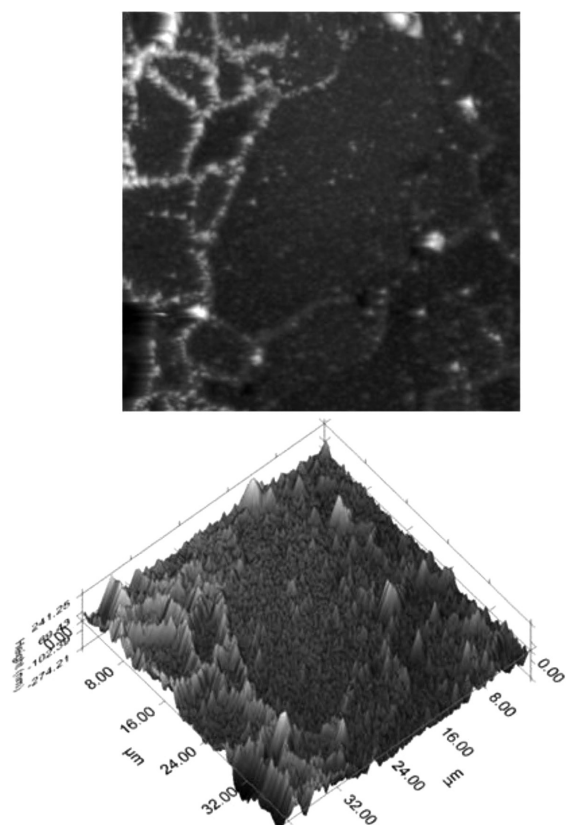


**Figure 11:** Surface morphology of the area of 40 μm × 40 μm for the sample milled for 50 h and annealed

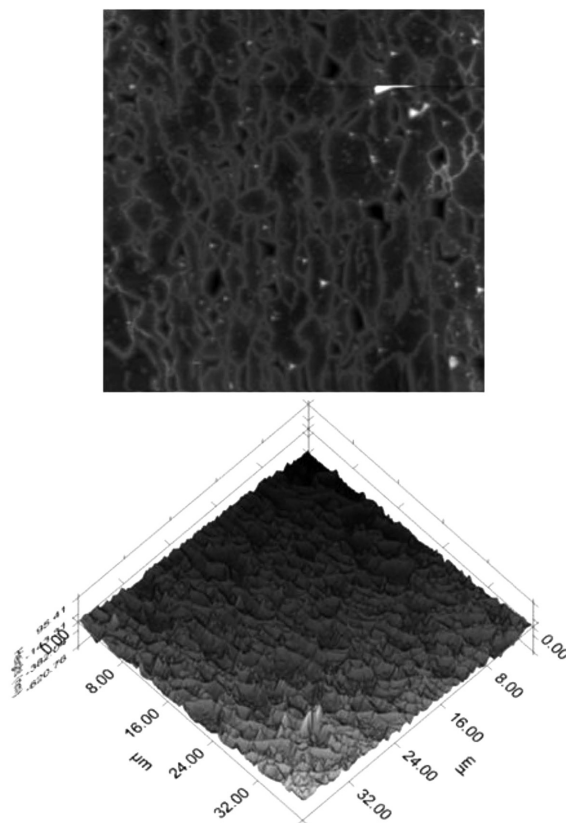


**Figure 12:** Surface morphology of the area of 40 μm × 40 μm for the sample milled for 70 h and annealed

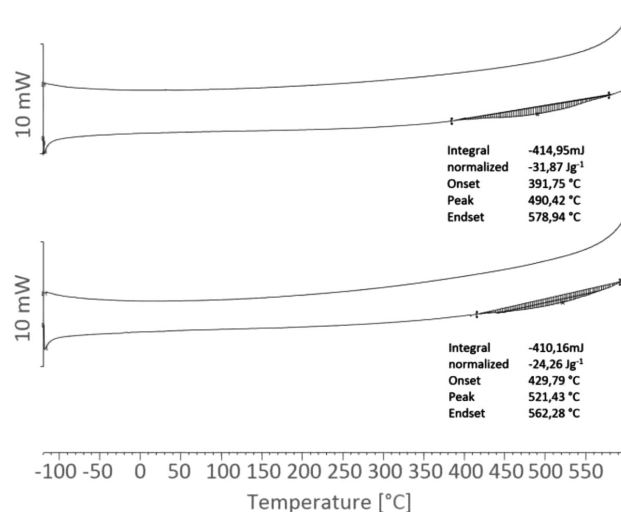


**Figure 13:** DSC analysis of the samples milled for 50 h and 70 h and also annealed

Another important aspect of the produced material is its properties. DSC results showed (**Figure 13**) the presence of an endothermic peak on the heating curve for both samples. In the case of the sample milled for 70 h, the peak was slightly shifted toward higher temperatures. The peaks occurred at about 490 °C and 520 °C for the samples milled for 50 h and 70 h, respectively. The presence of the peaks can indicate the presence of a partial phase transformation  $\alpha \rightarrow \beta$ . Moreover, the milling time has an impact on the temperature of transformation. However, no significant changes were noticed on the cooling curves.

The nanoindentation method allowed the determination of the reduced Young's modulus and hardness of the material, and the results of this analysis of the material after different milling times and sintering are presented in **Table 7**.

**Table 7:** Results of the nanoindentation analysis – hardness and modulus of both samples

Samples	Contact depth (nm)	Hardness (GPa)	Modulus (GPa)
50 h	89(14)	0.99(0.31)	48(19)
70 h	42(12)	3.86(1.71)	95(32)

The measurement is based on the curves of the load and the penetration depth of the indenter (**Figures 14** and **15**). After 50 h of milling, the material obtained much lower values of hardness and modulus in comparison to the material milled for 70 h. For the samples milled for 50 h and 70 h, the hardness was 0.99±0.31 GPa and 3.86±1.71 GPa, respectively. A similar situation applied to the values of the modulus. For the material milled for 50 h, it was 48±19 GPa, and for the material milled for 70 h, it was 95±32 GPa. Such low modulus values, especially in the case of the sample with the shorter milling time, are very promising as they are close to the value of the modulus of a human bone.

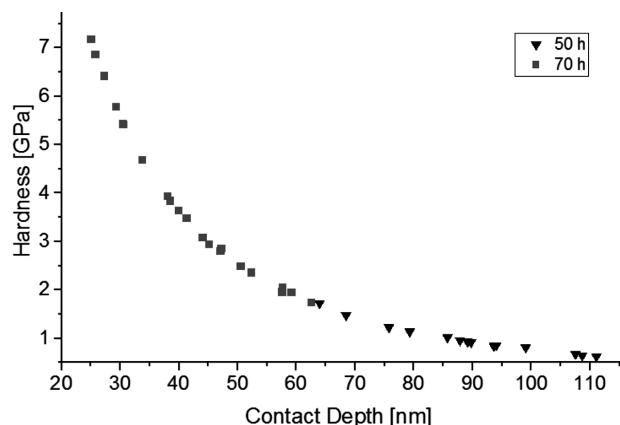


Figure 14: Diagram of hardness to contact depth for both samples, after 50 h and 70 h of milling

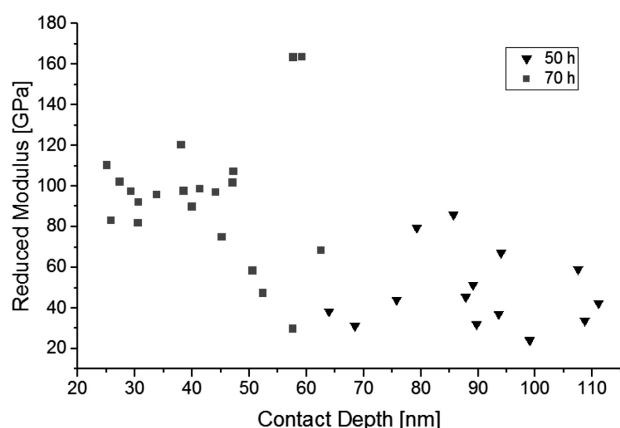


Figure 15: Diagram of reduced modulus to contact depth for both samples, after 50 h and 70 h of milling

The nanosized indentation measurements of the mechanical properties are from the selected specific areas, which neutralize the effects of the pores or defects on the results. A large measurement uncertainty is even more surprising. Assuming that the material is mechanically widely heterogeneous, it seems necessary to apply heat treatment to the material. The microhardness measurement of the sample milled for 50 h revealed a higher value of the microhardness and it is  $288.6(\pm 31.0)$  HV0.5, which is around 2.82 GPa. For the sample milled for 70 h, the revealed value is  $256.2(\pm 14.6)$  HV0.5, which is approximately 2.51 GPa. However, we observed a relatively high uncertainty of the measurement, which made it difficult to clearly evaluate the differences in the microhardness measurement.

#### 4 CONCLUSIONS

Based on the investigation into the microstructure and mechanical properties of the Ti-26Nb (at%) alloy, the main conclusions can be drawn:

- It was proved that the microstructure, the degree of porosity and mechanical properties can be adjusted by means of mechanical alloying.

- A longer milling time (70 h) resulted in an increased degree of structure fragmentation. Young's modulus increased twice as well.
- The porous samples sintered from the powders milled for 50 hours have a very low elastic modulus of 48(19) GPa, which is similar to that of natural bones.
- Ball-milling for 50 h led to the formation of a relatively equiaxed shape and powder particles of a smaller size and with a more asymmetrical particle-size distribution than that of the powders ball milled for 70 h.
- Based on XRD, it was found that the process of high-energy milling for 50 h and 70 h makes it possible to obtain a solid nanocrystalline solution  $\beta + \alpha$ .

#### Acknowledgments

This work was supported by the Polish National Science Centre (Polish: Narodowe Centrum Nauki, abbr. NCN) under the research project no. UMO-2011/03/D/ST8/04884

#### 5 REFERENCES

- <sup>1</sup> M. Long, H. J. Rack, Titanium alloys in total joint replacement – a materials science perspective, *Biomaterials*, 19 (1998) 18, 1621–1639, doi:10.1016/S0142-9612(97)00146-4
- <sup>2</sup> Y. Li, C. Yang, H. Zhao, S. Qu, X. Li, Y. Li, New Developments of Ti-Based Alloys for Biomedical Applications, *Mater.*, 7 (2014) 3, 1709–1800, doi:10.3390/ma7031709
- <sup>3</sup> M. Niinomi, Mechanical biocompatibilities of titanium alloys for biomedical application, *J. Mech. Behav. Biomed. Mater.*, 1 (2008) 1, 30–42, doi:10.1016/j.jmbbm.2007.07.001
- <sup>4</sup> A. Biesiekierski, J. Wang, M. Gepreel, C. Wena, A new look at biomedical Ti-based shape memory alloys, *Acta Biomater.* 8 (2012) 5, 1661–1669, doi:10.1016/j.actbio.2012.01.018
- <sup>5</sup> S. Miyazaki, H.Y. Kim, Basic characteristics of titanium–nickel (Ti–Ni)-based and titanium–niobium (Ti–Nb)-based alloys, *Shape Memory and Superelastic Alloys*, Appl. Technol., (2011), 15–42, doi:10.1016/B978-1-84569-707-5.50002-X
- <sup>6</sup> M. Tahara, H. Y. Kim, H. Hosoda, S. Miyazaki, Cyclic deformation behavior of Ti-26 at.% Nb alloy, *Acta Mater.*, 25 (2009), 2461–2469, doi:10.1016/j.actamat.2009.01.037
- <sup>7</sup> H. Y. Kim, Y. Ikehara, J. I. Kim, H. Hosoda, S. Miyazaki, Martensitic transformation, shape memory effect and superelasticity of Ti–Nb binary alloys, *Acta Mater.* 54 (2006), 2419–2429, doi:10.1016/j.actamat.2006.01.019
- <sup>8</sup> G. Dercz, I. Matuła, M. Zubko, A. Liberska, Structure characterization of biomedical Ti–Mo–Sn prepared by mechanical alloying method, *Acta Phys. Pol. A*, 130 (2016), 1029–1032, doi:10.12693/APhysPolA.130.1029
- <sup>9</sup> I. Matuła, G. Dercz, M. Zubko, L. Pająk, Influence of high energy milling time on the Ti-50Ta biomedical alloy structure, *Acta Phys. Pol. A*, 130 (2016), 1033–1036, doi:10.12693/APhysPolA.130.1033
- <sup>10</sup> X. Rao, C. L. Chu, Y. Y. Zheng, Phase composition, microstructure, and mechanical properties of porous Ti–Nb–Zr alloys prepared by a two-step foaming powder metallurgy method, *J. Mech. Behav. Biomed.*, 34 (2014), 27–36, doi:10.1016/j.jmbbm.2014.02.001
- <sup>11</sup> G. Ryan, A. Pandit, D. P. Apatsidis, Fabrication methods of porous metals for use in orthopaedic applications, *Biomaterials*, 27 (2006) 13, 2651–2670, doi:10.1016/j.biomaterials.2005.12.002

- <sup>12</sup> H. M. Rietveld, A Profile Refinement Method for Nuclear and Magnetic Structures, *J. Appl. Cryst.*, 3 (1969), 65–69, doi:10.1107/S0021889869006558
- <sup>13</sup> R. J. Hill, C. J. Howard, Quantitative phase analysis from neutron powder diffraction data using the Rietveld method. *J. Appl. Cryst.*, 20 (1987), 467–474, doi:10.1107/S0021889887086199
- <sup>14</sup> G. Dercz, D. Oleszak, K. Prusik, L. Pająk, Rietveld-based quantitative analysis of multiphase powders with nanocrystalline NiAl and FeAl phases, *Rev. Adv. Mater. Sci.*, 8 (2008), 764–768
- <sup>15</sup> Y. Li, Y. Cui, F. Zhanga, H. Xua, Shape memory behavior in Ti–Zr alloys, *Scripta Mater.*, 64 (2011) 6, 584–587, doi:10.1016/j.scriptamat.2010.11.048
- <sup>16</sup> A. Nouri, P. D. Hodgson, C. Wen, Effect of ball-milling time on the structural characteristics of biomedical porous Ti–Sn–Nb alloy, *Mater. Sci. Eng. C*, 31 (2011), 921–928, doi:10.1016/j.msec.2011.02.011
- <sup>17</sup> G. Dercz, I. Matuła, M. Zubko, J. Dercz, Phase composition and microstructure of new Ti–Ta–Nb–Zr biomedical alloys prepared by mechanical alloying method, *Powder Diffr.*, (2017), 1–7, doi:10.1017/S0885715617000045
- <sup>18</sup> L. Lü, M. O. Lai, *Mechanical Alloying*, Kluwer Academic Publishers, Boston, 1998
- <sup>19</sup> C. Suryanarayana, Mechanical alloying and milling, *Prog. Mater. Sci.*, 46 (2001) 1–2, 1–184, doi:10.1016/S0079-6425(99)00010-9
- <sup>20</sup> A. Omran, K. Woo, H. B. Lee, Mechanical properties of  $\beta$ -Ti–35Nb–2.5Sn alloy synthesized by mechanical alloying and pulsed current activated sintering, *Metall. Mater. Trans. A*, 43 (2012) 12, 4866–4874, doi:10.1007/s11661-012-1298-y
- <sup>21</sup> G. Dercz, B. Formanek, K. Prusik, L. Pająk, Microstructure of Ni(Cr)–TiC–Cr<sub>3</sub>C<sub>2</sub>–Cr<sub>7</sub>C<sub>3</sub> composite powder, *J. Mater. Process. Tech.*, 162 (2005), 15–19, doi:10.1016/j.matprotec.2005.02.004
- <sup>22</sup> G. Dercz, L. Pająk, B. Formanek, Dispersion analysis of NiAl–TiC–Al<sub>2</sub>O<sub>3</sub> composite powder ground in a high-energy attritorial mill, *J. Mater. Process. Tech.*, 175 (2006), 334–337, doi:10.1016/j.jmatprotec.2005.04.060
- <sup>23</sup> M. Tahara, H. Y. Kim, H. Hosoda, S. Miyazaki, Cyclic deformation behavior of a Ti–26 at.% Nb alloy, *Acta Mater.*, 57 (2009), 2461–2469, doi:10.1016/j.actamat.2009.01.037
- <sup>24</sup> E. K. Molchanova, *Phase Diagrams of Titanium Alloys* (Translation of Atlas Diagram Sostoyaniya Titanovykh Splavov), Israel Program for Scientific Translations, Jerusalem, 1965, 116
- <sup>25</sup> S. N. Patankar, F. H. Froes, Transformation of mechanically alloyed Nb–Sn powder to Nb<sub>3</sub>Sn, *Metall. Mater. Trans. A*, 35 (2004), 3009–3012, doi:10.1007/s11661-004-0248-8
- <sup>26</sup> P. J. James, Particle Deformation During Cold Isostatic Pressing of Metal Powders, *Powder Metall.*, 20 (1977), 199–204, doi:10.1179/pom.1977.20.4.199
- <sup>27</sup> L. Lu, M. O. Lai, G. Li, Influence of sintering process on the mechanical property and microstructure of ball milled composite compacts, *Mater. Res. Bull.*, 31 (1996), 453–464, doi:10.1016/S0025-5408(96)00024-4





## EFFECTS OF AN ADDITION OF COIR-PITH PARTICLES ON THE MECHANICAL PROPERTIES AND EROSION-WEAR BEHAVIOR OF A WOOD-DUST-PARTICLE-REINFORCED PHENOL FORMALDEHYDE COMPOSITE

VPLIVI DODATKA KOKOSOVH VLAKEN  
FENOL-FORMALDEHIDNEMU KOMPOZITU, OJAČANEM Z  
LESNIM PRAHOM, NA NJEGOVE MEHANSKE LASTNOSTI IN  
EROZIJSKO OBRABOArul Sujin Jose<sup>1</sup>, Ayyanar Athijayamani<sup>2</sup>, Kalimuthu Ramanathan<sup>3</sup>,  
Susaiyappan Sidhardhan<sup>4</sup><sup>1</sup>Lourdes Mount College of Engineering and Technology, Department of Mechanical Engineering, Kanyakumari, Tamilnadu, India<sup>2</sup>Government College of Engineering, Department of Mechanical Engineering, Bodinayakanur, Tamilnadu, India<sup>3</sup>Alagappa Chettiar College of Engineering and Technology, Department of Mechanical Engineering, Karaikudi, Tamilnadu, India<sup>4</sup>Government College of Engineering, Department of Civil Engineering, Tirunelveli, Tamilnadu, India  
athimania@gmail.com*Prejem rokopisa – received: 2016-09-23; sprejem za objavo – accepted for publication: 2017-01-22*

doi:10.17222/mit.2016.284

Several attempts were made to investigate the effects of various process parameters on the mechanical properties and wear behavior of synthetic and natural cellulosic fibers and also particle-reinforced polymer composites. However, very few studies were carried out on the effects of various process parameters on the mechanical and wear behavior of phenol formaldehyde (PF) composites reinforced with natural cellulosic fibers and particles. Therefore, in the present study, an attempt was made to observe the effects of various process parameters on the mechanical and wear behavior of wood-dust (WD) and coir-pith (CP) particle-reinforced resole-type PF composites. First, the mechanical properties of a WD/PF composite were studied based on the content of CP particles. Then, the erosive-wear behavior of the WD/PF composite was studied with respect to five different parameters such as particle content, erodent size, impact velocity, impingement angle, and standoff distance. The erosive experiments were carried out for five different parameters based on the Taguchi experimental design ( $L_{27}$ ). The results show that the mechanical properties of the WD/PF composite increase with an addition of CP particles. The increment in the composite modulus was higher than that of the composite strength. The erosive test results indicate that the erosion-wear rate is affected by the particle content, impingement angle, erodent size and impact velocity. Brittle-erosion behavior was identified on the surface of the composite with a heavy erosive wear occurring at a 60° impingement angle.

**Keywords:** biowaste particles, phenol formaldehyde, composites, mechanical properties, erosive-wear resistance, Taguchi method

Izvedenih je bilo že kar nekaj poizkusov v zvezi z učinki različnih procesnih parametrov na mehanske lastnosti in obrabo polimernih kompozitov ojačanih s sintetičnimi in naravnimi celuloznimi vlakni in/ali delci. Toda zelo malo raziskav je bilo izvedenih glede vpliva različnih procesnih parametrov na mehanske lastnosti in obrabo fenolformaldehidnih (angl. PF) kompozitov, ojačanih z naravnimi celuloznimi vlakni in delci. Tako je v pričujočem delu predstavljen vpliv različnih procesnih parametrov na mehanske lastnosti in obrabo PF kompozitov, ki so bili ojačani z delci lesnega prahu (angl. WD) in delci kokosa (angl. CP). Te vrste kompozitov se uporabljajo za izdelavo podplatov čevljev. Najprej so bile določene mehanske lastnosti WD/PF kompozitov glede na vsebnost CP delcev. Sledili so preizkusi in analize erozijske obrabe WD/PF kompozitov glede na vsebnost (količino) delcev v kompozitu, velikost, hitrost in razdaljo učinkovanja erozijskega sredstva ter njegov vpadni kot. Preizkusi so temeljili na analizi s Taguchijevo metodo ( $L_{27}$ ) s petimi različnimi parametri. Rezultati so pokazali, da se mehanske lastnosti WD/PF kompozitov izboljšujejo z dodajanjem CP delcev. Povišanje modula kompozitov je bilo večje od povečanja trdnosti kompozita. Erozijski testi kažejo, da je hitrost erozijske obrabe posledica vseh procesnih parametrov, to je: vsebnosti delcev, udarnega kota, hitrosti in velikosti delcev izbranega erozijskega sredstva. Največja obraba zaradi erozije je bila dosežena (ugotovljena) pri 60 stopinjskem vpadnem kotu abrazijskega sredstva z nastalimi poškodbami krhkega značaja.

**Ključne besede:** delci biopadkov, fenolformaldehid, kompoziti, mehanske lastnosti, odpornost proti erozijski obrabi, Taguchi metoda

## 1 INTRODUCTION

Recently, polymer composites reinforced with synthetic materials have been replaced with polymer composites reinforced with bio-based natural materials. The bio-based natural materials have many advantages over the synthetic materials like renewability, biodegradability, abundant availability, low costs, etc.<sup>1-3</sup> In India,

particularly in the South Indian region, the biowaste materials like wood dust, coir pith, groundnut shell, coconut shell, cashew nut shell, etc. are abundantly available because in that region, coconut, groundnut and cashew nut are cultivated in large amounts. A number of timber and oil mills are also available in the Southern region of Tamilnadu, India. Therefore, bioparticles are thrown away after producing useful materials and

dumped on the land of the village nearest to these industries.

Many studies have already reported on the properties of different bio-based natural-fiber-reinforced polymer composites in different conditions.<sup>3–7</sup> But, only few reports are available on the properties of polymer composites filled with biowaste particles.<sup>8–11</sup> In this investigation, an attempt was made to study the mechanical and wear behavior of PF composites reinforced with biowaste particles (WD and CP). Mechanical properties of wood-dust-particle-reinforced PF composites were evaluated based on the content of coir pith. The erosive-wear behavior of the composites was studied using five different parameters such as particle content, erodent size, impingement angle, impact velocity and standoff distance. The erosive experiments were conducted as per the Taguchi experimental design. The parameters used for erosive-wear tests were also analyzed using an analysis of variance with the wear rate.

## 2 MATERIALS AND METHODOLOGY

### 2.1 Materials

Wood-dust particles were collected from the Kumar Timber and Sawmill, Karaikudi, Tamilnadu, India. Coir-pith particles were collected from the Coir Industry, Sozhavanthan, Tamilnadu, India. From the collected wood-dust and CP particles, microparticles with the average size of 800 microns were separated using a sieving machine available in our composite laboratory. The resole-type PF liquid resin was procured, together with a cross-linking agent (divinylbenzene) and acidic catalyst (hydrochloric acid), from POOJA Chemicals, Madurai, Tamilnadu, India.

### 2.2 Preparation of the composites

A hardboard mold box with dimensions of 150 mm × 150 mm × 3 mm was used to prepare the wood-dust and coir-pith-particle composite plates using the hand lay-up technique. Wood dust/coir pith/phenol formaldehyde composites were fabricated at three different concentrations of wood-dust and coir-pith particles, i.e., (20, 30 and 40) % mass fractions. The amount of WD particles was maintained at a fixed level of 20 % mass fraction. Three different amounts of CP particles (0–20 % mass fractions) were hybridized with the constant amount of WD particles, i.e., 20WD/0CP, 20WD/10CP, 20WD/20CP. The weight percentage of WD and CP particles and

designation of the composites are given in **Table 1**. Prior to the process, the particles were dried in sunlight for 12 h. The PF resin with the particles was mixed with a mechanical stirrer at room temperature for 30 min. Then, the cross-linking agent and acidic catalyst were also mixed into the mixture of phenol formaldehyde/particles and once again stirred with the mechanical stirrer for 15 min. After that, the mixture was poured into the mold box and allowed to cure at room temperature for 48 h.

### 2.3 Testing composite specimens

Composite specimens were characterized using mechanical tests such as tensile, flexural and impact tests. The tensile tests were conducted on an FIE universal testing machine (UTE 40 HGFL) in accordance with ASTM D638-10.<sup>12</sup> The flexural tests were performed on the same testing machine in accordance with ASTM D790-10.<sup>13</sup> The impact tests were carried out on an Izod impact machine according to ISO 180.<sup>14</sup> All the tests were conducted at room temperature and atmospheric pressure.

### 2.4 Taguchi experimental design

The erosive behavior of the WD/CP/PF composite was studied based on the Taguchi method and analysis of variance techniques. Experiments were performed as per Taguchi experimental design (an orthogonal array) because it is a systematic and efficient approach to get the optimum range of process parameters with a good performance. The number of experiments can be reduced due to the constructed orthogonal array, which provides a set of well-balanced experiments.<sup>15</sup> The results obtained with this experimental design are transformed into signal-to-noise (*S/N*) ratios, which serve as objective functions for the optimization of parameters and help with the result analysis. There are three *S/N* ratios available for the optimization of several static problems: the smaller-the-better (used to minimize the response), the nominal-the-better (used whenever an ideal quality is equated with a particular nominal value.) and the larger-the-better ratio (used to maximize the response). Among these three characteristics, the minimum erosion rate comes under the smaller-the-better characteristic, which can be expressed as Equation (1):

$$S/N = -10 \log_{10} \left( \frac{1}{n} \sum_{i=1}^n y_i^2 \right) \quad (1)$$

(the mean of the sum of squares of the measured data)

**Table 1:** The weight percentage of WD and CP particles and designation of the composites

Total weight percentage of particles in the composites	Weight percentage of resin	Weight percentage of WD particles	Weight percentage of CP particles	Designation of composites
20	80	20	0	20WD/0CP
30	70	20	10	20WD/10CP
40	60	20	20	20WD/20CP

The five different process parameters at three levels are used in this study to observe the erosive behavior of the WD/CP/PF composite. Therefore, the actual number of experiments, based on the traditional experimental design, should be 243 ( $3^5$ ). But, this number is reduced to 27 experiments using the Taguchi technique. The process parameters and their setting levels for the erosion test of the WD/CP/PF composite are presented in **Table 2**. In these experiments, the following parameters are fixed throughout the process: the type of erodent is silica, the erodent feed rate is  $10.0 \pm 1.0$  g/min, the nozzle length is 80 mm, and the nozzle diameter is 3 mm.

**Table 2:** The erosive process parameters with their designation and setting levels

Process Parameters and their designation	Level I	Level II	Level III
Particle content: (A) wt%	20	30	40
Impact velocity: (B) m/sec	41	52	63
Impingement angle: (C) degree	30	60	90
Erodent size: (D) $\mu\text{m}$	300	500	700
Stand-off distance: (E) mm	80	120	160

## 2.5 Erosion test

The erosive tests of the WD/CP/PF composite specimens were conducted as shown in the schematic diagram of the erosion process (**Figure 1**). The main components of the erosion-test apparatus are the erodent feeder box, erodent feeder nozzle, mixing chamber, nozzle of the mixing chamber, air-flow vent, sample holder and erodent collector. Dry silica sand with three different sizes (300, 500 and 700)  $\mu\text{m}$  was used as the erodent in the erosion tests. After the test, the composite samples were taken from the apparatus and cleaned with acetone.

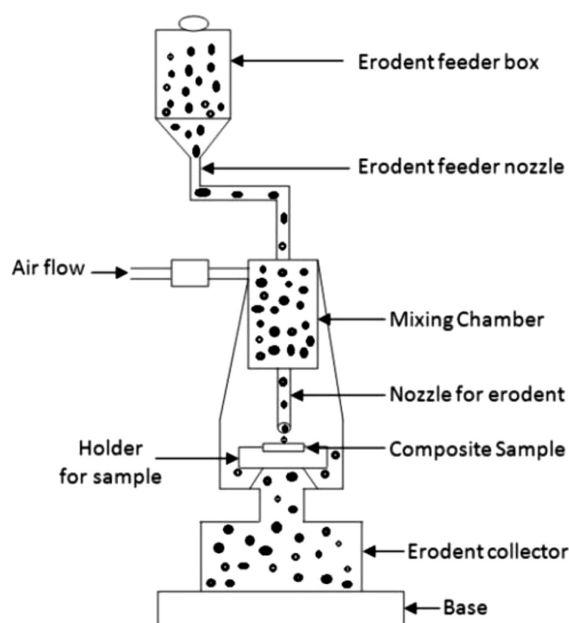


**Figure 1:** Schematic diagram of the erosive process of the WD/CP/PF composite

Then, the cleaned composite specimens were dried and weighed using a precision digital balance at an accuracy of  $\pm 0.1$  mg. The composite samples were weighed before and after the erosion tests and their difference is termed as the weight loss. Then, the weight loss was recorded and used for the erosion-rate calculation. Generally, the erosion rate can be obtained as the ratio of the weight loss of samples to the weight of the eroding particle. The process was repeated until the steady-state erosion was reached.

## 3 RESULTS AND DISCUSSION

### 3.1 Mechanical properties of the composites

Mechanical tests were carried out on the WD/CP/PF composites and their results are presented in **Figure 2a**. The neat-resin sample had a tensile strength of 29.8 MPa, tensile modulus of 1168.4 MPa, flexural strength of 34.7 MPa, flexural modulus of 1257.4 MPa, and impact strength of 1.24 KJ/m<sup>2</sup>. It can be seen that the tensile strength and modulus of the PF composite increase with an increase in the particle content. The tensile strength of the 20WD/PF composite is almost the same as that of the neat-resin sample. It shows that the addition of WD particles enhances the strength of the PF composite. The WD/PF composite without the addition of CP particles has a tensile strength of 30.4 MPa and this value increases to 41.7 MPa with the incorporation of 10 % mass fraction of CP particles; after that, it decreases to 36.8 MPa with the addition of 20 % mass fraction of CP particles. This may be due to a poor interfacial bonding between the particles and the matrix, i.e., a weak transfer of stress. Moreover, the stress concentration in the PF matrix may be created due to the corner edges of the irregularly shaped WD and CP particles.

Due to the addition of 10 % mass fraction and 20 % mass fraction of CP particles, the tensile strength of the WD/PF composite increases by about 37.17 % and 21.1 %, respectively. **Figure 2a** also shows the tensile-modulus values of the WD/CP/PF composites with respect to the particle content. The composite also reached the tensile-modulus value of the neat-resin sample with the particle addition of 20 % mass fraction. The tensile-modulus value of the WD/PF composite increased with the further addition of CP particles. The maximum modulus value was observed at 40 % mass fraction of the particles.

The results of the flexural tests of the WD/CP/PF composites with respect to the particle content are given in **Figure 2b**. It is interesting to note that the flexural strength and modulus of the WD/PF composite increase with the addition of CP particles. The flexural strength of the WD/PF composite is slightly lower than the value of the neat-resin sample. The maximum values of the flexural strength and modulus were identified at the 40 % addition. The flexural strength of the WD/PF composite



A. SUJIN JOSE: EFFECTS OF AN ADDITION OF COIR-PITH PARTICLES ON THE MECHANICAL AND ...

was increased by about 68.99 % due to the incorporation of 20 % mass fraction of CP particles.

The impact-strength values of the WD/CP/PF composites after the impact tests are presented in **Figure 2c**. It can be seen that the impact strength of the WD/PF composite is slightly lower than the value of the neat-resin sample. It is also shown that the impact strength of the WD/PF composite increases with the addition of 10 % mass fraction of CP particles, but it decreases with the incorporation of 20 % mass fraction of CP particles. This may be due to a poor adhesion between the particles and the matrix. It may also be due to the stress concentration of the resin matrix. It is also observed that the incorporation of 10 % mass fraction and 20 % mass fraction of CP particles shows 15.57 % and 8.19 % higher impact values compared to the WD/PF composite.

### 3.2 Steady-state erosion: effects of the impingement angle

Generally, the erosive-wear behavior of polymer composite materials can be categorized as brittle and ductile. A ductile erosive situation is created in thermo-plastic polymer composites, whereas the a brittle erosive situation may be created in thermosetting polymer composites. For the steady-state-erosion analysis of the WD/CP/PF composites, an erosion test was carried out based on eight different impingement angles (20, 30, 40,

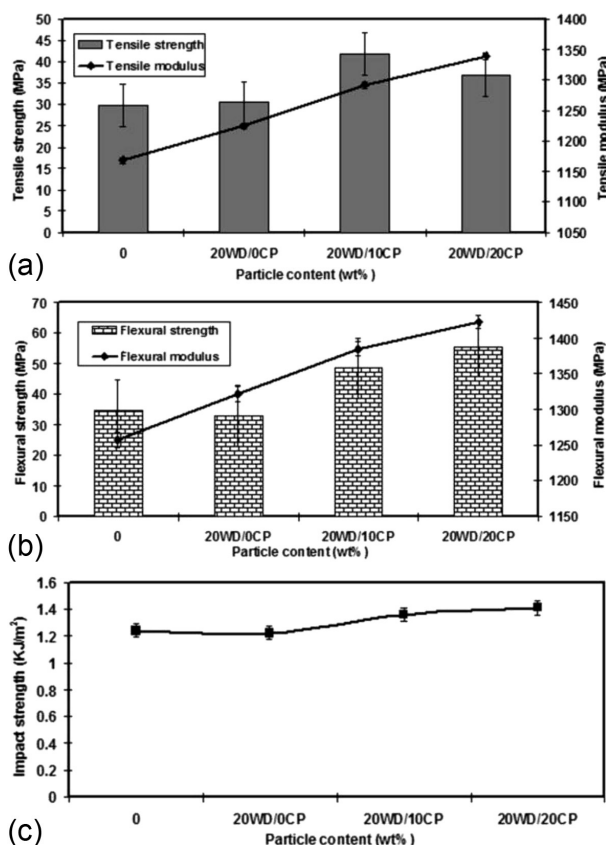


**Figure 2:** Variation of: a) tensile property, b) flexural property, and c) impact strength based on the particle content

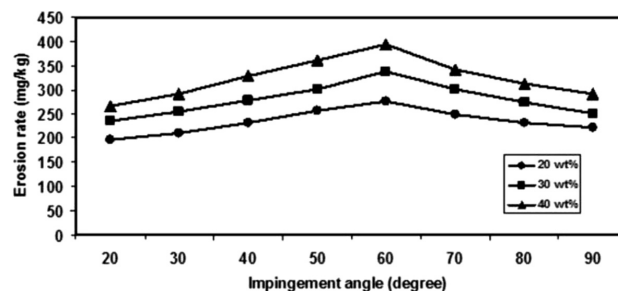


**Figure 3:** Steady-state erosive behavior of WD/CP/PF composites for eight different impingement angles

50, 60, 70, 80 and 90)°, keeping all the other process parameters constant (the initial level values).

The effects of the impingement angles on the erosion rate of the WD/CP/PF composites are presented in **Figure 3**. From this figure, it can be observed that the erosion rate is high at the impingement angle of 60° for all the composite specimens, irrespective of the particle content. However, a more brittle erosive behavior was identified for the 40 % mass-fraction (20WD/20CP) composite specimen. However, in the 20 % and 30 % mass-fraction composite specimens, a semi-brittle erosive behavior was identified. This may be due to the addition of WD and CP particles to the PF composites. When the higher amounts of particles are added to the polymer material, it behaves as a typical brittle material. Therefore, the brittleness of the composites with 20 % mass fraction and 30 % mass fraction of particles is lower than the composite with 40 % mass fraction of particles. Due to this, a semi-brittle erosive situation exists during the erosive process. It is also clear from **Figure 3** that the erosion rate increased with the increase in the particle content. This may be due to the increased hardness of the PF composite material caused by the addition of WD and CP particles.

### 3.3 Analysis of the erosion rate

The erosion rates for 27 combinations of the erosive experiments conducted on the WD/CP/PF composites are given in **Table 3**. The erosion analysis was made with popular software, namely, MINITAB 17. From **Table 3**, it can be concluded that the parameter combination of particle loading-A (level II = 30 % mass fraction), impact velocity-B (level I = 41 m/s), impingement angle-C (level I = 30°), erodent size-D (level II = 500  $\mu$ m) and standoff distance-E (160 mm) gives the minimum erosion rate (189.8 mg/kg). Moreover, another parameter combination (experiment number 4) allows the next level of the minimum erosion rate (194.1 mg/kg). The difference between these two erosion rates is small, as seen from **Table 3**. Anyway, the first parameter combination mentioned above is recognized as the better combination of parameters to obtain the minimum erosion rate. The overall mean of the signal-to-noise ratio for the erosion rate is found to be 49.75 dB.

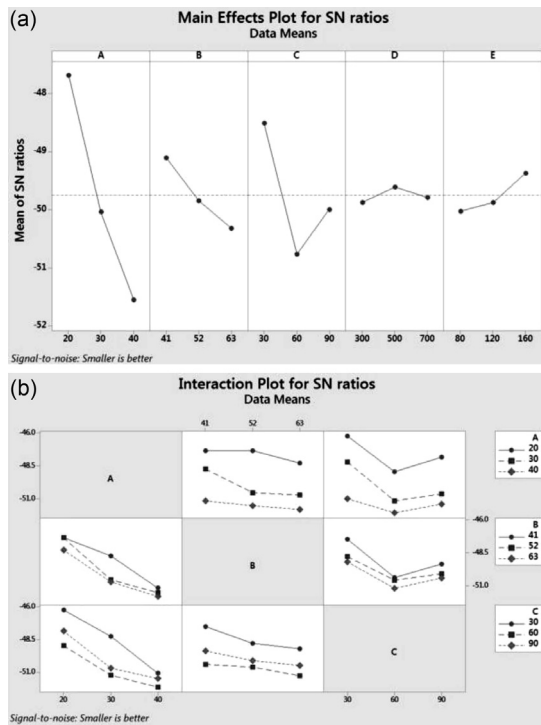


**Figure 4:** a) Effects of erosive-process parameters and b) effects of interactions of erosive-process parameters on the erosion rate

**Table 3:** The erosion rates and their S/N ratio of WD/CP/PF composites for 27 combinations

Experiment No.	A	B	C	D	E	Erosion rate mg/kg	S/N ratio dB
1	20	41	30	300	80	209.5	-46.42
2	20	41	60	500	120	273.8	-48.75
3	20	41	90	700	160	220.7	-46.87
4	20	52	30	500	120	194.1	-45.76
5	20	52	60	700	160	267.3	-48.54
6	20	52	90	300	80	246.2	-47.82
7	20	63	30	700	160	211.9	-46.52
8	20	63	60	300	80	301.3	-49.58
9	20	63	90	500	120	277.1	-48.85
10	30	41	30	500	160	189.8	-45.65
11	30	41	60	700	80	343.5	-50.72
12	30	41	90	300	120	312.7	-49.90
13	30	52	30	700	80	298.9	-49.51
14	30	52	60	300	120	367.2	-51.29
15	30	52	90	500	160	351.3	-50.91
16	30	63	30	300	120	300.8	-49.56
17	30	63	60	500	160	378.5	-51.56
18	30	63	90	700	80	361.9	-51.17
19	40	41	30	700	120	332.8	-50.44
20	40	41	60	300	160	387.5	-51.76
21	40	41	90	500	80	370.6	-51.37
22	40	52	30	300	160	359.1	-51.10
23	40	52	60	500	80	398.3	-52.00
24	40	52	90	700	120	381.7	-51.63
25	40	63	30	500	80	379.2	-51.58
26	40	63	60	700	120	427.6	-52.62
27	40	63	90	300	160	369.8	-51.36

The effects of five erosive-process parameters on the erosion rate are graphically presented in **Figure 4a**. From this figure, it can be clearly concluded that parameter A (the particle content), parameter B (the impact velocity) and parameter C (the impingement angle) are the most significant parameters. Parameter E (the standoff distance) shows a moderately significant influence, while parameter D (the erodent size) has a relatively less significant influence. **Figure 4b** shows the interaction between the erosive parameters. From this figure, it is observed that a moderate interaction exists between parameters A and B, and between A and C. The interaction between parameters B and C is below the moderate level.

**Figures 5a to 5c** show 3D surface plots of the erosion rate with significant process parameters. The observation is similar to the one made of the interaction plots of the erosion rate. From the erosion test analysis of the WD/CP/PF composites, it can be concluded that the erodent size is most insignificant for the erosion rate. The standoff distance shows relatively less significance when compared to the other three process parameters (particle content, impact velocity and impingement

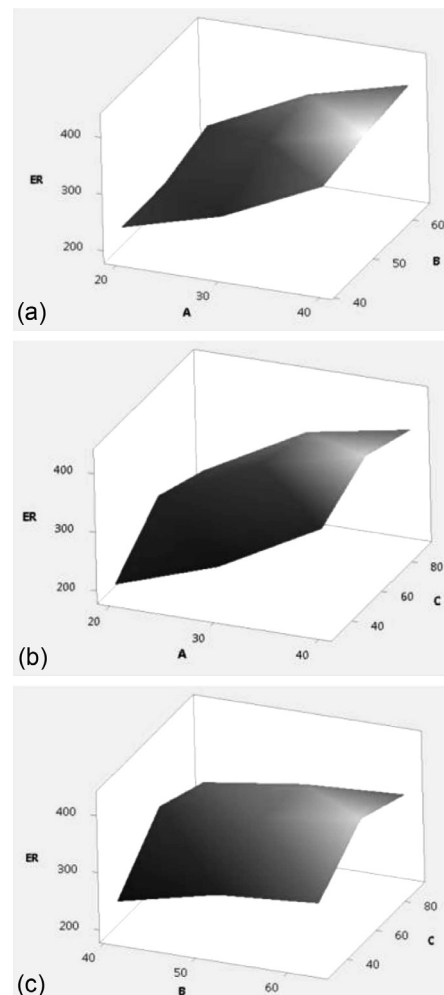


**Figure 5:** 3D surface plots of erosion rate vs process parameters: a) A × B, b) A × C, and c) B × C

angle). It can be concluded that the combination of the parameters – the particle content at level II, the impact velocity at level I and the impingement angle at level I – gives the minimum erosion rate. Therefore, this combination is recognized as the best combination of the erosive-process parameters to get the minimum erosion rate within the selected parameter range.

### 3.4 Analysis of the variance for the erosion rate

Taguchi's analysis of variance can be used to find the set of significant parameters as well as their interactions in any system. In this study, ANOVA is used to understand the contribution of the parameters to the erosion rate and the effects of their interactions on the erosion rate of the WD/CP/PF composite. The ANOVA results for the erosion rate of the WD/CP/PF composite are given in **Table 4**. The last column (*p*-value) in this table indicates the highly significant parameters and their main effects depend upon the value of *p*. The *p* values for the particle content, impact velocity, impingement angle and standoff distance are 0.000, 0.023, 0.003 and 0.186, indicating their great influence on the erosion rate of the composite. The *p* values of the interactions of the process parameters show a moderate significance and a significance below the moderate level. **Table 5** shows the responses for the *S/N* ratio (the small-the-better characteristic). The order of the erosive-process parameters based on their contributions to obtain the minimum erosion rate is the particle content, impingement angle, impact velocity, standoff distance and erodent size.

**Table 4:** Analysis of variance for Means of erosion rate

Source	DF	Seq SS	Adj SS	Adj MS	F	P
A	2	81404	81403.9	40701.9	120.99	0.000
B	2	7520	7519.9	3759.9	11.18	0.023
C	2	25188	25188.1	12594.0	37.44	0.003
D	2	97	96.7	48.4	0.14	0.870
E	2	1778	1778.4	889.2	2.64	0.186
A*B	4	2698	2698.2	674.6	2.01	0.258
A*C	4	3305	3305.3	826.3	2.46	0.203
B*C	4	791	791.1	197.8	0.59	0.690
Residual Error	4	1346	1345.6	336.4		
Total	26	124127				

**Table 5:** Response table for signal to noise ratios (smaller is better)

Level	A	B	C	D	E
1	-47.68	-49.10	-48.51	-49.87	-50.02
2	-50.03	-49.84	-50.76	-49.61	-49.87
3	-51.54	-50.31	-49.99	-49.78	-49.37
Delta	3.86	1.21	2.25	0.26	0.65
Rank	1	3	2	5	4

### 3.5 Confirmation experiment

At the end of this study, we carried out a confirmatory experiment as the final test to validate the estimated

results obtained during the erosive analysis of the WD/CP/PF composite. Therefore, the experimental results were verified with the estimated results using the confirmation test. This test was conducted to predict the erosion rate caused by a new set of erosive-process-parameter levels ( $A_2B_1C_1E_3$ ). To predict the *S/N* ratio, the following equation can be used:

$$S/N_p = (A_2-T) + (B_1-T) + (C_1-T) + (E_3-T) + T \quad (2)$$

where *T* is the overall experimental average of the *S/N* ratio and *S/N<sub>p</sub>* is the value of the predicted *S/N* ratio. The comparison results for the predicted and experimental *S/N* ratio of the optimum process parameters are given in **Table 6**. The difference between the predicted and experimental *S/N* ratio is 0.51, i.e., an error of 1.1 %. It proves that the model can predict the erosion rate with a reasonable accuracy.

**Table 6:** Comparison results of predicted and experimental signal-to-noise ratio of optimal process parameters

	Optimal erosive process parameters		
	Predicted	Experimental	Difference
Parameter level	$A_2B_1C_1E_3$	$A_2B_1C_1E_3$	Predicted-Experimental
Erosion rate mg/kg	191.5	189.8	1.7
Signal-to-noise ratio dB	-46.17	-45.66	

## 4 CONCLUSIONS

Mechanical properties of a WD/CP/PF composite were analyzed based on the particle content. The results show that the tensile strength of the WD/PF composite increased with the addition of 10 % mass fraction of CP particles, but decreased with the addition of 20 % mass fraction of CP particles. The flexural properties of the WD/PF composite increased with the increase in CP particles. The impact strength of the WD/PF composite also increased with the addition of 10 % mass fraction of CP particles and decreased with further addition of CP particles. The steady-state erosion analysis was carried out for eight different impingement angles on the WD/CP/PF composite. The composite with the lower particle content shows a semi-brittle erosive behavior with a higher erosion wear at the 60° impingement angle. On the other hand, the composite with the higher particle content showed a fully brittle nature of the erosive behavior with a higher erosion wear at the 60° impingement angle. From the erosive analysis of the WD/CP/PF composite, the process parameters like the particle content, impingement angle and impact velocity are found to be the most significant parameters influencing the erosion rate. The standoff distance shows a moderate influence on the erosion rate, while the erodent size shows a less significant influence on the erosion rate.

## 5 REFERENCES

- <sup>1</sup> G. K. Mani, J. B. B. Rayappan, D. K. Bisoyi, Synthesis and characterization of kapok fibers and its composites, *J. of Appl. Sci.*, 12 (2012), 1661–1665, doi:10.3923/jas.2012.1661.1665
- <sup>2</sup> J. A. Khan, M. A. Khan, R. Islam, Mechanical, thermal and degradation properties of jute fabric – reinforced polypropylene composites: Effect of potassium permanganate as oxidizing agent, *Polym. Compos.*, 34 (2013), 671–680, doi:10.1002/pc.22470
- <sup>3</sup> S. Singh, D. Deepak, L. Aggarwal, V. K. Gupta, Tensile and flexural behavior of hemp fiber reinforced virgin recycled HDPE matrix composites, *Procedia Mater. Sci.*, 6 (2014), 1696–1702, doi:10.1016/j.mspro.2014.07.155
- <sup>4</sup> I. V. Surendra, K. V. Rao, K. V. P. P. Chandu, Fabrication and investigation of mechanical properties of sisal, jute & okra natural fiber reinforced hybrid polymer composites, *Int. J. Eng. Trends Technol.*, 19 (2015), 116–120, doi: 10.14445/22315381/IJETT-V19P220
- <sup>5</sup> D. Kurniawan, B. S. Kim, H. Y. Lee, J. Y. Lim, Effects of repetitive processing, wood content, and coupling agent on the mechanical, thermal, and water absorption properties of wood/polypropylene green composites, *J. Adhes. Sci. Technol.*, 27 (2013), 1301–1312, doi:10.1080/01694243.2012.695948
- <sup>6</sup> E. Muñoz, J. A. García-Manrique, Water absorption behaviour and its effect on the mechanical properties of flax fibre reinforced bioepoxy composites, *Int. J. Polym. Sci.*, (2015), 1–10, doi:10.1155/2015/390275
- <sup>7</sup> M. G. A. Selvan, A. Athijayamani, Mechanical properties of fragrant screw pine fiber reinforced unsaturated polyester composite: Effect of fiber length, fiber treatment and water absorption, *Fibers Polym.*, 17 (2016), 104–116, doi:10.1007/s12221-016-5593-x
- <sup>8</sup> S. I. Durowaye, G. I. Lawal, M. A. Akande, V. O. Durowaye, Mechanical properties of particulate coconut shell and palm fruit polyester composites, *Int. J. Mater. Eng.*, 4 (2014), 141–147, doi:10.5923/j.ijme.20140404.04
- <sup>9</sup> L. Netra, S. Thomas, C. K. Das, R. Adhikari, Analysis of morphological and mechanical behaviours of bamboo flour reinforced polypropylene composites, *Nepal J. Sci. Technol.*, 13 (2012), 95–100, doi:10.3126/njst.v13i1.7447
- <sup>10</sup> M. A. M. M. Idrus, S. Hamdan, M. R. Rahman, M. S. Islam, Treated tropical wood sawdust-polypropylene polymer composite: mechanical and morphological study, *J. Biomater. Nano-Biotechnol.*, 2 (2011), 435–444, doi:10.4236/jbnb.2011.24053
- <sup>11</sup> R. Panneerdhass, A. Gnanavelbabu, K. Rajkumar, Mechanical properties of luffa fiber and ground nut reinforced epoxy polymer hybrid composites, *Procedia Eng.*, 97 (2014), 2042–2051, doi:10.1016/j.proeng.2014.12.447
- <sup>12</sup> ASTM D 638–10, Standard test method for tensile properties of plastics, *Annual Book of ASTM Standards*, 08.01 (2010), 1–16, ASTM International, West Conshohocken
- <sup>13</sup> ASTM D 790–10, Standard test methods for flexural properties of un-reinforced and reinforced plastics and electrical insulating materials, *Annual Book of ASTM Standards*, 08.01 (2010), 1–11, ASTM International, West Conshohocken
- <sup>14</sup> ISO 180:2000, Plastics – determination of Izod impact strength, third edition, *ISO Central Secretariat*, Switzerland, 2000
- <sup>15</sup> U. S. Rao, L. L. R. Rodrigues, Influence of machining parameters on tool wear in drilling of GFRP composites – Taguchi analysis and ANOVA methodology, *Proc. of the Inter. Conf. on Advances in Mechanical and Robotics Engineering – MRE 2014*, 25–29, doi:10.15224/978-1-63248-002-6-84





# OPTIMUM BUSHING LENGTH IN THERMAL DRILLING OF GALVANIZED STEEL USING ARTIFICIAL NEURAL NETWORK COUPLED WITH GENETIC ALGORITHM

## OPTIMALNA DOLŽINA PODPORE (ŠABLONE, VODILA) PRI TERMIČNEM VRTANJU GALVANIZIRANEGA JEKLA Z UPORABO UMETNE NEVRONSKE MREŽE IN GENETSKEGA ALGORITMA

Navasingh Rajesh Jesudoss Hynes<sup>1</sup>, Ramar Kumar<sup>1</sup>, Jebaraj Angela Jennifa Sujana<sup>2</sup>

<sup>1</sup>Mepco Schlenk Engineering College, Department of Mechanical Engineering, Sivakasi, Vindhunagan, 626005 Tamil Nadu, India

<sup>2</sup>Mepco Schlenk Engineering College, Department of Information Technology, Sivakasi, Vindhunagan, 626005 Tamil Nadu, India  
findhynes@yahoo.co.in, mepcokumar@gmail.com, ang\_jenefa@mepcoeng.ac.in

*Prejem rokopisa – received: 2016-09-27; sprejem za objavo – accepted for publication: 2017-01-24*

doi:10.17222/mit.2016.290

Thermal drilling is a novel sheet-metal-hole-making technique that utilizes the heat produced at the interface of the rotating conical tool and workpiece in order to soften the workpiece and pierce a hole into it. In this work, experiments with thermal drilling of galvanized steel were conducted based on the Taguchi  $L_{27}$  orthogonal array. Significant process parameters such as rotational speed, tool angle and workpiece thickness were varied during the experimentation. In thermal drilling, the thermal-drill tool pushes aside a large amount of workpiece material to form a sleeve, which is often referred to as the bushing length. A predictive model for the bushing length was developed using a feed-forward artificial neural network based on experimental data. As the bushing length is closely associated with the tapping process, the influences of the input process parameters play a vital role in fastening galvanized steel with threaded fasteners in diverse engineering applications. The optimization problem was solved by implementing a genetic algorithm under constraint limits to maximize the bushing length. Further, a confirmation test was conducted with the intention to compare the optimum value and its corresponding bushing length predicted by the genetic algorithm. Good agreement was observed between the predicted and the experimental values.

**Keywords:** thermal drilling, artificial neural network, genetic algorithm, galvanized steel, bushing length

Termično vrtanje je nova, za vrtanje lukenj v pločevino, uporabljena tehnika, ki izkorišča toploto, proizvedeno na površini vrteče se konice orodja na obdelovancu z namenom, da ga zmehča in vanj naredi luknjo. V delu so bili izvedeni preizkusi na osnovi metode Taguchi  $L_{27}$  z ortogonalno matriko s termičnim vrtanjem galvaniziranega jekla. Pomembni parametri postopka, kot so: hitrost vrtenja, kot orodja in debelina obdelovanca, so se med eksperimentiranjem spreminjali. Pri toplotnem vrtanju, vrtanje orodja potisne stran več materiala obdelovanca tako, da se tvori navarek (rokav) okoli luknje, ki se pogosto omenja kot dolžina šablone. Napovedni model za dolžino šablone, je razvit z uporabo umetne nevrnske mreže, ki temelji na znanstvenih podatkih. Ker je dolžina šablone precej povezana s procesom izdelave navoja, vplivi teh vhodnih procesnih parametrov igrajo ključno vlogo pri pritrditvi galvaniziranega jekla z navojem pritrdilnih elementov v različnih inženirskih aplikacijah. Problem optimizacije je bil rešen z implementacijo genetskega algoritma na podlagi omejitev za povečanje dolžine šablone. Ugotovljeno je bilo dobro ujemanje med napovedano in eksperimentalno vrednostjo.

**Ključne besede:** termično vrtanje, umetna nevrnska mreža, genetski algoritem, galvanizirano jeklo, dolžina šablone

## 1 INTRODUCTION

Thermal drilling is an emerging hole-making process with significant breakthroughs in many drilling situations in both automobile and aerospace applications. This process uses the heat energy produced at the interface in order to soften and then pierce the workpiece.<sup>1</sup> Moreover, this heat energy enhances the flow ability of the workpiece material, which is extruded onto both the front and back sides of a drilled hole. Finally, the extruded or deformed material forms a bushing shape, which surrounds the drilled hole.<sup>2</sup> The length of the bushing formed on the workpiece after a thermal-drilling operation is called the bushing length. Achieving a sufficient bushing length is very important since the bushing length can increase the threading depth and the clamp-load-bearing capability in various engineering applications.

Contrary to the conventional drilling process, in thermal drilling, there is no chip and wastage of the material, since all the deformed material contributes to developing a bushing. As it abolishes chip generation, it can be seen as a clean, eco-friendly and chipless hole-making technique. When joining metal sheets or thin-walled structures by drilling holes using the conventional-drilling process, just one or two threads can be made in them; however, reliability is a matter of great concern in such a situation. Alternatively, weld nuts and threaded rivet nuts are used, but due to thermal distortion, they get jammed and twisted during the fastening of the structures.<sup>3</sup> On the other hand, during the thermal-drilling process, the bushing formed is about 3 to 4 times thicker than the workpiece. The bushing thus allows a greater contact area and high structural rigidity of fasteners in joining situations.<sup>4</sup>

A. H. Streppel and H. J. J. Kals<sup>5</sup> suggested that the thermal-drilling process could be applied to different materials like carbon steels, stainless steel, copper, brass and aluminium. They carried out experimentation on the thermal drilling of aluminium. Due to strong pre-strain hardening, the process resulted in bad quality of the bushing. M. Kerkhofs and M. Van Stappen<sup>6</sup> compared the performance of (Ti, Al) N coated tungsten carbide thermal drills with uncoated drills. They reported that the coated thermal drills allowed a longer tool life than the uncoated flow drills. S. F. Miller et al.<sup>7</sup> conducted experiments with the thermal-drilling process on steel, aluminum and titanium. They studied the properties such as the hardness and microstructure of drilled holes. They concluded that in thermal drilling large deformation and high frictional heat are generated, resulting in the changes in the material properties and microstructure of a workpiece. They reported that the thermal conductivity of the material drilled affects the quality and integrity of the hole.

S. F. Miller et al.<sup>8</sup> conducted an experimental and numerical analysis of a thermal-drilling process on the AISI 1020 cold-rolled carbon steel under a constant feed rate. Moreover, they developed two classic models for the thermal-drilling process. They predicted the temperature distribution using a finite-element-based thermal model and in another attempt, they predicted the thrust force and torque using the basic principles of physics. S. F. Miller et al.<sup>9</sup> thermally drilled into aluminium and magnesium alloys using tungsten carbide and titanium carbide in a cobalt matrix under different rotational speeds and feed rates. They analyzed the thrust force, torque, energy, power and peak power required for drilling. They also evaluated the formation of the bushing shape of cast metals. The bushings produced during the thermal drilling of brittle cast metals demonstrated a radial fracture. In their conclusions, they suggested to pre-heat a cast metal workpiece and create a high rotational speed for obtaining a cylindrically shaped bushing without a significant radial fracture.

S. F. Miller et al.<sup>10</sup> developed a three-dimensional finite-element model for the thermal-drilling process in order to evaluate the plastic strain and deformation of a workpiece. S. F. Miller et al.<sup>11</sup> investigated thermal-drill tool-wear characteristics during the thermal drilling of an AISI 1015 carbon steel workpiece. Furthermore, the thrust force and torque were analyzed. They concluded that the carbide tool is durable and it demonstrates the least tool wear after drilling 11.000 holes. However, progressively severe abrasive grooving on the tool tip was observed. S. M. Lee et al.<sup>12</sup> carried out thermal drilling into the IN-713LC super alloy under different rotation speeds and feed rates. They investigated the material properties such as hardness, roundness, and surface roughness of the holes drilled into the IN-713LC super alloy. They reported that the hardness is higher near the wall of a drilled hole and it decreases with the

increasing distance from the edge of the hole. In addition to that, higher rotational speeds and feed rates demonstrate better roundness and lower surface roughness.

H. M. Chow et al.<sup>13</sup> optimized the process parameters of a thermally drilled austenite stainless-steel workpiece using the Taguchi method.<sup>14</sup> They considered the input parameters such as friction angle, friction/contact-area ratio, feed rate and drilling speed, and studied their influence on the response parameters like surface roughness. Moreover, the hardness and microstructural aspects of drilled holes were studied. It was observed that the surrounding area of a drilled hole acquired a fine grain size and a compact structure with a higher microhardness than that of the area away from the drilled region. S. M. Lee et al.<sup>15</sup> employed thermal drilling for the AISI 304 stainless steel using tungsten carbide drills with and without coating. Their results illustrated that at the same rotational speed and for the same number of holes drilled, the coated drills experienced less tool wear than the uncoated drills. Furthermore, they investigated the changes in the relationship between the drilled-surface temperature, tool wear and axial thrust force.

W. L. Ku et al.<sup>16</sup> optimized the parameters of thermal drilling into austenite stainless steel using the Taguchi method. They studied the effects of the friction angle, friction/contact-area ratio, feed rate and rotational speed on the response-quality characteristics such as the surface roughness and bushing length. They revealed that at optimized drilling conditions, the bushing length of a drilled hole was nearly three times longer than the plate thickness, and a mirror-like quality wall surface of the drilled hole could be obtained. M. Folea et al.<sup>17</sup> investigated the thermal drilling of a maraging-steel workpiece. The authors reported that the temperature was the most important factor in the thermal-drilling process. They also revealed that a greater quality of the holes drilled into maraging steel could be achieved with higher rotational speeds. T. K. Mehmet et al.<sup>18</sup> studied the effects of the thermal-drilling parameters such as friction angle, friction/contact-area ratio, feed rate and rotational speed on workpiece temperature, thrust force and torque in thermal drilling of the ST12 material. They revealed that the thrust force and torque reduce with the increasing rotational speed and increase with the friction angle, feed rate and friction/contact-area ratio.

D. Biermann and Y. Liu<sup>19</sup> demonstrated the feasibility of the thermal drilling of a magnesium wrought alloy and analyzed the thrust forces and torque. They measured the process temperature online and examined the strength of the joint through tapping and thread forming. B. B. Mehmet<sup>20</sup> experimentally and numerically investigated the thermal drilling of the AISI 1020 steel. In their study, an analytical model for the torque, axial power and heat-transfer coefficient was developed. Good agreement was observed between experimental and numerical values.

Similar work was performed by P. Krasauskas et al.<sup>21</sup> on the thermal drilling into the AISI 304 steel. P. D. Pantawane and B. B. Ahuja<sup>22</sup> carried out regression modelling of the thermal drilling of the AISI 1015 steel using the Taguchi method. They studied the effects of the tool-diameter ratio and rotational speed on the material thickness and the effect of the feed on the response parameters including the thrust force, torque and surface roughness of drilled holes. G. Somasundaram et al.<sup>23</sup> carried thermal drilling on the Al-SiC composite material and studied the roundness errors on drilled holes. They considered the input process parameters such as the composition of workpiece, workpiece thickness, rotational speed and feed rate. They developed an empirical relation between the process parameters and the roundness error using the response surface methodology.

Artificial neural network (ANN) is a biologically inspired computer program designed to simulate the way, in which the human brain processes information.<sup>24</sup> ANN is widely applied in modeling many machining operations like turning, milling and drilling. S. R. Karnik and V. N. Gaitone<sup>25</sup> used a multilayer feed-forward ANN to predict the influence of the process parameters such as the cutting speed, feed, drill diameter, point angle and lip-clearance angle on the burr height and burr thickness in drilling the AISI 316L stainless steel. R. S. Mamilla et al.<sup>26</sup> applied a multilayer ANN for modeling an abrasive flow-finishing process on the AISI 1040 and AISI 4340 steel. S. Assarzadeh and M. Ghoreishi<sup>27</sup> successfully used a multilayer ANN for modeling the metal-removal rate and surface roughness in an electrical discharge machining process involving the BD3 steel. O. Babur et al.<sup>28</sup> developed an ANN model according to experimental measurement data for the end milling of Inconel 718. They coupled a genetic algorithm (GA) with an ANN to forecast the surface roughness. S. Sarkar et al.<sup>29</sup> produced a multilayer feed-forward-ANN model to predict the process parameters of the machining of  $\gamma$  titanium aluminide with a wire-electrical-discharge machine. A. K. Singh et al.<sup>30</sup> used a multilayer feed-forward ANN to predict the flank wear of high-speed steel drill bits for drilling holes into a copper workpiece.

The literature review on thermal drilling reveals that experimental investigations and numerical simulations of the effects of mechanical and physical properties on the thermal-drilling process was mainly carried out on copper, brass, aluminium, magnesium and stainless-steel alloys, maraging steel, ST12 steel and IN-713LC super alloy. Galvanized steel is being widely used for car body structures and it is a good candidate for the implementation of the thermal-drilling process. The application of galvanized steel is widely used in the areas of roofing material, doors, ship's ducts and panels, electrical-appliance automobile parts, etc.<sup>31</sup>

In the present work, thermal drilling was carried out on galvanized steel. Based on experimental measurement

data, an ANN model was developed to predict the formation of the bushing length in thermal drilling of galvanized steel. This model considers rotational speed, tool angle and workpiece thickness as significant thermal-drilling process parameters. Then the optimum values of these drilling parameters were computed, with the aim of achieving the maximum bushing length, by solving the optimization problem implementing a GA. Thus, the present work allows us to achieve the maximum bushing length, which is highly desirable for the subsequent tapping and joining in automotive applications. A schematic diagram of the combined ANN-GA optimization<sup>24</sup> is shown in **Figure 1**. It indicates the stages of the GA process and its relation with the ANN process.

## 2 THERMAL DRILLING

### 2.1 Physical description of the process

**Figure 2** shows a schematic representation of the thermal-drilling process. Based on the thermal-drill geometry, there are four steps involved in thermal drilling. Initially, the center point zone of a drill approaches and pierces the workpiece. Secondly, the produced heat softens the workpiece as a result of the friction between the thermal drill and the workpiece. Thirdly, the softened material is pushed downward and the drill moves forward to form the bushing using the cylindrical zone of the tool. Fourthly, the extruded burr on the workpiece surface is pressed to form a boss with the shoulder zone

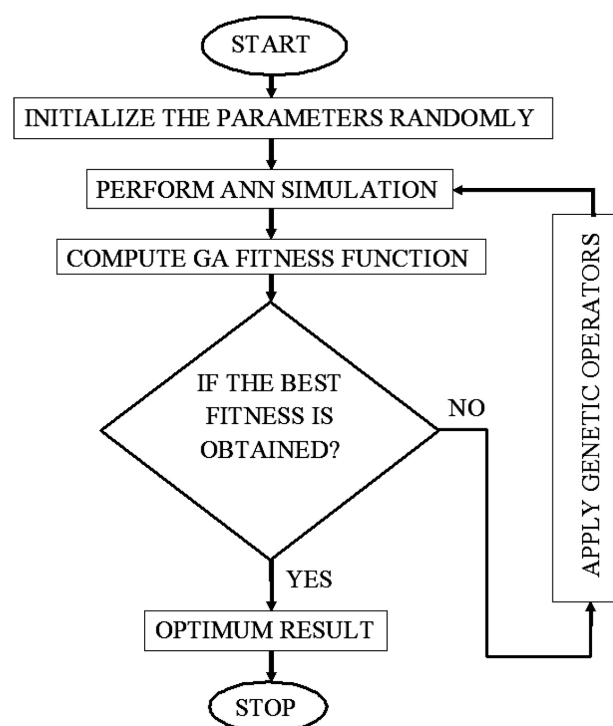


**Figure 1:** Flow chart of the integrated ANN-GA optimization process



of the thermal drill. Finally, the thermal drill retracts leaving a hole with a bushing length.<sup>37</sup>

## 2.2 Formation of the bushing length

The initial volume of the material ( $V_i$ ) available to produce a hole by thermal drilling is given in Equation (1).<sup>33</sup> As shown in **Figure 2**,  $D_1$  and  $P_t$  represent the inner-hole diameter in mm and the thickness of the workpiece in mm, respectively.

$$V_i = \frac{\pi}{4} D_1^2 P_t \quad (1)$$

During thermal drilling, the volume of the material to be displaced ( $V_f$ ) in order to produce a bushing is given in Equation (2).<sup>33</sup> As shown in **Figure 2**,  $D_2$  and  $L$  represent the outer-bushing diameter in mm and the bushing length in mm, respectively.

$$V_f = \frac{\pi}{4} [D_2^2 - D_1^2] L \quad (2)$$

It is known that the initial approximation of the volume of the material for producing a hole is the same as the volume of the material to be displaced during the formation of the bushing. Therefore, Equations (1) and (2) are assumed to be equal. Equating Equations (1) and (2), Equation (3) is obtained:

$$\frac{\pi}{4} D_1^2 P_t = \frac{\pi}{4} [D_2^2 - D_1^2] L \quad (3)$$

While rearranging the terms in Equation (3), the bushing length ( $L$ ) can be determined as shown in Equation (4):

$$L = \frac{D_1^2}{[D_2^2 - D_1^2]} P_t \quad (4)$$

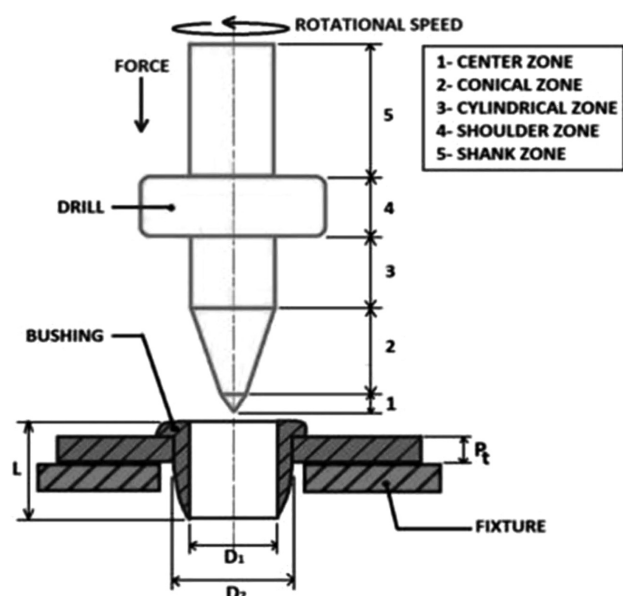


**Figure 2:** Schematic representation of the thermal-drilling process

## 3 EXPERIMENTAL PART

In the present work, the experiments were carried out at in a vertical drilling machine. A hot-dip-galvanized steel workpiece with thickness values of 1, 1.5, 2 mm and with dimensions of 50 mm × 150 mm was used. 6-mm-diameter thermal drills with different tool angles were used in the experimentation. They were machined out of high-speed steel rods, having the required dimensions as shown in **Figure 3**. The feed rate of the thermal-drilling process is kept constant at 240 mm/min. The chemical composition of the galvanized steel is given in **Table 1**. Axial forces were measured using a digital drilling-tool dynamometer. Temperature measurements were done on-line using a non-contact-type infra-red thermometer and the temperature profile of the process was obtained using the DATA TEMP MX software with a time increment of 0.016 s. The micro-structure of the holes drilled into galvanized steel was measured using a scanning electron microscope (Carl Zeiss EVO18, Germany). Three different levels of the input process parameters were used, as shown in **Table 2**.

Based on the proper selection of the input process parameters, the desirable output parameters can be obtained during the experimentation. The selected input process parameters such as the rotational speed, tool

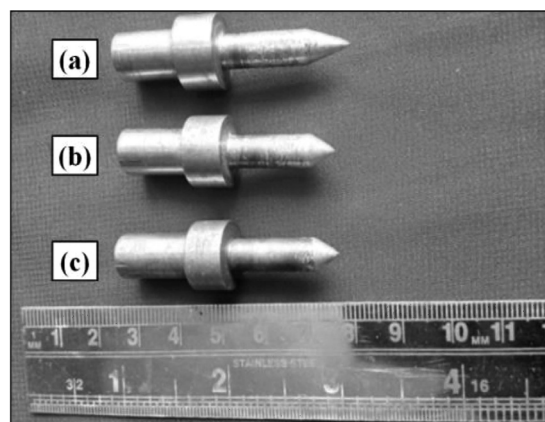


**Figure 3:** Obtained thermal drills with different tool angles: a) 35 degree tool angle b) 37.5 degree tool angle, c) 45 degree tool angle

**Table 1:** Chemical composition of galvanized steel (w%)

C	Si	S	P	Mn	Ni	Cr	
0.003	0.006	0.005	0.018	0.173	0.011	0.031	
Mo	V	Cu	Al	Nb	Zn	Ti	Fe
0.001	0.002	0.017	0.035	0.001	0.004	0.05	Balance

**Table 2:** Input process parameters and their levels

Factors	Levels		
	1	2	3
Rotational speed (min <sup>-1</sup> )	1944	2772	3600
Tool angle (°)	30	37.5	45
Workpiece thickness (mm)	1	1.5	2

angle and workpiece thickness, and the output parameter, the bushing length of the thermally drilled galvanized steel sheet, were analyzed in this work. Based on the Taguchi's  $L_{27}$  orthogonal array, experiments were conducted at three levels of the drilling-process parameters and the corresponding bushing length was measured using a digital vernier caliper (Model No CD-12C, Mitutoya Corporation, Japan). All the experimental values of the bushing length are displayed in **Table 3**. Samples of the thermally drilled holes are shown in **Figure 4**. During the thermal drilling, the burr is extruded onto the top surface, and it is leveled when it comes in contact with the shoulder of the thermal-drill tool as shown in **Figure 5a**. The formation of the bushing at the rear side of the galvanized steel plate is shown in **Figure 5b**. It can be used to act as a cylindrical sleeve bearing and it can be taped to fabricate an internal screw. Additionally, it widely reduces the complexity of joining components in the aerospace and automotive industries.

**Table 3:** Experimental results of the thermal-drilling process

Expt No.	Rotational speed (min <sup>-1</sup> )	Tool angle (°)	Workpiece thickness (mm)	Bushing length (mm)
1	1944	30	1	2.54
2	1944	30	1.5	3.42
3	1944	30	2	4.38
4	1944	37.5	1	3.24
5	1944	37.5	1.5	3.21
6	1944	37.5	2	4.41
7	1944	45	1	2.97
8	1944	45	1.5	4.87
9	1944	45	2	5.26
10	2772	30	1	2.67
11	2772	30	1.5	3.84
12	2772	30	2	4.02
13	2772	37.5	1	2.91
14	2772	37.5	1.5	3.83
15	2772	37.5	2	4.42
16	2772	45	1	2.94
17	2772	45	1.5	4.31
18	2772	45	2	5.57
19	3600	30	1	3.55
20	3600	30	1.5	4.64
21	3600	30	2	5.84
22	3600	37.5	1	2.78
23	3600	37.5	1.5	3.85
24	3600	37.5	2	5.92
25	3600	45	1	2.42
26	3600	45	1.5	4.42
27	3600	45	2	5.61

#### 4 ARTIFICIAL-NEURAL-NETWORK MODELING

Recently, the use of the artificial intelligence performance has been remarkable in the entire engineering field.<sup>24</sup> To understand and manage any industrial course

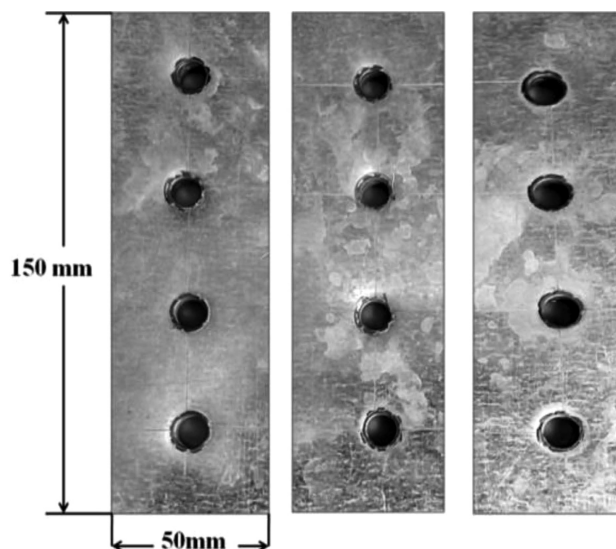


**Figure 4:** Holes made by thermal drilling in galvanized steel plates

of action, modeling and optimization of the process are essential. An accurate control is a requirement necessary to accomplish better quality and productivity. ANN plays a significant role in forecasting the solutions for non-linear problems in all engineering fields. Using statistical techniques, numerous researchers endeavored to develop a model based on experimental data. In general, a neural network represents a network of many processors operating in parallel. Each processor contains a small size of the local memory. Then, these units are coupled through communication channels, which typically carry numeric data. An excellent instance of a biological neural network is the brain of a human. It comprises the most demanding and controlling arrangement, in which learning along with training controls the behavior of a human to take action to solve any problem met in day-by-day life.

ANN can be successfully employed to predict the output parameters for any given input parameters, based on the training set for a given complex problem.<sup>28</sup> In the

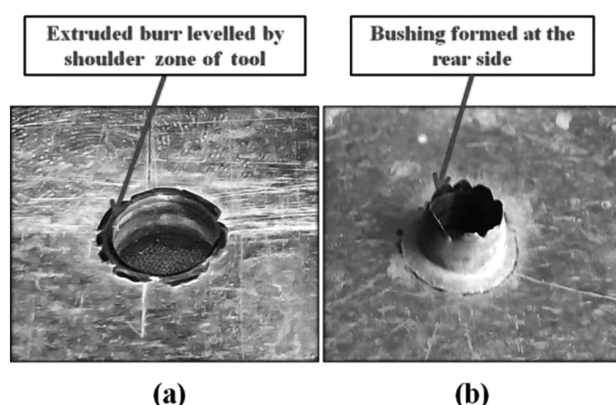


**Figure 5:** Appearance of a hole made by thermal drilling: a) top view and b) rear view

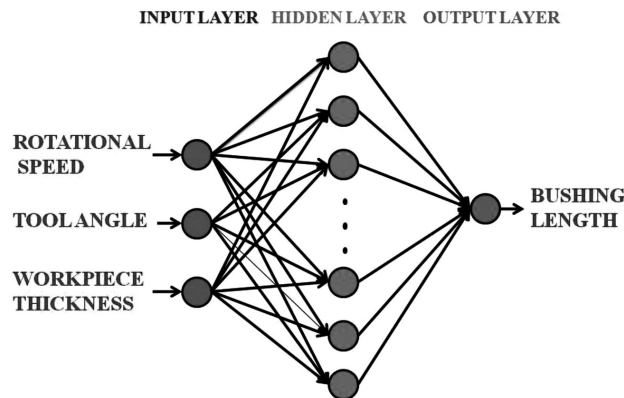


Figure 6: ANN modeling of the bushing length in thermal drilling

present work, an ANN is developed using MATLAB version 7.10, neural network toolbox, with the intention of predicting the bushing length as a function of three input process parameters including the rotational speed, tool angle and workpiece thickness. Figure 6 shows the neural-network architecture of the bushing length obtained with thermal drilling. The input data is provided through input layer neurons, and it is fed forward through the hidden layer. Then the response is obtained at the output layer neurons. The neurons are linked by weights that take part in the learning process. The weights help in attaining the optimum solution and escape from the local minima. To establish the optimum structural design, we apply the trial-and-error method with the appropriate activation function and the most excellent training algorithm. A number of models were created and tested. A hyperbolic tangent sigmoid transfer function is considered as the hidden-layer activation function, and it is given in Equation (5):

$$f(x) = \text{tansig}(x) = \frac{2}{1 + e^{-2x}} - 1 \quad (5)$$

The most important selection criteria used for the suitable model are the mean squared error and the regression-coefficient value. The mean sum of the squared error (MSE) is the average squared difference between the predicted value and the actual experimental value as shown in Equation (6). A lower value of the MSE indicates a better model. The regression coefficient ( $R$ ) was measured by correlating the predicted and the actual values as given in Equation (7). An  $R$  value of 1 indicates a close relationship between the predicted and actual experimental value, i.e., a very small error.

$$MSE = \frac{1}{n} \sum_i |A_i - P_i|^2 \quad (6)$$

$$R = 1 - \left( \frac{\sum_{i=1}^n |A_i - P_i|^2}{\sum_{i=1}^n |P_i|^2} \right) \quad (7)$$

where  $A_i$  is the actual experimental value,  $P_i$  is the predicted value and  $n$  is the number of patterns. With the intention of measuring the accuracy of the prediction model, the percentage of error is calculated with Equation (8):

$$z = \left| \frac{E - P}{E} \right| \times 100 \quad (8)$$

where  $z$  = % of prediction error,  $E$  = experimental value,  $P$  = predicted value

## 5 RESULTS AND DISCUSSION

The results of the ANN coupled with the GA<sup>34</sup> are utilized to predict and optimize the bushing length based on the input process parameters such as the rotational speed, tool angle and workpiece thickness in the thermal-drilling process, and they are discussed below.

### 5.1 Prediction of the bushing length by the ANN

Table 4 displays the parameters used with this modeling technique. The developed ANN model of the bushing length was trained by means of the selected parameters. During the training process, a 19 set input for training trials were presented each time and the resultant output was acquired. The number of the hidden-layer neurons varied from 1 to 20. It was determined based on trial and error, through step-by-step increasing the number of neurons and examining their result against the forecast value. The final neuron number of the hidden layer obtained was 10. The ul-

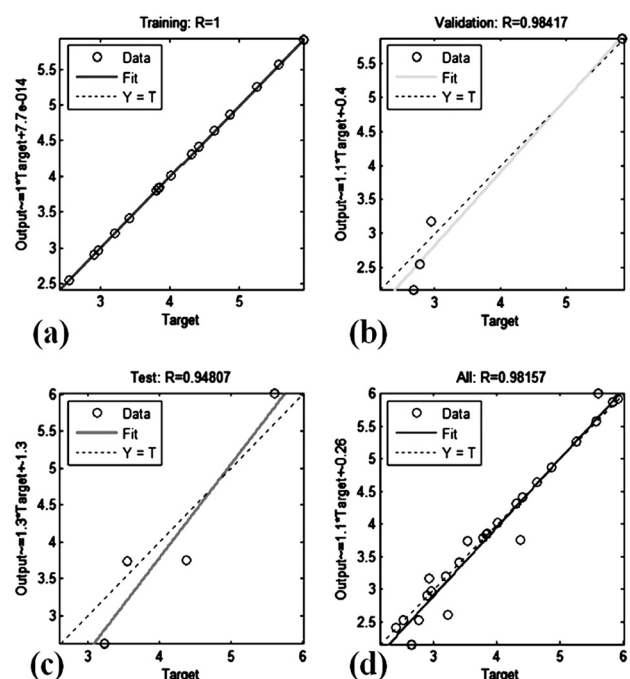


Figure 7: Correlation between the predicted values of the ANN model and the experimental data for the prediction of the bushing length using: a) training data, b) validation data, c) test data and d) entire data

mate weights between the input layer and hidden layer ( $w_1$ ,  $w_2$ ,  $w_3$ ), the bias ( $b$ ) and weights between the hidden layer and the output layer ( $w_4$ ) are shown in **Table 5**. Finally, the lowest MSE value achieved was 0.00415 when the configuration of the ANN was 3-10-1. There are three input neurons, each indicating one input variable from the input layer, 10 neurons in the hidden layer and the output layer with one neuron correspond to the bushing length.

**Table 4:** Parameters used in the ANN modeling

Input variables	Rotational speed, tool angle, workpiece thickness
Output variable	Bushing length
Network type	Feed-forward back propagation
Algorithm	Levenberg-Marquardt back-propagation algorithm (trainlm)
Activation function	Hyperbolic tangent sigmoid transfer function
Data division	70 % (training); 15 % (validation); 15 % (testing)
Number of neurons in the hidden layer	10

**Table 5:** Final weights in between the layers

No. of neurons	Weights				
	Input to hidden layer				Hidden to output layer
	$w_1$	$w_2$	$w_3$	$b$	
1	-0.682	-1.572	1.929	3.529	0.680
2	-0.865	1.620	-2.115	2.483	-0.576
3	3.045	0.934	-0.191	-1.179	0.111
4	1.722	-2.097	1.179	-1.184	-0.253
5	-1.826	-1.470	1.863	0.273	-0.183
6	-0.027	-0.448	3.025	-0.131	1.113
7	-0.619	2.955	0.332	-0.694	0.268
8	0.855	-1.318	-2.373	1.895	0.036
9	1.645	0.306	-2.767	2.418	0.939
10	1.822	-1.597	-1.613	3.188	-0.638

The output performance of the established ANN is examined on the basis of the regression-correlation coefficient ( $R$  value) between the predicted values and the experimental values. The predicted responses of the ANN model are in excellent conformity with the experimental values, i.e., the correlation regression coefficients of 100 % for the training set, 98.41 % for the validation set and 94.80 % for the testing set are achieved as shown in **Figure 7**. It was concluded that the feed-forward back-propagation algorithm of the configuration of 3-10-1 gives the most excellent results for the prediction of the bushing length as shown in **Table 6**. The graphical representation of the experimental and predicted values of the bushing length by the ANN is shown in **Figure 8**. It shows that the ANN prediction values are very close to the experimental values of the bushing length. The average prediction error between the

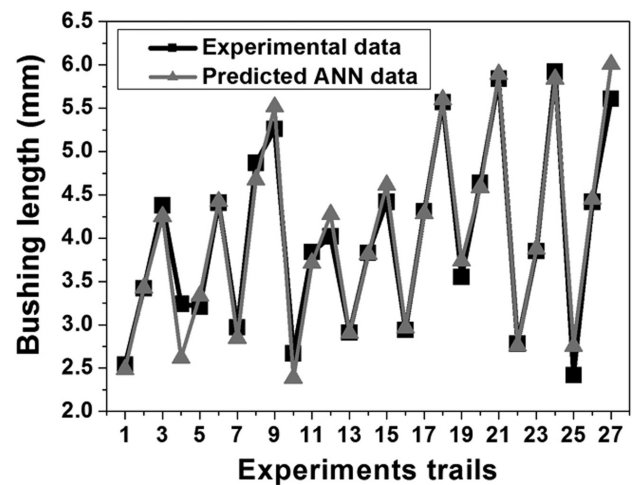


**Figure 8:** Correlation between experimental and predicted values

**Table 6:** Comparison of experimental and predicted values of the bushing length

Expt No.	Bushing length (mm)		Prediction error (%)
	Experimental value	Predicted ANN value	
1	2.54	2.485	2.165
2	3.42	3.427	0.204
3	4.38	4.252	2.922
4	3.24	2.618	19.197
5	3.21	3.336	3.925
6	4.41	4.425	0.340
7	2.97	2.843	4.276
8	4.87	4.677	3.963
9	5.26	5.517	4.886
10	2.67	2.385	10.674
11	3.84	3.714	3.281
12	4.02	4.275	6.343
13	2.91	2.905	0.172
14	3.83	3.814	0.418
15	4.42	4.615	4.412
16	2.94	2.964	0.816
17	4.31	4.284	0.603
18	5.57	5.599	0.521
19	3.55	3.738	5.296
20	4.64	4.585	1.185
21	5.84	5.893	0.907
22	2.78	2.760	0.719
23	3.85	3.875	0.649
24	5.92	5.836	1.419
25	2.42	2.755	13.843
26	4.42	4.450	0.679
27	5.61	6.007	7.077

experimental and predicted values of the bushing length is 1.843 %. Therefore, it is demonstrated that the developed ANN model is suitable for forecasting the bushing length of drilled holes in thermal drilling of galvanized steel, having the highest accuracy of 98.157 %.



### 5.2 Optimization of the bushing length using a GA

The optimization of the thermal drilling process is performed using the GA in MATLAB toolbox, with the intention of enhancing the effectiveness of the drilling process in order to achieve high structural rigidity for fasteners in joining situations.<sup>35,36</sup> This algorithm makes a binary coding system to characterize the variables such as rotational speed (RS), tool angle (TA) and workpiece thickness (WT). All of the process variables are symbolized by a ten-bit binary equivalent. In the chromosome, the process variables are represented as a substring. The GA employs different types of crossover and mutation operators to predict the maximum values of the bushing length. At this time, the second-order mathematical model is considered as an objective function with the aim of maximizing the output bushing length (BL). In this model, the rotational speed (RS), tool angle (TA) and workpiece thickness (WT) are considered as the input parameters. The aim of the optimization is to maximize the bushing length; however, usually, a GA is used to achieve the minimum function value for a minimization problem. Hence, in the present situation, the objective function was converted into a minimization problem. A unity negative factor is multiplied to the objective function in the larger-the-best-type bushing length (L) of the responses characteristic of thermal drilling to make them minimize the type objective. The parameters used in the GA technique are shown in Table 7. Equation (9) is a developed regression model of the bushing length and it is used as the fitness function or objective function for this problem. It is developed with the knowledge gained from ANN values.<sup>37,38</sup>

Table 7: GA parameters

Population type	Double vector
Population size	100
Scaling function	Rank
Selection function	Roulette wheel
Elite count	2
Crossover fraction	0.8
Mutation function	Adaptive feasible
Crossover function	Heuristic
Stall generations	50

$$\begin{aligned} \text{Maximum bushing length (L)} = & 6.56203 - 4.64305 \times 10^{-4} \times \text{RS} - 0.210894 \times \text{TA} - 1.04080 \times \text{WT} + \\ & 3.54118 \times 10^{-7} \times \text{RS}^2 - 0.00413827 \times \text{TA}^2 - 0.282222 \times \text{WT}^2 - 5.82394 \times 10^{-5} \times \text{RS} \times \text{TA} + 0.000668277 \times \\ & \text{RS} \times \text{WT} + 0.0584444 \times \text{TA} \times \text{WT} \end{aligned} \quad (9)$$

is subjected to constrained variables such as:

$$1944 \text{ min}^{-1} = \text{RS} = 3600 \text{ min}^{-1} \quad (\text{RS} - \text{rotational speed})$$

$$30^\circ = \text{TA} = 45^\circ \quad (\text{TA} - \text{tool angle})$$

$$1 \text{ mm} = \text{WT} = 2 \text{ mm} \quad (\text{WT} - \text{workpiece thickness}).$$

Figure 9 shows the bushing-length fitness-function plot obtained with the genetic algorithm. The negative sign from the final result can be eliminated to get the

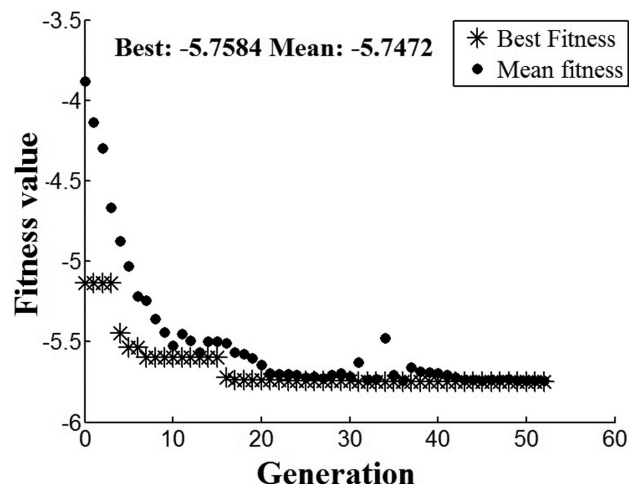


Figure 9: Fitness-function plot of the bushing length from the genetic algorithm

maximum value of the bushing length. The optimum result is achieved at the 52<sup>nd</sup> iteration of the genetic algorithm. It is found that the mean fitness value is 5.7472 mm, whereas the best fitness value is 5.7584 mm.

Table 8 presents the optimized and experimental value of the bushing length. Very close agreement between the optimized and experimental values of the bushing length is obtained. It confirms the potential applicability of these GA techniques for the industry-related problems.

Figure 10 shows the cross-section of the bushing length of a hole drilled in galvanized steel under the condition of the optimal process parameter. The bushing length can offer a longer contact-surface area, which can uphold a shaft securely, and the drilled-hole inner surface has a thermally affected zone.

Table 8: Comparison of predicted and experimental values of the bushing length

	Optimum drilling input process parameters			Output parameters
	Rotational speed (min <sup>-1</sup> )	Tool angle (°)	Work-piece thickness (mm)	Bushing length (mm)
Parameters optimized with genetic algorithm	3552.461	45	2	5.758
Experimentally used parameters	3600	45	2	5.6

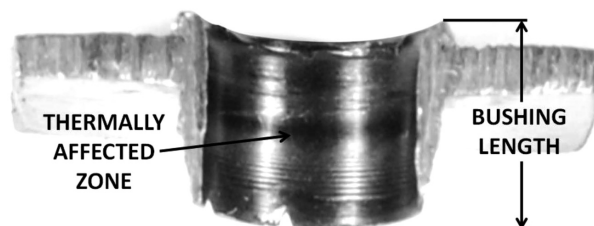


Figure 10: Cross-section of a thermally drilled hole

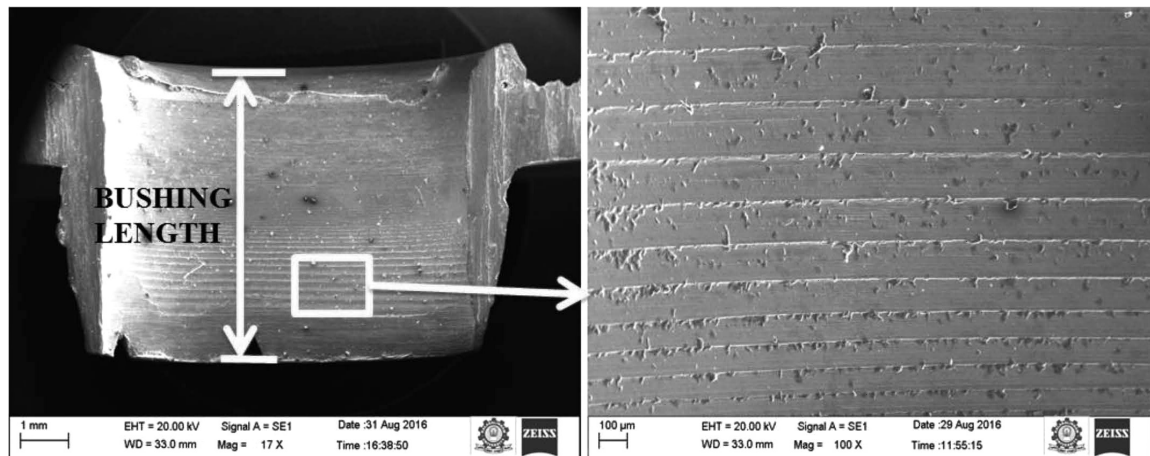


Figure 11: Microstructure of a thermally drilled hole

### 5.3 Microstructural investigation

Figure 11 shows a macrograph obtained with scanning electron microscopy at a magnification of 17 $\times$ . The scanning electron microscope was utilized to observe and investigate the inside surface of a hole drilled in galvanized steel. During the thermal-drilling operation, the rubbing action between the interface of the thermal drill and the galvanized-steel workpiece led to a rise in the temperature of up to 798 °C as recorded on-line during the experimentation. Due to such frictional heating and application of the axial tensile force, Luders bands were formed to relieve the high amount of the internal stresses experienced in the galvanized steel.<sup>39,40</sup> Luders bands started to form at the tail end of the bushing at a distance of 914  $\mu\text{m}$ , after the piercing of a hole with the center zone of the thermal drill. Until a distance of 1725  $\mu\text{m}$ , stretcher-strain markings such as Luders bands are observed in the micrograph shown in Figure 11. The width of each band thus formed is different because of non-uniform yielding of the galvanized steel during the contact with the cylindrical zone of the thermal drill.

## 6 CONCLUSIONS

The present work demonstrates the possibility of thermal drilling of galvanized steel that has tremendous applications in the domain of automobile and aerospace engineering. Owing to its importance, the mechanism and formation of the bushing length is studied.

Due to frictional heating and applied axial force, internal stresses tend to increase in that region and subsequently lead to the formation of Luders bands at the tail end of the bushing. The formation of these stretcher-strain marks is due to discontinuous non-uniform yielding of the galvanized steel.

The relationship between the input parameters such as the rotational speed, tool angle and workpiece thickness, and the output parameters like the bushing length is modeled through an ANN technique. The developed

ANN model is appropriately incorporated with the GA to optimize the thermal-drilling process parameters.

A good correlation was observed between the experimental measurements and the predicted optimum values. This shows that the ANN model combined with the GA can be successfully applied to find the optimum conditions for achieving the maximum bushing length in the thermal drilling of galvanized steel.

The modeling and optimization are valid for one material and coating only. For different materials, the building of a new ANN model is required, and the genetic optimization is to be performed again.

## Acknowledgements

The authors are grateful for the financial grant by the Mepco Schlenk Engineering College (Autonomous), Sivakasi, under the Students Project Scheme (Letter No. OF/EDC/2840/2015-2016 dated 24.10.2015) for establishing an experimental set-up. The authors acknowledge the support and encouragement by Dr. S. Arivazhagan, Principal and Dr. P. Nagaraj, Head of Mechanical Engineering, towards this work.

## 7 REFERENCES

- <sup>1</sup> N. R. J. Hynes, M. V. Maheshwaran, Numerical analysis on thermal drilling of aluminum metal matrix composite, AIP. Conf. Proc., 1728 (2016), 1–5, doi:10.1063/1.4946597
- <sup>2</sup> O. Cebeli, D. Zulkuf, Investigate the friction drilling of aluminium alloys according to the thermal conductivity, Tem. J., 2 (2013) 1, 93–101
- <sup>3</sup> S. F. Miller, Experimental analysis and numerical modeling of the friction drilling process, Thesis, University of Michigan, 2006
- <sup>4</sup> N. R. J. Hynes, M. Muthukumar, N. Rakesh, C. K. Gurubaran, Numerical analysis in friction drilling of AISI1020 steel and AA 6061 T6 alloy, Recent Advances in Environmental and Earth Sciences and Economics, 39 (2015), 145–149
- <sup>5</sup> A. H. Streppel, H. J. J. Kals, Flow drilling: a preliminary analysis of a new bush-making operation, CIRP Ann. Manuf. Techn., 32 (1983) 1, 167–171, doi:10.1016/S0007-8506(07)63383-6

- <sup>6</sup> M. Kerkhofs, M. Van Stappen, The performance of (Ti, Al) N-coated flow drills, *Surf. Coat. Technol.*, 68 (1994) 69, 741–746
- <sup>7</sup> S. F. Miller, P. J. Blau, A. J. Shih, Microstructural alterations associated with friction drilling of steel, aluminum, and titanium, *J. Mater. Eng. Perform.*, 14 (2005), 647–653, doi:10.1361/105994905X64558
- <sup>8</sup> S. F. Miller, R. Li, H. Wang, A. J. Shih, Experimental and numerical analysis of the friction drilling process, *J. Manuf. Sci. Eng.*, 128 (2006), 802–810, doi:10.1115/1.2193554
- <sup>9</sup> S. F. Miller, J. Tao, A. J. Shih, Friction drilling of cast metals, *Int. J. Mach. Tools Manuf.*, 46 (2006), 1526–1535, doi:10.1016/j.jmachtools.2005.09.003
- <sup>10</sup> S. F. Miller, A. J. Shih, Thermo-mechanical finite element modeling of the friction drilling process, *J. Manuf. Sci. Eng.*, 129 (2007), 531–538
- <sup>11</sup> S. F. Miller, P. J. Blau, A. J. Shih, Tool wear in friction drilling, *Int. J. Mach. Tools Manuf.*, 47 (2007), 1636–1645, doi:10.1016/j.jmachtools.2006.10.009
- <sup>12</sup> S. M. Lee, H. M. Chow, B. H. Yan, Friction drilling of IN-713LC cast superalloy, *Mater. Manuf. Proces.*, 22 (2007), 893–897, doi:10.1080/10426910701451697
- <sup>13</sup> H. M. Chow, S. M. Lee, L. D. Yang, Machining characteristic study of friction drilling on AISI 304 stainless steel, *J. Mater. Process. Technol.*, 207 (2008), 180–186, doi:10.1016/j.jmatprotec.2007.12.064
- <sup>14</sup> B. Mehmet, C. Ibrahim, G. Mustafa, O. Feridun, Application of the taguchi method to optimize the cutting conditions in hard turning of a ring bore, *Mater. Tech.*, 49 (2015) 5, 765–772, doi:10.17222/mit.2014.246
- <sup>15</sup> S. M. Lee, H. M. Chow, F. Y. Huang, B. H. Yan, Friction drilling of austenitic stainless steel by uncoated and PVD AlCrN- and TiAlN-coated tungsten carbide tools, *Int. J. Mach. Tools Manuf.*, 49 (2009), 81–88, doi:10.1016/j.jmachtools.2008.07.012
- <sup>16</sup> W. L. Ku, C. L. Hung, S. M. Lee, H. M. Chow, Optimization in thermal friction drilling for SUS 304 stainless steel, *Int. J. Adv. Manuf. Technol.*, 53 (2011), 935–944, doi:10.1007/s00170-010-2899-5
- <sup>17</sup> M. Folea, D. Schlegel, E. Gete, C. Langlade, A. Roman, Preliminary tests on flow drilling of maraging steels, *Acad. J. Manuf. Eng.* 10 (2012) 4, 42–47
- <sup>18</sup> T. K. Mehmet, A. Alaattin, B. Bertan, K. A. Hamza, An experimental study on friction drilling of ST12 steel, *T. Can. Soc. Mech. Eng.*, 38 (2014), 319–329
- <sup>19</sup> D. Biermann, Y. Liu, Innovative flow drilling on magnesium wrought alloy AZ31, *Proc. CIRP*, 18 (2014), 209–214, doi:10.1016/j.procir.2014.06.133
- <sup>20</sup> B. B. Mehmet, G. Kadir, G. Arif, Three-dimensional finite element model of friction drilling process in hot forming processes, *J. Proc. Mech. Eng.*, (2015), 1–7, doi:10.1177/0954408915614300
- <sup>21</sup> P. Krasauskas, S. Kilikevičius, R. Česnavičius, D. Pačenga, Experimental analysis and numerical simulation of the stainless AISI 304 steel friction drilling process, *Mecha.*, 20 (2014) 6, 590–595, doi:10.5755/j01.mech.20.6.8664
- <sup>22</sup> P. D. Pantawane, B. B. Ahuja, Parametric analysis and modelling of friction drilling process on AISI 1015, *Int. J. Mecha. Manuf. Sys.*, 7 (2014) 1, 60–79, doi:10.1504/IJMM.2014.062771
- <sup>23</sup> G. Somasundaram, B. S. Rajendra, K. Palanikumar, Modeling and analysis of roundness error in friction drilling of aluminum silicon carbide metal matrix composite, *J. Compos. Mater.*, 46 (2011) 2, 169–181, doi:10.1177/0021998311410493
- <sup>24</sup> S. Changyu, W. Lixia, C. Wei, W. Jinxing, Optimization for injection molding process conditions of the refrigeratory top cover using combination method of artificial neural network and genetic algorithms, *Poly. Plast. Tech. Eng.*, 46 (2007), 105–112, doi:10.1080/03602550601152853
- <sup>25</sup> S. R. Karnik, V. N. Gaitone, Development of artificial neural network models to study the effect of process parameters on burr size in drilling, *Int. J. Adv. Manuf. Technol.*, 39 (2008), 439–453, doi:10.1007/s00170-007-1231-5
- <sup>26</sup> R. S. Mamilla, S. Mondal, J. Ramkumar, V. K. Jain, Experimental investigations and modeling of drill bit-guided abrasive flow finishing (DBG-AFF) process, *Int. J. Adv. Manuf. Technol.*, 42 (2009), 678–688, doi:10.1007/s00170-008-1642-y
- <sup>27</sup> S. Assarzadeh, M. Ghoreishi, Neural-network-based modeling and optimization of the electro-discharge machining process, *Int. J. Adv. Manuf. Technol.*, 39 (2008), 488–500, doi:10.1007/s00170-007-1235-1
- <sup>28</sup> O. Babur, O. Hasan, K. Hasan, Optimum surface roughness in end milling Inconel 718 by coupling neural network model and genetic algorithm, *Int. J. Adv. Manuf. Technol.*, 27 (2005), 234–241, doi:10.1007/s00170-004-2175-7
- <sup>29</sup> S. Sarkar, S. Mitra, B. Bhattacharyya, Parametric optimisation of wire electrical discharge machining of  $\gamma$  titanium aluminide alloy through an artificial neural network model, *Int. J. Adv. Manuf. Technol.*, 27 (2006), 501–508, doi:10.1007/s00170-004-2203-7
- <sup>30</sup> A. K. Singh, S. S. Panda, S. K. Pal, D. Chakraborty, Predicting drill wear using an artificial neural network, *Int. J. Adv. Manuf. Technol.*, 28 (2006), 456–462, doi:10.1007/s00170-004-2376-0
- <sup>31</sup> S. M. Hamidinejad, F. Kolahan, A. H. Kokabi, The modeling and process analysis of resistance spot welding on galvanized steel sheets used in car body manufacturing, *Mater. Des.*, 34 (2012), 759–767, doi:10.1016/j.matdes.2011.06.064
- <sup>32</sup> Y. Lieh-Dai, K. Wei-Liang, C. Han-Ming, W. Der-An, L. Yan-Cherng, Mar-M247, Haynes-230 & Inconel-718 study of machining characteristics for Ni-based super alloys on friction drilling, *Adv. Mat. Res.*, 459 (2012), 632–637, doi:10.4028/www.scientific.net/AMR.459.632
- <sup>33</sup> J. B. Peter, C. J. Brian, Q. Jun, Feasibility of thermally drilling automotive alloy sheet, castings, and hydro formed shapes, (2007), <http://web.ornl.gov/info/reports/2007/3445605662084.pdf>, 08/2016
- <sup>34</sup> P. Sathiya, K. Panneerselvam, M. Y. Abdul Jaleel, Optimization of laser welding process parameters for super austenitic stainless steel using artificial neural networks and genetic algorithm, *Mater. Des.*, 36 (2012), 490–498, doi:10.1016/j.matdes.2011.11.028
- <sup>35</sup> K. Girish, S. S. Kuldip, Predictive modelling and optimization of machining parameters to minimize surface roughness using artificial neural network coupled with genetic algorithm, *Proc. CIRP*, 31 (2015), 453–458, doi:10.1016/j.procir.2015.03.043
- <sup>36</sup> S. S. Kuldip, S. Sachin, K. Girish, Optimization of machining parameters to minimize surface roughness using integrated ANN-GA approach, *Proc. CIRP*, 29 (2015), 305–310, doi:10.1016/j.procir.2015.02.002
- <sup>37</sup> D. S. Nagesh, G. L. Datta, Genetic algorithm for optimization of welding variables for height to width ratio and application of ANN for prediction of bead geometry for TIG welding process, *App. Soft. Comp.*, 10 (2010), 897–907, doi:10.1016/j.asoc.2009.10.007
- <sup>38</sup> M. Z. Azlan, H. Habibollah, S. Safian, Genetic algorithm and simulated annealing to estimate optimal process parameters of the abrasive water jet machining, *Eng. Comp.*, 27 (2011), 251–259, doi:10.1007/s00366-010-0195-5
- <sup>39</sup> V. S. Ananthan, E. O. Hall, Macroscopic aspects of Luders band deformation in mild steel, *Actametall. Mater.*, 39 (1991) 12, 3153–3160, doi:10.1016/0956-7151(91)90049-7
- <sup>40</sup> F. H. Julian, K. Stelios, On the effect of Luders bands on the bending of steel tubes. Part II: Analysis, *Int. J. Solids. Struct.*, 48 (2011), 3285–3298, doi:10.1016/j.ijsolstr.2011.07.012



GELLING POLYSACCHARIDE AS THE ELECTROLYTE MATRIX  
IN A DYE-SENSITIZED SOLAR CELLŽELIRNI POLISAHARID KOT ELEKTROLITNA OSNOVA V  
SOLARNIH CELICAH, OBČUTLJIVIH NA BARVILAJose Paolo Bantang<sup>1</sup>, Drexel Camacho<sup>1,2</sup><sup>1</sup>De La Salle University, Chemistry Department, 2401 Taft Avenue, 1004 Manila, Philippines<sup>2</sup>De La Salle University, Organic Materials and Interfaces Unit, CENSER, 2401 Taft Avenue, 1004 Manila, Philippines  
drexel.camacho@dlsu.edu.ph

Prejem rokopisa – received: 2016-09-30; sprejem za objavo – accepted for publication: 2017-03-16

doi:10.17222/mit.2016.294

Hydrophilic polysaccharide,  $\kappa$ -carrageenan, was utilized as the polymer matrix in gel-electrolyte systems for dye-sensitized solar-cell (DSSC) applications. The influence of the solvent system was investigated to optimize the solubility of  $\kappa$ -carrageenan and tetrabutylammonium-iodide (TBAI)/I<sub>2</sub> electrolytes by minimizing the water content because of its unfavorable effect on DSSCs. We report herein that two solvent systems, a water/acetonitrile mixed solvent and DMSO, were found to effectively dissolve the components. The composite natures of the  $\kappa$ -carrageenan-electrolyte systems in these solvents were confirmed with an FTIR analysis. The presence of  $\kappa$ -carrageenan did not impede the electrochemical properties of the electrolytes, as confirmed with cyclic voltammetry, electrochemical impedance spectroscopy and linear sweep voltammetry. The incorporation of the gel electrolytes in DSSCs showed that the DMSO system exhibited better solar-cell efficiency compared to the mixed-solvent system.

Keywords: dye-sensitized solar cell,  $\kappa$ -carrageenan, gel electrolyte, electrochemical impedance spectroscopy, ionic conductivity

Hidrofilni polisaharid,  $\kappa$ -karagen, je bil uporabljen kot polimerna osnova v želirno elektrolitskih sistemih za uporabo v barvno občutljivih sončnih celicah (angl. DSSC). Da bi izboljšali topnost  $\kappa$ -karagena in elektrolitov tetrabutylamonijevega iodida (TBAI)/I<sub>2</sub> z zmanjšanjem vsebnosti vode, zaradi njenega neželenega učinka na DSSC, je bila preiskovana občutljivost sistema topil. Članek poroča, da sta bila najdena dva nova sistema topil, mešanica topila voda/acetoni-tril in DMSO, ki učinkovito raztopita komponente. Lastnosti oz. obnašanje kompozitov elektrolitskega sistema  $\kappa$ -karagen v teh raztopinah, so bile potrjene z FTIR-analizo. Prisotnost  $\kappa$ -karagenskega elektrolitnega sistem ni predstavljala ovire za imepdančno spektroskopijo in lenarno "sweep" voltometrijo. Vključitev gel-elektrolitov v DSSC je pokazala, da DMSO-sistem kaže boljše solarno celično učinkovitost kot sistem mešanih topil.

Ključne besede: barvno občutljive sončne celice, rastlinska želatina  $\kappa$ -karagen, gel-elektrolit, elektrokemična imepdančna spektroskopija, ionska prevodnost

## 1 INTRODUCTION

Gel-polymer electrolytes are promising materials for a potential incorporation in electrochemical devices<sup>1</sup> such as dye-sensitized solar cells (DSC). This is because their mechanical behavior is that of solids, yet their internal structure is flexible and their conductivity behavior resembles that of a liquid state allowing a good electrode/electrolyte contact.<sup>2,3</sup> Moreover, its ease of fabrication allows more tunability in designing systems for specific applications.

Natural polysaccharide is a potential matrix for polymer electrolytes owing to its hydrophilic and gel-forming capacity that traps the solvent together with the redox couple inside the polymer matrix. The high water-retention property of polysaccharide-based polymer-electrolyte systems was shown to promote good ionic conductivities and thermal stability.<sup>4,5</sup> Agarose,<sup>6,7</sup> cellulose and its derivatives<sup>8,9</sup> and  $\kappa$ -carrageenan<sup>10</sup> are the gel-forming natural polysaccharides that have been used as polymer-electrolyte (PE) systems for dye-sensitized-solar-cell (DSSC) applications. To maximize the

water-retention property of these polysaccharide-based gel systems, an aqueous medium is necessary. However, we can see that water disturbs the interfacial attachment of dyes to TiO<sub>2</sub>. Thus, it is highly desirable to develop a polysaccharide-based electrolyte system in a smaller amount of water or in a non-aqueous medium.

$\kappa$ -Carrageenan, which is composed mainly of disaccharide units of  $\beta$ -D-galactopyranose with either an  $\alpha$ -D-galactopyranose or 3,6-anhydrogalactose is a promising polysaccharide matrix for electrolytes due to its hydrophilic, linear and sulfated properties. The electrostatic interactions of ions with hydroxyl groups and sulfate groups in the main chain are essential to the conduction mechanism of a polysaccharide electrolyte system.<sup>11,12</sup> The promising features of  $\kappa$ -carrageenan as a polymer-electrolyte system can be potentially applied to DSSCs. Solid-state DSSCs using carrageenan-gel electrolyte systems were fabricated by soaking the aqueous polymer gel with the redox electrolytes<sup>11</sup> and forming thin polymer membranes<sup>13</sup> leading to decent efficiencies. To date, studies on the preparation and characterization of carrageenan-electrolyte systems have been limited



only to pure aqueous systems. A significant amount of water present in the electrolyte systems applied to DSSCs causes a decrease in the photocurrent of the device associated with dye desorption, iodate formation and a decrease in the electron lifetime.<sup>14</sup> Hence, the amount of water must be controlled, if not eliminated. It is the objective of this paper to investigate the influence of the solvent system on carrageenan electrolyte and its performance in a DSSC. This paper reports, for the first time, on a novel carrageenan-based electrolyte system with an iodide/tri-iodide redox couple prepared using a mixed solvent system and a non-aqueous solvent.

## 2 MATERIALS AND METHODS

### 2.1 Optimization of the $\kappa$ -carrageenan electrolyte system

Different  $\kappa$ -carrageenan (Shemberg, Philippines) biopolymer gel electrolytes were optimized by varying the ratio of water/acetonitrile and the amount of polymer with a constant amount of tetrabutylammonium iodide (TBAI, Sigma Aldrich, a reagent grade of 98 %; 20 % w/w of TBAI with respect to  $\kappa$ -carrageenan) and iodine ( $I_2$ , Aldrich, = 99.99 % metal basis). The molar ratio of TBAI/ $I_2$  was 4:1. The ratio of water/ACN was optimized by dissolving  $\kappa$ -carrageenan (0.2 g) with TBAI/ $I_2$  in different solvent systems consisting of 100 % water, 3:1 water/ACN, 1:1 water/ACN, 1:3 water/ACN, and 100 % ACN at 80 °C until a homogeneous solution was formed. Thin films were formed by casting solutions on plastic petri dishes and slowly drying in air. Different biopolymer electrolytes were prepared using the same procedure by varying the concentration of  $\kappa$ -carrageenan (0, 0.5, 1.0, 1.5 and 2 % w/v). Using the optimized parameters,  $\kappa$ -carrageenan gel electrolytes containing 20 % w/w (with respect to the amount of  $\kappa$ -carrageenan) of other salts such as potassium iodide (Sigma Aldrich) and trimethylsulfonium iodide (TMSI, Sigma Aldrich) were also prepared.

A liquid-state polymer electrolyte and a gel-state polymer electrolyte based on  $\kappa$ -carrageenan were prepared by dissolving 1 % w/v or 2 % w/v of the polysaccharide in 2 mL of dimethylsulfoxide at 70 °C. Tetrabutylammonium iodide (0.5 M),  $I_2$  (0.05 M) and LiI (0.1 M) were added to the  $\kappa$ -carrageenan solution. As the control, the same composition was used without adding the biopolymer.

### 2.2 Fabrication of dye-sensitized solar cells (DSSCs)

The photoanode was prepared spreading a  $TiO_2$  paste (Solaronix, Ti-Nanoxide T/SP) on a fluorine-doped tin-oxide (FTO) conducting glass (TCO22-7) with the doctor-blading method. The active area of the photoanode was fixed to 1 cm  $\times$  1 cm with adhesive tapes. The deposited paste was sintered at 450 °C for 30 min and cooled down slowly to room temperature. The deposited

$TiO_2$  film was soaked in a dye solution containing a ruthenium dye (Ruthenizer 535-bisTBA, Solaronix) in ethanol for 24 h. The counter electrode was prepared by sintering an FTO conducting glass coated with a platinum solution (Platisol 41121, Solaronix) at 450 °C for 30 mins. The photoanode and counter electrode were sealed with a hot-melt thermoplastic material called Surlyn (DuPont, thickness of 60  $\mu$ m), also acting as a spacer. A dye-sensitized solar cell was fabricated by inserting a hot gel-electrolyte solution in a pre-drilled hole on the counter electrode. Three different solar cells were fabricated containing different iodide salts (KI, TMSI, and TBAI) in a water/ACN  $\kappa$ -carrageenan matrix. A control DSSC was prepared using an acetonitrile-based liquid electrolyte (Iodolyte AN50, Solaronix). The same process was used for the fabrication of a DSSC incorporating gel electrolytes in DMSO.

### 2.3 Characterization

The surface morphology and thickness of the thin films were characterized using scanning electron microscopy (JEOL JSM-5310). The electrical conductivity was measured using the 4-point probe Van der Pauw method. In brief, four wires were attached to the corners of a 1 cm  $\times$  1 cm thin film using a silver paste. The voltage at a constant current was measured. The resistivity and electrical conductivity were calculated using the following equations:

$$\text{Resistivity, } s = \frac{\pi d}{\ln 2} \left( \frac{V_1}{l_2} + \frac{V_2}{l_1} \right) f \left( \frac{R_1}{R_2} \right) \text{ and Electrical}$$

conductivity,  $\rho = 1/s$ , where  $d$ ,  $V$ ,  $I$  and  $f(R_1/R_2)$  refer to the thickness, potential, current and van der Pauw function, respectively.

The redox properties of the  $\kappa$ -carrageenan gel electrolyte were characterized using 3-electrode cyclic voltammetry (Powerlab/4SP potentiostat). The electrodes composed of the Ag/AgCl reference electrode, platinum-wire counter electrode and glassy-carbon working electrode were pierced through the gel. Electrochemical impedance spectroscopy (Metrohm Autolab potentiostat PGSTAT128N) was obtained by sandwiching the gel electrolyte in between two platinum-coated FTO conducting-glass electrodes. The active area was fixed to 1  $\times$  1 cm<sup>2</sup> and the thickness of the spacer was about 50  $\mu$ m. The frequency was set from 10<sup>6</sup> Hz to 10<sup>-1</sup> Hz with an AC applied voltage of 10 mV. The ionic conductivity ( $\sigma$ ) of the gel electrolyte was calculated from the solution resistance ( $R_s$ ) using Equation (3):

$$\sigma = \frac{L}{AR_s} \quad (3)$$

The solution resistance ( $R_s$ ) is determined as the intercept of the Nyquist plot against the real part of the impedance or the horizontal axis. The variables  $L$  and  $A$  correspond to the thickness of the spacer and the active area, respectively. The solar-cell parameters such as the

open-circuit voltage, short-circuit current, fill factor and efficiency of the fabricated dye-sensitized solar cells with  $\kappa$ -carrageenan gel electrolyte were assessed using a 100 mW/cm<sup>2</sup> AM 1.5 solar simulator (Abet Technologies) coupled with a potentiostat to obtain a current-voltage (IV) curve.

### 3 RESULTS AND DISCUSSIONS

#### 3.1 Carrageenan-electrolyte system in a mixed solvent system

Acetonitrile (ACN), which is a common organic solvent used for preparing liquid electrolytes for DSSC applications, does not dissolve  $\kappa$ -carrageenan. Thus, to form  $\kappa$ -carrageenan electrolytes containing a redox couple  $I^-/I_3^-$  (from TBAI and  $I_2$ ), the amount of water is crucial to dissolve the hydrophilic polysaccharide.<sup>15</sup> Using water only as the solvent, a black film was formed with observable colorless crystals (**Figure 1a**) indicating the unsuccessful dissolution of both TBAI salt and iodine. Likewise, crystallization of the salt was formed on the surface of the film prepared using a 3:1 v/v water/ACN system (**Figure 1b**). The salt crystallization is attributed to the relative insolubility of the salt in a water-rich solvent. Moreover, the presence of the salt and iodine crystals on the film surface indicates that it fails to dissociate in the polymer matrix, leading to an unsuccessful incorporation of the charge-carrier redox couple  $I^-/I_3^-$ . For a 1:1 v/v water/ACN mixed-solvent system, a uniform orange polymer-electrolyte film without visible crystals was formed (**Figure 1c**), indicating

good dissolution and incorporation of the  $I^-/I_3^-$  redox couple in the polymer matrix. No films were cast for the 1:3 v/v water/acetonitrile solvent systems and in 100 % acetonitrile because of the relative insolubility of carrageenan in an acetonitrile-rich solvent.

The concentration of carrageenan in the polymer electrolyte containing 20 % w/w TBAI (w.r.t.  $\kappa$ -carrageenan) in the 1:1 H<sub>2</sub>O/acetonitrile mixed solvent affects the property and the ionic conductivity of the electrolyte. A liquid polymer electrolyte is formed when the concentrations of carrageenan are in a range of 0.1–0.5 % w/v. Increasing the carrageenan concentration to  $\geq 1.0$  % w/v gave a gel polymer electrolyte. Consequently, the ionic conductivity of the polymer electrolytes changes in response to its composite form. The ionic conductivity (**Figure 2**) of  $\kappa$ -carrageenan-electrolyte systems increases as the carrageenan concentration increases from 0.1 to 1.0 % w/v. The increase in the ionic conductivity at low  $\kappa$ -carrageenan concentrations is attributed to high free-ion concentrations due to their interaction with the functional group present in  $\kappa$ -carrageenan.<sup>16</sup> The ionic conductivity decreases at carrageenan concentrations of 1.0–2.0 % w/v. The increase in the polymer concentration causes chain entanglements, impeding the movement of the ions, thus, decreasing its ionic conductivity.<sup>16</sup>

Different iodide salts were incorporated in  $\kappa$ -carrageenan to prepare the gel electrolytes. Films were formed and the IR spectra of the electrolyte films contained typical functional-group vibrations of  $\kappa$ -carrageenan.<sup>17</sup> The bands at 1272 cm<sup>-1</sup> were identified as an O=S=O symmetric vibration that would respond in the presence of a cation. A shift in the frequency was observed in the O=S=O symmetric vibration compared with the pure  $\kappa$ -carrageenan reference (**Table 1**, entry 1). This shift is attributed to the electrostatic interaction between the negatively charged sulfate ions in the carrageenan chains and the positively charged cations from the iodide salt.<sup>4</sup> The effect of the addition of iodide salts generally increased the electrical conductivity (**Table 1**, entry 2) of the films formed, as compared with

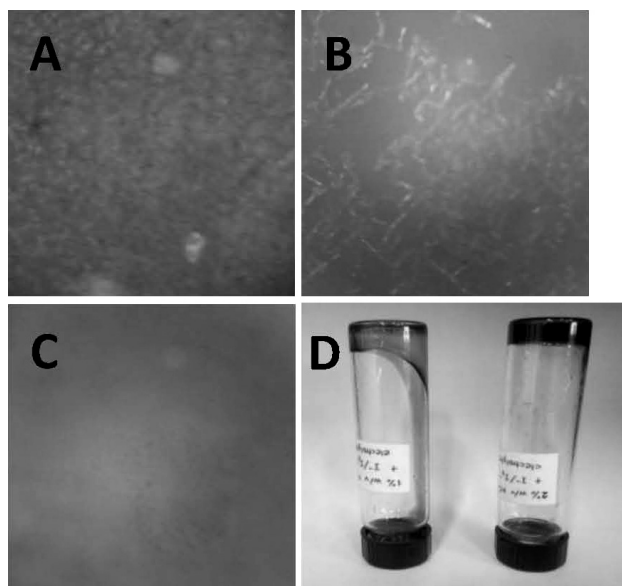


**Figure 1:** Optical images of 1 % w/v  $\kappa$ -carrageenan films mixed with 40 % w/w TBAI (w.r.t.  $\kappa$ -carrageenan) in 4:1 mole ratio TBAI /  $I_2$  electrolyte in varying solvents a) in 100 % water, b) in 3:1 H<sub>2</sub>O/acetonitrile, c) in 1:1 H<sub>2</sub>O/acetonitrile, d) polymer gel electrolytes containing  $\kappa$ -carrageenan and TBAI/LiI/ $I_2$  electrolyte: left: 1 % w/v  $\kappa$ -carrageenan in DMSO (liquid state), right: 2 % w/v  $\kappa$ -carrageenan in DMSO (gel-state)

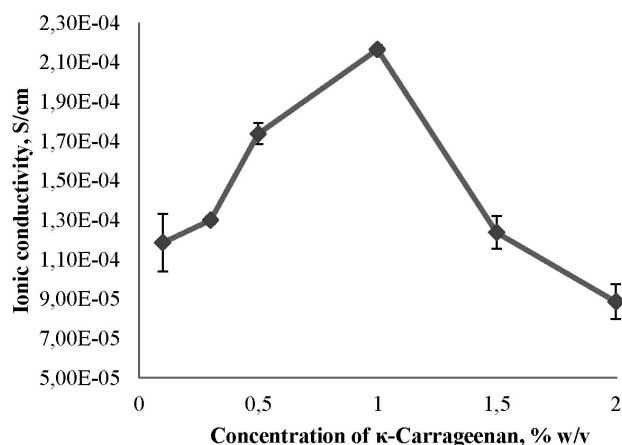


**Figure 2:** Effect of  $\kappa$ -carrageenan concentration on ionic conductivity of carrageenan/TBAI/ $I_2$  systems

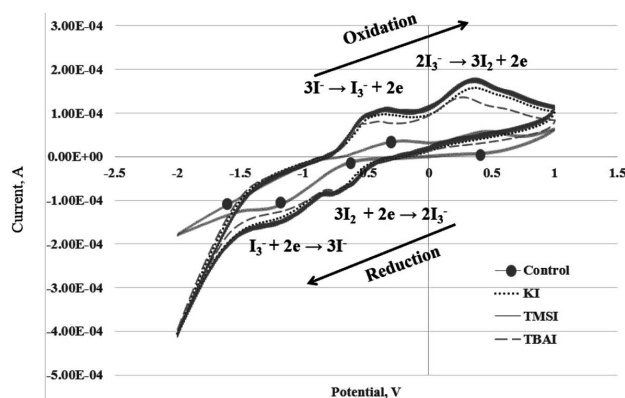
**Table 1:** FTIR and conductivity of the  $\kappa$ -carrageenan electrolytes containing different salts

Entry		Pure $\kappa$ -carrageenan (reference)	Iodolyte AN50 (control)	KI/I <sub>2</sub>	TMSI/I <sub>2</sub>	TBAI/I <sub>2</sub>
				in $\kappa$ -carrageenan		
1	FTIR O=S=O vibration (cm <sup>-1</sup> )	1272	–	1261	1274	1263
2	Electrical conductivity of polymer-electrolyte films <sup>a</sup> (S cm <sup>-1</sup> )	0.127	–	0.281	0.189	0.326
3	Ionic conductivity of polymer-electrolyte gels <sup>b</sup> (x10 <sup>-4</sup> S cm <sup>-1</sup> )	–	1.66	2.52	3.05	2.17

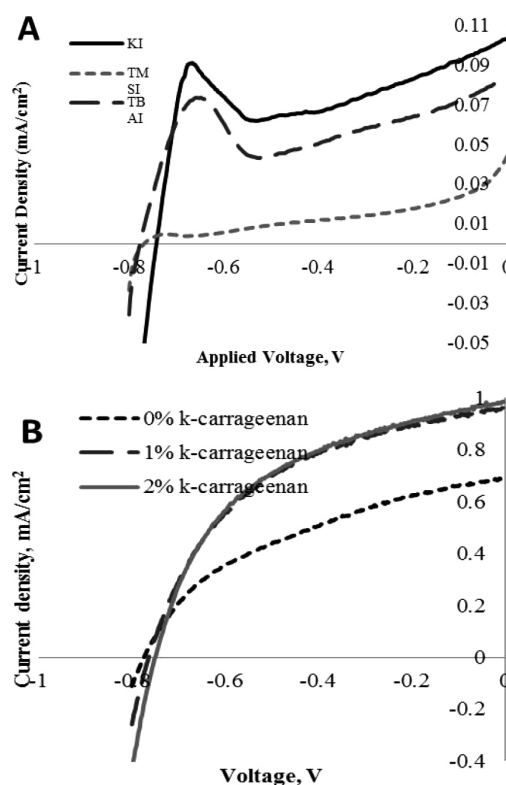
<sup>a</sup>Measured with 4-point probe Van der Pauw technique<sup>b</sup>Measured with electrochemical impedance spectroscopy (EIS)

the reference pure  $\kappa$ -carrageenan due to the addition and incorporation of the redox species. The ionic conductivities (**Table 1**, entry 3) of the gel electrolytes are generally higher than that of the acetonitrile-based liquid electrolyte, indicating a facile transport of the redox couple in the carrageenan matrix. Cyclic voltammetry of the gel electrolytes with and without  $\kappa$ -carrageenan (**Figure 3**) showed that the addition of the polymer does not impede the electrochemical behavior of the I<sup>-</sup>/I<sub>3</sub><sup>-</sup> redox couple in the mixed water/acetonitrile system. Two redox processes were observed, indicating the migration of I<sup>-</sup>/I<sub>3</sub><sup>-</sup> in the 3D matrix of  $\kappa$ -carrageenan.<sup>18</sup>

Solar cells were fabricated using the conventional set-up composed of a TiO<sub>2</sub>/ruthenium dye as the photoanode and a platinum counter electrode sandwiching the  $\kappa$ -carrageenan-gel electrolyte systems in water/ACN. I-V characteristics of the DSSCs (**Table 2** and **Figure 4a**) containing the  $\kappa$ -carrageenan-gel electrolytes showed poor efficiency (<0.10 %) as compared to the liquid electrolyte (2.33 %), attributed to a much lower short-circuit current, which can be associated with the presence of a significant amount of water in the electrolyte system. The presence of water causes dye detachment due to the weakening of the dye-TiO<sub>2</sub> linkage, resulting in a limited amount of electrons injected from the excited state of the dye and consequently leading to the lowering of the short-circuit current.<sup>16</sup> The obtained efficiencies of

**Figure 3:** Electrochemical-behavior (cyclic voltammetry) analysis of the  $\kappa$ -carrageenan-gel electrolytes containing different salts; control: LiI/I<sub>2</sub> in 1:1 v/v water/ACN without carrageenan

different  $\kappa$ -carrageenan-gel electrolytes with a mixture of acetonitrile and water suggest that imparting a large amount of water (50 %) in the electrolyte system for

**Figure 4:** I-V curves of the DSSCs: a) containing different iodide salts (KI, TMSI and TBAI) in the water/ACN  $\kappa$ -carrageenan matrix and b) containing  $\kappa$ -carrageenan-based electrolytes in DMSO under a 100 mW/cm<sup>2</sup> illumination**Table 2:** Characteristics of the fabricated DSSCs under a 100 mW/cm<sup>2</sup> illumination

Electrolyte	V <sub>oc</sub> (V)	I <sub>sc</sub> (mA/cm <sup>2</sup> )	FF	$\eta$ (%)
Iodolyte (control)	0.695	6.444	0.521	2.333
KI:I <sub>2</sub>	0.746	0.100	0.819	0.061
TMSI:I <sub>2</sub>	0.776	0.0414	0.152	0.005
TBAI:I <sub>2</sub>	0.778	0.0817	0.765	0.049

**Table 3:** I-V electrochemical properties of the carrageenan electrolyte in DMSO measured using two platinized FTO conducting glasses and I-V characteristics of DSSCs under a 100 mW/cm<sup>2</sup> illumination\*

Electrolytes in DMSO	Electrochemical properties of electrolyte				I-V characteristics of DSSC			
	$R_b^{**}$ ( $\Omega$ )	$R_{Pt}$ ( $\Omega$ )	Ionic conductivity, $\times 10^{-4}$ (S/cm)	Diffusivity of $I_3^-$ , $\times 10^{-9}$ (cm <sup>2</sup> s <sup>-1</sup> )	Short-circuit current (mA/cm <sup>2</sup> )	Open-circuit voltage (V)	Fill factor	Efficiency (%)
Control (without $\kappa$ -carrageenan)	21.28	218.13	2.82	1.48	0.690	0.781	0.410	0.221
1% w/v $\kappa$ -carrageenan	25.33	296.41	2.37	1.41	0.960	0.763	0.483	0.354
2% w/v $\kappa$ -carrageenan	25.25	338.46	2.38	1.11	0.983	0.751	0.488	0.360

\*The electrolyte used was composed of tetrabutylammonium iodide (0.5 M),  $I_2$ , (0.05 M) and LiI (0.1 M)

\*\* $R_b$  corresponds to the solution resistance, which corresponds to the intercept at the real part of the EIS spectrum

DSSCs is still detrimental to the performance of a solar-cell device.

### 3.2 Carrageenan-electrolyte system in a non-aqueous solvent

Carrageenan is not known to dissolve in purely non-aqueous solvents. However, in the course of our investigation of electrolyte systems, we observed that it dissolves in dimethylsulfoxide (DMSO).<sup>19,20</sup> We investigated the solubility properties of  $\kappa$ -carrageenan in DMSO, dissolving different amounts of the biopolymer

at 60 °C. A liquid solution is formed with 1 % w/v  $\kappa$ -carrageenan (a solubility of 0.01 g/mL DMSO at room temperature and at 60 °C). Increasing the  $\kappa$ -carrageenan concentration from 1.5 to 3.5 % w/v allows the dissolution of the biopolymer in DMSO, forming a transparent solution at 60 °C. However, upon cooling down at room temperature, it forms into a stable gel (**Figure 1d**). A further increase in the concentration of  $\kappa$ -carrageenan of 4–5 % w/v leads to the formation of a stable gel even at 60 °C. Other organic solvents such as ethanol, methanol, acetonitrile, tetrahydrofuran, dimethylformamide and methoxyethanol did not show good solubility. The advantages of using DMSO are its relatively low vapor pressure and relatively non-volatile nature, which are useful for maintaining its gel state. Moreover, this organic solvent shows a relatively low toxicity and is considered environmentally benign.<sup>6</sup> The addition of electrolyte systems TBAI and  $I_2$  turned the  $\kappa$ -carrageenan DMSO solution into a dark-brown one indicating the incorporation of the electrolytes. The IR spectrum of the polymer-electrolyte system showed functional groups typical of  $\kappa$ -carrageenan. A shift in the O=S=O symmetric vibration from typical 1272 for pure  $\kappa$ -carrageenan to 1226 cm<sup>-1</sup> for carrageenan gel electrolyte is attributed

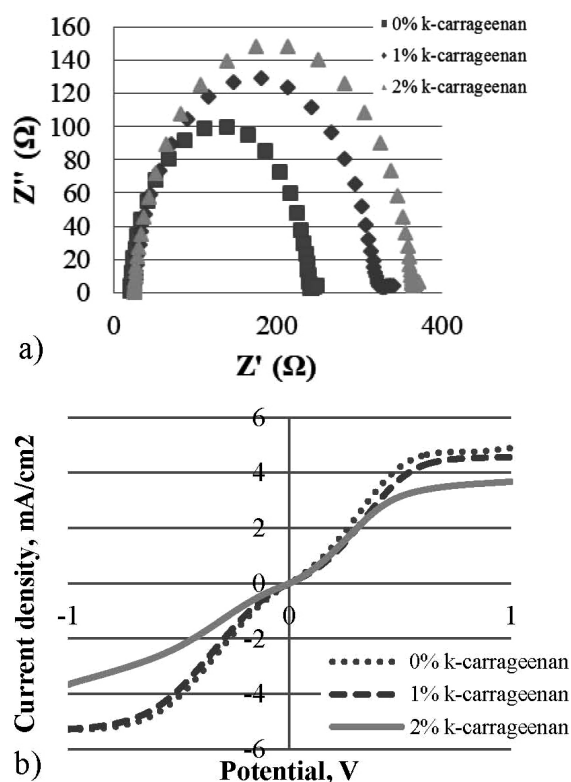


**Figure 5:** a) EIS spectra of electrolytes measured using a symmetrical-cell set-up between two platinized FTO conducting glasses in a frequency range of 1 MHz to 0.1 Hz, b) linear sweep voltammogram of the electrolytes measured between two platinized FTO conducting glasses swept between -1 V to 1 V. Scan rate: 10 mV/s

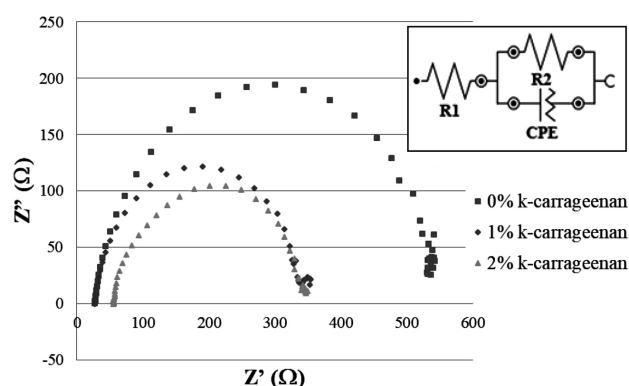


**Figure 6:** EIS spectrum of a DSSC containing  $\kappa$ -carrageenan-based electrolytes in DMSO; inset: equivalent circuit model ( $R_1$  = series resistance,  $R_2$  =  $TiO_2$ /dye/electrolyte interface resistance,  $CPE$  = constant phase element)



to the interaction of the cation with the sulfate functional groups.<sup>5</sup>

The ionic conductivity and diffusivity of the tri-iodide ion (**Table 3**) in DMSO showed that the addition of  $\kappa$ -carrageenan decreases the ionic conductivity of the electrolyte system in comparison to the DMSO-based liquid-electrolyte system. EIS spectra (**Figure 5a**) of the electrolytes in DMSO show a broader semi-circle arc upon the addition of  $\kappa$ -carrageenan, which is associated with an increase in the charge-transfer resistance at the platinum/electrolyte interface ( $R_{\text{Pt}}$ ). A higher  $R_{\text{Pt}}$  indicates a less efficient electro-activity at the Pt/electrolyte interface attributed to a slower ionic conductivity.<sup>21</sup> The concentration of iodide ions is in excess in comparison with the amount of tri-iodide ions. Hence, the limiting current density of the gel electrolytes is associated with the diffusion coefficient of the tri-iodide ions. The limiting current densities of the electrolytes (**Figure 5b**) show negative and positive values due to the transport of charge carriers from one electrode to the other through the whole electrolyte system.<sup>8</sup> A slow diffusion of the tri-iodide ions is consistent with the slow ionic conductivity of the carrageenan-electrolyte system. The slow tri-iodide ion diffusion in the  $\kappa$ -carrageenan electrolytes resulted in a higher recombination.<sup>22</sup> These results were consistent with the decreasing trend in the open-circuit voltage of the electrolytes with  $\kappa$ -carrageenan. The photovoltaic performance of the  $\kappa$ -carrageenan-based dye-sensitized solar cells (**Figure 4b** and **Table 3**) showed that the addition of  $\kappa$ -carrageenan to the  $\text{I}^-/\text{I}_3^-$  redox electrolyte system in dimethylsulfoxide decreases the open-circuit voltage and increases the short-circuit current of a solar cell. The improvement in the short-circuit current of the DSSCs with a  $\kappa$ -carrageenan/DMSO electrolyte system is attributed to the ability of the hydroxyl functional group and negatively charged sulfate ions of  $\kappa$ -carrageenan to allow dissociation of the ions in the polymer matrix through the electrostatic interaction with the cations. The enhancement in the short-circuit current of the  $\kappa$ -carrageenan/DMSO electrolytes is the major contribution to the improvement of the overall efficiency of the dye-sensitized solar cells. Good dissociation of ions in the polymer matrix increases the concentration of  $\text{I}^-$ , its counterion, and  $\text{I}_3^-$  leading to an increase in the short-circuit current.<sup>23</sup>

A typical liquid-electrolyte-based DSSC show an EIS spectrum consisting of three semi-circle arcs corresponding to the interfacial resistances occurring during the electrochemical reaction at the platinum/electrolyte interface, during the charge-transfer process at the  $\text{TiO}_2$ /dye/electrolyte interface and Warburg diffusion of  $\text{I}^-/\text{I}_3^-$  in the electrolyte. A frequency-response-analyzer (FRA) impedance analysis of the  $\kappa$ -carrageenan/DMSO DSSC (**Figure 6**) showed a unique single semi-circle arc, associated with the charge-recombination process occurring at the  $\text{TiO}_2$ /dye/electrolyte interface ( $R_2$ ). The

other parameters such as  $R_1$  and CPE corresponded to the series resistance and constant phase element, respectively. A decreasing trend in the semi-circle arc radius was observed when the  $\kappa$ -carrageenan concentration was increased. A quantitative approach of the recombination resistance was done by fitting the Nyquist plot with its corresponding equivalent circuit model. Chi-square values for the fitted equivalent circuit model range from 0.02–0.07, indicating good value fitting. The charge-recombination resistances ( $R_2$ ) of the DSSCs without  $\kappa$ -carrageenan (control), with 1 % w/v  $\kappa$ -carrageenan (liquid state) and 2 % w/v  $\kappa$ -carrageenan (gel state), obtained from the plot are 515.19  $\Omega$ , 317.88  $\Omega$  and 292.86  $\Omega$ , respectively. A higher  $R_2$  value signifies lower charge recombination between the photoanode conduction-band electrons and  $\text{I}_3^-$  ions at the  $\text{TiO}_2$ /dye/electrolyte interface resulting in a higher  $V_{\text{oc}}$ .<sup>24</sup> The higher charge recombination of the polymer electrolytes with  $\kappa$ -carrageenan, compared to the electrolyte without the polymer, is generally attributed to the slow ionic conductivity of the ions in the gel matrix of carrageenan (**Table 3**). Moreover, the  $\kappa$ -carrageenan electrolyte penetrates poorly into the  $\text{TiO}_2$  layer due to its polymeric nature contributing to the less efficient charge-transfer process.<sup>21</sup> The results were consistent with the photovoltaic characteristics of the fabricated dye-sensitized solar cells.

## 4 CONCLUSIONS

A hydrophilic polysaccharide,  $\kappa$ -carrageenan, was successfully used as the polymer matrix for a gel-electrolyte system in a mixed solvent of water and acetonitrile for dye-sensitized solar cells. The solvent system improved the dissolution of the components and the electrolyte properties. Efficiencies of less than 0.1 % of the fabricated DSSCs are attributed to the significant amount of water. A novel gel-polymer electrolyte consisting of  $\kappa$ -carrageenan electrolyte gel in DMSO was developed for DSSCs. Removal of the water from the polymer-electrolyte system improved the DSSC performance from 0.049 to 0.36 %, a seven-fold increase in the magnitude. The presence of  $\kappa$ -carrageenan in the DMSO-based gel-electrolyte system helps improve the solar-cell efficiency from 0.221 to 0.360 %.

## Acknowledgments

The authors are grateful to Dr. Erwin Enriquez, Dr. Arnel Salvador and Dr. Armando Somintac for the use of the solar simulator and Ms. Anna San Esteban for guidance in solar measurements. This work was supported by research grants from DOST-PCIEERD of the Republic of the Philippines; DOST-SEI-ASTHRDP and DLSU-PhD Fellowship Grants to J. P. O Bantang; DLSU Research Faculty Grant, DLSU Science Foundation and DLSU-URCO to D. H. Camacho.

## 5 REFERENCES

- <sup>1</sup> J. R. MacCallum, C. A. Vincent, *Polymer Electrolytes Reviews-I*, Elsevier Applied Science, London, 1989
- <sup>2</sup> K. N. Kumar, T. Sreekanth, M. J. Reddy, U. V. S. Rao, Study of transport and electrochemical cell characteristics of PVP:NaClO<sub>3</sub> polymer electrolyte system, *J. Power Sources*, 101 (2001), 130–133 doi:10.1016/S0378-7753(01)00658-9
- <sup>3</sup> T. M. W. J. Bandara, P. Ekanayake, M. A. K. L. Dissanayake, I. Albinsson, B. E. Mellander, A polymer electrolyte containing ionic liquid for possible applications in photoelectrochemical solar cells, *J. Solid State Electrochem.*, 14 (2010), 1221–1226, doi:10.1007/s10008-009-0951-x
- <sup>4</sup> X. Guo, P. Yi, Y. Yang, J. Cui, S. Xiao, W. Wang, Effects of surfactants on agarose-based magnetic polymer electrolyte for dye-sensitized solar cells, *Electrochim. Acta*, 90 (2013), 524–529, doi:10.1016/j.electacta.2012.12.028
- <sup>5</sup> R. Singh, A. R. Polu, B. Bhattacharya, H.-W. Rhee, C. Varlikli, P. K. Singh, Perspectives for solid biopolymer electrolytes in dye sensitized solar cell and battery application, *Renew. Sustainable Energy Rev.*, 65 (2016), 1098–1117, doi:10.1016/j.rser.2016.06.026
- <sup>6</sup> W. Wang, X. Guo, Y. Yang, Lithium iodide effect on the electrochemical behavior of agarose based polymer electrolyte for dye-sensitized solar cell, *Electrochim. Acta*, 56 (2011), 7347–7351, doi:10.1016/j.electacta.2011.06.032
- <sup>7</sup> H.-L. Hsu, W.-T. Hsu, J. Leu, Effects of environmentally benign solvents in the agarose gel electrolytes on dye-sensitized solar cells, *Electrochim. Acta*, 56 (2011), 5904–5909, doi:10.1016/j.electacta.2011.04.117
- <sup>8</sup> P. Li, Y. Zhang, W. Fa, Y. Zhang, B. Huang, Synthesis of a grafted cellulose gel electrolyte in an ionic liquid ([Bmim]I) for dye-sensitized solar cells, *Carbohydr. Polym.*, 86 (2011), 1216–1220, doi:10.1016/j.carbpol.2011.06.017
- <sup>9</sup> X. Huang, Y. Liu, J. Deng, B. Yi, X. Yu, P. Shen, S. Tan, A novel polymer gel electrolyte based on cyanoethylated cellulose for dye-sensitized solar cells, *Electrochim. Acta*, 80 (2012), 219–226, doi:10.1016/j.electacta.2012.07.014
- <sup>10</sup> M. Kaneko, T. Hoshi, Y. Kaburagi, H. Ueno, Solid type dye-sensitized solar cell using polysaccharide containing the redox electrolyte solution, *J. Electroanal. Chem.*, 572 (2004), 21–27, doi:10.1016/j.jelechem.2004.05.021
- <sup>11</sup> H. Ueno, M. Kaneko, Investigation of a nanostructured polysaccharide solid medium for electrochemistry, *J. Electroanal. Chem.*, 568 (2004), 87–92, doi:10.1016/j.jelechem.2003.12.044
- <sup>12</sup> N. N. Mobarak, N. Ramli, A. Ahmad, M. Y. A. Rahman, Chemical interaction and conductivity of carboxymethyl  $\kappa$ -carrageenan based green polymer electrolyte, *Solid State Ionics*, 224 (2012), 51–57, doi:10.1016/j.ssi.2012.07.010
- <sup>13</sup> F. Bella, N. N. Mobarak, F. N. Jumaah, A. Ahmad, From seaweeds to biopolymeric electrolytes for third generation solar cells: An intriguing approach, *Electrochim. Acta*, 151 (2015), 306–311, doi:10.1016/j.electacta.2014.11.058
- <sup>14</sup> C. Law, S. C. Pathirana, X. Li, A. Y. Anderson, P. R. F. Barnes, A. Listorti, T. H. Ghaddar, B. C. O'Regan, Water-Based Electrolytes for Dye-Sensitized Solar Cells, *Adv. Mater.*, 22 (2010), 4505–4509, doi:10.1002/adma.201001703
- <sup>15</sup> D. H. Camacho, S. J. M. Tambio, M. I. A. Oliveros, Carrageenan-Ionic Liquid Composite: Development of Polysaccharide-Based Solid Electrolyte System, *The Manila J. of Science*, 6 (2011), 8–15
- <sup>16</sup> H.-L. Lu, Y.-H. Lee, S.-T. Huang, C. Su, T. C.-K. Yang, Influences of water in bis-benzimidazole-derivative electrolyte additives to the degradation of the dye-sensitized solar cells, *Sol. Energy Mater. Sol. Cells*, 95 (2011), 158–162, doi:10.1016/j.solmat.2010.02.018
- <sup>17</sup> C. Tranquilan-Aranilla, N. Nagasawa, A. Bayquen, A. Dela Rosa, Synthesis and characterization of carboxymethyl derivatives of kappa-carrageenan, *Carbohydr. Polym.*, 87 (2012), 1810–1816, doi:10.1016/j.carbpol.2011.10.009
- <sup>18</sup> S. Yuan, Q. Tang, B. He, P. Yang, Efficient quasi-solid-state dye-sensitized solar cells employing polyaniline and polypyrrole incorporated microporous conducting gel electrolytes, *J. Power Sources*, 254 (2014), 98–105, doi:10.1016/j.jpowsour.2013.12.112
- <sup>19</sup> S. Chan, J. P. Bantang, D. Camacho, Influence of Nanomaterial Fillers in Biopolymer Electrolyte System for Squaraine-Based Dye-Sensitized Solar Cells, *Int. J. Electrochem. Sci.*, 10 (2015), 7696–7706
- <sup>20</sup> J. P. Bantang, D. Camacho, A Novel Biopolymer Gel Electrolyte System for DSSC Applications, *Proceedings of the DLSU Research Congress*, 3, 2015
- <sup>21</sup> S. Venkatesan, N. Obadja, T.-W. Chang, L.-T. Chen, Y.-L. Lee, Performance improvement of gel- and solid-state dye-sensitized solar cells by utilization of the blending effect of poly (vinylidene fluoride-cohexafluoropropylene) and poly (acrylonitrile-co-vinyl acetate) co-polymers, *J. Power Sources*, 268 (2014), 77–81, doi:10.1016/j.jpowsour.2014.06.016
- <sup>22</sup> H.-L. Hsu, C.-F. Tien, Y.-T. Yang, J. Leu, Dye-sensitized solar cells based on agarose gel electrolytes using allylimidazolium iodides and environmentally benign solvents, *Electrochim. Acta*, 91 (2013), 208–213, doi:10.1016/j.electacta.2012.12.133
- <sup>23</sup> K. Hara, T. Horiguchi, T. Kinoshita, K. Sayama, H. Arakawa, Influence of electrolytes on the photovoltaic performance of organic dye-sensitized nanocrystalline TiO<sub>2</sub> solar cells, *Sol. Energy Mater. Sol. Cells*, 70 (2001), 151–161, doi:10.1016/S0927-0248(01)00019-8
- <sup>24</sup> Y. Yang, J. Cui, P. Yi, X. Zheng, X. Guo, W. Wang, Effects of nanoparticle additives on the properties of agarose polymer electrolytes, *J. Power Sources*, 248 (2014), 988–993, doi:10.1016/j.jpowsour.2013.10.016



DEVELOPMENT OF A HEAT TREATMENT FOR INCREASING  
THE MECHANICAL PROPERTIES AND STRESS CORROSION  
RESISTANCE OF 7000 Al ALLOYSRAZVOJ TOPLOTNE OBDELAVE ZA IZBOLJŠANJE MEHANSKIH  
LASTNOSTI IN NAPETOSTNO KOROZIJSKO ODPORNOST 7000  
AL ZLITINMehdi Shakouri<sup>1</sup>, Mohammad Esmailian<sup>1</sup>, Saeed Shabestari<sup>2</sup><sup>1</sup>Advanced Material and Renewable Energy Department, Iranian Research Organization for Science and Technology (IROST),  
P. O. Box 3353-5111, Tehran, Iran<sup>2</sup>Center of Excellence for High Strength Alloys Technology (CEHSAT), School of Metallurgy and Materials Engineering,  
Iran University of Science and Technology (IUST), Narmak, 16846, Tehran, Iran  
mshakoori@yahoo.com*Prejem rokopisa – received: 2016-10-10; sprejem za objavo – accepted for publication: 2017-04-19*

doi:10.17222/mit.2016.297

A retrogression and re-ageing (RRA) treatment is a three-step heat treatment that can improve both the mechanical strength and the corrosion resistance in aluminum alloys. In this work, the mechanical and stress corrosion properties under various ageing treatment conditions were investigated in an Al–8.5Zn–2.1Mg–2Cu–0.2Ag (w/w%) alloy. The treatments were the T6 conventional method followed by a retrogression and re-ageing (RRA) treatment. Tensile test, scanning electron microscopy (SEM), energy-dispersive X-ray spectroscopy (EDS) and differential scanning calorimetry (DSC) were used to investigate the mechanical and stress corrosion cracking (SCC) properties. The results showed that both, the strength and the corrosion resistance criteria (SCR), which is defined as the ratio between the remaining strength percent in stressed and un-stressed conditions, improve after the RRA treatment. The tensile strength and SCR criteria for the T6 heat treatment were 547 MPa and 71 % initially and then increased to 612 MPa and 95 % for the RRA treatment, respectively. Moreover, the EDS results showed that in grain-boundary precipitates the Cu concentration is much higher for the RRA in comparison with the T6 treatment, but it is lower for the matrix precipitates in the RRA treatment.

Keywords: aluminium alloys, stress corrosion resistance, precipitation, retrogression and re-ageing

Obdelava z retrogresijo in ponovno oživitvijo (angl. RRA) je tristopenjska toplotna obdelava, s katero lahko izboljšamo tako mehansko trdnost kot odpornost proti koroziji pri aluminijevih zlitinah. V pričujočem delu so bile raziskovane mehanske lastnosti in lastnosti odpornosti proti koroziji pri zlitini Al–8.5Zn–2.1Mg–2Cu–0.2Ag (w/w%) pod različnimi pogoji obdelave staranja. Izvedeni so bili testi po konvencionalni T6 metodi, z upoštevanjem RRA obdelave. Natezni preiskus, vrstična elektronska mikroskopija (SEM), energijsko disperzijska rentgenska spektroskopija (EDS) in DSC-testiranja so bili izvedeni, da bi raziskali mehanske in napetostno-korozijske lomne lastnosti (angl. SCC). Rezultati so pokazali, da se oba kriterija tako trdnost kot odpornost proti koroziji, ki definirata razmerje med procentom zaostale trdnosti pri napetostnih in nenapetostnih pogojih, po RRA-obdelavi izboljšata.

Ključne besede: aluminijeve zlitine, odpornost proti koroziji, oborine, retrogresija in ponovno staranje

## 1 INTRODUCTION

The Al–Zn–Mg–Cu series aluminum alloys are precipitation-hardening alloys that are used extensively for light-weight structural applications, in particular in the aircraft industry. They have a combination of good strength and good stress corrosion resistance.<sup>1</sup>

The most popular heat treatment to gain the peak-aged strength (T6X temper) is a solution treatment, quenching, stretching (for stress relief purposes) followed by artificial aging at 120 °C for 24 h, but this temper is highly susceptible to SCC. In order to reduce this susceptibility, an over-aging treatment (T7X temper) is needed.<sup>2</sup> This requirement becomes increasingly demanding as the solute contents are increased in commercial alloys in order to improve the mechanical properties even further.

To improve both the mechanical strength and corrosion resistance, it has been proposed to utilize an RRA treatment. This three-step heat treatment has been shown to offer a stress corrosion resistance as good as that of a T7X heat treatment, while keeping a strength comparable to that of a T6X temper.<sup>3,4</sup> This type of heat treatment comprises three steps. First, an ageing step that leads to a T6 state. A second step (called retrogression or reversion) of short duration at high temperature dissolves part of the initially formed precipitates. Third heat treatment step at lower temperature leads to the desired microstructure.<sup>5</sup>

Stress corrosion cracking occurs under loading in a corrosive environment. Several investigations have reported that the SCC mechanism involves anodic dissolution, hydrogen-induced cracking, passive film rupture, hydrogen embrittlement, magnesium segregation to the



grain boundaries and a precipitate-free zone (PFZ) along the grain boundary.<sup>6–10</sup> However, the microstructural characteristics of Al–Zn–Mg–Cu high strength aluminum alloys are well known to have a strong influence not only on the mechanical properties but also on the SCC susceptibility. Larger grain-boundary precipitates can trap more atomic hydrogen to nucleate hydrogen bubbles, thereby decreasing the hydrogen concentration at grain boundaries below a critical value is considered to prevent intergranular SCC fracture.<sup>11</sup> Furthermore, the cathodic grain-boundary precipitates grow by depleting solute atoms. Studies showed that this leads to the broadening of the anodic PFZ, which contained no strengthen precipitation phase and as a result was soft and weak.<sup>12</sup> The combination of tensile stress and anodic dissolution caused SCC.

SCC resistance is of practical importance for the industrial applications of the Al–Zn–Mg–Cu series aluminum alloys. Various heat treatments in these alloys offer very different SCC properties. The SCR criteria are proposed to compare the SCC resistance.

The aim of this paper is to investigate the mechanical strength and SCC of a 7000 series aluminum alloy after conventional T6 and RRA treatments. The SCR criteria have been defined to easily compare the SCC resistance of this alloy after various treatments. SEM investigations were used to determine the effect of the heat treatments on the alloy's microstructure with the aim of studying its effect on SCC susceptibility. For comparison, the stress corrosion resistance of the alloy with different heat treatments was studied by the breaking load method according to ASTM G139 standard.<sup>13</sup>

## 2 EXPERIMENTAL PART

The samples used in this study were received as 8-mm-thick sheets that were homogenized, hot rolled and heat treated after being alloyed and casted. The chemical composition of the alloy is shown in **Table 1**.

**Table 1:** Chemical composition (in mass fractions, w/%) of fabricated alloy

Alloy No.	Zn	Cu	Mg	Fe	Si	Zr	Ag
1	8.5	2	2.1	0.18	0.16	0.20	0.19

An induction melting furnace used for melting and the melt was poured in a water-cooled copper mold. The as-cast specimens were homogenized at 460 °C for 24 h and hot rolled to about 33 % reduction. Hot rolling was

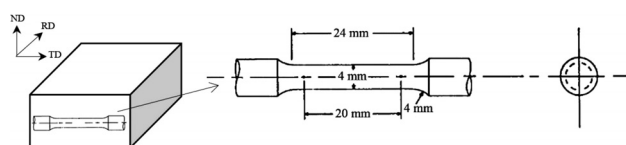


**Figure 1:** Schematic showing the preparation of tensile samples from the specimens

performed with 40 min<sup>-1</sup> rolling speed at 430 °C. The specimens were milled to tensile samples according to the ASTM E8M standard. A schematic showing the preparation of tensile samples from the specimens is given in **Figure 1**.

A solution heat treatment was done at 471 °C for 6 h followed by a water quenching. T6 ageing was performed for 24 h at 120 °C (T6 temper). The scheme of the retrogression and re-ageing treatment is shown in **Figure 2**.

Mechanical properties measurements were made at ambient temperature on the specimens machined according to the ASTM E8M-04 small size standard. The average of three tests was used for each result. The test's strain rate was 10<sup>-3</sup> /s.

The SEM analysis was performed on a TESCAN scanning electron microscope. Thermal analysis was performed in a DSC 1 Mettler Toledo differential scanning calorimeter. Polished alloy disks with a diameter of 5 mm and 0.6 mm thick were sealed in aluminum pans and heated in a flowing argon atmosphere at a constant heating rate of 10 °C/min. The flowing rate of the argon was 100 mL/min.

The stress corrosion tests were performed according to the ASTM G139 standard. The Neutral 3.5 % Sodium Chloride Solution was prepared in accordance with the requirements of the ASTM G44 standard. The ASTM G49 standard was used for preparation of direct tension stress corrosion test specimens. A 207 MPa stress for the cycle of 4 d was applied as per section 8-2 of the ASTM G139 standard. In order to eliminate the corrosion other than SCC (such as pitting), some specimens were tested unstressed. The ratio of remaining strength of stressed and unstressed samples represented in percent, were calculated as SCR criteria for different treatment.

## 3 RESULTS AND DISCUSSION

### 3.1 Mechanical strength

The mechanical strength of the alloy was 547 MPa after the T6 treatment and was 612 MPa after the RRA treatment. The RRA treatment leads to an about 12 % increase in mechanical strength. While T6 treatment is carried out to ensure maximum strength; the RRA

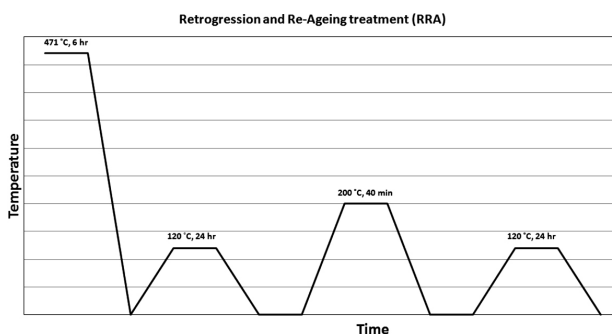


**Figure 2:** Scheme of the RRA treatment

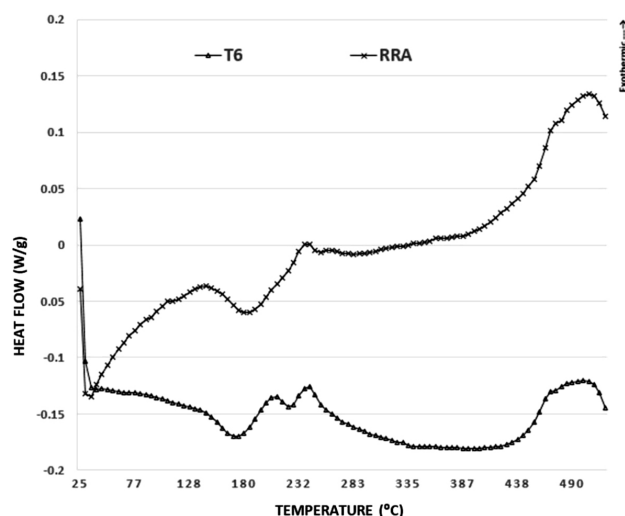


Figure 3: DSC curves for T6 and RRA treatment

treated samples show higher strength. It seems that the performed T6 treatment does not lead to precipitation of all the alloying elements and yet there are elements in the solution. To investigate this further, DSC analysis was conducted on the samples.

### 3.2 DSC results

Figure 3 shows the DSC analysis for the T6 and RRA treatment. Unlike the RRA treatment, the T6 curve shows two exothermic peaks at temperatures between 200 °C and 245 °C. The RRA curve in this region has only one small peak at about 240 °C. These peaks are results of  $\eta$  and  $\eta'$  precipitation from solid solution.<sup>14–16</sup> In the RRA curve, there exists only one peak related to  $\eta$  precipitation. This means that there are still a lot of elements in solid solution after T6 treatment suggesting that either time or temperature or both are not enough for diffusion and precipitation of the elements. As a result, the maximum strength has not achieved.

### 3.3 Stress corrosion cracking

Stress corrosion tests were performed according to the ASTM G139 standard for direct tension stress corrosion test method. Figure 4 shows the strength of T6 and RRA samples after exposure to corrosive 3.5 % sodium chloride solution without stressing and with a 207 MPa stress after 4 d. As expected, strength is dropped in both the T6 and RRA treatment after the SCC test. After the SCC test with 207 MPa constant stresses for 4 d in corrosive solution, the strength of RRA treated samples decreased from 612 MPa to 545 MPa. Accordingly, the strength of the T6 treated samples dropped from 547 MPa to 367 MPa. Calculating the results in percentages, gives us a better understanding of the strength reduction.

The test was conducted in corrosive solution in two stress conditions: un-stressed and with constant 207 MPa tension stress. The mechanical strength decreased for

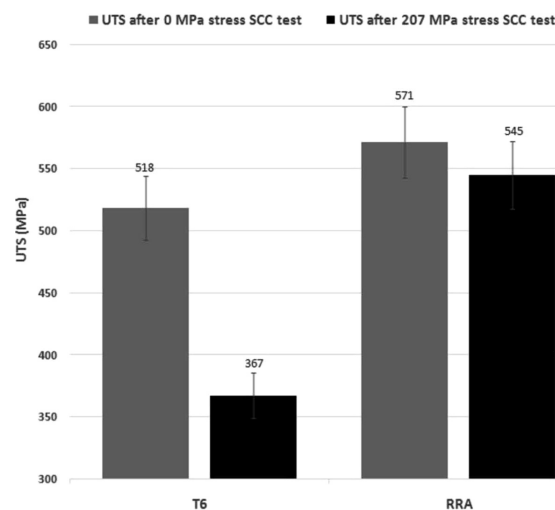


Figure 4: Direct tension stress corrosion cracking test after T6 and RRA treatment

both conditions. In order to better demonstrate the SCC results, it is most useful to calculate the remaining strength after SCC test and subtract the effect of corrosion methods other than SCC (such as pitting). To achieve this, the percentage of SCR ratio of remaining strength of stressed and unstressed samples is defined as stress corrosion resistance SCR. The SCR results of the alloy after the T6 and RRA heat treatments are shown in Figure 5. The remaining strengths of the unstressed samples after RRA and T6 treatments were 94.7 % and 93.3 %, respectively, which are not much different. It means that unstressed corrosion results for both treatments were almost identical. However, the remaining strength percentages in the constant stress condition were very different. The remaining strength percentage was 89 % for the RRA treatment and 68 % for the T6 treatment. The SCR for the RRA treatment was 95 % and for the T6 treatment it was 71 %. A significant im-

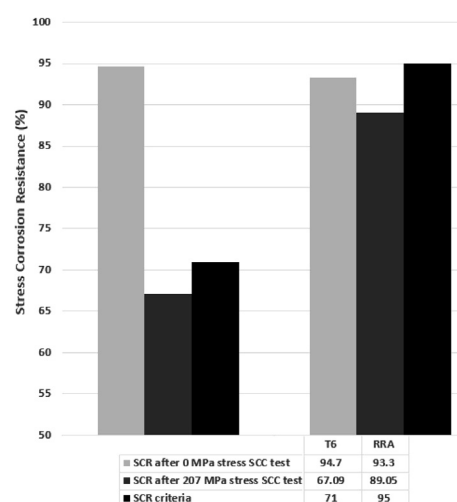


Figure 5: The SCR results of the alloy after T6 and RRA heat treatments

provement in the stress corrosion cracking has been achieved after the RRA treatment.

### 3.4 SEM and EDS analysis

The SEM micrographs of the T6 and RRA samples are shown in **Figures 6** and **7**.

Comparison of these two micrographs shows that, after the RRA treatment the grain-boundary precipitates have lost their continuity and divided to relatively larger particles. This is an essential factor for reducing the intergranular corrosion and consequently reducing the stress corrosion cracking. Two basic mechanisms of the SCC in 7000 series aluminum alloys have been proposed: anodic dissolution and cathodic dissolution (hydrogen embrittlement).<sup>6</sup> The precipitates in the grain boundaries have the electrode potential different from the Al matrix. This would result in the anodic dissolution and form defects in a chloride solution. The hydrogen atoms produced in the crack tip also lead to the hydrogen embrittlement in the grain boundaries. The large size and distance of the grain-boundary particles could decrease the anodic dissolution speed. These particles can also act as the trapping sites for atomic hydrogen and transform

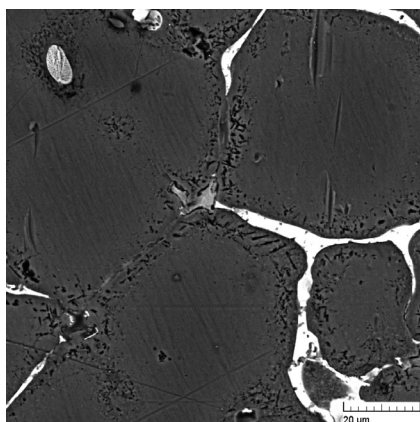


**Figure 6:** SEM micrograph of T6 sample showing continuous precipitates along the grain boundary

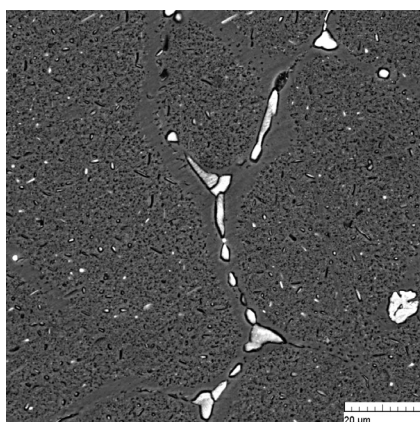


**Figure 7:** SEM micrograph of RRA sample showing less continuous precipitates along the grain boundary in comparison to the T6 sample

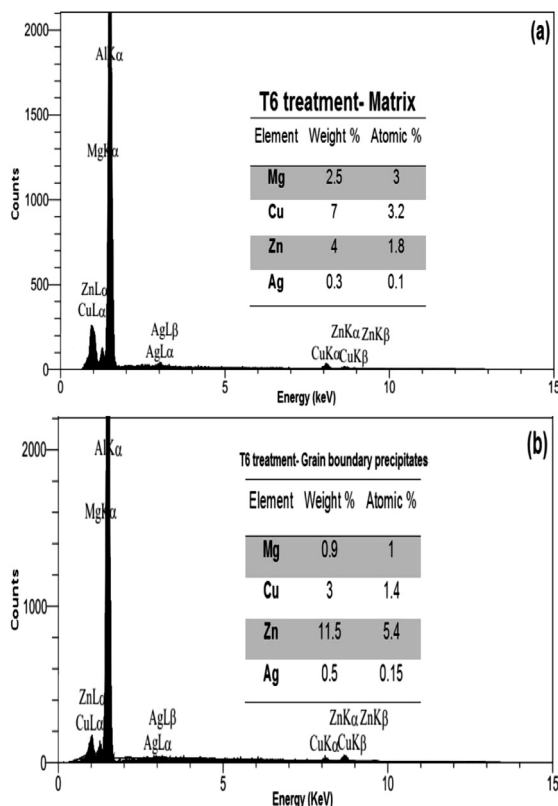


**Figure 8:** EDS analysis of T6 sample: a) matrix, b) grain boundary precipitates

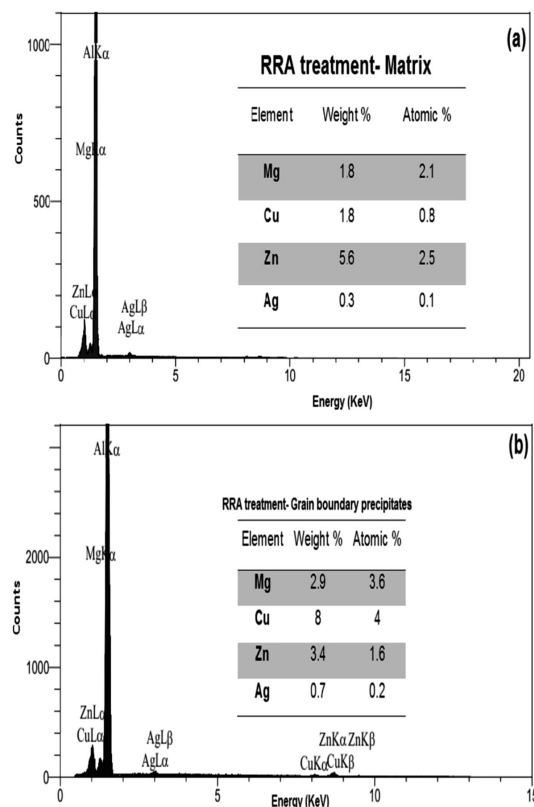


**Figure 9:** EDS analysis of RRA sample: a) matrix; b) grain boundary precipitates

them to molecular hydrogen bubbles to reduce the concentration of the atomic hydrogen at the grain boundaries. Both the size and distance of the grain-boundary precipitates in RRA treated alloy were larger than that in T6 treated alloy, therefore, the SCR criteria after RRA treatment is higher than the T6 treatment.

Another factor showing SCC resistance improvement after RRA treatment is the concentration changes of precipitates and matrix. The Zn and Cu atoms have opposite effects on the electrochemical properties of aluminum.<sup>17,18</sup> In a corrosive medium, the  $\eta$  phase in grain boundary is very active and anodic with respect to the matrix.<sup>19</sup> Cu enrichment of precipitates after RRA increases the electrode potential of the grain boundaries and decreases the activity of grain-boundary phases. **Figures 9** and **10** show the EDS analysis of the grain-boundary precipitates and matrix after RRA and T6 treatment. **Figure 8a** shows the Cu-rich matrix after the T6 treatment while according to **Figure 8b**, the precipitates are Zn-rich. After RRA treatment, the matrix depleted from Cu atoms and the grain boundary precipitates were Cu-enrichment (**Figures 9a** to **9b**). Large variations in concentration of solute atoms happen during the RRA treatment. Zn atoms have a higher diffusivity than Cu atoms and leave the precipitates first after the reversion stage.<sup>20</sup> As a result, the Zn content of the matrix increases and a corresponding increase in the Cu precipitate content happens. This happens reversely in the T6 treatment, where Zn incorporates first the precipitates, resulting in a high Zn content of the precipitates and high Cu matrix content. The Zn and Cu atoms have opposite effects on the electrochemical properties of aluminum.<sup>21</sup> A change in the corrosion behavior of the 7000 series aluminum alloy is related to changes in precipitate composition and particularly to a Cu enrichment of the precipitates.<sup>22</sup> During the RRA treatment, the precipitates enrich by Cu atoms (**Figure 9b**) and this factor as well as other factors improves the SCC resistance.

## 4 CONCLUSIONS

The mechanical strength of an Al–8.5Zn–2.1Mg–2Cu–0.2Ag (w/%) alloy after conventional T6 treatment was lower than the mechanical strength after RRA treatment.

SCR is a useful criteria to compare the SCC in Al–Zn–Mg–Cu alloys after various heat treatments. The SCR of the Al–8.5Zn–2.1Mg–2Cu–0.2Ag (w/%) alloy after conventional T6 treatment was 71 % and was 95 % after RRA treatment. The SCC improved significantly after the RRA treatment.

The SCC improvement after the RRA treatment related to Cu enrichment of the precipitates along with the discontinuities of the grain-boundary precipitates.

## 5 REFERENCES

- T. Dursun, C. Soutis, Recent developments in advanced aircraft aluminium alloys, *Materials & Design*, 56 (2014), 862–871, doi:10.1016/j.matdes.2013.12.002
- D. Liu, B. Xiong, F. Bian, Z. Li, X. Li, Y. Zhang, F. Wang, H. Liu, In situ studies of microstructure evolution and properties of an Al–7.5Zn–1.7Mg–1.4Cu–0.12Zr alloy during retrogression and reaging, *Materials & Design*, 56 (2014), 1020–1024, doi:10.1016/j.matdes.2013.12.006
- J. Li, N. Birbilis, C. Li, Z. Jia, B. Cai, Z. Zheng, Influence of retrogression temperature and time on the mechanical properties and exfoliation corrosion behavior of aluminium alloy AA7150, *Materials Characterization*, 60 (2009) 11, 1334–1341, doi:10.1016/j.matchar.2009.06.007
- R. Bucci, C. Warren, E. Starke, The Need for New Materials in Aging Aircraft Structures, *Journal of Aircraft*, 37 (2000) 1, 122–129, doi:10.2514/2.2571
- D. Feng, X. M. Zhang, S. D. Liu, and Y. L. Deng, Non-isothermal retrogression and re-ageing treatment schedule for AA7055 thick plate, *Materials & Design*, 60 (2014), 208–217, doi:10.1016/j.matdes.2014.03.064
- D. Najjar, T. Magnin, T. J. Warner, Influence of critical surface defects and localized competition between anodic dissolution and hydrogen effects during stress corrosion cracking of a 7050 aluminium alloy, *Materials Science and Engineering: A*, 238 (1997) 2, 293–302, doi:10.1016/S0921-5093(97)00369-9
- T. Burleigh, The postulated mechanisms for stress corrosion cracking of aluminum alloys: a review of the literature 1980–1989, *Corrosion*, 47 (1991) 2, 89–98, doi:10.5006/1.3585235
- R. Jones, D. Baer, M. Danielson, J. Vetrano, Role of Mg in the stress corrosion cracking of an Al–Mg alloy, *Metallurgical and Materials Transactions A*, 32 (2001) 7, 1699–1711, doi:10.1007/s11661-001-0148-0
- E. Pugh, Progress toward understanding the stress corrosion problem, *Corrosion*, 41 (1985) 9, 517–526, doi:10.5006/1.3583022
- A. Sedriks, J. Green, D. Novak, Corrosion processes and solution chemistry within stress corrosion cracks in aluminum alloys, *Proceedings of NACE*, 1971, 569–575
- T. Tsai, T. Chuang, Role of grain size on the stress corrosion cracking of 7475 aluminum alloys, *Materials Science and Engineering: A*, 225 (1997) 1–2, 135–144, doi:10.1016/S0921-5093(96)10840-6
- T. Pardoen, D. Dumont, A. Deschamps, Y. Brechet, Grain boundary versus transgranular ductile failure, *Journal of the Mechanics and Physics of Solids*, 51 (2003) 4, 637–665, doi:10.1016/S0022-5096(02)00102-3
- ASTM 139:2005(G)- Standard test method for determining stress-corrosion cracking resistance of heat-treatable aluminum alloy products using breaking load method, ASTM International, West Conshohocken
- K. Ghosh, N. Gao, Determination of kinetic parameters from calorimetric study of solid state reactions in 7150 Al–Zn–Mg alloy, *Transactions of Nonferrous Metals Society of China*, 21 (2011) 6, 1199–1209, doi:10.1016/S1003-6326(11)60843-1
- T. Marlaud, A. Deschamps, F. Bley, W. Lefebvre, B. Baroux, Influence of alloy composition and heat treatment on precipitate composition in Al–Zn–Mg–Cu alloys, *Acta Materialia*, 58 (2010) 1, 248–260, doi:10.1016/j.actamat.2009.09.003
- J. G. Tang, H. Chen, X. M. Zhang, S. D. Liu, W. J. Liu, H. Ouyang, H. P. Li, Influence of quench-induced precipitation on aging behavior of Al–Zn–Mg–Cu alloy, *Transactions of Nonferrous Metals Society of China*, 22 (2012) 6, 1255–1263, doi:10.1016/S1003-6326(11)61313-7
- R. W. Revie, H. H. Uhlig, *Uhlig's corrosion handbook*: vol. 51, John Wiley & Sons, Hoboken 2011
- G. Silva, B. Rivolta, R. Gerosa, U. Derudi, Study of the SCC Behavior of 7075 Aluminum Alloy After One-Step Aging at 163 °C, *Journal of Materials Engineering and Performance*, 22 (2013) 1, 210–214, doi:10.1007/s11665-012-0221-4



M. SHAKOURI et al.: DEVELOPMENT OF A HEAT TREATMENT FOR INCREASING THE MECHANICAL PROPERTIES ...

- <sup>19</sup> S. Maitra, G. English, Mechanism of localized corrosion of 7075 alloy plate, *Metallurgical and Materials Transactions A*, 12 (1981) 3, 535–541, doi:10.1007/BF02648553
- <sup>20</sup> H. Bakker, H. Bonzel, C. Bruff, M. Dayananda, W. Gust, J. Horvath, I. Kaur, G. Kidson, A. LeClaire, H. Mehrer, *Diffusion in solid metals and alloys/Diffusion in festen metallen und legierungen*: vol. 26, Springer, Berlin 1990
- <sup>21</sup> E. Hollingsworth, H. Hunsicker, Corrosion of aluminum and aluminum alloys, *ASM Handbook*, 13 (1987), 583–609
- <sup>22</sup> J. T. Staley, S. Byrne, E. Colvin, K. Kinnear, Corrosion and stress-corrosion of 7xxx-w products, *Materials Science Forum*, 217 (1996), 1587–1592, doi:10.4028/MSF.217-222.1587

CORROSION RESISTANCE OF AS-PLATED AND HEAT-TREATED  
ELECTROLESS DUBLEX Ni-P/Ni-B-W COATINGSKOROZIJSKA ODPORNOST PLATIRANIH IN NEELEKTRIČNO  
TOPOLOTNO OBDELANIH DUPEKS Ni-P/Ni-B-W PREVLEKBehiye Yüksel<sup>1</sup>, Garip Erdogan<sup>2</sup>, Fatih Erdem Bastan<sup>2</sup>, Rasid Ahmed Yıldız<sup>3</sup><sup>1</sup>Istanbul Aydin University, Mechanical Engineering Department, 34668 Istanbul, Turkey<sup>2</sup>Sakarya University, Engineering Faculty, Department of Metallurgy and Materials Engineering, 54187 Sakarya, Turkey<sup>3</sup>TU Istanbul, Mechanical Engineering Faculty, 34437 Istanbul, Turkey  
behiyeyuksel@aydin.edu.tr*Prejem rokopisa – received: 2016-10-20; sprejem za objavo – accepted for publication: 2017-03-10*

doi:10.17222/mit.2016.304

In this study, Ni-P/Ni-B-W duplex coatings were deposited on carbon steel substrates (AISI 1020) using the electroless plating process and their microstructure and corrosion properties were systematically evaluated based on different heat-treatment temperatures. Both, the surface morphology and cross-sectional morphology of the Ni-P/Ni-B-W coatings were studied using a scanning electron microscope (SEM), while X-ray diffraction (XRD) was applied for examining the structural modifications. The amorphous coating began to crystallize at a heat-treatment temperature of 350 °C. Potentiodynamic polarization measurements were carried out in an aqueous medium containing 3.5 % NaCl for evaluating the corrosion resistance of as-plated and heat-treated duplex coatings. The corrosion potentials of duplex coatings were observed to shift toward more positive values with increased heat-treatment temperatures. Depending on the heat-treatment temperature, it was identified that the crystallized duplex coatings generally had better corrosion resistance than the amorphous coating.

Keywords: Ni-P/Ni-B-W coating, corrosion, heat treatment

V študiji so bile dvojne Ni-P/Ni-B-W prevleke nanešene na substrate iz ogljikovega jekla (AISI 1020) s postopkom neelektričnega platiranja. Sistematično so bile ocenjene mikrostruktura ter korozijske lastnosti izdelanih prevlek, glede na različne temperature toplotne obdelave. Morfologije površin in profili izdelanih Ni-P/Ni-B-W prevlek so bili pregledani z vrstičnim elektronskim mikroskopom (SEM), medtem ko so bile z rentgensko difrakcijsko analizo (XRD) ugotovljene strukturne spremembe. Amorfná prevleka je začela kristalizirati pri temperaturi toplotne obdelave 350 °C. Korozijska odpornost platiranih in toplotno obdelanih dupleks prevlek je bila ocenjena s pomočjo meritev potenciodinamične polarizacije v 3,5 % vodni raztopini NaCl. Opazovali so korozijske potenciale dupleks prevlek, da bi dobili bolj pozitivne vrednosti z zvišanimi temperaturami toplotne obdelave. Ugotovljeno je bilo, da imajo kristalizirane dupleks prevleke na splošno boljše korozijsko odpornost kot amorfne prevleke.

Ključne besede: Ni-P/Ni-B-W dvojna prevleka, korozija, toplotna obdelava

## 1 INTRODUCTION

Studied for the first time in 1946 by Brenner and Riddell, the electroless plating process has been used in many industrial applications because of its superior characteristics over electroplating, such as the ability to plate insulation materials and having a homogeneous coating-thickness distribution.<sup>1</sup> Among electroless coating types, electroless nickel coating is the most popular for having good hardness, wear and corrosion resistance properties.<sup>2</sup> If the electroless Ni coating family is reviewed, besides pure Ni coatings, Ni-P and Ni-B coatings deposited using reducing agents such as hypophosphite, borohydride or dimethylamine borane stand out. The major advantages of Ni-P coatings are their low cost, high corrosion resistance and easy process control.<sup>3</sup> Nonetheless, a borohydride reduced nickel coating is harder and has higher wear resistance than tool steel and hard chrome coatings.<sup>4,5</sup> On the other hand, some studies – although they are limited in number – have highlighted the addition of tungsten to this coating system for in-

creasing its corrosion resistance, which is lower than that of a Ni-P coating.<sup>6–9</sup> As a result of the co-deposition of this refractory material (which cannot be reduced in an aqueous solution as metallic tungsten) together with iron group metals, developing coatings with attractive corrosion and tribological properties is possible.<sup>10–12</sup> Recently, research for obtaining multilayer coatings to increase existing coating corrosion resistance to higher levels has also been conducted.<sup>13,14</sup>

The aim of the present study was to evaluate the effect of different heat-treatment temperatures on the microstructure and corrosion properties of electroless Ni-P/Ni-B-W coatings. To the best of our knowledge, no others studies are available on this topic.

## 2 EXPERIMENTAL PART

For this experiment, 10 mm × 10 mm × 60 mm plain carbon steel (AISI 1020) plates were used as a substrate material for developing Ni-P/Ni-B-W duplex coatings. Prior to the plating process, the surfaces of all the

samples were mechanically cleaned (up to 1200 grade) and then soaked in trichloroethylene and cleaned with detergent in an ultrasonic bath at 70 °C. Finally, sample surfaces were activated in 30 % of volume fractions. HCl for two minutes and then rinsed in distilled water. The cleaned substrates were then soaked in Ni-P and Ni-B-W electroless plating baths for two hours, respectively.

Reagent-grade chemicals and distilled water were used for the preparation of all the electrolytes and the pH was adjusted to  $4.8 \pm 0.2$  and  $13.5 \pm 0.2$  with  $\text{H}_2\text{SO}_4$  or NaOH in Ni-P and Ni-B-W plating baths, respectively. The temperature of the baths was maintained at  $90 \pm 2$  °C for Ni-P and  $88 \pm 2$  °C for Ni-B-W.

Deposition of Ni-P and Ni-B-W was carried out in an aqueous bath containing 15 g/L  $\text{NiSO}_4 \cdot 6\text{H}_2\text{O}$ , 26 g/L  $\text{Na}_2\text{H}_2\text{PO}_4 \cdot \text{H}_2\text{O}$ , 13 g/L  $\text{NaC}_2\text{H}_3\text{O}_2$ , 12 mL/L HF and 8 g/L  $\text{NH}_4\text{HF}_2$  for the Ni-P coating, and 24 g/L NiCl<sub>2</sub>, 60 mL/L EDTA, 26.5 g/L KOH, 120 g/L  $\text{NaBH}_4$ , 263 g/L NaOH, 2.6 g/L  $\text{PbWO}_4$ , 13 g/L EDTA and 40 g/L  $\text{Na}_2\text{WO}_4 \cdot 2\text{H}_2\text{O}$  for Ni-B-W coatings, respectively.

The coated specimens were heat treated at 250 °C, 300 °C, 350 °C and 650 °C for 1 h each at a heating rate of 5 °C/min in an air-circulated furnace, followed by slow furnace cooling to room temperature.

The composition of the duplex coatings was determined by energy-dispersive X-ray analysis (EDX) using a Link Analytical QX-2000 attached to the SEM apparatus. The crystal structures of the duplex coatings were examined using a Philips PW 3710 grazing incidence x-ray diffractometer ( $\text{Cu-K}\alpha$  radiation). A Jeol JSM-7000F FE-SEM was used to characterize the microstructures and morphology of the coatings. The corrosion behavior was investigated using a PGZ 301 Dynamic Voltammetry and VoltaMaster4 software.

Electrochemical experiments were carried out in a 3.5 % NaCl aqueous solution in a three-electrode cell at room temperature. In this cell, a platinum electrode was used as a counter electrode and a saturated calomel electrode was used as a reference electrode; the duplex coating was used as a working electrode and by masking

with silicon, only a 1 cm<sup>2</sup> surface area was left on the samples for exposure to the electrolyte. The dynamic potential scanning technique was used for obtaining the polarization curves of duplex coating samples. Prior to the potentiodynamic measurement, samples were held for approximately 15 min in the electrolyte and then electrode potential was raised from -600 mV to +200 mV at a rate of 10 mV/min.

### 3 RESULTS

The XRD patterns of the as-plated and heat-treated Ni-P/Ni-B-W coatings, and their chemical compositions are in **Figure 1** and in **Table 1**. SEM micrographs of Ni-P/Ni-B-W coatings before and after the heat treatments are in **Figure 2**.

**Table 1:** Chemical compositions of the Ni-P/Ni-B-W duplex coatings

Type of coating	Ni (w/%)	P (w/%)	B (w/%)	W (w/%)
Ni-P	87.27	12.73	-	-
Ni-B-W	87.45	-	7.86	4.69

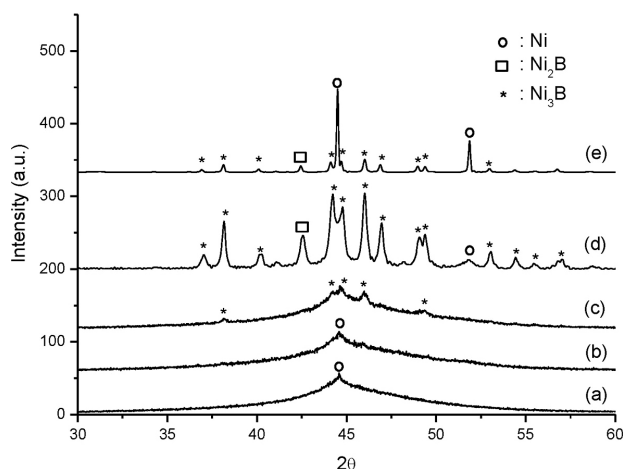


**Figure 1:** XRD spectra for a): as-plated Ni-P/Ni-B-W, b) 250 °C, c) 300 °C, d) 350 °C and e) 650 °C

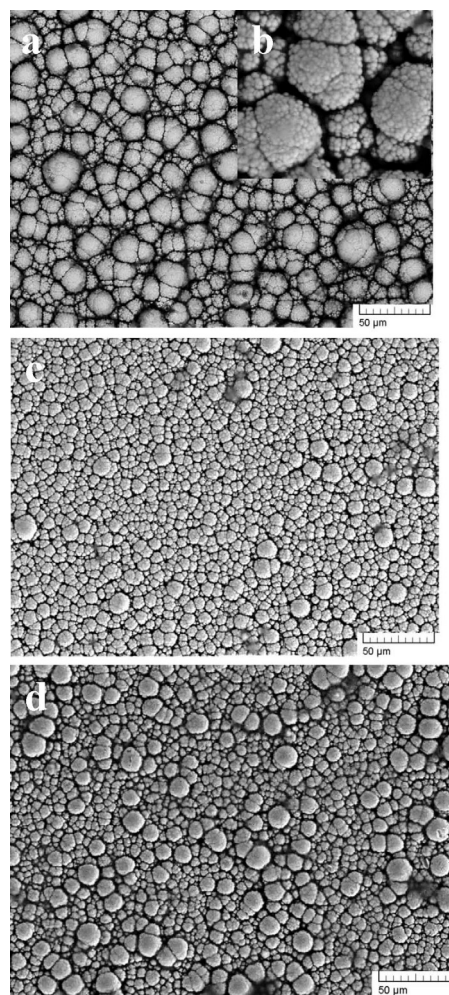


**Figure 2:** Surface morphology of duplex coating a), b) as-plated Ni-P/Ni-B-W, c) heat treated at 300 °C, d) heat treated at 650 °C



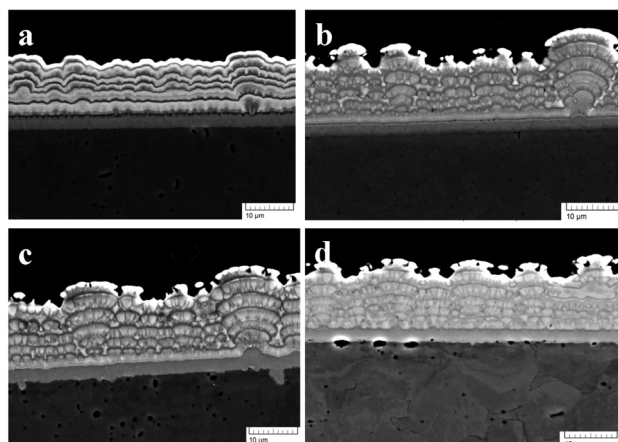


**Figure 3:** Cross-section of Ni-P/Ni-B-W duplex coating: a) as-plated, b) heat treated at 250 °C c) heat treated at 350 °C, d) heat treated at 650 °C

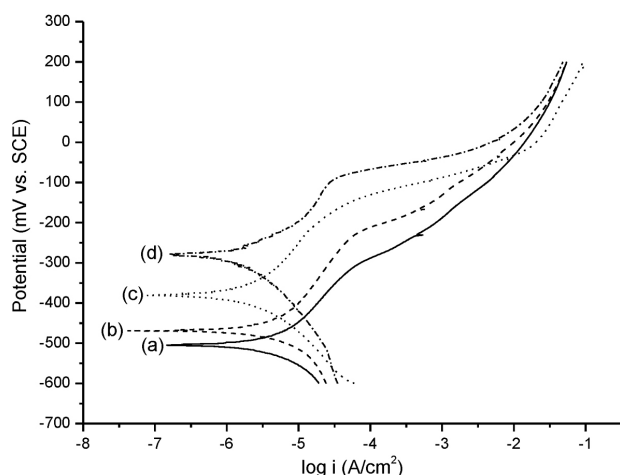


**Figure 4:** Polarization curves in a 3.5 % NaCl aqueous medium of as-plated and heat-treated Ni-P/Ni-B-W coatings: a) as-plated NiP/NiBW, b) heat treated at 300 °C, c) heat treated at 350 °C d) heat treated at 650 °C

The cross-sections of the Ni-P/Ni-B-W duplex coatings are shown in **Figure 3**.

Potentiodynamic curves of as-plated and heat-treated Ni-P/Ni-B-W coatings at different temperatures obtained in a 3.5 % NaCl aqueous medium are shown in **Figure 4**.

The changes in the corrosion current density ( $I_{\text{corr}}$ ) values with heat treatment are given in **Table 2**.

**Table 2:** Corrosion resistance of as-plated and heat-treated Ni-P/Ni-B-W duplex coatings at different temperatures in 3.5 % NaCl solution

NiP/NiBW	$I_{\text{corr}}$ ( $\mu\text{A}/\text{cm}^2$ )	$E_{\text{corr}}$ (mV)
As-plated	$1.55 \pm 0.59$	$-506 \pm 32$
300 °C	$1.70 \pm 0.41$	$-470 \pm 23$
350 °C	$0.71 \pm 0.20$	$-382 \pm 18$
650 °C	$0.57 \pm 0.09$	$-280 \pm 11$

The surface morphologies of the as-plated sample and heat-treated sample at 650 °C following potentiodynamic polarization measurements are shown in **Figure 5**.

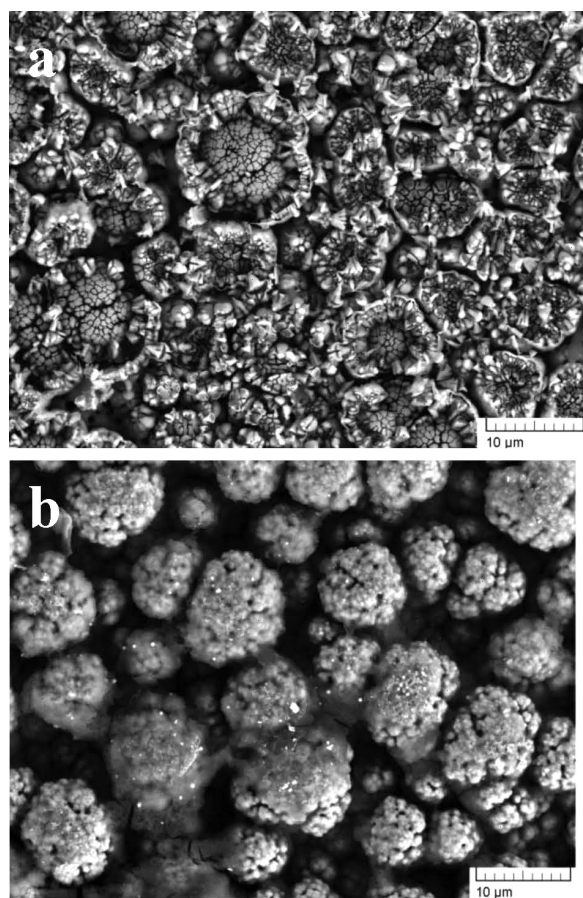


**Figure 5:** Surface morphology of NiP/NiBW duplex coatings detected by SEM after potentiodynamic measurement: a) as-plated, b) heat treated at 650 °C

The corrosion current density and corrosion potential values obtained by Tafel interpolation are shown in **Table 3**.

The corrosion current density and corrosion potential values obtained by Tafel interpolation are shown in **Table 3**.

**Table 3:** Corrosion resistance of substrate and Ni-B-W and Ni-P/Ni-B-W duplex coatings heat treated at 650 °C in 3.5 % NaCl solution

Sample	$I_{\text{corr}}$ ( $\mu\text{A}/\text{cm}^2$ )	$E_{\text{corr}}$ (mV)
Carbon steel substrate	$4.59 \pm 1.01$	$-598 \pm 46$
NiBW	$3.40 \pm 0.35$	$-298 \pm 17$
NiP/NiBW	$0.57 \pm 0.09$	$-280 \pm 11$

**Figure 6** shows the polarization curves of the Ni-B-W and duplex Ni-P/Ni-B-W coatings heat treated at 650 °C and the steel substrate obtained in a 3.5 % NaCl aqueous medium.

#### 4 DISCUSSION

The Ni-P/Ni-B-W coating diffraction patterns up to 300 °C reveal a single broad peak indicating an amorphous coating structure under these conditions (**Fig-**



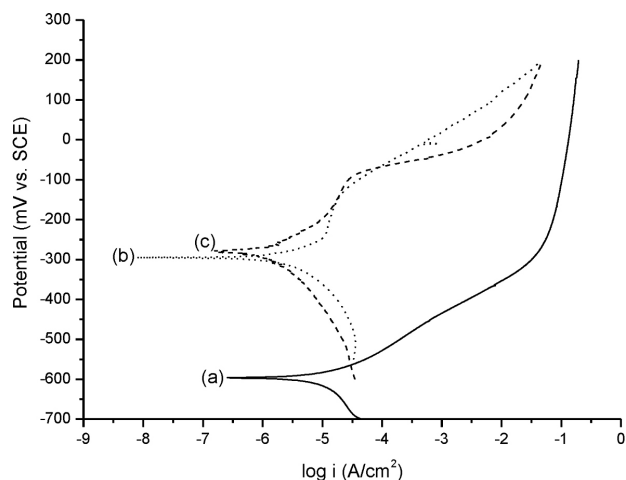


**Figure 6:** Polarization curves: a) steel substrate, b) Ni-B-W coating heat treated at 650 °C, c) duplex Ni-P/Ni-B-W coating heat treated at 650 °C

ure 1). For heat-treatment temperatures up to 300 °C, the duplex coating preserved its amorphous structure. However, after heat treatment at and above 300 °C, the diffraction patterns showed the formation of  $\text{Ni}_3\text{B}$  intermetallic crystals. For the higher heat-treatment temperatures up to 650 °C, formation of the nickel borides progressively increased. Drovosekov et al., reported chemical bond formations between boron and tungsten in the Ni-B-W coating system. However, the major nickel borides formed during the heat treatments might have prevented the formation of the B-W bond.<sup>9,15</sup> In other words, the quantity of the boron in the coating was high enough to prevent the formation of Ni-W compounds in the structure.<sup>16</sup>

SEM micrographs of the Ni-P/Ni-B-W coatings before and after the heat treatments showed the formation of typical spherical nodular structures (Figure 2). Each nodule appears to be formed by the unification of many grains existing as colonies (Figure 2b), similar to the case suggested by S. Ruan et al.<sup>17</sup> Some microcracks were noticeable on the surfaces of the as-plated Ni-P/Ni-B-W samples. The microcracks may be due to the internal stress caused by the relatively larger tungsten atoms in the coating structure.<sup>18,19</sup>

With the heat treatments, the structure progressively crystallized and, as consequence, a substantial reduction of the microcracks was noticed (Figure 2c and 2d). In a Ni-B-W coating system, W atoms may selectively exist at the boundaries of the nodules, from there, they may segregates to the coating surface, during the heat treatments.<sup>16,17</sup> This process may decrease the internal stress inside the coating, resulting in a substantial decrease of the microcracks on the coating surface.

The thickness of the Ni-P coating in the duplex coating system was measured as 2  $\mu\text{m}$ , while the average thickness of the Ni-B-W (the other coating in the system) was measured as 11  $\mu\text{m}$  (Figure 3). On the other hand, it was obvious that the nodular structure seen in

the surface morphology of the Ni-B-W coating showed columnar growth starting from the Ni-P layer to the topmost surface of the coating (Figure 3a). Furthermore, it was observed that adherence of the Ni-P coating to the substrate was good and there was no pore formation between the substrate and Ni-P coating. Pores seen in the interface of Ni-P/Ni-B-W, in addition to pores partially observed inside the Ni-B-W coating had a columnar structure and they were considered to have been formed due to the capturing of released hydrogen – even if in small amounts – during the oxidation reaction of sodium borohydride used as a the boron source.<sup>5</sup> The pores disappear with increasing heat-treatment temperatures. This may be a result of the diffusion of hydrogen atoms to the surface. They may promote better crystallization of the coating and ease the formation of the  $\text{Ni}_3\text{B}$  and  $\text{Ni}_2\text{B}$  phases (Figure 3b and 3c). After 650 °C heat treatment the major phase of the coating was noticed to be  $\text{Ni}_3\text{B}$ . At that stage adherence between the coatings reached its best level, while the Ni-B-W coating showed columnar grains with a denser structure (Figure 3d).

As Figure 4, a difference of approximately 220 mV was detected between corrosion potentials ( $E_{\text{corr}}$ ) of as-plated and 650 °C heat-treated duplex coatings. This is the shifting of  $E_{\text{corr}}$  values of the coatings toward nobler values with increased heat treatments applied to the coatings. The anodic branch of the polarization curve of the coating before heat treatment showed the breakdown potential at values around -310 mV (Figure 4a). But the current density increased at a constant rate, indicating that the unstable passive film formation on the coating has disappeared rapidly. For heat treatment at 300 °C, the breakdown potential was observed to shift toward -220 mV. At 300 °C, which is the onset temperature of crystallization, corrosion potential shifted towards a positive end approximately 40 mV, compared to the as-plated sample. At 350 °C, crystallization was nearly completed and the corrosion potential had shifted towards more positive values. However, the breakdown potential was observed (as with other samples) at around -180 mV. Nonetheless, it was detected that the current density of this sample became higher as the potential value increased compared with that for the to as-plated and heat-treated samples at 300 °C. For the heat treatment at 650 °C, a passive film formation on the coating surface was seen at around -190 mV, suggesting that corrosion rate was restrained at such potential range. However, as this protective film began to dissolve at around -90 mV, a steep increase in the current density was observed.

The major reason for the difference between the corrosion resistance of as-plated and heat-treated Ni-P/Ni-B-W coatings exposed to chloride ions was undoubtedly associated with the transformation of the microstructure from an amorphous to a crystalline morphology. The main reason for having a higher  $E_{\text{corr}}$  value the heat-treated coating at 300 °C (where an amorphous

structure still prevailed) compared to the as-plated sample was the result of the borides formed during the onset of crystallization. The heat-treated sample at 350 °C (where the microstructure had completely been transformed to a crystalline structure) had a higher corrosion resistance compared to the sample heat-treated at 300 °C.<sup>20</sup> On the other hand, it is a known fact that corrosion resistance generally increases with addition of tungsten to a electroless nickel-boron coating system, because of the tendency to form an oxide film on the surfaces.<sup>7,18</sup> However, as seen in **Figure 4**, the corrosion resistance of the as-plated Ni-P/Ni-B-W sample having a nodular structure did not increase, with the addition of tungsten. This is because the tungsten atoms were stuck in the colony boundaries, not to be segregated to the surfaces during the corrosion process and therefore, could not be oxidized to promote the formation of a mixed oxide film. However, depending on the increased heat treatment temperatures segregation of W atoms toward surfaces at 650 °C was more likely to occur. The mixed oxide film a passive zone formed this way may be the main reason for the substantial decrease of the current density as observed here.

It can be seen that uniform corrosion occurred on the surface of the as-plated sample in the amorphous structure that has the lowest corrosion resistance (**Figure 5a**). Conversely, on the surface of the heat-treated sample at 650 °C complete crystallization were noted and the pits (indicated by arrows) in the grains within the colonies were observed (**Figure 5b**).

To interpret the effect of the duplex coating on corrosion resistance, the potentiodynamic polarization measurements of the Ni-P/Ni-B-W and Ni-B-W coatings, as well as which were deposited under the same process conditions and heat-treated at 650 °C, and carbon steel substrate were studied (**Table 3**).

As can be observed from **Figure 6**, while the Ni-B-W coating and the duplex coating almost had the same corrosion potential, more positive values at about 300 mV, compared with that of the substrate. Among the coating studied the duplex coating has the lowest corrosion current density. The anodic branches of polarization curves of both the duplex and the Ni-B-W coatings have a passive zone, and both coatings had an  $E_{pit}$  value of approximately -90 mV. Additionally, the current density of the Ni-B-W coating at a constant rate increases, depending on the increased potential value. On the other hand, the anodic branch of the duplex coating indicated that an entrance to a second passive zone at approximately 20 mV. This passive zone may be related to the existence of Ni-P in the duplex coating. A similar interpretation was reported by Zhang et al. for the corrosion of Ni-B-W surfaces.<sup>14</sup> In general, corrosion starts at the outermost surface of the substrate and proceed inward. However, the stable passive film formed on the Ni-P layer on the substrate may act as a barrier for corrosion propagation, causing the duplex coating to have better

corrosion resistance than the single-layer Ni-B-W coating.

## 5 CONCLUSIONS

The effect of heat treatments on the corrosion resistance of a Ni-P/Ni-B-W duplex coating deposited on carbon steel was studied. The Ni-P/Ni-B-W coatings have an amorphous structure for a heat treatments up to 300 °C. The coatings start to crystallize at about 350 °C and completed at about 650 °C with the major phases being the nickel borides. The heat treatment, besides causing nickel boride formation within Ni-B-W, also caused obtaining a denser Ni-P/Ni-B-W coating when increasing heat treatment temperature.

The corrosion resistance of the duplex coating increases substantially with increasing the heat treatment temperature. The duplex coating and the single-layer Ni-B-W coating heat-treated at 650 °C indicated higher corrosion resistance as compared to that of steel substrate. When these two coatings were compared in terms of corrosion resistance, the duplex coating showed better performance.

## 6 REFERENCES

- A. Brenner, G. Riddell, Nickel Plating on Steel by Chemical Reduction, *J. Res. Nat. Bur. Std.*, 37 (1946), 31–35
- J. Sudagar, J. Lian, W. Sha, Electroless nickel, alloy, composite and nano coatings-A critical review, *J. Alloys Compd.*, 571(2013), 183–204, doi:10.1016/j.jallcom.2013.03.107
- Y. F. Shen, W. Y. Xue, Z. Y. Liu, L. Zuo, Nanoscratching Deformation and Fracture Toughness of Electroless Ni-P Coatings, *Surf. Coat. Technol.*, 205 (2010), 632–640, doi:10.1016/j.surfcoat.2010.07.066
- K. M. Gorbunova, M. V. Ivanov, V. P. Moiseev, Electroless Deposition of Nickel-Boron Alloys – Mechanism of Process, Structure, and Some Properties of Deposits, *J. Electrochem. Soc.*, 120 (1973), 613–618, doi:10.1149/1.2403514
- R. N. Duncan, T. L. Arney, Operation and Use of Sodium-Borohydride-Reduced Electroless Nickel, *Plat. Surf. Finish.*, 71 (1984) 12, 49–54
- R. A. C. Santana, S. Prasad, A. R. N. Campos, F. O. Araujo, G. P. DA Silva, P. Lima-Neto, Electrodeposition and Mechanical Properties of Ni-W-B Composites from Tartrate Bath, *Prot Met Phys Chem.*, 46 (2010) 1, 117–122, doi:10.1134/S207020511001017X
- M. G. Hosseini, M. Abdolmaleki, H. Ebrahimzadeh, S. A. Seyed Sadjadi, Effect of 2-Butyne-1, 4-Diol on the Nanostructure and Corrosion Resistance Properties of Electrodeposited Ni-W-B Coatings, *Int. J. Electrochem. Sci.*, 6 (2011) 4, 1189–1205
- T. Osaka, N. Takano, T. Kurokawa, T. Kaneko, K. Ueno, Characterization of chemically-deposited NiB and NiWB thin films as a capping layer for ULSI application, *Surf. Coat. Technol.*, 169–170 (2003), 124–127, doi:10.1016/S0257-8972(03)00186-5
- G. Graef, K. Anderson, J. Groza, A. Palazoglu, Phase evolution in electrodeposited Ni-W-B alloy, *Mater. Sci. Eng.*, B41 (1996), 253–257, doi:10.1016/S0921-5107(96)01656-X
- E. Lassner, W. D. Schubert, Tungsten: Properties, Chemistry, Technology of the Element, Alloys, and Chemical Compounds, Kluwer Academic, New York, 1999
- E. Beltowska-Lehman, Kinetics of Induced Electrodeposition of Alloys Containing Mo from Citrate Solutions, *Phys. Stat. Sol.*, 5 (2008) 11, 3514–3520, doi:10.1002/pssc.200779404

B. YÜKSEL et al.: CORROSION RESISTANCE OF AS-PLATED AND HEAT-TREATED ELECTROLESS ...

- <sup>12</sup> A. I. Aydeniz, A. Göksenli, G. Dil, F. Muhaffel, C. Calli, B. Yüksel, Electroless Ni-B-W Coatings for Improving Hardness, Wear And Corrosion Resistance, MTAEC9, 47 (2013) 6, 803–806
- <sup>13</sup> T. S. N. Sankara Narayanan, K. Krishnaveni, S. K. Seshadri, Electroless Ni–P/Ni–B Dublex Coatings: Preparation and Evaluation of Microhardness, Wear and Corrosion Resistance, Mater. Chem. Phys., 82 (2003), 771–779, doi:10.1016/S0254-0584(03)00390-0
- <sup>14</sup> W. X. Zhang, Z. H. Jiang, G. Y. Li, Q. Jiang, J. S. Lian, Electroless NiP/NiB Dublex Coatings For Improving The Hardness and The Corrosion Resistance of AZ91 D Magnesium Alloy, Appl. Surf. Sci., 254 (2008), 4949–4955, doi:10.1016/j.apsusc.2008.01.144
- <sup>15</sup> A. B. Drovosekov, M.V. Ivanov, V. M. Krutskikh, E. N. Lubnin, Y. M. Polukarov, Chemically Deposited Ni-W-B Coatings: Composition, Structure and Properties, Prot. Met., 41(2005) 1, 55–62, doi:10.1007/s11124-005-0008-1
- <sup>16</sup> F. Z. Yang, Z. H. Ma, L. Huang, S. K. Xu, S. M. Zhou, Electrodeposition and Properties of an Amorphous Ni-W-B Alloy before and after Heat Treatment, Chin. J. Chem., 24 (2006), 114–118, doi:10.1002/cjoc.200690004
- <sup>17</sup> S. Ruan, C. A. Schu, Mesoscale Structure and Segregation in Electrodeposited Nanocrystalline Alloys, Scripta Mater., 59 (2008) 11, 1218–1221, doi:10.1016/j.scriptamat.2008.08.010
- <sup>18</sup> R. A.C. Santana, S. Prasad, A. R. N. Campos, F. O. Araújo, G.P. Silva, P. Lima-Neto, Electrodeposition and Corrosion Behaviour of a Ni–W–B Amorphous Alloy, J. Appl. Electrochem., 36 (2006), 105–113, doi:10.1007/s10800-005-9046-2
- <sup>19</sup> R. A. Yildiz, A. Göksenli, B. Yüksel, F. Muhaffel, A. Aydeniz, Effect of Annealing Temperature on The Corrosion Resistance of Electroless Produced Ni-B-W Coatings, Adv Mat Res., 652 (2013), 263–268, doi:10.4028/www.scientific.net/AMR.651.263
- <sup>20</sup> Z. Z. Hamid, H. B. Hassan, A. M. Attyia, Influence of Deposition Temperature and Heat Treatment on The Performance of Electroless Ni–B Films, Surf. Coat. Technol., 205 (2010) 7, 2348–2354, doi:10.1016/j.surfcoat.2010.09.025

# SHORT-TERM CREEP OF P91 HEAT-RESISTANT STEELS AT LOW STRESSES AND AN INSTANTANEOUS-STRESS-CHANGE TESTING

## KRATKOTRAJNO LEZENJE TOPLOTNO ODPORNEGA JEKLA P91 PRI NIZKIH NAPETOSTIH IN NENADNI MENJAVI NAPETOSTI OBREMENJEVANJA

Jiang Zhe, Shen Junjie, Zhao Pengshuo

Tianjin University of Technology, Tianjin Key Laboratory for Advanced Mechatronic System Design and Intelligent Control, National Demonstration Center for Experimental Mechanical and Electrical Engineering Education, 391 Binshui Road, Xiqing District, Tianjin, China  
sjj1982428@sina.com, j211209977@live.com

*Prejem rokopisa – received: 2016-11-20; sprejem za objavo – accepted for publication: 2017-03-21*

doi:10.17222/mit.2016.305

For the short-term creep behavior to be evaluated and the creep mechanism of P91 heat-resistant steels at low stresses and high temperatures to be clarified, stress-change testing was conducted with a “helicoïdal-spring creep test” demonstrating a high strain resolution. The creep deformation consists of the primary creep stage, whereas no secondary creep stage was observed. Blackburn’s law was suggested to be the best choice for a short-term-creep-behavior description because it provides a good representation of an experimental creep curve. An anelastic backflow at a low stress was confirmed, following a high reduction in the stress. The absolute value of the instantaneous strain for a load increase was equal to the value for a load decrease and the creep of the P91 steels at low stresses might have been controlled by the viscous glide of dislocations.

Keywords: P91 heat-resistant steel, creep, anelastic, stress change

Da bi bilo moč oceniti kratkotrajno lezenje in njegov mehanizem toplotno obstojnega jekla P91 pri nizkih napetostih in visokih temperaturah, so bili izvedeni preizkusi spremembe napetosti z uporabo t.i. testa spiralne vzmeti, ki omogoča veliko ločljivost deformacije. Deformacija lezenja sestoji iz primarne in sekundarne faze lezenja, vendar sekundarne faze niso analizirali oz. opazovali. Blackburnov zakon je najbolj uporaben zakon za opis obnašanja jekla med kratkotrajnim lezenjem, ker se z njim najbolj približamo rezultatom, dobljenim z eksperimenti. Neelastični povratni tok pri nizki napetosti je bil potrjen z večjim zmanjšanjem napetosti. Zaradi absolutne vrednosti trenutne deformacije za dano obremenitev je bil narastek deformacije enak zmanjšanju obremenitve, medtem ko je lezenje pri nizkih napetostih jekla P91 kontrolirano z viskoznim drsenjem dislokacij.

Ključne besede: P91 jeklo za delo v vročem, lezenje, neelastičnost, sprememba napetosti

## 1 INTRODUCTION

The P91 ferritic heat-resistant steel is utilized for the material production of thermal-power-plant components, which are exposed to elevated temperatures for extensive periods. This requires that the P91 structural materials resist creep deformation at both high temperatures and low stresses. The creep strength obtained with the extrapolation method based on the data of the creep deformation at a high stress is higher than the true creep strength under these conditions (at low stresses).<sup>1,2</sup> The creep-strength degradation is not only based on the microstructural degradation<sup>3–6</sup>, but it is also related to the change in the creep mechanism.<sup>7–9</sup> The creep-mechanism clarification has to depend on the instantaneous creep behavior because the long-term creep is associated with the microstructural degradation. The stress-change test constitutes an effective method for a creep-deformation-mechanism clarification based on the instantaneous-strain and creep-rate-variation evaluation at the stress changes during the creep testing.<sup>10–12</sup>

At a high strain rate (a high stress) and a high temperature, a sudden-stress-change experiment has been widely utilized for pure metals and solution-strengthened alloys.<sup>10–12</sup> In contrast, at a low strain rate  $\dot{\epsilon}$ , especially the ultra-low  $\dot{\epsilon}$ , lower than  $10^{-10} \text{ s}^{-1}$ , it is usually impossible for a conventional tension-creep technique to distinguish the instantaneous plastic strain from the total strain under a sudden stress change, due to the unsatisfactory strain resolution, existing between  $10^{-6}$  and  $10^{-5}$ . As an additional creep technique, the helicoïdal-spring creep test based on torsion deformation provides a significantly high strain resolution, even up to  $10^{-9}$ .<sup>13</sup> Due to this high strain resolution, it is possible for very low instantaneous strains to be measured during a sudden stress change.<sup>14</sup>

In the present study, the instantaneous creep of the P91 ferritic heat-resistant steels was studied during sudden-stress-change experiments using the helicoïdal-spring-specimen technique for the creep mechanism under both a low stress and a high temperature.



**Table 1:** Chemical components of P91

Element	Cr	Mo	Si	V	C	Nb	Cu	N	P	Ni	Ti	Al	S
Content (%)	9.50	0.91	0.60	0.20	0.10	0.10	0.07	0.04	0.02	0.02	0.01	0.01	0.01

## 2 EXPERIMENTAL PART

### 2.1 Materials

The P91 heat-resistant steel was utilized in this experiment. The chemical components are presented in **Table 1**.

### 2.2 Specimen processing

The steel was processed into helicoidal-spring specimens using the method of high-speed wire-electrode cutting machining; the outer and inner diameters of the specimens were 12 mm and 8 mm, respectively. The cross-section of the helicoidal-spring specimens was a rectangle. The side length of the rectangle was 2 mm, as presented in **Figure 1**.

The helicoidal-spring specimens were annealed at 1313 K for 60 min and consequently tempered at 1033 K for 60 min.

### 2.3 Test methods

**Figure 2** presents the experimental apparatus, which includes an electric furnace with three adjacent heaters, a high-precision optical micrometer, a load, a weight and a system for receiving and processing information. By measuring the helicoidal-spring-specimen pitch change, the creep curves could be obtained. The test-apparatus details were previously reported.<sup>14</sup>

During the testing, the number of weights was increased or decreased for the instantaneous stress change

to be observed. The weight was suspended under a load with a flammable thread. In order for a load to be increased, the load was hooked quickly. For a load to be decreased, the flammable thread was burned.

The test was performed at a temperature of 923 K and a slight oscillation. The specimen was loaded subsequently for five days when the strain rate was down to  $10^{-9}$ – $10^{-8}$  s<sup>-1</sup>. Also, the stress consequently increased or decreased at various applied levels and the instantaneous strain was measured. The following equations<sup>15,16</sup> were utilized for calculating the mean surface shear stress,  $\tau$ , and the surface shear strain,  $\gamma$ , with the assumption of the pure torsion of the helicoidal-spring specimen:

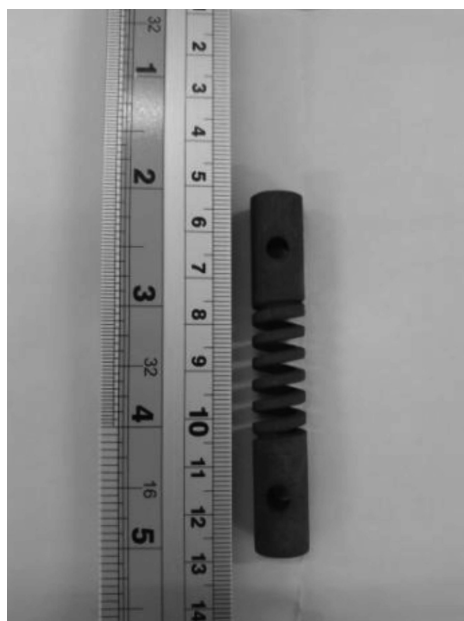
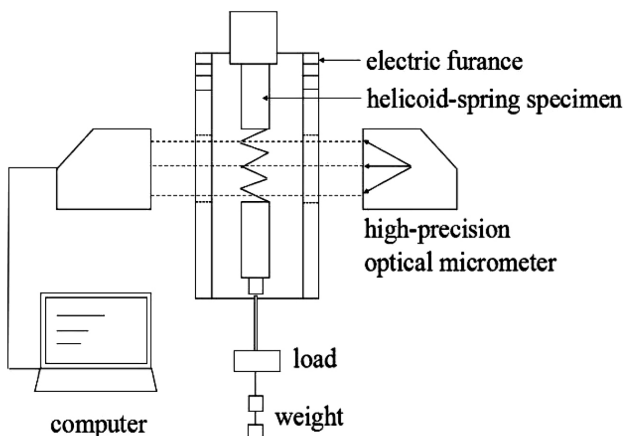
$$\tau = \frac{PD}{2a^2b} \quad (1)$$

$$\gamma = \frac{2a}{\pi D^2} \Delta\delta \quad (2)$$

where  $P$  is the average load,  $D$  is the coil diameter (12 mm) and  $\Delta\delta$  is the displacement of the mean coil-pitch spacing. In this study, the torsion was the dominant component of deformation, because  $D$  was quite higher than  $d$  ( $D/d > 12$ )<sup>17</sup> and the value of  $\delta$  was between 2 mm and 4 mm.<sup>18</sup> Since the stress and strain in the helicoidal spring had essentially shear components, the former could be transformed into the equivalent tensile quantities with the von Mises equations for the tensile stress  $\sigma = \sqrt{3}\tau$  and the tensile strain  $\varepsilon = \gamma/\sqrt{3}$ .

## 3 RESULTS AND DISCUSSION

**Figure 3** demonstrates the creep curves obtained at 923 K and at various stresses: (34.85, 27.75 and 19.35) MPa.

**Figure 1:** Helicoidal-spring specimen for the stress-change testing**Figure 2:** Experimental apparatus including electric furnace, high-precision optical micrometer, load, weight and information-receiving and processing system

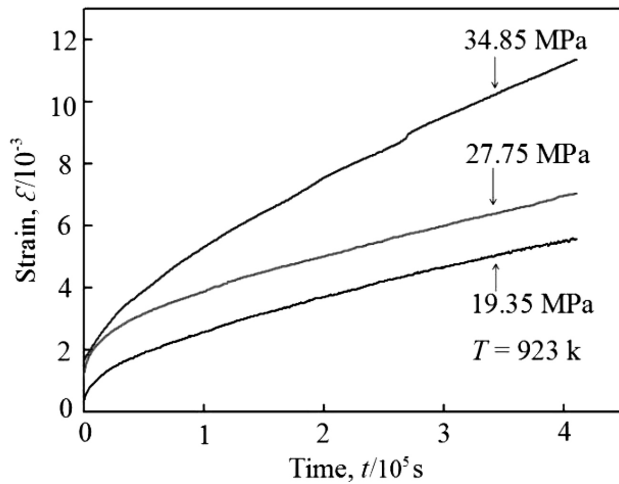


**Figure 3:** Strain/time creep curves for P91 at 923 K and various stresses

The creep rate which corresponded to the slope of the curves decreased as the duration increased.

**Figure 4** presents the strain rate on a logarithmic plot versus the strain at 923 K and various stresses. The creep deformation of the P91 steels consisted of the primary creep stages where the creep rate decreased along with the strain and no apparent secondary (steady-state) creep stage was observed where the creep rate would not change along with the strain.

The constitutive creep equations expressing the primary stages should be utilized in the experimental creep-curve analysis. The following constitutive creep equations were utilized, being widely accepted as the basic creep equations.<sup>19,20</sup>

Power law:

$$\varepsilon = \varepsilon_0 + at^b \quad (3)$$

Exponential law:

$$\varepsilon = \varepsilon_0 + a[1 - \exp(-bt)] \quad (4)$$

Logarithmic law:

$$\varepsilon = \varepsilon_0 + a \ln(1+bt) \quad (5)$$

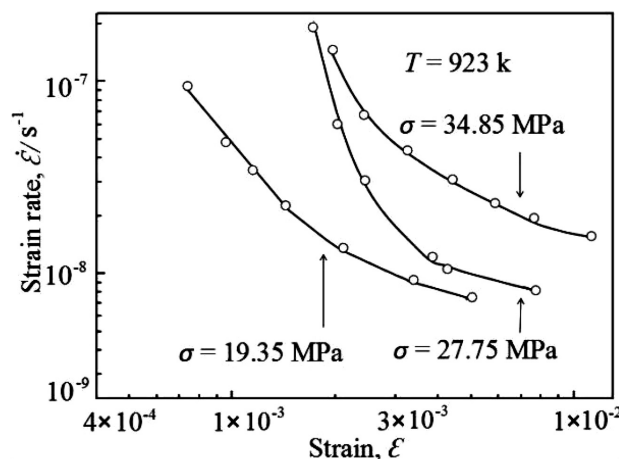


**Figure 4:** Strain rate/strain creep curves at 923 K and various stresses

Blackburn's law:

$$\varepsilon = \varepsilon_0 + ac[1 - \exp(-bt)] + c[1 - \exp(-dt)] \quad (6)$$

where  $\varepsilon$  is the strain,  $\varepsilon_0$  is the instantaneous strain on dead weight,  $t$  is the elapsed time and  $a$ ,  $b$ ,  $c$  and  $d$  are the parameters characterizing the primary creep region. The  $a$ ,  $b$ ,  $c$  and  $d$  values were called the "scaling factors".<sup>21</sup>

**Figure 5** presents representative results of a regression analysis, for the creep at 923 K and 27.75 MPa. The exponential-law and power-law equations did not reproduce the experimental data. Compared to the logarithmic-law equation, the Blackburn equation provided a better representation of the experimental creep curve. Therefore, the short-term creep for the P91 heat-resistant steels at low stresses could be described with the Blackburn equation.

In order for the creep mechanism of the P91 steels at low stresses to be studied, the instantaneous creep behavior was investigated. The specimens were loaded for  $4.3 \times 10^5$  s until the strain reached  $6 \times 10^{-3}$ . In this case, the dislocations could be expected to move. The stress increased or decreased at various levels that were consequently applied and the instantaneous strain was measured.

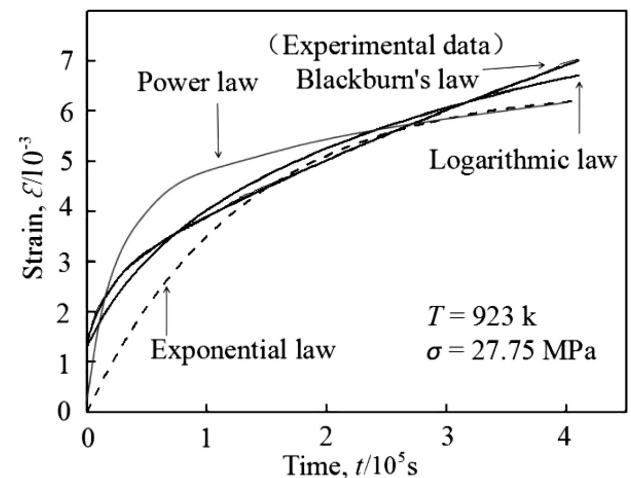


**Figure 5:** Comparison of experimental data and predicted curves of strain versus time at 923 K and 27.75 MPa

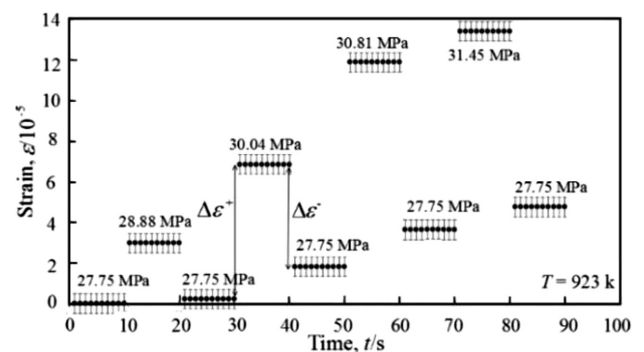


**Figure 6:** Example of instantaneous elongation and contraction upon low stress changes at a high temperature

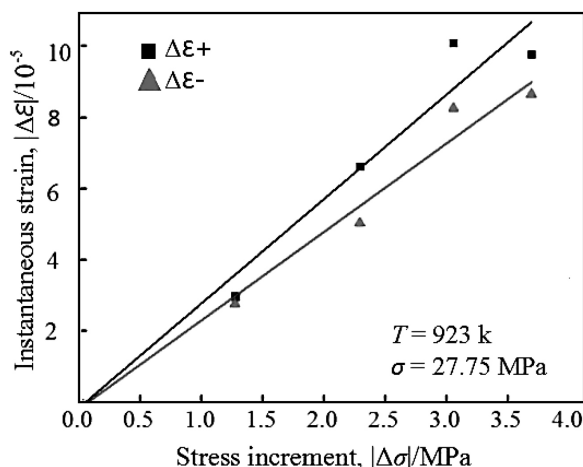


**Figure 7:** Instantaneous strain at a high temperature ( $T = 923$  K) versus the stress change during P91 steady-state creep

**Figure 7** presents instantaneous-elongation and contraction examples upon low changes in the stress of the P91 steels. In the figure, the  $\Delta\epsilon^-$  was the instantaneous strain under a stress decrease and the  $\Delta\epsilon^+$  was the instantaneous strain under a stress increase.

The relationship between the stress increment  $|\Delta\sigma|$  and the instantaneous strain  $|\Delta\epsilon|$  is presented in **Figure 7**. The creep demonstrates a viscous behavior because the absolute values of the instantaneous strain for the load increase were equal to the values for the load decrease.

Two types of creep at low stress exist. One is creep controlled by the diffusion including the lattice diffusion creep (Nabarro-Herring type)<sup>22</sup> at a high-T and grain boundary diffusion creep (Coble type)<sup>22</sup> at an intermediate-T. The other is creep associated with dislocation movement including free flight motion (climb controlled) and viscous motion (glide controlled)<sup>23</sup>. When creep is controlled by the diffusion, the creep should be a non-viscous behavior. In this case, the absolute values of the instantaneous strain for a small-load increase should be apparently larger than the values for a small-load

decrease. If creep is controlled by free flight motion of dislocation, plastic strain can occur instantaneously when the stress is increased by a small amount. Therefore, creep shows non-viscous behavior. When creep is controlled by the viscous glide of dislocations, instantaneous plastic strain does not occur even if the applied stress is increase suddenly. Thus, creep shows viscous behavior. In this study, the creep demonstrates a viscous behavior, because non instantaneous strain is observed during the stress increase. It means creep may be controlled by the viscous glide of dislocations.

**Figure 8** gives an example of the anelastic backflow, observed for a high reduction in the stress during the transient-creep stage. Specifically, the helicoidal spring specimen was loaded at 27.75 MPa and 923 K for 120 h and consequently unloaded all the stress for 120 h. Two different parts of the creep strain existed: the anelastic strain was reversible, which is presented with solid double arrows, whereas the plastic strain was irreversible and it is presented with dashed double arrows. Therefore, the instantaneous strain that occurred under a sudden stress change included both elastic and anelastic components.

## 4 CONCLUSIONS

The short-term creep behavior in the P91 heat-resistant steels was investigated using instantaneous-stress-change tests. The results were as follows:

- 1) The creep deformation consisted of the primary creep stages, but no secondary creep stage was observed.
- 2) The Blackburn equation could be utilized for the creep-curve description because it provided an improved representation of the experimental creep curve.
- 3) The viscous glide of dislocations might have been the dominant creep mechanism because the creep displayed a viscous behavior.
- 4) The short-term creep at a low stress displayed an anelastic behavior.

## Acknowledgment

This project was supported by the National Natural Science Foundation of China (Grant No. 51605330).

## 5 REFERENCES

- <sup>1</sup> K. Kimura, Y. Takahashi, ASME 2012 Pressure Vessels & Piping Division Conference, American Society of Mechanical Engineers, 18 (2012) 2, 177, doi:10.1016/0308-0161(93)90110-f
- <sup>2</sup> K. Maruyama, J. S. Lee, Creep & Fracture in High Temperature Components: Design & Life Assessment Issues, DEStech
- <sup>3</sup> H. G. Armaki, R. Chen, K. Maruyama, M. Igaras, Premature creep failure in strength enhanced high Cr ferritic steels caused by static recovery of tempered martensite lath structures, Materials Science and Engineering A, 527 (2010) 24–25, 6581–6588, doi:10.1016/j.msea.2010.07.037

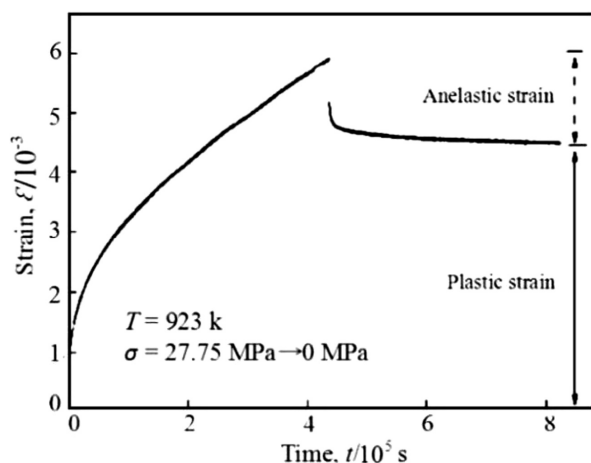


**Figure 8:** Elongation versus time during a high stress reduction without an elastic strain

- <sup>4</sup> O. Prat, J. Garcia, D. Rojas, G. Sauthoff, G. Inden, The role of Laves phase on microstructure evolution and creep strength of novel 9%Cr heat resistant steels, *Intermetallics*, 32 (2013) 32, 362–372, doi:10.1016/j.intermet.2012.08.016
- <sup>5</sup> L. Kyu-Ho, H. Sung-Min, S. Jae-Hyeok, S. Jin-Yoo, H. Joo-Youl, J. Woo-Sang, Effect of Nb addition on Z-phase formation and creep strength in high-Cr martensitic heat-resistant steels, *Materials Characterization*, 102 (2015) 2, 79–84, doi:10.1016/j.matchar. 2014. 12. 028
- <sup>6</sup> X. Dong, Q. Z. Gao, C. Li, 9Cr-1.7W-0.4Mo-Co Ferritic Heat-Resistant Steel Isothermal Aging Microstructural Evolution, *Publications, Lancaster*, 85 (2008) 1–2, 372–379, doi:10.1016/j.ijpvp. 2007. 06. 006
- <sup>7</sup> *Transactions of Materials and Heat Treatment*, 36 (2015) 3, 81–86, doi:10. 1016/j.msea.2013.09.033
- <sup>8</sup> K. Kimura, H. Kushima, K. Sawada, Long-term creep deformation property of modified 9Cr–1Mo steel, *Materials Science and Engineering A*, 511 (2009) 18, 58–63, doi:10.1016/j.msea.2008.04.095
- <sup>9</sup> K. Kimura, Y. Toda, H. Kushima, K. Sawada, Creep strength of high chromium steel with ferrite matrix, *International Journal of Pressure Vessels and Piping*, 87 (2010) 6, 282–288, doi:10.1016/j.ijp.2010.03. 016
- <sup>10</sup> E. M. Haney, F. Dalle, M. Sauzay, L. Vincent, I. Tournié, L. Allais, B. Fournier, Macroscopic results of long-term creep on a modified 9Cr–1Mo steel (T91), *Materials Science and Engineering A*, 510 (2009) 18, 99–103, doi: 10.1016/j.msea. 2008. 04.099
- <sup>11</sup> K. Maruyama, S. Karashima, Theoretical Consideration of Measurement of Work-Hardening and Recovery Rates during High Temperature Creep, *Trans. Japan Inst. Metals*, 16 (1975) 11, 671–678, doi:10.2320/matertrans1960.16.671
- <sup>12</sup> K. Abe, H. Yoshinaga, S. Morozumi, A Method of Discerning Frictional Stress and Internal Stress by the Stress Relaxation Test, *Journal of the Japan Institute of Metals and Materials*, 18 (1997) 6, 479–487, doi:10.2320/matertrans1960.18.479
- <sup>13</sup> H. Oikawa, H. Sugawara, Instantaneous plastic strain associated with stress increments during the steady state creep of Al and Al - 5.5 At. Pct. Mg alloy, *Scripta Metall.*, 12 (1978) 1, 85–89, doi:10.1016/0036-9748(78)90234-x
- <sup>14</sup> A. Magnin, Measurement of Very Low Creep Strains, *Journal of Testing and Evaluation*, 37 (2009) 1, 53–58, doi:10.1122/1.5550242
- <sup>15</sup> J. J. Shen, K. Ikeda, S. Hata, H. Nakashima, Instantaneous creep in face-centered cubic metals at ultra-low strain rates by a high-resolution strain measurement, *Journal of Wuhan University of Technology (Materials Science Edition)*, 28 (2013) 6, 1096–1100, doi:10.1007/s11595-013-0826-y
- <sup>16</sup> S. Timoshenko, D. H. Yong, *Elements of Strength of Materials*, 5th ed., New York, Van Nostrand, 1968, 77–80
- <sup>17</sup> A. M. Wahi, *Mechanical Springs*, 2nd ed., New York, McGraw Hill, 1963, 229–230
- <sup>18</sup> M. R. Mitchel, R. E. Link, P. Marecek, Measurement of Very Low Creep Strain, A Review, *J. Test. Eval.*, 37 (2009) 1, 53–58, doi:10. 15 20/jte101475
- <sup>19</sup> P. S. Zhang, J. J. Shen, H. Zhang, Short-Term Creep Behavior in P91 Heat-Resistant Steel at Low Stress, *J. Material Science Forum*, 850 (2016) 1, 922–926, doi:10.4028/www. scientific. net/ MSF.850.922
- <sup>20</sup> S. Holdsworth, Developments in the assessment of creep strain and ductility data, *Materials at High Temperatures*, 21 (2004) 1, 25–32, doi:10.3184/096034004782750041
- <sup>21</sup> R. P. Reed, N. J. Simon, R. P. Walsh, Creep of copper: 4–300 K, *Materials Science and Engineering A*, 147 (1991) 1, 23–32, doi:10.1016/0921-5093(91)90801-s
- <sup>22</sup> W. D. Nix, Effects of Grain Shape on Nabarro-Herring and Coble Creep Processes, *Metals Forum*, 4 (1981) 1, 38–43
- <sup>23</sup> H. Hiroyuki, N. Satoshi, K. Junichi, K. Akihiro, Creep deformation characterization of heat resistant steel by stress change test, *International Journal of Pressure Vessels and Piping*, 24 (2009) 9, 556–562, doi:10.1016/j.ijpvp.2008.06.003
- <sup>24</sup> K. Maruyama, S. Karashima, Theoretical Consideration of Measurement of Work-Hardening and Recovery Rates during high temperature Creep, *Trans. Japan Inst. Metals*, 16 (1975) 11, 671–678, doi:10.2320/matertrans1960.16.671





EFFECT OF SEVERE PLASTIC AND HEAVY COLD  
DEFORMATION ON THE STRUCTURAL AND MECHANICAL  
PROPERTIES OF COMMERCIAL PURE TITANIUMUČINEK PLASTIČNOSTI IN DEFORMACIJE PRI  
PODHLAJEVANJU NA STRUKTURNE IN MEHANSKE LASTNOSTI  
ČISTEGA KOMERCIALNEGA TITANAJan Palán<sup>1</sup>, Pavol Šutta<sup>2</sup>, Tomáš Kubina<sup>1</sup>, Mária Dománková<sup>3</sup><sup>1</sup>COMTES FHT, Prumyslova 995, 334 41 Dobruška, Czech Republic<sup>2</sup>New Technologies – Research Centre Westbohemian Region, University of West Bohemia, 306 14 Plzeň, Czech Republic<sup>3</sup>Institute of Materials Science, Faculty of Materials Science and Technology Trnava, STU Bratislava, Bottova 25, 917 24 Trnava, Slovakia  
jpalan@comtesfht.cz*Prejem rokopisa – received: 2016-10-25; sprejem za objavo – accepted for publication: 2017-01-23*

doi:10.17222/mit.2016.307

SPD (severe plastic deformation) processing of materials provides a great potential associated with the enhancement of their properties by refining the initial grain structure. The present experiments involved mechanical working of commercial-purity titanium (Ti Grade 2) with the CONFORM SPD technique, which is one of the SPD methods, and with rotary swaging. The objective was to process the material at as low temperatures as possible in order to avoid softening processes and, therefore, to achieve the maximum strengthening through a microstructure refinement. Three passes through a CONFORM SPD machine were completed and the resulting ultimate strength was 673 MPa. The average grain size was 330 nm. The greatest improvement of the mechanical properties was achieved in the first pass. In the subsequent passes, the contributions were minor. The processing in the CONFORM SPD machine did not impair the ductility of the material. Subsequently, the wires were rotary swaged. The ultimate strength achieved was 1070 MPa. The response of the properties to this forming method was markedly different. The reason is that rotary swaging does not belong to SPD techniques. It causes rapid work hardening and reduces the ductility of the material. The workpiece was subsequently investigated with the aid of several techniques. Light and transmission electron microscopy and X-ray diffraction were employed for evaluating the grain size, distribution and orientation.

Keywords: equal-channel angular pressing, CONFORM SPD technique, rotary swaging, titanium, extrusion

Velika plastična deformacija (angl. SPD) pri obdelavi materialov omogoča veliko možnosti, povezane z izboljšanjem njihovih lastnosti z izboljšavo izvorne strukture zrn. Pričujoči preizkus je vključeval mehansko obdelavo komercialno dostopnega čistega titana (Ti Grade 2) s CONFORM SPD-tehniko, ki je ena od SPD-metod, in s kovanjem. Namen je bil, da bi se material obdelalo pri čim nižjih temperaturah, kot je mogoče, da bi se izognili procesom mehčanja in, da bi dosegli maksimalno krepitev s prečiščenjem strukture. Narejeni so bili trije nizi v CONFORM SPD-stroju in končna moč je dosegla 673 MPa. Povprečna velikost zrn je bila 330 nm. Največje izboljšave mehanskih lastnosti so bile dosežene v prvem nizu. V sledečih nizih so bile le-te manjše. Obdelava v CONFORM SPD-stroju ni škodovala duktilnosti materiala. Posledično so bile žice zvite. Končna moč je bila 1070 MPa. Odziv lastnosti na to metodo oblikovanja je bil izrazito drugačen. Razlog je v tem, da rotacijsko zvijanje ne sodi v tehnike SPD. Rotacijsko zvijanje povzroči hitro utrjevanje in zmanjšuje duktilnost materiala. Vzorec je bil nato raziskan s pomočjo več tehnik. Za ovrednotenje velikosti, razporeditve in orientacije zrn, sta bili uporabljeni transmisijška elektronska mikroskopija in rentgenska difrakcija.

Ključne besede: enakomerno kotno stiskanje, CONFORM SPD-tehnika, rotacijsko zvijanje, titan, iztiskanje

## 1 INTRODUCTION

Severe plastic deformation (SPD) is a generic term for a group of methods which cause grain refinement in a material and produce equiaxed grains.<sup>1</sup> The occurrence of an ultrafine structure or nanostructure is conditional on high hydrostatic pressure ( $P > 1$  GPa) and large shear deformation applied at relatively low temperatures. The temperatures of SPD processes should meet the condition of  $T(\text{SPD}) < 0.4 T(\text{melting})$ .<sup>1</sup> Another aspect is the strain magnitude, defined as  $\epsilon(\text{true strain}) > 6-8$ . When the above conditions are met, the forming process leads to a high density of lattice defects, predominantly dislocations, and to the formation of subgrains, which reduces the stored energy.<sup>2</sup> The relationship between the mechanical properties and the grain size is described

with the Hall-Petch equation<sup>3,4</sup>. In the present study, commercially pure (CP) titanium Grade 2 was worked by means of the CONFORM SPD (CONSPD) method. This method uses continuous angular pressing through a die chamber of a modified design to produce ultrafine structures and nanostructures of the materials.<sup>5-7</sup> The design modification reflects the principles of the ECAP method (equal-channel angular pressing), as described in studies.<sup>5-7</sup> Continuous operation is the key advantage of this forming method. The processing of CP titanium Grade 2 with the CONFORM SDP machine was described in multiple papers.<sup>5,7</sup> The main outcomes were the improved mechanical properties (ultimate tensile strength (UTS) = 698 MPa, 0.2 % offset yield stress (0.2 OYS) = 637 MPa), no significant decrease in the

elongation, and an equiaxed ultrafine-grained (UFG) microstructure.<sup>7</sup>

The present study proposes a process route which involves CONFORM SPD forming and rotary swaging (RS) in order to enhance the mechanical properties of a workpiece.<sup>8–10</sup> The effects of severe plastic deformation and work hardening are thus combined. The proposed technology allows the mechanical properties of pure titanium to be improved dramatically. The ultrafine-grained CP Ti Grade 2 has a great potential because its mechanical properties are comparable to the Ti6Al4V alloy, which is mostly used in medicine. Recently, it was suggested that Al and V might be toxic for the human body.<sup>11,12</sup>

## 2 EXPERIMENTAL PART

The material under investigation was CP titanium Grade 2 with the chemical composition given in **Table 1**. The composition was measured by means of the Bruker Q4 Tasman optical emission spectrometer and the Bruker G8 Galileo gas analyser. The diameter of Ti rods was 10 mm.

**Table 1:** Chemical composition of feedstock in weight percent

Fe	O	C	H	N	Ti
0.046	0.12	0.023	0.0026	0.0076	99.822

The processing was carried out in a CONFORM SPD machine, type 315i with a modified die chamber (**Figure 1**), and in a HMP R4-4 rotary-swaging machine. During the CONFORM SPD process, the temperature was 220 °C, the wheel speed was 0.5 min<sup>-1</sup>, and the angle of the die chamber was 90°. Three passes through the CONFORM SPD machine were completed. The product's cross-section was identical to that of the feedstock. Rotary swaging, the subsequent process, was carried out at ambient temperature. In this operation, the cross-section area was reduced by 20 % in each pass. The total area reduction was 90 %.

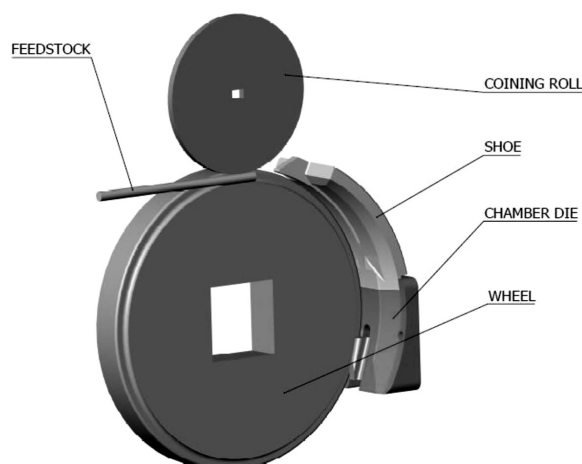


**Figure 1:** Schematic illustration of the CONFORM SPD process

For the purpose of observation with a transmission electron microscope (TEM), thin foils were prepared with the final electrolytic thinning in a Tenupol 5 device, using a solution of 300 mL CH<sub>3</sub>OH + 175 mL 2-butanol + 30 mL HClO<sub>4</sub> at –10 °C and a voltage of 40 V. The TEM analysis was performed with a JEOL 200CX instrument with an acceleration voltage of 200 kV. Selective electron diffraction was used for the determination of the phases. The grain size was measured using the linear intercept method.

The preferred orientation of crystallites (texture) was analysed with an automatic powder diffractometer X'Pert-Pro equipped with an ultra-fast semiconductor position-sensitive detector Pixcel. Cu-K<sub>α1</sub> radiation (λ = 0.154056 nm) was used. The texture was characterized from the radial X-ray diffraction patterns using the Harris (1952) texture index, Equation (1):

$$T_i = \frac{n \cdot I_i / R_i}{\sum_{j=1}^n I_j / R_j} \quad (1)$$

where  $n$  is the number of the reflections investigated,  $I_i$  is the observed intensity and  $R_i$  is the corresponding intensity for the sample with randomly oriented crystallites. The  $R_i$  values were obtained from the ICDD PDF standard diffraction data file (reference code 00-005-0682). The texture was analysed in the direction of the material flow, both after CONFORM SPD (longitudinal direction), and after CONFORM SPD + rotary swaging.

## 3 MICROSTRUCTURE

The mean grain size in the initial condition of the feedstock was 5390 nm. After the first pass, the mean grain size was  $d_{\text{average}} \sim 320 \pm 35$  nm in the transverse direction. After the first pass, the microstructure was equiaxed with a non-uniform dislocation density (**Figure 2a**). Some locations exhibited a preferential orientation (**Figure 2b**). After the second pass (**Figure 2c**), the mean grain size was  $d_{\text{average}} \sim 250 \pm 25$  nm in transverse direction. The dislocation density was still non-uniform after the second pass. After the third pass, the mean grain size was  $d_{\text{average}} \sim 330 \pm 30$  nm (**Figure 3d**): the grain was larger than after the second pass. This increase can be attributed, in part, to the non-uniform deformation and to the high surface activity of the UFG microstructure. High surface activity and dislocation density (strain magnitude) lower the temperatures of softening processes. A certain grain growth can be expected to occur during the forming due to deformation heat and the heat retained in the die chamber (220 °C). The grain growth upon multiple passes through the CONFORM SPD machine was already reported in <sup>9</sup>.

**Figure 3a** is a micrograph of the structure in the transverse direction after three passes through the CONFORM SPD machine and after a 35 % area reduction

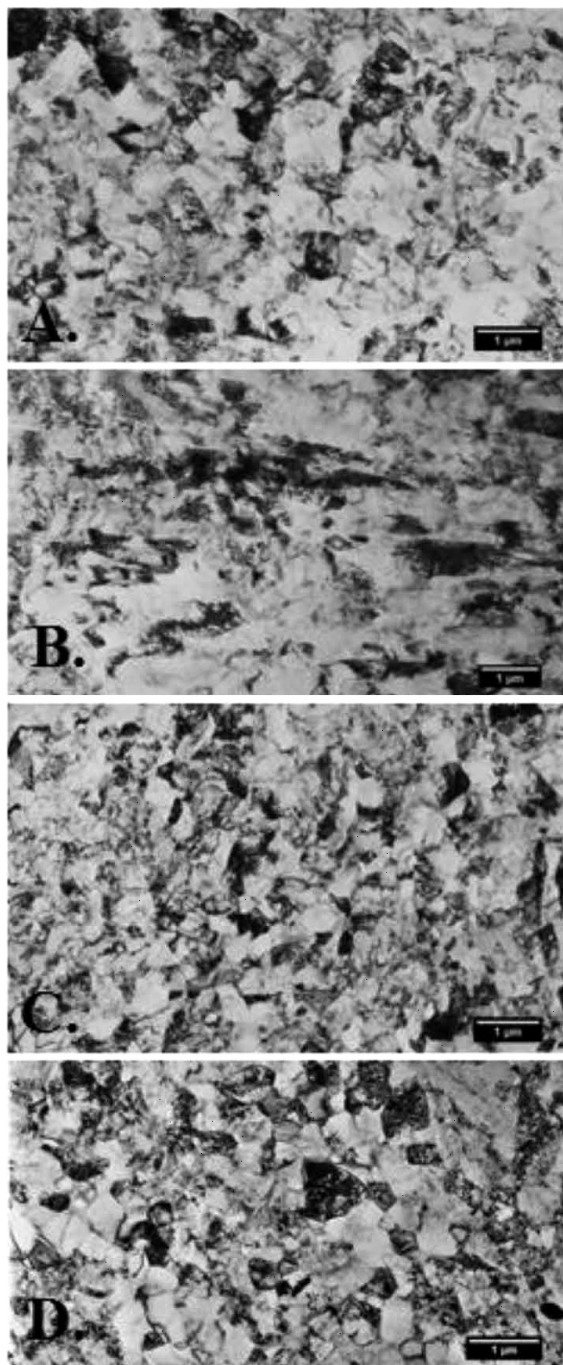


**Figure 2:** TEM images: a) CON SPD – 1 pass (transverse), b) CON SPD – 1 pass (longitudinal), c) CON SPD – 2 passes (transverse), d) CON SPD – 3 passes (transverse)

with rotary swaging (RS). The mean grain size in the transverse direction is  $d_{\text{average}} \sim 300 \pm 150$  nm. The large standard deviation is due to a large variation in the grain size. **Figure 3b** is a micrograph taken in the longitudinal direction after CONFORM SPD and RS. The grains are elongated and aligned in the direction of forming due to the nature of the deformation introduced by rotary swaging. Unlike in CONFORM SPD, the grains become elongated instead of being refined or converted into new

polyhedral grains. After the additional reduction due to rotary swaging (3 passes through CONFORM SPD + the total area reduction of 50 % by RS), it became impossible to determine the grain size due to the high dislocation density, as seen in **Figure 3c**. The summary of the average grain sizes is given in **Table 2**.

**Table 2:** Average grain size in the transverse and longitudinal sections obtained from TEM images

Condition	Grain size (nm)	
	Transverse	Longitudinal
as received	5390±20	
CON SPD – 1 pass	320±35	340±30
CONSPD – 2 passes	250±25	310±30
CONSPD – 3 passes	330±30	420±30
CON SPD – 3 passes + RS (35 %)	300±150	220±50
CONSPD – 3 passes + RS (50 %)	Not possible to evaluate due to high dislocation density	

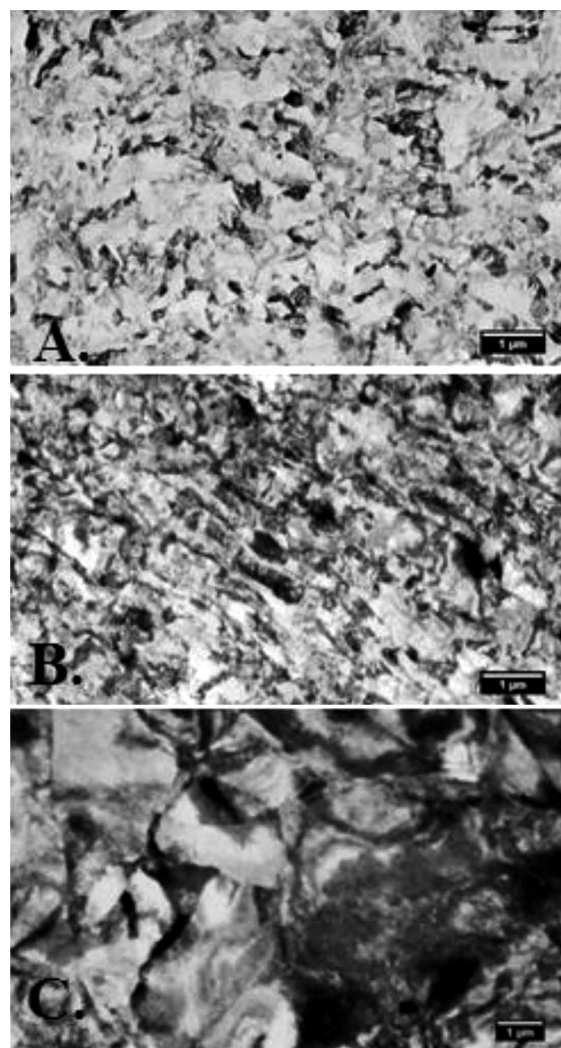


**Figure 3:** TEM images: a) CON SPD – 3 passes + RS (area reduction by 35 %) in the transverse direction, b) CON SPD – 3 passes + RS (35 %) in the longitudinal direction, c) CON SPD – 3 passes + RS (50 %) in the transverse direction



#### 4 TEXTURE EVALUATION

The preferred orientation of crystallites expressed with the texture index  $T_i$  (Equation 1, **Table 3**) is, in all the cases, in the [001] direction perpendicular to the sample surface analysed. The highest value was found for CONSPD – 3 passes + RS (75 %) titanium sample, i.e., the sample that was processed using the CONFORM SPD device and rotary swaging (basal texture, **Figure 5**). An increased value of the texture index can be seen in the initial state, due to the previous wire-drawing process (**Figure 4**). The texture index is lower for the samples that were processed with the CONFORM SPD device. Texture indices for the [101] direction are listed for the sake of comparison. Nevertheless, all their values are lower than 1. It means that no preferred orientation of crystallites in the [101] direction is present, as opposed to the sample surface.

**Table 3:** Texture evaluation using X-ray diffraction

Plane (h k l)	Texture index		
	as received	CONSPD – 1 pass	CONSPD – 2 passes
$T_i(002)$	3.13	2.49	2.67
$T_i(101)$	0.66	0.69	0.86
	CONSPD – 3 passes	CONSPD – 3 passes + RS (75 %)	Standard
$T_i(002)$	2.37	3.48	1
$T_i(101)$	0.97	0.24	1

#### 4 MECHANICAL PROPERTIES

**Table 4** indicates that the largest increase in the mechanical properties was obtained during the first pass through CONFORM SPD. The subsequent passes led to smaller increments. It is important to note that the increase in the ultimate strength and yield stress upon CONFORM SPD is not offset by a decrease in the ductility. The improvement in the mechanical properties is mainly due to the grain refinement and the increased

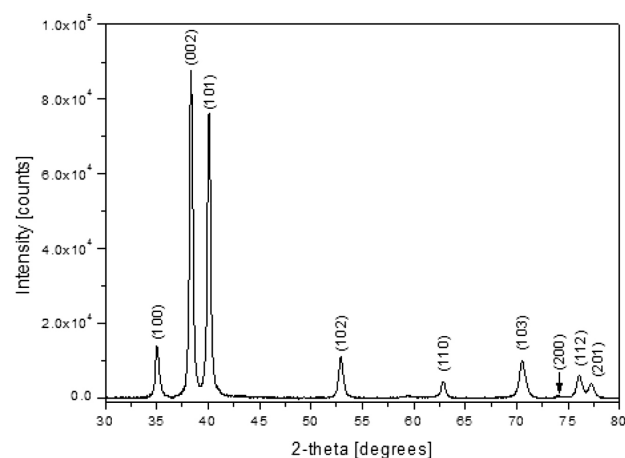


**Figure 4:** Diffraction radial profile of the as-received specimen

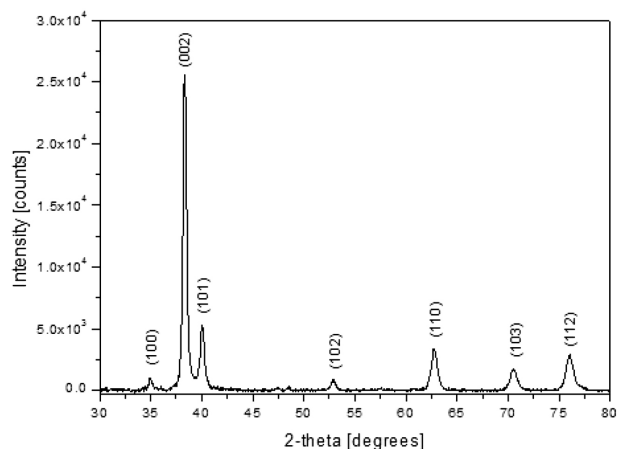


**Figure 5:** Diffraction radial profile of the specimen with the strongest texture: CONSPD – 3 passes + rotary swaging (75 %)

dislocation density, which impede the dislocation movement. A further increase in the mechanical properties was obtained with rotary swaging applied after the three passes through the CONFORM SPD machine. In comparison with the CONFORM SPD process, rotary swaging leads to a decrease in the ductility as a result of work hardening.

**Table 4:** Mechanical properties in the as-received condition, after CONFORM SPD processing and after RS

Condition	0.2 OYS	UTS	A <sub>5</sub>	RA
	MPa	MPa	%	%
as received	370	480	25	52
CONSPD – 1 pass	540	580	23	62
CONSPD – 2 passes	560	600	23	62
CONSPD – 3 passes	570	623	20	64
CONSPD – 3 passes + RS (50 %)	830	885	13	54
CONSPD – 3 passes + RS (75 %)	930	1000	12	57
CONSPD – 3 passes + RS (85 %)	950	1070	12	58
RS only (85 %)	780	850	12	50

#### 5 DISCUSSION

The CONFORM SPD processing led to higher ultimate strengths and yield stresses without a reduced ductility. This is characteristic of the process of the formation of a UFG equiaxed structure shown in **Figure 2**. The grain size and distortion are non-uniform due to non-uniform deformation during the forming process. The preferred orientation of crystallites in the [001] direction perpendicular to the surfaces of the investigated samples is not too significant, except for the sample which was processed with CONFORM SPD and the rotary swaging machine where the highest value of the texture index was observed (the basal texture).

Major increases in the ultimate strength and yield stress were found after the first pass through the CON-

FORM SPD machine, whereas the increments from the subsequent passes were small. This is closely related to the grain size, which did not decrease during the subsequent passes. It is possible to say that the additional deformation causes the subgrains to rotate into high-angle grain boundaries, typically with an equiaxed shape of the grains.<sup>5,7,9</sup> The subsequent rotary swaging led to a further increase in the mechanical properties, but the strengthening mechanism was different this time. Instead of the formation of equiaxed grains, the grains became elongated in the direction of forming, with a much higher dislocation density (**Figure 3**).<sup>10,11</sup> When compared to the CONFORM SPD route, rotary swaging led to a reduced ductility as a consequence of work hardening.

## 6 CONCLUSION

This study involved the processing of Ti Grade 2 using CONFORM SPD and rotary swaging with the goal of improving its mechanical properties. The results and findings are described below:

- The CONFORM SPD processing substantially refined the grain from its initial size of 5390 nm to 350 nm. The subsequent rotary swaging did not provide for a further grain refinement but led to a grain elongation and to a higher dislocation density.
- The processing led to the basal texture. The most significant form of texture was found in the specimen processed with CONFORM SPD and rotary swaging.
- Three passes through the CONFORM SPD machine led to a strength of 623 MPa and a yield stress of 570 MPa without any notable decrease in the elongation.
- After CONFORM SPD, the specimens were rotary swaged, which brought their strength to 1070 MPa and the yield stress to 950 MPa. In the initial condition, the ultimate strength was 480 MPa and the yield stress was 370 MPa.

## Acknowledgment

These results were obtained under the project entitled "Development of West-Bohemian Centre of Materials

and Metallurgy" No. 101412, financed by the Ministry of Education of the Czech Republic.

## 7 REFERENCES

- <sup>1</sup> R. Z. Valiev, R. K. Islamgaliev, I. V. Alexandrov, Bulk nanostructured materials from severe plastic deformation, *Progress in Materials Science*, 45 (**2000**) 2, doi:10.1016/S0079-6425(99)00007-9
- <sup>2</sup> N. J. Petch, The cleavage strength of polycrystals, *J. Iron Steel Inst.*, 174 (**1953**), 25–28
- <sup>3</sup> E. O. Hall, The Deformation and Ageing of Mild Steel: III Discussion of Results, *Proc. Phys. Soc. London*, 64 (**1951**), 747–753, doi:10.1088/0370-1301/64/9/303
- <sup>4</sup> A. Mishra, B. Kad, F. Gregori, M. Meyers, Microstructural evolution in copper subjected to severe plastic deformation, *Acta Materialia*, 55 (**2007**), 2, doi:10.1016/j.actamat.2006.07.008
- <sup>5</sup> M. Duchek, T. Kubina, J. Hodek, J. Dlouhý, Development of the production of ultrafine-grained titanium with the conform equipment, *Mater. Tehnol.*, 47 (**2013**), 4
- <sup>6</sup> G. J. Raab, R. Z. Valiev, T. C. Lowe, Y. T. Zhu, Continuous processing of ultrafine grained Al by ECAP–Conform, *Materials Science and Engineering*, 382 (**2004**) 1/2, doi:10.1016/j.msea.2004.04.021
- <sup>7</sup> T. Kubina, J. Dlouhý, M. Kover, Preparation and thermal stability of ultra-fine and nano-grained commercially pure titanium wires using CONFORM equipment, *Mater. Tehnol.*, 49 (**2015**), 2, doi:10.17222/mit.2013.226
- <sup>8</sup> L. Ostrovska, L. Vistejnova, J. Dzigan, P. Slama, T. Kubina, E. Ukrainsev, D. Kubies, M. Kralickova, M. Kalbacova, Biological evaluation of ultra-fine titanium with improved mechanical strength for dental implant engineering, *J. Mater. Sci.*, 23 (**2015**), doi:10.1007/s10853-015-9619-3
- <sup>9</sup> M. Zemko, T. Kubina, J. Dlouhý, J. Hodek, Technological aspects of preparation of nanostructured titanium wire using a CONFORM machine, *IOP Conference Series: Materials Science and Engineering*, 63 (**2014**), 2, doi:10.1088/1757-899X/63/1/012049
- <sup>10</sup> D. V. Gunderov, A. V. Polyakov, I. P. Semenova, Evolution of microstructure, macrotexture and mechanical properties of commercially pure Ti during ECAP-conform processing and drawing, *Materials Science and Engineering*, 562 (**2013**), 128–136, doi:10.1016/j.msea.2012.11.007
- <sup>11</sup> I. P. Semenova, R. Z. Valiev, E. B. Yakushima, G. H. Salimgareeva, T. C. Lowe, Strength and fatigue properties enhancement in ultra-fine-grained Ti produced by severe plastic deformation, *Journal of Materials Science*, 43 (**2008**), 23–24, doi:10.1007/s10853-008-2984-4
- <sup>12</sup> H. Alkhazraji, E. El-Danaf, M. Wollmann, L. Wagner, Enhanced Fatigue Strength of Commercially Pure Ti Processed by Rotary Swaging, *Advances in Materials Science and Engineering*, (**2015**), 1–12, doi:10.1155/2015/301837



EFFECT OF YTTRIUM AND ZIRCONIUM MICROALLOYING ON  
THE STRUCTURE AND PROPERTIES OF WELD JOINTS OF A  
TWO-PHASE TITANIUM ALLOYUČINEK MIKROLEGIRANJA ITRIJA IN CIRKONIJA NA  
STRUKTURO IN LASTNOSTI NA SPOJE ZAVROV DVOFAZNE  
ZLITINE TITANA

Anatoly Illarionov, Artemy Popov, Svetlana Illarionova, Dmitry Gadeev

Ural Federal University, 620034, 28 Mira str., Yekaterinburg, Russia  
d.v.gadeev@urfu.ru*Prejem rokopisa – received: 2016-11-10; sprejem za objavo – accepted for publication: 2017-04-19*

doi:10.17222/mit.2016.317

The effect of microalloying of the Ti-4.8Al-1.2Mo-2.6V-0.6Cr-0.25Fe titanium alloy with yttrium and zirconium on the phase composition, structure and mechanical properties of welded sheets was studied using light and transmission electron microscopy, X-ray diffraction analysis and microindentation-hardness testing. A differential thermal analysis was employed to model the welding thermal cycle. It was found that alloying with yttrium led to the precipitation of  $Y_2O_3$  oxide particles resulting in refining the microstructure of the alloy. In addition, yttrium additions were shown to stabilise the  $\beta$ -phase of the alloy that decreases the hardness of the alloy.

Keywords: microalloying, rare-earth elements, titanium alloy, welding

Učinek mikrolegeriranja zlitine titana Ti-4.8Al-1.2Mo-2.6V-0.6Cr-0.25Fe z itrijem in cirkonijem na sestavo faze, strukturne in mehanske lastnosti je bil raziskovan s svetlobno elektronsko mikroskopijo, z rentgensko difrakcijsko analizo in s testiranjem trdote mikroindentacije. Uporabili smo diferencialno termično analizo za pridobitev modela za varilni termični cikel. Ugotovljeno je bilo, da legiranje z itrijem vodi k razpršenosti  $Y_2O_3$  oksidnih delcev, kar se kaže pri rafiniranju mikrostrukture zlitine. Poleg tega je bilo dokazano, da so dodatki itrija stabilizirali  $\beta$ -fazo v zlitini, ki zmanjšuje trdoto zlitine.

Ključne besede: mikrolegeranje, elementi redke zemlje, zlitina titana, varjenje

## 1 INTRODUCTION

Titanium alloys, due to their high specific strength and good corrosion resistance, are widely used in the aerospace and marine industries as structural materials and it is desirable to further enhance their properties. The latter is possible by means of complex multicomponent alloying.<sup>1,2</sup> In addition to the specific strength, good weldability is usually necessary to maximise the material utilisation.

Since  $\alpha$ -titanium and  $\alpha+\beta$  alloys are considered to have a better weldability compared to metastable  $\beta$ -titanium alloys,<sup>3</sup> a number of  $\alpha+\beta$ -alloys were developed in Russia to meet these requirements. One of them is Ti-4.8Al-1.2Mo-2.6V-0.6Cr-0.25Fe, which is a typical martensite-type two-phase alloy.<sup>4</sup>

Despite good weldability, the welding usually negatively affects the mechanical properties of titanium alloys.<sup>5</sup> This is partly due to the oxygen absorbed from the shield atmosphere followed by its diffusion to the weld-fusion zone (FZ), partly due to a high heat input resulting in significant grain coarsening. One way to overcome such a problem is to refine the prior grain size by the grain-boundary pinning effect of second-phase particles and promote heterogeneous nucleation in the

FZ.<sup>6</sup> It was shown that microalloying with transition elements, especially rare-earth metals, is a promising way to refine the structure of titanium alloys.<sup>7</sup> One of the most frequently employed alloying elements is yttrium.<sup>8–11</sup>

Although it was already shown what microalloying of the Ti-4.8Al-1.2Mo-2.6V-0.6Cr-0.25Fe alloy with 0.06 % mass fraction of yttrium decreases the oxygen concentration in  $\alpha$ - and  $\beta$ -solid solutions due to the formation of  $Y_2O_3$  particles,<sup>4</sup> detailed studies of a weld structure were not conducted. This is why our study aimed at investigating the influence of microalloying titanium alloys with zirconium and yttrium on the microstructure formation and mechanical properties of the weld joints of this alloy.

## 2 EXPERIMENTAL PART

Two-millimeter-thick hot-rolled sheets of an ( $\alpha+\beta$ ) martensitic titanium alloy alloyed with yttrium (alloy 1) and zirconium (alloy 2) were used in this study. The chemical compositions of the alloys are shown in **Table 1**. Prior to their use, the sheets were subjected to vacuum annealing at 750 °C for 1 h followed by arc welding using non-consumable tungsten electrodes.



**Table 1:** Chemical compositions of the test materials, in mass fractions (w/%)

Materials	Alloying elements, in mass fractions (w/%)							
	Ti	Al	Mo	V	Cr	Fe	Y	Zr
Alloy 1	Bal	4.80	1.20	2.60	0.60	0.60	0.06	-
Alloy 2							-	0.07

The microstructures of the alloys were analyzed with light optical (LOM) and transmission electron (TEM) microscopy on Olympus GX51 and JEM 200C microscopes, respectively. A qualitative phase analysis was carried out using X-ray diffraction (XRD) with Cu- $K_\alpha$  radiation on a DRON-3M powder diffractometer. A differential thermal analysis (DTA) was performed on a Du Pont appliance in DTA-1600 crucibles. The average grain size and grain-size distribution were determined with an Epiquant optical microscope.

Vickers microhardness was measured at a 1 N load in accordance with the formula below (ISO 6507) and multiplied with the standard gravity ( $g = 9.81$ ) to get the values in MPa in Equation (1):

$$HV = 0.1891 \cdot (F/d^2) \quad (1)$$

with  $F$  being the applied load (Newton) and  $d$  being the average length of the diagonal of the residual indent (millimeters).

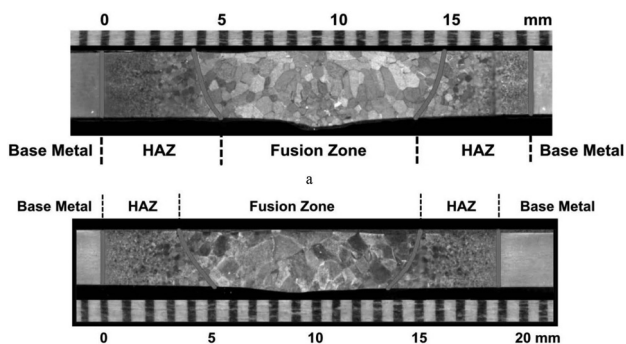
Metallographic samples were prepared according to the standard procedures. The steps consisted of grinding with 120–2400 grit SiC paper, polishing with 0.3  $\mu\text{m}$  colloidal alumina, followed by the final polishing with a 0.05  $\mu\text{m}$  colloidal silica suspension. Kroll's reagent with a composition of 100 mL water + 2 mL HF + 5 mL HNO<sub>3</sub> was used to etch the specimens.<sup>12</sup> Thin foils for the TEM investigation were prepared with electrolytic polishing in a methanol-containing electrolyte (300 mL methanol, 175 mL butanol, 30 mL perchloric acid (70–72 %)) at -30 °C.<sup>12</sup>

### 3 RESULTS AND DISCUSSION

With respect to the differences in the microstructure, weld joints generally consist of three distinct zones, i.e., the base metal, the fusion zone and the heat-affected zone. In the fusion zone (FZ), materials melt during the welding and crystallize during the subsequent cooling. The heat-affected zone (HAZ) corresponds to the narrow transition region between the base metal and the fusion zone where the material is heated up to sub-transus or even superheated above the critical temperature. The latter might obviously cause significant microstructure changes in comparison with the base metal.

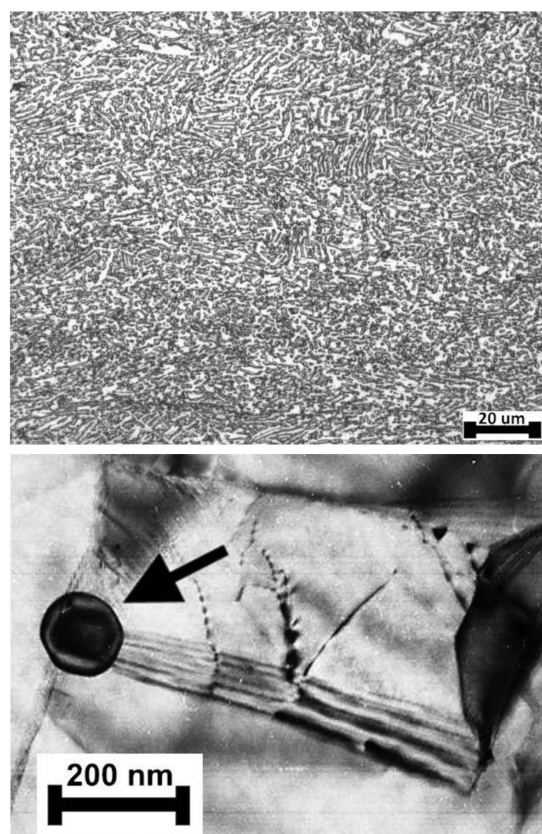
On the present samples, the zone width was measured and it was around 12 mm and 4.5 mm for the fusion and heat-affected zones, respectively (**Figure 1**).

The base-metal microstructure of both alloys is represented by primary  $\alpha$ -phase precipitates of a mixed, globular and lamellar, morphology in a  $\beta$ -phase matrix

**Figure 1:** Structures of welded joints: a) alloy 1 with Y; b) alloy 2 with Zr

(**Figure 2a**). The yttrium-containing alloy 1 is distinguished by a dispersive oxide precipitation of Y<sub>2</sub>O<sub>3</sub> particles with the average diameter of up to 120 nm (**Figure 2b**). These particles were found to be almost spherical and to precipitate mainly near the grain boundaries. The TEM micrograph (**Figure 2b**) shows a specific 'comet-tail-like' contrast around these particles, which is attributed to the elastic-stress field caused by the difference between the thermal-expansion coefficients of the oxides and the matrix.

The average  $\beta$ -phase grain size decreased with the increasing distance from the FZ (**Figure 1**) due to the higher temperatures achieved in the HAZ close to the

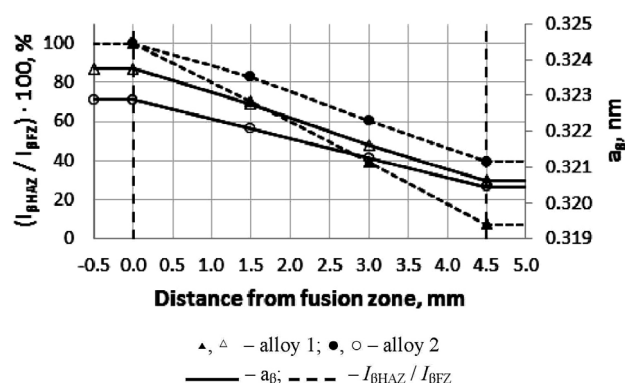
**Figure 2:** Microstructures of base metals: a) alloy 2 (LOM); b) alloy 1 (TEM)

FZ. The coarsest grains of alloy 2 reached about 400  $\mu\text{m}$  in diameter, whereas in alloy 1, they did not exceed 330  $\mu\text{m}$ , i.e., the yttrium-containing alloy 1 was characterized by a 1.2 times finer grain size. A similar relationship was previously observed in the solution-treated and water-quenched alloys of the same composition<sup>4</sup> and it was attributed to the presence of the yttrium-oxide particles in the Y-containing alloy that inhibited the grain-boundary movement.

The X-ray diffraction analysis showed that the volume fractions of the  $\alpha$ - and  $\beta$ -phases varied significantly in different parts of the HAZ (Figure 3). The intensity of  $\beta$ -phase peaks in the XRD patterns decreased with the increasing distance from the FZ, clearly indicating that the volume fraction of the  $\beta$ -phase was significantly higher in the near-FZ areas. At the same time, the  $a_\beta$  lattice parameter changed in the opposite direction.

It can be seen that the  $(200)_\beta$ -peak intensity ratio for alloy 1 was considerably higher than that for alloy 2. This confirms the assumption that yttrium binds oxygen, thus increasing the stability of the supercooled  $\beta$ -phase upon cooling.<sup>4,8–9</sup> Furthermore, such a behaviour resulted in a higher  $\beta$ -phase volume fraction, decreasing the hardness of the alloy. This was confirmed with the microhardness-indentation tests. Alloy 1 had a lower microhardness ( $2800 \pm 50$  MPa) than alloy 2 ( $3300 \pm 50$  MPa). It was also found that the  $\alpha$ -phase morphology along the HAZ changed from a complex one (Figure 2) to a lamellar one consisting of thin platelets (Figure 4).

The analysis of the microstructures of the alloys revealed a noticeable feature of both alloys, i.e., a jagged shape of the grain boundaries. A similar phenomenon was seen previously, for instance, in Ni–Mn–In-based alloys after thermal cycling<sup>13</sup> and near-alpha titanium alloys<sup>14</sup> and it was attributed to the formation of martensite crystals, which grow towards the grain boundaries curving them. Figure 4a shows that such a shape coincides closely with the lamellar  $\alpha$ -phase precipitations on both sides of the grain boundaries. Thin  $\alpha$ -lamellae were formed during the cooling from the single-phase



$I_{\text{HAZ}}, I_{\text{FZ}} - (200)_\beta$  XRD peak intensity in the heat-affected and fusion zones

**Figure 3:**  $\beta$ -phase lattice parameter ( $a_\beta$ ) and  $(200)_\beta$  XRD-peak intensity ratio ( $I_{\beta\text{HAZ}} / I_{\beta\text{FZ}}$ ) as a function of distance from the fusion zone of a welded joint

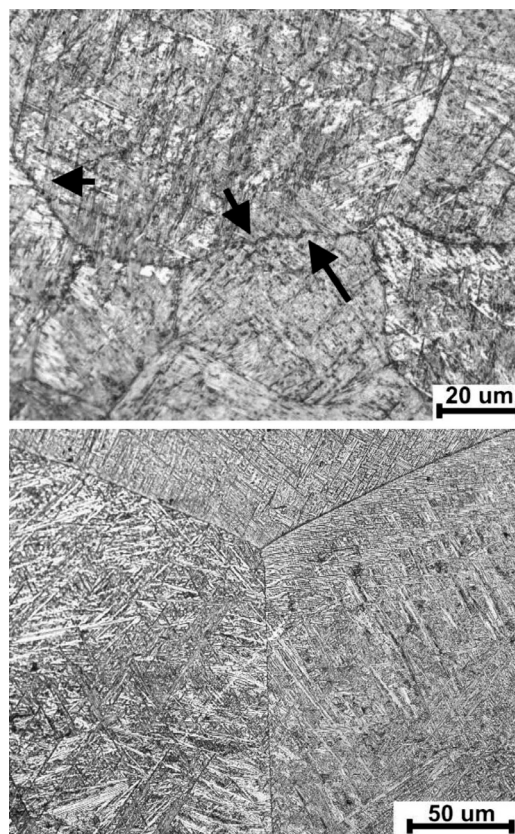


**Figure 4:** Microstructures of heat-affected zones of weld joints: a) alloy 1, b) alloy 2

$\beta$ -region. The stress field next to the growing  $\alpha$ -lamellae could interact with the grain boundaries curving them. The same process occurred in the neighbouring grains resulting in the jag formation. Since this process can occur in preferentially oriented grains, the jags were found only on the corresponding parts of the grains. On the whole, we suppose that the jagged shape of the grain boundaries is associated with the interaction of the boundaries with the products of the  $\beta \rightarrow \alpha$ -transformation occurring upon the cooling.

To summarize the above, it can be concluded that the welding thermal cycle results in significant changes of the grain structure, phase composition and morphology of the phases. Yttrium binds oxygen forming oxide particles that inhibit the grain growth and improve the  $\beta$ -phase stability. In turn, microalloying the alloy with zirconium does not result in the formation of additional phases and leads to the solution hardening of the alloy.

The average grain sizes for the weld joints of the samples of alloys 1 and 2 did not show any significant difference and was about 480–600  $\mu\text{m}$  (Figure 1). The fine structure of the alloys mainly consists of the  $\alpha$ -phase, with dislocations perpendicular to the lamellae (Figure 5b).

The  $\alpha$ -lamellae in the FZs of the alloys tend to form small colonies that may cross differently oriented lamellae (Figure 5c). Interlamellar  $\alpha/\beta$  spacings in



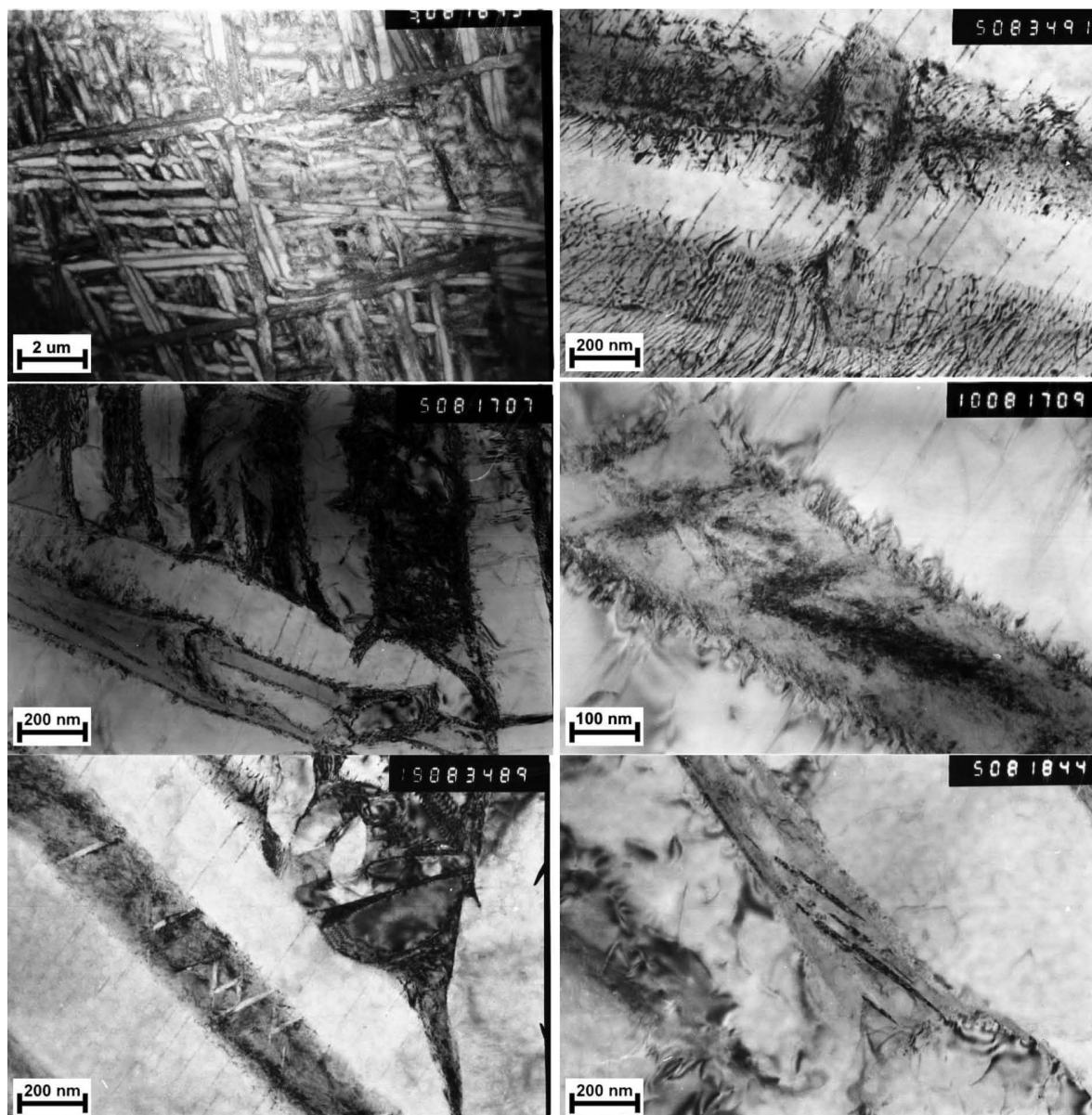


Figure 5: Thin structures of the weld joints of alloys 1 and 2: a), c), d) alloy 1; b), e), f) alloy 2

alloy 2 have a complex structure and high dislocation density (Figure 5d).  $\beta$ -phase interlayers are relatively wide (up to 200 nm) and non-uniform throughout the bulk of the alloy. Secondary  $\alpha$ -phase precipitations were observed in the interlamellar spacings, both along and across the  $\beta$  interlayers as well as at the  $\alpha/\beta$ -interphase boundaries (Figure 5d).

Generally, the coarse  $\alpha$ -platelets with a small dislocation density prevail in both yttrium- and zirconium-containing alloys (Figures 5e, 5f). However, alloy 1 is distinguished by a more conventional structure of interlamellar spacing. Although the thin lenticular platelets of the secondary  $\alpha$ -phase were still present, no highly dispersive precipitates were found on the interphase boundaries and within the  $\beta$ -layers. It should be noted that no  $Y_2O_3$  particles were detected in the FZ. This

might be connected with the intense overheating of the alloy caused by welding that resulted in a dissociation of the oxide.

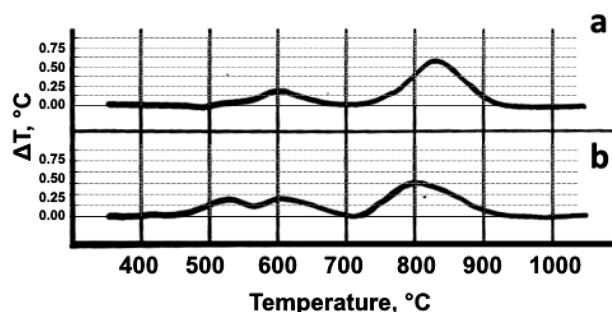


Figure 6: DTA curves for continuous cooling (20 °C/min cooling rate) from 1200 °C: a) alloy 1, b) alloy 2

In order to model the welding thermal cycle, a number of DTA experiments involving continuous heating up to 1200 °C and the subsequent cooling to 20 °C/min were carried out. Continuous-cooling DTA curves allowed us to determine the temperature ranges of the  $\beta \rightarrow \alpha$ -transformation (**Figure 6**).

A comparative analysis of the curves showed that the  $\beta$ -phase decomposition process in alloy 2 consisted of three distinctive stages, whereas only two exothermal effects were found for alloy 1. Stages I and II (at 920–750 and 700–550 °C, respectively) were attributed to the formation of coarse primary  $\alpha$ -colonies with a low defect density and secondary  $\alpha$ -platelets within the  $\beta$ -matrix. Stage III (500–400 °C) was assigned to the precipitation of the highly dispersed  $\alpha$ -precipitates mentioned above (**Figure 5 d**).

The formation of the  $\alpha$ -phase upon supercooling below the transus temperature of the titanium alloys is initiated by the crystallographic defects of the structure such as grain boundaries, dislocations, etc. Yttrium binds oxygen and thus refines the alloy. The products of the  $\beta$ -phase decomposition were quite free of precipitates. On the other hand, the precipitation of the secondary  $\alpha$ -platelets was possible in both alloys studied during supercooling of up to about 600 °C. At lower temperatures, the  $\beta$ -phase was stabilized in alloy 1, whereas its further decomposition occurred in alloy 2 resulting in the formation of highly dispersed  $\alpha$ -precipitates. We believe that all these differences in the behaviour of the alloys are associated with different  $\beta$ -phase stability values, which are primarily defined by the concentration of impurities in the alloys. Specifically, the interstitial elements in alloy 1, mainly oxygen, are bound to yttrium in the form of oxides. Zirconium has a lower affinity for oxygen and thus oxygen atoms remain in the solid solution leading to a more complete  $\beta$ -phase decomposition upon the cooling (**Figure 2**) resulting in a lower  $\beta$ -phase lattice parameter. With an increase in the volume fraction of the body-centred cubic  $\beta$ -phase, the strength of the titanium alloys usually decreases.<sup>12</sup> This is why the microhardness of Y-containing alloy 1 was found to be lower (3300±100 MPa for alloy 2) and 3000±100 MPa for alloy 1).

#### 4 CONCLUSIONS

The influence of the microalloying of titanium alloy Ti–4.8Al–1.2Mo–2.6V–0.6Cr–0.25Fe with yttrium and zirconium on the structure and microhardness was considered. It was found that the alloying with yttrium has the most noticeable effect on the structure of a weld joint and the phase transformation of the alloy.

A yttrium addition refines the alloy by means of binding with oxygen atoms and forming Y<sub>2</sub>O<sub>3</sub> particles. These particles pin the grain boundaries in both the

heat-affected and fusion zones, inhibiting the grain growth during a welding thermal cycle. In addition, due to a lower concentration of oxygen in the  $\alpha$ -phase, yttrium decreases the  $\beta$ -transus temperature of the alloy leading to the stabilization of the supercooled  $\beta$ -phase.

Due to a higher volume fraction of the "soft"  $\beta$ -phase in the yttrium-containing alloy, its microhardness was shown to be lower than that of the alloy with zirconium.

#### Acknowledgment

We hereby acknowledge the support of the Ministry of Science and Education of the Russian Federation, in accordance with the decree of the Government of 9 April 2010, No. 218, project No. 03.G25.31.0234.

#### 5 REFERENCES

- <sup>1</sup> A. I. Khorev, Development of structural titanium alloys for components and sections in aerospace technology, 10 (2010), 13–23, doi:10.1080/09507116.2010.486188
- <sup>2</sup> A. I. Khorev, Complex alloying and heat treatment of titanium alloys, 6 (2008), 364–368, doi:10.1080/09507110802288312
- <sup>3</sup> M. J. Donachie, Titanium, A Technical Guide, 2<sup>nd</sup> ed., ASM International, 2000
- <sup>4</sup> A. G. Illarionov, A. A. Popov, S. M. Illarionova, Effect of Microalloying, with Rem Inclusively, on the Structure, Phase Composition and Properties of ( $\alpha$  +  $\beta$ )-Titanium Alloy, Metal Science and Heat Treatment, 57 (2016), 719–725, doi:10.1007/s11041-016-9948-0
- <sup>5</sup> E. W. Collings, The physical metallurgy of titanium alloys, American Society for Metals, 1984, 261
- <sup>6</sup> Rios PR. Overview No. 62: A theory for grain boundary pinning by particles, Acta Metall., 35 (1987) 12, 2805–2814
- <sup>7</sup> A. I. Khorev, Theory and practices of microalloying of near- $\alpha$  and  $\alpha$ + $\beta$  titanium alloys with REE, zirconium, hafnium and rhenium, Technologii machinostroeniya, 1 (2015), 5–10
- <sup>8</sup> H. Wu, Y. Han, X. Chen, Effects of Yttrium on Mechanical Properties and Microstructures of Ti-Si Eutectic Alloy, Chinese Journal of Aeronautics, 18 (2005), 171–174, doi:10.1016/S1000-9361(11)60324-5
- <sup>9</sup> R. P. Kolli, A. A. Herzing, S. Ankem, Characterization of yttrium-rich precipitates in a titanium alloy weld, Materials Characterization, 122 (2016), 30–35, doi:10.1016/j.matchar.2016.10.014
- <sup>10</sup> B. Poorganji, A. Kazahari, T. Narushima, C. Ouchi, T. Furuhashi, Effect of yttrium addition on grain growth of  $\alpha$ ,  $\beta$  and  $\alpha$ + $\beta$  titanium alloys, Journal of Physics: Conference Series, 240 (2010), 12170, doi:10.1088/1742-6596/240/1/012170
- <sup>11</sup> W. F. Cui, C. M. Liu, L. Zhou, G. Z. Luo, Characteristics of microstructures and second-phase particles in Y-bearing Ti-1100 alloy, Materials Science and Engineering: A, 323 (2002), 192–197, doi:10.1016/S0921-5093(01)01362-4
- <sup>12</sup> G. Lütjering, J. C. Williams, Titanium, 2<sup>nd</sup> ed., Springer, Berlin, 2007, 442
- <sup>13</sup> Y. V. Kaletina, E. D. Efimova, E. G. Gerasimov, A. Y. Kaletin, Effect of thermal cycling on structure and properties of Ni–Mn–In-based alloys, Technical Physics, 12 (2016), 1894–1897
- <sup>14</sup> H. M. Flower, P. R. Swann, D. R. F. West, The effect of Si, Zr, Al and Mo on the structure and strength of Ti martensite, Journal of Materials Science, 8 (1972), 929–938





MICROSTRUCTURE EVOLUTION AND STATISTICAL ANALYSIS  
OF Al/Cu FRICTION-STIR SPOT WELDSRAZVOJ MIKROSTRUKTURE IN STATISTIČNA ANALIZA  
VRTILNO-TORNIH TOČKASTIH ZVAROV Al/CuMukuna Patrick Mubiayi<sup>1</sup>, Esther Titilayo Akinlabi<sup>1</sup>,  
Mamookho Elizabeth Makhatha<sup>2</sup><sup>1</sup>University of Johannesburg, Department of Mechanical Engineering Science, Auckland Park Kingsway Campus,  
2006 Johannesburg, South Africa<sup>2</sup>University of Johannesburg, Department of Metallurgy, School of Mining, Metallurgy and Chemical Engineering, Doornfontein Campus,  
2028 Doornfontein, South Africa  
patrickmubiayi@gmail.com*Prejem rokopisa – received: 2016-11-18; sprejem za objavo – accepted for publication: 2017-03-16*

doi:10.17222/mit.2016.320

In this paper, friction-stir spot welding (FSSW) is performed on 3 mm thick AA1060 and C11000 using different process parameters and tool geometries. The microstructure- and the microhardness-profile analyses were conducted and the probability distribution function (PDF) of the obtained microhardness values was determined. Optical images showed a good material mixing in most of the spot welds produced, whereas the energy-dispersive-spectroscopy (EDS) analysis showed the presence of intermetallic compounds. Microhardness results revealed that process parameters and tool geometries have significant effects on the distribution of microhardness values in different locations of the produced spot welds. Furthermore, goodness-of-fit values showed that most of the  $R^2$  values ranged between 0.8842 and 0.9999, which indicated how well the model fits with the experimental data. On the other hand, the residuals comprised positive and negative runs which also indicated the existence of a certain correlation with the experimentation.

Keywords: aluminium, copper, friction-stir spot welding, statistical analysis

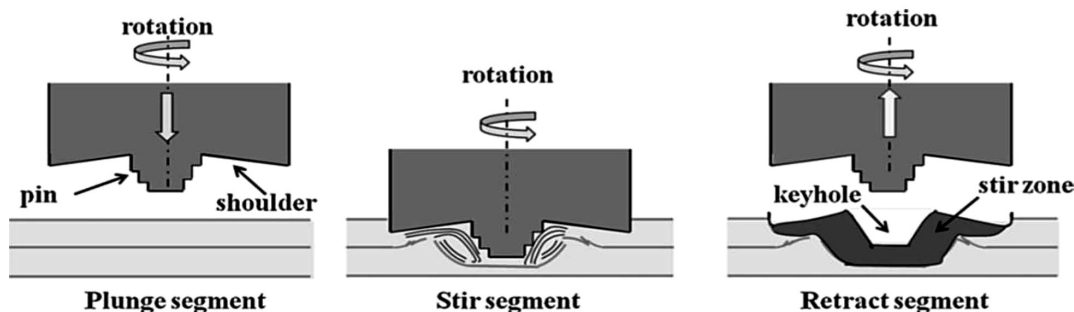
V prispevku je predstavljeno vrtilno-torno točkovno varjenje (angl. FSSW) na 3 mm debeli pločevini AA1060 in C11000 z uporabo različnih procesnih parametrov in različno geometrijo orodij. Izvedene so bile analize profila mikrostrukture in mikrotvdote in določena je bila porazdelitvena funkcija verjetnosti za dobljene vrednosti mikrotvdote. Posnetki so pokazali dobro mešanje materiala na večini izdelanih točkovnih zvarov, medtem ko je EDS-analiza pokazala prisotnost intermetalnih spojin. Meritve mikrotvdote so pokazale, da imajo procesni parametri in geometrija orodij pomemben vpliv na porazdelitev mikrotvdote glede na različne lokacije izdelanih točkovnih zvarov. Nadalje je serija opazovanj oz. ocena pokazala, da je večina  $R^2$  vrednosti rangiranih med 0,8842 in 0,9999. To potrjuje, da se model dobro ujema z eksperimentalnimi podatki. Po drugi strani pa razlika med pozitivnimi in negativnimi cikli kaže na obstoj določene korelacije s preizkušanjem.

Ključne besede: aluminij, baker, vrtilno-torno točkovno varjenje, statistična analiza

## 1 INTRODUCTION

Friction-stir welding (FSW) is a fairly new solid-state joining technique created and patented by The Welding Institute (TWI) in 1991 for butt and lap welding of ferrous and non-ferrous metals and plastics.<sup>1</sup> Friction-stir spot welding (FSSW) is a novel variant of linear friction-stir welding (FSW) used for spot-welding

applications.<sup>2</sup> The FSSW process uses a non-consumable rotating tool which is plunged into the workpieces to be welded. Before attaining the selected plunge depth, the rotating tool is held at the same position for a fixed time, which is defined as the dwell time. Consequently, the rotating tool is withdrawn from the welded joint, leaving a solid-phase friction-stir spot weld behind. Throughout the FSSW process, the tool penetration depth and the

Figure 1: Schematic diagram of the friction-stir spot-welding process<sup>3</sup>

dwelt time fundamentally determine the heat generation, material plasticization around the tool's pin, weld geometry and, hence, the mechanical properties of the welded joint.<sup>2</sup> **Figure 1** depicts a schematic illustration of the FSSW technique.

It should be noted that the FSSW process uses a non-consumable tool, which is similar to the FSW tool.<sup>4</sup> The shoulder produces the frictional heat, whereas the pin creates the material flow between the work sheets.<sup>2,3</sup> In addition to the tool, the other parameters involved in FSSW include the tool rotation speed, the tool plunge depth and the tool dwell time. These parameters have an effect on the strength, the surface texture of the welded joints<sup>2</sup> and the existence of weld defects.<sup>3</sup>

A typical cross-section of a friction-stir spot weld displays five different structures including the parent material (PM), the heat-affected zone (HAZ), the thermomechanically affected zone (TMAZ), the stir zone (SZ) and the hook.<sup>2</sup>

Friction-stir welding (FSW) and friction-stir spot welding (FSSW) of aluminium and copper have thus far not been fully investigated due to the huge difference between their melting temperatures and the high chemical affinity of both materials which facilitate the formation of brittle intermetallic Al/Cu phases.<sup>6–18</sup> Vickers hardness measurement is a common technique used to characterise the hardness of materials and it was reported that the presence of intermetallics affects the hardness values of the produced FS welds and FSS welds.<sup>11,17</sup> On the other hand, statistical analyses of Al/Cu friction-stir welds and spot welds have not been well researched. S. Akinlabi and E. T. Akinlabi<sup>19</sup> conducted statistical analyses on the data obtained from dissimilar friction-stir butt welds of aluminium (AA5754) and copper (C11000) to understand the link between the process parameters and the properties of the resulting welds. They concluded that the downward vertical force has a significant effect on the ultimate tensile strength (UTS) of the produced welds. A robust relationship between the electrical resistivity and the heat input into the welds was also observed.<sup>19</sup>

Statistical analyses evaluate the effects of process parameters on the properties of the produced spot welds and establish the relationships amongst the process parameters.

Therefore, in the current study, an effort was made to further understand the relationships between the process parameters and the microhardness profiles of FSSW welds between copper and aluminium using the probability distribution function (PDF). Furthermore, the microstructure and the chemical analyses of the produced spot welds were also studied.

## 2 MATERIALS AND WELDING PARAMETERS

In this study, AA1060 and C11000 base materials with dimensions of 3 mm thickness, 600 mm length and

120 mm width were friction-stir spot lap welded. The chemical compositions of the two parent materials were determined using a spectrometer. The chemical composition of the aluminium sheet is as follows: 0.058 % mass fraction of Si, 0.481 % mass fraction of Fe, 0.011 % mass fraction of Ga, 0.05 % mass fraction of other elements and the rest is Al. The chemical composition of the copper sheet is: 0.137 % mass fraction of Zn, <0.1 % mass fractions of Pb, 0.02 % mass fraction of Ni, 0.023 % mass fraction of Al, 0.012 % mass fraction of Co, 0.077 % mass fraction of B, 0.036 % mass fraction of Sb, 0.043 % mass fraction of Nb, <0.492 % mass fraction of other elements and the rest is Cu.

The sheets were friction-stir spot welded in a 30 mm overlap configuration. The spot welds were produced at the eNtsa of Nelson Mandela Metropolitan University, Port Elizabeth, South Africa using an MTS PDS I-Stir. The tool material used was H13 tool steel hardened to 50–52 HRC with a 4 mm tool pin, 5 mm tool diameter and 15 mm tool shoulder. The friction-stir spot welds were produced at rotational speeds of 800 min<sup>-1</sup> and 1200 min<sup>-1</sup>, the tool-shoulder-plunge depths employed were 0.5 mm and 1 mm at a constant dwell time of 10 s. The two different tool profiles used in the current study were flat pin/flat shoulder and conical pin/concave shoulder tool, designated as FPS and CCS, respectively. The produced welds were designated as XX\_XX\_XX with the first part describing the tool geometry, the second part indicating the rotational speed and the third part indicating the shoulder plunge depth.

The weld samples were sectioned using wire electrical discharge machining (WEDM), grinded and polished, mounted and prepared, using the ASTM standard metallographic procedure and ASTM Standard E3-11.<sup>20</sup>

A solution of FeCl<sub>3</sub> (10g) + HCl (6 mL) + ethanol (C<sub>2</sub>H<sub>5</sub>OH) (20 mL) + H<sub>2</sub>O (80 mL) was used to etch the copper side of the spot welds, while the aluminium side was etched with H<sub>2</sub>O (190 mL) + HNO<sub>3</sub> (5 mL) + HCl (10 mL) + HF (2 mL). The microstructure of the spot welds was studied using an optical microscope (Olympus BX51M) equipped with the Stream software. Scanning electron microscopy combined with energy dispersive spectroscopy (SEM/EDS) was used to further examine the microstructure and the chemical analyses, respectively. A TESCAN equipped with Oxford Instruments X-Max was used for the SEM/EDS analyses. The Vickers microhardness was determined using a dia-

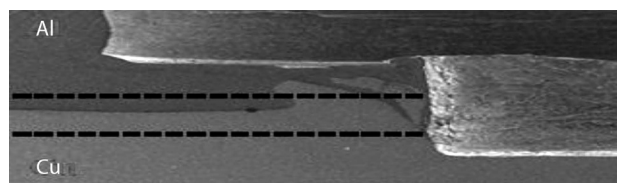


**Figure 2:** Representation of a spot weld with dashed lines illustrating the location of the microhardness-profile measurements

mond-pyramid-indenter EMCO Test DuraScan tester. Two different locations on the spot welds were used, viz., the top and the bottom, as illustrated in **Figure 2**. The microhardness measurements were carried out from the keyhole for all the different parameters and tool geometries, to find the probability density function (PDF) of each one. The Matlab 2014 software program was used to determine the PDF.

### 3 RESULTS AND DISCUSSION

The microstructure of the friction-stir spot welds was studied using an optical microscope and the results are depicted in **Figures 3** and **4**.

**Figure 3** illustrates the microstructures of the spot welds produced at: a) 800 min<sup>-1</sup> and b) 1200 min<sup>-1</sup>, a 1 mm shoulder plunge depth using a flat pin and a flat shoulder tool. On the other hand, **Figure 4** shows the microstructure of the spot weld produced at: a) 800 min<sup>-1</sup> and b) 1200 min<sup>-1</sup>, a 0.5 mm shoulder plunge depth using a conical pin and a concave shoulder tool.

It can be seen in **Figure 3a** that there are a copper ring and a mixture of Al/Cu particles in the stir zone. There is no palpable welding defect in the weld and copper is disseminated in this zone with different shapes. In the upper part of the joint, a large bulk of copper with

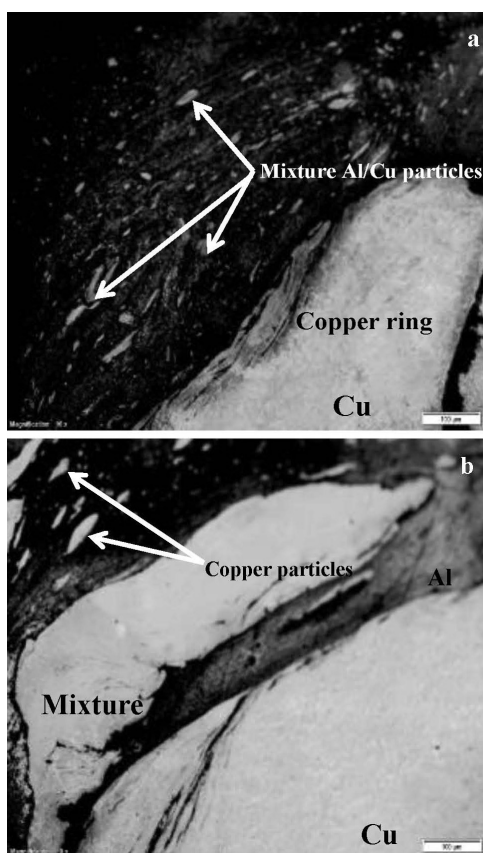


**Figure 3:** Optical microscope images showing the macrostructures of the joints at: a) 800 min<sup>-1</sup> and b) 1200 min<sup>-1</sup>, 1 mm shoulder plunge depth using a flat pin and flat shoulder tool

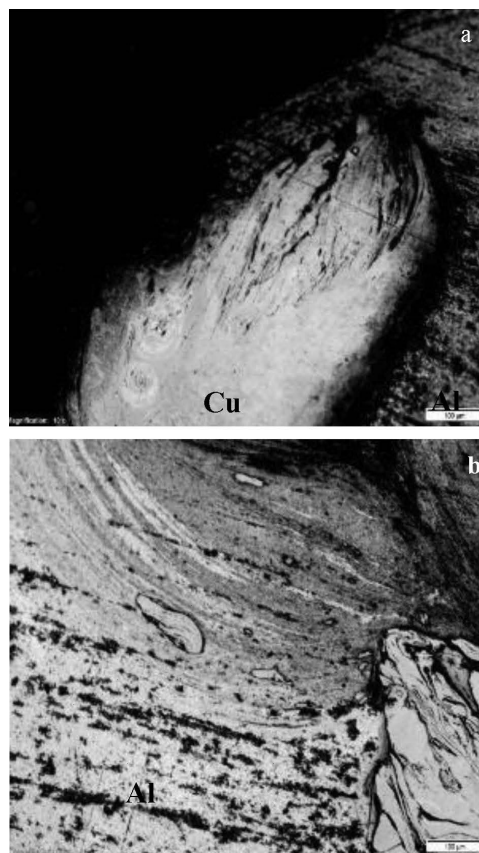


**Figure 4:** Optical microscope images showing the macrostructures of the joints at: a) 800 min<sup>-1</sup> and b) 1200 min<sup>-1</sup>, 0.5 mm shoulder plunge depth using a conical pin and concave shoulder tool

irregular shapes can be observed (**Figure 3a**). The tool pin was inserted in the aluminium plate and the copper ring extruded upward from the lower copper plate into the aluminium plate was observed. This was in agreement with the previous work.<sup>15</sup>

Additionally, the intermixing of copper and aluminium was not homogenous for different spot welds and different microstructures were formed in different regions of the welds. It was reported that the FSW of dissimilar materials is different from that of similar materials due to the formation of a complex, intercalated vortex-like and related flow pattern.<sup>21</sup>

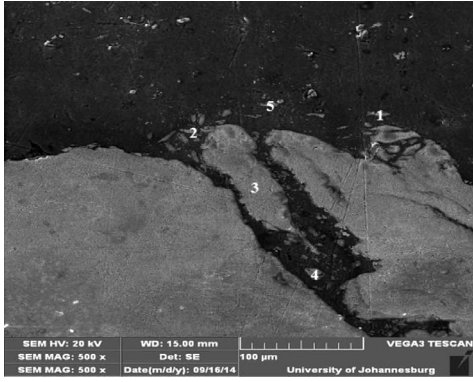
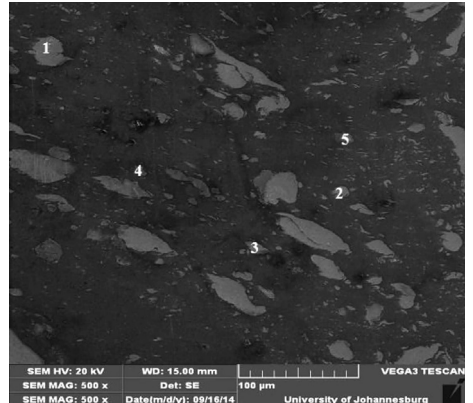
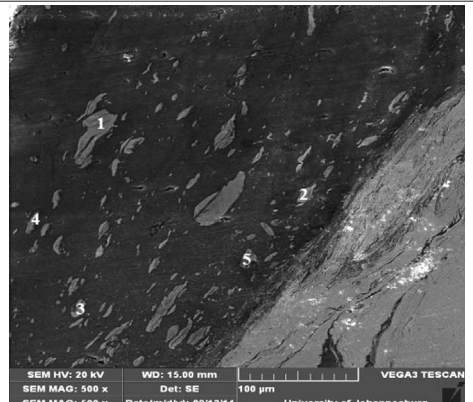
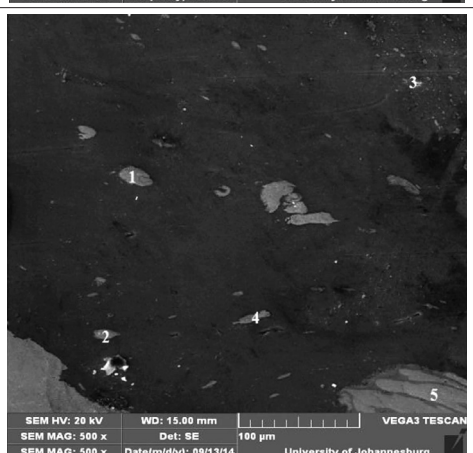
In **Figure 4b**, a good interlaced structure can be seen. This is formed by aluminium and copper, thereby indicating that the two plates are bonded firmly in this region, which is composed of a lamellar structure of copper particles with a streamlined shape of aluminium strips. In this region, a few disseminated copper particles were also observed.

The energy-dispersive-spectrometry analyses at the selected points in the stir zone were recorded using SEM micrographs (**Table 1**). Intermetallic compounds were found in most of the produced welds. Two intermetallic compounds, viz., Al<sub>2</sub>Cu and Al<sub>3</sub>Cu<sub>4</sub> were found in the weld produced at 1200 min<sup>-1</sup>, 0.5 mm shoulder plunge



M. P. MUBIAYI et al.: MICROSTRUCTURE EVOLUTION AND STATISTICAL ANALYSIS OF Al/Cu ...

**Table 1** displays SEM micrographs and the EDS analysis of selected points on the produced friction-spot welds: a) (FFS\_1200\_0.5), b) (FFS\_1200\_1), c) (CCS\_1200\_0.5) and d) (CCS\_1200\_1).

	Point	Composition		Intermetallic compound
		Al	Cu	
	1	54.94	45.06	-
	2	48.5	51.5	Al <sub>2</sub> Cu
	3	4.34	95.66	-
	4	24.55	75.45	Al <sub>3</sub> Cu <sub>4</sub>
	5	41.98	58.02	Al <sub>2</sub> Cu
	Point	Composition		Intermetallic compound
		Al	Cu	
	1	1.46	98.54	-
	2	17.71	82.29	Al <sub>4</sub> Cu <sub>9</sub>
	3	36.27	63.73	AlCu
	4	94.53	5.07	-
	5	16.98	83.02	Al <sub>4</sub> Cu <sub>9</sub>
	Point	Composition		Intermetallic compound
		Al	Cu	
	1	3.1	96.9	-
	2	7.82	92.18	-
	3	49.49	50.27	Al <sub>2</sub> Cu
	4	29.22	70.78	AlCu
	5	13.77	86.23	AlCu <sub>3</sub>
	Point	Composition		Intermetallic compound
		Al	Cu	
	1	2.26	97.74	-
	2	1.33	98.67	-
	3	92.77	6.97	-
	4	37.35	62.65	AlCu
	5	9.15	90.85	-

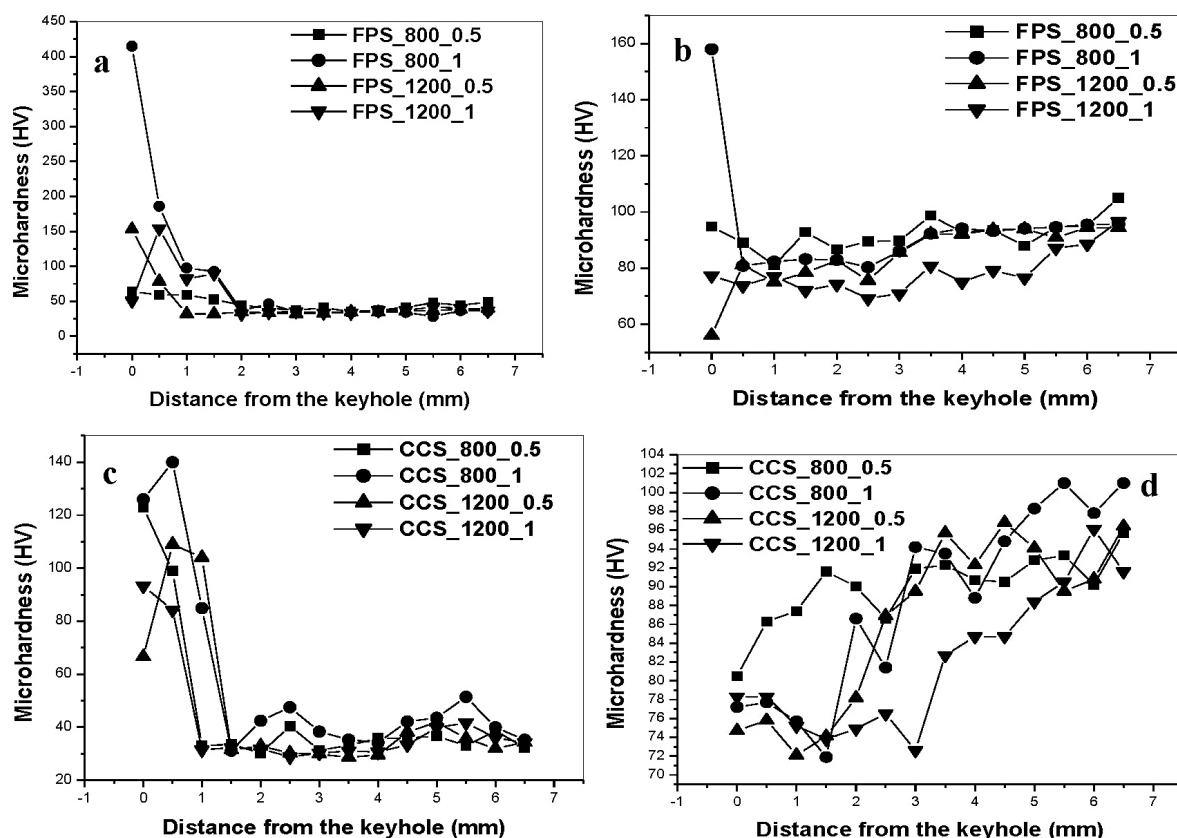


**Figure 5:** Microhardness distributions along the welds produced using different tools and process parameters: a) flat pin/flat shoulder (FPS), top; b) bottom; c) conical pin/concave shoulder (CCS), top; d) bottom

depth, whereas the weld produced at  $1200 \text{ min}^{-1}$  and 1 mm shoulder plunge depth contained  $\text{Al}_4\text{Cu}_9$  and  $\text{AlCu}$  intermetallic compounds. These intermetallics were found in the welds produced using a flat pin and flat shoulder tool. On the other hand, the spot welds produced using a conical pin and concave shoulder contained  $\text{Al}_2\text{Cu}$ ,  $\text{AlCu}_3$  and  $\text{AlCu}$  intermetallic compounds. These intermetallic compounds were found in the weld produced at  $1200 \text{ min}^{-1}$  and 0.5 mm shoulder plunge depth. Only the  $\text{AlCu}$  intermetallic was found in the weld produced at  $1200 \text{ min}^{-1}$  and 1 mm shoulder plunge depth, but the concentration of this intermetallic compound was relatively small. It was reported that the presence of intermetallic compounds could affect the microhardness profile.<sup>17</sup>

**Figure 5** (a, b, c and d) shows the microhardness values of the spot welds produced using a flat pin and a flat shoulder tool, or a conical pin and a concave shoulder at different process parameters. The microhardness values of the parent materials were in the range of 86.7–96.3 HV for Cu while for Al, the range was between 34.6–40.3 HV. In all the samples, high microhardness values were recorded at the top, in the region close to the keyhole.

It was reported that all the mechanical tests are subject to large statistical variations, which should be evaluated.<sup>22</sup>

The probability distribution function (PDF) of the Vickers hardness was reported in the literature to correspond to the Gaussian (or normal) distribution<sup>23</sup> and log-normal distribution.<sup>24</sup> A. M. Hassan et al.<sup>25</sup> studied the significance of the process parameters of friction-stir welding of aluminium-matrix composites to set the optimum level for each of these parameters and to further predict which responses are affected when using analyses of variance (ANOVA).<sup>25</sup> The present study used the Matlab 2014a statistical toolbox to analyse the probability density function (PDF) of the obtained microhardness results. This was done to understand how different parameters and tool geometries affect the probability of obtaining specific microhardness values.

A probability density function (PDF) is a function that defines the relative possibility for a random variable to take on a given value. The probability of the random variable falling within a particular range [a, b] of values is given with a finite integral of the PDF within that range [a, b], Equation (1):

$$p(x) = \int_b^a f(x, \mu, \sigma) = \int_b^a \frac{1}{\sqrt{2\pi\sigma^2}} e^{-\frac{(x-\mu)^2}{2\sigma^2}} \quad (1)$$

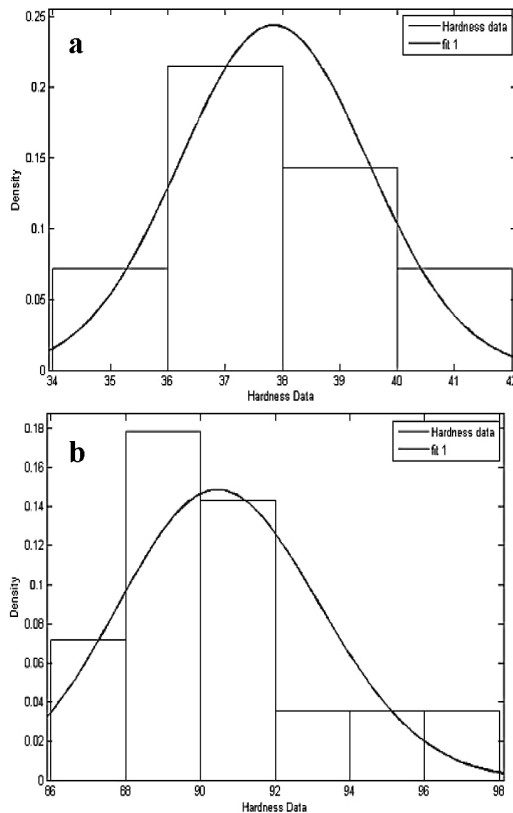


**Figure 6:** Depicting the microhardness PDF histograms of the parent materials: a) aluminium, b) copper

where  $\sigma$  is the standard deviation,  $\sigma^2$  is the variance and  $\mu$  is the mean.

It is given by the area under the density function, nonetheless above the horizontal axis and in between the lowest and highest values of the range. The probability density function is a non-negative value and its integral over the entire space is equal to one.

PDF histograms of the microhardness and their fits for the parent materials, namely, aluminium and copper, are depicted in **Figures 6a** and **7b**, respectively. The PDFs of the top and bottom hardness measurements were investigated, **Figures 7a** and **7b** depict the PDF histograms of the microhardness for the weld produced at 800 min<sup>-1</sup>, 0.5 mm shoulder plunge depth, using a flat pin and a flat shoulder tool.

It can be seen that the probability of having the microhardness values between 40 and 45 HV is high in the histogram, as shown in **Figure 7a**, which represents the microhardness measured at the top of the spot weld. This corresponds mostly to the microhardness of the aluminium parent material, whereas the possibility of getting high microhardness values between 50 and 60 HV is low.

On the other hand, the PDF of the bottom measurement (**Figure 7b**) shows that there is a high possibility of getting microhardness values between 85 and 95 HV. This corresponds to the microhardness of the copper-parent sheets, while the microhardness values between

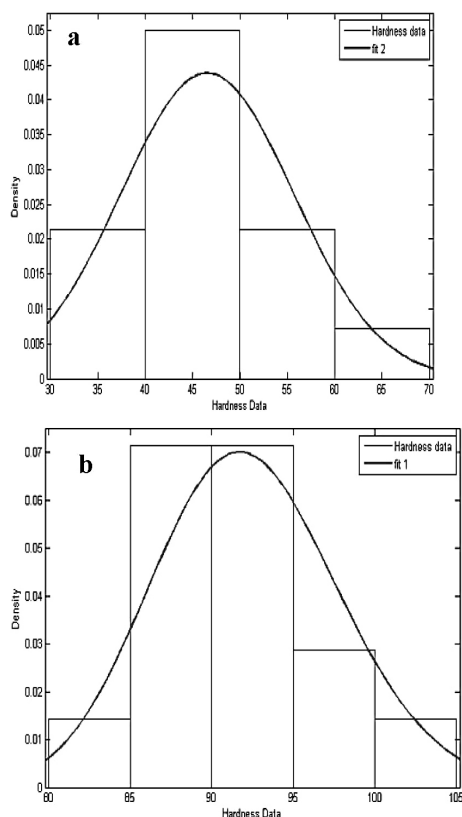


**Figure 7:** PDF histograms of the microhardness of FPS\_800\_0.5 spot weld: a) top and b) bottom

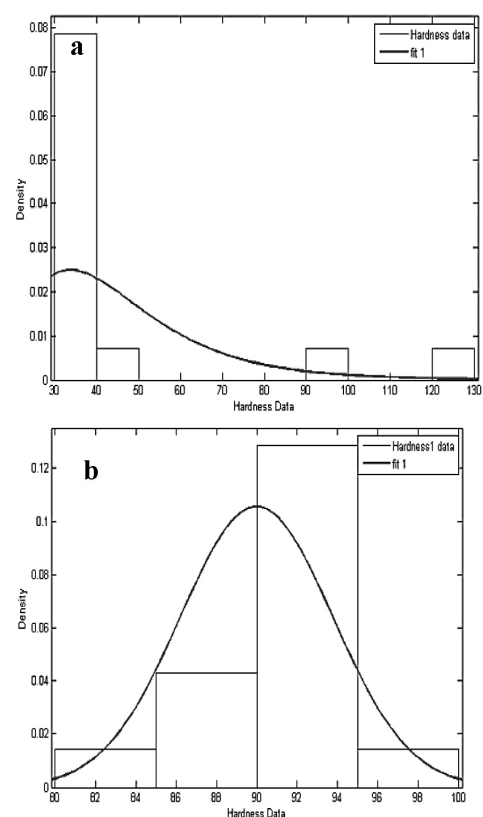


**Figure 8:** PDF histogram of the microhardness of CCS\_800\_0.5 spot weld: a) top and b) bottom

100 HV and 105 HV are likely to show a lower possibility of being obtained when using the same process parameters as those used in this research work. The possibility of having higher microhardness values compared to the values of the parent materials in the two different sheets (copper and aluminium) was observed to be due to the presence of a mixture of copper and aluminium in the vicinity of the keyhole. Additionally, **Figure 8** depicts a PDF histogram of the microhardness measurements ((a) top and (b) bottom) for the weld produced at  $800 \text{ min}^{-1}$ , 0.5 mm shoulder plunge depth, using a conical pin and a concave shoulder.

The results show that there is a higher possibility for obtaining microhardness values between 30–50 HV and 50–70 HV, whereas the possibility for high values between 120 and 130 HV is low (**Figure 8a**). The trend for the bottom area (**Figure 8b**) is similar to the one discussed above for the PDF of the bottom microhardness obtained using a flat pin and a flat shoulder.

Moreover, when the rotational speed of  $1200 \text{ min}^{-1}$  is increased, the possibility of getting high microhardness values ranging between 100–110 HV and 90–100 HV increases for the top area of the spot weld produced using a conical pin and a concave shoulder, and for the top and bottom microhardness values, respectively. It can be seen that the rotational speed and the tool geometry may influence the possibility of different probability distributions.

The model shows that, in order to get the probability in a specific region, the integral of the PDF for the region of interest need to be computed. The PDF found in the current research work is a normal distribution (called a Gaussian distribution as well). In order to get any probability, we can compute the finite integral of the normal distribution equation (1).

The goodness of fit and the residuals were also analysed. The results show that most of the  $R^2$  values range between 0.8842 and 0.9999, which is an indication of how well the model fits with the experimental data shown in **Table 2**.

**Table 2:**  $R^2$  and adjusted  $R^2$  of the welds produced using a flat pin/flat shoulder tool and conical pin/concave shoulder tool for the microhardness measured on the top and at the bottom

Sample ID	$R^2$ square	Adjusted $R^2$ square
FPS_800_0.5	0.9896	0.8842
FPS_800_1	0.9996	0.9999
FPS_1200_0.5	0.9999	0.9937
FPS_1200_1	0.9993	0.9298
CCS_800_0.5	0.9924	0.9818
CCS_800_1	0.9976	0.9424
CCS_1200_0.5	0.9893	0.987
CCS_1200_1	0.9997	0.9866

**Figures 9a to 9b** depict the goodness of fit and the residuals for the weld produced at  $1200 \text{ min}^{-1}$ , 1 mm shoulder plunge depth, using a flat pin and a flat shoulder (the top-microhardness measurement). In

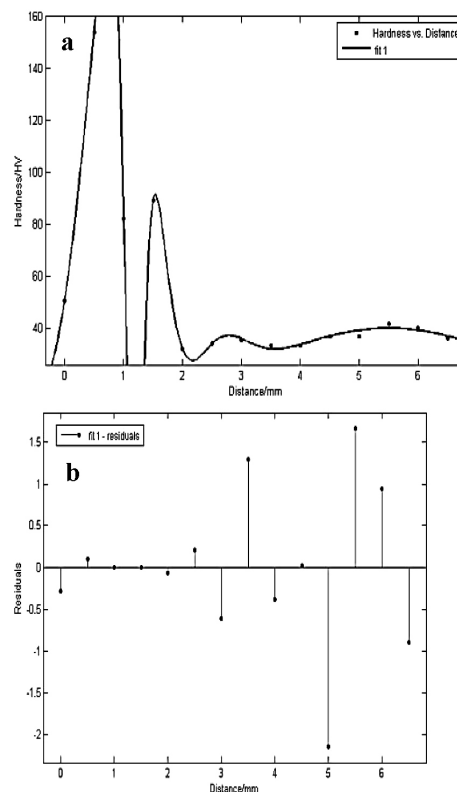


**Figure 9:** a) goodness of fit and b) the residuals for the spot weld produced at  $1200 \text{ min}^{-1}$ , 1 mm shoulder plunge depth, using a flat pin and a flat shoulder (top-microhardness measurements)

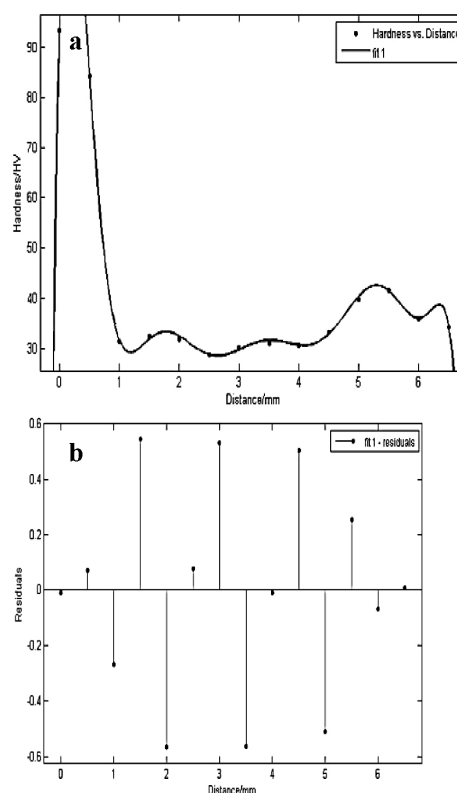


**Figure 10:** a) goodness of fit and b) the residuals for the spot weld produced at  $1200 \text{ min}^{-1}$ , 1 mm shoulder plunge depth, using a conical pin and a concave shoulder (top-microhardness measurements)



addition, **Figures 10a to 10b** depict the goodness of fit and the residuals for the weld produced at  $1200 \text{ min}^{-1}$ , 1 mm shoulder plunge depth, using a conical pin and a concave shoulder (the top-microhardness measurement). Besides the  $R^2$  values, the residual analysis was also employed in the study in order to check the adequacy of the models. **Figures 9b and 10b** show the residual plots for the microhardness values obtained at the top, using a flat pin/flat shoulder and a conical pin/concave shoulder, using the  $1200 \text{ min}^{-1}$  speed and 1 mm shoulder plunge depth, respectively. It was reported that the tendencies to have runs of positive and negative residuals indicate the existence of a certain correlation with the experimentation.<sup>26</sup>

**Tables 3 and 4** present the standard deviation, the variance and the mean obtained from the statistical analyses of the measured microhardness values for the two different positions, namely, the top and bottom of the spot welds produced with different tools and using different process parameters.

**Table 3:** Mean, variance, mu and sigma of the spot samples produced using a flat pin/flat shoulder tool and a conical pin/concave shoulder tool for the microhardness taken on the top

Sample ID	Mean	$\sigma^2$	$\mu$	$\sigma$
FPS_800_0.5	46.543	82.8442	46.5429	9.102
FPS_800_1	75.099	4994.97	4.00167	0.796
FPS_1200_0.5	45.121	441.806	3.71115	0.443
FPS_1200_1	51.731	672.845	3.83391	0.474
CCS_800_0.5	44.575	409.802	3.70341	0.433
CCS_800_1	55.887	813.763	3.90757	0.481
CCS_1200_0.5	45.453	482.889	3.71166	0.458
CCS_1200_1	40.942	248.04	3.64315	0.371

**Table 4:** Mean, variance, mu and sigma of the spot samples produced using a flat pin/flat shoulder tool and a conical pin/concave shoulder tool for the microhardness taken at the bottom

Sample ID	Mean	$\sigma^2$	$\mu$	$\sigma$
FPS_800_0.5	92.234	32.7196	4.52241	0.062
FPS_800_1	84.7	119.974	84.7	10.95
FPS_1200_0.5	84.7	119.974	84.7	10.95
FPS_1200_1	78.429	58.0637	78.4286	7.62
CCS_800_0.5	89.986	14.2859	89.9857	3.78
CCS_800_1	88.564	102.307	88.5643	10.11
CCS_1200_0.5	86.252	89.6604	4.45128	0.109
CCS_1200_1	82.043	54.8519	4.40318	0.09

It should be noted that the mean is equal to  $\mu$  if the distribution is normal. It can be seen that in some cases in the current work  $\mu$  and the mean have different values, which shows that the distributions in some of the analyses were not normal. The standard deviation  $\sigma$  should be close to zero, but in the current work, the value of the standard deviation is not close to zero in some of the cases. This shows that the microhardness values are not close to the expected values and this could be due to the microhardness values measured in different locations of the weld samples, far apart from each other.

This was further suspected due to the presence of intermetallics, which could have been the cause of the high microhardness values since intermetallics are invariably hard and brittle.

Each figure contains residuals versus the distance (the distance from the keyhole), taking into account the data and the constant variance of the residuals. In the plot of residuals versus distance, it is shown that the models are adequate to predict the responses in an acceptable manner.

## 4 CONCLUSIONS

According to the presented results, some conclusions can be drawn:

- The microstructure of the produced spot welds shows a good material mixing, the presence of a copper ring and a mixture of Al/Cu particles present in the stir zone.
- The EDS analyses of the produced friction-stir spot welds exhibited the presence of intermetallic compounds, which are known to affect the microhardness.
- The microhardness values obtained at the top were high for all the samples and this was in the region close to the spot-weld keyhole. In addition, all the microhardness values obtained at the bottom of the samples, in the region close to the keyhole, have lower values, which were close to the average value of the copper base material. This occurred for all the spot welds produced using a conical pin and concave shoulder.
- The probability-density-function (PDF) histograms of the microhardness results revealed that the process parameters and the tool geometries have significant effects on the distribution of the microhardness values in different locations of the produced spot welds.
- Additionally, goodness-of-fit values were also analysed and these showed that most of the  $R^2$  values ranged between 0.8842 and 0.9999, which is an indication of how well the model fits with the produced experimental data.

## Acknowledgements

The authors wish to acknowledge the financial support of the University of Johannesburg and the assistance from Mr. Riaan Brown (eNtsa at Nelson Mandela Metropolitan University).

## 5 REFERENCES

- <sup>1</sup> W. M. Thomas, E. D. Nicholas, J. C. Needham, M. G. Murch, P. Temple-Smith, C. J. Dawes, International Patent No. PCT/GB92/02203, GB patent application No. 9125978.8, 1991
- <sup>2</sup> H. Badarinarayan, Fundamentals of Friction Stir Spot Welding, PhD Thesis, 2009, Missouri

- <sup>3</sup> W. Yuan, R. S. Mishra, B. Carlson, R. Verma, R. K. Mishra, Material flow and microstructural evolution during friction stir spot welding of AZ31 magnesium alloy, *Materials Science and Engineering, A* 543 (2012), 200–209
- <sup>4</sup> J. Podržaj, B. Jerman, D. Klobčar, Welding defects at friction stir welding, *Metalurgija*, 54 (2015) 2, 387–389
- <sup>5</sup> J. M. Timothy, Friction Stir Welding of Commercially Available Superplastic Aluminium, PhD thesis, 2008, Department of Engineering and Design, Brunel University, Brunel
- <sup>6</sup> J. Ouyang, E. Yarrapareddy, R. Kovacevic, Microstructural evolution in the friction stir welded 6061 aluminum alloy (T6-temper condition) to copper, *Journal of Materials Processing Technology*, 172 (2006), 110–122
- <sup>7</sup> P. Liu, Q. Shi, W. Wang, X. Wang, Z. Zhang, Microstructure and XRD analysis of FSW joints for copper T2/aluminium 5A06 dissimilar materials, *Materials Letters*, 62 (2008), 4106–4108
- <sup>8</sup> P. Xue, B. L. Xiao, D. R. Ni, Z. Y. Ma, Enhanced mechanical properties of friction stir welded dissimilar Al–Cu joint by intermetallic compounds, *Materials Science and Engineering A*, 527 (2010), 5723–5727
- <sup>9</sup> A. Esmaeili, M. K. Besharati Givi, H. R. Zareie Rajani, A metallurgical and mechanical study on dissimilar friction stir welding of aluminum 1050 to brass (CuZn30), *Materials Science and Engineering, A* 528 (2011), 7093–7102
- <sup>10</sup> A. Abdollah-Zadeh, T. Saeid, B. Sazgari, Microstructural and mechanical properties of friction stir welded aluminum/copper lap joints, *Journal of Alloys and Compounds*, 460 (2008), 535–538
- <sup>11</sup> E. T. Akinlabi, Characterisation of Dissimilar Friction Stir Welds between 5754 Aluminium Alloy and C11000 Copper, D-Tech thesis, Nelson Mandela Metropolitan University, South Africa, 2010
- <sup>12</sup> M. N. Avettand-Fenoel, R. Taillard, G. Ji, D. Goran, Multiscale Study of Interfacial Intermetallic Compounds in a Dissimilar Al 6082-T6/Cu Friction-Stir Weld, *Metallurgical and Materials Transactions A*, (2012), 4655–4666
- <sup>13</sup> M. F. X. Muthu, V. Jayabalan, Tool Travel Speed Effects on the Microstructure of Friction Stir Welded Aluminium – Copper Joints, *Journal of Materials Processing Technology*, 217 (2015), 105–113
- <sup>14</sup> M. P. Mubiayi, E. T. Akinlabi, Friction Stir Spot Welding between Copper and Aluminium: Microstructural Evolution, *Proceedings of the International MultiConference of Engineers and Computer Scientists, Vol II, IMECS 2015, March 18–20, 2015, Hong Kong*
- <sup>15</sup> R. Heideman, C. Johnson, S. Kou, Metallurgical analysis of Al/Cu friction stir spot welding, *Science and Technology of Welding and Joining*, 15 (2010) 7, 597–604
- <sup>16</sup> U. Özdemir, S. Sayer, Ç. Yeni, Bornova-Izmir, Effect of Pin Penetration Depth on the Mechanical Properties of Friction Stir Spot Welded Aluminum and Copper, *Materials Testing in Joining Technology*, 54 (2012) 4, 233–239
- <sup>17</sup> M. Shiraly, M. Shamanian, M. R. Toroghinejad, M. Ahmadi Jazani, Effect of Tool Rotation Rate on Microstructure and Mechanical Behavior of Friction Stir Spot-Welded Al/Cu Composite, *Journal of Materials Engineering and Performance*, 23 (2014) 2, 413–420
- <sup>18</sup> M. P. Mubiayi, E. T. Akinlabi, Evolving properties of friction stir spot welds between AA1060 and commercially pure copper C11000, *Transactions of Nonferrous Metals Society of China*, 26 (2016), 1852–1862
- <sup>19</sup> E. T. Akinlabi, S. A. Akinlabi, Friction stir welding of dissimilar materials – statistical analysis of the weld data, *Proceedings of the International MultiConference of Engineers and Computer Scientists*, 2012, 1368–1373
- <sup>20</sup> ASTM Standard E3-11, Standard guide for preparation of metallographic specimens, ASTM International, West Conshohocken, PA, 2011, doi: 10.1520/E0003-11, www.astm.org
- <sup>21</sup> L. E. Murr, A Review of FSW Research on Dissimilar Metal and Alloy Systems, *Journal of Materials Engineering and Performance*, 8 (2010) 19, 1071–108
- <sup>22</sup> J. M. Schneider, M. Bigerelle, A. Iost, Statistical analysis of the Vickers hardness, *Materials Science and Engineering, A* 262 (1999), 256–263
- <sup>23</sup> A. L. Yurkov, N. V. Jhuravleva, E. S. Lukin, Kinetic microhardness measurements of sialon-based ceramics, *Journal of Materials Science*, 29 (1994), 6551–6560
- <sup>24</sup> I. Y. Yanchev, E. P. Trifonova, Analysis of microhardness data in Tlx In 1-x Se, *Journal of Materials Science*, 30 (1995), 5576–5580
- <sup>25</sup> A. M. Hassan, M. Almomani, T. Qasim, A. Ghaithan, Statistical analysis of some mechanical properties of friction stir welded aluminium matrix composite, *Int. J. Experimental Design and Process Optimisation*, 3 (2012) 1, 91–109
- <sup>26</sup> K. Palanikumar, R. Karthikeyan, Optimal machining conditions for turning of particulate metal matrix composites using Taguchi and response surface methodologies, *Machining Science and Technology*, 10 (2006) 4, 417–433



SYNTHESIS OF PMMA/ZnO NANOPARTICLES COMPOSITE  
USED FOR RESIN TEETHSINTEZA PMMA/ZnO NANODELCEV KOMPOZITOV ZA  
IZDELAVO ZOB IZ UMETNIH SMOL**Danica Popović<sup>1</sup>, Rajko Bobovnik<sup>2</sup>, Silvester Bolka<sup>2</sup>, Miroslav Vukadinović<sup>1</sup>,  
Vojkan Lazić<sup>1</sup>, Rebeka Rudolf<sup>3,4</sup>**<sup>1</sup>University of Belgrade, School of Dental Medicine, Dr. Subotića 8, 11000 Belgrade, Serbia<sup>2</sup>Faculty of Polymer Technology, Ozare 19, 2380 Slovenj Gradec, Slovenia<sup>3</sup>Zlatarna Celje d.o.o., Kersnikova ulica 19, 3000 Celje, Slovenia<sup>4</sup>University of Maribor, Faculty of Mechanical Engineering, Smetanova 17, 2000 Maribor, Slovenia  
d.popovic984@gmail.com*Prejem rokopisa – received: 2017-02-24; sprejem za objavo – accepted for publication: 2017-03-31*

doi:10.17222/mit.2017.025

Wear resistance is one of the most important physical properties of the artificial teeth used in acrylic dentures. The goal of this research was to synthesize a new composite material made of matrix Poly-(methyl methacrylate)-PMMA with different percentages (2 % and 3 % of volume fractions) of zinc-oxide nanoparticles (ZnO NPs) as reinforcing elements, to improve its mechanical properties. The dynamic mechanical behaviour of this composite was studied through the DMA method in comparison to the pure PMMA supported by the characterization of their microstructures. Then the wear resistance was analysed on the samples, which were prepared in the form of teeth. In this context their vertical height loss was measured after 100,000 chewing cycles on a chewing simulator, before and after the artificial thermal ageing. Investigations showed that the PMMA/ZnO NP composites dampened the vibrations better than the pure PMMA, which could be assigned to the homogenous distribution of ZnO NPs in the PMMA matrix. It was found that the mean vertical height loss for the pure PMMA teeth was significantly higher (more than 4 times) compared to composite teeth made with ZnO NPs. Introducing the thermal artificial ageing led to the finding that there was no effect on the height loss by the composite material with 3 % of volume fractions of ZnO NPs. Based on this it was concluded that PMMA/ZnO NPs composites showed improved in-vitro wear resistance compared to acrylic-resin denture teeth, so this new composite material should be preferred when occlusal stability is considered to be of high priority.

Keywords: poly-(methyl methacrylate)-PMMA, zinc-oxide nanoparticles, composite, resin teeth

Odpornost proti obrabi je ena izmed najbolj pomembnih fizikalnih lastnosti umetnih zob pri akrilnih protezah. Cilj te raziskave je bil sintetiziranje novega kompozitnega materiala, izdelanega iz matrice poli-(metil meta akrilata) – PMMA z različnimi volumskimi odstotki (2 % in 3 %) nanodelcev cinkovega oksida (ZnO NPs), uporabljenimi kot ojačitveni element za izboljšanje mehanskih lastnosti materiala. Dinamično mehansko obnašanje teh kompozitov smo raziskali z metodo DMA v primerjavi s čistim PMMA, ter s karakterizacijo njihovih mikrostruktur. Nato je bila analizirana odpornost proti obrabi na vzorcih, ki so bili pripravljeni v obliki zob. Izmerjena je bila njihova navpična izguba višine po 100.000 žvečilnih ciklov na žvečilnem simulatorju, pred in po umetnem toplotnem staranju. Preiskave so pokazale, da so PMMA/ZnO NPs kompoziti bolje blažili vibracije kot čisti PMMA, kar lahko pripišemo homogeni porazdelitvi ZnO NPs v PMMA matrici. Ugotovili smo, da je bila povprečna navpična izguba višina za čisti PMMA zob znatno višja (več kot 4x) v primerjavi s kompozitnimi zobmi z ZnO NPs. Umetno toplotno staranje ni imelo učinka na izgubo navpične višine zoba iz kompozitnega materiala s 3 volumskimi % ZnO NPs. Na podlagi tega smo sklenili, da imajo kompoziti PMMA/ZnO NPs izboljšano in vitro odpornost proti obrabi, v primerjavi z zobno protezo iz akrilne smole, zato naj bi imel ta novi kompozitni material prednost pri uporabi, kadar je potrebna okluzalna stabilnost.

Ključne besede: poli-(metil meta akrilat)-PMMA, nanodelci cinkovega oksida, kompoziti, zobje iz umetnih smol

**1 INTRODUCTION**

Teeth loss in the human population is associated with numerous problems such as chewing difficulties, alteration of speech and facial expressions, which all leads to de-socialization. According to the Oral Health-Healthy People 2010: Objectives for Improving Health 26 % of the US population and 33 % of the Central Europe population aged between 65 years and 74 years are toothless; but some dramatic data and a wide variation in edentulism prevalence among adults aged 50 and above was found in the following countries: 48.3 % in Ireland, Malaysia 56.6 % and Netherlands 65.4 %, which indicates an international problem.<sup>1-3</sup>

The problems of toothless people in the region of the Balkan peninsula and South-Eastern Europe are usually solved with a complete or partial acrylic denture, which is the easiest and the cheapest solution, because more than 90 % of these patients are in a bad financial situation and incapable of buying dental implants and hybrid bridges above them. With an acrylic denture the wear resistance represents one of the most important physical properties because, in the case that the material has excessive wear, that might cause loss of the vertical dimension of occlusion (VDO) which is associated with decreased occlusal forces, loss of masticatory efficiency, improper tooth relationship, and fatigue of masticatory muscles.<sup>4</sup> Recently, a study examined how VDO can



affect brain function in complete denture wearers, and also measured occlusal forces when there is a change in VDO in which electroencephalograms were used.<sup>5</sup> Many authors have pointed out the necessity of creating complete new dentures, or relining of the denture base, which is not a simple procedure and presents financial pressure for the patients.<sup>6</sup> So, finding the new combination of materials with improved mechanical properties, which include better wear resistance, would be helpful for many reasons for those patients.

Many basic researches based on polymer materials represent the challenge. One of these are made of supramolecular polymers as a new high-tech material.<sup>7,8</sup> Over the past two decades a great effort has been made by the community of researchers for the synthesis and utilization of nanomaterials in the field of medical materials.<sup>9</sup> Using fine nanoparticles as reinforcing elements could improve the functional properties of conventional materials such as PMMA, which has been used for dentures since 1937. The ZnO NPs are small objects that behave as an entire unit regarding their transport and properties. The introduction of ZnO NPs represents a new approach in dentistry by the production of a denture, because they could decrease the level of residual monomer and, besides this, they also have antimicrobial activity. This was shown in recent studies.<sup>10,11</sup> Namely, ZnO NPs are environmentally friendly materials in the nanometre size range, and could be synthesized in a wide range of particle shapes and structures.<sup>12–14</sup> ZnO in bulk form is a largely inert, white powder compound that has a very broad application, from the chemical industry through cosmetic and medical products. In dentistry they have an important place as a medicament for healing injuries after periodontal surgical treatment, in the cementation of temporary, as well as definitive, crowns etc. ZnO is also a biocompatible material that exhibits antimicrobial properties against gram-negative as well as gram-positive bacteria.<sup>15</sup> A recent study also investigated, proved and determined the minimal inhibitory concentration of ZnO NPs against *Candida Albicans*.<sup>16</sup>

Nanostructured materials with unique and fascinating properties motivate scientists tremendously to explore and understand their formation and growth processes and following the critical volume in several studies we tried to find the right percentage of ZnO NPs in a PMMA matrix which could advance the properties of this new composite, because increasing the percentage of added NPs could downgrade some of them.<sup>17,18</sup>

According to the presented state-of-the-art study, the aim of this research was:

- (i) To synthesize a composite PMMA/ZnO NPs material, to test its mechanical properties, and evaluate the developed microstructures;
- (ii) To investigate the wear resistance of resin teeth in a chewing simulator with two combinations, before and after thermal artificial ageing. This investigation

included not only the classical testing samples, but also the real model of the shapes of first upper molars (testing resin teeth) and showed possible practical applications in dentistry.

## 2 EXPERIMENTAL PART

### 2.1 Materials for composite PMMA/ZnO NPs

Commercially available ZnO nanopowder (purity 99.99 %, density 5.606 g/cm<sup>3</sup>, insoluble in water, formula weight 81.37, melting point 1975 °C) was purchased from Interdent (Belgrade, Serbia). The average size of the ZnO NPs was 30 nm and they were in the form of a sphere. The typical shape and morphology of characteristic ZnO NPs are shown in **Figure 1**, which was made on a transmission electron microscope (TEM).

PMMA matrix (polymethylmethacrylate powder with benzoyl-peroxide, pigments and for a liquid-methylmethacrylate HQ 60, ethylene glycoldimethacrylate, methylmethacrylate composite) was distributed by Galenika (Belgrade, Serbia). This material was used for Biogal® acrylic teeth (Galenika, Belgrade, Serbia) and has already passed through the applied ISO Standards.

### 2.2 Measurement of ZnO nanoparticles' size distribution and zeta potential in water and MMA

Because of the frequent problem with agglomeration among nanoparticles, especially ZnO NPs in water, we used the DLS technique to confirm or deny this fact indirectly and compare them with ZnO NPs in suspension with MMA. Initially, ZnO NPs powder (0.05 g) with water and MMA monomer (15 mL by volume in both cases) was mixed through magnetic stirring for the time duration of 45 min. The size distributions and surface charge of the nanoparticles were determined with a Malvern Zetasizer Nano ZS (Malvern Instruments Ltd., U.K.) by the DLS technique. The suitable parameters for ZnO NPs Absorption: 0.1 and Refractive index: 2.0. were chosen according to <sup>19</sup>.

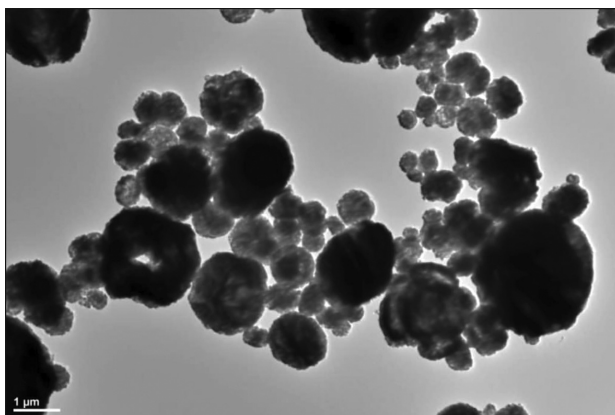


**Figure 1:** Micrograph of shape and morphology of characteristic ZnO NPs (TEM, 10 000×)

### 2.3 Preparation of samples

Samples were made in two shapes: Lamina (dimension: 45 mm × 3 mm × 7 mm) for characterization of the new composite and then in the form of the first upper molar for direct potential use in dentistry.

The ZnO NPs in the PMMA matrix were mixed with PMMA powder and then free radical polymerization was performed of MMA monomer in bulk. The new composite was synthesized at the selection of the appropriate technological regime, which started in the moment of adding monomer liquid PMMA/ZnO NPs powder for 1 h and 45 min at 100 °C. The procedure for both samples followed by shaping the samples firstly in wax, then duplicated and changed in to the pure PMMA, PMMA filled with 2 % of volume fractions and 3 % of volume fractions of ZnO NPs. The volume % were chosen according to our previous experiences and based on <sup>7,16,18</sup>. All samples in the form of the first upper molar were identical in form, plan parallel and highly polished. They were prepared for a wear test in a chewing simulator. Schematic presentations of the composite PMMA/ZnO NPs synthesis and their corresponding testing are shown in **Figure 2**. A list of samples' names, their mixing ratio PMMA/ZnO NPs and technical descriptions are given in **Table 1**. PMMA1 was chosen for a comparison with the new composites.

### 2.4 Characterization

Thermo-mechanical properties were examined using a Perkin Elmer DMA 8000 dynamic mechanical analyser. The TT\_DMA software, Version 14310, was used for the evaluation of the results. The viscoelastic properties of the samples were analysed by recording the storage modulus ( $E'$ ), loss modulus ( $E''$ ) and loss factor ( $\tan \delta$ ) as a function of temperature. The height of the peak of the loss factor determined the damping behaviour – with decreasing peak height the damping behaviour was increasing. For the analyses of test samples, the DMA instrument was operated in the dual cantilever mode. The viscoelastic analyses were carried out on samples with dimensions of approximately 42 mm × 5 mm × 2 mm. The samples were heated at 2 °C/min from room temperature to 180 °C under an air atmosphere. A frequency of 10 Hz and amplitude of 20  $\mu$ m were used.

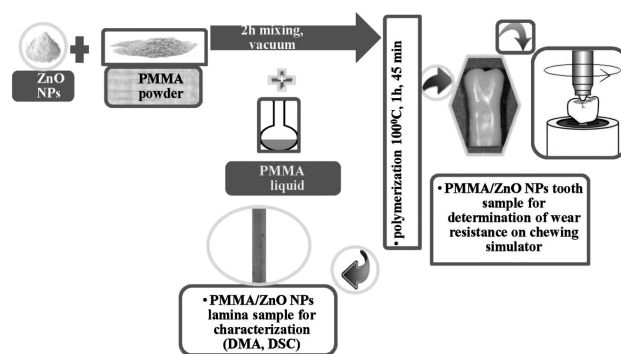


**Figure 2:** Schematic presentation of synthesis composite PMMA/ZnO NPs and samples for testing

A flash differential scanning calorimeter (Flash DSC) was used for the identification of the glass transition and reorganisation of the polymers for all the samples. Flash DSC works by ultra heating and cooling rates that induce physical transitions and chemical processes. This characterization was very important for dentistry practice because it allowed us to follow the level of polymerization in the residual monomer, which could produce an allergic reaction by the use of the new composite for the resin teeth in removable dentures in the mouths of patients.

### 2.5 Determination of wear resistance

The wear tests of the samples in the shape of upper first molar were performed in a chewing simulator CS-4.2 economy line (SD Mechatronics, Germany). The simulator has two identical sample chambers and two stepper motors which allow computer-controlled vertical and horizontal movements. The masticatory cycle in this research consisted of three phases: contact with a vertical load of 5 kg, horizontal sliding of 0.4 mm, vertical sliding of 0.2 mm and separating the teeth and machine antagonist. In our investigation, two types of tests were made: before and after thermal artificial ageing including all samples from **Table 1**. The machine was set at 100.000 cycles, which simulated chewing over a period of one year. The loss of substance was measured with an electronic digital calliper – Globathronics GmbH (Germany). Accelerated thermal ageing was carried out by immersing the samples in a water bath at a temperature of 70 °C.<sup>20,21</sup>

**Table 1:** Composition, mixing ratio and forms of samples for different testing

Samples/ abbreviation	Composition	Mixing ratio	Form for characterization	Form for wear test
PMMA1	Pure PMMA	15 mL MMA + 23.4 g PMMA	Lamina	Tooth model
PMMA2	PMMA/2vol%ZnO NPs	15 mL + 22.93 g PMMA + 0,47 g ZnO NPs	Lamina	Tooth model
PMMA3	PMMA/3vol%ZnO NPs	15 mL + 22.7 g PMMA + 0,7 g ZnO NPs	Lamina	Tooth model

**Table 2:** Composition and the type of mixing used in the preparation of the solvent with the DLS measurements

Exp. No.	Composition	Methodology	DLS Measurement				
			Run of measurement	Average size range (µm)		Zeta potential (mV)	
1	0.05 g ZnONPs + 15 mL H <sub>2</sub> O	Magnetic stirring (45 min)	I	3.50	4.01 ± 0.40	–3.45	–3.38 ± 0.81
			II	4.08		–2.35	
			III	4.48		–4.35	
2	0.05 g ZnONPs + 15 mL MMA	Magnetic stirring (45 min)	I	2.28	2.21 ± 0.10	–3.40	–3.48 ± 0.07
			II	2.28		–3.57	
			III	2.06		–3.49	

## 2.6 Microstructure analysis

Microstructural characterizations of all the samples were carried out with scanning electron microscopy (SEM-Sirion 400 NC and Quanta 200 3D). The specimens, without previous preparation, were broken in an atmosphere of N<sub>2</sub> to minimise the influence of metallographic preparation regarding changes in the structure of the composite. After breaking, the samples were sprayed with Au (Jeol JSM 8310 appliance), which enables the observation of the non-conductive surfaces of the samples with an electron beam. The samples were positioned into the chamber of the microscope and observations were performed with an accelerating voltage of 15 kV.

## 2.7 Statistical analysis

The statistical analysis included all the parameters involved in the laboratory tests and it was performed in the statistical package SPSS® 17.0. Multivariate linear regression analysis was used to determine the predictors of differences between the analysed groups of samples. The threshold value for accepting the working hypothesis was set at  $p < 0.05$ .

# 3 RESULTS AND DISCUSSION

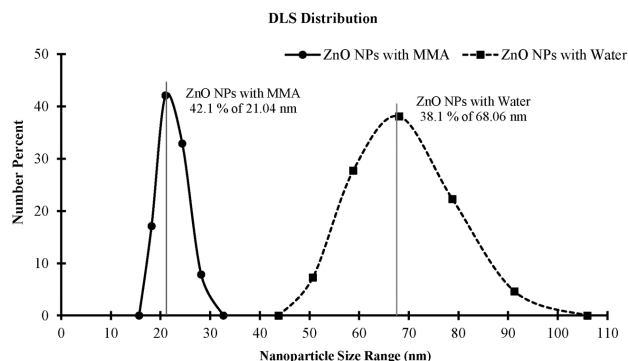
## 3.1 Macroscopic view

A macroscopic view of both samples' shapes confirmed the homogenous structure of PMMA and PMMA/ZnO NPs. There was only an acceptable difference in colour.

Adding ZnO NPs to the mixture with PMMA gave a brighter colour as the percentage of nanoparticles grew. This could be solved in the future by the addition of proper pigment, which results in a similar colour as in the teeth or oral mucosa, which are replicated in resin teeth and denture bases.

## 3.2 Size distribution and zeta-potential by DLS

The statement of the homogeneous distribution of ZnO NPs in samples was also confirmed by DLS measurement of the results, which are shown in **Table 2**. In ZnO NPs with MMA suspension, the average particle size was  $2.21 \pm 0.10 \mu\text{m}$ , while 42.1 % of the particles were in the size range of 21.04 nm, whereas in ZnO NPs with water suspension, the average particle size was  $4.01 \pm 0.4 \mu\text{m}$ , while 38.1 % of the particles were in the size range of 68.06 nm. Therefore, the average size of the particles was greater in ZnO NPs with water suspension with more presence of larger-sized clusters of particles. Distribution of ZnO NPs in MMA suspension was homogenous, which showed additionally the insolubility of ZnO NPs in water. ZnO NPs with MMA had a sharp and narrow intensity vs. size curve, as compared to ZnO NPs with water; thereby, it can be stated that there is a higher degree of agglomeration in the ZnO NPs with water suspension (**Figure 3**). The present study showed how it is possible to predict, simulate and characterize the composite material, which is aimed for use in dentistry. The DLS technique could confirm indirectly that ZnO NPs in an MMA suspension give a smaller agglomeration, which was also proven through the calculated large hydrodynamic diameters. ZnO NPs which have a zeta-potential between minus 30 mV and plus 30 mV show a tendency for coagulation. Therefore, ZnO NPs suspensions with water were unstable solutions and showed the tendency of agglomerate, while adding MMA in the ZnO NPs did not show much difference in the stability of the suspension as compared with the water. The samples in our work were made by mixing first ZnO NPs nanopowder and PMMA powder matrix in vacuum, at room temperature for 2 h then adding MMA, which reduced the aggregation among ZnO NPs. This may allow us to prepare homogenous nanocomposites with organic matrices without additional surface modification. The chosen average ZnO NPs size showed

**Figure 3:** Number vs. size distribution curve of ZnO NPs with MMA and water



that is of vital importance for the final properties of the new developed composite PMMA/ZnO NPs since it affected the UV-vis absorption and thermal stability. During the synthesis it was found that smaller ZnO NPs showed a higher degree of agglomeration, which is in accordance with the literature.<sup>22–24</sup>

### 3.3 Determination of properties

The results obtained by the DMA (**Figure 4**) showed the following results. The difference in the elastic modulus at low temperatures which may be due to a slight decrease in the cross linking of PMMA by adding ZnO NPs. At elevated temperatures, the incidence of chain transfer increased (at termination). With chain transfer, the propagating polymer radical reacts with another molecule by proton abstraction and this leads to branching and cross-linking.

Partly, the E modulus increases due to the addition of ZnO NPs, but this increase is minimal. Because of the absence of good interactions between the ZnO NPs and the PMMA matrix, the loss factor increases with the amount of addition of ZnO NPs in the PMMA matrix. ZnO NPs added to the PMMA increased the E modulus and reduced the level of cross-linking. At the same time, the poor interaction between the filler and the matrix results in a less elastic response, which means that the composite of PMMA/ZnO NPs dampen the vibrations better than pure PMMA. With the increasing of the loss factor ( $\tan \delta$ ) the damping of the material also increases. In our case, the height of the loss factor peak of the sample PMMA3 was the highest; therefore, the damping of the vibrations of the sample PMMA3 is the highest (**Figure 5**).

Characterization using the DMA method showed that changes in the vibration-damping behaviour of the new composite could mean that at the gingival a more gentle feeling appears, which leads to this material being more friendly to oral mucosa due to vibration damping. This should also be proven through practice. Composite PMMA/ZnO NPs would require longer curing times in

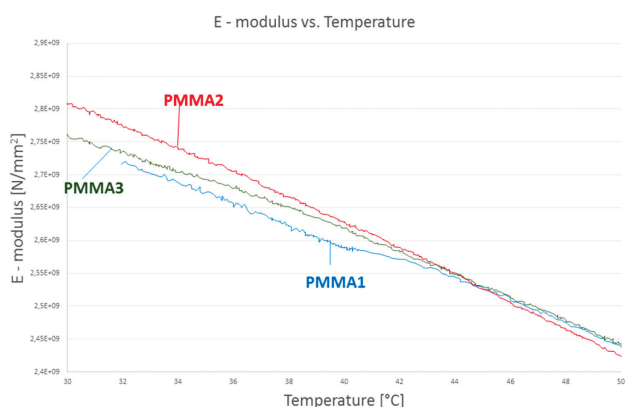


**Figure 4:** DMA results- diagram  $E$  – modulus ( $\text{N/mm}^2$ ) –  $T$  ( $^{\circ}\text{C}$ ) for all samples

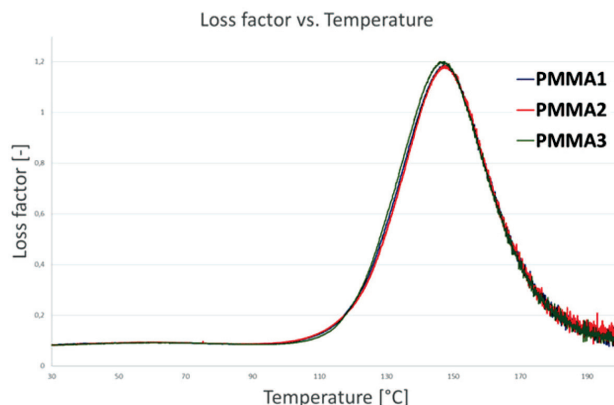


**Figure 5:** DMA results-loss factor vs. temperature for all samples

comparison with the pure PMMA. Based on this finding it is expected to obtain a better material with the surface modification of ZnO NPs where good interactions between filler and matrix can be formed.

From the Flash DSC measurements (**Figure 6**), the lowest glass-transition temperature was measured in the PMMA3 sample ( $129.6^{\circ}\text{C}$ ), followed by PMMA2 ( $131.0^{\circ}\text{C}$ ) and the highest glass-transition temperature was in the pure PMMA1 ( $131.1^{\circ}\text{C}$ ). This fact is also confirmed by the position of the peaks of the loss factor ( $\tan \delta$ ), where the lowest glass-transition temperature was measured in the PMMA3 ( $146.1^{\circ}\text{C}$ ), followed by PMMA2 ( $147.2^{\circ}\text{C}$ ) and the highest glass-transition temperature in the pure PMMA1 ( $147.8^{\circ}\text{C}$ ). In this context it was found that the degree of cross-linking was reduced by the addition of ZnO NPs. With increasing glass-transition temperature the loss factor decreased, which indicates that the material PMMA3 ( $\tan \delta = 1.2003$ ) has the best vibration-damping behaviour, followed by PMMA2 ( $\tan \delta = 1.1856$ ). The pure PMMA1 ( $\tan \delta = 1.1839$ ) showed the most elastic response. From the height of  $\tan \delta$  it can be concluded that the 3 % addition of ZnO NPs in PMMA is needed to obtain a significant change in the vibration-damping behaviour of the composite. Despite the small differences measured, as well on DMA ( $E$  modulus,  $\tan \delta$ ) as on Flash DSC (glass-transition temperatures), all the results had the same tendency.

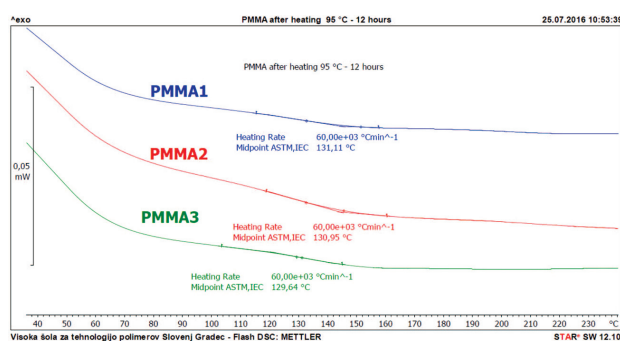


**Figure 6:** Results of flash DSC analysis for all samples, heating  $1.000^{\circ}\text{C/s}$  (diagram heat flow ( $\text{mW}$ ) –  $T$  ( $^{\circ}\text{C}$ ))



The difference in the E modulus at low temperatures may have been due to the slight decrease in the cross-linking of the PMMA by adding ZnO NPs. The degree of cross linking by adding ZnO NPs decreased, as shown by the measurements on the Flash DSC and the level of the peak of  $\tan \delta$ . This results, at temperatures up to about 45 °C, in a minimum E modulus in the PMMA3 and a maximum E modulus in the PMMA2 (the difference between the glassy transition of PMMA2 and pure PMMA1 was minimal). Partly, the E modulus increased due to the addition of ZnO NPs, but this increase was minimal. Because of the absence of good interactions between the ZnO NPs and the PMMA matrix, the loss factor increased with the amount of addition of ZnO NPs in the PMMA matrix.

### 3.4 Wear resistance

The mean vertical dimension of each tooth sample was measured (from the top of the field where the wear test was performed to the bottom) before the artificial chewing action and after. All the samples were subjected to artificial thermal ageing (the samples were in warm water at 70 °C for one month) and, after that, to mechanical ageing on the chewing simulator. The results of mean height loss of the control (PMMA1) and tested group (PMMA2, PMMA3) are shown in **Figure 7**. Recently, a study showed that the median vertical wear of polymer denture teeth, made by different materials, has been reported to be above 0.2 mm after 2 years of observation and, in over 50 % of these, variability of wear. This could be attributed to specific patient factors such as biting force, nutrition habits and other unknown factors. Gender differences were also found in the spatial and temporal parameters of masticatory movement path

and rhythm.<sup>25–27</sup> On the other hand, we used the same material and improved these mechanical properties by adding a different percentage of ZnO NPs; we also checked the height loss of the material only after one year of mechanical ageing on a chewing simulator.

The tested PMMA2/3 samples showed a higher wear resistance than the tooth sample PMMA1 by 4 times. Artificial thermal ageing had an effect on the pure PMMA1 and PMMA2, but there was no effect in the group with samples made of PMMA3. There was no statistically significant difference in the loss of height between samples made of PMMA2 with PMMA3. Occlusal wear values of the samples made of pure PMMA1 and PMMA2 after thermal artificial ageing were 2-times as big compared to the samples made from PMMA3. Wear resistance of restorative materials under clinical conditions is a rather complicated phenomenon compared to other mechanical and physical properties of materials.<sup>25</sup> Furthermore, the cause of thermal stability and its effect on the wear resistance of both PMMA2 and PMMA3 samples could be linked significantly. Long-term polymerization at 70 °C, after polymerization at the usual 100 °C for 1 h and 45 min can be recommended, because of its positive effect on the wear resistance of PMMA1 and PMMA2 after artificial ageing (70 °C, one month). PMMA3 had lower height loss before, as well as after, thermal artificial ageing compared to the other samples.

### 3.5 Microstructure

The microstructure of the fracture surface of the newly developed PMMA2 is shown in micrographs (**Figure 8**), where the visible fracture is brittle. Detailed observation by higher magnification revealed that ZnO NPs (coloured in white) are distributed homogeneously through the PMMA matrix with some small evidence of ZnO NPs' agglomeration (about 1  $\mu\text{m}$ ) and signs of de-polymerized dark fields around them. This led to the deteriorated final properties of the composite. In the future, it is necessary to avoid the de-polymerization process by the adequate preparation of ZnO NPs' surface

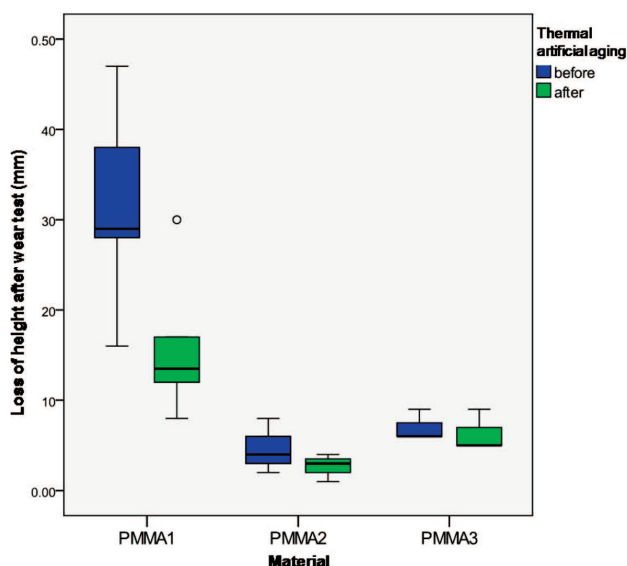


**Figure 7:** Loss of height of resin teeth after wear test on chewing simulator before and after thermal artificial aging

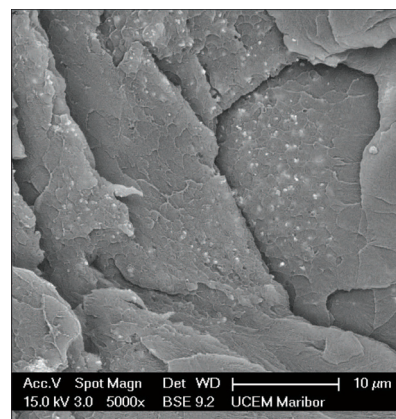


**Figure 8:** Micrographs of characteristic surface fracture in PMMA2

modification.<sup>23</sup> On the other hand, from the literature it is known that homogeneously dispersed ZnO NPs in the PMMA matrix can be explained by the theory of the different kinds of integration by grafting copolymer chains.<sup>28,29</sup>

#### 4 CONCLUSIONS

Based on the methodology applied in this study, and by considering the obtained results, the following conclusions can be drawn:

- The newly developed composite of PMMA/ZnO NPs has a better vibrations damping effect than pure PMMA1. This could lead to the gingival's more gentle feeling of appearance.
- Composite resin denture PMMA teeth reinforced by the ZnO NPs showed better wear resistance by about 4 times compared to the pure PMMA1.
- The microstructure of PMMA/ZnO NPs consists of a PMMA matrix and homogeneously distributed ZnO NPs.
- Combinations of different characterization techniques in the designing of polymer composites reinforced by nanoparticles with in vitro chewing simulation enable the determination of functional composite's behavior in dentistry.

#### Conflicts of interests

There are no conflicts of interests to declare.

#### Acknowledgment

This study was supported by the research project "Development of PMMA composite enriched/enhanced with nanoparticles (Ag, ZnO) and biocompatibility testing", number of project 451-03-2802-IP Type 1/144 and by the Infrastructure Programmes IO-0046 and IO-0029 financed by the Slovenian Agency ARRS. Thanks to the Ministry of Education, Science and Sport, Republic of Slovenia (Programme MARTINA, OP20.00369), which enabled the research with co-financing.

Special acknowledgements go to Mohammed Shariq for work on DLS.

#### Note:

The responsible translator for the English language is mag. Shelagh Hedges, Faculty of Mechanical Engineering, University of Maribor, Slovenia.

#### Abbreviations:

PMMA – Poly-(Methyl-Methacrylate)(powder)  
 MMA – Methyl-Methacrylate(liquid)  
 ZnO NPs – Zinc-Oxide Nanoparticles  
 DMA – Dynamic mechanical analysis  
 PMMA2 – PMMA + 2 vol. %ZnO NPs  
 PMMA3 – PMMA + 3 vol. %ZnO NPs  
 Flash DSC – Flash differential scanning calorimeter

DLS – Dynamic light scattering

TEM – Transmission Electron Microscope

#### 5 REFERENCES

- <sup>1</sup> Healthy people, 2010, vol. 2, section 21, Oral Health, www.healthy-people.gov/Publications, 21–18 to 21–19, 25.11.2008
- <sup>2</sup> F. Müller, M. Naharro, G. E. Carlsson, What are prevalence and incidence of tooth loss in the adult and elderly population in Europe?, Clin. Oral Implants Res., 18 (2007) 3, 2–14, doi:10.1111/j.1600-0501.2007.01459.x
- <sup>3</sup> D. A. Felton, Edentulism and comorbid factors, J. Prosthodont., 18 (2009) 2, 86–88, doi:10.1111/j.1532-849X.2009.00437.x
- <sup>4</sup> J. Zeng, Y. Sato, C. Ohkubo, T. Hosoi, In vitro wear resistance of three types of composite resin denture teeth, J. Prosthet. Dent., 94 (2005) 5, 453–457, doi:10.1016/j.prodent.2005.08.010
- <sup>5</sup> M. Risa, Y. Yoshikazu, M. Masakazu, O. Chikahiro, The influence of vertical dimension of occlusion changes on the electroencephalograms of complete denture wearers, J. Prosthodont. Res., 58 (2014) 2, 121–126, doi:10.1016/j.jpor.2014.01.003
- <sup>6</sup> A. L. Machado, E.T. Giampaolo, C. E. Vergani, A. C. Pavarina, D. Salles, J. H. Jorge, Weight loss and changes in surface roughness of denture base and relined materials after simulated tooth brushing in vitro, Gerodontology, 29 (2012) 2, 121–127, doi:10.1111/j.1741-2358.2010.00422.x
- <sup>7</sup> M. Žigon, G. Ambrožič, Supramolecular polymers, Mater. Tehnol., 37 (2003) 5, 231–236
- <sup>8</sup> B. M. Geilich, T. J. Webster, Reduced adhesion of Staphylococcus aureus to ZnO/PVC nanocomposites, Int. J. Nanomed., 8 (2013), 1177–1184, doi:10.2147/IJN.S42010
- <sup>9</sup> I. Bilecka, M. Niederberger, New developments in the nonaqueous and/or non-hydrolytic sol–gel synthesis of inorganic nanoparticles, Electrochim. Acta, 55 (2010) 26, 7717–7725, doi:10.1016/j.electacta.2009.12.066
- <sup>10</sup> K. Memarzadeh, M. Vargas, J. Huang, J. Fan, R. P. Allaker, Nano metallic-oxides as antimicrobials for implant coatings, Key Eng. Mater., 493–494 (2012) 489–494, doi:10.4028/www.scientific.net/KEM.493-494.489
- <sup>11</sup> M. Bitenc, Z. Crnjak Orel, Synthesis and characterization of crystalline hexagonal bipods of zinc oxide, Mater. Res. Bull., 44 (2009) 2, 381–387, doi:10.1016/j.materresbull.2008.05.005
- <sup>12</sup> Y. Li, J. Z. Zhang, Hydrogen generation from photoelectron chemical water splitting based on nanomaterials, Laser Photonics Rev., 4 (2010) 4, 517–528, doi:10.1002/lpor.200910025
- <sup>13</sup> C. Buzea, I. Pacheco, K. Robbie, Nanomaterials and nanoparticles: Sources and toxicity, Biointerphases, 2 (2007) 4, 17–71, doi:10.1116/1.2815690
- <sup>14</sup> G. R. Patzke, Y. Zhou, R. Kontic, F. Conrad, Oxide nanomaterials: synthetic developments, mechanistic studies, and technological innovations, Angew. Chem. Int. Edit., 50 (2011) 4, 826–859, doi:10.1002/anie.201000235
- <sup>15</sup> J. Sawai, Quantitative evaluation of antibacterial activities of metallic oxide powders (ZnO, MgO and CaO) by conductimetric assay, J. Microbiol. Meth., 54 (2003) 2, 177–182
- <sup>16</sup> M. Cierech, J. Wojnarowicz, D. Szmigiel, B. Bączkowski, A. M. Grudniak, K. I. Wolska, Preparation and characterization of ZnO-PMMA resin nanocomposites for denture bases, Acta Bioeng. Biomech., 18 (2016) 2, 31–41
- <sup>17</sup> P. Patil, G. Gaikwad, D. R. Patil, J. Naik, Synthesis of 1-D ZnO nanorods and polypyrrole/1-D ZnO nanocomposites for photocatalysis and gas sensor applications, Bull. Mater. Sci., 39 (2015) 3, 655–665, doi:10.1007/s12034-016-1208-9
- <sup>18</sup> M. Demir, M. Memesa, P. Castignolles, G. Wegner, PMMA/Zinc Oxide Nanocomposites Prepared by In-Situ Bulk Polymerization, Macromol. Rapid Comm., 27 (2006) 10, 763–770, doi:10.1002/marc.200500870

D. POPOVIĆ et al.: SYNTHESIS OF PMMA/ZnO NANOPARTICLES COMPOSITE USED FOR RESIN TEETH

- <sup>19</sup> M. Roman, Particle Size and Zeta Potential of ZnO, APCBEE Procedia 9 (2014) 13–17, doi:10.1016/j.apcbee.2014.01.003
- <sup>20</sup> A. Mahomed, D. W. L. Hukins, S. N. Kukureka, Effect of accelerated aging on the viscoelastic properties of Elast-Eon™: A polyurethane with soft poly(dimethylsiloxane) and poly(hexamethylene oxide) segments, Mat. Sci. Eng. C, 30 (2010) 8, 1298–1303, doi:10.1016/j.msec.2010.07.014
- <sup>21</sup> P. Spasojevic, B. Adnadjevic, S. Velickovic, J. Jovanovic, Influence of microwave heating on the polymerization kinetics and application properties of the PMMA dental materials, J. Appl. Polym. Sci., 119 (2011) 6, 3598–3606, doi:10.1002/app.33041
- <sup>22</sup> C. Feldmann, Polyol mediated synthesis of oxide particle suspensions and their application, Scripta Mater., 44 (2001) 8–9, 2193–2196, doi:10.1016/S1359-6462(01)00902-2
- <sup>23</sup> R. Y. Hong, J. Z. Qian, J. X. Cao, Synthesis and characterization of PMMA grafted ZnO nanoparticles, Powder Technol., 163 (2006), 160–168, doi:10.1016/j.powtec.2006.01.015
- <sup>24</sup> A. Anžlovar, A. Crnjak, M. Žigon, Poly(methyl methacrylate) composites prepared by in situ polymerization using organophilic nano-to-submicrometer zinc oxide particles, Eur. Polym. J., 46 (2010) 6, 1216–1224, doi:10.1016/j.eurpolymj.2010.03.010
- <sup>25</sup> M. Ghazal, B. Yang, K. Ludwig, M. Kern, Two-body wear of resin and ceramic denture teeth in comparison to human enamel, Dent. Mater., 24 (2008) 4, 502–507, doi:10.1016/j.dental.2007.04.012
- <sup>26</sup> S. D. Heintze, G. Zellweger, S. Sbicego, V. Rousson, C. Muñoz-Viveros, T. Stober, Wear of two denture teeth materials in vivo-2-year results, Dent. Mater., 29 (2013) 9, 191–204, doi:10.1016/j.dental.2013.04.012
- <sup>27</sup> T. Kyoko, S. Hiroshi, Gender differences in masticatory movement path and rhythm in dentate adults, J. Prosthodont. Res., 58 (2014) 4, 237–242, doi:10.1016/j.jpor.2014.06.001
- <sup>28</sup> E. Thang, G. Cheng, X. Ma, Preparation of nano-ZnO/PMMA composite particles via grafting of the copolymer onto the surface of zinc oxide nanoparticle, Powder Technol., 161 (2006) 3, 209–214, doi:10.1016/j.powtec.2005.10.007
- <sup>29</sup> A. Anžlovar, Z. Crnjak Orel, M. Žigon, Sub micrometer and nano-ZnO as filler in PMMA materials, Mater. Tehnol., 45 (2011) 3, 269–274

## ERRATUM

In Materiali in tehnologije/Materials and Technology 50 (2016) 5, 797-804, doi: 10.17222/mit.2015.307 in the article entitled:

***Measurement of bio impedance on an isolated rat sciatic nerve elicited with specific current stimulating pulses – Meritev bioimpedance na izoliranem živcu ischiadicusu podgane vzbujene s posebnimi tokovnimi stimulacijskimi impulzi***

written by Janez Rozman<sup>1,3</sup>, Monika C. Žužek<sup>2</sup>, Robert Frangež<sup>2</sup>, Samo Ribarič<sup>3</sup>

<sup>1</sup>Center for Implantable Technology and Sensors, ITIS d. o. o., Lepi pot 11, 1000 Ljubljana, Slovenia

<sup>2</sup>Institute of Physiology, Pharmacology and Toxicology, Veterinary Faculty, University of Ljubljana, Gerbičeva 60, 1000 Ljubljana, Slovenia

<sup>3</sup>Institute of Pathophysiology, Zaloška 4, Medical Faculty, University of Ljubljana, Republic of Slovenia

two additional authors are missing. The correct authorship of this article is:

Robert Brajkovič<sup>1</sup>, Dejan Križaj<sup>1</sup>, Janez Rozman<sup>2,3</sup>, Monika C. Žužek<sup>4</sup>, Robert Frangež<sup>4</sup>, Samo Ribarič<sup>3</sup>

<sup>1</sup>Faculty of Electrical Engineering, University of Ljubljana, Tržaška 25, 1000 Ljubljana,

<sup>2</sup>Center for Implantable Technology and Sensors, ITIS d. o. o. Ljubljana, Lepi pot 11, 1000 Ljubljana,

<sup>3</sup>Institute of Pathophysiology, Medical Faculty, University of Ljubljana, Vrazov trg 2, 1000 Ljubljana,

<sup>4</sup>Institute of Physiology, Pharmacology and Toxicology, Veterinary Faculty, University of Ljubljana, Gerbičeva 60, 1000 Ljubljana, Republic of Slovenia

MIT Editorial







**MEGATEL**  
poslovna IP telefonija

# instrumentalia

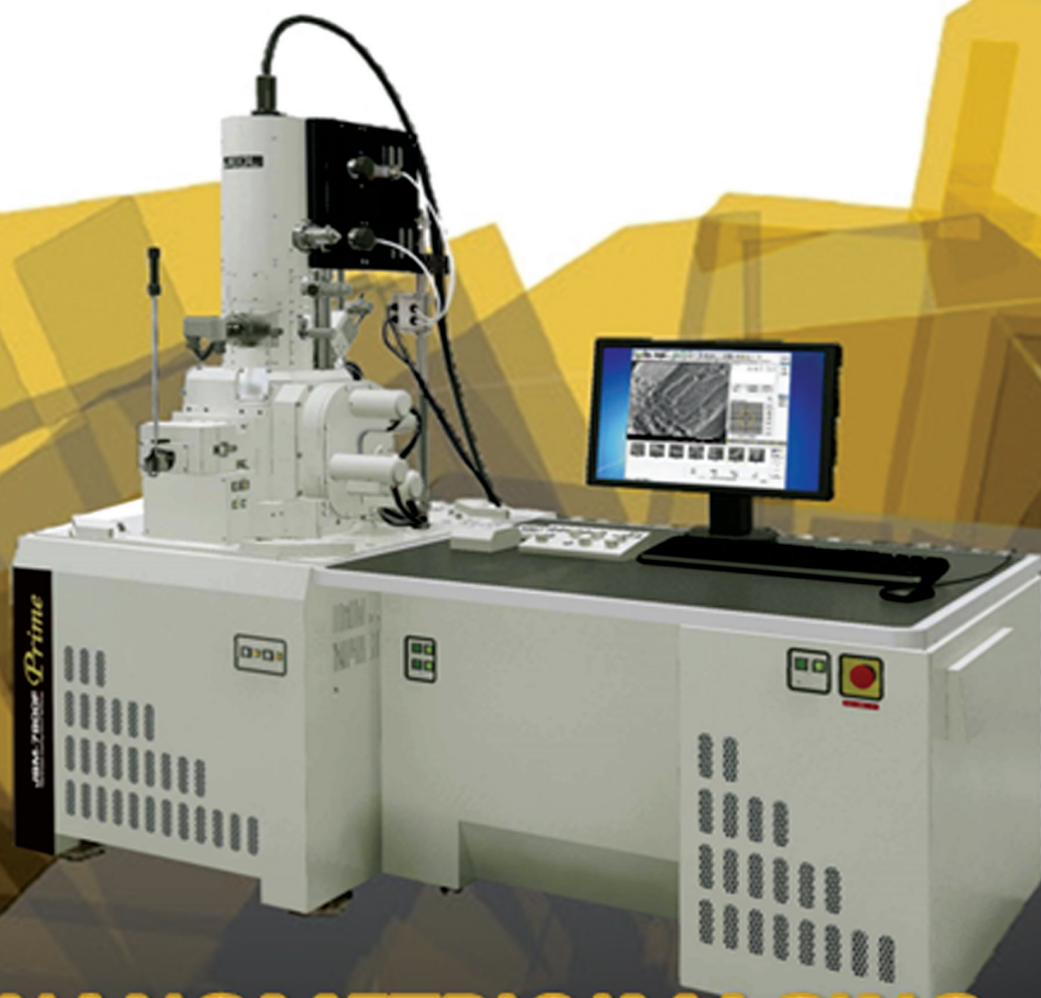
Instrumentalia, d.o.o.  
Leskoškova cesta 9 E  
SI – 1000 Ljubljana  
Tel: + 386 1 524 0196  
Fax: + 386 1 524 0198  
GSM: + 386 51 385 007

---



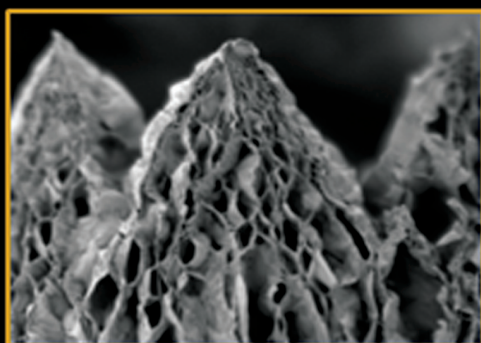
Instruments

# JSM-7800F *Prime*

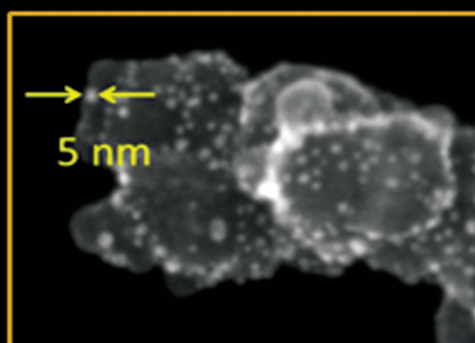


## SUB-NANOMETRIC IMAGING & NANOMETRIC ANALYSIS

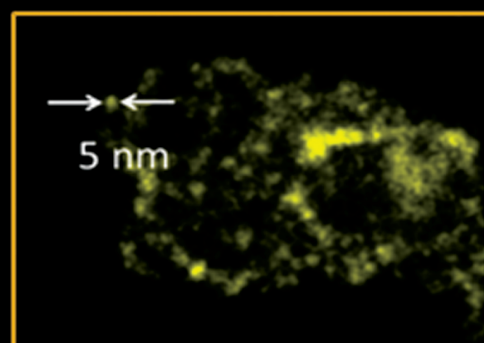
Resolution: 0.7nm from 30kV to 1kV



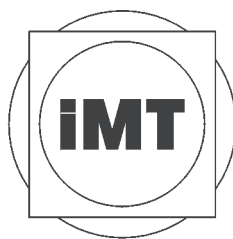
Graphene (80V)



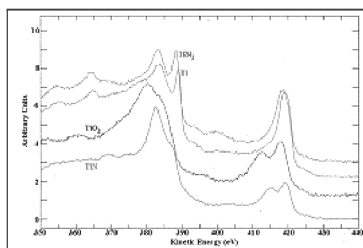
EDS analysis of nanoparticles







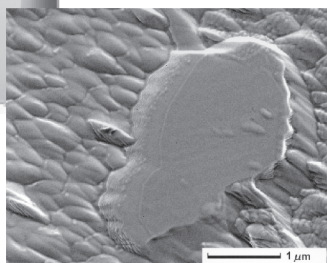
## INŠTITUT ZA KOVINSKE MATERIALE IN TEHNOLOGIJE



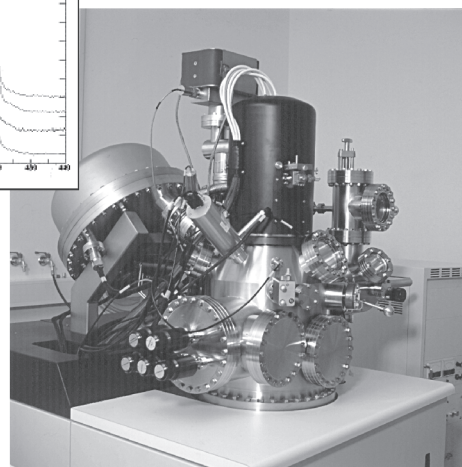
AES spekter štirih različnih kemijskih stanj titana (levo)



Elektronski mikroskop Jeol JSM-6500F opremljen z ED, WD in EBSD



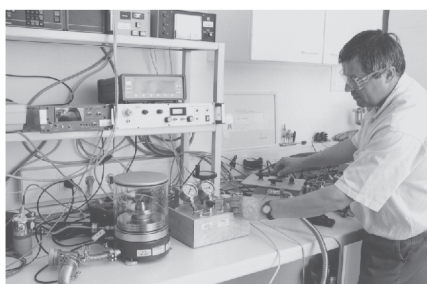
Zrno kromovega karbida (desno)



Elektronski spektrometer Microlab 310-F za HRAES, SAM, SEM in XPS analize površin

### Naslov:

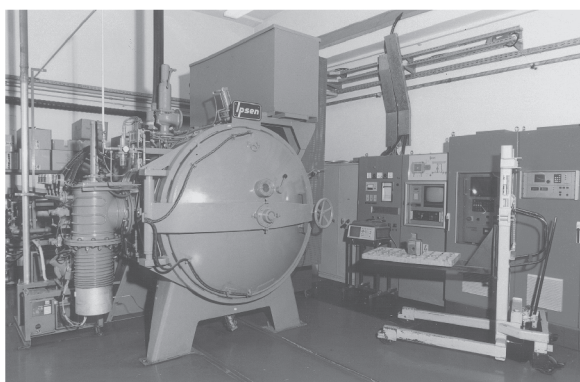
IMT, Lepi pot 11,  
SI-1000 Ljubljana,  
Slovenia  
Tel.: +386 1 4701 800,  
Faks: +386 1 4701 939  
<http://www.imt.si>,  
e-pošta: [imt@imt.si](mailto:imt@imt.si)



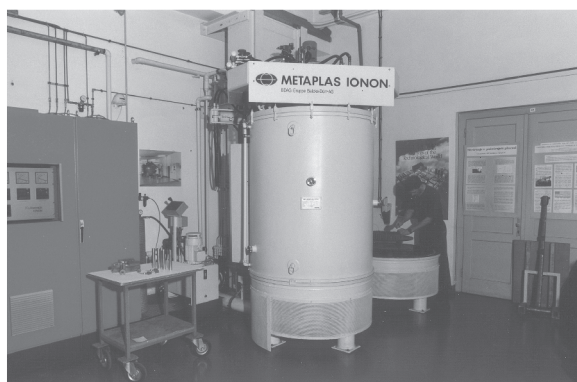
Tlačna tehnika RUSKA 2465A za kalibracije merilnikov tlaka



Akreditacijska listina L-030



Vakuumna peč VTTC-324R za toplotno obdelavo kovinskih materialov



METAPLAS IONON HZIW 600/1000 peč za nitiranje v pulzirajoči plazmi



aluminijaska industrija

1825-2000

IMPOL d.d.

Partizanska 38

2310 Slovenska Bistrica

SLOVENIJA

tel: +386-2-8453 100

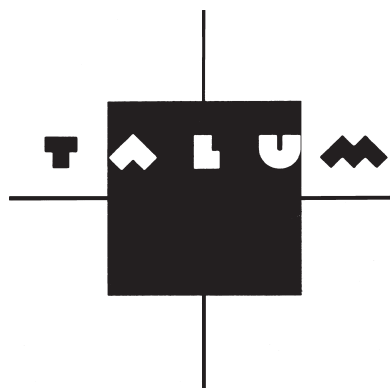
fax: +386-2-8181 219

e-mail: [info@impol.si](mailto:info@impol.si)

<http://www.impol.si>

IZDELKI IZ ALUMINIJA: palice in cevi, profili, pločevine, folije





**TALUM, d.d., KIDRIČEVO**

Tovarniška ulica 10  
2325 Kidričevo, Slovenia  
Telephone: +386 2 799 51 00  
Telefax: +386 2 799 51 03

# INSTRUCTIONS FOR AUTHORS

## 1 SUBMISSION OF MANUSCRIPT

An electronic version (using Microsoft Word or similar) of the manuscript, complete with abstract, keywords, figures and tables must be submitted to the MIT Editorial Office (mit@imt.si) as an e-mail attachment.

All contributions must be written in Slovene or English, following the MIT template.

The manuscript must be accompanied by the MIT checklist, data and cover letter.

Authors must provide the details of two potential reviewers who can make an independent assessment of the quality of the manuscript. The purpose of the reviewing procedure is to have the manuscripts evaluated objectively, and so suggested reviewers with local affiliations and who may be too closely associated with the authors, will be disregarded.

Authors must provide details of two potential referees who are not associated with the specific study, nor with the general research activities of the authors.

After the review process the manuscript will be returned to the author, with the decision of the Editor and, if appropriate, the reviews of the referees. If the paper is accepted the author will be asked to amend the manuscript in accordance with the referees' comments and return it to the MIT Editorial Office.

Authors must state that the results in their manuscript have not been published before, nor are they included in a paper that has been submitted to another journal.

Upon acceptance of an article, the copyright is transferred to the publisher. This transfer will ensure the widest possible dissemination of the article.

### 1.1 Preparation of the manuscript

The paper must be as short as possible and should not exceed 4-6 printed pages (approx. 20.000 characters). Papers presented at conferences must be restricted to 2-4 printed pages (approx. 10.000 characters).

#### *Title page*

Papers must have a concise but informative title, which should not exceed one line. The words from the title must be suitable for indexing and searching.

The title must be followed by the name(s) of the author(s) and by the name and address of the institution(s) where the work was carried out. An e-mail address for the contact author must be supplied.

#### *Abstract*

Papers must include an abstract, which should provide an overview of the content and conclusions of the paper and highlight the new information they contain. The abstract must be understandable in isolation

and written in the past tense, because it refers to work that was already done.

The length of the abstract should not exceed 250 words.

#### *Keywords*

The author must supply 3-4 keywords that describe the content of the article and are suitable for indexing and searching.

### 1.2 Symbols, equations (units of measurement)

Units of measurement must comply with the Law of Units of Measurement and Measures (Official Gazette of the Republic of Slovenia 2001/26), i.e., international SI units.

Equations must be marked on the right-hand side of the text with numbers in round brackets.

**Symbols in text should be written as text, not as equation.**

### 1.3 Tables

Tables must be clearly referred to in the text using Arabic numerals.

Each table must have a title which makes the general meaning understandable without reference to the text.

### 1.4 Figures

Figures are reduced to a single-column width (7.9 cm) except in special cases (max. printed size ~16 cm).

The lettering used on a figure should be chosen so that after reduction the height of numbers and capital letters falls within the range (1.2-2.4) mm.

Lines and arrows should also be of sufficient thickness so as to remain clear after the reduction process.

Figures must be saved in any supported format, e.g. JPG, TIFF.

Figures and figures captions must be inserted in the text.

Illustrations can be printed in colour when they are judged by the Editor to be essential to the presentation. Further information concerning colour illustrations and the costs to the author can be obtained from the publisher. Colour figures can be included, but with an additional page charge of €80.

Maximum number of figures and tables in paper is 10, for papers presented at conferences must be restricted to 8.

### 1.5 References

The references must be collected at the end of the article, and numbered in the order of their appearance in the text.

Each reference must be complete, the use of *ibid.*, *idem.*, *et al.*, etc. is not permitted.



References to unpublished or not readily accessible reports must be avoided.

References must be cited in English.

All references should have a DOI number, if it exists for the given reference.

Authors should avoid self-citing in the references as far as possible.

In the list of references, monographs, articles in journals, journals, contributions to conference proceedings, patent documents, electronic monographs, articles and other electronic documents must be cited in accordance with the following examples:

1. **Monographs**

H. Ibach, H. Luth, *Solid State physics*, 2<sup>nd</sup> ed., Springer, Berlin 1991, 245

2. **Articles in journals**

T. Mauder, J. Stetina, Improvement of the casting of special steel with a wide solid liquid interface, *Mater. Tehnol.*, 50 (2015) 1–2, doi:10.17222/mit.2014.122

3. **Contributions to conference proceedings, symposiums or conferences**

I. Rak, M. Kocak, V. Gliha, N. Gubelj: Fracture behaviour of over-matched high strength steel welds containing soft root layers, *Proc. of the 2<sup>nd</sup> Inter. Symp. on Mis-Matching of Interfaces and Welds*, Reinsford, 1997, 627–641

4. **Contributions in electronic form/online**

- Articles: M. P. Wnuk: Principles of fracture mechanics for space applications, <http://mit.imt.si/Revija/izvodi/kzt996/wnuk.pdf>, 30.01.2000
- Other: <http://www.imt.si/>, 15.03.2016

5. **Standards**

ISO 15787:2001(E) Technical product documentation, Heat treated ferrous part, Presentation and indication ISO Committee, Geneva

## **SPECIAL NOTICE TO AUTHORS**

In the past few years we have received an increasing number of articles that include computer simulations, with 3D colour images as a result. As the journal charges €80 per page for colour printing, some authors have

decided to convert their colour images to grey-scale images. We believe that this lessens both the impact and the clarity of the results. Since the Materials and Technology journal consistently strives for better quality presentation and a higher impact factor, we will be rejecting articles of this type.

## **2 ARTICLE PROOFS**

Authors will receive a set of proofs. They are requested to return the proofs with any corrections within two days. In the case of a delay the Editor will postpone publication of the article until the article proof is received.

## **3 COPYRIGHT**

In addition to the paper, authors must also enclose a written statement that the paper is original work and has not been published in this form anywhere else and that it is not under consideration for publication elsewhere.

On publication, copyright will pass to the publisher. The Journal of Materials and Technology must be stated as the source in all later publications.

The Editorial Board of the Journal of Materials and Technology:

- decide whether to accept a paper for publication;
- obtain professional reviewers for papers and decide on any proposals to shorten or extend them;
- obtain correct terminology and edit language.

The e-files of papers will be kept in the archives of the Materials and Technology journal.

## **4 PUBLICATION FEE**

Authors will be asked to pay a publication fee for each article before its publishing in MIT journal. After the article has been accepted for publishing, this fee needs to be paid. The fee is € 300 for regular articles, and € 150 for articles, presented at ICMT annual conference in Portorož. The additional cost for coloured printing for one page is € 80. These fees do include value-added tax (VAT).

# MATERIALI IN TEHNOLOGIJE / MATERIALS AND TECHNOLOGY

Lepi pot 11, 1000 Ljubljana, Slovenia

Phone: +386 1 4701 860, +386 1 4701 857, Fax: +386 01 4701 939, e-mail: mit@imt.si

Editor-in-chief: dr. Paul John McGuinness

---

## MIT TEMPLATE

### TITLE

(The fewest possible words that adequately describe the contents of the paper in English)

### NASLOV

(v slovenskem jeziku, for Slovenian authors only)

Author's Name Author's Surname<sup>1</sup>, Author's Name Author's Surname<sup>2</sup>, Author's Name  
Author's Surname<sup>3\*</sup>

<sup>1</sup> Author's Affiliation, Address, City, State

<sup>2</sup> Author's Affiliation, Address, City, State

<sup>3</sup> Author's Affiliation, Address, City, State

\*Corresponding author's e-mail

### Abstract (in English)

The abstract must be viewed as a miniversion of the paper and should not exceed 250 words. It must be written in 'past tense', because it refers to work already done. It must state the principal objectives and scope of the investigation, describe the methodology employed, summarize the results and state the principal conclusions.

It must not give information or conclusions that are not included in the paper and it must not cite references to the literature.

### Keywords (in English)

Up to 3-4 words (abbreviations of the expressions are not allowed, only the common used ones: SEM, XRD, XPS, etc.)

# MATERIALI IN TEHNOLOGIJE / MATERIALS AND TECHNOLOGY

Lepi pot 11, 1000 Ljubljana, Slovenia

Phone: +386 1 4701 860, +386 1 4701 857, Fax: +386 01 4701 939, e-mail: mit@imt.si

Editor-in-chief: dr. Paul John McGuiness

---

**Povzetek** (v slovenskem jeziku, for Slovenian authors only)

Do 250 besed

**Ključne besede** (v slovenskem jeziku, for Slovenian authors only)

Od 3 do 4 besede (okrajšave izrazov niso dovoljene, razen splošno sprejetih: SEM, XRD, XPS, itd.)

## 1 INTRODUCTION

The purpose of the introduction is to supply sufficient background information to allow the reader to understand and evaluate the results of the present study. It should state briefly and clearly the purpose in writing paper, present as clearly as possible the nature and scope of the problem investigated, review recent literature to orient the reader, state the method of the investigation, and if necessary, the reasons for the choice of a particular method.

## 2 EXPERIMENTAL PART

The experimental part must give full details of the experimental apparatus and the methods used in obtaining results. It must include accurate details relating to the equipment and materials used, including quantities, temperatures, times etc. It must provide sufficient information for a colleague in the same field to reproduce the experiment. The data must be presented clearly and concisely, using graphs and tables. Figures and Tables must be written bold and not abbreviated throughout text. Figures and Tables must also follow the numerical order of appearance in the text. Once mentioned, they can be repeated. Equations must be written with Equation Editor and must be marked on the right-hand side of the text with numbers in round brackets. Throughout the text they must not be abbreviated. Physical quantities in the text have to be written as a plain text.

Equation 1 (1)

Equation 2 (2)

## 3 RESULTS

Results section should provide an overall picture of the experiments without repeating any of the details in the experimental section. The data should be presented clearly and concisely, using graphs and tables. Figures and Tables should be written bold and not abbreviated throughout text.

# MATERIALI IN TEHNOLOGIJE / MATERIALS AND TECHNOLOGY

Lepi pot 11, 1000 Ljubljana, Slovenia

Phone: +386 1 4701 860, +386 1 4701 857, Fax: +386 01 4701 939, e-mail: [mit@imt.si](mailto:mit@imt.si)

Editor-in-chief: dr. Paul John McGuinness

---

Figures and Tables must also follow the numerical order of appearance in the text. Once mentioned they can be repeated.

## 4 DISCUSSION

The purpose of the discussion is to present the principles, relationships, and generalisations shown by the results. The discussion must make clear the significance of the results and compare the findings with previously published work. It must discuss the results not simply repeat them.

## 5 CONCLUSIONS

The conclusion section should be short. It must present one or more conclusions which have to be drawn from the results and the subsequent discussion. Conclusions must be concise and easily understood by the reader.

## Acknowledgment

## 6 REFERENCES

All references need a DOI number if it exists for the given reference.

In the list of references monographs, articles in journals, journals, contributions to conference proceedings, patent documents, electronic monographs, articles and other electronic documents must be cited in accordance with the following examples:

1. ***Monographs:***

H. Ibach, H. Luth, Solid State physics, 2<sup>nd</sup> ed., Springer, Berlin 1991, 245

2. ***Articles in journals:***

T. Mauder, J. Stetina, Improvement of the casting of special steel with wide solid liquid interface, Mater. Tehnol., 50 (2015) 1, doi:10.17222/mit.2014.122

3. ***Contributions to conference proceedings, symposiums:***

I. Rak, M. Kocak, V. Gliha, N. Gubelj, Fracture behaviour of over-matched high strength steel welds containing soft root layers, Proc. of the 2<sup>nd</sup> Inter. Symp. on Mis-Matching of Interfaces and Welds, Reinsford 1997, 627–641

4. ***Contributions in electronic form/online:***

- Articles: M. P. Wnuk: Principles of fracture mechanics for space applications, <http://mit.imt.si/Revija/izvodi/kzt996/wnuk.pdf>, 30.01.2000
- Other: <http://www.imt.si>, 15.03.2016

5. ***Standards:***

ISO 15787:2001(E) Technical product documentation, Heat treated ferrous part, Presentation and indication ISO Committee, Geneva



# **MATERIALI IN TEHNOLOGIJE / MATERIALS AND TECHNOLOGY**

Lepi pot 11, 1000 Ljubljana, Slovenia

Phone: +386 1 4701 860, +386 1 4701 857, Fax: +386 01 4701 939, e-mail: [mit@imt.si](mailto:mit@imt.si)

Editor-in-chief: dr. Paul John McGuinness

---

## **MIT CHECKLIST**

PLEASE READ CAREFULLY THE STATEMENTS WRITTEN BELOW AND FULFILL IT WITH MARKING THE CHECKBOX.

THIS DOCUMENTATION IS REQUIRED TO PROCESS YOUR SUBMITTED MANUSCRIPT, ENTITLED: \_\_\_\_\_ FOR PUBLICATION IN MATERIALS AND TECHNOLOGY JOURNAL.

- ☐ Have you included a cover letter that makes clear the novelty of the investigation?
- ☐ Have you supplied the names of at least two potential referees?
- ☐ Is the manuscript written in accordance with the Instructions for Authors and with the MIT template?
- ☐ Does the number of figures and tables in your paper not exceed the required number according with Instructions for Authors?
- ☐ Are the figures and captions positioned in the text?
- ☐ Do you accept the terms of the MIT journal policy about the publication fee?

Signature: \_\_\_\_\_

**SPECIAL NOTICE:**

From **1<sup>st</sup> October 2016** the journal Materials and Technology will be introducing a publication fee. All fees listed below, were agreed by the Editorial Board of Materials and Technology during its meeting on 15<sup>th</sup> June 2016:

Publication fee -regular	€300, 00
Publication fee – ICM&T conference paper	€150, 00
Additional charge for colour printing	€ 80, 00 /page
MIT journal subscription (Slovenia)	€42, 00
MIT journal subscription (abroad)	€85, 00

MIT (Materials and Technology journal) Editorial Office

Editor-in-Chief: dr. Paul John McGuiness

Ljubljana, September 2016

**OBVESTILO!**

Od **1.10.2016** dalje objava člankov v reviji Materiali in tehnologije (MIT) ni več brezplačna. Objavo članka Uredništvo revije MIT zaračunava na podlagi sklepa iz seje Uredniškega odbora revije Materiali in tehnologije/Materials and Technology, dne 15. junija 2016, po spodnjem ceniku:

Objava prispevka	300, 00 €
Objava konferenčnega prispevka (ICM&T)	150, 00 €
Doplačilo za barvni tisk	80, 00 €/stran
Naročnina na revijo MIT (Slovenija)	42, 00 €
Naročnina na revijo MIT (tujina)	85, 00 €

Uredništvo revije Materiali in tehnologije (MIT)

Glavni in odgovorni urednik: dr. Paul John McGuiness

Ljubljana, september 2016



ELECTRONIC  
ACCESS

<http://mit.imt.si>

ISSN 1580-2949



9 771580 294004